Efficient Computation of Sommerfeld Integral by Cubic Spline Interpolation to Determine Spatial Domain Dyadic Green's Function in Horizontally Layered TI Medium

Jianmei Zhou and Hongnian Wang
School of Physics, Jinlin University, Changchun 130012, China

Abstract— It is very important to fast compute the spatial domain dyadic Green's function in horizontal layered TI formations for use of integral equation to solve 3D EM field. The Green's function is usually expressed by the Sommerfeld integral with complex kernel functions. Their integrands always contain singular points so their numerical integrations often show rapid oscillations and slow convergent characteristics and their computations are very time-consuming.

Based on the complexity of the kernel function in horizontal layered TI formations in magnetotelluric exploration, we advance a simple and novel approach called as cubic spline interpolation method (CSIM) to quickly solve the Sommerfeld integral. First, we divide the integral range into a series of small segments with gradual increase of the lengths and compute the values of the kernel functions at all nodes. Then we use cubic spline functions to interpolate the kernel function and obtain the semianalytic expression of the function. We can further transform the integral into a series of simple Bessel integral with kernel of polynomial functions at each segment. Furthermore, using Bessel function recursion formula and the asymptotic expansion of Lommel formula to analytically solve all the integrals and sum them, we can efficiently obtain numerical results of spatial domain dyadic Green's function. The numerical results show that the new algorithm largely increases efficiency of computation of the Green's function and faster than other digital filter techniques.

1. INTRODUCTION

Modeling electromagnetic field distribution and propagation in layered media is essential in many application areas, such as geophysical prospecting [1] and EM scattering [2]. Integral equation (IE) theory is widely used to solve the problem because it can reduce unknowns and flexible application [3]. But the IE method need to solving lots of dyadic Green's function in space domain, which is usually expressed by the Sommerfeld integrals with complex kernel functions. Difficulties in the computation arise from the singular nature, highly oscillatory behavior and slow convergent characteristics of the integrals [2].

Several methods have been proposed to address the difficulties. For example, the DCIM [4], extrapolation methods based on a variety of acceleration [5], and method using window function [2, 6]. In magnetotelluric exploration, mainly use the digital filter method [7, 8] due to the large offset and low frequency range. The basic idea of the digital filter method (DFM) is to turn the direct integrals into convolution integrals; these are discretized to a finite convolutional sum. Without numerical integration of the Bessel function, this method has greatly improved the computational speed of the SI. However, this method mainly processes the Bessel function, while ignoring the time of calculation of the kernel function. For media with many layers, the kernel function is so complex, which leading to the time of calculation of it can not be ignored, or even occupy most of the time of calculation of SI.

In this paper, we present a simple and novel approach called as cubic spline interpolation method (CSIM). Considering the complexity of the kernel function in multilayer TI medium, we use cubic spline functions to interpolate the kernel function and obtain the semianlytic expression of the function. Then transform the integral into a series of simple Sommerfeld integral with kernel of polynomial functions at each segment. Furthermore, using Bessel function recursion formula and the asymptotic expansion of Lommel formula to analytically solve all the integrals and sum them, we can efficiently obtain numerical results of spatial domain dyadic Green's function. Finally, the numerical results demonstrate the algorithm can largely increases efficiency of computation of the Green's function and faster than other digital filter techniques.

2. DYADIC GREEN'S FUNCTIONS

In horizontally layered TI medium, the field due to arbitrary current distributions $(\mathbf{J}, \mathbf{M})$ can be expressed as [9]:

$$\begin{aligned} \mathbf{E} &= \int \bar{\mathbf{G}}^{JE}(r, r') \cdot \mathbf{J}(r')dr' + \int \bar{\mathbf{G}}^{ME}(r, r') \cdot \mathbf{M}(r')dr' \\ \mathbf{H} &= \int \bar{\mathbf{G}}^{JH}(r, r') \cdot \mathbf{J}(r')dr' + \int \bar{\mathbf{G}}^{MH}(r, r') \cdot \mathbf{M}(r')dr' \end{aligned} \tag{1}$$

where $\bar{\mathbf{G}}^{PQ}(r, r')$ is the DGF relating P-type fields at r and Q-type currents at r'. And its each component can be expressed as a range of Sommerfeld integral:

$$G(\rho) = \int_0^{+\infty} \tilde{G}(k_\rho; z, z') J_m(k_\rho \rho) k_\rho^n dk_\rho, \quad m = 0, 1, \quad n = 0, 1, 2, 3 \tag{2}$$

where $J_m(k_\rho\rho)$ is the Bessel function of order m and kernel function $\tilde{G}(k_\rho; z, z')$ is the DGF in frequency domain.

3. FAST CALCULATION OF SOMMERFELD INTEGRAL

For numerical integration, we replace the semi-infinite with a finite range large enough:

$$G(\rho) \approx \int_{k_{\rho,MN}}^{k_{\rho,MX}} \tilde{G}(k_\rho; z, z') J_m(k_\rho \rho) k_\rho^n dk_\rho = \sum_{i=1}^{K} \int_{k_{\rho,i}}^{k_\rho,i+1} \tilde{G}(k_\rho; z, z') J_m(k_\rho \rho) k_\rho^n dk_\rho \tag{3}$$

where $[k_{\rho,MN}, k_{\rho,MX}]$ is a given range. $k_{\rho,j} = k_{\rho,1} \exp[(j-1) \cdot \Delta k]$, $j = 2, 3, \ldots, K+1$ is a sequence of selected interpolation points based on the exponential decay behavior of the kernel function and $\Delta k = \frac{\log(k_{\rho,MX}/k_{\rho,MN})}{K}$. Then the integral is evaluated as a sum of a series of partial integrals over finite subintervals. If the coordinates of the field and source points are determinate, the values of the kernel function $\tilde{G}(k_\rho)$ at each interpolation point $k_{\rho,j}$ become known. And the kernel function in each subinterval $(k_{\rho,j}, k_{\rho,j+1})$ can be replaced by the asymptotic form with the using of cubic spline interpolation:

$$\begin{aligned} \tilde{G}_j \;=\; & \frac{M_j}{6h_j}(k_{\rho,j+1} - k_\rho)^3 + \frac{M_{j+1}}{6h_j}(k_\rho - k_{\rho,j})^3 + \left(\frac{\tilde{G}(k_{\rho,j+1})}{h_j} - \frac{M_{j+1}h_j}{6}\right)(k_\rho - k_{\rho,j}) \\ & + \left(\frac{\tilde{G}(k_{\rho,j})}{h_j} - \frac{M_j h_j}{6}\right)(k_{\rho,j+1} - k_\rho) \end{aligned} \tag{4}$$

where $k_{\rho,j} \le k_\rho \le k_{\rho,j+1}$, $j = 1, 2, \ldots, K$, $h_j = k_{\rho,j+1} - k_{\rho,j}$ and $M_j = \tilde{G}''(k_{\rho,j})$ is the second derivative of $\tilde{G}_j$ at point $k_{\rho,j}$. Using the boundary conditions $2M_1 + \lambda_1 M_2 = d_1$, $\mu_{K+1}M_K + 2M_{K+1} = d_{K+1}$ and choice $\lambda_1 = \mu_{K+1} = 1$, $d_1 = d_2$, $d_{K+1} = d_K$, we can obtain the cubic polynomial expression of $\tilde{G}(k_\rho)$. With the Bessel function recursion formula $xJ_0(x) = \frac{d}{dx}[xJ_1(x)]$, $J_0'(x) = -J_1(x)$, the SI can be simplification as:

$$G(\rho) = \sum_{i=1}^{K} \left(A_i + B_i \int_{x_i}^{x_{i+1}} J_0(t)dt\right) \tag{5}$$

where A_i and B_i are the parameters easy to solve in each subinterval.

3.1. Calculation of $\int_0^x J_0(t)dt$

If we have the value of $\int_0^x J_0(t)dt$, we can get the value of (5). Here we combine the asymptotic expansion of Lommel formula with the analytic express of Bessel function to solve the problem.

(I) $x > 15$, use the asymptotic expansion of Lommel formula [10]:

$$\int_0^x J_0(t)dt = 1 - xS_{-1,-1}(x)J_0(x) + xS_{0,0}(x)J_1(x) \tag{6}$$

where $xS_{0,0}(x) =_3 F_0(1, \frac{1}{2}, \frac{1}{2}; \frac{-4}{x^2})$, $x^2S_{-1,-1}(x) = {}_3F_0(1, \frac{3}{2}, \frac{1}{2}; \frac{-4}{x^2})$ and the generalized hypergeometric series is defined as ${}_pF_0(a_1, a_2, \ldots, a_p; z) = \sum_{k=0}^{+\infty} \frac{(a_1)_k(a_2)_k \ldots (a_p)_k \cdot z^k}{k!}$, where $(a)_0 = 1$, $(a)_k = a(a+1)(a+2)\ldots(a+k-1)$.

(II) $x < 15$, use the analytic express of Bessel function:

$$\int_0^x J_0(t)dt \cong \sum_{k=0}^{30} (-1)^k \frac{x}{(2k+1)\cdot(k!)^2} \left(\frac{x}{2}\right)^{2k} \tag{7}$$

where the relative truncation error is less than 5×10^{-15}.

3.2. Error Analysis of CSI Function

The error function for cubic spline interpolation is:

$$\|f - s\|_\infty \leq \frac{5}{384} h^4 \left\| f^{(4)} \right\|_\infty \tag{8}$$

where h is maximum of the subintervals of width and s is the cubic spline interpolating f. In order to clearly analyze, we consider as a model problem a horizontal electrical dipole over an isotropic homogeneous half-space medium. Accordingly, the kernel function is simplify as

$$f = 0.5e^{ik_z^e(z-z')} \tag{9}$$

where $k_z^e = \sqrt{\omega^2\mu_0\varepsilon_0 - k_\rho^2}$. The calculated results demonstrate that error tends to 0 as $k_{\rho,MX} > 10^6$.

4. NUMERICAL RESULTS

To validate of our method we consider as a model problem a horizontal electrical dipole over a TI half space, horizontal resistivity $R_H = 100\,\Omega \cdot \mathrm{m}$ and vertical resistivity $R_V = 400\,\Omega \cdot \mathrm{m}$. The transmitter and receiver coordinate is (0, 0, 0) and (500 m, 500 m, 0) respectively. Fig. 1 shows a comparison of the electric field component computed with the CSIM and analytic solution [11]. We observe good agreement of the CSIM with the analytic solution.

Further to study a 5 layer TI model with parameters given in Table 1, and the receiving dipoles are parallel to the horizontal electrical dipole transmitter but offset by 2 km. We compute the EM response by CSIM and digital filter method (DFM), respectively. Fig. 2 shows that, CSIM get the same result with DFM. Running on the same computer, the time CSIM using is 1.1 s, while DFM is 6.4 s.

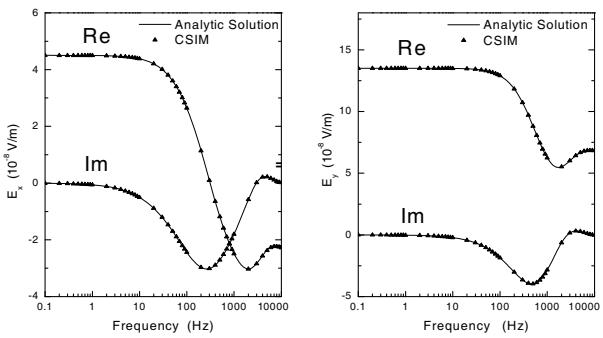

Figure 1: Comparison of E_x and E_y obtained by CSIM and analytic solution in TI half-space model.

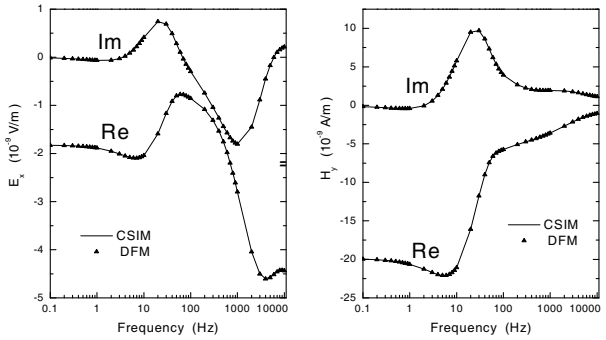

Figure 2: Comparison of E_x and H_y obtained by CSIM and DFM in 5-layer model.

Table 1: Parameters of the 5 layer horizontally layered TI model.

Layer	Depth (m)	R_H ($\Omega \cdot$ m)	R_V($\Omega \cdot$ m)
1	100	100	400
2	90	10	90
3	300	50	450
4	20	400	1000
5		100	100

5. CONCLUSION

We have developed an effective algorithm for Computation the Sommerfeld Integral to determine spatial domain dyadic green's function in a horizontally layered TI medium. Using cubic spline interpolation technique, the kernel function can be simplified as polynomial functions. Furthermore, using Bessel function recursion formula and the asymptotic expansion of Lommel formula to analytically solve the SI, we can efficiently obtain numerical results of spatial domain dyadic Green's function. The numerical results validate the method and show that the new algorithm largely increases efficiency of computation of the Green's function and faster than other digital filter techniques.

REFERENCES

1. Wang, H. N., S. Poman, et al., "Numerical modeling of multicomponent induction well-logging tools in the cylindrically stratified anisotropic media," *IEEE Trans. Geosci. Remote Sens.*, Vol. 46, No. 4, 1134–1147, 2008.
2. Cai, W. and T. J. Yu, "Fast calculation of dyadic Green's function for electromagnetic scattering in the multi-layered medium," *J. Comput. Phys.*, Vol. 165, 1–21, 2000.
3. Chen, G. B., H. N. Wang, et al., "Modeling of electromagnetic responses of 3-D electrical anomalous body in a layered anisotropic earth using integral equations," *Chinese J. Geophys.*, Vol. 52, No. 8, 2174–2181, 2009 (in Chinese).
4. Yuan, M. T., T. K. Sarkar, and M. Salazar-Palma, "A direct discrete complex image method from the closed-form Green's functions in multilayered media," *IEEE Trans. Microwave Theory Tech.*, Vol. 54, No. 3, 1025–1032, 2006.
5. Michalski, K. A., "Extrapolation methods for sommerfeld integral tails," *IEEE Trans. Antennas Propagat.*, Vol. 46, No. 10, 1405–1418, 1998.
6. Chen, G. B., H. N. Wang, et al., "An efficient algorithm of the electromagnetic dyadic Green's function in a horizontal-layered anisotropic medium," *Acta. Phys. Sin.*, Vol. 58, No. 3, 1608–1618, 2009.
7. Anderson, W. L., "Computer program numerical integration of related Hankel transforms of orders 0 and 1 by adaptive digital filtering," *Geophysics*, Vol. 44, No. 4, 1287–1305, 1979.
8. Anderson, W. L., "Fast hankel transforms using related and lagged convolutions," *ACM Trans. Math. Softw.*, Vol. 8, No. 4, 344–368, 1982.
9. Michalski, K. A. and J. R. Mosig, "Multilayered media Green's functions in integral equation formulations," *IEEE Trans. Antennas Propagat.*, Vol. 45, No. 3, 508–519, 1997.
10. Luke, Y. L., *Integrals of Bessel Functions*, McGraw-Hill Book Company, INC., New York, 1962.
11. Wait, J. R., *Geo-electromagnetism*, Academic Press, New York, 1982.

Relationships between the RCSR Properties of a Coated Slab and Absorbing Characteristic of the Coated RAM

Hai-Yan Chen, **Long-Jiang Deng**, **Pei-Heng Zhou**, **Liang Chen**, **Jian-Liang Xie**, **and Zhi-Wei Zhu**
State Key Laboratory of Electronic Thin Film Integrated Device
University of Electronic Science and Technology of China, Chengdu 610054, China

Abstract— Relationships between the radar cross section reduction (RCSR) properties of a coated slab and the characteristic of the coated radar absorbing materials (RAM) are studied. The slab with radar cross section (RCS) patterns coated with RAM are calculated for either horizontal polarization (HH) or vertical polarization (VV) incident plane wave using a uniform geometrical theory of diffraction for loss surfaces. Comparing the reflection or absorption characteristic of the RAM to the properties of the bi-static RCS of the coated slab, approximate analysis results show that the two are dependent. Surface waves are considered wherever there is reactive surface impedance. The mono-static RCS of the coated slab can be mainly benefited from edge effectiveness for surface wave. The attenuation constants of surface wave in the coated RAM are analyzed. Examining the RCS patterns, we can observe that the effect of RCSR for the coated slab can achieve an optimum at 75° of incidence angle, which can be also interpreted from the characteristic of the coated RAM. The most difficult part in the RCSR design occurs at low frequency, which can be improved by optimizing the characteristic of the coated RAM.

1. INTRODUCTION

E lectromagnetic scattering from finite coated surface arises in many physical contexts. Therefore, it is desirable to understand the interrelationships between the RCSR properties and the characteristic of its coated RAM. In the past researching for RCSR of a target using RAM, some important electromagnetic scattering problems including the quantitative interrelationships between the coating materials sorts, coating layers, coating thickness and the shaping design such as curvature adjustment, have been extensively investigated [1–3]. Yet the intrinsic electromagnetic characteristic of the coated RAM are rarely concerned. Due to its growing application, RAM is widely researched [4–6]. In designing RAM, it becomes important to obtain an optimized intrinsic electromagnetic characteristic such as reflection or absorption coefficient. However, the contributions of RAM to the RCSR of the coated target and the electromagnetic scattering mechanism of the target are seldom considered in RAM design. Thus, it is necessary to study the relationships between the RCSR properties of a coated target and the characteristic of its coated RAM.

The relative permittivity and relative permeability of the considered RAM are obtained from measured data. Based on these intrinsic parameters, the reflection or absorption coefficient can be computed for various electromagnetic wave incidence conditions according to electromagnetic field theory. Moreover, the attenuation characteristic of surface waves in radar absorbing layer is also considered. Based on the discussion for surface waves, the interrelationships between the intrinsic parameters of RAM and the attenuation characteristic of the surface waves can be founded [7, 8].

By coating a given target with a thin layer of suitable electromagnetic properties, the RCS can be reduced and it is of interest to investigate the resulting RCSR. In this paper, the RCS patterns of a target with RAM coating for horizontal polarization and vertical polarization plane wave are calculated using a uniform geometrical theory of diffraction for loss surfaces [9, 10]. By changing the polarization and frequency bands of incidence plane wave, and keeping the coating thickness, the relationship between the electromagnetic scattering properties and these parameters can be obtained. In efficient frequency bands of the absorbing material, the effects of RCSR are considerable large. Comparing these results to those obtained from the numerical calculation for the electromagnetic characteristic of the coated RAM, the relationships between the RCSR properties of the coated slab and the absorbing characteristic of its coated RAM can be founded.

2. DESIGN

In this paper, the electromagnetic scattering properties presented by coated slab will be discussed. In all of the following discussion, unless otherwise indicated, the slab will be considered to lie in the xy-plane with a plane wave incident at an angle θ with respect to the z-axis, as shown in Fig. 1

of Ref. [11], and all of the corresponding parameters are built similarly. All results presented in this paper are obtained from some actual absorbing material, and its relative permittivity ε and relative permeability μ are gained from measured results, see RAM A in Ref. [11]. The frequencies of 1, 8, and 18 GHz, representing L, X, and Ku wave bands respectively, will be discussed.

The calculations are made in the principal plane and the radar cross section values are presented in decibels relative to one square wavelength (dB). The incidence angle θ are defined in Fig. 1 of Ref. [11], and the incidence angle 0° is perpendicular to the direction of the target surface.

3. RESULTS AND ANALYSIS

3.1. Bi-static RCS and the Reflection Properties

To analyze the relationships between the effect of RCSR of the target and the characteristic of the coated RAM, we propose the bi-static RCS pattern of the target and the reflection (or absorbing) properties of the coated RAM. The bi-static RCS patterns of the proposed target for HH-polarization with RAM and without RAM for incidence angle at 0°, 30°, and 75° respectively are shown in Fig. 1. Aspect angle 0° is defined as mirror angle of the corresponding bi-static angle, and the aspect angle increases in the incidence direction along the z axis. All the results showed a peak at the direction of the mirror of the bi-static angle. With the increasing bi-static angle, the peak values will decrease slightly. The RCS patterns were relatively flat at 75° of the bi-static angle, but showed shock strengthening at 0° of the bi-static angle. At the frequency of 1 GHz in aspect angle range of 0° to +90°, it is observed that the effects of the RCSR were not obvious in the case of several different bi-static angles. At 8, and 18 GHz, the most significant effects of the RCSR can be obtained at 75° of the bi-static angle. Similar conclusions can be drawn from the reflection characteristic of the coated RAM, just as shown in Fig. 3. At 0.5 mm of the thickness of the coated RAM, the peak of absorbing can be obtained at about 12 GHz at 75° of the bi-static angle for HH-polarization.

From Figs. 1–2, at the aspect angle 0°, we can observe that the RCS values of the coated target are equal to the product of the RCS values of uncoated target and the square of the reflection coefficient of the coated RAM. Therefore, the reflection characteristic of RAM can be considered as a guideline for the evaluation of its RCSR. By reciprocity theory, similar conclusion can be obtained for VV-polarized.

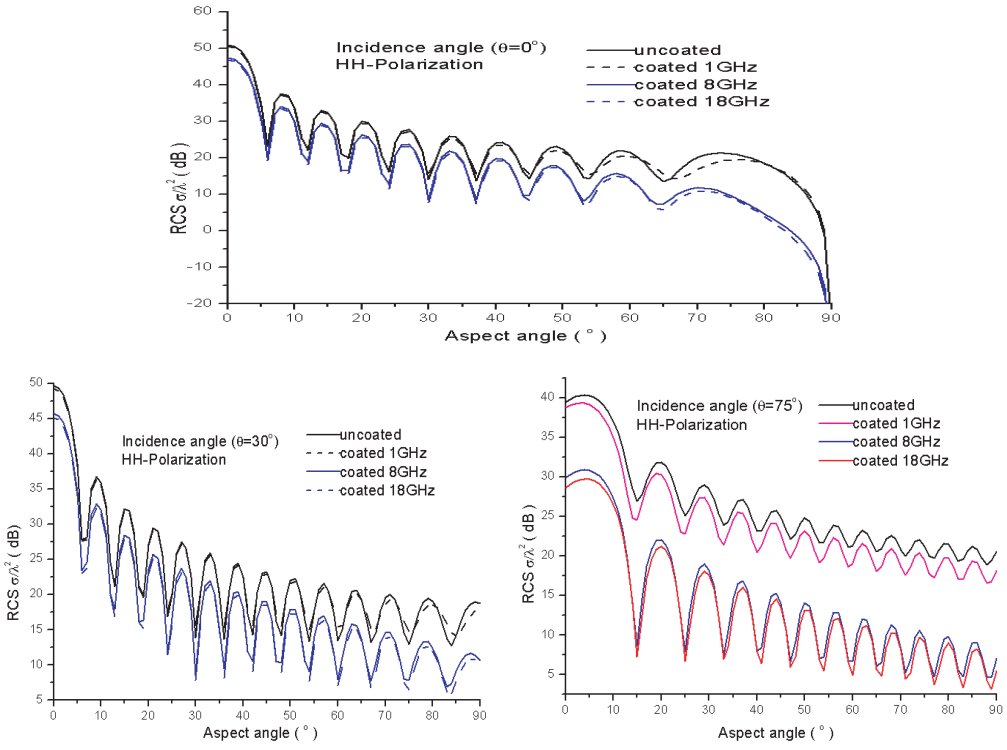

Figure 1: Return loss of a circular corrugated horn.

3.2. Mono-static RCS and Surface Wave Characteristic

As for electromagnetic scattering problem of a target, the mono-static RCS is mainly concerned. In most cases, the mono-static RCS of a target is due to the electrical or magnetic discontinuity existed at the structure of the target. Surface wave must be considered when the electrical or magnetic discontinuity happens [11, 12]. The mono-static RCS pattern is computed for the uncoated slab and RAM coated slab under the horizontal polarization of incidence plane wave.

Based on the definition of surface wave and the theory of electromagnetic field, attenuation characteristic of the considered RAM is obtained for the 0.5 mm of the coated thickness using numerical calculation, just as shown in Fig. 3. Only transverse magnetic (TM) waves are considered corresponding to the analysis of the considered target's RCS pattern. The characteristics of surface waves are dependent on the values of the attenuation and phase constants, and their transmission mechanisms are rally complicated. In this paper, the attenuation constants at x and z direction has been considered. From Fig. 3, we can observed that there is an exponential increase in the wave amplitude with increasing distance from the surface under the frequency of 10 GHz, and the wave decays exponentially with the increasing x at other frequencies. Due to the existing improper wave and the lower values of attenuation at x direction, the absorbing characteristics of the RAM will be poor. With increasing frequency, the absorbing characteristic of the RAM can be improved because of the increasing attenuation. As for the frequencies beyond 10 GHz, the surface waves will transport backward leaky wave with increasing attenuation, and its absorbing properties can be enhanced.

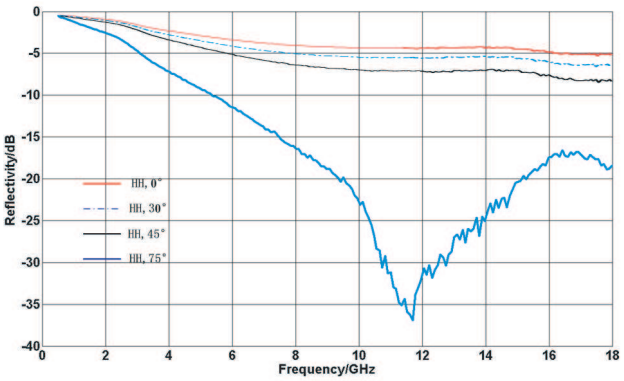

Figure 2: Reflection properties of the coated RAM for HH-polarization with incidence angle $\theta = 0°$, 30°, 45°, 75°.

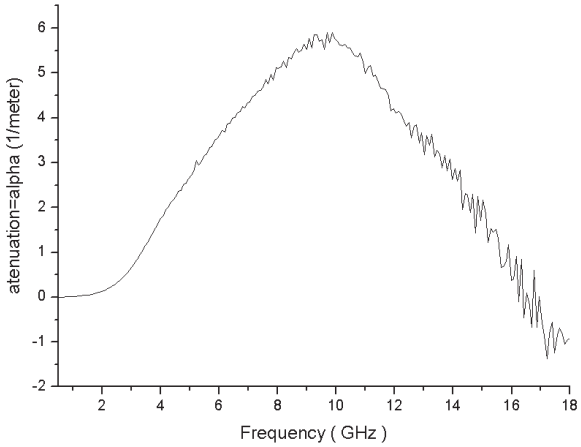

Figure 3: Attenuation characteristic of the considered RAM with 0.5 mm of its thickness.

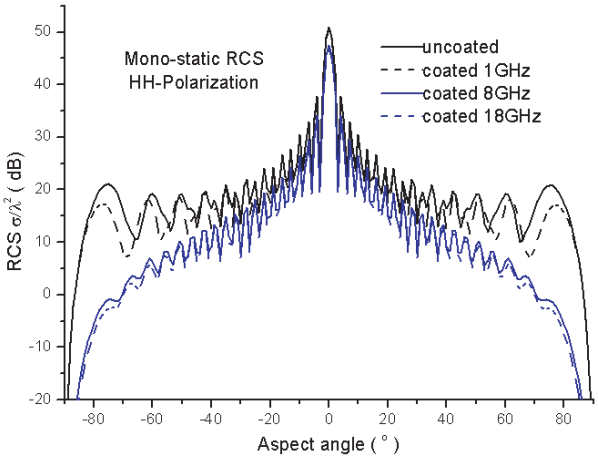

Figure 4: HH-polarization mono-RCS diagram of the proposed target with RAM coated and without RAM coated for 1, 8, 18 GHz respectively.

In Fig. 4, the considered target is examined in the full pitching plane for both coated and uncoated conducting plates for the horizontal polarization. All RCS diagrams of the targets show a peak at 0° due to the normal incidence of the electromagnetic wave. This position of the targets is not a critical point for actual application. The maximum attenuation values of 5, 24 and 25 dB are observed at 1, 8 and 18 GHz in the vicinity of the pitching angle ±75°, respectively. At the frequency of 1 GHz, the RCSR effects are apparently poor compared with those of the other two frequencies.

4. CONCLUSION

We have studied the relationships between the RCSR properties of a coated target and the characteristic of its coated RAM. At mirror angle of the corresponding bi-static angle, the RCS values of the coated target are equal to the product of the RCS values of uncoated target and the square of the reflection coefficient of the coated RAM. The reflection characteristic of the RAM has certain relation to RCSR. The mono-static RCS pattern of the considered target were presented for HH and VV polarization, and have found that the effects of the RCSR in horizontal polarization is superior to those in vertical polarization for coating given actual RAM. In HH polarization, the maximum attenuation values of 5, 24 and 25 dB are observed at 1, 8 and 18 GHz in the vicinity of the pitching angle ±75° for the considered RAM, respectively. The unsatisfied effects of the RCSR occurs at low frequency for both polarization, especially an anti-reduction effect can appear when the incidence angle $|\theta| > 78°$. The properties of the material have certain correspondence to its contributions to RCSR.

REFERENCES

1. Mosallaei, H. and Y. Rahmat-Samii, "RCS reduction of canonical targets using genetic algorithm synthesized RAM," *IEEE Trans. on Antenna and Propagation*, Vol. 48, No. 10, 1594–1606, Oct. 2000.
2. Smith, F. C., "Edge coatings that reduce monostatic RCS," *IEE Proc. — Radar Sonar Navig.*, Vol. 149, No. 6, 310–314, Dec. 2002.
3. Geng, Y.-L., C.-W. Qiu, and N. Yuan, "Exact solution to electromagnetic scattering by an impedance sphere coated with a uniaxial anisotropic layer," *IEEE Trans. on Antennas and Propagation*, Vol. 57, No. 2, 572–576, Feb. 2009.
4. Wright, P. V., B. Chambers, A. Barnest, et al., "Progress in smart microwave materials and structures," *Smart Mater. Struct.*, Vol. 9, 273–279, 2000.
5. Chen, H. Y., H. B. Zhang, and L. J. Deng, "Design of an ultra-thin magnetic-type radar absorber embedded with FSS," *IEEE Antennas and Wireless Propagation Letters*, Vol. 9, 899–901, 2010.
6. Mitrano, C., A. Balzano, M. Bertacca, et al., "CFRP-based broad-band radar absorbing materials," *Radar Conference, RADAR '08, IEEE*, 1–6, May 26–30, 2008.
7. Ufimtsev, P. Y., R. T. Ling, and J. D. Scholler, "Transformation of surface waves in homogeneous absorbing layers," *IEEE Trans. on Antennas and Propagation*, Vol. 48, No. 2, 214–222, Feb. 2000.
8. Ufimtsev, P. Y. and R. T. Ling, "New results for the properties of TE surface waves in absorbing layers," *IEEE Trans. on Antennas and Propagation*, Vol. 49, No. 10, 1445–1452, Oct. 2001.
9. Sheng, X.-Q., J.-M. Jin, J. Song, et al., "On the formulation of hybrid finite-element and boundary-integral methods for 3-D scattering," *IEEE Trans. on Antennas and Propagation*, Vol. 44, No. 3, 303–310, Mar. 1998.
10. Marceaux, O. and B. Stupfel, "High-order impedance boundary conditions for multilayer coated 3-D objects," *IEEE Trans. on Antennas and Propagation*, Vol. 48, No. 3, 429–436, Mar. 2000.
11. Chen, H.-Y., P.-H. Zhou, L. Chen, and L.-J. Deng, "Study on the properties of surface waves in coated RAM layers and monostatic RCSR performances of the coated slab," *Progress In Electromagnetics Research M*, Vol. 11, 123–135, 2010.
12. Chen, H.-Y., L.-J. Deng, and P.-H. Zhou, "Suppression of surface wave from finite conducting surfaces with impedance loading at margins," *Journal of Electromagnetic Waves and Applications*, Vol. 24, Nos. 14–15, 1977–1989, 2010.

Experimental Study of Microwave Permeability of FeCoBSi Thin Films Prepared on Thin Flexible Substrates

Haipeng Lu, **Jing Yang**, **and Longjiang Deng**
State Key Laboratory of Electronic Thin Films and Integrated Devices
University of Electronic Science and Technology of China, Chengdu 610054, China

Abstract— The microwave permeability of FeCoBSi thin films prepared on thin flexible substrates is studied. The film as deposited showed as an amorphous and isotropic structure in film plane. The permeability is measured in the frequency range of 0.5–18 GHz using coaxial techniques. The paper deals with two different technological methods in preparing the spiral measuring sample. Alteration of the technological process allows the microwave properties of the thin films to be varied. The microwave permeability of thin film wound with FeCoBSi layer inward is significantly larger than that of the thin film wound with FeCoBSi layer outward. The reason is attributed to varied types of stresses are caused at the process of spiral sample preparing. The stress affect the measured values of permeability by changing the orientation of in-plane magnetic moments. Therefore, the effect of stress could be avoided or be rationally used in our study.

1. INTRODUCTION

Materials with high microwave permeability are of practical importance for a number of applications. As ferromagnetic films with in-plane anisotropy are able to overcome the Snoek's limits, they might obtain larger values of microwave permeability than bulk magnets [1]. So a lot of research has been carried out to develop ferromagnetic thin films for the use in high frequency devices such as high-frequency micro inductors or micro transformers. However, more and more new applications such as flexible EMI suppressors require flectional samples which under a suitable form [2]. This is the motivation for the experimental study of thin films deposited on thin flexible substrates.

Iron-based films are known with high saturation magnetization. Alloying iron with cobalt, boron and silicon may result in the materials with high saturation magnetization and appropriate anisotropy or resistivity. Such films may have high permeability at frequencies of several GHz [3, 4].

The paper deals with FeCoBSi films based on flexible mylar substrates, aiming at the structure and microwave properties of the films. The influence of the different winding methods of the samples on microwave permeability is specialized studied. The objective is deriving correlations between the preparation process and dynamic parameters by analyzing the experimental data on thin ferromagnetic films.

2. EXPERIMENTAL

$Fe_{66}Co_{17}B_{16}Si_1$ thin films are produced on flexible 11.5 μm thick mylar substrates by DC magnetron sputtering in Ar atmosphere at pressure 0.6 Pa. The structure of the films is studied with X-ray diffraction (XRD). The hysteresis loops are obtained by vibrating sample magnetometer (VSM) measurements. The permeability has been measured from 500 MHz up to 18 GHz using a coaxial technique described elsewhere [5, 6]. This technique is suitable for films deposited on a flexible substrate and implies winding a film into a hollow spiral sample that adapts to the geometry of the coaxial line cavity. Since an alternating electric field is normal to the film plane and magnetic field is in-plane, the technique simulates the magnetic performance of laminates. As the relationships between the intrinsic properties of inclusion and the effective properties of the composite are well known, measuring the composite properties leads to the intrinsic electromagnetic properties of the ferromagnetic inclusions.

3. RESULTS AND DISCUSSION

The X-ray diffraction spectrum for FeCoBSi thin film deposited on a flexible mylar substrate is shown in Figure 1. There is only one peak at the position about 25.5° in the figure, which is the characteristic peak of mylar substrate. The XRD spectrum does not exhibit any clear (110) peak of α-Fe or α-FeCo phase. It means the FeCoBSi films prepared on thin flexible mylar substrates have an amorphous structure. Actually, it is difficult to obtain crystallized metal films on such flexible thin substrate by our sputtering process. The temperature of the centre area for magnetron

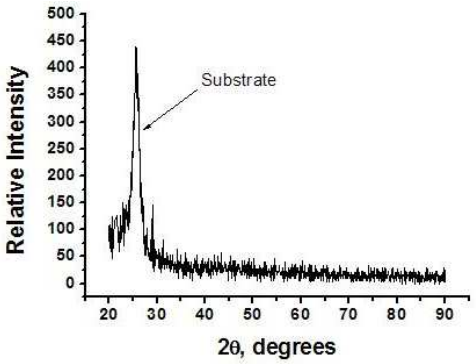

Figure 1: XRD spectra of FeCoBSi thin film deposited on a flexible mylar substrate.

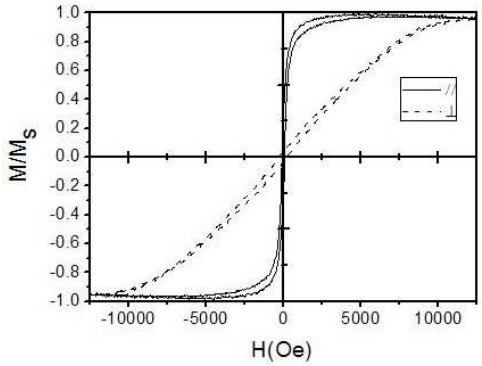

Figure 2: Hysteresis loop of a FeCoBSi thin film deposited on mylar substrate.

sputtering is much higher than the temperature the flexible mylar substrates could endure. In order to avoid the bending deformation of films, the film's substrate was firmly stuck to a component of cooling system during the course of deposition. It also cannot be imposed any heat treatment after sputtering. So the films usually present amorphous structure.

Figure 2 shows the magnetic hysteresis loop of FeCoSi thin film. Solid line and the dashed line represent respectively the hysteresis loop which parallels to the film surface and perpendicular to the film surface. As we did not induce anisotropy by applying field sputtering, the film is isotropic in-plane. The in-plane coercivity is found to be about 11 Oe.

Permeability of ferromagnetic thin films can be described in the frames of the Landau–Lifschitz FMR model:

$$\mu(f) = 1 + \frac{\mu_s}{1 - i(f/f_r) - (f/f_0)^2}, \tag{1}$$

where μ_s is the static permeability, f_r and f_0 are the relaxation and resonance frequencies. The microwave performance of an arbitrary magnetic film can be estimated from the experiment by the use of Acher's coefficient [7]:

$$k_A = \int_{f_1}^{f_2} \mu''(f) f df \Big/ \left(\frac{\pi}{2}(\gamma 4\pi M_s)^2\right), \tag{2}$$

The integration in Eq. (2) is over the ferromagnetic resonance (FMR) line, and μ'' is the imaginary part of the permeability component related to microwave magnetic field applied in the film plane along the hard axis. Value of k_A helps to understand film quality. The closer is k_A to unity, the better is the film from the viewpoint of microwave application. A perfect film with uniform magnetization and in-plane anisotropy has $k_A = 1$, and the best value for the isotropic in-plane sample, $k_A = 0.5$. But if the microwave magnetic field applied in the film plane is perpendicular to the hard axis, the microwave properties of thin films are typically worse. The reason is attributed to the component of magnetic moments which is perpendicular to the microwave magnetic field is considerable little.

There are two winding methods for preparing the measuring samples which are suitable for the geometry of the coaxial line cavity. One method is to wind the thin film with FeCoBSi layer inward and the other method is to wind the film with FeCoBSi layer outward (Figures 3(a), (b)). Although there is no significant difference from the appearance point of view to the spiral samples, the different winding methods may typically lead to different measure results on microwave permeability.

Alteration of the technological process allows the microwave properties of the thin films to be varied. Two examples of the measured microwave permeability as a function of frequency are given in Figure 4, where the spiral samples with the same thickness of FeCoBSi film are made by the above two methods, respectively. The lines with solid symbols are the real part and the lines with hollow symbols are the imaginary part of permeability. The microwave permeability of thin film wound with FeCoBSi layer inward is significantly larger than that of the thin film wound with FeCoBSi layer outward (Figure 4).

The difference is attributed to different arranging states of magnetic moments caused by internal stress of the thin films. When we wind the films to be measuring samples, different types of stresses

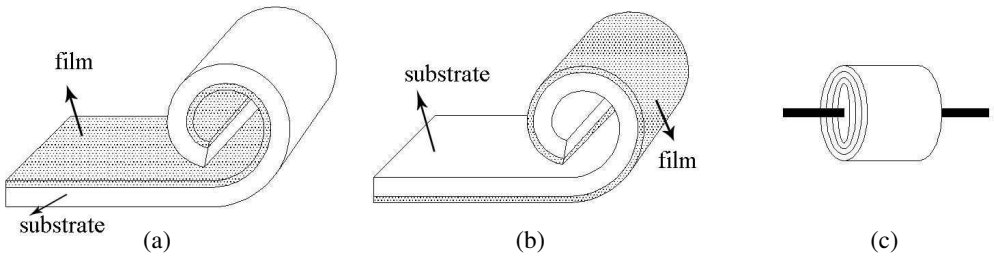

Figure 3: Two winding methods for preparing the spiral samples for measuring. (a) FeCoBSi layer inward, (b) FeCoBSi layer outward, (c) spiral sample for measuring.

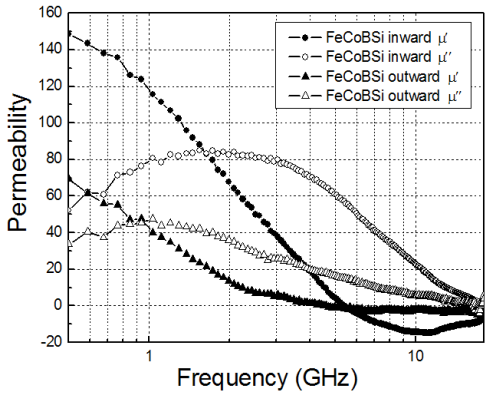

Figure 4: Permeability as a function of frequency for FeCoBSi thin films.

are induced in ferromagnetic thin films. Then magneto-elastic energy is formed by the stresses. The magneto-elastic energy allows re-orientation of magnetization vector, and thus changing the permeability at the direction of stress. The relation between the stress and the magneto-elastic energy is given by:

$$F_\sigma = -\frac{3}{2}\lambda_s \sigma \cos^2\theta, \tag{3}$$

where λ_s is the magnetostrictive coefficient, σ is the stress, θ is the angle between the stress and M_s. In accordance with the minimum energy principle, for material with positive magnetostrictive coefficient ($\lambda_s > 0$), if the stress is tensile stress ($\sigma > 0$), the magnetic moments will tend to arrange in the direction parallel to the stress direction. And if the stress is compressive stress ($\sigma < 0$), the magnetic moments will tend to arrange in the direction perpendicular to the stress direction. For material with negative magnetostrictive coefficient ($\lambda_s < 0$), the situation is the opposite. That means if $\lambda_s\sigma > 0$, $\theta = 0°$ or $180°$, if $\lambda_s\sigma < 0$, $\theta = 90°$ or $270°$ (Figure 5).

As we did not induce anisotropy during the sputtering process, the FeCoBSi film shows isotropic in-plane. So the internal in-plane magnetic moment is random orientation. In this case, k_A in Eq. (2) is approximately equal to 0.5. When we wind the films into spiral samples by the two methods above mentioned, the in-plane magnetic moments tend to re-oriented by the induced magneto-elastic energy. They tend to be parallel or perpendicular to the direction of stress as well as the direction of microwave magnetic field. Easy and hard magnetization axis appeared in film plane. The FeCoBSi film began to show anisotropy.

FeCoBSi film is a material with positive magnetostrictive coefficient ($\lambda_s > 0$). When we wind the film into a spiral sample by the method that ferromagnetic film inward, a compressive stress ($\sigma < 0$) is caused. Then the in-plane magnetic moments of the ferromagnetic film tend to re-orientated perpendicular to the direction of compressive stress. In this case, $k_A \approx 1$. When we prepared a spiral sample by the method that ferromagnetic film outward, a tensile stress ($\sigma > 0$) is caused. Then the in-plane magnetic moments of the ferromagnetic film tend to re-orientated along the direction of tensile stress as well as the circumferential direction. In this case, the component of magnetic moments which is perpendicular to the microwave magnetic field is very little, so the coefficient $k_A \ll 0.5$ then. The microwave properties of thin films are worse.

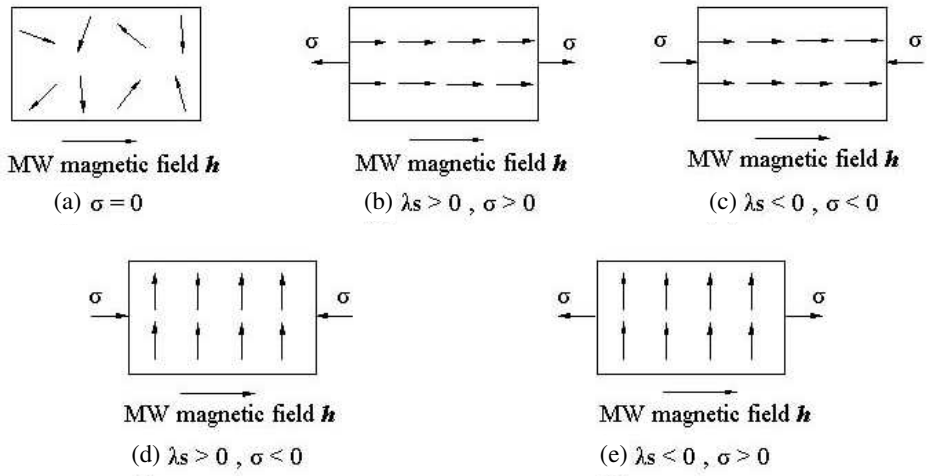

Figure 5: The effect of stress on the orientation of magnetic moments.

4. CONCLUSIONS

The experimental study of microwave permeability of FeCoBSi thin films prepared on thin flexible substrates allows the following conclusions to be made. Firstly, the ferromagnetic thin films deposited on thin flexible mylar substrates by magnetron sputtering usually present an amorphous structure. Secondly, if we use the coaxial technique to measure the permeability of thin films, stress may be formed at the process of spiral sample preparing. It may affect the measured values by changing the orientation of in-plane magnetic moments. Therefore, we should avoid this circumstance or use the effect of stress rationally in our study.

ACKNOWLEDGMENT

The authors would like to thank Prof. Mangui Han for fruitful discussion and valuable remarks. The work was supported by the Pre-research Funds for the General Armament Department, and the Fundamental Research Funds for the Central Universities (Grant No. ZYGX2009J032).

REFERENCES

1. Iakubov, I. T., A. N. Lagarkov, S. A. Maklakov, A. V. Osipov, K. N. Rozanov, I. A. Ryzhikov, and S. N. Starostenko, "Microwave permeability of composites filled with thin Fe films," *Journal of Magnetism and Magnetic Materials*, Vol. 300, No. 1, e74–e77, 2006.
2. Valls, O., D. Damiani, and O. Acher, "High frequency permeability of CoFeV thin films deposited on thin flexible substrates," *Digests of the Intermag Conference*, FD07, Amsterdam, Netherlands, April 2002.
3. Chen, L. H., S. L. Cheng, C. T. Hsieh, Y. H. Shih, S. Jin, and R. B. van Dover, "Ultrahigh frequency properties of amorphous Co-Fe-Zr-B thin films," *IEEE Transactions on Magnetics*, Vol. 37, No. 4, 2242–2244, 2001.
4. Frommberger, M., J. McCord, and E. Quandt, "High-frequency properties of FeCoSiB thin films with crossed anisotropy," *IEEE Transactions on Magnetics*, Vol. 40, No. 4, 2703–2705, 2004.
5. Acher, O., J. L. Vermeulen, and P. M. Jacquart, "Permeability measurement on ferromagnetic thin films from 50 MHz up to 18 GHz," *Journal of Magnetism and Magnetic Materials*, Vol. 136, No. 3, 269–278, 1994.
6. Acher, O., P. L. Gourrierec, G. Perrin, P. Baclet, and O. Roblin, "Demonstration of anisotropic composites with tuneable microwave permeability manufactured from ferromagnetic thin films," *IEEE Transactions on Microwave Theory and Techniques*, Vol. 44, No. 5, 674–684, 1996.
7. Iakubov, I. T., A. N. Lagarkov, S. A. Maklakov, A. V. Osipov, K. N. Rozanov, I. A. Ryzhikov, and S. N. Starostenko, "Microwave permeability of laminates with thin Fe-based films," *Journal of Magnetism and Magnetic Materials*, Vol. 272–276, No. 3, 2208–2210, 2004.

GMI Output Stability of Glass-coated Co-based Microwires for Sensor Application

Jing-Shun Liu[1], **Xiao-Dong Wang**[1], **Fa-Xiang Qin**[2], **and Fu-Yang Cao**[1], **Da-Wei Xing**[1], **Hua-Xin Peng**[2], **Xiang Xue**[1], **and Jian-Fei Sun**[1]

[1]School of Materials Science and Engineering, Harbin Institute of Technology, Harbin 150001, China
[2]Advanced Composite Center for Innovation and Science (ACCIS), University of Bristol
University Walk, Bristol BS8 1TR, United Kingdom

Abstract— We report a study here on the technique of Cu electro-plated wire-connecting for stabilizing the GMI output of $Co_{68.15}Fe_{4.35}B_{15}Si_{12.5}$ glass-coated amorphous microwires at the magnetic field ranging from 0 Oe to 4.2 Oe. The GMI output stability was characterized by a precision impedance analyzer and in a magnetically shielded space (MSS). The results show that this method could reduce the emission of RF electro-magnetic wave and driving signal attenuation, minimize the disturbance of stray capacity and parasitic capacity, and suppress high frequency destabilization and concussion at the relatively high frequency ($\geq$ MHz), hence effectively improve the GMI output stability for high-resolution magnetic sensor application.

1. INTRODUCTION

Glass-coated amorphous magnetically microwires have recently attracted much attention because of their potential industrial applications: they can be used as GMI and GSI (giant stress impedance) sensor elements in the CMOC IC circuitry to detect weak magnetic fields, small weights and slight vibrations. They find wide applications particularly in the car industry, biomedicine and navigation fields [1–4].

For the weak GMI and GSI magnetic sensors, researchers tend to enhance their stability, precision, repeatability and linearity by optimizing the design of electrical circuit, in that even a slight fluctuation of impedance could induce voltage signal magnified by further amplification circuit [5]. But little effort has been given in the wire-connecting perspective. Therefore, it is significant to study on the effect of wire-connecting on GMI output stability of the glass-coated Co-rich amorphous microwires. In general, for the as-cast glass-coated microwires, it is very challenging to achieve a stable electrical interconnection between amorphous wire and microelectronic circuit. The issue can be tackled from the following two aspects: (i) to remove the insulating glass thoroughly using hydrofluoric acid to assure a total exposure of the metal core. (ii) to seek for novel wire-connecting technique of improving wetting characteristic of two-terminal surface of the wire. Copper electro-plating, with higher electrical and thermal conductivity, good wettability with solder and weak destabilization of high frequency signal, is an effective way to ensure the bondability and reliability in wire-connecting process applied for packaging of chips with wire interconnects [6–8]. In this context, we employed the Cu-plating technique to stabilize GMI output.

This paper aims to achieve a stable interconnection between Co-based glass-coated wires and solder by controlling copper electro-plating process of wire-end, and explore the best conditions to maximize its GMI output stability. The results presented here are useful for high-performance GMI sensor applications.

2. EXPERIMENTAL DETAILS

Soft magnetic amorphous glass-coated microwires of nominal composition of $Co_{68.15}Fe_{4.35}B_{15}Si_{12.5}$ (the metallic nucleus diameter, $d = 32\,\mu m$, the glass-coating thickness, $t = 1.5\,\mu m$) was prepared using an experimental facility based on the modified Taylor-Ulitovskiy method [2, 3]. The fabricated thin microwires possessed excellent soft magnetic properties owing to the nearly zero or negative magnetostriction constant ($\lambda \leq -10^{-6}$). We selected the samples with whole length of 24 mm, and glass-coated layers of the two terminals (each about 4 mm long) were removed by hydrofluoric acid (HF) for 180 s, then Cu electro-plating was employed by minitype device. The improved electrolyte include copper sulphate, sulfuric acid, sodium chloride, glucose and sulfocarbolate acid with proper proportion. In order to obtain good electro-plating layer, process parameters were controlled effectively, (such as temperature is about 40°C, hyperpure copper is used as anode) [9]. The surface morphology of the studied microwires and electro-plated layers were measured by

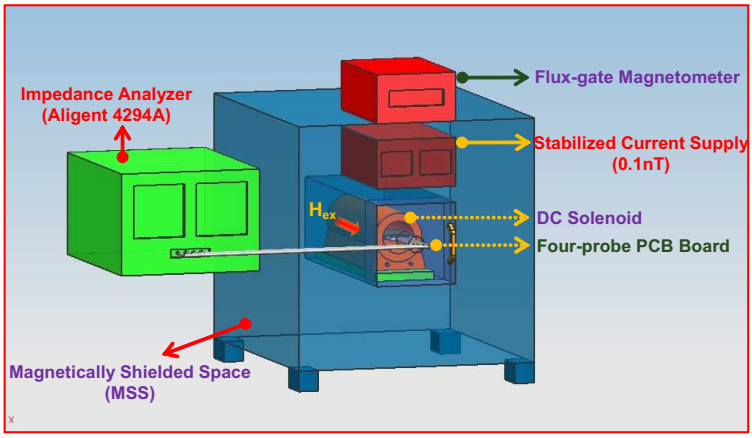

Figure 1: Schematic illustrations of magneto-impedance measurement system and magnetically shielded space (MSS). The unidirectional arrow represents the axial applied external magnetic field.

scanning electron microscopy (SEM). Video-based contact angle measurement device (OCA 20LHT) was employed to measure the dynamic contact angles based on the analysis of the drop shape of the different types of interfaces in a pipe-still heater with 10^{-3} torr vacuum. Figure 1 illustrates impedance measurement system and magnetically shielded space (MSS).

The magnetoimpedance was measured by an Aligent 4294A impedance analyzer in the frequency range of 40 Hz–110 MHz. The glass-covered microwire with two-end electro-plated was connected into PCB board adopting the four-probe connecting method. The composition of solder (SAC) is tin (96.5%), silver (3.0%), copper (0.5%) in weight percent, respectively. The magnetoimpedance ratio $\Delta Z/Z_{\max}$ is defined as [10]:

$$\frac{\Delta Z}{Z_{\max}}(\%) = \left[\frac{Z(H_{ex}) - Z(H_{\max})}{Z(H_{\max})}\right] \times 100\% \tag{1}$$

where H_{ex} denotes the dc axial external magnetic field, which is supplied by a solenoid; $H_{\max}$ denotes the maximum field along the wire axis, which is 4.2 Oe in the present work. All measurements were performed at room temperature.

3. RESULTS AND DISCUSSION

As was shown in Figure 2, the morphology and thickness (precisely measured from the SEM images) of copper electroplated layer depend on the current density of cathode and electro-plating time. The uniform electro-plating layer is critical for the final stable wire-connecting, as well as impedance output stability. At the cathode current density of 147.12 A/dm^2, at the initial stage of electro-plating, the thickness of wires obviously increases to 0.77 µm in 45 s, the microstructure of Cu electro-plated layer is uniform, dense, slightly coarse and of no macroscopic irregularity. In 75 s and 120 s, hydrogen liberation occurred in these stages. The surface of microwires becomes rougher and porous, resulting in stress concentration in some regions because of different plating rate, thereby forming some long cracks. The thicknesses in 75 s and 120 s are up to 1.08 µm, 1.31 µm, respectively. In 240 s, copper particles grow rapidly, and the brittleness of Cu layer with 2.08 µm thick increases. The microstructure becomes much more coarse, with the occurrence of abnormal deposited regions, making the wire unsuitable for wire-connecting. Further, the relations between thickness (T) of copper layer and electro-plating time (t) can be fitted by the following expression of parabola type with small error of fitting: $T = 0.063 + 0.014t - 0.000024t^2$. Thus, the thickness of copper electro-plated layer can be effectively controlled by the above expression. Overall, the uniform layer and proper layer thickness are essential for wire-connecting. With the comparison of above presented morphology for different times, the following parameters (147.12 A/dm^2, 45 s) can be chosen as the final choice for wire-end electroplating in the present work.

In order to evaluate the wetting characteristic of copper electro-plated layer at wire ends, the dynamic wetting morphologies of as-cast glass-removed microwires with two typical interfaces are shown in Figure 3. Contact angles of non-electroplated interface (a), θ_a, is 85.54°, and the contact angles of Cu electro-plated interface (b), θ_b, is 30.28° For the latter, it indicates that copper electro-plated layer as a transition medium interconnecting CoFeBSi alloy and solder has good wettability

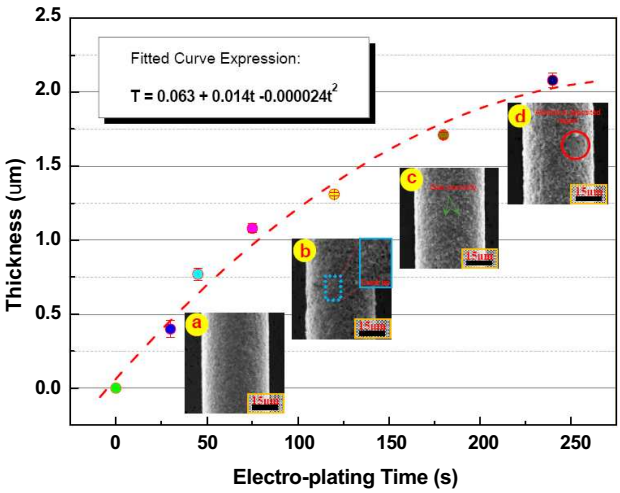

Figure 2: Variation in the surface morphology and thickness of Cu electroplated layer at the current density of 147.12 A/dm^2 with different electro-plating time: (a) 45 s, (b) 75 s, (c) 120 s, (d) 240 s.

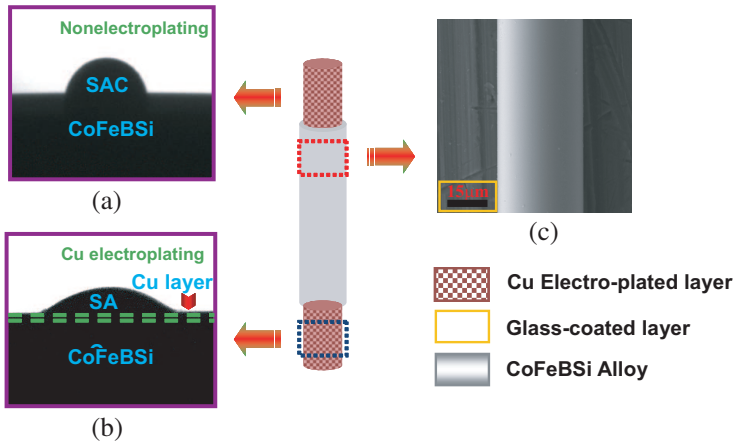

Figure 3: The wetting morphology of as-cast glass-coated amorphous microwires with two typical interfaces: (a) non-electro-plated interface [8] and (b) Cu electro-plated interface. The OCA images (a) and (b) indicate contact angles of θ_a and θ_b are 85.54° and 30.28°, respectively. (c) is a SEM image of surface morphology of the glass-coated wire with total diameter of around 32 μm.

for wire-connecting and that the solder has small surface tension. Therefore, wire-connecting of copper electro-plated layer at wire ends exhibits stability and reliability even in unfavorable working conditions.

The microwire with copper electro-plated two-terminal is connected into PCB board, placed in magnetically shielded space (MSS) to avoid the disturbing of geomagnetic or other magnetic field, to analyze impedance output stability of wires accurately at the same ambient temperature (25°C) and the driving current amplitude (20 mA) [11]. The impedance stabilities and the corresponding GMI output stabilities dependence of the magnetic field (0 Oe–4.2 Oe) at the frequency range of 0.1 MHz–15 MHz are shown in Figure 4. For non-electro-plated at wire-terminal (as seen in Figures 4(a) and (b)), the impedance variation has some obvious inhomogeneous variation regions (IVRs) at 0.1 MHz–15 MHz, especially, at 3 MHz–6 MHz and 8 MHz–13 MHz. From GMI ratio ($\Delta Z/Z_{\max}$) output stability variation, impedance fluctuation almost runs through all of frequency region, and the magnified meshes in partial magnifications (as shown in Figure 4(b)) present flectional variation, or macroscopic fluctuant variation. For copper electro-plated at wire-terminal (as seen in Figures 4(c) and (d)), as mentioned above, the IVRs are improved effectively, the impedance and its GMI output stability vary stably and smoothly as the magnetic field and frequency are increased, even at relatively high frequency ($\geq$ 8 MHz), and the maximum GMI ratio $[\Delta Z/Z_{\max}]_{\max}$ is up to 124%. In a word, copper electro-plating at wire-terminal is an effective approach to im-

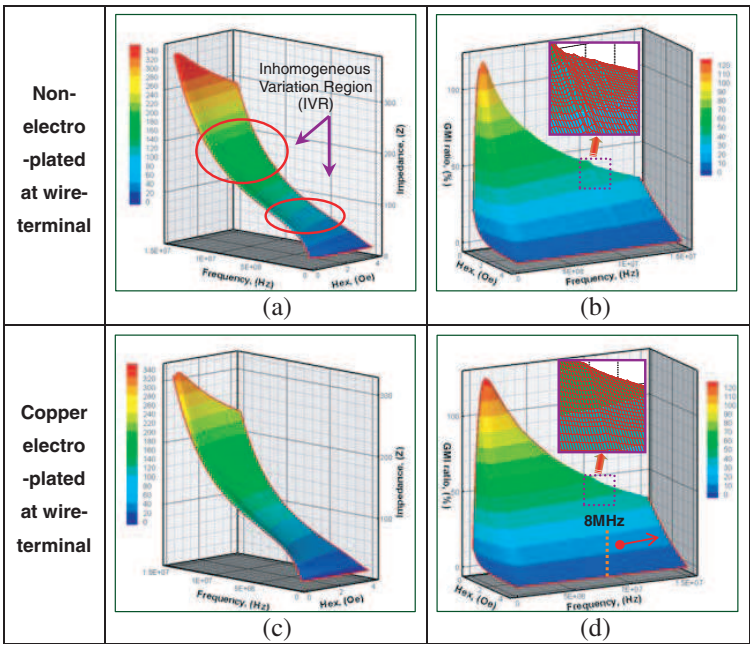

Figure 4: The impedance output stabilities ((a) and (c)) and their GMI ratio $\Delta Z/Z_{\max}$ output stabilities ((b) and (d)) vs. frequency (0.1 MHz–15 MHz) and magnetic field. The red ellipses indicate the inhomogeneous variation regions (IVRs) of impedance. The partial magnifications (imaginary purple line) in (b) and (d) are shown in order to illustrate the variation in GMI ratios with increasing applied field (0 Oe–4.2 Oe) at different frequencies.

prove the GMI output stability of glass-coated microwires. In conclusion, electro-plated copper is an excellent conductor with good wettability interconnecting solder. As a result, it reduces the contact resistance of spot weld, and help to achieve stable wire-connecting. Meanwhile, this type wire-connecting also can avoid the disturbance of stray capacity and parasitic capacity in spot weld and reduce the emission of RF electro-magnetic wave and driving signal attenuation, more importantly, suppress destabilization and concussion resulting from contact instability of wire-connecting ends at the relative high frequency ($\geq$ MHz).

4. CONCLUSIONS

The wire-connecting with Cu electro-plated terminal has been demonstrated to have the significant effects of stabilizing the GMI output of glass-coated Co-based wires. A uniform and dense granular structure of Cu electro-plated layer obtained from optimized electro-plating process at 147.12 A/dm^2 for 45 s has smaller contact angle (30.28°) and lower contact resistance. Compared with non-electro-plated wire-terminals, Cu electro-plated wire-connecting reduced the fluctuation of impedance and enhanced effectively the GMI output stability at different magnetic field and frequency. This is of significant importance for the development of high performance GMI magnetic sensors.

ACKNOWLEDGMENT

The authors would like to express their appreciation to Prof. G. H. Tu, Nanjing Normal University, China, for useful discussion and advice.

REFERENCES

1. Zhukov, A., J. Gonzalez, M. Vazquez, V. Larin, and A. Torcunov, *Nanocrystalline and Amorphous Magnetic Microwires Encyclopedia of Nanoscience And Nanotechnology*, Chapter 62, American Scientific Publishers, California, 2004.
2. Zhukov, A., V. Zhukova, J. M. Blanco, and J. Gonzalez, "Recent research on magnetic properties of glass-coated microwires," *J. Magn. Magn. Mater.*, Vol. 294, No. 2, 182–192, 2005.
3. Phan, M. H. and H. X. Peng, "Giant magnetoimpedance materials: Fundamentals and applications," *Prog. Mater. Sci.*, Vol. 53, No. 2, 323–420, 2008.

4. Garcia, C., V. Zhukova, M. Ipatov, J. Gonzaleza, J. M. Blanco, and A. Zhukov, "High-frequency GMI effect in glass-coated amorphous wires," *J. Alloy. Compd.*, Vol. 488, No. 1, 9–12, 2009.
5. Hauser, H., L. Kraus, and P. Ripka, "Giant magnetoimpedance sensors," *IEEE Trans. Magn.*, Vol. 4, No. 2, 28–32, 2001.
6. Nguyen, L. T., D. McDonald, A. R. Danker and P. Ng, "Optimization of copper wire bonding on Al-Cu metallization," *IEEE Trans. Compon. Pack. A*, Vol. 18, No. 2, 423–429, 1995.
7. Zhong, Z. W., H. M. Ho, Y. C. Tan, W. C. Tan, H. M. Goh, B. H. Toh, and J. Tan, "Study of factors affecting the hardness of ball bonds in copper wire bonding," *Microelectron. Eng.*, Vol. 84, No. 2, 368–374, 2007.
8. Liu, J. S., J. F. Sun, D. W. Xing, X. Xue, S. L. Zhang, H. Wang, and X. D. Wang, "Experimental study on the effect of wire bonding by Cu electroplating on GMI stability of Co-based amorphous wires," *Phys. Status Solidi A*, Vol. 208, No. 3, 530–534, 2011.
9. Lee, C. M., J. H. Lim, S. M. Hwang, E. C. Park, J. H. Shim, J. H. Park, J. Joo, and S. B. Jung, "Characterization of flexible copper laminates fabricated by Cu electro-plating process," *Trans. Nonferrous Met. Soc. China*, Vol. 19, No. 4, 965–969, 2009.
10. Vazquez, M., M. Knobel, M. L. Sanchez, R. Valenzuela, and A. P. Zhukov, "Giant magnetoimpedance effect in soft magnetic wires for sensor applications," *Sens. Acta. A-Phys.*, Vol. 59, No. 1–3, 20–29, 1997.
11. Sun, J. F., J. S. Liu, D. W. Xing, and X. Xue, "Experimental study on the effect of alternating-current amplitude on GMI output stability of Co-based amorphous wires," *Phys. Status Solidi A*, Vol. 208, No. 4, 910–914, 2011.

On the Electrically Driven Motion

S. L. Vesely[1], **A. A. Vesely**[2], **and C. A. Dolci**[3]

[1]I.T.B. — C.N.R., Italy
[2]Via L. Anelli 13, Milano, Italy
[3]Liceo Einstein, Milano, Italy

Abstract— Comprehension of electric currents can be sought in several ways. We note two issues: On the one hand, the experimental evidence that electric power can be converted into mechanical power. On the other hand, the long-established theoretical habit of reducing electric phenomena to the mechanical paradigm. Both of them involve electrically driven motion, but reductionism prevents the use of *electrical signals* as a theoretical basis for process control. Thus we leave it and re-explore conversions. In this article, we briefly review the interpretation in terms of ionic transport of two classical approaches to electrolysis. Then we describe isoelectric focusing, whereby protein migration in an immobilized pH gradient can be achieved by means of an electric field without meaningful ionic current between the electrodes. We finally propose an acoustic analogy for the latter technique and similar ionic transports.

1. INTRODUCTION

Continuous and low-frequency alternate currents result in phenomena that are perceived differently than those exclusively related with high frequencies and electric transients. In facts, the former currents lend themselves to conversions into mechanical movements, as it was initially observed by Galvani on frog's legs, while the latter ones result in radiation and other effects that can be interpreted in mechanical terms by means of analogies or similar constructs only. Considering that dynamos are even better than voltaic batteries at generating current, electromechanical conversions evoke, for the "electric conflict", images of conduction in the internals of conductors and electrolytic cells, and images of mechanical impulses transferred from generators to loads. The classical physical approach deals with electric current by adapting the laws of mechanics, and a mathematical account for it is given using either one of two methods that are incompatible with one another. The first one applies functional analysis to an homogeneous uncompressible fluid, and depicts the steady-state flow in the complex plane by means of potential flow diagrams. The second one treats the fluid in accordance with kinetic gas theory; that is, it considers the flow a convective motion of a system of points, and applies the theory of probability for an infinite number of points. Either method can be specified and tweaked in accordance with experimental results. Vice-versa, smart mathematical refinements can suggest new experiments. However, the first method, tagged "field", cannot be tweaked so as to find corpuscles inside the fluid, nor specified so as to match streamlines with trajectories. Thus, in order to easily switch between the field and the particle pictures, both descriptions have to be reformulated. For this sake, transport theories have been reformulated in the sample space, so that field variables and particle variables alike can be outcomes of an event. The latter formulations take into account both the current flow and its fluctuations, as an integral part of their core concepts. Because of their ability to simultaneously consider fields and particles, they allow to investigate interactions of electricity with matter. Such interactions are usually expressed as perturbations of particles' laws due to the field. These modern transport theories are flexible and modular, so as to cover the whole body of condensed matter physics.

In the rest of this article, we examine the *concepts* of electric current and related fluctuations inferred from transport theories, as far as their relationship with electrolysis is concerned. In Section 4, we describe a biochemical technique (isoelectric focusing) as an example of an electrokinetic phenomenon that differs from electrolysis in some respects. Finally, we sketch an interpretation of electric current and related fluctuations, based on an acoustic analogy.

2. ON THE MOTION DRIVEN BY LOCAL ELECTRICAL FORCES

Since transport theories deal with electric current by considering it a motion of charged particles subject to an electric field[1], we wish to make two preliminary remarks about extending the dynamical concept of force to electromagnetism. First one, on the cause-and-effect relationship between

[1]Assuming that irreversible processes admit a statistical approach, transport theories apply the fluctuation-dissipation theorem (Nyquist) and the Onsager reciprocal relations to the reciprocal processes. They conclude that, at steady equilibrium,

a body's motion and the force that determines it[2]. Since the correspondence is bijective only if the motion is the sole outcome of the cause, we note that $F = ma$ exhibits a dependence upon an intrinsic quantity of the body, its inertial mass m. In Newton's theory of gravitation, the inertial mass cancels with the gravitational one. That allows tracing all trajectories on a graph with a single metric scale. Applying such paradigm to an electric or magnetic mass, e or μ, the electric/magnetic force can be defined in the same way, without considering any mechanical mass. Instead, extending the paradigm so as to formally include both mechanical and electric forces, and assuming an intrinsic dependence upon e/m[3], all extrinsic causes being equal, the results differ for each different value of the ratio. In the general case of multiple forces, where each one is related to its specific intrinsic attribute of bodies, and where additionally the ratios e/m change as objects approach the speed of light, it is still possible to obtain accurate numerical results, but the effectiveness of the original paradigm is lost.

The second remark concerns the question of *random causes* of motion. They start out in modeling "macroscopic" phenomena as systems comprised of a huge number of mass-points. The cause-and-effect paradigm is individually applied to each point subject to a force. *Free points*[4], instead, are considered to be in random thermal motion. Since Einstein's work, Brownian motion is considered an experimental evidence of that thermal motion, leading to diffusion phenomena at a "macroscopic" level. If that is accepted, "averaging" has an experimental ground different from accounting for measurement errors. Whatever we may believe about the existence of atoms, the concept of stochastic motion originated from ancient Greek atomism, which predates R. Brown's observations, and implies a paradigm different from Newton's determinism. From this perspective, the conceptions of causality and randomness encompass two of the many possible philosophical approaches to the problem of motion. Two conceptions are enough to bother both concepts of average force and random force, making them hybrid.

3. ELECTRICAL NETWORK AND CHEMICAL APPROACHES TO ELECTROLYSIS

Electric currents are referenced in relation with contact potential differences, also known as Volta potentials. As such potentials zero out in closed conductor loops, except in case some electrolytes are suitably inserted, as a matter of facts Volta potentials can be used to feed direct current in that case only. Concerning the generation of electric current, chronicles report a dispute between Volta and Galvani about the necessity that the electrolytes be of animal origin, involving the then relevant question of whether electricity depends upon some sort of vital fluid. The problem was dismissed because voltaic piles use inorganic electrolytes. Further disagreements on the nature of current also originated from metaphysical considerations. Leaving them aside, we can summarize Kohlrausch's approach by saying that it led to the (energetic) analysis of linear networks, while Faraday's approach was related to the chemistry of Dalton and Proust[5]. In the first case, circuit analysis valid for ohmic circuits is formally extended to electrolytes. That allows attributing to both passive circuit elements and generators of electromotive force (emf) a current as well as a voltage drop. In particular, emf is assigned a potential difference with sign reversed. This framework does not allow to tackle questions about the nature of current — convective versus conductive — because electrolytes are treated exactly like passive circuit elements. Faraday's approach, instead, correlates the current delivered with the formation of gaseous reaction products[6], thus evidencing a relationship between chemical and electrical phenomena. The quest for a logical link between chemical reactions and current doesn't result in a key to comprehend the nature of current either. However, the ability to discriminate between potential difference and current now depends on the identification of the two respective quantities on the chemical side. Faraday missed to identify them. He coined the names *cation* and *anion* for the hydrogen and the oxygen that are formed at

noise is due solely to the conduction current, whereas the linear response includes the particles motion, because fluctuations depend on the autocorrelation spectra of all the conjugate variables in the system. Thus, the linear response is linear only as far as its expectation value is being considered.

[2]D. Hume considers the cause-and-effect relation an inductive result that can be achieved by means of logical deduction.

[3]Lorentz's renowned 1892 book entitled "The theory of the electron" didn't hold the necessity of assigning a mass to charged particles. In relation to Mie's theory, the question was then posed of whether the mass as a whole should be considered of electromagnetic origin. A dependence upon the product em might have been more convenient for developing the theory, but the interpretation of cathodic rays experiments by J. J. Thomson in 1897 and most importantly Aston's spectrometer separation criterion required to consider the ratio e/m.

[4]Random force has null mean.

[5]To Dalton is due the law of multiple proportions, to Proust that of definite proportions. Both laws become marginal in organic chemistry.

[6]Faraday considered polarization a cohesive force opposite to electrolytic dissociation.

the cathode and the anode, respectively, when flowing current split the water. After verifying that, when he was able to dissociate solutes, their weights were proportional to the current integral, he suggested to adopt their electrochemical equivalent as the chemical equivalent of reactants. At the time, however, chemistry was based on mechanics. A "chemical equivalent" denoted the mass rather than concentration of a substance. Furthermore, chemical affinity used to denote the strength of the force that binds elements together[7]. Thus, the emf, rather than the current, was believed to perform the work required to dissociate the compounds. As a consequence, current was also explained in mechanical terms. It wasn't until J. J. Thomson's experiments allowed a convective interpretation of the whole of the current, that Berzelius' theory of chemical dissociation could be brushed up again. Then both of the currents could be explained as electrically driven motions, and electrons could be taught to participate in the formation of neutral gases at a cell's electrodes. However, in the meantime chemistry had evolved taking avail of interpretations rooted in thermodynamics. The concepts of work performed by a reversible electrolytic cell, and chemical affinity had both been revisited: the former was related to Gibb's free energy, while the latter was taken as proportional to the chemical reaction rate. The link between electromagnetism and chemistry thus stopped at electrolysis laws, the more and more increasing use of electronics and optical methods in chemical analysis notwithstanding.

4. MORE COMPLEX ELECTROKINETIC PHENOMENA

In biochemistry, it is important to separate from one another and identify the compounds in organic mixtures. Ionic transport, as implied by electrolysis, is not a general means for separation of colloids and various classes of macromolecules in aqueous solution, because their net charge is undefined. Nevertheless, as it results from titrations that around physiologic pH several macromolecules are amphoteric (that is, exhibit acid as well as basic functional groups), it is possible to separate them within an electrolytic cell by migration through a porous diaphragm. We say "migration" to mean that, absent any convective motion within the solvent, different molecules take different times to pass through a partition, either a porous diaphragm or a gel matrix. Electrolysis laws don't hold, and the migration of organic compounds is attributed to the need to pass across the pores, that is, to electro-osmosis[8]. Such migration is also associated with an electric current, so that one can hypothesize that some traits of Faraday's law are still valid[9], but cannot verify it by gurgling ions at the electrodes, since that would corrupt the electro-osmotic process. At any rate, the counterions of acid and basic protein groups, and the solvent, are generally blamed for the current. In particular, the solvent is also responsible for a variety of effects, as organic substances are capable of swelling, coagulation, precipitation. To achieve fractionation avoiding unwanted side effects, biochemists seek to control the solvents' buffering capacity and salt concentration (ionic strength), while the amount of current — as long as not exceeding — is deemed of secondary importance. In electrochemistry the explanation of electrophoresis led to a bunch of electrokinetic theories, the first of whom goes back to Helmholtz. Present theories have to account for several secondary effects. For example, it is generally agreed that electric force depends upon the formation of double layers of electrostatic charges on the surfaces of electrodes, as well as on those of pores in the gel, and also upon the layers wrapped around macromolecules.

Among the techniques used in biochemistry to separate different molecules, isoelectric focusing (isoelectrofocusing) is a very sophisticate one, whereby the separation of the components of a mixture is attained as protein fractionation at the isoelectric point of each substance [1]. To apply the method, it is necessary to produce and immobilize a predefined pH gradient in a gel matrix between the electrode compartments. On the one hand, it is agreed that each kind of protein is electrically driven to its isoelectric point, defined as the location of minimal ionization of the solute. On the other hand, there are no practical means to evaluate the relationship between the amount of current measured at the electrodes and the amount of separated chemical equivalents, because $\mathrm{pH} = -\log_{10}[H^+]$ varies along the matrix. Inorganic chemistry experiences show that, in cases without gurgling at the electrodes, the pH of the solution varies with time while current flows, as

[7] That means they believed the more "affine" the chemical reactants, the stronger they bind, independently of their concentrations. Such belief is contrary to the law of mass action.

[8] We note that the osmotic method, based on Van't Hoff's law $\Pi = RTn$, where n is the number of molecules, is used to determine the molecular weight of proteins from $M = RTc/\Pi$, where c is the concentration in g/liter and Π the pressure in atm. Even if the atomic mass is no more determined that way nowadays, Arrhenius' dissociation theory bases on exactly this law (besides the freezing point depression and the vapor pressure lowering), in order to assert that monovalent inorganic salts are dissociated into ions in solution.

[9] Alternatively, small ions can be assumed to migrate by ionophoresis.

a consequence of ionic depletion. Because of thermal convections in the bulk of the liquid, ionic depletion is measured near the electrodes. However, in isoelectric focusing with immobilized pH gradients (IEF-IPG) current flows through the gel even if ions are neither transported nor depleted. There is an earlier variations of IEF, Isoelectric focusing with carrier ampholynes (IEF-CA), which provides for cathodic and anionic solutions separated by a solid matrix, usually a polyacrylamide gel. Before injecting the mixture to be treated, one runs a large pool of ampholyte molecules of different isoelectric points (pI) between pH 3.5 and 10; that serves as buffer, as it stabilizes a gradient of pH=pI in the gel. That is possible because the ampholyne are special amphoteric compounds that simultaneously exhibit prominent acid and basic groups with similar pK[10]. The assumption for pH gradient immobilization by CA is that, according to Kohlrausch electro-migration law, when carrier ampholynes arrive to the zone near their pI[11], their migration under the electric field ceases. In this case, the ΔpK between different carrier species contributes to conductivity, but it also affects the sharpness in focusing separated substances. The IEF-IPG technique that sharpens isoelectric lines was published in 1982 [2]. It allows to stably graft "Immobilines"[12], i.e., bifunctional acrylamide derivatives, onto the support ($\frac{1}{2}$ mm thickness). That way, one can shape a linear gradient encompassing a couple of pH units around pH = 7, where the water has no buffering capacity, so that proteins focus in sharp bands around their isoelectric points, as said, after having essentially zeroed diffusion and convection in the solute. In these conditions, having avoided additional unbound ions, specific conductivity is that of pure water: $\approx 1\,\mu$S/cm. According to the description of IEF-IPG, no ionic transport can be detected in conjunction with electric current; even the resulting fractionation is not compatible with a current due to ion motion.

5. AN ACOUSTIC ANALOGY

In the preceding sections we brought some examples of cells containing aqueous solution, considered passive elements of an electric circuit, and the chemical dissociations and separations obtained with them. The phenomenology is rather extended, and can admit different interpretative approaches, depending on the particular phenomenon and the intended theoretical framework. We stem from isoelectric focusing, which reminds us of Kundt's dust patterns in air. Those patterns are obtained inside a closed tube by gently and continuously rubbing it to make it sound [3]. Water is a quite reacting solvent, and plays a role similar to that of the air inside Kundt's tube. Firstly, water conductivity is small compared to metal's, but still considerably higher than that of most non-aqueous solvents[13]. Electric current can be thought of as a sign of excitation of a conductor[14]. Thus, the easily occurring polarization of pure water under CC may suggest that the excitation has a high-Q band, whose center corresponds to the null frequency. Secondly, conductivity betters when the water is doped with some acids, salts, or bases, and that corresponds to a lowering of the band's Q. Reciprocally[15], controlling the rate of some inorganic reactions, it is possible to build voltaic piles and batteries that will deliver continuous current. Thirdly, water also catalyzes a broad number of reactions of a much more diversified nature than those met in inorganic chemistry. We note that current flows are often associated with fractionations, in organic chemistry. They too are compatible with the alternative interpretation that attributes a mild electrical excitation to current-conducting aqueous systems. Imagining that colloids in the gel with a pH (and density) gradients separate by type under a continuous electrical solicitation, much like different kind of dust form different patterns in a Kundt's tube, it is possible to derive an explanation of the chemical fractionation described in Section 4, by analogy [4].

It is taught that the active delivery of current by piles and batteries is sustained by chemical

[10]For example, aminoacids can be used with higher or lower effectiveness to attain stable pH gradients.

[11]The pI depends upon the ΔpK between acid and basic groups.

[12]Two types of components are used: acid acrylamides with a carboxyl buffering group and basic polyacrylamides. They are added to the gel while casting it, by using a two-chamber gradient mixer. The mixing ratio is such that the required pH gradient along the polymerized matrix is attained without further titrations.

[13]Models usually attribute a high permittivity $\epsilon'(0)$ ($\approx$ 80) to pure water, while they attribute conductivity to the small electrolytic dissociation. In effects, the equation $\nabla \times \mathbf{H} = \mathbf{J} + \partial\mathbf{D}/\partial t$ makes a clear distinction between conduction and displacement, even if successively positing $\mathbf{J} + \partial\mathbf{D}/\partial t \rightarrow (\sigma_e + j\omega\epsilon')\mathbf{E}$, where σ_e includes both the static conductivity and the lossy part of permittivity, the distinction fades away.

[14]Excitation does not necessarily imply that the output oscillates. In particular, electric current is posited at null frequency because it is interpreted as a continuous flow.

[15]We regard this reciprocity as "symptomatic" for the onset of resonant conversion. The phenomenon is rather complex. In our opinion, the system response can be considered linear only when taking into account just the electric response; that is, substituting the word "fluctuation" with "modulation".

reactions[16] [5]. The requisite of inserting separators reflects that, in order for the current to stay steady while reactions are occurring, it is necessary that the prevailing reaction rates *be kept* steady[17]. According to modern statistical thermodynamics interpretations, the strength of an electrolytic current is determined by ionic transport; its fluctuation gives the power spectrum[18]. Instead, we suggest that the current be the result of an electric cross talk between a band at null frequency and some of the bands belonging to that huge water band that runs from IR to microwaves. The latter bands include the contributions of a variety of solutes. During the course of reactions, some of these bands become more prominent, and some of them quench; overtones and combination modes may appear. Modes from infrared upward are irradiated, while power at lower frequencies usulaay is not. Detection of continuous current relies in the first place on the existence in the system of the corresponding (low) frequency band, and then on the fact that connecting an electric load does not substantially alter the process underway. In case a frequency band coincides with one of the bands "hijacked" by the reaction, the reaction presumably gets altered. This interpretation differs from established explanations as it suggests that CC is just one of the bands of aqueous solutions on which reactions can be monitored. Current fluctuations in batteries happen both because the cross talk is a modulation, and because any other excited mode, unless filtered, can superimpose on current. These are preliminary remarks meant to express intuitively that some processes can excite the CC band of water, and that, reciprocally, a steady excitation of this band contributes to separation/dissociation of solutes.

6. CONCLUSIONS

We recounted how the correlation between ionic mass and charge represented Faraday's contribution to chemistry at a time when its salient problem consisted in compiling a periodic table of elements. In electrochemistry, inorganic salts dissociations are considered processes directly coupled to the measured electric current. As today's chemistry has evolved far beyond the subject area of simple inorganic redox reactions, toward the comprehension of organic processes, the position of Faraday's ideas must translate to the corresponding study of electronic monitoring and control of those processes. Many electrical and optical techniques, besides electrolysis, are already widely applied in chemistry for *analytical* purposes. For *preparative* purposes, we hold that electronic control of processes can be expanded by learning which of the monitored electrical responses can reciprocally control which reactions. Electrolysis is traditionally understood by assuming that chemical dissociations produce ionic transport currents directly. Instead, we argue that electrochemical conversions are primarily engaged at some higher frequencies (IR or even UV). Then, electrolytic currents result from cross talk, and can be assimilated to an electromagnetic band at null frequency. The latter band contains the reaction's small signal response, which is as linear as any modulation, even if the corresponding electrochemical process is not. Indeed, control aims at "linearizing" processes, maintaining that their products are delivered at given rates.

REFERENCES

1. Kolin, A., "Isoelectric spectra and mobility spectra: A new approach to electrophoretic separation," *PNAS*, Vol. 41, No. 3, 101–110, 1955.
2. Gianazza, E. and P. G. Righetti, "Immobilized pH gradients," *Electrophoresis*, Vol. 30, S112–S121, 2009.
3. Kundt, A., "Über eine neue Art akustischer Staubfiguren und über die Anwendung derselben zur Bestimmung der Schallgeschwindigkeit in festen Körpern und Gasen," *Ann. Phys.*, Vol. 203 No. 4, 497–523, 1866.
4. Waller, M. D., *Chladni Figures: A Study in Symmetry*, G. Bell & Sons LTD, London, 1961.
5. Heiman, A., and S. Licht, "Fundamental baseline variations in aqueous near-infrared analysis," *Anal. Chim. Acta*, Vol. 394, 135–147, 1999.

[16] The cited article shows the effect of monovalent electrolytes on the features of the water IR band from 900 nm to 1700 nm. In particular, it shows a quench in the zone around 1450 nm, where a lower Q may imply an increased channel capacity. Most importantly, the article underlines how difficult it is to determine a solute's base-line in aqueous solution, because of alterations in the water spectrum w.r.t. that of pure water.

[17] Besides using separators, there may be other means to control the course of reactions. Incidentally, we observe that usually chemical reaction rates are assumed to satisfy statistical laws provided by nonlinear thermodynamics. A strict dependence of each process' outcome upon the experimental conditions, as stated in some experimental protocol, doesn't seem to us to be a violation of natural laws. However, that's a tricky question.

[18] A power spectrum is the Fourier transform of the process' correlation function.

Novel Nonlocal Gauge Functions in Electrodynamics and Their Effect on Quantum Mechanical Phases

Konstantinos Moulopoulos
Department of Physics, University of Cyprus, Nicosia 1678, Cyprus

Abstract— We point to previously overlooked solutions of the standard gauge transformation equations of Electrodynamics: the generalized "gauge functions" go beyond the usual Dirac phase factors (spatial or temporal integrals of potentials) and exhibit a new form of nonlocal quantal behavior, with the well-known Relativistic Causality of classical fields affecting directly the phases of quantum mechanical wavefunctions. Because of the new solutions, the phases of wavefunctions in the Schrödinger picture are affected nonlocally by spatially and temporally remote magnetic and electric fields, in specific ways that are briefly demonstrated. The new nonlocalities, apparently overlooked in path-integral approaches, compete with Aharonov-Bohm behaviors and they provide: (i) a correction to a number of erroneous results in the literature (either an uncritical use of Dirac phases that persists since the time of Feynman's work on path integrals, or a sign error that still propagates in the literature and that regards the connection of Aharonov-Bohm phases to semiclassical phases picked up inside nonvanishing fields due to path-deflections by the Lorentz force), (ii) a new interpretation of semiclassical observations and further extensions to delocalized states (a "generalized Werner & Brill cancellation"), (iii) a natural remedy of earlier "paradoxes" (such as the van Kampen thought-experiment, as well as Peshkin's discussion of the electric Aharonov-Bohm effect that is made "causal" by the new solutions), and (iv) a new formulation directly applicable to the study of time-dependent slit-experiments and their causal issues.

The Dirac phase factor — with a phase containing spatial or temporal integrals of potentials (of the general form $\int^{\mathbf{r}} \mathbf{A}\cdot d\mathbf{r}' - c\int^{t}\phi dt'$) — is the standard and widely used solution of the usual gauge transformation equations of Electrodynamics (with $\mathbf{A}$ and ϕ vector and scalar potentials respectively). In a quantum mechanical context, it connects wavefunctions of two systems (with different potentials) that experience the same classical fields at the observation point $(\mathbf{r}, t)$, the two more frequently discussed cases being: either systems that are gauge-equivalent (a trivial case with no physical consequences), or systems that exhibit phenomena of the Aharonov-Bohm (AB) type (magnetic or electric) [1] — and then this Dirac phase has nontrivial observable consequences. In the above two cases, the classical fields experienced by the two (mapped) systems are equal *at every point* of the accessible spacetime region. However, it has not been widely realized that the gauge transformation equations, viewed in a more general context, can have *more general solutions* than simple Dirac phases [2], and these lead to wavefunction-*phase-nonlocalities* that have been widely overlooked and that seem to have important physical consequences. These apply to cases where the two systems are allowed to experience *different fields* at spacetime points (or regions) that are remote to (and do not contain) the observation point $(\mathbf{r}, t)$, see Fig. 1 for two examples. In this brief report we emphasize the existence of the new solutions and demonstrate them in simple examples, presenting therefore cases (and closed analytical results (see [2]) for the wavefunction-phases) that actually connect (or map) two quantal systems that are **neither physically equivalent nor of**

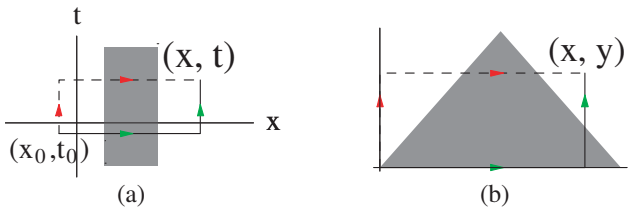

Figure 1: Examples of field-configurations where the nonlocal terms are nonzero: (a) a strip in 1+1 spacetime, where the electric flux enclosed in the "observation rectangle" is dependent on t but independent of x; (b) a triangular distribution in 2-D space, where the magnetic flux inside the "observation rectangle" depends on both x and y. The phase difference at the outside observation point (for each case) can be given in analytical form (see [2]).

the usual Aharonov-Bohm type. The consequences of the new (*nonlocal*) contributions (that appear in the wavefunction-phases) are found to be numerous and important; they are also of a different type in static and in time-dependent configurations (and in the latter cases they seem to lead to Relativistically *causal* behaviors, that apparently resolve earlier "paradoxes" arising in the literature from the use of standard Dirac phase factors).

Let us first recall that for the solutions $\Psi(\mathbf{r},\mathbf{t})$ of the t-dependent Schrödinger equation (SE) for a quantum particle of charge q moving in two distinct sets of classical vector and scalar potentials $(\mathbf{A}_1,\phi_1)$ and $(\mathbf{A}_2,\phi_2)$, that are generally spatially- and temporally-dependent [and such that, at the spacetime point of observation $(\mathbf{r},t)$, the magnetic and electric fields are the same in the two systems], are formally connected through $\Psi_2(\mathbf{r},t) = e^{i\frac{q}{\hbar c}\Lambda(\mathbf{r},t)}\Psi_1(\mathbf{r},t)$, with the function $\Lambda(\mathbf{r},t)$ required to satisfy $\nabla\Lambda(\mathbf{r},\mathbf{t}) = \mathbf{A}_2(\mathbf{r},t) - \mathbf{A}_1(\mathbf{r},t)$ and $-\frac{1}{c}\frac{\partial\Lambda(\mathbf{r},t)}{\partial t} = \phi_2(\mathbf{r},t) - \phi_1(\mathbf{r},t)$. For general potentials it is usually stated that the general gauge function that connects the above wavefunctions is (with $\mathbf{A} = \mathbf{A}_2 - \mathbf{A}_1$ and $\varphi = \varphi_2 - \varphi_1$)

$$\Lambda(x,t) = \Lambda(x_0,t_0) + \int_{x_0}^{x} \mathbf{A}(\mathbf{x}',t)\cdot d\mathbf{x}' - c\int_{t_0}^{t}\phi(x,t')dt', \tag{1}$$

which, however, is generally **incorrect** for x and t uncorrelated variables**:** it does **not** generally satisfy the above system (viewed as a system of partial differential equations (PDEs)), namely $\nabla\Lambda = \mathbf{A}$ and $-\frac{1}{c}\frac{\partial\Lambda}{\partial t} = \phi$. Indeed**:** (i) When the ∇ operator acts on (1), it gives the correct $A(x,t)$ from the 1st term, but it also gives some annoying additional nonzero quantity from the 2nd term (that survives because of the x-dependence of ϕ); hence it invalidates the first of the above basic system of PDEs. (ii) Similarly, when the $-\frac{1}{c}\frac{\partial}{\partial t}$ operator acts on (1), it gives the correct $\phi(x,t)$ from the 2nd term, but it also gives some annoying additional nonzero quantity from the 1st term (that survives because of the t-dependence of $\mathbf{A}$); hence it invalidates the second of the basic system of PDEs. It is only when $\mathbf{A}$ is t-independent, and ϕ is spatially-independent, that (1) is correct. It is also interesting to note that the line integrals appearing in (1) do *not* form a path (in spacetime) that connects the initial to the final point (although our new solutions *do* (see [2]). [An alternative form that is also given in the literature is again Eq. (1), but with the variables that are not integrated over implicitly assumed to belong to the initial point (hence a t_0 replaces t in $\mathbf{A}$, and an x_0 replaces x in ϕ). However, one can see again that the basic system is *not* satisfied (the above differential operators, when acted on Λ, give $\mathbf{A}(x,t_0)$ and $\phi(x_0,t)$, hence *not* the values of the potentials at the point of observation (x,t) as they should), *this not being an acceptable solution either*. And in this case also there is no spacetime-path connecting the initial (x_0,t_0) to the final point (x,t) either, as the reader can easily verify].

It turns out from this work [2] that the full form of a general Λ goes beyond Eq. (1), and

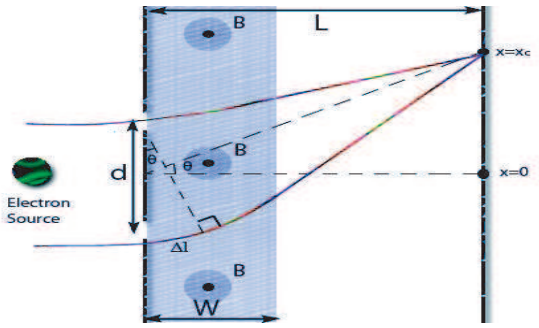

Figure 2: The standard double-slit apparatus with an additional strip of a perpendicular magnetic field B of width W placed between the slit-region and the observation screen. The deflection shown is for a negative charge q (and it is assumed small, due to $W \ll L$).

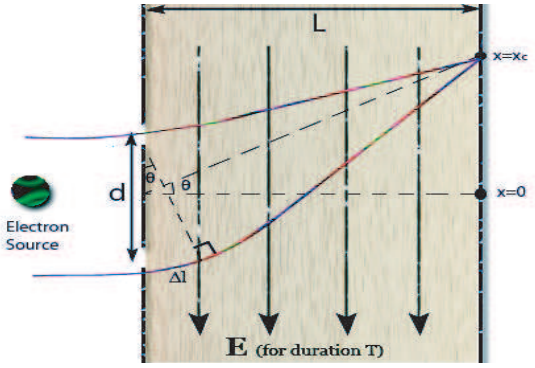

Figure 3: The analog of Fig. 2 (again for negative q) but with an additional electric field parallel to the observation screen that is turned on for a time interval T (with $T \ll t$, and t the time of travel). For both Fig. 2 and 3, it can directly be shown that $\Delta\varphi^{semiclassical} = -2\pi\frac{q}{e}\frac{\Phi}{\Phi_0} = -\Delta\varphi^{AB}$, hence an extra minus sign compared to reports in the literature.

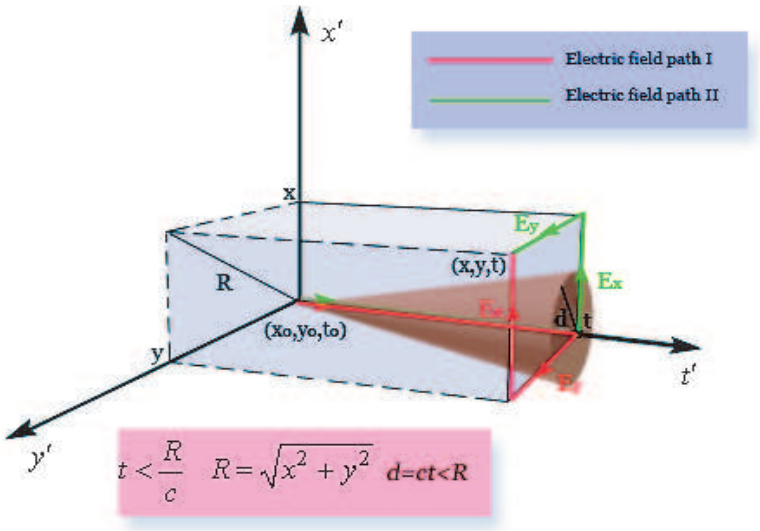

Figure 4: The analog of paths of Fig. 1 but now in $2+1$ spacetime for the van Kampen thought-experiment, when the instant of observation t is so short that the physical information has not yet reached the spatial point of observation (x, y). The strips of Fig. 1(a) have now given their place to a light-cone. At the point of observation, the AB phase has now become "causal" due to cancellations between two solutions (the two "electric field paths").

also beyond the usual Dirac phases: apart from integrals over potentials, it also generally contains terms of classical fields that act *nonlocally* (in spacetime) on the solutions of the t-dependent SE. As a result, the phases of wavefunctions in the Schrödinger picture are affected nonlocally by magnetic and electric fields — nonlocal contributions that have apparently escaped from path-integral approaches. The full solutions and a number of physical examples are given in detail in [2]. We then focus on two types of application of the new formulation: (i) Application to particles passing through fully-nonvanishing magnetic or electric fields leads to cancellations of AB phases at the observation point; these cancellations are linked to behaviors at the semiclassical level (to early experimental observations by Werner & Brill [3] or to recent reports of Batelaan & Tonomura [4]) but are far more general (valid not only for narrow wavepackets in semiclassical motion but also for completely delocalized quantum states). By using them we provide a new interpretation of semiclassical results and we point out a number of sign errors in popular reports in the literature: we show that semiclassical phase-differences picked up by classical trajectories (deflected by fields) are *opposite* (and *not* equal, as usually stated or implied) to the corresponding "AB phase" (due to the flux enclosed by the same trajectories), see Figs. 2 and 3 for examples, where one can directly show the extra sign, namely $\Delta\varphi^{semiclassical} = -\Delta\varphi^{AB}$. (ii) Application to t-dependent situations provides a remedy for a number of misconceptions (on improper use of simple Dirac phase factors) propagating in the literature (Feynman [5], Erlichson [6] and others), and leads to nontrivially extended phases that contain an AB part and a nonlocal field-part: their competition is shown to recover Relativistic Causality in earlier "paradoxes" (such as the van Kampen thought-experiment [7], see Fig. 4) and also provides a fully quantitative formulation of Peshkin's qualitative discussion (on expected causal behavior) in the electric AB effect [8] (discussion that was also based on a simple Dirac phase factor). The temporal nonlocalities found in this work demonstrate in part *a causal propagation of phases of quantum wavefunctions in the Schrödinger picture* (through the well-known causal propagation of fields), something that may open a new and direct way for addressing t-dependent double-slit experiments and the associated causal issues, without the absolute need of modular variables in the Heisenberg picture [9].

To evaluate in a broader sense the crucial nonlocal influences found in the present work, we should emphasize that at the level of the basic Lagrangian $L(\mathbf{r}, \mathbf{v}, t) = (1/2)m\mathbf{v}^2 + (q/c)\mathbf{v}\cdot\mathbf{A}(\mathbf{r}, t) - q\varphi(\mathbf{r}, t)$ there are no fields present, and the view holds in the literature [10] that electric or magnetic fields cannot contribute directly to the phase of quantum wavefunctions. This view originates from the path-integral treatments widely used (where the Lagrangian determines directly the phases of Propagators), but, nevertheless, our canonical formulation treatment shows that fields *do* contribute

nonlocally, and they are actually crucial in recovering Relativistic Causality. Furthermore, SU(2) generalizations of the present work would be an obviously interesting extension of the above U(1) theory, and such generalizations are rather formally direct and not difficult to make (an immediate physically interesting question being whether the new nonlocal terms might have a nontrivial impact on i.e., spin-(1/2)-states, since these terms would act asymmetrically on opposite spins). Finally, one can always wonder what the consequences of these new nonlocalities would be, if these were included in other systems of High-Energy or Condensed Matter Physics *with a gauge structure*; alternatively, it is worth noting that, if E's were substituted by gravitational fields and B's by Coriolis force fields arising in non-inertial frames of reference, the above nonlocalities (and their apparent causal nature) could possibly have an interesting story to tell about quantum mechanical phase behavior in a Relativistic/Gravitational framework.

ACKNOWLEDGMENT

Graduate student G. Konstantinou is acknowledged for having drawn Figures 2, 3 and 4.

REFERENCES

1. Aharonov, Y. and D. Bohm, *Phys. Rev.*, Vol. 115, 485, 1959.
2. Moulopoulos, K., *J. Phys. A*, Vol. 43, 354019, 2010.
3. Werner, F. G. and D. R. Brill, *Phys. Rev. Lett.*, Vol. 4, 344, 1960.
4. Batelaan, H. and A. Tonomura, *Physics Today*, Vol. 62, No. 9, 38, September 2009.
5. Feynman, R. P., R. B. Leighton, and M. Sands, *The Feynman Lectures on Physics*, Vol. 2, Chapter 15, 10 & 13, Addison-Wesley, 1964.
6. Erlichson, H., *Amer. Journ. Phys.*, Vol. 38, 162, 1970.
7. Van Kampen, N. G., *Phys. Lett.*, Vol. 106A, 5, 1984.
8. Peshkin, M. and A. Tonomura, *Lecture Notes in Physics*, 340, Springer-Verlag, 1989.
9. Tollaksen, J., Y. Aharonov, A. Casher, T. Kaufherr, and S. Nussimov, *New J. Phys.*, Vol. 12, 013023, 2010.
10. Brown, R. A. and D. Home, *Il Nuovo Cimento*, Vol. 107B, 303, 1992.

Investigation of Illusion Optics Devices Implemented by Transmission-line Metamaterials with Full Tensors

Guo Chang Liu, **Chao Li**, **and Guang You Fang**
Institute of Electronics, Chinese Academy of Sciences, Beijing 100190, China

Abstract— With the proposition of transformation optics, there emerged a lot of novel electromagnetic devices such as the invisibility cloaks, field concentrators, illusion optics devices and so on, which provide a unconventional functions for arbitrarily control the behaviors of electromagnetic waves. The practical implementation of such devices must take use of metamaterials(MTMs) for that the devices needs anisotropic and non-uniform medium parameters. As a candidate of MTMs with wideband and low loss properties, periodic transmission line (TL) networks were widely used to mimic MTMs with unique characteristics. However, the effective medium parameters possessed by TL MTMs before are all diagonal in the Cartesian basis, which limit the development of MTMs with more complex parameters. Recently, a group in the University of Michigan proposed a new structure of TL MTMs with arbitrary full tensors, in other words it can achieve any 2D anisotropic and non-uniform materials. In this paper, this kind of tensor TL metamaterials was introduced to the field of illusion optics invisibility system. Two circuit simulations are presented, one is an illusion optics system which optically transforms one object to another and the other is a rectangle invisibility cloak that cloaks objects at a distance outside the cloaking shell. It's found that TL MTMs with full tensors can be well applied to mimic transformation optics devices with complex medium parameters distributions.

1. INTRODUCTION

Transformation optics [1] made it possible for people to control the electromagnetic (EM) arbitrarily, combined with the concept complementary medium, people have proposed several novel EM device such as superscatterer, the anti-cloak and illusion optics devices [2–7]. But the EM parameters of such kind of devices are usually non-uniform and anisotropy, which must be implemented by MTMs. As a candidate of MTMs with wideband and low loss properties, periodic TL networks were widely used to mimic MTMs. However, the effective medium parameters possessed by TL MTMs before are all diagonal in the Cartesian basis [8], which limits the development of MTMs with more complex parameters. Recently, a group in the University of Michigan proposed the tensor TL MTMs which can achieve any 2D anisotropic and non-uniform materials [9]. In this paper, we implemented two novel device of illusion optics invisibility system by this new TL MTMs, one is an illusion optics system which optically transforms one object to another [5] and the other is a rectangle invisibility cloak that cloaks objects at a distance outside the cloaking shell [6]. We found the TL MTMs with full tensors can be well applied to mimic transformation optics devices with complex medium parameters distributions.

2. TENSOR TRANSMATION-LINE MTMS

From Fig. 1(a), we can see the structure of tensor TL unit cell, which has 4-branch in plane x-y [9]. Now I will show why this new structure can achieve tensor non-uniform and anisotropy parameters.

The propagation characteristics of TL network with the unit cell depicted in Fig. 1(b) can be described by three equations.

$$\frac{\partial V}{\partial x} = -\frac{1}{d}(z_{xx}I_x + z_{yy}I_y) \tag{1}$$

$$\frac{\partial V}{\partial y} = -\frac{1}{d}(z_{yx}I_x + z_{yy}I_y) \tag{2}$$

$$-\frac{\partial I_x}{\partial x} - \frac{\partial I_y}{\partial y} = \frac{1}{d}YV \tag{3}$$

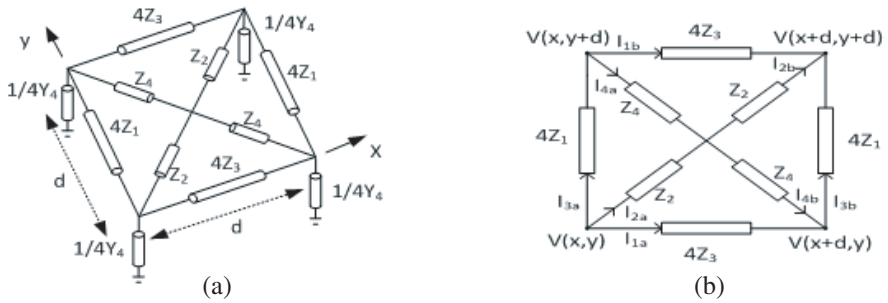

Figure 1: (a) Perspective view of the 4-branch TL MTMs unit cell. (b) Top view of the 4-branch TL MTMs unit cell.

where,

$$I_x = I_{3a} + I_{3b} + I_{2a} + I_{4a} \tag{4}$$

$$I_y = I_{1a} + I_{1b} + I_{2a} - I_{4b} \tag{5}$$

$$Z = \begin{pmatrix} z_{xx} & z_{xy} \\ z_{yx} & z_{yy} \end{pmatrix} \tag{6}$$

$$Y = Z^{-1} = \begin{pmatrix} \frac{1}{2Z_3} + \frac{1}{2Z_2} + \frac{1}{2Z_4} & \frac{1}{2Z_2} - \frac{1}{2Z_4} \\ \frac{1}{2Z_2} - \frac{1}{2Z_4} & \frac{1}{2Z_1} + \frac{1}{2Z_2} + \frac{1}{2Z_4} \end{pmatrix} \tag{7}$$

The propagation characteristics of this network are analogous to those for an TE wave (electric field polarized in the z direction). Compare the Maxwell equations with (1)–(3), we notices that there is a one-to-one relationship between a medium with material parameters and the electrical network shown in Fig. 1(b) with circuit parameters. The following substitutions can be made to go from the material to the electrical network.

$$E_z \leftrightarrow V,\ H_y \leftrightarrow -I_x H_x \leftrightarrow I_y,\ j\omega\mu_{yy}d \leftrightarrow Z_{xx},\ j\omega\mu_{xx}d \leftrightarrow Z_{yy},\ -j\omega\mu_{yy}d \leftrightarrow Z_{yx},$$
$$-j\omega\mu_{yx}d \leftrightarrow Z_{xy},\ j\omega\varepsilon_z d \leftrightarrow Y \tag{8}$$

For some special situation which can be seen in Fig. 2, the one to one relationship is still available.

3. CIRCUIT SIMULATION

Now, let's consider the first example. The illusion device [5] depicted in Fig. 3(a) is composed of four parts. The upper triangle part is composed of negative index homogenous medium of $\varepsilon = -1,\ \mu = -1$, embedded with a 'anti-object' of the rectangle object with $\varepsilon = -0.01,\ \mu = -100$, it's a complementary medium of the lower one, aimed to annihilate the optical signature of the rectangle object below. The left and right rectangle parts combined with the middle rectangle part constitute the 'restoring medium', which is used to restore the illusion and create a new signature, where the left and right triangle part is composed of homogenous media of $\mu_{xx} = 1.1622,\ \mu_{xy} = \pm 0.2162,\ \mu_{yy} = 0.9007,\ \varepsilon = 1.1622$ respectively, while the middle rectangle part is composed of homogenous media of $\mu_{xx} = 1.1622,\ \mu_{yy} = 0.8605,\ \varepsilon = 1.1622$ with an embedded compressed version of rectangle object illusion of $\mu_{xx} = 116.2162,\ \mu_{yy} = 86.0465,\ \varepsilon = 0.0116$.

To implement the illusion device using tensor TL MTMs, the substitutions given by Eq. (8) are applied to attain corresponding circuit parameter. The unit cell depicted in Fig. 2(a) and Fig. 2(b) are used to implement the upper left and right triangle parts respectively, and the rest parts are implemented by the structure depicted in Fig. 2(c).

An operation frequency is selected at 0.3 GHz, the dimensions of each unit cell are assumed to be 5 cm ($1/20\lambda_0$).The voltages at the corner of each unit cell were computed using Matlab. A time snapshot of the steady-state voltages is plotted in Fig. 3(b). We find that we have implemented the novel device successfully and at the same time verified the utility of the tensor TL MTMs directly.

Now, let's consider the other example. The rectangle cloak [6] shown in Fig. 4(a) is composed of three main parts. The layer between boundary c and b is a part composed of homogenous medium, where we can embed object. For simplify we set the medium parameter $\varepsilon = 1,\ \mu = 1$

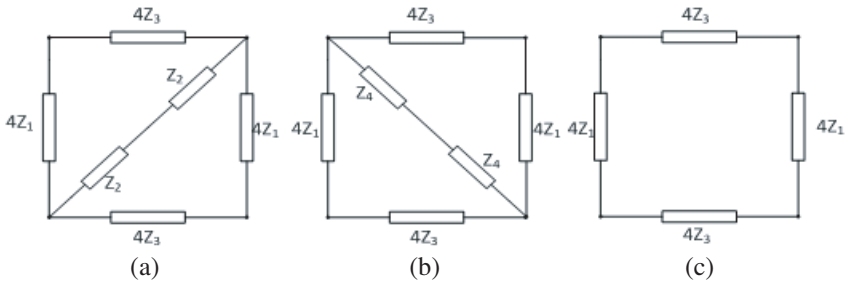

Figure 2: Top view of some special tensor TL unit cell. (a) One kind of 3-branch TL structure. (b) Another kind of 3-branch TL structure. (c) 2-branch TL structure.

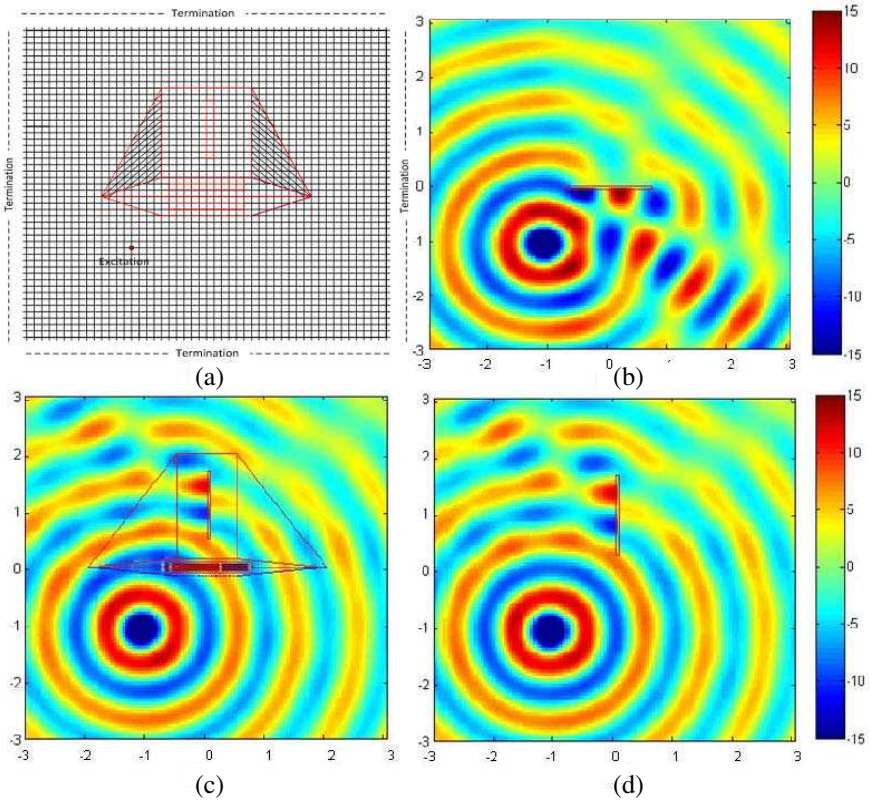

Figure 3: (a) Simulation set up for a transmission-line (TL) based illusion optics system (transform one object to another), embedded within isotropic, homogeneous TL medium. (b)–(d) Time snapshot of the simulated, steady-state voltages(excited by a current source)when we set. (b) The original object. (c) The original object with the illusion device. (d) Illusion.

without any object. This part is optically cancelled by the layer between boundary b and a, which is called a complementary medium. The EM parameter of such region can be attained from folded transformation. The middle core material is optically equal to free space enclosed by the red-dashed line, whose parameters are $\varepsilon = (R_3/R_1)^2,\ \mu = 1$.

To implement the rectangle cloak using tensor TL MTMs, the substitutions given by Eq. (8) are applied to attain corresponding circuit parameter. The unit cell depicted in Fig. 2(a) and Fig. 2(b) are used to implement the complementary medium between the boundary a and b respectively according to situation shown in Fig. 4(a). The rest parts are implemented by using the unit cell depicted in Fig. 2(c).

The dimension of the structure is $R_1 = 1.2$, $R_2 = 1.6$, $R_3 = 1.8$ and other simulation conditions are the same as the illusion system, which is not going to be elaborated here.

The voltages at the corner of each unit cell were computed using Matlab. A time snapshot of the steady-state voltages is plotted in Fig. 4(b), we find that we have implemented the novel device successfully and verified the utility of the tensor TL MTMs directly.

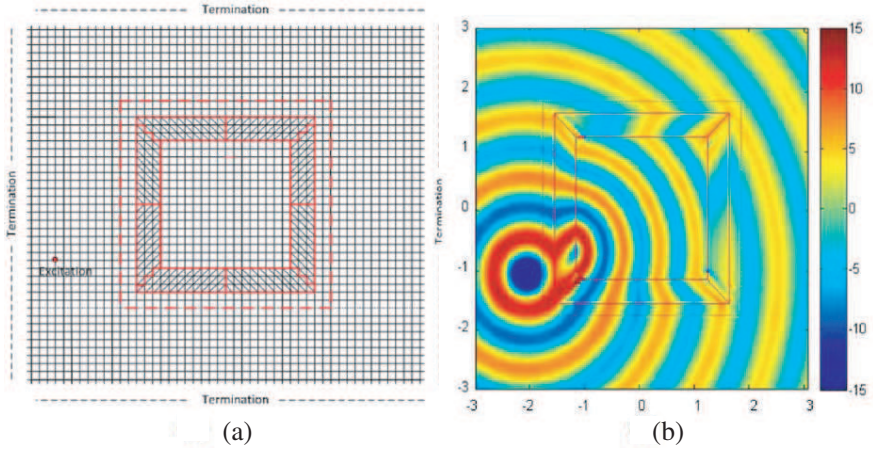

Figure 4: (a) Simulation set up for a transmission-line (TL) based rectangle cloak (cloaks object outside cloaking shell) embedded within isotropic, homogeneous TL medium. (b) Time snapshot of the simulated, steady-state voltages (excited by a current source).

4. CONCLUSION

This paper implemented two novel illusion optics devices by tenor TL MTMs, and at same time verified the utility of the new TL structure which can implement medium with arbitrary 2D full tensor.

REFERENCES

1. Ward, A. J. and J. B. Pendry, "Refraction and geometry in Maxwell's equations," *Journal of Modern Optics*, Vol. 43, No. 4, 773–793, 1996.
2. Yang, T., H. Y. Chen, X. D. Luo, and H. R. Ma, "Superscatterer: Enhancement of scattering with complementary media," *Optics Express*, Vol. 16, No. 22, 18545–18550, 2008.
3. Luo, X. D., T. Yang, Y. W. Gu, H. Y. Chen, and H. R. Ma, "Conceal an entrance by means of superscatterer," *Appl. Phys. Lett.*, Vol. 94, No. 22, 223513–223515, 2009.
4. Chen, H. Y., X. D. Luo, H. R. Ma, and C. T. Chen, "The anti-cloak," *Optics Express*, Vol. 16, No. 19, 14603–14608, 2008.
5. Lai, Y., H. Y. Chen, D. Z. Han, J. J. Xiao, Z.-Q. Zhang, and C. T. Chan, "Illusion optics: The optical transformation of an object into another object," *Phys. Rev. Lett.*, Vol. 102, No. 25, 253902–253905, 2009.
6. Lai, Y., H. Y. Chen, Z.-Q. Zhang, and C. T. Chan, "Complementary media invisibility cloak that cloaks objects at a distance outside the cloaking shell," *Phys. Rev. Lett.*, Vol. 102, No. 9, 093901–093904, 2009.
7. Chen, H. Y., C. T. Chan, S. Y. Liu, and Z. F. Lin, "A simple route to a tunable electromagnetic gateway," *New J. Phys.*, Vol. 11, No. 8, 083012–083024, 2009.
8. Grbic, A. and G. V. Eleftheriades, "Periodic analysis of a 2-D negative refractive index transmission line structure," *IEEE Trans. Antennas Propag.*, Vol. 51, No. 26, 2604–2611, 2003.
9. Gok, G. and A. Grbic, "Tensor transmission-line metamaterials," *IEEE Trans. Antennas Propag.*, Vol. 58 , No. 5, 1559–1566, 2010.

About the Zero Point Energy, Zero Point Mass, Zero Point Temperature and Zero Point Motion in the Subatomic World and Photonics

Antonio Puccini
Department of Neurophysiology of Order of Malta, Naples, Italy

Abstract— The Heisenberg Uncertainty Principle states that no particle can be completely motionless (since it is not possible to know two *complementary parameters* of e a particle at the same time), it will at least oscillate around a plane: in this case we will talk about *Zero Point Motion*. From Quantum Mechanics we learn that a real particle will never have a null energy, but it will always have a minimum possible energy called *Zero Point Energy*. We also learn from Quantum Mechanics that Absolute Zero temperature can never be reached. At this temperature, in fact, the motion would cease and we would be able to know simultaneously the two *complementary parameters* we mentioned before: the position and the momentum of the same particle. In a number of cases, in fact, extremely low temperature have been reached, but never touching $-273,15^\circ$ Celsius. Thus we will talk about *Zero Point Temperature*.

Relativity's Theory, on its turn, tells us that mass and energy are equivalent. Einstein, in fact, realized that scientists were wrong keeping about the mass and E as two phenomena which though linked, were basically different. On the contrary, he understood that they had exactly equal behaviours: both expanded and contracted according to an identical factor. Under every significant aspect, Einstein concluded mass and E were entities *indistinguishable and interchangeable*, and formulated his famous formula: $E = mc^2$. So any particle having energy should carry a mass, though tiny, corresponding to the energy of the examined particle divided the square of the speed of light.

1. INTRODUCTION

We learn from Quantum Mechanics(QM) that "just as a particle will never have a null energy (E), that is zero, but a fundamental minimal E: the Zero Point Energy (ZPE). In the same way the particle, because of its *undulation aspect*, will never be able to remain completely still, that is with a zero motion" [1]: in this case we will talk about Zero Point Motion (ZPMt). This goes in accordance with Heisenberg's Uncertainty Principle (HUP): it is not possible to know two *complementary parameters* of a particle at the same time, such as its *position* (x) and *momentum* (p). As it is known, the p is given by the mass (m) of the particle times its speed (v): $p = m \cdot v$. Thus, a completely motionless particle would give us simultaneously quite precise information about its x and p which, in this case, would be zero. However, this will never be possible, this is why a particle will never be completely still — even if it is apparently motionless, (as inside a solid) — at least it will keep *vibrating*, that is it will preserve a vibrating motion, also the smallest possible.

Thus, as Chandrasekhar reminds us "there is a ZPMt which corresponds to the ZPE" [1]. Still in accordance with HUP [2, 3], a particle will never be at a temperature of Absolute Zero. At this temperature, in fact, the motion would cease and we would be able to know simultaneously the two *complementary parameters* we mentioned before. We will talk about Zero Point Temperature (ZPT), which can never coincide with the unreachable temperature of the Absolute Zero. In fact extremely low temperatures have been reached, but never touching -273.15° Celsius. Thus, Hawking reminds us that "the temperature is just a measurement of the mean E — or of the mean speed — of the particles" [4]. As in the case of a particle there should not be a zero E, as we should never reach a temperature of Absolute Zero, in the same way (also considering what Hawking and HUP stated) a particle should never reach a zero speed, or motion. We need to consider, besides, that the ZPE and the ZPMt are worth both for a subatomic particle and for the atom in itself.

2. DISCUSSION

We cannot forget the worries and the doubts which bothered Einstein in the first years of last century, till he traced the fundamental concepts of Restricted Relativity. "Einstein realized that scientists were wrong keeping thinking about the mass and the E as two phenomena which, though linked, were basically *different*. Einstein understood that they had also exactly equal behaviors: both expanded and contracted according to an identical factor. He concluded that mass and E

were entities *indistinguishable and interchangeable*: as a person wearing different clothes or showing different hairstyle. The mass and the E could be compared to the American dollars and the British pounds: though they appeared different, they were basically the same thing, that is a kind of exchange currency. Besides, even though the two currencies had different values, there was an exchange rate between them, that is a formula which fixed the rate between them" [5]. Essentially the problem the young Einstein had to face was the following: which was the formula of the rate of exchange relating the mass and the E? Einstein managed to find the right inspiration and he formulated mathematically the Principle of Equivalence Mass-Energy:

$$E = mc^2 \tag{1}$$

Here it is, at last, the long-desired formula of the exchange rate! Einstein's satisfaction was big, since the relation between Mass and Energy had revealed so easy, so elegant: since the mass and the E were two entities interchangeable, science did not have to deal with two Principles of Conservation. "The mass could be destroyed and transformed in E, in the same way the E could be destroyed and transformed in mass" [5]. The Principle of Equivalence Mass-Energy are two faces of the same coin, since they are *interchangeable* and since we mentioned the ZPE, why can't we think about a Zero Point Mass (ZPM)? After all mass and E are equivalent!. According to Planck-Einstein equation, the E of the P is:

$$E = h \cdot f \tag{2}$$

where h is the Planck's constant, equal to $6.625 \cdot 10^{-27}$ [erg $\cdot$ s] and f is the frequency of oscillation of the P per second, which we indicate with $10^n \cdot$ [1/s]. We get that the E of the P is not constant, but changes in a rate directly proportional to the f of the considered P.

Einstein explained its Equivalence Principle: "It represents the connection between *inertial mass* and energy" [6]. Let's consider, thus, which could be the *inertial* E of the P, that is its minimum E, as to say its ZPE. Well, we cannot know with accuracy: it depends on the minimum number of oscillations that a P can make in a second, that is it depends on the value of 10^n. We cannot exclude that the P is able to reach the minimum limit of one oscillation per second, that is $f = 10^{\circ}$ [1/s]: nothing forbids it and HUP allows it. In this case, with reference to Eq. (2), let's calculate which could be the ZPE of the P:

$$\text{ZPE} = h \cdot f = (6.625 \cdot 10^{-27}, [\text{erg} \cdot \text{ s}]) \cdot 10^{\circ}\,[1/\text{s}] \tag{3}$$

That is:

$$\text{ZPE} = 6.625 \cdot 10^{-27}\,[\text{erg}] \tag{4}$$

We have that the ZPE of the P corresponds to the value of h, which is an energetic value. In this case we got the possible value of the minimum oscillating motion allowed to the P. Whereas, if the minimum limit of oscillations of the P was (i.e.) 100, this value would be indicated with 10^2 [1/s]. In this case we would have:

$$E = h \cdot f = h \cdot 10^2\,[1/\text{s}] = 6.625 \cdot 10^{-25}\,[\text{erg}] \tag{5}$$

Along with Eq. (1), let's try to calculate the value of the *inertial mass* of the P, which can be indicated with the value of its *minimal mass*, that is with its ZPM:

$$\text{ZPM} = \text{ZPE}/c^2 \tag{6}$$

If we consider that the minimum possible value of the ZPE of the P can correspond to the one emerging from Eq. (4), we have:

$$\text{ZPM} = 6.625 \cdot 10^{-27}\,[\text{erg}]/(2.9979 \cdot 10^{10}\,[\text{cm/s}])^2 \tag{7}$$

Since the erg value is expressed in [g $\cdot$ cm/s$^2\cdot$ cm], that is in [g $\cdot$ cm^2/s^2], developing the (7), we have:

$$\text{ZPM} = 6.625/8.9874) \cdot 10^{-27-20}\,[\text{g} \cdot \text{ cm}^2/\text{s}^2] \cdot [\text{s}^2/\text{cm}^2] \tag{8}$$

That is

$$\text{ZPM} = 0.7372 \cdot 10^{-47}\,[\text{g}] \tag{9}$$

That is:

$$\text{ZPM} = 7.37 \cdot 10^{-48}\,[\text{g}] \tag{10}$$

3. CONCLUSIONS

Thus, also considering the minimum possible oscillation of the P (it twill never be able to be completely still: HUP forbids it), and, as consequence, considering its minimum possible E (ZPE), we get that the P has a its own *inertial mass*, which coincides with its ZPM [7].

It is certainly an extremely low value, yet $\neq 0$. Just incidentally let's mention something about the neutrino. The neutrino too, up until short ago, was considered massless, though having a certain E (thus in contrast with the Mass-Energy Equivalence Principle). Later the control of its *oscillation* and the well known Superkamiokande experiment permitted to consider the neutrino as having a its own mass, though extremely small.

There is also another particle, still hypothetical, considered massless: the graviton. As we know it is the *quantum*, the boson of the gravity force (GF). However the GF, as a *force*, subtends a E: its force, always of attraction, so evident in galactic systems, is carried out through a E, that is through a continuous *work* carried out by the graviton. Indeed the Quantum Field Theory gives an energetic value to the graviton, just to justify the way the GF is carried out.

However, still long with the Mass-Energy Equivalence Principle, since it has been given an energetic value to the graviton, in the same way it should correspond also an *equivalent mass*, the smallest we can imagine, certainly smaller than the ZPM of the P. In fact, the ZPM should coincide with the ZPE corresponding to the examined particle divided c^2. With regard to this Feynman wrote: "E and mass differ only by a factor c^2 which is merely a question of units, so we can say *E is mass* " [8]. In other words, the mass of any particle having E — all real particles have! — corresponds to the specific E of the examined particle, divided the square of the speed of light in vacuum.

We can just conclude that it is much more likely that as every physical system or every particle, even a real boson, has a minimal quantity of E (ZPE), following the Equivalence Principle they will have an *equivalent ZPM*, and preserve a ZPMt.

REFERENCES

1. Chandrasekhar, B. S., *Why Things Are the Way They Are*, Vol. 84, 125, Il Saggiatore ed., Cambridge University Press, Milano, 1988.
2. Heisemberg, W., *Z. Phys.*, Vol. 43, 184–185, 1927.
3. Puccini, A., "Uncertainty principle and electromagnetc waves," *Journal of Electromagnetic Waves and Applications*, Vol. 19, No. 7, 885–890, 2005.
4. Hawking, S., *A Brief History of Time*, Vol. 137, 128, Bibl. Univ. Rizzoli, Milano, 1990.
5. Guillen, M., *Five Equations That Changed the World*, 267–269, TEA Ed., Milano, 1995.
6. Galison, P., "L'equazione del sestante," *It Must Beautiful: Great Equations of Moderne Science*, 119, Il Saggiatore ed., Graham Farmelo, Milano, 2005.
7. Puccini, A., "About the restmass of photon; Session: Electromagnetic theory and design on the optical dispersive materials, invisible cloak and photonic crystals," *PIERS Proceedings*, Marrakesh, Morocco, March 20–23, 2011.
8. Feynman, R. P., *The Feynman Lectures on Physics*, Vol. 3, No. 12, 1617, Zanichelli, Ed., 1989 California Institute of Technology, Bologna, 1965.

Comment on "Permanence of Light Velocity" by Applying the New Theory on Electromagnetic Wave

Yelin Xu[1] and Qiang Xu[2]

[1]Institute of Biophysics, Chinese Academy of Sciences, Beijing 100101, China
[2]Institute of Theoretical Physics of Haikou, Haikou 570206, China

Abstract— The author's latest paper on electromagnetic wave indicated that, electromagnetic wave had the function of continuously adjusting it self's velocity automatically, namely CAVA. Here, we will continue to discuss CAVA. After the theoretical analyses based on experimental results, this paper reaches the conclusion that CAVA has advantage as well as disadvantage. The advantage is that, under the condition that the light source is stationary, the velocity of electromagnetic wave keeps invariable because of CAVA, and this improves the quality of radio communication; the disadvantage is that real light velocity is variable when the light source is moving, but CAVA is not able to distinguish its true features and adjusts it to C stereotyped, and this brings us the false appearance of the permanence of light velocity. This paper indicates that, when the light source is stationary, light velocity is invariable; when the light source is moving, light velocity is variable.

1. INTRODUCTION

Reference [1] points out that the velocities of electromagnetic wave have a reference system. Since it is so, they inevitably obey Galileo's composition formulas of velocities. This point of view was proved by French scientist G. Sagnac's experiment [2] in 1913.

Reference [1] also indicates that electromagnetic wave has the function of CAVA, the velocity problem of electromagnetic wave is the character of electromagnetic wave itself. The velocity and space-time of electromagnetic wave are two matters which are completely independent and irrelevant to each other.

Reference [3] abandoned the hypotheses of "Permanence of Light Velocity" and "Space-time is variable", it successfully derived the formulas of Relativity by applying Galileo's view of space-time and Newton mechanics. It was also simple and easy to be understood. Thus, how to comment on "Permanence of Light Velocity" turns to be a problem that interests all of us, and this paper will solve the problem.

2. ANALYSIS ON THE LENS OF AN EQUIPMENT

Figure 1(a) is a lens in cosmic space ($\varepsilon_2\mu_2$). To show it more clearly, an eye is drawn to express the location of the observer. A ray is divided into three parts which are connected with the eye by dotted lines. If the velocity of the incident ray is $(C-u)$, obviously the velocity of the ray while it is rushing in the lens v_7 is $(\varepsilon_2\mu_2)^{-1/2}$, and when the ray goes into vacuity again, its velocity becomes C.

From reference [1] we can know that the consecutive changes of light velocity can be expressed by Figure 1(b), where curve ① stands for the velocity changes of a ray in vacuity and curve ② stands for that in a lens. When the ray reaches the lens of an equipment, the numerical value of it's velocity correspondingly locates at point M, but because of CAVA, M moves to N, then to B,

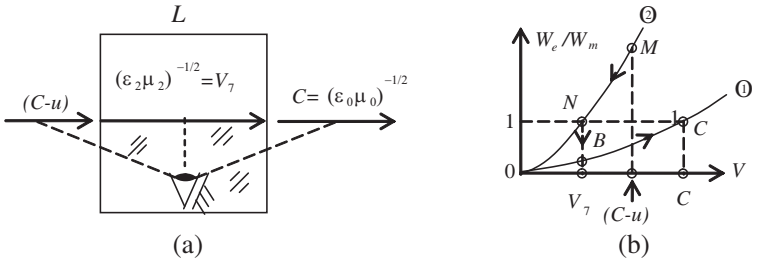

Figure 1: For a beam of light with arbitrary speed in vacuity, its velocity will turn to C once it passes the lens.

and finally reaches C. That is to say, for a ray with arbitrary speed in vacuity, its velocity will turn to C once it passes the lens. Any equipment has lens, therefore, we should be cautious to any measurement result.

When we are asked about the light velocity of a ray after it passes the lens, if the answer is C, then it's correct; but if we are asked about the velocity of this ray when it's rushing towards the lens, the answer "C" will be incorrect, and this mistake is brought to us by CAVA.

The method to avoid this mistake is to place two receivers on the route of the ray. Assume that the distance between these two receivers is ΔS, and it takes the light pulse Δt to pass the two receivers, then the actual light velocity will be $\Delta S/\Delta t$. It is obvious that the problems of light velocity are complicated, and they should be treated differently.

We will analyze the situations when the light source or emitter is on the star and on the earth respectively.

3. ANALYSIS ON LIGHT VELOCITY WHEN THE LIGHT SOURCE OR EMITTER IS ON A STAR

As Figure 2 shows, S expresses a star, V is the cosmic vacuity, and E stands for the earth. We stay on the earth and see the star moving away from us in uniform rectilinear motion with the velocity of u. In Figure 2(a), we assume that the star is motionless and the earth is moving to the right. The light velocity is analyzed as following.

When the emitter and the observer are relatively stationary, light velocity in vacuity is constant C, there is:

$$V_1 = V_2 = C \tag{1}$$

When the light enters into atmosphere, because of the acceleration function from CAVA [1], we can know that:

$$V_3 = C + u \tag{2}$$

When the observer and the light are moving to the same direction, there is:

$$V_4 = C - u \tag{3}$$

Because that CAVA can adjust light velocity to a constant, let $\varepsilon_1\mu_1$ be the capability of the atmosphere, we get:

$$V_5 = (\varepsilon_1\mu_1)^{-1/2} \approx C \tag{4}$$

When this ray leaves the earth atmosphere, the surface of the earth that the ray is emitted can be regarded as a light source, there is:

$$V_6 = C \tag{5}$$

If we regard that the earth is motionless and the star moves to the left, see Figure 2(b), the results are completely identical with formula (1) to (5). This is because that the earth and the star all stay in the cosmic vacuity.

4. ANALYSIS ON LIGHT VELOCITY WHEN THE LIGHT SOURCE OR EMITTER IS ON THE EARTH

As Figure 2 shows, S is the emitter train, V is the earth atmosphere, and E the receiver train. In Figure 2(a), the emitter train is still and the receiver train is moving.

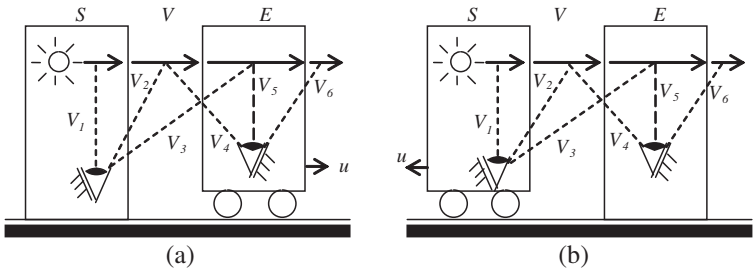

Figure 2: The method of defining light velocity.

As the emitter and the observer are relatively stationary, there is:

$$V_1 = V_2 = C \tag{6}$$

After the light (ray) enters into the receiver train, because of the acceleration of CAVA, there is:

$$V_3 = C + u \tag{7}$$

For the observer and the ray are moving to the same direction, we get:

$$V_4 = C - u \tag{8}$$

Because of CAVA, there is:

$$V_5 = C \tag{9}$$

When this ray leaves the receiver train and reenters into the atmosphere, its velocity in the atmosphere is C, the observer and the ray are traveling to the identical direction, we get:

$$V_6 = C - u \tag{10}$$

Figure 3 illustrates the light velocity changes because of CAVA. Where ① stands for the light velocity curve in the air in the sealed receiver train, curve ② represents that in the atmosphere on the earth. If the velocity of light is C in the atmosphere, then it locates at point M correspondingly. When the ray enters into the receiver train, it locates at point N correspondingly, because of CAVA function of the air in the train, point N moves to point B automatically. When the ray leaves the receiver train and reenters into the atmosphere, it locates at point D correspondingly, and because of CAVA of the earth atmosphere, D moves to M automatically. If the receiver train is an open vehicle, the conclusion remains unchanged, because the lens of the equipment also has the function of CAVA.

In Figure 2(b), the emitter train S is moving and the receiver train E is still, the light velocity at this moment is analyzed as:

$$V_1 = C \tag{11}$$

As the velocity of the light in the atmosphere is C, there is:

$$V_2 = V_3 = C + u \tag{12}$$

For the receiver train is motionless, so:

$$V_4 = V_5 = V_6 = C \tag{13}$$

As both S and E are in the atmosphere, Figures 2(a) and 2(b) lead to different results.

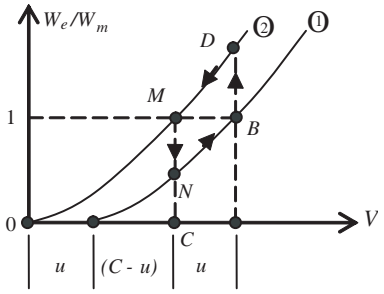

Figure 3: Changes of the light velocity because of CAVA when the receiver train is moving.

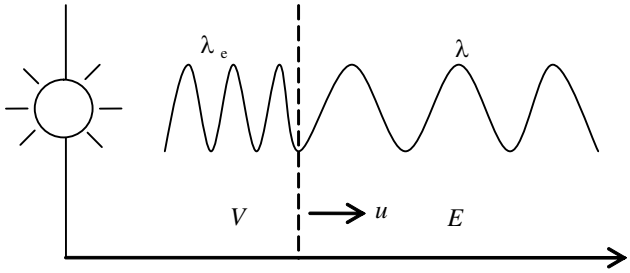

Figure 4: Change of the wavelength of the star light after it enters the earth atmosphere.

Table 1: The measurement results of light velocity.

Year	C (km/sec)
1849	315000
1950	299789.3 ± 0.8
1956	299791 ± 2
1958	299795 ± 0.1

Table 2: Real light velocity under different conditions.

	Light velocity						
	V_1	V_2	V_3	V_4	V_5	V_6	
Universe	C	C	$C+u$	$C-u$	C	C	Fig. 2(a) and (b)
the Earth	C	C	$C+u$	$C-u$	C	$C-u$	Fig. 2(a)
	C	$C+u$	$C+u$	C	C	C	Fig. 2(b)

5. EXPERIMENTAL BASIS OF "PERMANENCE OF LIGHT VELOCITY"

Experiments indicate that under the condition that the light source and the receiver are relatively stationary, light velocity is constant C. Table 1 lists part of the results [4] which support this viewpoint. Obviously, the statement of "Permanence of Light Velocity" is tenable here.

6. EXPERIMENTAL BASIS OF "LIGHT VELOCITY IS VARIABLE"

Experiments reveal that under the condition that the light source and the receiver have a relative motion, light velocity is variable. The following listed events support this viewpoint.

(1) French scientist G. Sagnac's experiment in 1913 proved that light velocity is variable.

(2) The existence of Doppler Effect of light explains that light velocity is variable.

(3) The red-shift measurement result of optical spectrum of the stars in universe is the most powerful proof of "light velocity is variable". The analysis is as following:

We'll go on discussing the topic in Section 2. The dotted line in Figure 4 expresses the edge of the earth atmosphere. Take the star as the reference system, the electromagnetic wave is consecutive, after the electromagnetic wave enters the earth atmosphere, its frequency f is invariant; the velocity of the electromagnetic wave rises, so its wavelength increases. Assume that the original wavelength of the light is λ_e, the increased wavelength is λ, there is:

$$f\lambda_e + u = f\lambda \tag{14}$$

$$\lambda - \lambda_e = \frac{u}{f} \tag{15}$$

$$Z = \frac{\lambda - \lambda_e}{\lambda_e} = \frac{u}{C} \tag{16}$$

Formula (16) is namely the red-shift formula, it is consistent with the observation results on the universe [4, 5], where λ and λ_e are all length. In Galileo's space-time, length is invariable. Therefore, when observing from the earth, formula (16) is still correct.

7. CONCLUSION

(1) To summarize this paper, we can get Table 2.

It can be seen from Table 2 that because of the participation of CAVA, the problem of light velocity gets complicated. And this reminds engineers to be cautious to the problems related to light velocity and do not treat them the same. Only with our careful analysis can our radio ranging technique be more accurate.

(2) Rule of light velocity: when the light source is stationary, light velocity is invariable; when the light source is moving, light velocity is variable.

REFERENCES

1. Xu, Y. L., "Study on description of electromagnetic wave," *PIERS Online*, Vol. 6, No. 1, 41–45, 2010.
2. Zhao, G. C., *The Principles and Technologies of Fiber-Optic Gyroscope*, 32, National Defense Industry Press, Beijing, China, 2008.
3. Xu, Y. L., "A simple method for deriving the formulas of relativity," *Proceeding of IEEE-2010 International Conference on Physics Science and Technology*, Hong Kong, China, http://www.icpst.org/, 2010.
4. Liang, L. F. and P. Jiang, *Physics*, Fudan University Press, Vol. 573, 130, 2005.
5. Ohanian, H. C. and R. Ruffini, *Gravitation and Spacetime*, W. W. Norton & Company, Inc., Section 3, Chapter 9, 1994.

A Note on Variational Theory for Piezoelectricity with Voids

Ji-Huan He
National Engineering Laboratory for Modern Silk, College of Textile and Engineering
Soochow University, 199 Ren-ai Road, Suzhou 215123, China

Abstract— A classical (not Gurtin-type) variational theory for piezoelectric materials with voids is established by the semi-inverse method.

1. INTRODUCTION

Generally speaking, there exist two basic ways to describe a physical problem: 1) by partial differential equations (PDEs) with boundary conditions (BCs); 2) by variational principles (VPs). The PDE model requires strong local differentiability (smoothness) of the physical field, while its VP partner requires weaker local smoothness or only local integrability. The VP model is also a sound theoretical foundation of the finite element method (FEM) and other direct variational methods such as Ritz's, Trefftz's and Kantorovitch's methods.

In the theory of elasticity, variational formulations have provided not only a unifying point of view but they also have facilitated the development of many approximate methods of analysis. There exists an innumerable literature on the variational theory of elasticity. However, for piezoelectricity, the variational theory has not received extensive attention. Applying the semi-inverse method [1–3], the present author obtained a coupled variational principles of piezoelectricity [4], a variational principle for thermopiezoelectricity [5], some generalized variational principles for nonlinear thermopiezoelectricity [6], a variational theory for piezoelectric ceramics with surface electrodes [7], and a Hamilton principle of linear thermopiezoelectricity [8]. Liu obtained a family of unified classical variational principles in coupled thermoelastical dynamics [9].

Recently Luo and Kuang established a Gurtin-type variational principle for piezoelectric materials with voids [10].

The theory of elastic materials with voids or vacuous pores was first established by Nunziato and Cowin [11, 12]. This theory enables us to analysize the behaviour of elastic porous solids, which can be widely found in engineering, such as rock and soil, bone, manufactured porous materials.

Ciarletta and Scalia [13] studied a linear thermoelastic theory of material with voids, and established a uniqueness and reciprocal theorems. Dhaliwal and Wang [14] proposed a domain of influence theorem for the linear theory of elastic materials with voids. Iesan [15] established a variational theory for thermoelastic materials with voids, and Pi and Jin [16] obtained a generalized variational principle for static linear elastic materials with voids.

2. MATHEMATICAL RELATIONS

Let x_i $(i = 1, 2, 3)$ be rectangular Cartesian coordinates and Ω be a regular region of three dimensional space occupied by an elastic material with voids. According to Cowin and Nunziato's linear elastic theory of elastic materials with voids, we have the following equations

1) Equilibrium Equations

$$\sigma_{ij,j} + \rho \bar{f}_i = 0, \tag{1}$$

$$h_{i,i} + g + \rho l = 0, \tag{2}$$

where σ_{ij} is the symmetric stress tensor, ρ is the mass density, $\bar{f}_i$ is the body force, h_i is the equilibrated stress vector, l and g represent the extrinsic equilibrated body force and the intrinsic equilibrated body force respectively.

2) Geometrical Equations

$$\varepsilon_{ij} = \frac{1}{2}(u_{i,j} + u_{j,i}), \tag{3}$$

$$e_i = \varphi_{,i}. \tag{4}$$

3) Constitutive Equations

$$\sigma_{ij} = E_{ijkl}\varepsilon_{kl} + M_{ijk}e_k - \beta_{kij}E_k + \gamma_{ij}\varphi, \tag{5}$$
$$D_i = \beta_{ijk}\varepsilon_{jk} + a_{ij}E_j - p_{ij}e_j - d_i\varphi, \tag{6}$$
$$h_i = A_{ij}e_j + M_{ikli}\varepsilon_{kl} + p_{ik}E_k + b_i\varphi, \tag{7}$$
$$g = \varsigma\varphi + \eta_{ij}\sigma_{ij} + a_ih_i + c_iD_i. \tag{8}$$

in which, u_i is the elastic displacement vector, ε_{ij} is the strain vector, E_{ijkl}, M_{ijk}, β_{kij}, γ_{ij}, a_{ij}, p_{ij}, d_iA_{ij}, b_i, ς, η_{ij}, a_i, c_i are characteristic coefficients of material, and the comma followed by a subscript stands for partial derivatives with respect to the coordinates.

4)Maxwell Equations

$$D_{i,i} = \rho_e, \tag{9}$$
$$E_i = -\Phi_{,i}, \tag{10}$$

where D_i is the vector of the electric displacement, E_i is the vector of the electric field, Φ is the electric potential and ρ_e is the volume density of free charges.

3. GENERALIZED VARIATIONAL PRINCIPLE

By the semi-inverse method, we establish a variational principle with 10 kinds of independent variables (u_i, σ_{ij}, ε_{ij}, φ, e_i, h_i, g, E_i, D_i, Φ):

$$J(u_i, \sigma_{ij}, \varepsilon_{ij}, \varphi, e_i, h_i, g, E_i, D_i, \Phi) = \iiint_\Omega L d\Omega. \tag{11a}$$

where the Lagrangian is expressed in the form

$$\begin{aligned} L = {} & u_i(\sigma_{ij,j} + \rho\bar{f}_i) + \varphi(h_{i,i} + g + \rho l) + \varepsilon_{ij}\sigma_{ij} \\ & -\frac{1}{2}\varepsilon_{ij}E_{ijkl}\varepsilon_{kl} - \varepsilon_{ij}M_{ijk}e_k + \varepsilon_{ij}\beta_{kij}E_k \\ & +D_i(E_i + \Phi_{,i}) + \rho_e\Phi - \frac{1}{2}E_ia_{ij}E_j - E_ip_{ij}e_j \\ & +e_ih_i - \frac{1}{2}e_iA_{ij}e_j + \lambda(g - \varsigma\varphi - \eta_{ij}\sigma_{ij} - a_ih_i - c_iD_i)^2 \end{aligned} \tag{11b}$$

where λ is a penalty parameter, i.e., $\lambda \gg 0$.

[Proof] Calculating variation with respect to g, we have

$$\delta g: \quad \varphi + 2\lambda(g - \varsigma\varphi - \eta_{ij}\sigma_{ij} - a_ih_i - c_iD_i) = 0. \tag{12}$$

In case $\lambda \to \infty$, we have

$$g - (\varsigma\varphi + \eta_{ij}\sigma_{ij} + a_ih_i + c_iD_i) = 0. \tag{13}$$

In finite element application the value of λ should be very large, for example $\lambda = 10000$.

Now making the functional stationary, we obtain the following Euler equations:

$$\delta u_i: \quad \sigma_{ij,j} + \rho\bar{f}_i = 0, \tag{14}$$
$$\delta\sigma_{ij}: \quad -\frac{1}{2}(u_{i,j} + u_{j,i}) + \varepsilon_{ij} + 2\lambda G\eta_{ij} = 0, \tag{15}$$
$$\delta\varepsilon_{ij}: \quad \sigma_{ij} - E_{ijkl}\varepsilon_{kl} - M_{ijk}e_k + \beta_{kij}E_k = 0, \tag{16}$$
$$\delta E_i: \quad \varepsilon_{kl}\beta_{ikl} + D_i - a_{ij}E_j - p_{ij}e_j = 0, \tag{17}$$
$$\delta D_i: \quad E_i + \Phi_{,i} + 2\lambda Gc_i = 0, \tag{18}$$
$$\delta\Phi: \quad -D_{i,i} + \rho_e = 0, \tag{19}$$
$$\delta e_i: \quad -\varepsilon_{kl}M_{kli} - E_jp_{ij} + h_i - A_{ij}e_j = 0, \tag{20}$$
$$\delta\varphi: \quad h_{i,i} + g + \rho l - 2\lambda\varsigma G = 0, \tag{21}$$

where $G = g - \varsigma\varphi - \eta_{ij}\sigma_{ij} - a_ih_i - c_iD_i$. In view of Eq. (13), the above equations satisfy all field equations.

We can also obtain a variational principle with 9 kinds of independent variables (u_i, σ_{ij}, ε_{ij}, φ, e_i, h_i, E_i, D_i, Φ), the Lagrangian can be expressed in the form

$$\begin{aligned} L_1 &= u_i(\sigma_{ij,j} + \rho\bar{f}_i) + \varphi(h_{i,i} + \tilde{g} + \rho l) + \varepsilon_{ij}\sigma_{ij} - \frac{1}{2}\varepsilon_{ij}E_{ijkl}\varepsilon_{kl} - \varepsilon_{ij}M_{ijk}e_k + \varepsilon_{ij}\beta_{kij}E_k \\ &\quad + D_i(E_i + \Phi_{,i}) + \rho_e\Phi - \frac{1}{2}E_i a_{ij}E_j - E_i p_{ij}e_j + e_i h_i - \frac{1}{2}e_i A_{ij}e_j \end{aligned} \tag{22}$$

where $\tilde{g}$ is called restricted variable, i.e., $\delta\tilde{g} = 0$. In the simulation procedure, the value of g is prescribed by $g^{(n+1)} = \varsigma\varphi^{(n)} + \eta_{ij}\sigma_{ij}^{(n)} - a_i h_i^{(n)} - c_i D_i^{(n)}$, where the subscript n denotes the nth iteration value.

4. CONCLUSION

In the paper, by the semi-inverse method, we obtain a generalized variational principle for the discussed problem.

ACKNOWLEDGMENT

This work is supported by National Natural Foundation of China.

REFERENCES

1. He, J. H., "Generalized Hellinger-Reissner principle," *ASME Journal of Applied Mechanics*, Vol. 67, No. 2, 2000, 326–331.
2. He, J. H., "A classical variational model for micropolar elastodynamics," *International J. of Nonlinear Sciences and Numerical Simulation*, Vol. 1, No. 2, 133–138, 2000.
3. He, J. H., "A variational model for micropolar fluids in lubrication journal bearing," *International J. of Nonlinear Sciences and Numerical Simulation*, Vol. 1, No. 2, 139–142, 2000.
4. He, J. H., "Coupled variational principles of piezoelectricity," *Int. J. Engineering Sciences*, Vol. 39, No. 3, 323–341, 2000.
5. He, J. H., "A variational principle for thermopiezoelectricity based on Chandrasekharaiah's generalized linear theory," *J. University of Shanghai for Science and Technology*, Vol. 21, No. 4, 356–365, 1999.
6. He, J. H., "Generalized variational principles for nonlinear thermopiezoelectricity," *Facta Universitatis, Series: Mechanics, Automatic Control & Robotics*, Vol. 2, No. 10/2, 1253–1261, 2000.
7. He, J. H., "A variational approach to electroelastic analysis of piezoelectric ceramics with surface electrodes," *Mechanical Research Communications*, Vol. 27, No. 4, 445–450, 2000.
8. He, J. H., "Hamilton principle and generalized variational principles of linear thermopiezoelectricity," *ASME J. Applied. Mechanics*, Vol. 68, No. 3, 2001.
9. Liu, G. L., "A family of unified classical variational principles in coupled thermoelastical dynamics," *ACTA Mechematica Sinica*, Vol. 31, 165–172, 1999.
10. Luo, E. and J. Kuang, "Energy principles in dynamic theory of piezoelectric materials with voids," *Acta Mechematica Sinica*, Vol. 33, No. 2, 195–204, 2001.
11. Nunziato, J. W. and S. C. Cowin, "A nonlinear theory of elastic materials with voids," *Arch. Rational Mech. Anal.*, Vol. 72, 175–201, 1979.
12. Cowin, S. C. and J. W. Nunziato, "Linear elastic materials with voids," *J. Elasticity*, Vol. 13, 125–147, 1983.
13. Clarletta, M. and A. Scalia, "On uniqueness and reciprocity in linear thermoelasticity of materials with voids," *J. Elasticity*, Vol. 32, 1–17, 1993.
14. Dhaliwal, R. S. and J. Wang, "Domain of influence theorem in the theory of elastic materials with voids," *Int. J. Engineering Science*, Vol. 32, No. 11, 1823–1828, 1994.
15. Iesan, D., "A theory of Thermoelastic materials with voids," *Acta Mech.*, Vol. 60, 67–89, 1986.
16. Pi, D.-H. and L.-H. Jin, "Structural function theory of generalized variational principles for linear elastic materials with voids," *Applied Math. Mech.*, Vol. 12, No. 6, 565–575, 1991.

Parametric Transformation and Parametric Resonance of Confined Acoustic Phonons and Confined Optical Phonons by an External Electromagnetic Wave in Doping Superlattices

N. Q. Bau[1], N. V. Nghia[2], and L. T. Hung[3]

[1]Department of Physics, Viet Nam National University Hanoi, 334 Nguyen Trai, Hanoi, Vietnam
[2]Department of Physics, Water Resources University, 175 Tay Son, Hanoi, Vietnam
[3]University of Education, Viet Nam National University Hanoi, 144 Xuan Thuy, Hanoi, Vietnam

Abstract— The parametric transformation and parametric resonance of confined acoustic phonons and confined optical phonons by an external electromagnetic wave in doping superlattices are theoretically studied by using a set of quantum kinetic equations for phonons. The analytic expression of the parametric transformation coefficient K_1 and the threshold amplitude $E_{threshold}$ of the field in doping superlattices are obtained. Unlike the case of unconfined phonons, the formula of K_1 and $E_{threshold}$ contains a quantum number m characterizing confined phonons. Their dependence on the temperature T of the system, the wave vector $\vec{q}_\perp$ and the frequency Ω of the electromagnetic wave is studied. Numerical computations have been performed for n-$GaAs$/p-$GaAs$ doping superlattices. The results have been compared with the case of unconfined phonons, which show that confined phonons cause some unusual effects.

1. INTRODUCTION

As we know that the electron gas becomes non-stationary in the presence of an external electromagnetic wave (EEW). When the conditions of the parametric resonance are satisfied, parametric interactions and transformations (PIT) of the same kinds of excitations, such as phonon-phonon and plasmon-plasmon excitations, or of different kinds of excitations, such as plasmon-phonon excitations, will arise, i.e., the energy exchange processes between these excitations will occur [1, 2]. The PIT of acoustic and optical phonons has been considered in bulk semiconductors [3–5]. For semiconductor nanostructures, there have been several works on the generation and amplification of acoustic phonons [6–8].

Recently, there have been a lot of works on the behavior of low-dimensional system, in particular two-dimensional systems, such as semiconductor superlattices [9], quantum wells [10] and doped superlattices [11, 12]. The confinement of electrons and phonons in low-dimensional systems considerably enhances the electron mobility and leads to unusual behaviors under external stimuli. Many attempts have conducted dealing with these behaviors. For examples, the problem of the nonlinear absorption coefficient of a strong electromagnetic wave (EMW) by confined electrons in doping superlattices and quantum wells in both cases of confined phonons and unconfined phonons, have been investigated [13, 14].

The works on the PIT for low dimensional semiconductors have been studied only in the case of unconfined phonons [10, 12]. Therefore, in this paper, we have studied parametric transformation and parametric resonance of acoustic and optical phonons in doping superlattices in the case of confined phonons. The comparison of the result of confined phonons to one of unconfined phonons [12] shows that confined phonons cause some unusual effects.

2. THE PARAMETRIC RESONANCE OF CONFINED ACOUSTIC PHONONS AND CONFINED OPTICAL PHONONS IN DOPING SUPERLATTICES

We use a simple model for doping superlattices, in which electrons and phonons are confined by an infinite potential $V(z)$ of a parabolic well along the z direction and electrons are free in x-y plane. A laser wave irradiates the sample in the z direction, the electric field of the laser wave is polarized in the x-y plane and $\vec{E} = \vec{E}_0 \sin(\Omega t)$. The vector potential of the laser wave is $\vec{A}(t) = c \cdot \vec{E}_0 \cos(\Omega t)/\Omega$. Using the Hamiltonian similar the one for the system of the electron-acoustic and optical phonons in the case of unconfined phonons given in [11], we obtained a set of coupled quantum kinetic equations for the optical phonons and the acoustic phonons. Unlike the case of unconfined phonons, this quantum kinetic equations contain a quantum number m characterizing confined phonons. Using Fourier transformation, we obtain a general dispersion equation for the

PIT between confined acoustic and optical phonons in doping superlattices. Then, we limit our calculation to the case of the first-order resonance, in which $\omega_{\vec{q}}^m \pm \Omega = v_{\vec{q}}^m$. We also assume that the electron-phonon interactions is very weak. Thus, in the general dispersion equation [3, 5], we keep only the second order term in the electron-phonon interaction constant ($|C_{\vec{q}_\perp}^m|^2$ or $|D_{\vec{q}_\perp}^m|^2$) and the term $|C_{\vec{q}_\perp}^m|^2|D_{-\vec{q}_\perp}^m|^2$ is ignored. We obtain the resonant phonon modes [1, 3, 5, 10] from the general dispersion equation:

$$\omega_{\pm}^{(\pm)} = \omega_a + \frac{1}{2}\left\{(v_a \pm v_o)\Delta_q - i(\tau_a + \tau_o) \pm \sqrt{[(v_a \mp v_o)\Delta_q - i(\tau_a - \tau_o)]^2 \pm \Lambda^2}\right\} \tag{1}$$

with:

$$\tau_a \approx -\frac{1}{\hbar}\sum_{n,n'}\left|I_{n,n'}^m\right|^2\left|C_{\vec{q}_\perp}^m\right|^2 \mathrm{Im}\left[\Pi_0\left(m, \vec{q}_\perp, \omega_{\vec{q}_\perp}^m\right)\right] \tag{2}$$

$$\tau_o \approx -\frac{1}{\hbar}\sum_{n,n'}\left|I_{n,n'}^m\right|^2\left|D_{-\vec{q}_\perp}^m\right|^2 \mathrm{Im}\left[\Pi_0\left(m, \vec{q}_\perp, v_{\vec{q}_\perp}^m\right)\right] \tag{3}$$

$$\Lambda \approx \frac{2}{\hbar}\sum_{n,n'}\left|I_{n,n'}^m\right|^2\left|C_{\vec{q}_\perp}^m\right|\left|D_{-\vec{q}_\perp}^m\right|\Pi_l\left(m, \vec{q}_\perp, \omega_{\vec{q}_\perp}^m\right) \tag{4}$$

where $\Delta_q = q - q_0$, q_0 being the wave number for which the resonance is satisfied; $v_a\,(v_0)$ is the group velocity of the acoustic (optical) phonon; ω_a is the renormalization (by the electron-phonon interaction) frequency of the acoustic phonon; $\omega_{\vec{q}_\perp}^m$ ($v_{\vec{q}_\perp}^m$) is the frequency of confined acoustic (optical) phonons; m is the quantum number characterizing confined phonons; $I_{n,n'}^m$ is the electron form factor; and $C_{\vec{q}_\perp}^m$ ($D_{\vec{q}_\perp}^m$) is the electron-confined acoustic (electro-confined optical) phonon interaction constant.

From [15], we have:

$$\left|C_{\vec{q}_\perp}^m\right|^2 = \frac{\xi^2\hbar}{\rho v_s LS}\sqrt{\vec{q}_\perp^{\,2} + \left(\frac{m\pi}{L}\right)^2}; \quad \left|D_{\vec{q}_\perp}^m\right|^2 = \frac{e\hbar v_0}{\varepsilon_0 LS}\left(\frac{1}{K_0} - \frac{1}{K_\infty}\right)\frac{1}{\vec{q}_\perp^{\,2} + \left(\frac{m\pi}{L}\right)^2} \tag{5}$$

where L, S, ρ, v_s, and ξ are the length, across area, the mass density, the acoustic velocity and the deformation potential constant, respectively. ε_0 is the permittivity of free space, $\hbar v_0$ is the energy of optical phonon, K_0 and K_∞ are the static and high frequency dielectric constant, respectively.

In Eqs. (2), (3) and (4), we have:

$$\Pi_l\left(m, \vec{q}_\perp, \omega\right) = \sum_{v=-\infty}^{\infty} J_v\left(\frac{\lambda}{\Omega}\right) J_{v+l}\left(\frac{\lambda}{\Omega}\right)\Gamma\left(m,\, \vec{q}_\perp, \omega + l\Omega\right) \tag{6}$$

$$\Gamma\left(m,\, \vec{q}_\perp, \omega + l\Omega\right) = \sum_{\vec{k}_\perp}\frac{\left[f_n\left(\vec{k}_\perp\right) - f_{n'}\left(\vec{k}_\perp - \vec{q}_\perp\right)\right]}{\varepsilon_n\left(\vec{k}_\perp\right) - \varepsilon_{n'}\left(\vec{k}_\perp - \vec{q}_\perp\right) - \hbar\left(\omega + l\Omega\right)} \tag{7}$$

where $f_n(\vec{k}_\perp)$ is the Fermi-Dirac distribution function of the electron in the state $|n, \vec{k}_\perp\rangle$; $J_v(\frac{\lambda}{\Omega})$ is the Bessel function; $\lambda = \frac{e\hbar\vec{E}_0\vec{q}_\perp}{m_B\Omega}$; $\varepsilon_n(\vec{k}_\perp)$ is the energy spectrum of the electron in doping superlattices, $\varepsilon_n(\vec{k}_\perp) = \frac{\hbar^2\vec{k}_\perp^{\,2}}{2m_B} + \varepsilon_n$; $\varepsilon_n = \hbar\sqrt{\frac{4\pi e^2 n_D}{K_0 m_B}}(n + \frac{1}{2})$. Here n is the energy quantum number of the electron in the z direction; $\vec{k}_\perp$ is the electron wave vector in x-y plane; n_D is doping concentration; m_B is the electron effective mass.

In Eq. (1) the signs ($\pm$) in the subscript of $\omega_\pm^{(\pm)}$ correspond to the signs ($\pm$) in front of the root and the signs ($\pm$) in the superscript of $\omega_\pm^{(\pm)}$ correspond to other sign pairs. These signs depend on the resonance condition $\omega_{\vec{q}}^m \pm \Omega = v_{\vec{q}}^m$. For instance, the existence of a positive imaginary part of $\omega_+^{(-)}$ implies a parametric amplification of acoustic phonons. In the case that $\lambda \ll 1$, corresponding to the resonance, from Eq. (1) we obtain [10, 11]:

$$F = \mathrm{Im}\left(\omega_+^{(-)}\right) = \frac{1}{2}\left\{-(\tau_a + \tau_o) + \sqrt{(\tau_a - \tau_o)^2 + \Lambda^2}\right\} \tag{8}$$

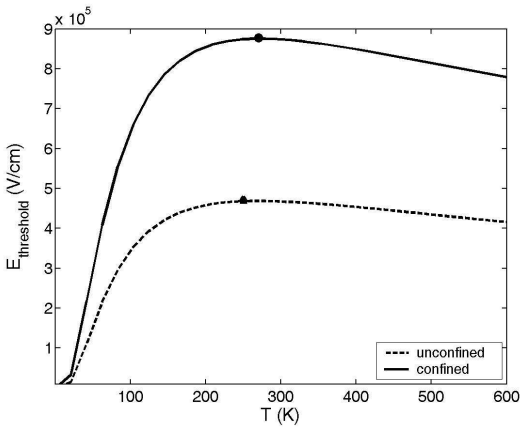

Figure 1: The dependence of $E_{threshold}$ on the temperature T.

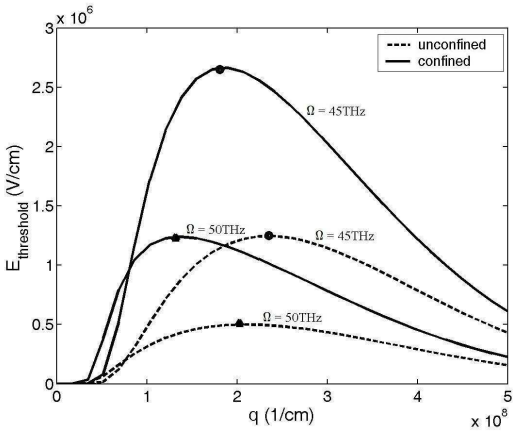

Figure 2: The dependence of $E_{threshold}$ on the wave vector $\vec{q}_\perp$.

From Eq. (8) the condition for the resonant acoustic phonon modes to have a positive imaginary part leads to $|\Lambda|^2 > 4\tau_a\tau_o$. Using this condition and Eqs. (2)–(4) then we obtain the threshold amplitude for EEW:

$$E_{threshold} = \sum_{m,n,n'} \frac{\sqrt{2\pi\beta} m_B^{3/2}\Omega^2\left[P_{nn'}(\omega^m_{\vec{q}_\perp})+\hbar\Omega\right]}{e\hbar^2\left[\vec{q}_\perp^{\,2}+\vec{q}_z^{\,2}\right]\{1-\exp(-\beta(\varepsilon_{n'}-\varepsilon_n))\}} \exp\left\{-\frac{\beta m_B}{4\hbar^2\left[\vec{q}_\perp^{\,2}+\vec{q}_z^{\,2}\right]}\left[P^2_{nn'}\left(\omega^m_{\vec{q}_\perp}\right)+P^2_{nn'}\left(v^m_{\vec{q}_\perp}\right)\right]\right\}$$
$$\times \exp\left(-\frac{\beta}{2}(\varepsilon_{n'}-\varepsilon_n)\right)\sqrt{\left(1-\exp\left(\beta\hbar\omega^m_{\vec{q}_\perp}\right)\right)\left(1-\exp\left(\beta\hbar v^m_{\vec{q}_\perp}\right)\right)}, \quad (9)$$

where $\beta = 1/(k_BT)$, $q_z = \frac{m\pi}{L}$, k_B is the Boltzmann constant,

$$P_{nn'}(\omega^m_{\vec{q}_\perp}) = \varepsilon_n - \varepsilon_{n'} - \hbar\omega^m_{\vec{q}_\perp} - \frac{\hbar^2[\vec{q}_\perp^{\,2}+\vec{q}_z^{\,2}]}{2m_B}; \quad P_{nn'}(v^m_{\vec{q}_\perp}) = \varepsilon_n - \varepsilon_{n'} - \hbar v^m_{\vec{q}_\perp} - \frac{\hbar^2[\vec{q}_\perp^{\,2}+\vec{q}_z^{\,2}]}{2m_B} \quad (10)$$

In order to clarify the mechanism for parametric resonance of acoustic and optical phonons in the case of confined phonons, we consider a *n-GaAs/p-GaAs* doping superlattices. The parameters used in this calculation are as follows: $\hbar v^m_{\vec{q}_\perp} \approx \hbar v_0 = 36.25\,\text{meV}$; $\Omega = 5\times10^{13}\,\text{s}^{-1}$; $L = 80\times10^{-10}\,\text{m}$; $\xi = 13.5\,\text{eV}$; $\rho = 5.32\,\text{gcm}^{-3}$; $\omega^m_{\vec{q}_\perp} \approx v_s = 5370\,\text{ms}^{-1}$; $K_\infty = 10.9$; $K_o = 12.9$; $m_B = 0.067m_0$; m_0 being the mass of free electron.

In Fig. 1, we show $E_{threshold}$ as a function of the temperature T, with $q_\perp = 2.8\times10^8\,\text{m}^{-1}$. When the temperature is decreased, the threshold amplitude for parametric amplification of acoustic phonons in which $\omega^m_{\vec{q}} + \Omega = v^m_{\vec{q}}$ decreases; the threshold amplitude, however, increases for the case of $\omega^m_{\vec{q}} - \Omega = v^m_{\vec{q}}$. These characteristics are the same in both case confined phonons and unconfined phonons. The figure shows that, in the case of confined phonons, the curve has a maximum value at $T = 280\,\text{K}$. In the case of unconfined phonons, the curve has a maximum value at $T = 255\,\text{K}$ [12].

In the Fig. 2, we show the dependent of $E_{threshold}$ on the wave vector $\vec{q}_\perp$ for two difference frequencies. The figure shows that the curves have maximal values and are non-symmetric around the maxima. This is due to the fact that a fixed EEF with an amplitude greater than the corresponding threshold amplitude can induce parametric amplification for acoustic phonons in two regions of the wave number corresponding to the two signs in $\omega^m_{\vec{q}} \pm \Omega = v^m_{\vec{q}}$.

In both figures, we can see the confined phonons increase the values of threshold amplitude, change the positions of the peak resonances are changed with the values of the frequency and temperature but they don't change the spectrum of $E_{threshold}$.

3. PARAMETRIC TRANSFORMATION OF CONFINED ACOUSTIC PHONONS AND CONFINED OPTICAL PHONONS IN DOPING SUPERLATTICES

Using the parametric resonant conditions $\omega^m_{\vec{q}_\perp} + s\Omega \approx v^m_{\vec{q}_\perp}$, $(s = 1, 2, 3, \ldots)$ the parametric transformation coefficient is obtained [15]:

$$K_s = \frac{1}{\hbar}\sum_{n,n'}\left|I^m_{n,n'}\right|^2 D^m_{-\vec{q}_\perp} C^m_{\vec{q}_\perp}\Pi_s(m,\vec{q}_\perp,\omega^m_{\vec{q}_\perp})\left[\frac{1}{\delta+i\gamma_0}\right], \quad (11)$$

where the quantity δ is infinitesimal.

Consider the case of $s = 1$ and note $|\delta| \ll \gamma_0$ [6], we get:

$$K_1 = \left|\frac{\Gamma}{2\gamma_0}\right|, \tag{12}$$

$$\Gamma = \frac{\lambda}{\hbar\Omega}\sum_{n,n'}\left|I^m_{n,n'}\right|^2 D^m_{-\vec{q}_\perp} C^m_{\vec{q}_\perp}\,\mathrm{Re}\,\Gamma(m,\vec{q}_\perp,\omega^m_{\vec{q}_\perp}), \tag{13}$$

$$\gamma_0 = -\frac{1}{\hbar}\sum_{n,n'}\left|I^m_{n,n'}\right|^2\left|D^m_{-\vec{q}_\perp}\right|^2\mathrm{Im}\,\Gamma(m,\vec{q}_\perp,v^m_{\vec{q}_\perp}), \tag{14}$$

$$\mathrm{Re}\,\Gamma(m,\vec{q}_\perp,\omega^m_{\vec{q}_\perp}) = -\frac{1}{A_1}\frac{m_B f_0}{2\pi\beta\hbar^2}\left[\exp(-\beta\varepsilon_n) - \exp(-\beta\varepsilon_{n'})\right], \tag{15}$$

$$\mathrm{Im}\,\Gamma(m,\vec{q}_\perp,v^m_{\vec{q}_\perp}) = -\frac{m_B f_0}{2\pi\hbar^3\sqrt{\vec{q}_\perp^{\,2}+\vec{q}_z^{\,2}}}\sqrt{\frac{2m_B\pi}{\beta}}\exp\left(-\frac{\beta m_B A_2^2}{2\hbar^2[\vec{q}_\perp^{\,2}+\vec{q}_z^{\,2}]}\right)\exp(-\beta\varepsilon_n)$$
$$\exp\left(\frac{\hbar\beta v^m_{\vec{q}_\perp}}{2}\right)sh\left(\frac{\hbar\beta v^m_{\vec{q}_\perp}}{2}\right) \tag{16}$$

$$A_1 = \frac{\hbar^2[\vec{q}_\perp^{\,2}+\vec{q}_z^{\,2}]}{2m_B} - (\varepsilon_n - \varepsilon_{n'}) + \hbar\omega^m_{\vec{q}_\perp}; \quad A_2 = \frac{\hbar^2[\vec{q}_\perp^{\,2}+\vec{q}_z^{\,2}]}{2m_B} - (\varepsilon_n - \varepsilon_{n'}) + \hbar v^m_{\vec{q}_\perp}, \tag{17}$$

where f_0 is the density of electron. K_1 is the parametric transformation coefficient of acoustic and

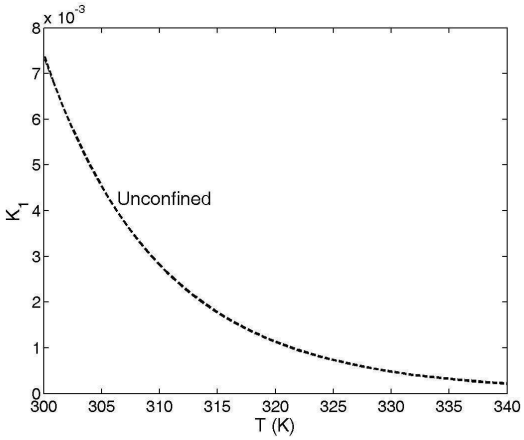

Figure 3: The dependence of K_1 on the temperature T in case unconfined phonons.

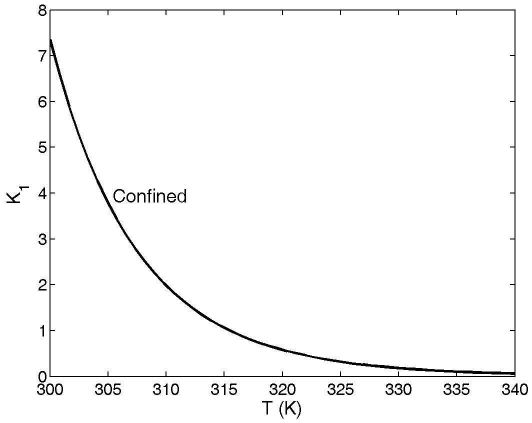

Figure 4: The dependence of K_1 on the temperature T in case confined phonons.

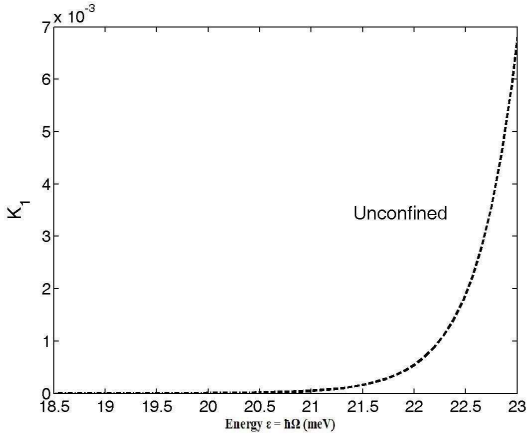

Figure 5: The dependence of K_1 on the energy $\varepsilon = \hbar\Omega$ in case unconfined phonons.

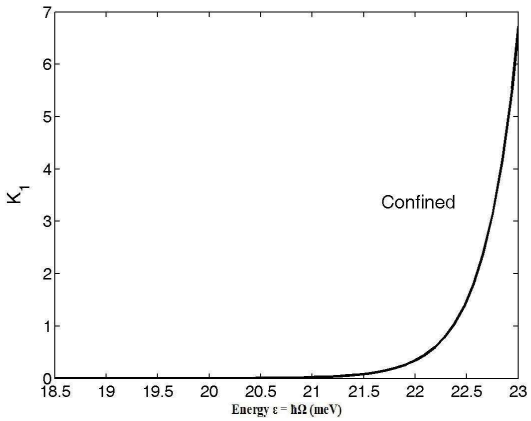

Figure 6: The dependence of K_1 on the energy $\varepsilon = \hbar\Omega$ in case confined phonons.

optical phonons in doping superlattices in the case of confined phonons when parametric resonant condition $\omega^m_{\vec{q}_\perp} + s\Omega \approx v^m_{\vec{q}_\perp}$ is satisfied.

In Figs. 3, 4, we show K_1 as a function of temperature T of the system, at frequency of the electromagnetic wave $\Omega = 3.5 \times 10^{13}\,\mathrm{s}^{-1}$. The figure shows that the curve of the parametric transformation coefficient K_1 strongly decreases when the temperature T of the system increases.

In Figs. 5, 6, we show K_1 as a function of the frequency of the electromagnetic wave, at room temperature $T = 300\,\mathrm{K}$. The figure shows that the curve strongly increases when the frequency of the EMW Ω increases.

From all figures above, we can see clearly the effect of confined phonons on the parameter transformation coefficient. Namely, the confined phonons increase the parameter transformation coefficient K_1 in doping superlattices.

4. CONCLUSION

In this paper, we have analytically investigated the possibility of parametric transformation and parametric resonance of confined acoustic phonons and confined optical phonons. We have obtained parametric resonant conditions, the threshold amplitude of the field and the parametric transformation coefficient K_1 for acoustic and optical phonons in doping superlattices in the case of confined phonons. We have also paid attention to K_1 in the case of unconfined phonons in comparison with the above result.

We have numerically calculated and graphed the threshold amplitude and the parametric transformation coefficient for *n-GaAs/p-GaAs* doping superlattices, to show that in the case of confined phonons, the curve of the parametric transformation coefficient K_1 strongly decreases when the temperature T of the system increases and strongly increases when the frequency of the electromagnetic wave Ω increases. This coefficient is decreased by a factor 10^{-3} in the case of unconfined phonons. We have shown that values of the threshold field $E_{threshold}$ in the case of confined phonons are much larger than those in the case of unconfined phonons [12].

ACKNOWLEDGMENT

This work is completed with financial support from the Viet Nam NAFOSTED.

REFERENCES

1. Phong, T. C., L. V. Tung, and N. Q. Bau, "Parametric resonance of acoustic and optical phonons in a doped semiconductor superlattice," *J. Kor. Phys. Soc.*, Vol. 53, 971–1975, 2008.
2. Silin, V. P., "Parametric action of the high-power radiation on plasma," *National Press on Physics Theory Literature*, Moscow, 1973.
3. Epstein, E. M., "Parametric resonance of acoustic and optical phonons in semiconductors," *Sov. Phys. Semicond.*, Vol. 10, 1164, 1976.
4. Vyazovskii, M. V. and V. A. Yakovlev, "Parametric resonance of acoustic and optical phonons in impurity semiconductors in low temperature," *Sov. Phy. Semicond.*, Vol. 11, 809, 1977.
5. Shmelev, G. M., N. Q. Bau, and V. H. Anh, "Parametric transformations of plasmons and phonons in semiconductors (firts part)," *Soviet Communication of JINR*, P-17-81-600, 1981.
6. Komirenko, S. M., K. W. Kim, A. A. Dimidenko, V. A. Kochelap, and M. A. Stroscico, "Generation and amplification of Sub-THz coherent acoustic phonons under the drift of two-dimensional electrons," *Phys. Rev. B*, Vol. 62, 7459, 2000.
7. Komirenko, S. M., K. W. Kim, A. A. Demidenko, V. A. Kochelap, and M. A. Stroscio, "Amplification of transverse acoustic phonons in quantum well heterostructures with piezoelectric interaction," *J. Appl. Phys.*, Vol. 90, 3934, 2001.
8. Shmelev, G. M. and N. Q. Bau, "The amplification of sound in semiconductors in the presence of two EMW," Soviet Book *Physics Effects in Semiconductors*, Kishinev, 1981.
9. Ploog, K. and G. H. Dholer, "Compositional and doping superlattices in III–V semiconductors," *Asvances in Physics*, Vol. 32, No. 3, 285–359, 1983.
10. Bau, N. Q. and T. C. Phong, "Parametric resonance of acoustic and optical phonons in a quantum well," *J. Kor. Phys. Soc.*, Vol. 42, No. 5, 647–651, 2003.
11. Bau, N. Q., N. V. Nhan, and T. C. Phong, "Calculations of the absorption coefficient of a weak Electromagnetic wave by free carriers in doped superlattices by using the Kubo-Mori method," *J. Korean. Phys. Soc.,* Vol. 41, 149–154, 2002.

12. Phong, T. C., L. V. Tung, and N. Q. Bau, "Parametric resonance of acoustic and optical phonons in a doped semiconductor superlattice," *J. Kor. Phys. Soc.*, Vol. 53, 971–1975, 2008.
13. Bau, N. Q., D. M. Hung, and L. T. Hung, "The influences of confined phonons on the nonlinear absorption coefficient of a strong electromagnetic wave by confined electrons in doping superlattices," *Progress In Electromagnetics Research Letters*, Vol. 15, 175–185, 2010.
14. Bau, N. Q., L. T. Hung, and N. D. Nam, "The nonlinear absorption coefficient of a strong electromagnetic wave by confined electrons in quantum wells under the influences of confined phonons," *Journal of Electromagnetic Waves and Applications*, Vol. 24, No. 13, 1751–1761, 2010.
15. Anh, V. H., "A quantum apprach to the parametric excitation problem in solids," Physic Report, Vol. 1, No. 64, 1–45, 1980.

All-optical Controllable Double State Switch Based on DIT by Using QD

K. Abbasian, **N. Pasyar**, **and A. Rostami**
School of Engineering Emerging-Technologies, University of Tabriz, Tabriz 51666, Iran

Abstract— In this article, we have simulated an all-optical double state controllable switch based on dipole induced transparency using photonic crystal (PC) cavity doped by a 4-level QD [1]. This switch operation is based on the dipole induced transparency phenomenon, where the optical signal has been coupled through the input fiber to the photonic crystal cavity and the optical control fields has been applied normally to the PC surface. We have realized this switch by solving Schrodinger and Poisson equations for inserted 4-level QD in photonic crystal rods, self consistently. Also, by using the proposed structure and applying the control field in the Purcell condition, the absorbing photonic crystal cavity has been converted to transparent one and switching operation has been obtained. In this paper, we have discussed frequency and dynamic operation of the switch and shown that a high quality all-optical switching operation can be obtained.

1. INTRODUCTION

In some of the reported researches in the past decade, all-optical switch is based on nonlinear optics and nonlinear phase shift which requires strong optical intensity. To avoid this requisite, EIT introduced as an important nonlinear effect on weak optical fields. Basic principles of EIT and applications of this phenomenon have been discussed by distinguished scientists [2, 3].

The main difficulty of solid state EIT is mismatching of optical probe and control fields group velocities. So, the effective length of nonlinear coupling via EIT is limited [4]. To avoid from this shortcoming, researchers have used quantum electrodynamics cavity (QED) and photon confining in it [5].

Already, we have suggested doping of multilevel atomic system in a PC cavity, which is coupled to input and output waveguides. DIT based systemhas been used, where the strong control field is applied perpendicular to the cavity. Therefore, we have gotten strong Purcell regime ($g^2/(\kappa\gamma) > 1$), where γ is the QD decay rate into modes other than the cavity modes, κ is the cavity field decay rate and g is the coupling between the cavity and the QD [1].

In this article, we have illustrated that a double state switch is realizable by two control fields in the case of 4-level nanocrystal doping in PC cavity. It has been shown that parameters such as switching power and speed are optically adjustable. We have discussed switching speed between both states of the switch and their relation with control fields' amplitudes.

2. THEORY OF OPERATION

We have studied the speed of the all-optical controllable switch illustrated in Fig. 1. Where, two waveguides 'a' and 'b' are coupled by a two dimensional photonic crystal cavity doped with a 4-level nanocrystal (QD). Input signal propagates in waveguide 'a', and the control fields are applied normally to the PC cavity. In absence of the control field, waveguides are transparent and PC cavity is opaque, so the input signal field propagates in waveguide 'a'. While in the presence of the second control field the cavity becomes transparent, so the input signal can be switched to the waveguide 'b'. Then, by applying the first control field simultaneously, the cavity changes to transparent one again.

The whole Hamiltonian of the all optical switch is written as following.

$$\begin{aligned} \mathrm{H} = {} & \hbar((\omega_{14} - i\Gamma/2)\ |4\rangle\langle 4| + \omega_{13}\,|3\rangle\langle 3| + (\omega_{12})\ |2\rangle\langle 2|) + \hbar\,(\omega_0 - i\kappa/2)\,\overset{+}{c}c + g\hbar\left(\overset{+}{c}\,\sigma_-^{14} + \sigma_+^{14}c\right) \\ & + \hbar\Omega_1\left(\sigma_+^{23}e^{-i\omega_1 t} + \sigma_-^{23}e^{i\omega_1 t}\right) + \hbar\Omega_2\left(\sigma_+^{34}e^{-i\omega_2 t} + \sigma_-^{34}e^{i\omega_2 t}\right) + \int_{-\omega_a}^{\omega_a} \hbar\, a^+(\omega)a(\omega)d\omega \\ & + \int_{-\omega_b}^{\omega_b} \hbar\omega\, b^+(\omega)b(\omega)d\omega + i\hbar\sqrt{\frac{\gamma}{2\pi}}\int_{-\omega_a}^{\omega_a}\left(\overset{+}{a}(\omega)c - \overset{+}{c}\,a(\omega)\right)d\omega + i\hbar\sqrt{\frac{\gamma}{2\pi}}\int_{-\omega_b}^{\omega_b}\left(\overset{+}{b}\,(\omega)c - \overset{+}{c}\,b(\omega)\right)d\omega, \quad (1) \end{aligned}$$

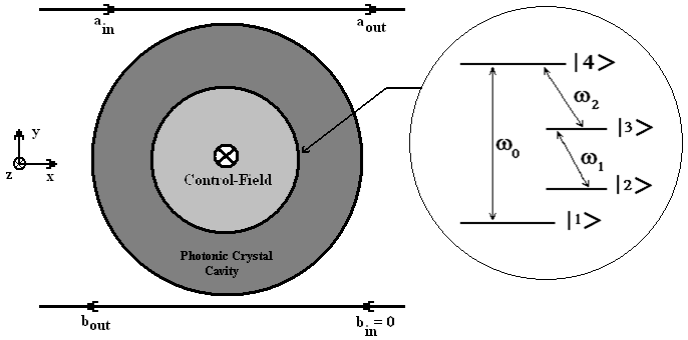

Figure 1: PC cavity-waveguide switch system, including schematic of 4-level nanocrystal doped in the cavity.

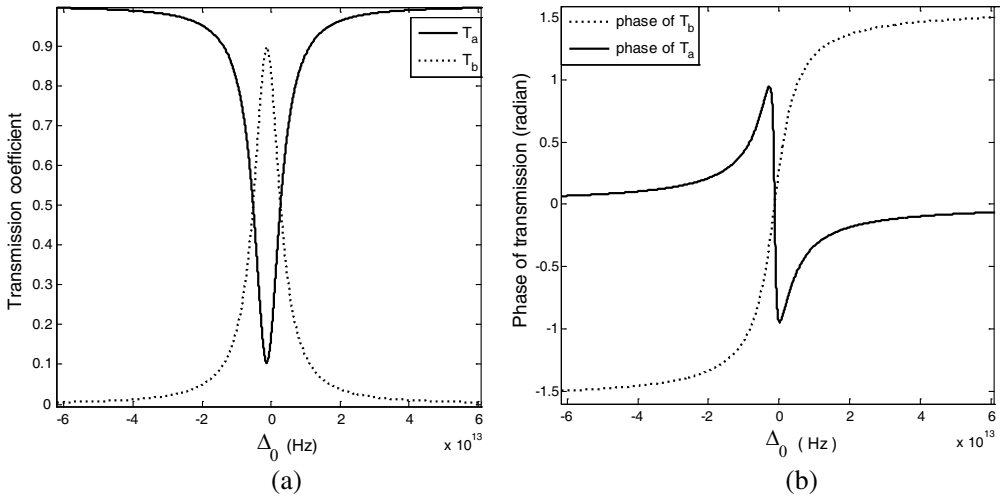

Figure 2: (a) Transmission coefficient. (b) Phase of transmission coefficient of 4-level nanocrystal doped in PC cavity versus detuning of the cavity mode from $|1> - |4>$ transition frequency. $\Delta_{14} = 0$, $\Delta_{23} = 5\,\mathrm{GHz}$, $\Delta_{34} = 5\,\mathrm{GHz}$, $\kappa = 100\,\mathrm{GHz}$, $g = 330\,\mathrm{GHz}$, $\gamma = 6\,\mathrm{THz}$, $\Gamma = 1\,\mathrm{GHz}$, $E_1 = 5.27\times10^4\,\mathrm{V/m}$, $E_2 = 1.32\times10^3\,\mathrm{V/m}$.

where, terms of the Hamiltonian are energy of the excited state $|4\rangle$ with spontaneous decay rate Γ, energy of the states $|3\rangle$ and $|2\rangle$, cavity mode ω_0 with κ as its decay rate, energy of the resonantly coupled transition $|1\rangle - |4\rangle$ to the cavity mode with a coupling rate g, off-resonantly transitions $|2\rangle - |3\rangle$ and $|3\rangle - |4\rangle$ by control fields, energy of the optical modes of the waveguides 'a' and 'b', the coupling energy between the cavity and waveguides 'a' and 'b', respectively.

The waveguides outputs have been obtained as following equations

$$\begin{aligned} a_{out} &= \frac{-\gamma\, b_{in} + \left(-i\Delta_0 + (\kappa/2) + \dfrac{g^2}{-i\Delta_{14} + (\Gamma/2) + SS}\right) a_{in}}{\left(-i\Delta_0 + \gamma + (\kappa/2) + \dfrac{g^2}{-i\Delta_{14} + (\Gamma/2) + SS}\right)}, \\ b_{out} &= \frac{-\gamma\, a_{in} + \left(-i\Delta_0 + (\kappa/2) + \dfrac{g^2}{-i\Delta_{14} + (\Gamma/2) + SS}\right) b_{in}}{\left(-i\Delta_0 + \gamma + (\kappa/2) + \dfrac{g^2}{-i\Delta_{14} + (\Gamma/2) + SS}\right)}, \end{aligned} \tag{2}$$

where, the only dependency of the output fields to the control fields is given by the following equation

$$SS = \frac{\Omega_2^2}{i\Delta_{34} + (\Gamma/2) - \dfrac{\Omega_1^2}{i\Delta_{23} + (\Gamma/2)}}, \tag{3}$$

where, cavity mode, probe and control field frequencies detuning with the corresponding resonant

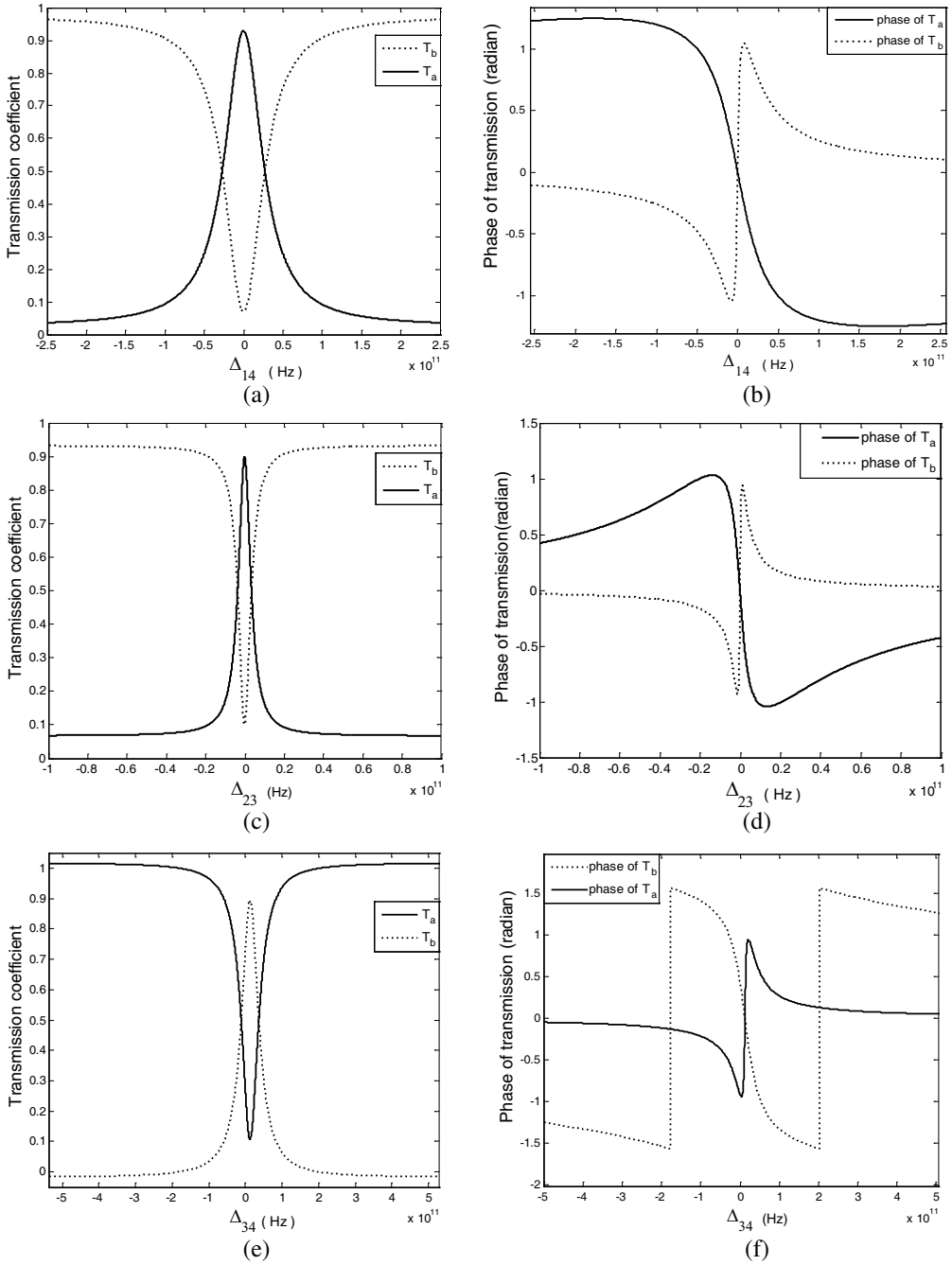

Figure 3: (a) and (b) $\Delta_0 = 0$, $\Delta_{23} = 5\,\mathrm{GHz}$, $\Delta_{34} = 5\,\mathrm{GHz}$, $\kappa = 100\,\mathrm{GHz}$, $g = 330\,\mathrm{GHz}$, $\gamma = 6\,\mathrm{THz}$, $\Gamma = 1\,\mathrm{GHz}$, $E_1 = 1.32 \times 10^3\,\mathrm{V/m}$, $E_2 = 5.27 \times 10^4\,\mathrm{V/m}$. (c) and (d) $\Delta_0 = 0$, $\Delta_{14} = 0$, $\Delta_{34} = 5\,\mathrm{GHz}$, $\kappa = 100\,\mathrm{GHz}$, $g = 330\,\mathrm{GHz}$, $\gamma = 6\,\mathrm{THz}$, $\Gamma = 1\,\mathrm{GHz}$, $E_1 = 5.27 \times 10^4\,\mathrm{V/m}$, $E_2 = 1.32 \times 10^3\,\mathrm{V/m}$. (e) and (f) $\Delta_0 = 0$, $\Delta_{14} = 0$, $\Delta_{23} = 5\,\mathrm{GHz}$, $\kappa = 100\,\mathrm{GHz}$, $g = 330\,\mathrm{GHz}$, $\gamma = 6\,\mathrm{THz}$, $\Gamma = 1\,\mathrm{GHz}$, $E_1 = 5.27 \times 10^4\,\mathrm{V/m}$, $E_2 = 1.32 \times 10^3\,\mathrm{V/m}$.

frequencies are defined by

$$\Delta_0 = \omega - \omega_0, \quad \Delta_{14} = \omega_0 - \omega_{14}, \quad \Delta_{34} = \omega_2 - \omega_{34}, \quad \Delta_{23} = \omega_1 - \omega_{23}, \tag{4}$$

Then, we have calculated the transmission coefficients of the waveguides.

3. SIMULATION RESULTS

Figure 2(a) shows that in resonant case of fiber mode with cavity, the fiber mode can pass through PC cavity to the output fiber '**b**', while the PC cavity become transparent by DIT effect. It is seen that we can couple about 90% of input signal from fiber '**a**' to fiber '**b**' with the speed of 18.3 THz which is slower than 3-level doped switch. Fig. 2(b) shows the phase of transmission coefficient,

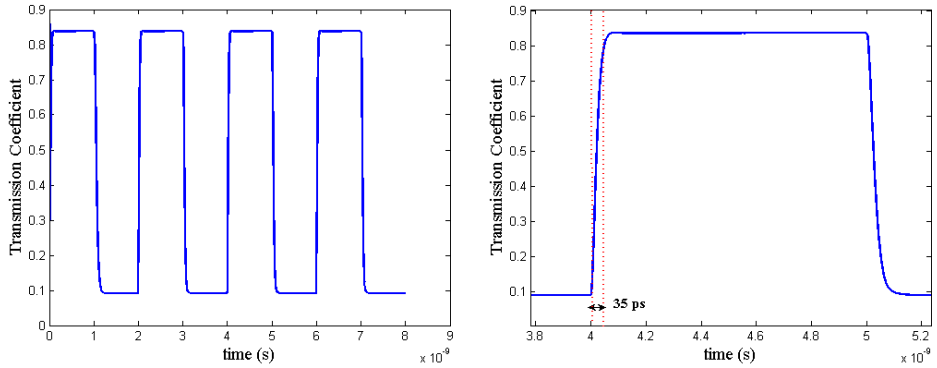

Figure 4: (a) Time evolution of switch with four level QD. (b) The rise time of output is 35 ps with the parameter values $G = 0.33\,\text{THz}$, $\gamma = 1\,\text{THz}$, $\kappa = 0.1\,\text{THz}$, $\Gamma_{21} = 0.6\,\text{GHz}$, $\Gamma_{31} = 6\,\text{GHz}$, $\Gamma_{41} = 9\,\text{GHz}$, $\Omega_1 = 0.07\,\text{THz}$.

we can deduce that the input optical field can transmits to a_{out} because of smaller delay time for large values of detuning, while for resonant case it transmit to b_{out} with negligible delay time.

Figure 3 illustrates transmission coefficient of PC cavity-waveguide switch system doped with 4-level nanocrystal versus optical control fields detuning. As we saw in Fig. 2, switching operation take place at $\Delta_0 \approx -12.26 \times 10^{12}\,\text{Hz}$, where in about $\Delta_0 \approx 0$ switch is at cross state. This is illustrated in Fig. 3(a), where switch reverts at $\Delta_{14} \approx 0\,\text{Hz}$ for $\Delta_0 = 0$. Fig. 3(c) illustrates the transmission coefficient versus the optical control field frequency detuning from $|2> - |3>$ transition frequency. The switching speed in this case slowdowns to 17.42 GHz where the transmission amplitude can reach up 90% of input signal. Fig. 3(d) illustrates the phase of transmission coefficient versus detuning Δ_{23}. It is shown that, in out of resonance phase of T_b is less than phase of T_a, so the most of input signal transmits to b_{out}. Fig. 3(e) illustrates the transmission coefficient versus optical control field frequency detuning from $|3> - |4>$ transition frequency. The switching speed in this case slowdowns to 69.2 GHz and other shortcoming is weak coupling where transmission amplitude can reach only 89.4% of input signal. Fig. 3(f) shows the phase of transmission coefficient versus detuning Δ_{34}. It is observed that, in out of resonance region, the phase of T_a is less than phase of T_b. So the most part of input signal transmits to a_{out}.

As we observe in Fig. 4, switching time has been reached to 35 ps, which introduces the four level nanocrystal suitable for insering in PhC cavity as a switch. So, we can implement an ultrahigh speed all-optical switch by means of 4-level QD doping in the cavity electrodynamics (QCED).

4. CONCLUSION

We have demonstrated that by doping 4 level nanocrystal, we can design a double state optical controllable switch, where any of control fields can change the state of switch between direct and cross states. We have shown that this switch can operate at about 20 THz by detuning of cavity mode with the fiber mode, but by control field detuning its speed slowdowns to 69.2 GHz by E_2 control field, to 17.42 GHz by E_1 control field. The possible cases of the switch have been illustrated. Also, by dynamic simulation the switching time of 35 ps has been obtained.

REFERENCES

1. Eftekhari, K., K. Abbasian, and A. Rostami, "Proposal for all-optical controllable switch using dipole-induced transparency (DIT)," *Optics Communications*, Vol. 283, 1817–1825, 2010.
2. Fleischhauer, M., A. Imamoglu, and J. P. Marangos, "Electromagnetically induced transparency: Optics in coherent media," *Rev. Mod. Phys.*, Vol. 77, 633, 2005.
3. Yadipour, R., K. Abbasian, A. Rostami, and Z. D. KoozehKanani, "A novel proposal for ultra-high resolution and compact optical displacement sensor based on electromagnetically induced transparency in ring resonator," *Progress In Electromagnetics Research*, Vol. 77, 149–170, 2007.
4. Zyaei, M., H. Rasooli Saghai, K. Abbasian, and A. Rostami, "Long wavelength infrared photodetector design based on electromagnetically induced transparency," *Optics Communications*, Vol. 281, 3739–3747, 2008.
5. Scully, M. O. and M. S. Zubairy, *Quantum Optics*, Cambridge University Press, ISBN: 0 521 43458 0, 2001.

Characteristics for Crosstalk between Dual Microstrip Transmission Lines in PCB

Xin Wang[1], **Hui Huang**[1,2], **and Qi Liu**[1]

[1]School of Electrical Engineering, Beijing Jiaotong University, Beijing 100044, China
[2]State Key Laboratory of Millimeter Waves, Nanjing 210096, China

Abstract— A detailed study of crosstalk between dual microstrip transmission lines in PCB is presented. The crosstalk response to signal frequency, the distance between microstrip transmission lines, the length of microstrip transmission line and the thickness of substrate are analyzed respectively. The calculation of S-parameter is obtained based on the finite element method. The simulation result indicates that crosstalk strength varies with the length of microstrip line, the distance between dual microstrip transmission lines and the substrate thickness.

1. INTRODUCTION

In the circuit, when two conductors are close with each other, there will be an electromagnetic coupling (crosstalk) between coupled strip transmission lines or coupled microstrip transmission lines [1]. This paper considers crosstalk between coupled microstrip transmission lines. This crosstalk is a completely symmetric coupled-line structure as shown in Figure 1.

When the source generates the signal (1), the signal (3) due to electric field coupling will suppress receiver. Generally we adopt mutual capacitance to analyze electric field coupling [2]. Since magnetic field coupling, the signal (2) also has an adverse effect on receiver. In general, mutual inductance can be used to explain magnetic field coupling. Both the signal (2) and the signal (3) are crosstalk. It is obvious that the directions of them are opposite [3, 4].

2. THEORY AND METHODS

When microstrip line operates in the lower microwave frequency range, impendence is [5]

$$Z_0 = \sqrt{\frac{L_1}{C_1}} = \frac{1}{v_p C_1} = \frac{\sqrt{\varepsilon_{re}}}{cC_1}, \tag{1}$$

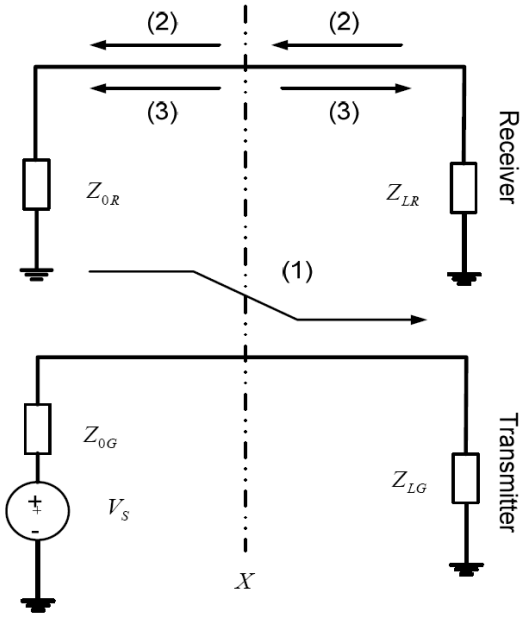

Figure 1: Crosstalk between two parallel wires in the circuit.

where C_1 is capacitance per unit length of microstrip line, v_p is the phase velocity of microstrip line, ε_{re} is equivalent permittivity and c is the speed of light.

$$C_1 = \frac{\varepsilon_r s}{h}, \tag{2}$$

where s is equivalent area, h is the thickness of media and ε_r is media permittivity.

In practical circuit design, the modified characteristic impedance is

$$Z_0 = \left(\frac{87}{\sqrt{\varepsilon_r + 1.41}}\right) \ln\left(\frac{5.98h}{0.8w + t}\right) \Omega. \tag{3}$$

When signal traveling along a wire generates an electromagnetic field, the electromagnetic coupling generates the crosstalk. $V_R(0)$ is interference voltage of receiver at $x = 0$. The definite of $V_R(L)$ is similar with $V_R(0)$. Near-end and far-end crosstalk are [6]

$$TR_0 = \frac{V_R(0)}{V_S}, \tag{4}$$

$$TR_L = \frac{V_L(0)}{V_S}. \tag{5}$$

The simulation model for crosstalk between dual microstrip transmission lines in PCB is shown in Figure 2. On the substrate two parallel microstrip transmission lines are perfect conductors. The varible h, d, l and w are the thickness of substrate, the distance from the receive transmission line to transmission line, the length and the width of microstrip line respectively. The substrate is made of FR-4 (epoxy laminated glass fiber) whose permittivity varies with the signal frequency.

We calculate S-parameter based on the finite element method. The size of PCB is 20 mm × 50 mm × 0.2 mm. Characteristic impedance of microstrip transmission lines is 50 Ω. The parameters we used are: $\varepsilon_r = 4.5$, $w/h = 1.85$, $h = 0.2$ mm, $d = 2$ mm, $l = 30$ mm and $w = 0.37$ mm.

Port P_1 (Transmission line) is interference source. To avoid distortion caused by the terminal mismatch, ports P_2, P_3 and P_4 need to connect 50 Ω resistors respectively. Generally this model can be considered as a four-port network. Near-end crosstalk parameter S_{13} ($St(P_1, P_3)$) and far-end crosstalk parameter S_{14} ($St(P_1, P_4)$) can be obtained. Actually S_{13} and S_{14} are scattering parameter [7].

Based on this model, we analyze the influence of each variable on crosstalk, i.e., we keep the other variable constant, and find out how S-parameter varies with one variable.

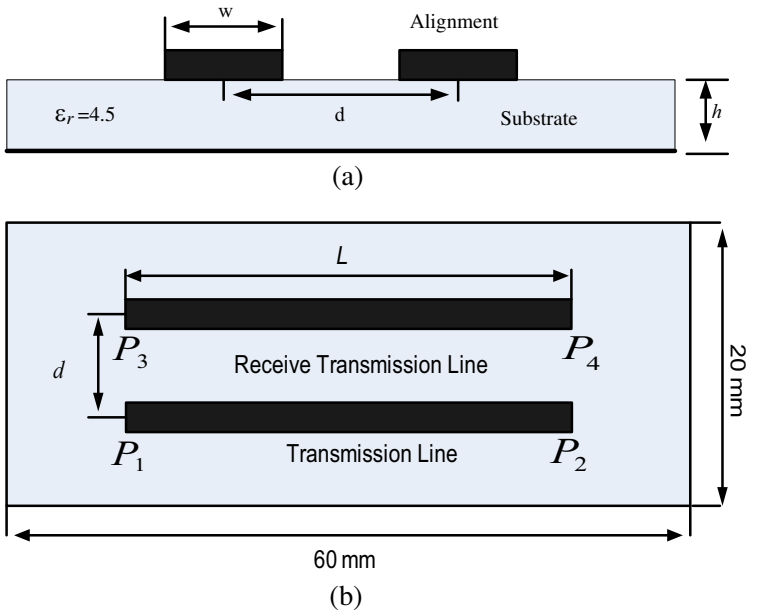

Figure 2: (a) Sectional view and (b) top view for dual microstrip transmission lines in PCB.

3. SIMULATION AND ANALYSIS

3.1. The Influence of Signal Frequency on Crosstalk

For the distance between microstrip transmission lines, we consider two cases: $d = 2\,\text{mm}$ and $d = 1\,\text{mm}$. The signal frequency range is from 0 GH to 15 GHz. the simulation result is shown in Figure 3.

For $d = 1\,\text{mm}$, the curves of S_{14}-parameter increase gently showing that far-end crosstalk is strengthening as signal frequency increases. The curves of S_{13}-parameter sustain oscillation. When signal frequency is greater than 14GHz this oscillation is obvious.

For $d = 2\,\text{mm}$, the variation of curves are almost the same with the variation at $d = 1\,\text{mm}$. The only difference is that crosstalk strength at $d = 2\,\text{mm}$ is smaller than crosstalk strength at $d = 1\,\text{mm}$.

Two cases illustrate the phases of two signals match with each other when inductive crosstalk and capacitive crosstalk reach far-end port simultaneously. So the curve of far-end crosstalk is gentle. For near-end crosstalk, these curves are apparently fluctuant due to the large phase difference.

3.2. The Influence of the Length of Microstrip Transmission Line on Crosstalk

The length interval of the microstrip line is [5 mm, 40 mm]. We consider four kinds of signal frequencies: 1 GHz, 5 GHz, 9 GHz and 13 GHz.

The curves of S_{13}-parameter and S_{14}-parameter are increasing as the length gets longer. Especially, S_{14}-parameter curves rise suddenly when the length is longer than 38 mm. In Figure 4(a)

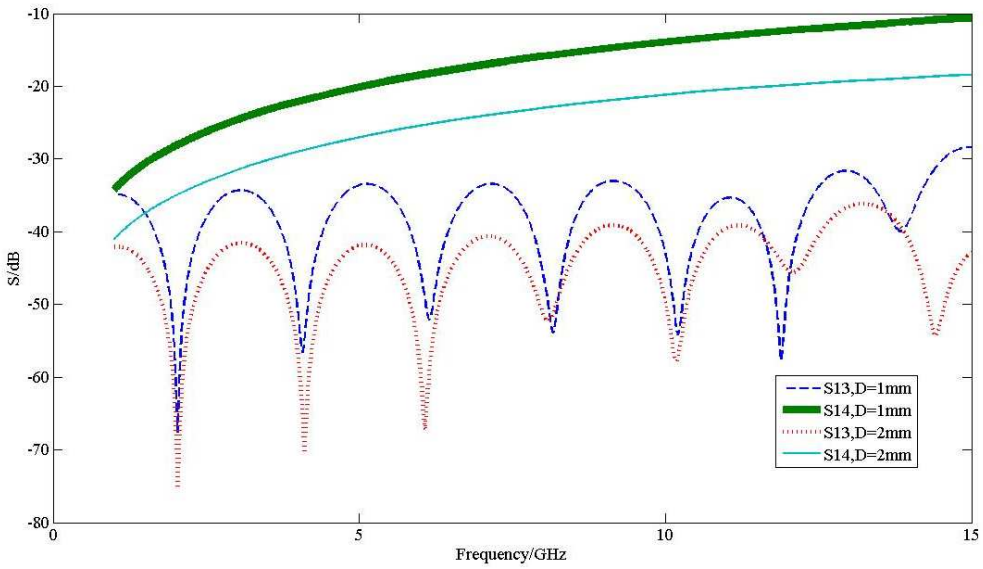

Figure 3: Crosstalk strength versus signal frequency.

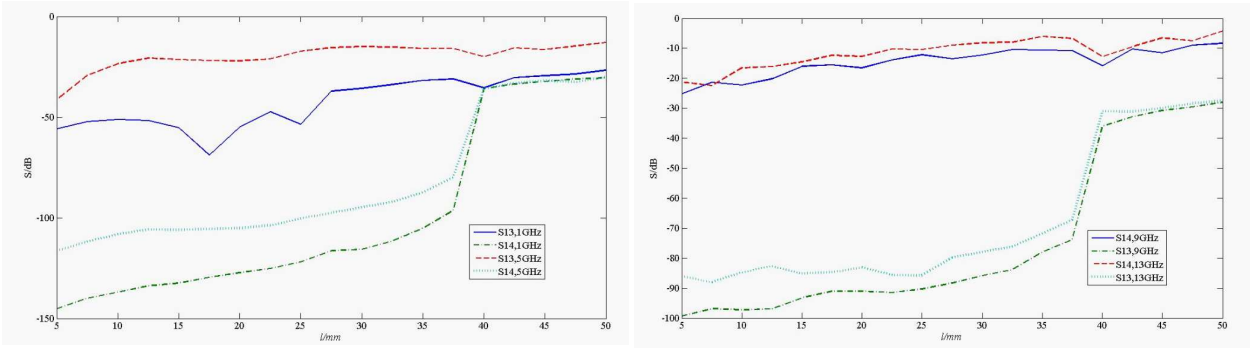

(a) (b)

Figure 4: Crosstalk versus the length of microchip line in PCB. Frequency for 1 GHz and 5 GHz in Fig. 4(a), frequency for 9 GHz and 13 GHz in Fig. 4(b).

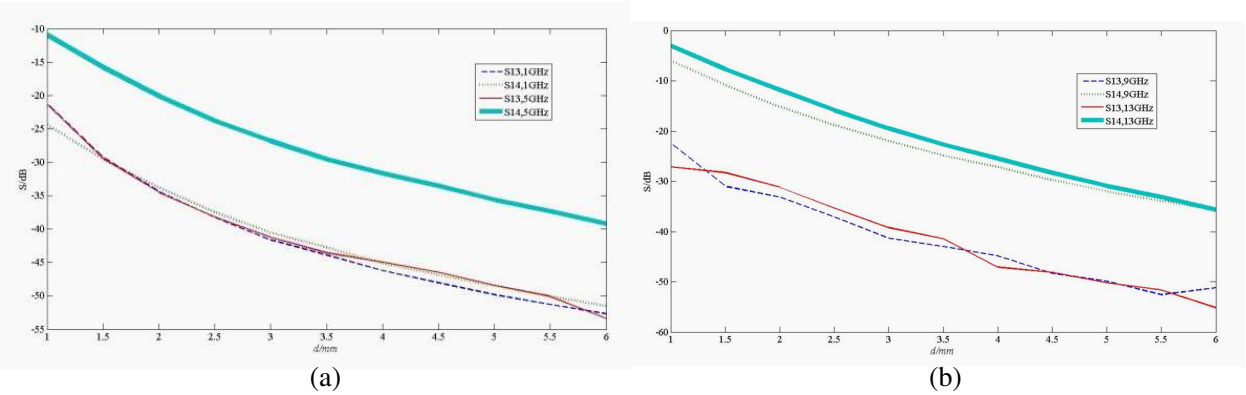

(a) (b)

Figure 5: Crosstalk versus the distance from the receiving line to transmission line. Frequency for 1 GHz and 5 GHz in Fig. 5(a), frequency for 9 GHz and 13 GHz in Fig. 5(b).

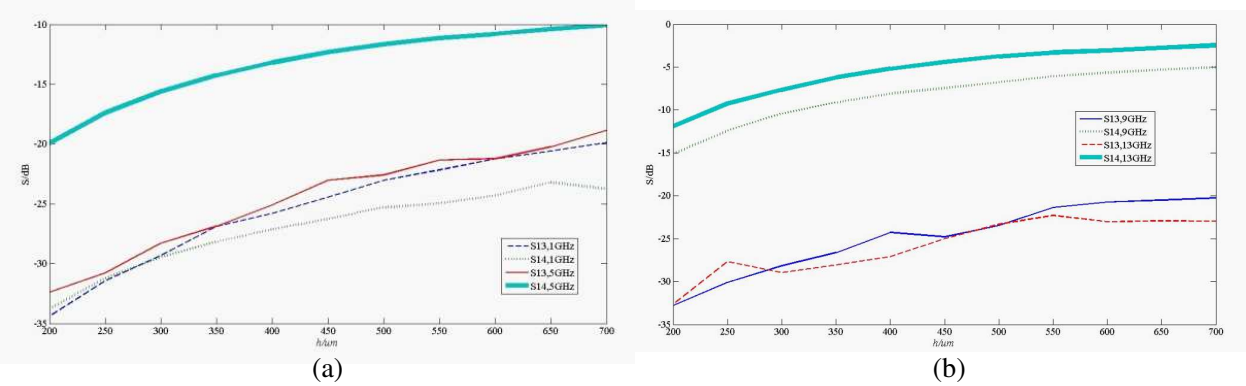

(a) (b)

Figure 6: Crosstalk versus the thickness of PCB. Frequency for 1 GHz and 5 GHz in Fig. 6(a), frequency for 9 GHz and 13 GHz in Fig. 6(b).

and Figure 4(b) the variations are similar with each other. The curve of S_{14}-parameter shocks strongly due to strengthening of mutual conductance and mutual capacitance.

3.3. The Influence of the Distance between Microstrip Transmission Lines on Crosstalk

The distance range between microstrip transmission lines is from 1 mm to 6 mm.

The curves of S_{13}-parameter and S_{14}-parameter decrease showing that strength of crosstalk is reversely proportional to the distance between dual transmission lines. For near-end crosstalk, crosstalk strength does not decline significantly until $d = 2.5$ mm. We notice irregular oscillation due to effect of mutual inductance and mutual capacitance in 9 GHz or higher.

3.4. The Influence of the Thickness of Substrate on Crosstalk

The thickness range of substrate is from 200 µm to 700 µm.

The curves of S_{13}-parameter and S_{14}-parameter increase showing that strength of near-end and far-end crosstalk is directly proportional to the thickness of substrate. In comparison of the other curve clusters in Figure 6(b), the curves of S_{13}-parameter shock more strongly due to the large phase difference on port P_3. Generally the distance between the top and the bottom of the substrate should be as small as possible, and it can suppress crosstalk strength to achieve the circuit function better.

4. CONCLUSION

We analyze S-parameter based on finite element method. Higher the frequency is, stronger crosstalk is. Signal transmission performance in low frequency is better than performance in high frequency. We also show how crosstalk strength varies with the length of microstrip line, the distance between dual microstrip transmission lines and the substrate thickness.

ACKNOWLEDGMENT

This work is sponsored by State Key Laboratory of Millimeter Waves under Contract K201012.

REFERENCES

1. Hill, D. A., K. H. Cavcey, and R. T. Johnk, "Crosstalk between microstrip transmission lines," National Institute of Standards and Technology, 1993.
2. Li, L. and W.-B. Li, "Crosstalk analysis between two parallel transmimission lines," *Chinese Journal of Radio Science*, Vol. 16, No. 2, 271–274, 2001.
3. Wang, Q. and F. Sha, "Analysis of crosstalk of two parallel transmission lines," *Journal of Electronic Measurement and Instrument*, Vol. 22, No. 6, 72–77, 2008.
4. Kotlan, V. and J. Machac, "High-frequency crosstalk between two parallel slotlines," *IET Microwave, Antennas & Propagation*, Vol. 12, No. 4, 2240–2246, 2009.
5. Lv, F. and S. Fei, "The coupling mechanism and optimization analysis model for crosstalk in PCB," *Electronics and Information Technology*, Vol. 1, No. 27, 1167–1170, 2005
6. Li, Z. and J. Mao, *Microwave and High-speed Circuit Theory*, Shanghai Jiaotong University Press, Shanghai, 2001.
7. Yan, R. and Y. Li, *Microwave Technology*, Beijing Institute of Technology Press, Beijing, 1997.

Surface Modes at Interface between Lossy Gyroelectric and Isotropic Media

Xin Wang[1], **Hui Huang**[1, 2], **and Bo Yi**[1]

[1]School of Electrical Engineering, Beijing Jiaotong University, Beijing 100044, China
[2]State Key Laboratory of Millimeter Waves, Nanjing 210096, China

Abstract— A detailed analysis of surface wave at the interface between gyroelectric and isotropic medium is presented. Two cases including lossless and lossy gyroelectric medium are considered. The conditions for the existence of surface modes in each case are analyzed, showing that the existence is determined by the components of wave vector k_y^2, k_{xi} and k_{xi2}. Take gyroelectric medium for an example, the existence interval of surface wave is obtained. Comparison of surface wave in lossy medium and lossless medium is presented.

1. INTRODUCTION

Nowadays surface wave is an increasingly hot research topic. The certain conditions of surface wave existence at the interface separating two semi-infinite half-spaces are studied. This research can contribute to understand material surface properties, and controlling the direction of such waves also helps potential application.

Lord Rayleigh has researched surface wave in 1885 [1], but his research was constrained due to the relative low manufacturing process. In 2005 Allan Boardman analyzed the surface magnetoplasmon ploaritons propagation at the interface between the gyroelectric medium and isotropic medium in Vogit configuration [2]. His research achievement can be applied to non-negative refracting medium. H. Huang analyzed surface wave propagation in uniaxial plasma in 2007 [3].

To our knowledge, however, no detailed research about surface modes at the interface between gyroelectric and isotropic medium has yet been given. In this paper, we consider surface wave propagation in lossy gyroelectric medium, furthermore, we compare the differences between lossless medium and lossy medium.

2. ANALYSIS METHODOLOGY

As shown in Figure 1, we establish a xyz coordinate system so that the interface is in the y-x plane and the z axis is perpendicular to it. Isotropic medium and gyroelectric medium are located at$x < 0$ and $x > 0$ semi-infinite region respectively. And the external magnetic field $\bar{B}_0$ is in the z direction. Region 1 is the isotropic medium, with permittivity ε_1 and permeability μ_1; region 2 is gyroelectric medium (Voigt configuration), with permeability μ_2 and permittivity tensor $\bar{\bar{\varepsilon}}_2$ [4].

In gyroelectric medium, the permittivity tensor is

$$\bar{\bar{\varepsilon}}_2 = \begin{bmatrix} \varepsilon_{xx} & i\varepsilon_{xy} & 0 \\ -i\varepsilon_{yx} & \varepsilon_{yy} & 0 \\ 0 & 0 & \varepsilon_{zz} \end{bmatrix}, \tag{1}$$

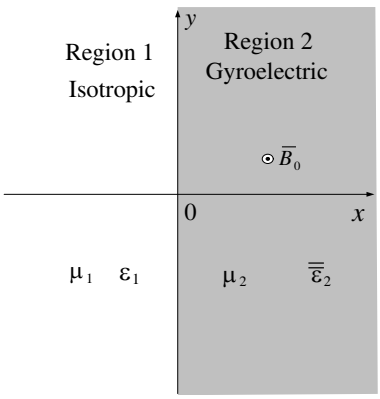

Figure 1: Diagram for an interface between a semi-infinite isotropic and gyroelectric media.

where the components of the tensor are [5]

$$\varepsilon_{xx} = \varepsilon_{yy} = \varepsilon_0 \left\{ 1 - \frac{(\omega_p/\omega)^2[1-(iv_c/\omega)]}{[1-(iv_c/\omega)]^2 - (\omega_b/\omega)^2} \right\}, \tag{2}$$

$$\varepsilon_{xy} = \varepsilon_{yx} = \varepsilon_0 \frac{(\omega_p/\omega)^2(\omega_b/\omega)}{[1-(iv_c/\omega)]^2 - (\omega_b/\omega)^2}, \tag{3}$$

$$\varepsilon_{zz} = \varepsilon_0 \left[1 - \frac{\omega_p^2}{\omega(\omega - iv_c)} \right], \tag{4}$$

where ω_p is the plasma frequency, ω_b is the cyclotron frequency (proportional to the static field $\bar{B}_0$), and v_c is the electron collision frequency representing the loss mechanism.

In isotropic medium ($x < 0$) (region 1), suppose the surface wave vector is $\bar{k}_1 = \hat{y}k_y + \hat{x}(-ik_{xi})$, we can obtain all quantities of incident wave

$$\bar{H}_1 = \hat{z}H_1 e^{ik_y y + k_{xi}x}, \tag{5}$$

$$\bar{E}_1 = \frac{1}{\omega\varepsilon_1}(-\hat{x}k_y - i\hat{y}k_{xi})H_1 e^{ik_y y - k_{xi}x}. \tag{6}$$

Notice x component of $\bar{k}_1$in isotropic medium is an imaginary number, we can obtain the dispersion relation [6, 7].

$$k_y^2 - k_{xi}^2 = \omega^2\mu_1\varepsilon_1. \tag{7}$$

In gyroelectric medium ($x > 0$) (region 2), we assume the wave vector is $\bar{k}_2 = \hat{y}k_y + \hat{x}(ik_{xi2})$, Ref. [2] gives the dispersion relation.

$$k_y^2 - k_{xi2}^2 = \omega^2\mu_2\varepsilon_v, \tag{8}$$

where $\varepsilon_v = \frac{\varepsilon_{xx}^2 - \varepsilon_{xy}^2}{\varepsilon_{xx}}$, it is the equivalent permittivity in Voigt configuration for TM wave [3].

According to boundary conditions, tangential component of electric field is continuous at the interface in medium: $\bar{E}_{1y}|_{x=0} = \bar{E}_{2y}|_{x=0}$.

Thus we can obtain

$$\frac{k_{xi}}{\varepsilon_1} = \frac{\varepsilon_{xy}k}{\varepsilon_{xx}\varepsilon_v} - \frac{k_{xi2}}{\varepsilon_v}. \tag{9}$$

Finally, based on the expression (7), (8) and (9), the components of wave vector are

$$k_y^2 = \omega^2\varepsilon_1 \frac{\mu_1[\varepsilon_{xx}^2(3\varepsilon_1^2 - \varepsilon_{xx}^2) + (\varepsilon_{xy}^2 - \varepsilon_1^2)(2\varepsilon_{xx}^2 - \varepsilon_{xy}^2)] - \mu_2\varepsilon_1\varepsilon_{xx}(\varepsilon_1^2 - \varepsilon_{xx}^2 + \varepsilon_{xy}^2) + 2\varepsilon_1 |\varepsilon_{xy}| \sqrt{\Delta}}{A} \tag{10}$$

$$k_{xi} = \sqrt{\omega^2\varepsilon_1^2 \frac{-[\mu_1\varepsilon_1(\varepsilon_{xx}^2 + \varepsilon_{xy}^2 - \varepsilon_1^2) + \mu_2\varepsilon_{xx}(\varepsilon_1^2 - \varepsilon_{xx}^2 + \varepsilon_{xy}^2)] + 2|\varepsilon_{xy}|\sqrt{\Delta}}{A}} \tag{11}$$

$$k_{xi2} = \sqrt{\omega^2\varepsilon_1^2 \frac{-[\mu_1\varepsilon_1(\varepsilon_{xx}^2 + \varepsilon_{xy}^2 - \varepsilon_1^2) + \mu_2\varepsilon_{xx}(\varepsilon_1^2 - \varepsilon_{xx}^2 + \varepsilon_{xy}^2)] + 2|\varepsilon_{xy}|\sqrt{\Delta}}{A} - \omega^2\mu_2 \frac{\varepsilon_{xx}^2 - \varepsilon_{xy}^2}{\varepsilon_{xx}}}, \tag{12}$$

where

$$\Delta = \varepsilon_1\varepsilon_{xx}[\varepsilon_1\varepsilon_{xx}(\mu_1^2 + \mu_2^2) + \mu_1\mu_2(\varepsilon_{xy}^2 - \varepsilon_1^2 - \varepsilon_{xx}^2)], \tag{13}$$

$$A = 4\varepsilon_1^2\varepsilon_{xx}^2 - (\varepsilon_{xx}^2 - \varepsilon_{xy}^2 + \varepsilon_1^2)^2. \tag{14}$$

According to expression (13), there are frequency bands in which physical solutions may exist but the solutions of k_y^2 are physically unacceptable. The existence of surface wave condition is that k_y^2, k_{xi} and k_{xi2} must be greater than zero.

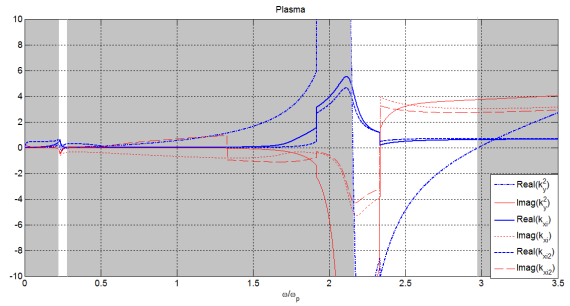

Figure 2: Wave vector k_y^2, k_{xi} and k_{xi2} versus frequency in lossy medium.

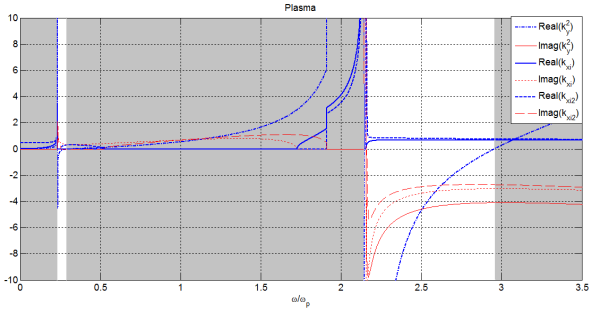

Figure 3: Wave vector k_y^2, k_{xi} and k_{xi2} versus frequency in lossless medium.

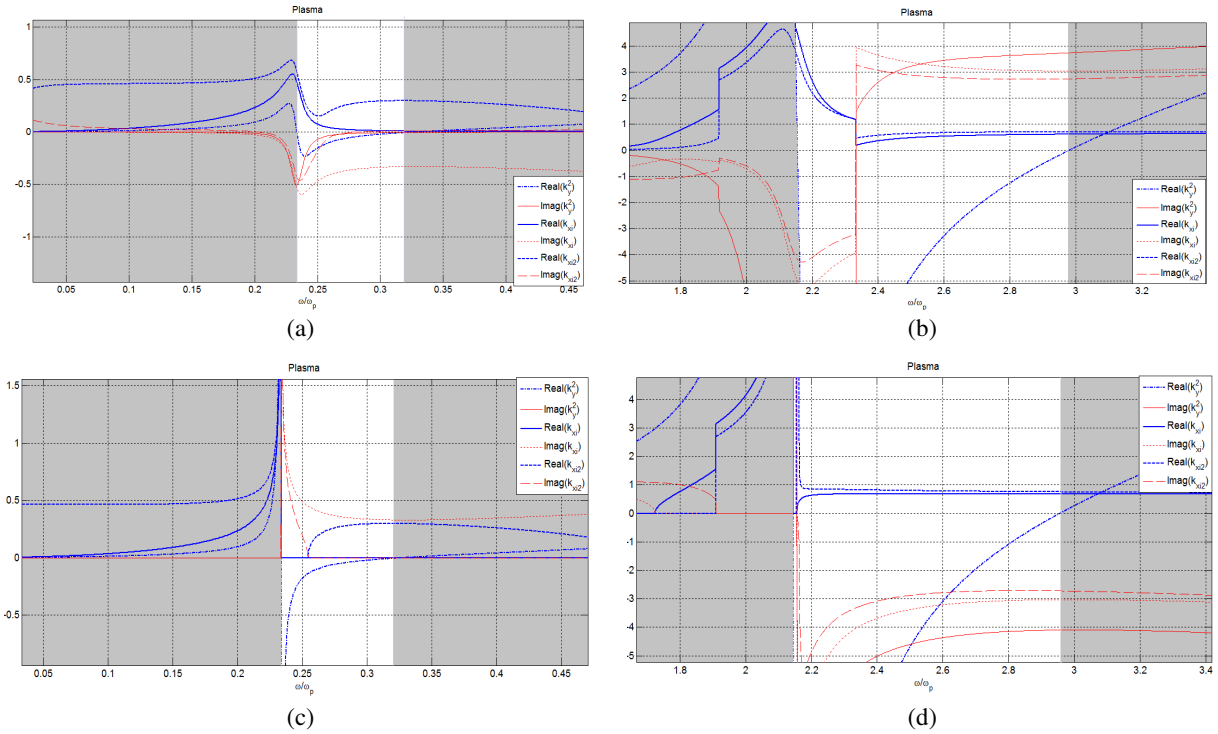

Figure 4: Magnification for wave vector k_y^2, k_{xi} and k_{xi2}, (a) and (b) in lossy medium (c) and (d) in lossless medium.

3. NUMERICAL RESULTS

Since it is hard to obtain the analytic existence conditions of the surface waves, we take a specific gyroelectric medium as an example. The parameters of the gyroelectric medium are: $\mu_2 = \mu_0$, $\omega_p = 10\pi \times 10^{10}$ rad/s and $\omega_b = 3.0 \times 10^{11}$ rad/s [5]. Furthermore, we consider two cases: Then we analyze graphics generated by MATLAB and consider two cases: one is lossy gyroelectric medium ($v_c = 2.0 \times 10^{10}$) [5] and the other is lossless gyroelectric medium ($v_c = 0$). In both cases, the isotropic medium is the vacuum with $\mu_1 = \mu_0$ and $\varepsilon_1 = \varepsilon_0$.

In lossy gyroelectric medium, the extreme point of the real parts of k_y^2, k_{xi} and k_{xi2} appear simultaneously where the value of ω/ω_p is 2.1550. When the value of ω/ω_p is 2.3325, the imaginary parts of k_y^2, k_{xi} and k_{xi2} attain the extreme point. Since k_y^2, k_{xi} and k_{xi2} must be greater than zero as shown in the shaded part of Figure 2, the existence frequency interval of surface wave is

$$\omega/\omega_p \in [0, 0.2336]\&[0.3286, 2.1550]\&[2.9796, +\infty].$$

In lossless gyroelectric medium, i.e., $v_c = 0$, $v_c = 0$, the extreme point of the real parts of k_y^2, k_{xi} and k_{xi2} appear simultaneously where the value of ω/ω_p is 0.2336 or 2.1438. When the value of ω/ω_p is 2.155, the imaginary parts of k_y^2, k_{xi} and k_{xi2} attain the extreme point as shown in the

shaded part of Figure 3. Thus the existence interval of surface wave is

$$\omega/\omega_p \in [0, 0.2336]\&[0.3291, 2.1438]\&[2.9569, +\infty].$$

It is not difficult to find that the existence frequency interval of surface wave in lossy medium and lossless medium are a little different. And the obvious difference is the trend curves of k_y^2, k_{xi} and k_{xi2} in lossy medium and lossless medium.

4. CONCLUSION

This paper analyzes surface wave at the interface between isotropic medium and gyroelectric medium which has dispersion characteristics. We consider two cases: lossy gyroelectric medium and lossless gyroelectric medium. The conditions for existence of surface wave of each case are analyzed, and for a given parameter medium, we obtain the frequency domain in which the surface wave can exist showing that the existence frequency domain for lossy medium or lossless medium has a little difference.

ACKNOWLEDGMENT

This work is sponsored by State Key Laboratory of Millimeter Waves under Contract K201012.

REFERENCES

1. Rayleigh, L., "On waves propagated along the plane surface of an elastic solid," *Proceedings of the London Mathematical Society*, Vol. 17, 4–11, 1885.
2. Boardman, A., N. King, and Y. Rapoport, "Gyrotropic impact upon negatively refracting surfaces," *New Journal of Physics*, Vol. 7, 191, 2005.
3. Huang, H., Y. Fan, B.-I. Wu, F. Kong, and J. A. Kong, "Surface modes at the interfaces between isotropic media and uniaxial plasma," *Progress In Electromagnetics Research*, Vol. 76, 1–14, 2007.
4. Walker, D. B., E. N. Glytsis, and T. K. Gaylord, "Surface mode at isotropic–uniaxial and isotropic–biaxial interfaces," *Journal of the Optical of America*, Vol. 15, 248–260, 1998.
5. Hunsberger, F., R. Luebbers, and K. Kunz, "Finite-difference time-domain analysis of gyrotropic media — I: Magnetized plasma," *IEEE Transactions on Antennas Propagation*, Vol. 40, No. 9, 1489–1495, 1992
6. Huang, H., Y. Fan, F. Kong, B.-I. Wu, and J. A. Kong, "Influence of external magnetic field on a symmetrical gyrotropic slab in terms of Goos-Hänchen shifts," *Progress In Electromagnetics Research*, Vol. 82, 137–150, 2008.
7. Darmanyan, S. A., M. Neviere, and A. A. Zakhidov, "Surface modes at the interface of conventional and left-handed media," *Optics Communication*, Vol. 225, 233–240, 2003.

Transmission Line Matrix Method for Two-dimensional Modeling of Terahertz Gaussian Beam Propagation

Daniel M. Hailu, **Shahed Shahir**, **Arash Rohani**, **and Safieddin Safavi-Naeini**
CIARS (Center for Intelligent Antenna and Radio Systems), Electrical and Computer Engineering Dept.
University of Waterloo, 200 University Avenue West, Waterloo, ON., N2L 3G1, Canada

Abstract— We present a two-dimensional Transmission Line Matrix (2D TLM) to simulate wave propagation and scattering inside and around an inhomogeneous cylinder for terahertz (THz) imaging. As a particular application, the proposed method is used to construct the dielectric profile or image of cylindrical sample. We compare and validate the 2D TLM with FDTD using TM-mode propagation through infinitely long lossless and lossy polyethylene cylinders.

1. INTRODUCTION

TERAHERTZ (THz) region of the electromagnetic (EM) spectrum is subject to extensive research for possible application to skin cancer detection, dental imaging, and pharmaceutical drug quality assurance. For THz Time-Domain Spectroscopy (THz-TDS), cylindrical, plano-convex and substrate lens designs are commonly used for imaging systems [1], and modeling THz communication channel [2].

In this work, we consider the problem of THz propagation through inhomogeneous cylindrical structures. The Transmission Line Matrix (TLM) [3–6] method is efficient in modeling inhomogeneous regions and dense finite regions. The TLM is applied to the THz range to exploit its advantages in modeling for inhomogeneous media, lossy media, nonlinear devices [7] and metamaterials. It has been implemented in 3D and 2D cases. In this work, THz propagation through an infinitely long electrically large inhomogeneous isotropic cylinder is modeled employing 2D TLM for THz applications. In addition effect of adding a hole in the cylindrical sample is examined.

The TLM method has been applied and studied extensively in the microwave and millimeter wave range [3–6]. In [8], TLM-IE is used to accurately model a waveguide polarizer based on an antiresonant reflecting optical waveguide (ARROW) structure operating at 230 THz. The three-dimensional transmission-line matrix and integral equation (TLM-IE) [8, 9], which combines the advantages of numerical TLM method in dense finite regions and those of IE method in open regions or electrically large homogeneous regions, is applied to analysis of ARROW polarizer and photonic bandgap gratings. The ARROW polarizer has severe aspect-ratio around 10^5 that most of numerical technique cannot handle, so by considering the very long polarizer as a periodic cascade connections of elementary short sections called "unit sections" and then apply TLM-IE to each section. Inside the unit section, the EM field is discretized using TLM and represented by analytical expression in free-space and numerical Green's function in substrate regions. The propagation/radiation properties of TE/TM modes is performed by comparing theoretical results of TE/TM losses and measured data in [8].

For electrically large homogenous structures, the 2D Spectral ray tracing (SRT) is applied by extending the 3D SRT [10, 11] formulated for this class of 2D Gaussian-beamC cylinder scattering problem. The 2D SRT is advantageous since it is fast for electrically large structures and homogeneous regions and can be incorporated in a hybrid approach with 2D TLM. The methods are then compared and verified using the Finite-difference time-domain (FDTD) method.

Section 2 describes the formulation for 2D TLM rigorous numerical solver. The 2D SRT, 2D TLM and 2D FDTD methods are then applied to THz Gaussian beam propagation through a polyethylene cylinder with and without holes. The results of the simulated electric field magnitude and phase are shown in Section 3. Finally, conclusions are made in Section 4.

2. TWO-DIMENSIONAL TRANSMISSION LINE MATRIX METHOD (2D TLMZ)

The 2D TLM algorithm is applied for modeling Terahertz (THz) Gaussian beam propagation through a cylindrical structure. The TLM is a time-domain space-discretizing method in which the dynamics of the EM field is found by applying Huygens' principle [5]. Other than an application of a hybrid method, TLM-IE [8] to model ARROW with large aspect ratio at 230 THz, to the authors' knowledge, it is the first time that TLM method [2, 6] is fully applied to model THz propagation in free-space and through curved electrically large lossy dielectric structure. The TLM is applied

to modeling of THz TMz-mode propagation through a cylinder. The 2D TLM algorithm for the case of TM-mode uses shunt nodes and involves sequence of scattering and connection steps. For each node, the total node voltage is given as

$$ {}_kV_z = \frac{2\left({}_kV_1^i + {}_kV_2^i + {}_kV_3^i + {}_kV_4^i\right) + 2{}_kV_s^i\hat{Y}_s}{4+\hat{Y}_s+\hat{G}_s}, \tag{1}$$

where incident sinusoid ${}_kV_1^i$ on line 1 and source sinusoid ${}_kV_s^i$ at kth time step, are scattered according to,

$$ {}_{k+1}\begin{bmatrix}V_1\\V_2\\V_3\\V_4\end{bmatrix}^r = \mathbf{S}\,{}_k\begin{bmatrix}V_1\\V_2\\V_3\\V_4\end{bmatrix}^i. \tag{2}$$

$$ \mathbf{S} = \frac{1}{\hat{Y}}\begin{bmatrix} 2-\hat{Y} & 2 & 2 & 2 & 2\hat{Y}_s \\ 2 & 2-\hat{Y} & 2 & 2 & 2\hat{Y}_s \\ 2 & 2 & 2-\hat{Y} & 2 & 2\hat{Y}_s \\ 2 & 2 & 2 & 2-\hat{Y} & 2\hat{Y}_s \\ 2 & 2 & 2 & 2 & 2\hat{Y}_s-\hat{Y} \end{bmatrix}. \tag{3}$$

The admittance $\hat{Y} = 4+\hat{Y}_s+\hat{G}_s$ and the normalized capacitive stub admittance is given by $\hat{Y}_s = 4(\varepsilon_r - 1)$, $\hat{G}_s = 0$. The loss is added in the TLM method by introducing a lossy stub with $\hat{G}_s = \frac{-\sigma\Delta l}{Z_{TL}^{-1}}$, where the characteristic impedance of each link line is Z_{TL}. Another advantage of TLM is that the scattering matrix is equal to its inverse implying that time reversal and time reversal radar-based imaging algorithms can be achieved by only reversing the process without changing the algorithm [6]. The structure and computation region is shown in Figs. 1 and 2. A TEM absorbing boundary condition is used to truncate the solution space. The input signal or incident field is a Gaussian beam given by

$$ E_z(x,y) = E_0 e^{-\left(\frac{y^2}{2w_0^2}\right)}, \tag{4}$$

in the space domain and modulated with exponential

$$ f_i(t) = E_z(x_0,y_i)\cdot\exp(-\omega(k-1)dt), \quad k=1,2,\ldots, \tag{5}$$

in time domain. The source is located at $x_i = x_0$ plane and $\omega_0 = \lambda$.

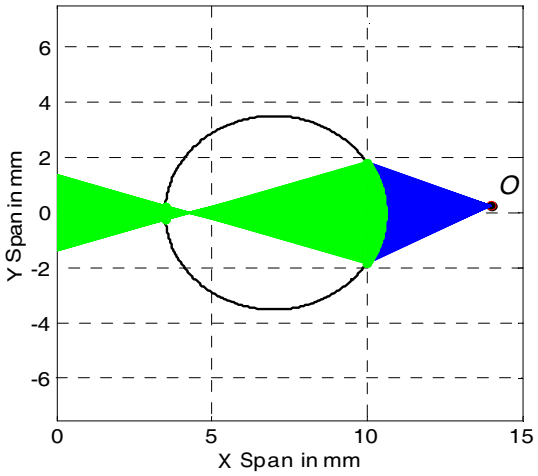

Figure 1: The geometry of cylindrical structure and SRT backward launched rays that hit the cylinder in the xy-plane is shown. Here the $x = 0$ is source plane and $x = 14$ mm is the observation plane.

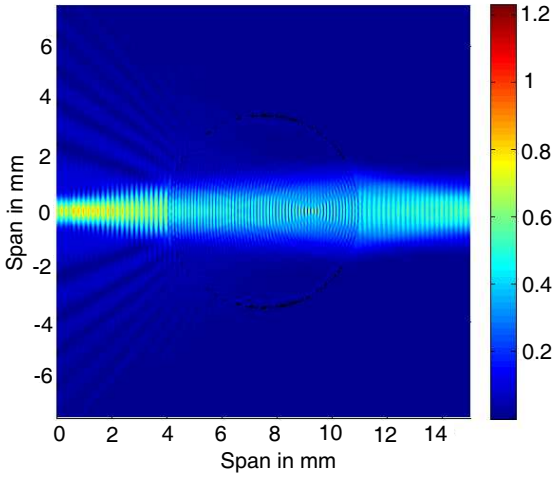

Figure 2: The $|E_z|$ total electric field shown is obtained from 2D TLM simulation for Gaussian beam propagation through a lossless 2D cylinder with beam width of 2λ or $w_0 = \lambda$. The cylinder has $R = 3.5$ mm $\approx 10\lambda$ and the source is 3.5 mm from the cylinder.

3. NUMERICAL EXAMPLES OF TLM NUMERICAL TECHNIQUE

To verify the accuracy of the proposed method we start with application of homogenous circular cylindrical geometry structures, shown in Fig. 1, for which analytical solutions exist [12, 13].

The far-field interaction with infinitely long inhomogeneous circular polyethylene cylinder, with radius of 10λ and $\varepsilon_r = 2.3$, was evaluated using 2D TLM and the $|E_z|$ total electric field is shown in Fig. 2. The simulation was for a Gaussian beam propagation through a lossless 2D cylinder with beam width of 2λ or $\omega_0 = \lambda$. For comparison, the electric field for TMz mode propagation at 860 GHz is simulated using 2D SRT, a fast asymptotic method, 2D TLM and 2D FDTD [14] for the 1500 points observations made at line of $x = 14$ mm is shown in Fig. 3. The source in this study is a Gaussian beam located at a plane 7 mm from the center of cylinder. A Gaussian beam is incident on the $x = 0.5$ mm plane, 3.5 mm from the cylinder. It is polarized along the z-direction as in Eq. (4), where $E_0 = 1$ V/m, beam waist of $w_0 = \lambda$ and $E_y(x, y) = 0$.

The corresponding spectral distribution is given by

$$\tilde{E}_z(k_x, k_y) = \frac{E_0 w_0}{\sqrt{2\pi}} e^{-\frac{w_0^2 k_y^2}{0.5}}, \quad \tilde{E}_y(k_x, k_y) = 0 \tag{6}$$

The Gaussian source, Eq. (4) and Eq. (6) has beam width of 2λ or $w_0 = \lambda$. The cylinder is 10λ or with approximate radius of 3.5 mm and the source is 3.5 mm from the cylinder.

For the TLM simulation of the cylinder with a hole, the maximum number of time steps is $K = 5,000$. An absorbing boundary condition applied to a computation region of cells 860×860, and $dl = 17.4\,\mu$m, where the descritization is 20 cells/wavelength. The elementary time step is $dt = 4.11 \times 10^{-5}$ ns. It took 4 hours on a PC with the Intel Centrino Duo 2.4 GHz processor and 6 GB of RAM. The magnitude of the electric field for Gaussian beam propagation through a cylinder is shown in Fig. 4.

Figure 5 shows the E-field distribution for the Gaussian beam propagation through a lossy cylindrical dielectric at 860 GHz. The TLM method is used for solving the direct problem in inverse scattering problems; we introduce a problem of cylinder with holes with different sizes. Fig. 6(a) shows the dielectric profile under study for THz imaging and Fig. 6(b) shows the magnitude of E_z obtained from 2D TLM simulation.

The 2D TLM and SRT codes were implemented using Matlab [15]. The time taken for 2D SRT simulation was 7 minutes and 43 seconds with 2^{10} backward rays launched and 1500 observation points on the same PC with the Intel Centrino Duo 2.4 GHz processor and 6 GB of RAM. The TLM method took 10 hours for resolution of 34.8 cells/wavelength and 10,000 time steps and FDTD took 11 hours to simulate on the same PC. The descritization for FDTD was 34 samples per wavelength with maximum number of time steps being 20,000. A PML absorbing boundary condition is applied around computation region with 100 PML cells.

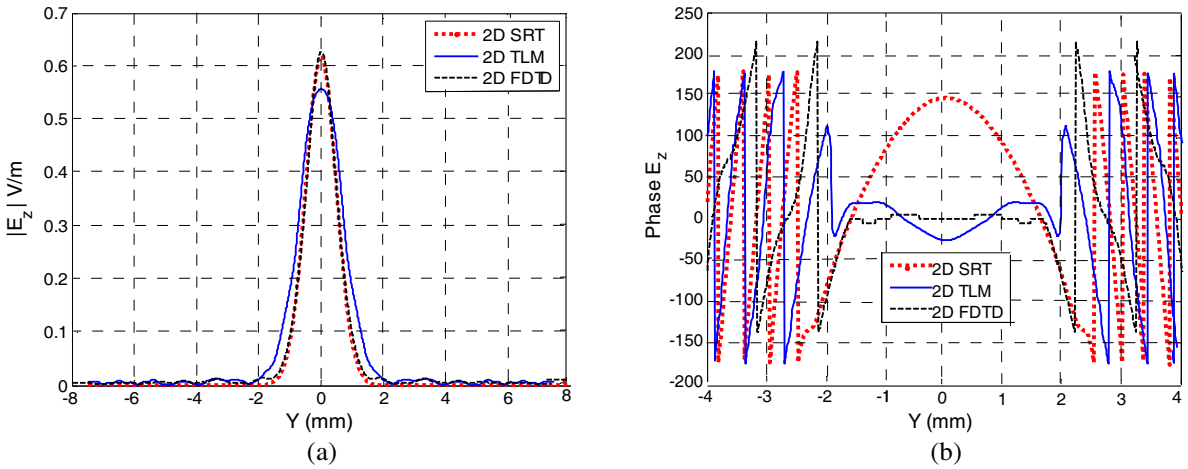

Figure 3: The (a) magnitude and (b) phase of E_z obtained from 2D SRT, 2D TLM and 2D FDTD simulations of Gaussian beam propagation through a 2D cylinder. The location of observation is 14 mm from the source.

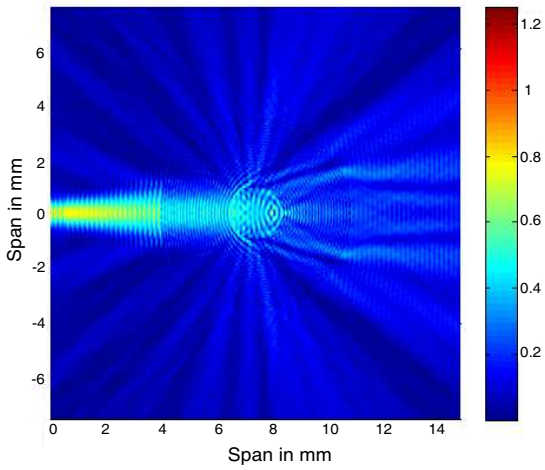

Figure 4: The magnitude of the total electric field E_z obtained after 2D TLM simulation for Gaussian beam propagation, $w_0 = \lambda$, through a 7 mm diameter cylinder with a circular hole with diameter of 2 mm at center.

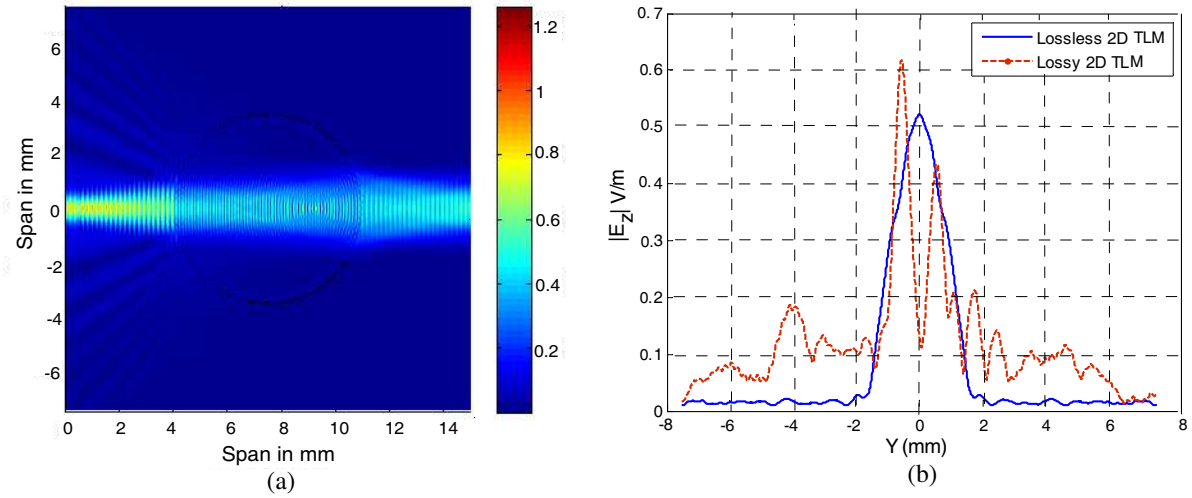

Figure 5: The (a) magnitude of E_z obtained from 2D TLM simulation for Gaussian beam propagation, $w_0 = \lambda$, through a lossy polyethylene cylinder ($\varepsilon_r = 2.3075$, $\sigma = 0.01\,\mathrm{S/m}$). (b) The 2D TLM lossy vs. lossless case at $x = 11\,\mathrm{mm}$.

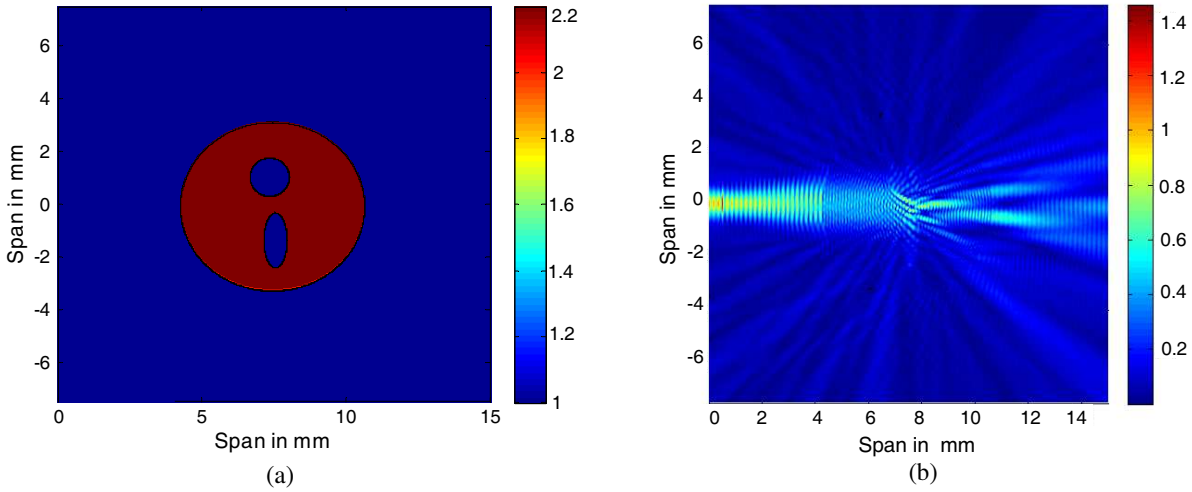

Figure 6: The (a) dielectric profile of the structure to image and (b) the magnitude of E_z obtained from 2D TLM simulation for Gaussian beam propagation, $w_0 = \lambda$, through a cylinder with a circular hole with diameter of 2.72 mm and elliptical hole with diameter of 1.6 mm along x and 4.16 mm along y.

4. CONCLUSIONS

The authors present a fast and computationally efficient two-dimensional Transmission Line Matrix (2D TLM) method applied in the terahertz (THz) range to simulate wave propagation and scattering inside and around an inhomogeneous cylinder. The 2D TLM is applied for cylinders of 10λ in size giving accurate magnitude and phase results as compared to FDTD. The direct solution obtained using 2D TLM can be used for THz image reconstruction and hybrid 2D TLM and 2D SRT techniques for future study.

ACKNOWLEDGMENT

This work was supported in part by the Natural Sciences and Engineering Research Council of (NSERC), and RIM.

REFERENCES

1. Wu, X., G. V. Eleftheriades, and T. E. Van Deventer Perkins, "Design and characterization of single-and-multiple-beam MM-wave circularly polarized substrate lens antennas for wireless communications," *IEEE Trans. Microwave Theory Tech.*, Vol. 49, March 2001.
2. Piesiewicz, R., J. Jemaia, M. Kochb, and T. Kurnera, "THz channel characterization for future wireless gigabit indoor communication systems," *The Proceedings of SPIE Conference*, Vol. 5727, 166–176, 2005.
3. Hoefer, W. J. R., "The transmission-line matrix method — Theory and applications," *IEEE Trans. Microwave Theory Tech.*, Vol. 33, March 1985.
4. Johns, P. B., "A symmetrical condensed node for the TLM-method," *IEEE Trans. Microwave Theory Tech.*, Vol. 35, No. 4, 370–377, April 1987.
5. Christopoulos, C., *Transmission-line Modeling (TLM) Method in Electromagnetics*, Morgan & Claypool, USA, 2006.
6. Forest, M. and W. J. R. Hoefer, "TLM synthesis of microwave structures using time reversal," *IEEE MTT-S Int. Microwave Symp. Dig.*, Vol. 2, 779–782, June 1992.
7. Stubbs, D. M., S. H. Pulko, and B. Wilson, "Application of transmission line matrix (TLM) method to numerical modelling of a MESFET distributed amplifier," *Electronics Letters*, Vol. 32, 1678–1680, August 1996.
8. Pierantoni, L., A. Massaro, and T. Rozzi, "Accurate modeling of TE/TM propagation and losses of integrated optical polarizer," *IEEE Trans. Microwave Theory Tech.*, Vol. 53, June 2005.
9. Pierantoni, L., A. Di Donato, and T. Rozzi, "Full-wave analysis of photonic bandgap integrated optical components by the TLM-IE method," *Journal Lightwave Tech.*, Vol. 22, October 2004.
10. Ehtezazia, I. A. and C. Letrou, "A spectral domain ray tracing method for quasi-optical devices modelling," *IEEE Int. Sym. Antennas and Prop.*, 1086–1089, June 1998.
11. Hailu, D. M., I. A. Ehtezazi, and S. Safavi-Naeini, "Fast analysis of terahertz integrated lens antennas employing the spectral domain ray tracing method," *IEEE Antennas and Wireless Lett.*, Vol. 8, 37–39, 2009.
12. Harrington, R. F., *Time-harmonic Electromagnetic Fields*, McGraw-Hill New York, 1961.
13. Lock, J. A., "Scattering of a diagonally incident focused Gaussian beam by an infinitely long homogeneous circular cylinder," *J. Opt. Soc. Am. A*, Vol. 14, 640–652, 1997.
14. Rohani, A., "A fast hybrid method for analysis and design of photonic structures," Ph.D. Thesis, University of Waterloo, 2006.
15. Matlab^{TM}, Version 7.8, The MathWorks, Inc., 3 Apple Hill Drive, Natick, MA 01760–2098, 2009.

Analysis of the Design and Optimization of a Yagi Antenna with High Gain in Meteorological Communication

Jue Li[1], **Bin Fang**[1], **Shi-Sheng Jin**[1], **and Wei-Wei Cheng**[2]

[1]Guizhou Meteorological Information Center, Guiyang, Guizhou 550002, China
[2]Institute of Microelectronics and Optoelectronics
Zhejiang University, Hangzhou, Zhejiang 310027, China

Abstract— This paper designs a 3-element Yagi beam aerial in free space for a frequency of 150 MHz using EZNEC, which has the maximum possible gain at the frequency, and is with front/back ratio of at least 10 dB, and input impedance to be purely resistive. Besides, it determines the optimum length of each element and the optimum spacing between elements (S), which requires readjustment of the element lengths.

1. INTRODUCTION

The Yagi-Uda antenna was invented by Shintaro Uda of Tohoku Imperial University, Sendai, Japan, with the collaboration of Hidetsugu Yagi, also of Tohoku Imperial University. The Yagi beam antenna is unidirectional. It can be vertically polarized or horizontally polarized with little difference in performance (other than the polarization) [1]. The Yagi antenna can be rotated into position with little effort. Yet the Yagi antenna shows power gain (so it puts out and receives a stronger signal), reduces the interfering signals from other directions, and is relatively compact [1].

2. YAGI ANTENNA DESIGN AND ADJUSTMENT

In fact, the structure of Yagi antenna is very simple. The basic Yagi antenna consists of three elements, as shown in Figure 1.

In order to minimize the number of variables, it does not use different spacing between the dipole and the other two elements. Hence, there are four variables to optimize: reflector length, director length, driven element length and spacing S [3].

Hence, it got the computing results from the above equations. The director length is 0.938 m; driven element length is 0.9713 m; reflector length is 1 m which is a half wavelength; spacing length is 0.2886 m. Considering the effect of environment, it got a wavelength 1.99862 m according to 150 MHz from the software EZNEC, so the above parameters change a little. And in practice, it adjusted the length of the three elements and the space. The following figures and some results are the most excellent parameters which are brought from the optimization process. The director length is 0.9373 m; driven element length is 0.9706 m; reflector length is 0.9993 m which is a half wavelength; spacing length is 0.2884 m. Figure 2 is the main window of EZNEC, and the operating frequency is set to 150 MHz, and the wavelength is 1.99862 m.

Figure 3 is the wire setting window of Yagi antenna, and it adopted 3-element structure which includes three wires in EZNEC.

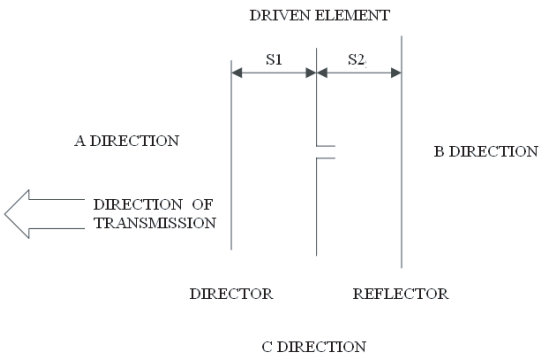

Figure 1: The basic Yagi antenna.

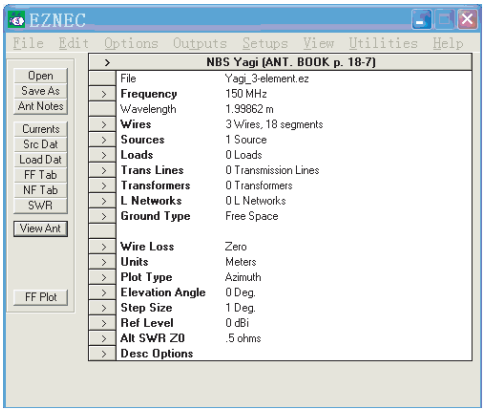

Figure 2: The main window of EZNEC.

Figure 4 is the 3D plot of the designed Yagi antenna with three elements, and it set the second wire as the source port.

Once finished the design, it provides the far field plot of designed Yagi antenna, shown in Figure 5. And in this figure, it is obvious that the front/back gain is 17.9 dB, which is more than the requirement that front/back gain is at least 10 dB.

Figure 6 is a snapshot of all the active windows of the design of Yagi antenna, which display the designed parameters, effect plot, wire setting and the FF plot.

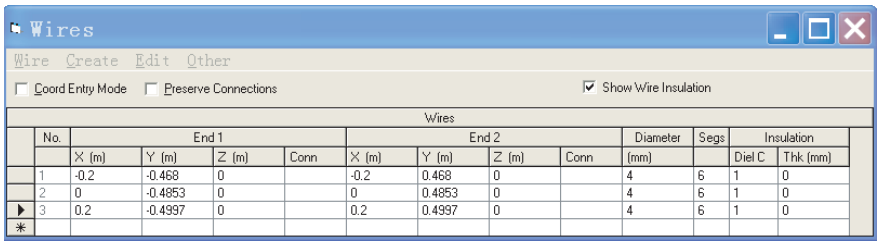

Figure 3: The wire setting window of Yagi antenna.

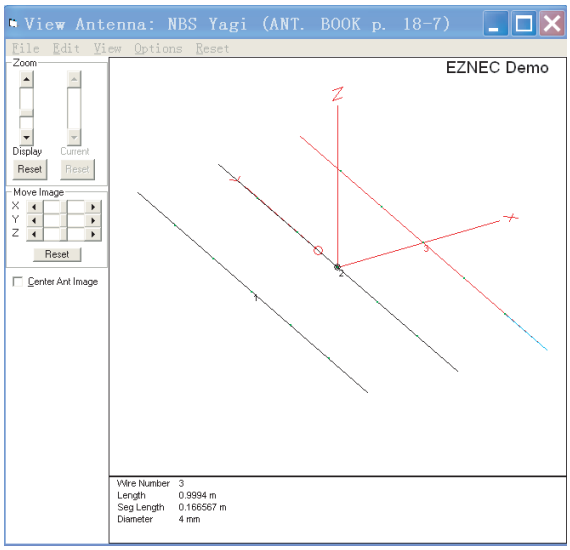

Figure 4: The 3D plot of the designed Yagi antenna with three elements.

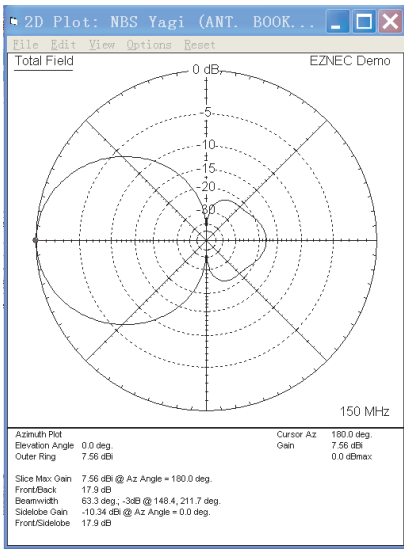

Figure 5: The far field plot of designed Yagi antenna.

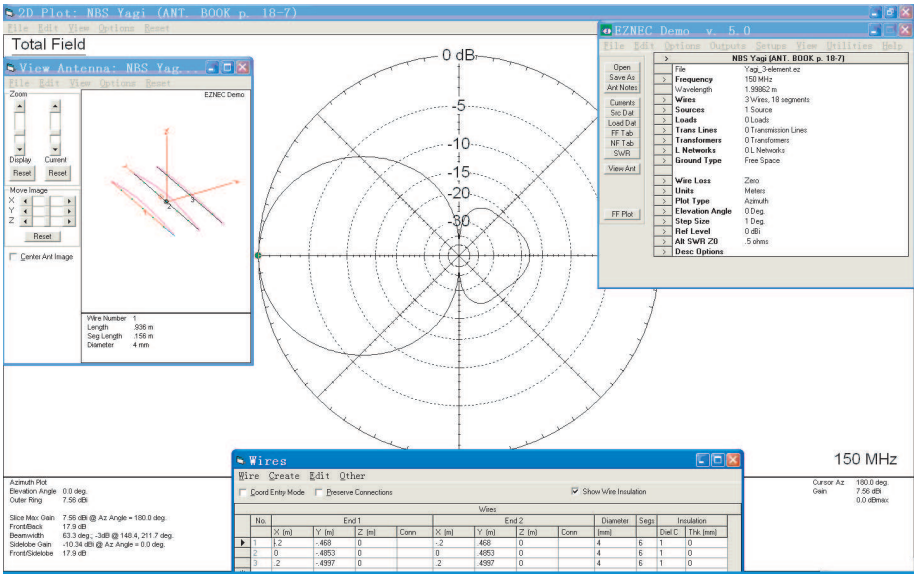

Figure 6: A snapshot of all the active windows of the design of Yagi antenna.

3. IMPEDANCE MATCHING OF YAGI ANTENNA

It is common practice to match impedances of antenna, transmission line, and either receiver or transmitter. The feedpoint impedance of most beam antennas is lower than the one of a half wavelength dipole, despite that the half wavelength dipole is a driven element.It adopts the gamma match shown in Figure 7 [4]. It consists of a piece of coaxial cable connector such that its shield is to the center point on the radiating element (L), and its center conductor goes to the matching device.

The dimensions of the gamma match of Figure 10 are as follows:

L is the driven element length, $A = \frac{L}{10}$, $B = \frac{L}{70}$, where: L, A and B are in meters.

4. EFFECT OF THE VARIATION OF FREQUENCY

Figure 8 is the far field plot of designed Yagi antenna with frequency varying in the frequency range $+/-6\%$ from the centre frequency.

From Figure 8, evidently the forward gain and F/B ratio of the designed Yagi antenna decrease according to the frequency shifting.

The resonant frequency depends on the dimensions of the Yagi antenna, and the dimensions of the Yagi antenna depend on the wavelength of the operating frequency, therefore, with the operating frequency shifting, the dimensions of the Yagi antenna keep their original values, then the forward gain and F/B ratio of the designed Yagi antenna are not the optimized situation, so they are decrease definitely [5].

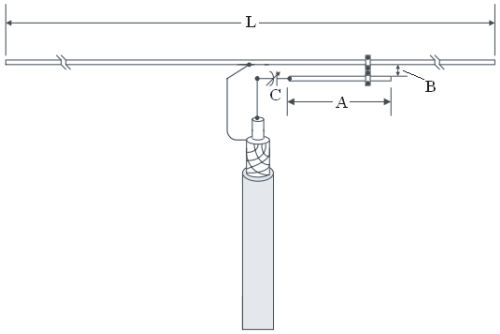

Figure 7: Gamma match.

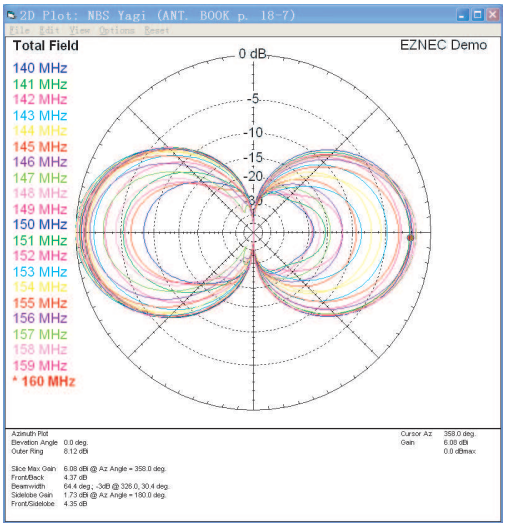

Figure 8: The far field plot of designed Yagi antenna with frequency varying in the frequency range $+/-6\%$ from the centre frequency.

5. CONCLUSIONS

This paper includes the process of designing a Yagi antenna, the design software usage, the diagrams of computing and simulation results, the rules of matching the antenna and the 50 Ω cable, and comments on the adjustment of the length and space of antenna, including discussion of gain variation and radiation. And the design of a 3-element Yagi beam aerial in free space for a frequency of 150 MHz using EZNEC, which has the maximum possible gain at the frequency, and is with front/back ratio of at least 10 dB, and input impedance to be purely resistive, meeting the requirements from the simulation results.

REFERENCES

1. Lim, S., "Design of a multidirectional, high-gain compact Yagi antenna," *IEEE Antennas Wireless Propag. Lett.*, Vol. 8, 418–420, 2009.
2. Balanis, C. A., *Antenna Theory: Analysis and Design*, Wiley, Hobo-ken, NJ, 2005.
3. Honma, N., T. Seki, and K. Nishikawa, "Compact planar four-sector antenna comprising microstrip Yagi-Uda arrays in a square configuration," *IEEE Antennas Wireless Propag. Lett.*, Vol. 7, 596–598, 2008.
4. Zhai, G., W. Hong, K. Wu, and Z. Kuai, "Printed quasi-Yagi antenna fed by half mode substrate integrated waveguide," *Asia-Pacific Microwave Conference*, 1–4, Suzhou, China, 2008.
5. Amadjikpe, A. L., D. Choudhury, G. E. Ponchak, and J. Papapoly-merou, "High gain quasi-Yagi planar antenna evaluation in platform material environment for 60 GHz wireless applications," *MTT IEEE MTT-S International Microwave Symposium Digest*, 385–388, Boston, MA, 2009.

Design and Analysis of a New Oscillator Circuit for Communication Based on Wien Bridge Structure

Qing Zhang[1], **Sheng-Yun Luo**[2], **and Wei-Wei Cheng**[3]

[1]Computer and Information Engineering College
Guizhou University for Nationalities, Guiyang, Guizhou 550002, China
[2]College of Science, Guizhou University for Nationalities, Guiyang, Guizhou 550002, China
[3]Institute of Microelectronics and Optoelectronics, Zhejiang University, Hangzhou, Zhejiang 310027, China

Abstract— This paper makes a detail analysis of the several important parameters of oscillator, which focus on the gain, distortion, stability of the gain, 180° phase shift, RC circuit for the oscillator design, and design a Wien bridge oscillator circuit based on the analysis, with the oscillating frequency 100 kHz by varying component values with 2.8% distortion.

1. INTRODUCTION

Oscillators are circuits that produce specific, periodic waveforms such as square, triangular, sawtooth, and sinusoidal. They generally use some form of active device, lamp, or crystal, surrounded by passive devices such as resistors, capacitors, and inductors, to generate output. There are two main classes of oscillator: relaxation and sinusoidal [1]. Thus, a sine wave may be the input to a device or circuit, with the output harmonics measured to determine t amount of distortion [2]. The waveforms in relaxation oscillators are generated from sine waves that are summed to provide specified shape.

2. ANALYSIS OF OSCILLATION

The canonical, or simplest, form of a negative feedback system is used to demonstrate the requirements for oscillation to occur. Figure 1 shows the block diagram for this system in which V_{IN} is the input voltage, V_{OUT} is the output voltage from the amplifier gain block (A), and β is the signal, called the feedback factor, that is fed back to the summing junction [3]. E represents the error term that is equal to the summation of the feedback factor and the input voltage.

The corresponding classic expression for a feedback system is derived as follows. Equation (1) is the defining equation for the output voltage; Equation (2) is the corresponding error:

$$V_{OUT} = E \times A \tag{1}$$

$$E = V_{IN} + \beta \cdot V_{OUT} \tag{2}$$

Eliminating the error term, E, from these equations gives

$$\frac{V_{OUT}}{A} = V_{IN} - \beta \cdot V_{OUT} \tag{3}$$

Rearrangement of the terms produces Equation (4), the classical form of feedback expression:

$$\frac{V_{OUT}}{V_{IN}} = \frac{A}{1 + A\beta} \tag{4}$$

Oscillators do not require an externally-applied input signal; instead, they use some fraction of the output signal created by the feedback network as the input signal.

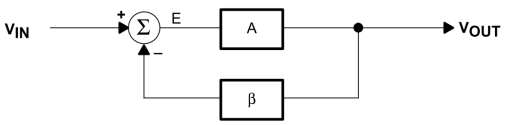

Figure 1: Canonical form of a feedback system with positive or negative feedback.

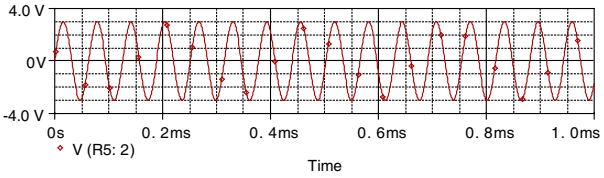

Figure 2: Oscillations occurring.

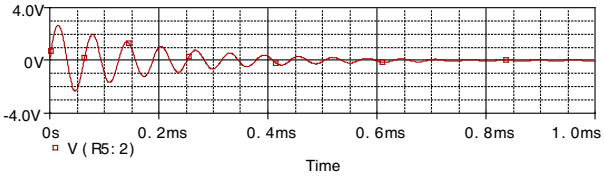

Figure 3: Oscillations attenuating.

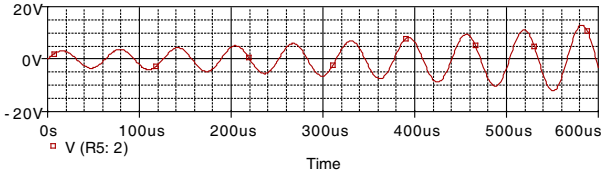

Figure 4: Oscillations amplifying.

The operational amplifier gain is

$$G = \frac{V_1(S)}{V_S(S)} = 1 + \frac{R_2}{R_1} \tag{5}$$

$$V_O(S) = V_1(S)\frac{Z_2(S)}{Z_1(S) + Z_2(S)} \tag{6}$$

We now have an equation for the overall circuit gain

$$T(S) = \frac{V_O(S)}{V_S(S)} = \frac{sRCG}{s^2R^2C^2 + 3sRC + 1} \tag{7}$$

If $G = 3$, oscillations occur, if $G < 3$, oscillations attenuate, if $G > 3$, oscillations amplify.

3. PHASE SHIFT IN OSCILLATOR

Phase shift determines the oscillation frequency because the circuit oscillates at whatever frequency accumulates a 180° phase shift. The sensitivity of phase to frequency, $d\varphi/d\omega$, determines the frequency stability [4].

In the region where the phase shift is 180°, the frequency of oscillation is very sensitive to the phase shift. Thus, a tight frequency specification requires that the phase shift, $d\varphi$, be kept within exceedingly narrow limits for there to be only small variations in frequency, $d\omega$, at 180° [5]. Although two cascaded RC sections eventually provide 180° phase shift, the value of $d\varphi/d\omega$ at the oscillator frequency is unacceptably small.

4. SINE WAVE OSCILLATOR CIRCUITS DESIGN

The transfer function for the circuit is derived using the technique described there. It is readily apparent that $Z_1 = R_G$, $Z_2 = R_F$, $Z_3 = (R_1 + 1/sC_1)$ and $Z_4 = (R_2 \| sC_2)$. Equation (8) shows the simple voltage divider at the non-inverting input. Each term is then multiplied by $(R_2C_2s + 1)$ and divided by R_2 to get Equation (9).

$$V_+ = V_{TEST}\left(\frac{Z_2}{Z_3 + Z_4}\right) = V_{TEST}\left[\frac{\dfrac{R_2}{R_2C_2s + 1}}{\left(\dfrac{R_2}{R_2C_2s + 1}\right) + \left(R_1 + \dfrac{1}{C_1s}\right)}\right] \tag{8}$$

$$\frac{V_+}{V_{TEST}} = \frac{1}{1 + R_1C_2s + \dfrac{R_1}{R_2} + \dfrac{1}{R_2C_1s} + \dfrac{C_2}{C_1}} \tag{9}$$

$$\frac{V_+}{V_{TEST}} = \frac{1}{1 + \dfrac{R_1}{R_2} + \dfrac{C_2}{C_1} + j\left(\dfrac{\omega_0}{\omega_1} - \dfrac{\omega_2}{\omega_0}\right)} \tag{10}$$

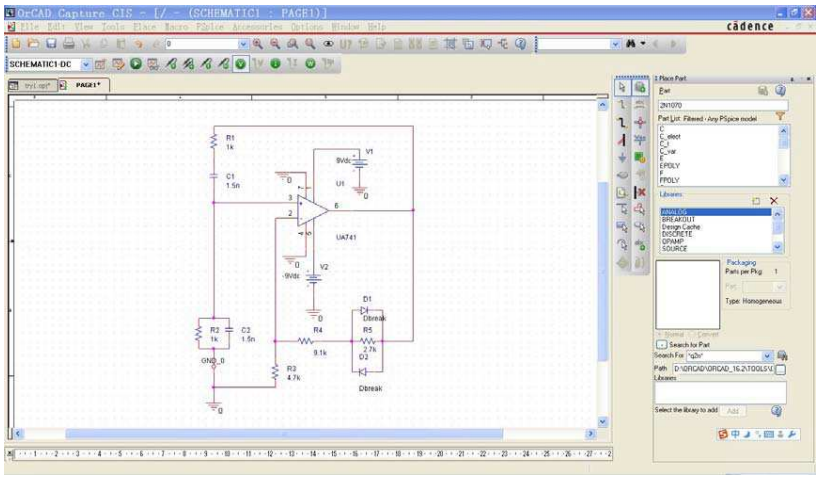

Figure 5: Wien-bridge circuit schematic in the window of OrCAD.

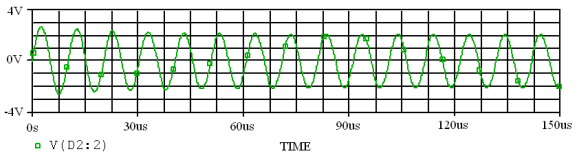

Figure 6: Time domain of wien-bridge circuit.

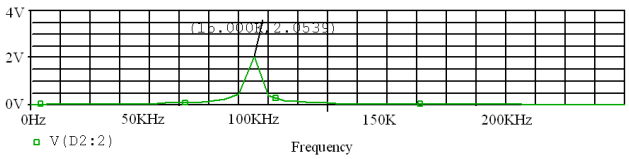

Figure 7: Frequency domain of wien-bridge circuit.

$$\frac{V_+}{V_{TEST}} = \frac{1}{1+\dfrac{R}{R}+\dfrac{C}{C}+j\left(\dfrac{\omega_0}{\omega_1}-\dfrac{\omega_2}{\omega_0}\right)} = \frac{1}{3+j\left(\dfrac{\omega_0}{\omega_0}-\dfrac{\omega_0}{\omega_0}\right)} = \frac{1}{3} \tag{11}$$

The final circuit is shown in Figure 5, with component values selected to provide an oscillation frequency of $\omega_0 = 2\pi f_0$, where $f_0 = 1/(2\pi RC) = 100\,\text{kHz}$. The circuit oscillated at 100 kHz, caused by varying component values with 2.8% distortion. Figure 6 and Figure 7 show the output voltage waveforms. The distortion grew as the saturation increased with increasing RF, oscillations ceased when RF was decreased by a mere 0.8%. The result of Wien bridge oscillator design is following.

In fact, due to limitations of the op-amp, frequencies above 1 MHz are unachievable.

5. CONCLUSION

This paper introduces the sinusoidal and relaxation type oscillator, and makes a detail analysis of the several important parameters of oscillator, and gives the result of Wien bridge oscillator circuit design which is according to the requirements and the design is based on the above analysis.

REFERENCES

1. Arena, P., L. Fortuna, and D. Porto, "Fractional integration via time-varying systems," *Proc. Int. Symp. on Nonlinear Theory and Its Applications (Nolta)*, 1125–1127, Switzerland, 1998.
2. Gottlieb, I. M., *Practical Oscillator Handbook*, Newnes, 1997.
3. "Single supply op amp design techniques," Application Note, Texas Instruments Literature Number SLOA030.
4. Elwakil, A. S. and A. M. Soliman, "A family of wien-type oscillators modified for chaos," *Int. Journal of Circuit Theory and Applications*, Vol. 25, 561–579, 1997.
5. Samavati, H., A. Hatimiri, A. Shahani, G. Nasser Bakht, and T. Lee, "Fractal capacitors," *IEEE J. Solid State Circuits*, Vol. 33, No. 10, 2035–2041, 1998.

The Research of the Turbo Coding Technology in the High-speed Underwater Communication with OFDM Mode

Wei Lan[1], **Bin Fang**[1], **Shi-Sheng Jin**[1], **and Wei-Wei Cheng**[2]

[1]Guizhou Meteorological Information Center, Guiyang, Guizhou 550002, China
[2]Institute of Microelectronics and Optoelectronics
Zhejiang University, Hangzhou, Zhejiang 310027, China

Abstract— This article describes the high-speed underwater acoustic communication of the key technologies of the OFDM underwater acoustic communication system, make an analysis of the advantages and disadvantages of the key technology of TURBO codes design based on high-speed underwater acoustic OFDM communication coding scheme, and it conducts the simulation and analysis, and finally, the reliability of the TURBO code in high-speed underwater acoustic OFDM communication is analyzed.

1. INTRODUCTION

Limited bandwidth, multi-path, the long propagation delay, and the fast time-varying of the channel structure, are the most difficult problems high-speed underwater acoustic communication faced, coupled with the background with high noise of the marine environment, which makes the underwater acoustic channel become by far the most difficult of wireless communication Channel [1].

The results show that acoustic communication in the water within an acceptable signal to noise ratio, using Turbo code BER performance is better than no channel coding and convolution coding; in the same bandwidth utilization using the program performance of underwater acoustic communication system better than that without channel coding and convolution codes [2]. Therefore, the combination of Turbo codes and OFDM system can significantly improve the transmission of underwater acoustic communication system transmission rate and reliability, resulting in underwater acoustic communication has a good application [3].

2. THE KEY TECHNOLOGIES OF HIGH-SPEED UNDERWATER ACOUSTIC COMMUNICATION

High-speed underwater acoustic communication of the key technologies including six directions, and that the new multi-path effects of reduced modulation; coding techniques, including image compression and transmission needed to improve the reliability of the system error correction coding; receiver structure embodies a powerful signal processor for the use and algorithms; underwater network system; a variety of fading channels were used in diversity and diversity techniques hidden; underwater acoustic channel physics, including the simulation and measurement of the channel [4]. OFDM underwater acoustic communication system is the key techniques, including spatial diversity techniques, anti-Doppler technology, PAPR technology and channel estimation and equalization.

The basic principle of OFDM is to convert the original signal through the string and split into N sub-signals, if the serial symbol rate is R, the conversion rate after the symbol R/N, sub-signal period is Δt, the integrity of the original signal cycle theory is $T = N * \Delta t$, then N sub-signals are modulated in the N-orthogonal subcarriers, and finally N Road, adding that the signal modulated by transmission signal; At the receiving end, the input signal is divided into N-branch, respectively, and mixing with N sub-carrier integration, to recover the parallel data, and then after string conversion and demodulation, and can recover the original data [5].

3. OFDM-BASED HIGH-SPEED UNDERWATER COMMUNICATION

Figure 1 shows the OFDM-based high-speed underwater acoustic communication system architecture including coding, interleaving, modulation module; OFDM (orthogonal frequency division multiplexing) module, with 52 sub-carriers, 64 point FFT, and 16 sample cyclic prefix; PLCP (Physical Fusion Protocol) module, pilot model for four long training sequence; multi-path fading channel dispersion module, can be used for multi-path channel parameters to configure the channel characteristics change; receiver equalizer module; Viterbi decoder module.

OFDM-based high-speed underwater acoustic communication system structure modified in each packet of data symbols and the number of missing bits; with continuous frame structure, omitting

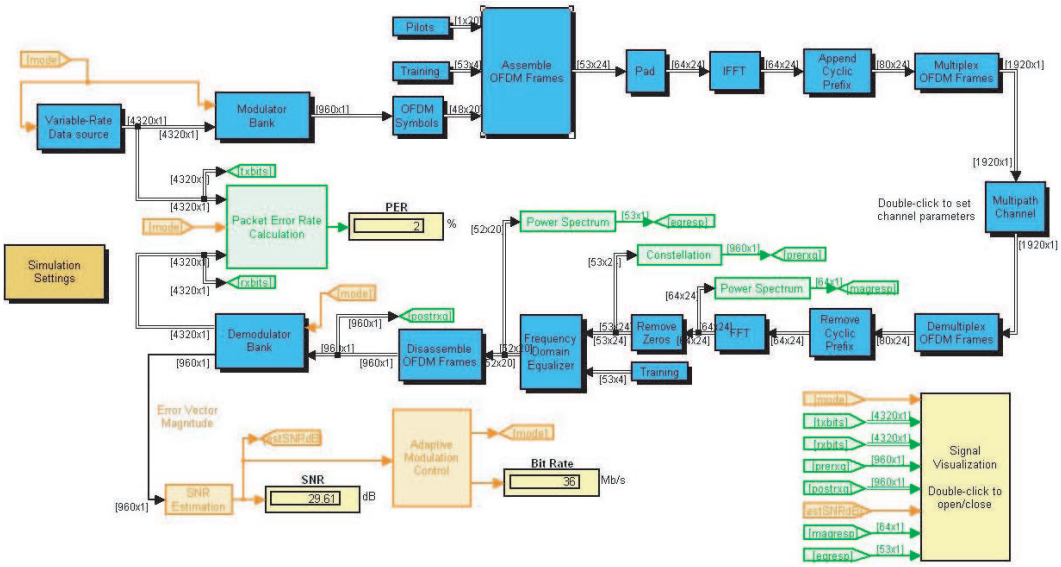

Figure 1: OFDM-based high-speed underwater acoustic communication system.

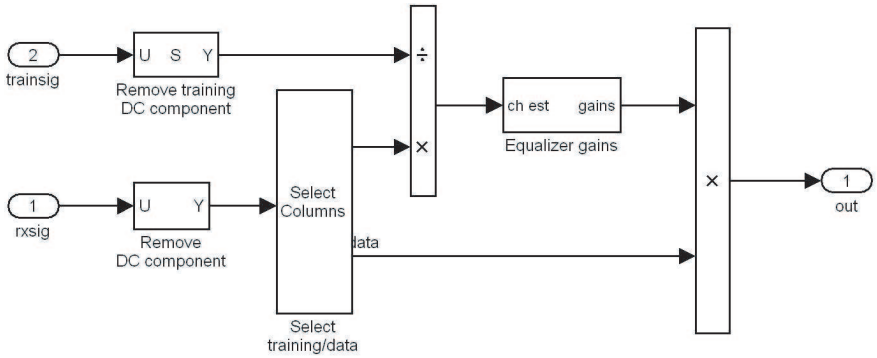

Figure 2: Structure of frequency domain equalizer.

the last part; decoder with a reset state; fixed transmit power level, instead of different channels Average signal to noise ratio.

As shown in Figure 2, Turbo frequency domain equalizer structure. Both the demodulator and decoder to use, input and output values of the prior processing operations, are provided for the next iteration of a Turbo incentive. The same principles also apply to Turbo coded CDMA systems, resulting in Turbo multiuser detection.

4. SIMULATION RESULTS

In accordance with the above-mentioned high-speed underwater acoustic communication in OFDM Turbo coding design, the simulation results are as follows.

Random binary data, you can see different data rates, see Figure 3 Turbo code based on high-speed underwater acoustic OFDM communication system simulation results — the data rate.

Plot before and after they receive a balanced signal, can know the modulation system is used, similar to a signal constellation of 2, 4, 8 or 64 points, Figure 4 Turbo Codes Based on high-speed underwater acoustic OFDM communication system simulation results — balanced.

Balance before and after encoding the received signal power spectrum. Before the equilibrium depends on the multipath fading channel model parameters of the dynamic signal block of spectrum, see Figure 5 Turbo codes based OFDM communication systems high-speed underwater acoustic simulation results — the received signal power spectrum, and Figure 6 Turbo-based high-speed underwater acoustic OFDM Code Communication System Simulation Results — Power spectrum equalization.

SNR estimation, error vector magnitude: Shows the maximum signal to noise ratio SNR estimation error vector magnitude. SNR in the multipath channel is the actual meaning of the received

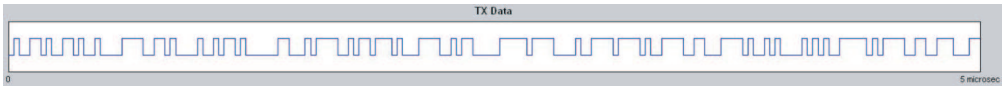

Figure 3: Data rate.

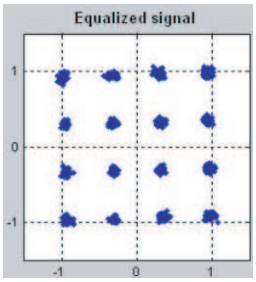

Figure 4: Balanced.

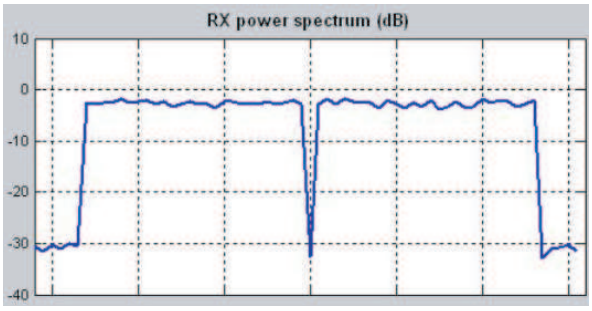

Figure 5: Received signal power spectrum.

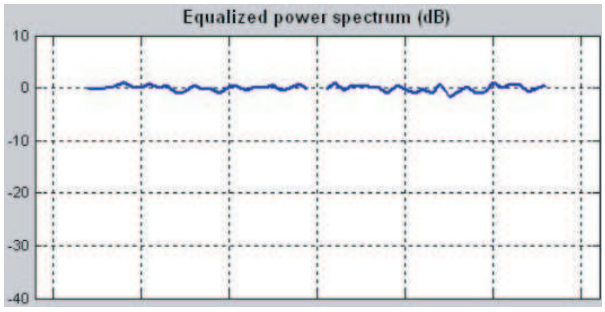

Figure 6: Power spectrum equalization.

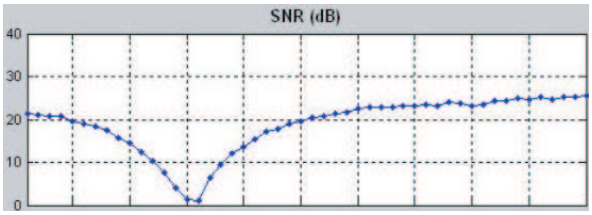

Figure 7: SNR.

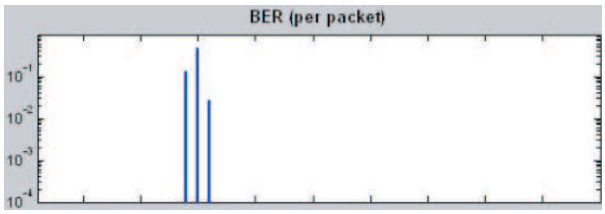

Figure 8: Error rate of every packet.

signal power subsystem, the signal to noise ratio, see Figure 7 Turbo codes based on high-speed underwater acoustic OFDM communication system simulation — SNR.

Each packet error rate: packet error rate as a percentage. For most of the data packet, the error rate is zero; see Figure 8 Turbo codes based on high-speed underwater acoustic OFDM communication system simulation results — every packet error rate.

5. CONCLUSION

Through this high-speed underwater acoustic communication of the key technologies of the presentation and OFDM underwater acoustic communication system of research, analysis of the OFDM underwater acoustic communication systems in the application of key technologies and the advantages and disadvantages, and code design based on high-speed TURBO OFDM underwater acoustic communication coding scheme for the system simulation, data rate, the signal is not balanced, balanced signal, the received signal power spectrum, balanced signal power spectrum, SNR, bit rate and packet error rate of each outcome were analyzed. Finally, BER and SNR under different conditions between the simulation results of the TURBO code in high-speed underwater acoustic OFDM communication reliability are analyzed.

REFERENCES

1. Stojanovic, M. and J. Presig, "Underwater acoustic communication channels: Propagation models and statistical characterization," *IEEE Communications Magazine*, 84–89, January 2009.
2. Stojanovic, M., "Efficient processing of acoustic signals for high rate information transmission over sparse underwater channels," *Elsevier Journal on Physical Communication*, 146–161, 2008.
3. Li, B., S. Zhou, M. Stojanovic, L. Freitag, and P. Willett, "Multicarrier communication over underwater acoustic channels with non-uniform doppler shifts," *IEEE Journal of Oceanic Engineering*, Vol. 33, No. 2, 198–209, April 2008.
4. Song, H. C., W. A. Kuperman, and W. S. Hodgkiss, "Basin-scale time reversal communications," *J. Acoust. Soc. Am.*, Vol. 125, 212–217, 2009.
5. Roy, S., T. M. Duman, V. McDonald, and J. G. Proakis, "High-rate communication for underwater acoustic channels using multiple transmitters and space-time coding: Receiver structures and experimental results," *IEEE Journal of Oceanic Engineering*, Vol. 32, No. 3, 663–688, July 2007.

Resonance Relation for Coated Spheres with Radial Anisotropy

H.-Z. Liu[1, 2], **K. Mouthaan**[1], **M. S. Leong**[1], **and S. Zouhdi**[2]

[1]National University of Singapore, Singapore
[2]Laboratoire de Génie Electrique de Paris, LGEP-Supélec, France

Abstract— In the long-wavelength limit, we establish the analytical resonance relation for coated rotationally uniaxial anisotropic spheres. We examine ranges of permissible constitutive parameters in conjunction with feasible radial ratios for two cases, one with a metallic shell and the other with a metallic core. In general, for the metallic shell case, an increase in core dielectric anisotropy leads to a larger permissible region constituted by both the shell permittivity and the core tangential permittivity for supporting localized surface plasmonic resonance (LSPR). A reverse trend is observed for having shell dielectric anisotropy. Furthermore, it is shown that for both above-mentioned arrangements, an increase in the order of LSPR results in a smaller permissible region. The derived relation serves as a design map of permissible values of the structural and material parameters, so that considerable time can be saved for future designs of resonant structures with radial anisotropy.

1. INTRODUCTION

For an electrically small sphere with positive permittivity, it is well-known that weak dipolar scattering prevails as described by Rayleigh scattering. On the other hand, for a small sphere with negative permittivity, giant scattering, termed plasmonic resonance, takes place due to the excitation of surface plasmons (polaritons), where surface plasmons are found in metals and surface polaritons in dielectrics [1]. With a core-shell structure, Alu and Engheta [2] speculated that LSPR can be supported when at least one layer possesses negative permittivity. Coated anisotropic spherical particles are of particular interest to this work due to their emerging applications in optical devices and plasmonic nanoantennas. Earlier work in the spectral domain [3–5] demonstrated that coated anisotropic spheres with either metallic shell or metallic core are capable of supporting LSPR. In this paper, we focus on the monochromatic case and generalize the resonance condition developed by Alu and Engheta by introducing an additional degree of freedom from dielectric anisotropy. The derived relation is analyzed pertaining to the role of dielectric anisotropy.

2. THEORETICAL FORMULATION

As illustrated in Fig. 1, a coated rotationally uniaxial anisotropic spherical scatterer of shell radius a_1 and core radius a_2 is centered at the origin and immersed in an isotropic host medium whose permittivity and permeability are denoted by ε_m and μ_m, respectively. An x-polarized monochromatic

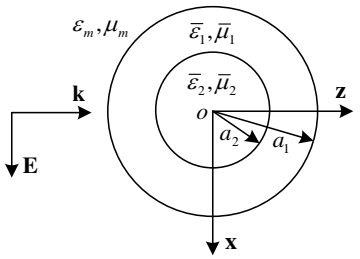

Figure 1: Configuration of scattering of incident plane wave by coated sphere with radial anisotropy.

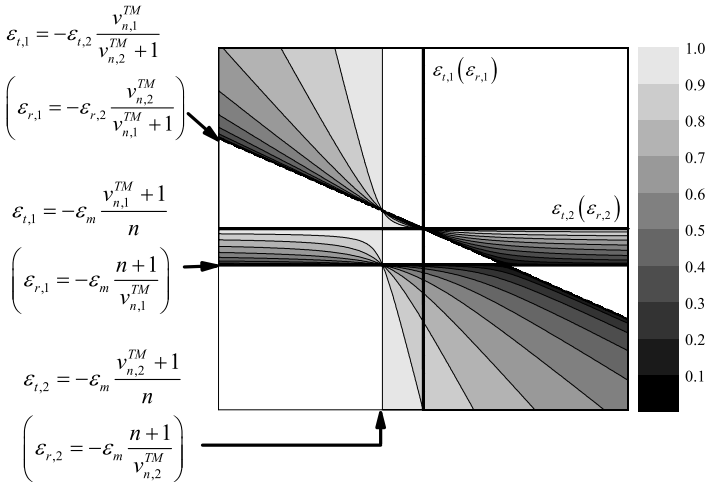

Figure 2: Contour plot of resonance condition over $\varepsilon_{t,1}$–$\varepsilon_{t,2}$ ($\varepsilon_{r,1}$–$\varepsilon_{r,2}$) space: gray region corresponds to $0 < a_2/a_1 < 1$; white region corresponds to forbidden region.

plane wave with unit amplitude travels along the z direction, as described by $\mathbf{E}^i = \hat{\mathrm{x}} e^{ik_m z} e^{-i\omega t}$, where $k_m = \omega\sqrt{\varepsilon_m \mu_m}$. The permittivity and permeability tensors of the scatterer are defined in the spherical coordinates as $\bar{\varepsilon}_j = (\varepsilon_{r,j} - \varepsilon_{t,j})\,\hat{r}\hat{r} + \varepsilon_{t,j}\bar{I}$ and $\bar{\mu}_j = (\mu_{r,j} - \mu_{t,j})\,\hat{r}\hat{r} + \mu_{t,j}\bar{I}$, where the identity tensor is given by $\bar{I} = \hat{r}\hat{r} + \hat{\theta}\hat{\theta} + \hat{\phi}\hat{\phi}$. The symbol j denotes the layer number ($j = 1$ for the shell region and $j = 2$ for the core region). It should be noted that $k_{t,j} = \omega\sqrt{\varepsilon_{t,j}\mu_{t,j}}$.

In the long-wavelength or small-radii limit, we derive the closed form expression of the scattering coefficient from the Mie solution [6]. The formulation presented below focuses on transverse magnetic (TM) waves with respect to the radial direction, whereas the transverse electric (TE) case can be inferred by duality. Following the approach presented in [6], the TM scattering coefficient of order n, corresponding to the n-th order component in the harmonic expansion of the incident wave, can be presented in symbolic form as

$$T_n^{TM} = \frac{C_n^{TM}}{C_n^{TM} + iD_n^{TM}}. \tag{1}$$

Both C_n^{TM} and D_n^{TM} are real with the assumption of negligible loss. Dissipative loss may cause severe attenuation to plasmonic resonance [1] and is not discussed in this paper.

In the limit of $z \to 0$, expressions of first- and second-kind Riccati-Bessel functions can be simplified with reference to those of pertinent cylindrical Bessel functions as [7]

$$\hat{J}_v(z) = \sqrt{\pi}(z/2)^{v+1} \Big/ \Gamma(v + 3/2), \tag{2}$$

$$\hat{Y}_v(z) = -\left(1/\sqrt{\pi}\right)\Gamma(v + 1/2)\,(z/2)^{-v}, \tag{3}$$

where $\Gamma(\cdot)$ denotes the Gamma function.

With reference to (2) and (3), the closed form expression for D_n^{TM} is given by

$$D_n^{TM} = \frac{n}{2n+1}\left(\frac{R_n^{TM}}{S_n^{TM}\varepsilon_m} + \frac{n+1}{n}\right), \tag{4}$$

where

$$R_n^{TM} = \varepsilon_{t,1}(n+1)\left\{\varepsilon_{t,1}\left(v_{n,2}^{TM}+1\right) + \varepsilon_{t,2}v_{n,1}^{TM} + \left(\frac{a_2}{a_1}\right)^{2v_{n,1}^{TM}+1}\left[\varepsilon_{t,2}\left(v_{n,1}^{TM}+1\right) - \varepsilon_{t,1}\left(v_{n,2}^{TM}+1\right)\right]\right\},$$

$$S_n^{TM} = \left(v_{n,1}^{TM}+1\right)\left[\varepsilon_{t,1}\left(v_{n,2}^{TM}+1\right) + \varepsilon_{t,2}v_{n,1}^{TM}\right] - v_{n,1}^{TM}\left(\frac{a_2}{a_1}\right)^{2v_{n,1}^{TM}+1}\left[\varepsilon_{t,2}\left(v_{n,1}^{TM}+1\right) - \varepsilon_{t,1}\left(v_{n,2}^{TM}+1\right)\right],$$

with $v_{n,j}^{TM} = \sqrt{\varepsilon_{t,j}/\varepsilon_{r,j}\,n(n+1) + 1/4} - 1/2$.

Resonance occurs when the scattering coefficient in (1) reaches its maximum of $T_n^{TM} = 1$, which is equivalent to setting $D_n^{TM} = 0$. As such, the n-th order LSPR become resonant in small scatterers. By setting (4) to zero, the resonance condition for the coated small sphere with radial anisotropy is derived as

$$\frac{a_2}{a_1} = \sqrt[2v_{n,1}^{TM}+1]{\frac{\left[\varepsilon_{t,1}n + \varepsilon_m\left(v_{n,1}^{TM}+1\right)\right]\left[\varepsilon_{t,1}\left(v_{n,2}^{TM}+1\right) + \varepsilon_{t,2}v_{n,1}^{TM}\right]}{\left(\varepsilon_m v_{n,1}^{TM} - \varepsilon_{t,1}n\right)\left[\varepsilon_{t,2}\left(v_{n,1}^{TM}+1\right) - \varepsilon_{t,1}\left(v_{n,2}^{TM}+1\right)\right]}}. \tag{5}$$

A graphical illustration of (5) is shown in the contour plot in Fig. 2, for given modal number n, dielectric anisotropy in core $\varepsilon_{t,2}/\varepsilon_{r,2}$ and shell $\varepsilon_{t,1}/\varepsilon_{r,1}$, and permittivity of the surrounding medium ε_m. In plotting Fig. 2, we presume that the dielectric anisotropy in all layers is positive, i.e., the tangential and radial permittivity in any layer must be of the same sign. The gray area corresponds to the permissible regions in which a combination of radial ratio a_2/a_1, tangential permittivity in the core $\varepsilon_{t,2}$ and shell $\varepsilon_{t,1}$ exists for resonance to take place. Lighter shades represent higher radial ratios. The white areas represent forbidden region for resonance. In addition, labels for the contour plot with respect to radial permittivity are provided in brackets.

By using duality ($\varepsilon \to \mu$), the resonance condition for the TE waves can be derived as

$$\frac{a_2}{a_1} = \sqrt[2v_{n,1}^{TE}+1]{\frac{\left[\mu_{t,1}n + \mu_m\left(v_{n,1}^{TE}+1\right)\right]\left[\mu_{t,1}\left(v_{n,2}^{TE}+1\right)+\mu_{t,2}v_{n,1}^{TE}\right]}{\left(\mu_m v_{n,1}^{TE} - \mu_{t,1}n\right)\left[\mu_{t,2}\left(v_{n,1}^{TE}+1\right)-\mu_{t,1}\left(v_{n,2}^{TE}+1\right)\right]}}. \tag{6}$$

In particular, when the material in both layers is isotropic, (5) and (6) converge to the formulae presented in [2].

3. NUMERICAL ANALYSIS

In this analysis, we presume the surrounding medium to be water (with $\varepsilon_m = 1.7689\varepsilon_0$ and $\mu_m = \mu_0$) and the scatterer is non-magnetic ($\mu_1 = \mu_2 = \mu_0$). Hence, under small-radii assumption, only TM resonance modes are relevant to our analysis. Furthermore, dissipative loss is assumed to be negligible everywhere. We investigate the properties of the contour plot over the shell–core tangential permittivity space, in particular, the $\varepsilon_{t,1}$–$\varepsilon_{t,2}$ space. Results can be easily extended to the $\varepsilon_{r,1}$–$\varepsilon_{r,2}$ space. As can be observed from Fig. 2, at least one layer of the particles has to possess negative permittivity for resonance to occur. Negative permittivity exists in certain metals near their plasma frequency, as described by the Drude model [3–5]. Therefore, we consider two kinds of particles in the following analysis, namely, one with anisotropic core and metallic shell, and the other with anisotropic shell and metallic core.

First we consider the metallic shell case with $\varepsilon_{t,1}/\varepsilon_{r,1} = 1$ for the isotropic shell, whose resonance condition is shown in 4th quadrant in Fig. 2. We are interested to know how anisotropy affects the permissible ranges of constitutive parameters. After some manipulations, a quantitative study is performed on the proportion of gray area to total area in the 4th quadrant. A higher proportion correlates with a wider permissible region. In Fig. 3, the proportion of permissible area in the 4th quadrant with varying core dielectric anisotropy between $0.01 \sim 100$ is presented for dipolar, quadrupolar and higher order multipolar resonance. In Fig. 3(a), the core tangential permittivity is limited between $0 \sim 15\varepsilon_0$, the shell permittivity is limited between $-15\varepsilon_0 \sim 0$. In Fig. 3(b), the constraint is relaxed, so that the two ranges become $0 \sim 100\varepsilon_0$ and $-100\varepsilon_0 \sim 0$ instead.

It can be observed in Fig. 3(a) that the proportion of permissible area increases with increasing core dielectric anisotropy, reaches a maximum and then gently decreases. For a low core anisotropy, the proportion of permissible area decreases with increasing modal number, whereas a reverse trend is observed for a high value of the core anisotropy. In Fig. 3(b), the proportion of permissible area increases with increasing core dielectric anisotropy and decreases with increasing modal number. By comparing Figs. 3(a) and (b), it can be concluded that when the choice of core tangential permittivity is limited, there exists an optimal core dielectric anisotropy that maximizes the proportion of permissible area. When the constraint is lifted, i.e., the ε_1–$\varepsilon_{t,2}$ space is expanded, a higher core dielectric anisotropy leads to a higher proportion of permissible area.

For a particle with metallic core, results are presented in Fig. 4. In general, increasing the shell dielectric anisotropy $\varepsilon_{t,1}/\varepsilon_{r,1}$ leads to decreasing proportion of permissible area, in contrast to the case with metallic shell.

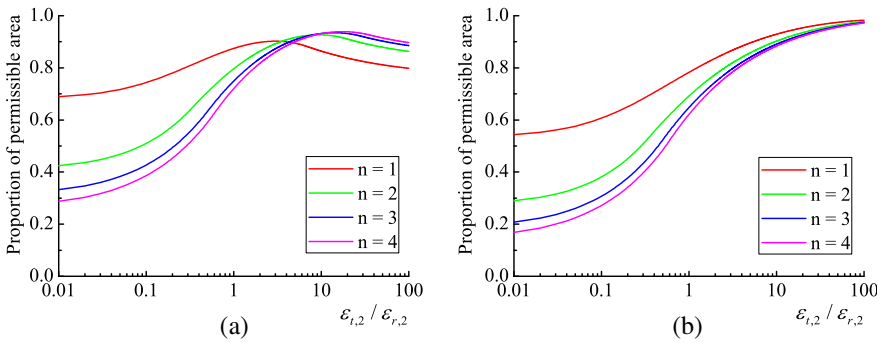

Figure 3: Proportion of permissible area in the 4th quadrant of contour map against $\varepsilon_{t,2}/\varepsilon_{r,2}$ with $\varepsilon_{t,1}/\varepsilon_{r,1} = 1$, $\varepsilon_m = 1.7689\varepsilon_0$ and (a) $|\varepsilon_{t,2,\max}| = |\varepsilon_{1,\max}| = 15\varepsilon_0$; (b) $|\varepsilon_{t,2,\max}| = |\varepsilon_{1,\max}| = 100\varepsilon_0$.

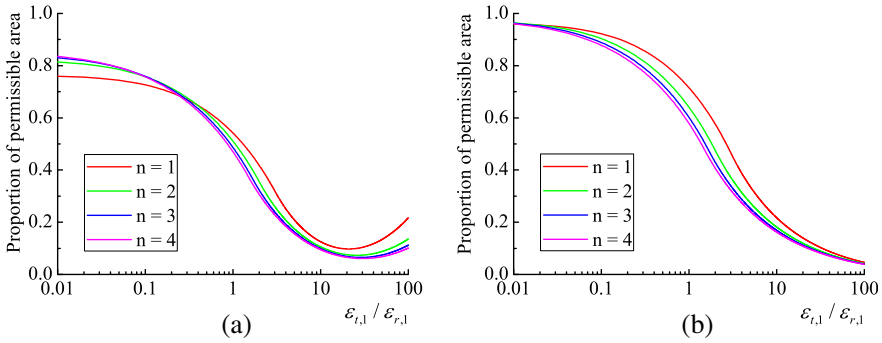

Figure 4: Proportion of permissible area in the 2nd quadrant of contour map against $\varepsilon_{t,1}/\varepsilon_{r,1}$ with $\varepsilon_{t,2}/\varepsilon_{r,2} = 1$, $\varepsilon_m = 1.7689\varepsilon_0$ and (a) $|\varepsilon_{t,1,\max}| = |\varepsilon_{2,\max}| = 15\varepsilon_0$; (b) $|\varepsilon_{t,1,\max}| = |\varepsilon_{2,\max}| = 100\varepsilon_0$.

4. CONCLUSION

In this paper, the effects of dielectric anisotropy on permissible ranges of constitutive parameters to support LSPR are quantitatively analyzed. The formulation is based on small-radii and low-loss assumption. Therefore the derived resonance relation will lose its accuracy when either the particle size or the dissipative loss increases. Nevertheless, the proposed resonance relation serves as a good starting point for selecting structural and material parameters in the design of resonant composite particles with radial anisotropy at given frequencies of interest.

REFERENCES

1. Tribelsky, M. I. and B. S. Luk'yanchuk, "Anomalous light scattering by small particles," *Phys. Rev. Lett.*, Vol. 97, No. 26, 263902-4, 2006.
2. Alu, A. and N. Engheta, "Polarizabilities and effective parameters for collections of spherical nanoparticles formed by pairs of concentric double-negative, single-negative, and/or double-positive metamaterial layers," *J. Appl. Phys.*, Vol. 97, 94310, 2005.
3. Ni, Y. X., et al., "Influence of spherical anisotropy on the optical properties of plasmon resonant metallic nanoparticles," *Appl. Phys. A*, Vol. 102, 673–679, 2011.
4. Wu, D. J. and X. J. Liu, "Influence of spherically anisotropic core on the optical properties of gold nanoshell," *Appl. Phys. A*, Vol. 94, No. 3, 537–541, 2009.
5. Liu, D. H., et al., "Effects of a coating of spherically anisotropic material in core-shell particles," *Appl. Phys. Lett.*, Vol. 92, No. 18, 181901, 2008.
6. Gao, L., et al., "Electromagnetic transparency by coated spheres with radial anisotropy," *Phys. Rev. E*, Vol. 78, 046609, 2008.
7. Abramowitz, M. and I. A. Stegun, *Handbook of Mathematical Functions with Formulas, Graphs, and Mathematical Tables*, Dover Publication, New York, 1965.

A Metal-dielectric Multilayer Film Applied to Enhance the Transmission of Two Counter-propagating Lights

Yaoju Zhang, **Xiaowei Ji**, **Youyi Zhuang**, **and Chongwei Zheng**
College of Physics and Electronic Information, Wenzhou University, Wenzhou, Zhejiang 325035, China

Abstract— Total internal reflection fluorescence microscopy (TIRFM) among several techniques of determining single molecule orientations by fluorescence measurements is a widely used imaging technique that is useful in probing the structure and dynamics of the basal surfaces of cells due to its excellent surface selectivity and ability to suppress background fluorescence. A single-layer metal film is often coated on surface of the coverslip in TIRFM to efficiently excite fluorescence molecules. However, the coated single-layer metal film decreases largely the transmission of emission fluorescence which propagation direction is contrary to that of the excitation light so that the intensity of detected image cannot be substantiality strengthened. In this paper, a metal-dielectric photonic crystal (MDPC) film is structured. The transmission of two counter-propagation lights from the MDPC film is analyzed by using the characteristic matrix method in the film optics. Compared with the single-layer metal thin film, the MDPC film consisted of 4.5 Ag-Si_3N_4 layers can increase not only the transmission of the excitation light but also the transmission of the emission light. If such a MDPC film is used to practical TIRFMs, the intensity of single-molecule fluorescence image can be markedly enhanced.

1. INTRODUCTION

Metallic devices at the nanometer scale have stimulated a broad range of interests in nanophotonics and near-field microscopy. For instance, sharp apertureless metal tips have been used to enhance the signal-to-noise ratio and the spatial resolution in a wide range of experiments [1–4]. A thin metal film can produce the surface plasmon-coupled emission (SPCE). Surface plasmon-coupled emission microscopy (SPCEM) was proposed as a high sensitivity technique that makes use of a thin layer of metal deposited on glass slides to efficiently excite fluorophores and to collect the emission light. The SPCEM technique with the total internal reflection fluorescence microscopy (TIRFM) configuration was used in the imaging of muscle fibrils to study the dynamics of interaction between actin and myosin cross-bridges [5]. The SPCEM method was first proposed as a high sensitivity and efficient fluorescence detection method by Lakowicz et al. [6, 7]. They showed, through imaging fluorophores near to a silver-coated glass substrate, that the fluorescence emission was highly directional and this increased the collection efficiency to nearly 50%, as well as contributed to low background noise. Experiments have also shown that the fluorescence of single molecules in the vicinity of a thin metallic film may appear enhanced up to a factor of 12 when detected through the metallic film [8]. Recently, Tang et al. proposed theoretically a model for SPCEM and show, through theoretical analysis and empirical results, that the point spread function of SPCEM is irregular and has an annular-like structure, significantly different from the familiar point spread function of the conventional wide-field microscopy [9]. This result is due to the highly polarized and anisotropic emission caused by the metal layer.

Theory and experimental results have shown that duo to the SPCE, the single-layer metal film coated on the surface of glass slides in the TIRFM can intensify the transmission of the excitation light so that the emission of fluorescent molecules is enhanced. On the other hand, the metal film also collects the emission light which propagating direction is contrary to the propagating direction of the excitation light in the TIRFM. The calculation in this paper shows that if the metal film coated on the glass slide in TIRFM is a single-layer metal film structure, its collection ability to the emission light is lower than that without the metal film. To overcome this disadvantage and further increase the intensity of fluorescent image, we propose a multilayer metal-dielectric photonic crystal (MDPC) film structure. The transmissions of two counter-propagating lights can be enhanced by use of the proposed MDPC film and consequently the fluorescent imaging intensity is larger than that by use of a single-layer metal film in the TIRFM.

2. MODEL AND FORMULAE

For simplicity, we calculate the transmission coefficients of plane wave passing through the MDPC film using the transfer matrix method [10]. For concreteness, we assume that the MDPC composite

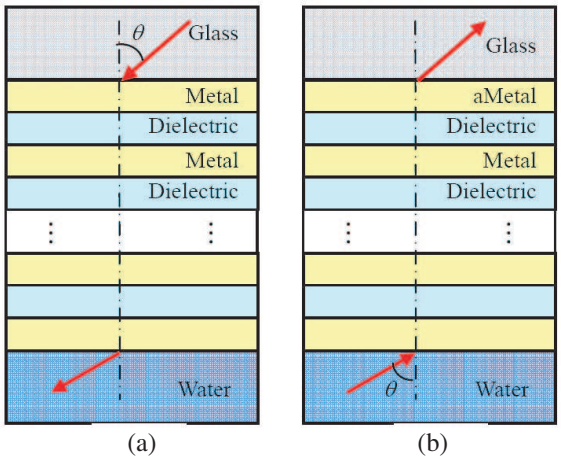

Figure 1: Metal-dielectric photonic crystal structure. (a) The incidence of excitation light from the glass and (b) the incidence of emission light from the water.

film consists of a Si_3N_4 dielectric layer with the dielectric constant $\varepsilon_d = 4.08$ and an Ag metal layer (as shown in Fig. 1) and the thickness of metal and dielectric layers are denoted t and h respectively. Both metal and dielectric are assumed nonmagnetic (i.e., $\mu = 1$). The glass slide in the TIRFM is on top of the MDPC film and water is below the MDPC film, fluorescence molecules is in water and in the vicinity of the interface between the MDPC film and water. We assume excitation light with 532 nm wavelength propagates along the route of glass→MDPC→water, while emission light with 560 nm wavelength propagates along the route contrary to the excitation light, i.e., water→MDPC→glass. (n_g, n_w n_m n_d) denote the refractive indices of glass slide, water, metal, and dielectric, respectively.

According to the film optics, the electric-filed transmission coefficient of the film can be written as [10]

$$t_s = \frac{2p_1}{(m_{11}^s + m_{12}^s p_l)p_1 + (m_{21}^s + m_{22}^s p_l)}, \tag{1}$$

$$p_1 = \sqrt{\frac{\varepsilon_1}{\mu_1}}\cos\theta_1, \quad p_l = \sqrt{\frac{\varepsilon_l}{\mu_l}}\cos\theta_l, \tag{2}$$

for the TE-polarized wave incident on the MDPC film and

$$t_p = \sqrt{\frac{\mu_l\varepsilon_1}{\mu_{1l}\varepsilon_l}}\frac{2q_1}{(m_{11}^p + m_{12}^p q_l)q_1 + (m_{21}^p + m_{22}^p q_l)}, \tag{3}$$

$$q_1 = \sqrt{\frac{\mu_1}{\varepsilon_1}}\cos\theta_1, \quad q_l = \sqrt{\frac{\mu_1}{\varepsilon_1}}\cos\theta_l, \tag{4}$$

for the TM-polarized wave incident on the MDPC film. In Eqs. (1) and (3), $m_{ij}^{s/p}$ is the elements of the characteristic matrix ($M(z_N) = M_1(z_1)M_2(z_2-z_1)\ldots M_N(z_N-z_{N-1})$) of the MDPC film where the superscripts s and p denote the components for the TE- and TM-polarized lights, respectively.

3. NUMERICAL RESULTS

It is well known that when the TE-polarized light is incident on a metal film, there is no the SPCE to come into being. Only for the TM-polarized light is incident on a metal film, the SPCE may be generated. Therefore, the TM-polarized light [8, 9] or radially polarized light [11, 12] are usually used in the TIRFM to effectively produce the SPCE. In the following calculations, we study only the transmission of the TM-polarized light from a metal film or a MDPC film. All calculation parameters are listed in Table 1.

As a starting point, we first calculate the transmission coefficient from a single-layer Ag film. Fig. 2 presents the amplitudes of the transmission coefficient $|t_p|$ from a single-layer Ag film as the incident angle θ, where (a) and (b) is the cases for the excitation light which propagating direction

Table 1: Calculation parameters.

parameter	value
$\lambda_{\text{excitation}}$	532 nm
$\lambda_{\text{emission}}$	560 nm
n_g of glass	1.518
n_m of Ag at $\lambda = \lambda_{\text{excitation}}$	0.12932-i3.19320
n_m of Ag at $\lambda = \lambda_{\text{emission}}$	0.12132-i3.42061
n_d of Si_3N_4	4.08
n_w of water	1.33

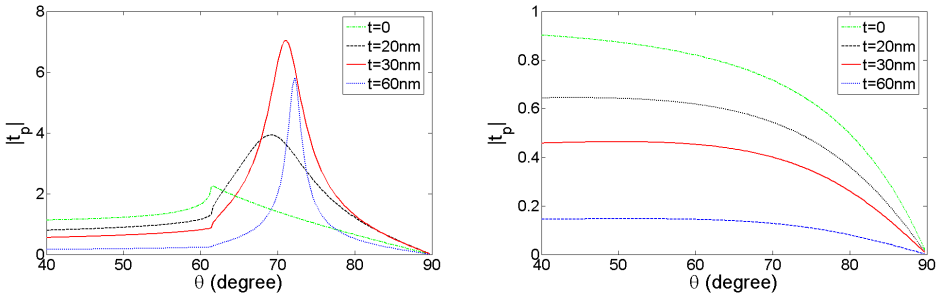

Figure 2: Amplitudes of transmission coefficients as a function versus the incident angle of the TM-polarized light. (a) For the excitation light propagating along the glass→metal→water direction and (b) for the emission light propagating along the water→metal→glass direction.

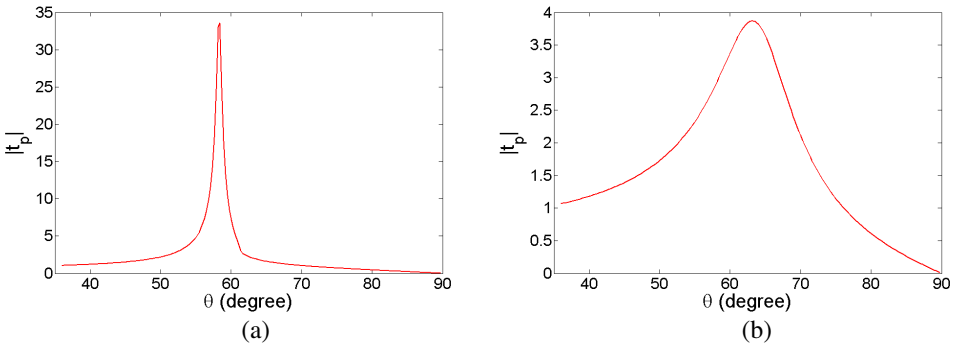

Figure 3: Amplitudes of transmission coefficients as a function versus the incident angle of the TM-polarized light incident on the MDPC. (a) For the excitation light propagating along the glass →MDPC→water direction and (b) for the emission light propagating along the water →MDPC→glass direction.

is from glass to water and for the emission light which propagating direction is from water to glass. As comparison, the transmission coefficient is also compiled together (dash-dot curves). From Fig. 2(a) it is seen that the metal film of Ag can enhance the transmission of the excitation light. The size of SPCE peak value has a non-monotone behaviour with the thickness t of Ag film. Our calculation shows that $|t_p|$ reaches its maximum value of 700 at $t = 42\,\text{nm}$. However, it is seen from Fig. 2(b) that the metal film result in the decrease of the transmission of the emission light which propagating direction is opposite to that of the excitation light and $|t_p|$ is smaller for larger t, which is disadvantage for enhancing the intensity of fluorescence image.

In order to overcome the shortcoming that a single-layer metal film reduces the transmission of the emission light, we propose a MDPC film structure as shown in Fig. 1. The MDPC film we designed consists of 4.5 metal-dielectric periodic layers, that is, the MDPC film consists of 5-layer Ag and 4-layer Si_3N_4 and the thickness of each layer is within the nanometer level. We find that when each Ag layer is 20 nm thick and each Si_3N_4 layer is 60 nm thick. such one-dimensional photonic crystal film can enhance the transmission of two counter-propagating lights. Figs. 3(a) and (b) show the transmission coefficients of the excitation light propagating along the glass→MDPC→water direction and the emission light along the opposite direction to the excitation light, respectively.

It is clear that the transmissions of the MDPC film for two counter-propagating lights are both enhanced compared with the case without any film. The brightness of fluorescent imaging patterns will be increased remarkably if such MDPC film is used in the TIRFM.

4. CONCLUSION

To enhance the image of single molecule fluorescence, one single-layer metal film is usually deposited on the glass slide in conventional localized TIRFMs. Our calculation has shown that one single layer metal film can enhance in faith the transmission of the excitation light but it reduces the transmission of the emission light propagating in the opposite direction of the excitation light. In this paper we have designed a MDPC film structure which consists of 4.5 Ag-Si_3N_4 layers. When the thickness of each Ag layer is 20 nm and the thickness of each Si_3N_4 layer is 60 nm in the MDPC with 4.5 Ag-Si_3N_4 periods, the MDPC film can enhance not only the transmission of the excitation light but also the transmission of the emission light. There is no doubt that if such MDPC film replaces the single layer metal film in the TIRFMs, the image quality of single molecule fluorescence will be improved markedly.

ACKNOWLEDGMENT

This work was supported by the National Natural Science Foundation of China under contract 61078023, the Public Welfare Project of Zhejiang Province science and technology office under contract 2010C31051, and the Natural Science Foundation of Zhejiang Province under contract Y6110505.

REFERENCES

1. Hayasawa, N., Y. Inouye, and S. Kawata, "Evanescent field excitation and measurement of dye fluorescence in a metallic probe near-field scanning optical microscope," *J. Microsc.*, Vol. 194, No. 2–3, 472–476, 1999.
2. Azoulay, J., A. D'ebarre, A. Richard, and P. Tch'enio, "Field enhancement and apertureless near-field optical spectroscopy of single molecules," *J. Microsc.*, Vol. 194, No. 2–3, 486–490, 1999.
3. Hamann, H. F., A. Gallagher, and D. J. Nesbitt, "Near-field fluorescence imaging by localized field enhancement near a sharp probe tip," *Appl. Phys. Lett.*, Vol. 76, No. 14, 1953–1957, 2000.
4. Sanchez, E. J., L. Novotny, and X. S. Xie, "Near-field fluorescence microscopy based on two-photon excitation with metal tips," *Phys. Rev. Lett.*, Vol. 82, No. 20, 4014–4017, 1999.
5. Borejdo, J., Z. Gryzyncski, N. Calander, P. Muthu, and I. Gryzyncski, "Application of surface plasmon coupled emission to study of muscle," *Biophys. J.*, Vol. 91, No. 7, 2626–2635, 2006.
6. Lakowicz, J. R., "Directional surface plasmon-coupled emission: A new method for high sensitivity detection," *Biochem. and Biophys. Res. Comm.*, Vol. 307, No. 3, 435–439, 2003.
7. Lakowicz, J. R., "Radiative decay engineering. 3. Surface plasmon-coupled directional emission," *Anal. Biochem.*, Vol. 324, No. 2, 153–169, 2004.
8. Stefani, F. D., K. Vasilev, N. Bocchio, N. Stoyanova, and M. Kreiter, "Surface-plasmon-mediated single-molecule fluorescence through a thin metallic film," *Phys. Rev. Lett.*, Vol. 94, No. 2, 023005-4, 2005.
9. Tang, W. T., E. Chung, Y. H. Kim, P. T. C. So, and C. J. R. Sheppard, "Investigation of the point spread function of surface plasmon-coupled emission microscopy," *Opt. Express*, Vol. 15, No. 8, 4634–4646, 2007
10. Born, M. and E. Wolf, *Principles of Optics*, 7th Edition, 61–64, United Kingdom at University Press, Cambridge, 1997.
11. Bharadwaj, P., P. Anger, and L. Novotny, "Nanoplasmonic enhancement of single-molecule fluorescence," *Nanotechnology*, Vol. 18, No. 4, 044017-5, 2007.
12. Lerman, G. M., A. Yanai, and U. Levy, "Demonstration of Nanofocusing by the use of Plasmonic Lens Illuminated with Radially Polarized Light," *Nano Lett.*, Vol. 9, No. 5, 2139–2143, 2009.
13. http://refractiveindex.info/.

Extraction of Non-thermal THz Emission from a High Electron Mobility Transistor

Y. Zhou, Y. D. Huang, W. Xue, X. X. Li, S. T. Lou, X. Y. Zhang, D. M. Wu, H. Qin, and B. S. Zhang

Key Laboratory of Nanodevice and Application, Suzhou Institute of Nano-Tech and Nano-Bionics Chinese Academy of Sciences, 398 Ruoshui Road, Suzhou Industrial Park, Jiangsu 215123, China

Abstract— In this paper, we propose and demonstrate a quantitative technique to extract the non-thermal terahertz (THz) emission from a high-electron-mobility transistor (HEMT). The THz emission is extracted from a strong background thermal radiation which lies in the terahertz spectrum too. Based on the technique, we obtained both efficiencies for terahertz emission and thermal emission. We found that the onset voltage of THz emission is below $V_{ds} \approx 1\,\mathrm{V}$ and the efficiency is maximized at $V_{ds} \approx 2\,\mathrm{V}$. Both THz emission and thermal emission saturate above $V_{ds} > 9\,\mathrm{V}$.

1. INTRODUCTION

The radiative decay of two-dimensional (2D) plasmons in semiconductor heterostructures is one of the most promising candidates for realising solid-state terahertz (THz) sources. Numbers of experimental studies have demonstrated THz emission from GaN/AlGaN, GaAs/AlGaAs heterostructures as well as Si MOSFETs [1–6]. Also there are a few rigorous theoretical studies on this subject [7, 8]. However, practical difficulties come from the fact that emission efficiency is low ($\sim 10^{-5} - 10^{-3}$) in such devices. This requires a highly sensitive detection technique to extract the weak THz emission from a strong thermal background which could be at room temperature or at an elevated device temperature. Hence, devices under test are usually cooled down to a low temperature to minimize the background emission. Cyrogenic narrow band detectors are often applied to achieve ultra high sensitivity and to enable spectrum analysis [5]. One of the widely used commercial detectors is cyrogenic silicon bolometer which normally works at liguid heilium temperature (4.2 K). A Fourier transform spectrometer (FTS) equipped with a silicon bolometer allows for sensitive detection and spectrum analysis [6]. These techniques have played an important role in extracting relatively strong THz emission with signal-to-noise ratio greater than one. In this paper, we present a scheme to extract weak THz emission which is submerged in a strong blackbody radiation.

2. EXPERIMENTAL SETUP

Our experiment was performed on a high-electron-mobility transistor (HEMT) fabricated from a GaN/AlGaN heterostructure, which provides a two-dimensional electron gas (2DEG) about 23 nm below the surface. The 2DEG has an electron mobility of $1400\,\mathrm{cm}^2/\mathrm{Vs}$ and an electron density of $1 \times 10^{13}\,\mathrm{cm}^{-2}$ at room temperature. The electron channel was formed by standard UV lithograph and has a length of 18 µm and a width of 400 µm. To couple the THz emission out of the electron channel, a metallic grating coupler (Ni/Au) with a period of 300 nm was fabricated on the surface by electron beam lithography (EBL).

The HEMT device was cooled down to 18 K in a pulse-tube cooler equipped with a 5 mm thick Polymethylpentene (TPX) window. As show in Fig. 1(a), the total emission from the HEMT was collected by a copper light pipe onto a Si bolometer (Model HDL5, *IRlabs, Inc.*). A DC source-drain bias (V_{ds}) is applied to excite two-dimensional plasmons. Here, we also superimposed a negative square-wave voltage ($V_{pp} = -1\,\mathrm{V}$) on the source-drain bias so that the induced emission power can be detected by a lock-in amplifier. The modulation frequency is tuned from 33 Hz to 2033 Hz in a step of 100 Hz. The duty cycle of the modulation signal is fixed at 50%. The average source-drain current is recorded by measuring the voltage drop on a $5\,\Omega$ resistor in series with the HEMT. The electrical power and detector signals as a function of the DC bias obtained at various modulation frequencies are plotted in Fig. 1(b).

3. DATA PROCESSING AND ANALYSIS

The total emission power seen by the bolometer contains two parts. One of them is caused by the radiative decay of 2D plasmons which is converted to electromagnetic radiation by means of grating coupler. The other is of thermal radiation due to the lattice heating by electric current. Both are

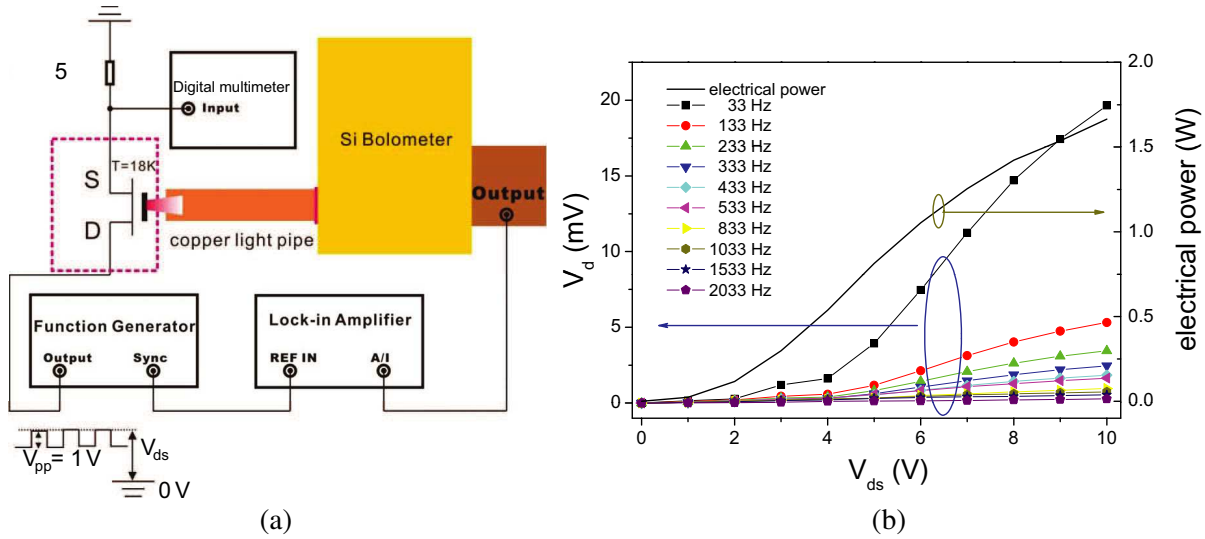

Figure 1: (a) Schematic of the experimental setup. (b) Electrical power and detector signal as a function of the DC bias at different modulation frequencies.

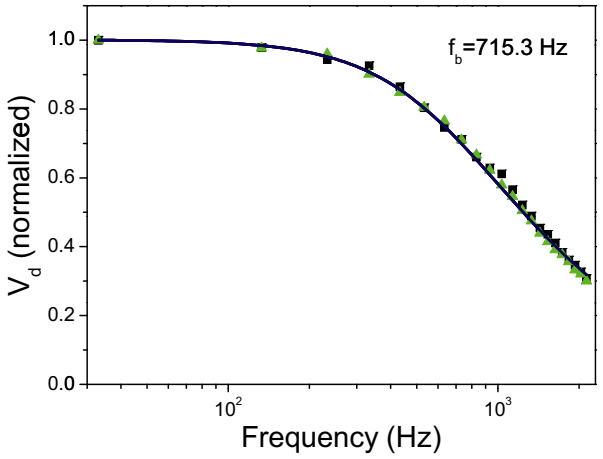

Figure 2: Frequency response of the silicon bolometer irradiated by a BWO THz source (≈ 1.0 THz).

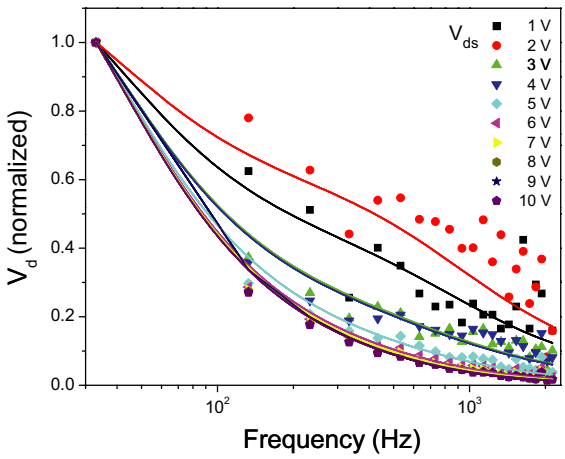

Figure 3: Frequency response of the detector signal from the device.

modulated by the 1 V square-wave source-drain voltage. These two emission processes have distinct characteristics of frequency response. For thermal emission, the characteristic frequency is low due to the device has a relatively large heat capacity and low thermal conductance. On the other hand, radiative decay of 2D plasmons has a much higher frequency response which is mainly determined by the damping of 2D plasmons. Nevertheless, when both emission energies are rendered onto the silicon bolometer, the silicon bolometer determines the highest response frequency.

Based on the above qualitative analysis, the detector signal can be written as

$$V_d = p_0[\alpha(V_{ds})Q_h + \beta(V_{ds})]sQ_b. \tag{1}$$

In Eq. (1), p_0 is the total electrical power delivered to the device, s is the responsivity of the silicon bolometer which is about 8000 V/W. $\alpha(V_{ds})$ and $\beta(V_{ds})$ are the bias-dependent efficiencies for thermal emission and THz emission, respectively. Q_h and Q_b are the frequency responses for thermal emission and silicon bolometer, respectively, and can be expressed as

$$Q_h = \frac{1}{\sqrt{1+(f/f_h)^2}}, \tag{2}$$

$$Q_b = \frac{1}{\sqrt{1+(f/f_b)^2}}, \tag{3}$$

Table 1: Parameter $k(V_{ds})$ at different DC bias voltages.

V_{ds} (V)	1	2	3	4	5	6	7	8	9	10
$k(V_{ds})$	0.40346	0.7564	0.14688	0.1406	0.05632	0.02944	0.02265	0.0168	0.0156	0.01513

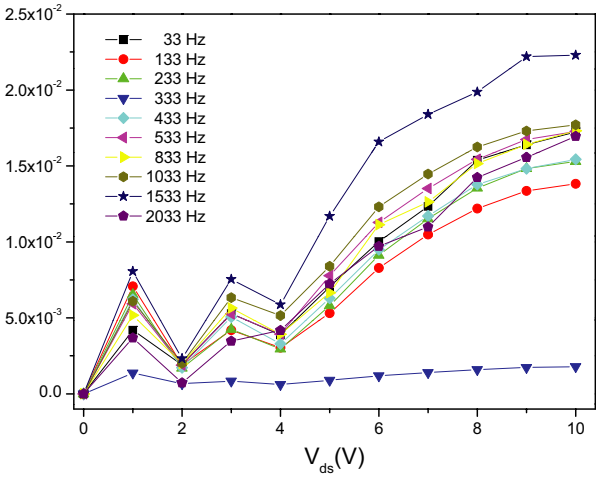

Figure 4: The efficiency of thermal emission.

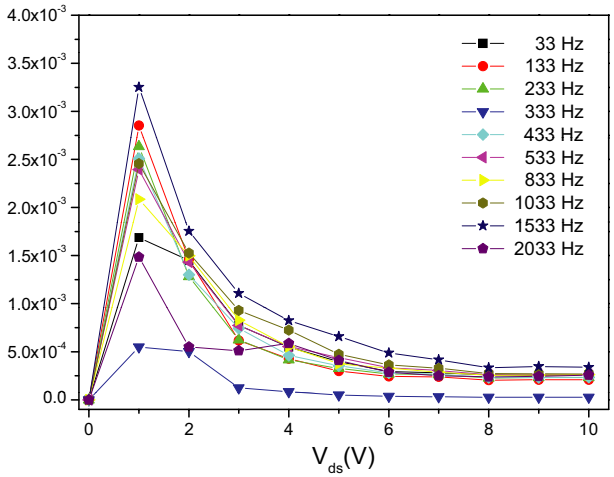

Figure 5: The efficiency of THz emission.

where, f is the modulation frequency, f_h and f_d are the characteristic frequency for thermal emission and THz emission, respectively. The detector signal can be further rewritten as

$$V_d = p_0 \alpha(V_{ds}) s[Q_h + k] Q_b, \tag{4}$$

where $k = \beta(V_{ds})/\alpha(V_{ds})$ is the ratio of THz emission to thermal emission.

The characteristic frequency f_b is determined in an experiment by chopping the THz output from a backward wave oscillator (BWO) as a standard THz source. As shown in Fig. 2, the frequency response is well fitted by Eq. (3) and f_b is found to be 715.3 Hz. By fitting the experimental data obtained at a constant DC bias and different modulation frequencies according to Eq. (1), both $f_h = 30$ Hz and parameter k are obtained. In the fitting, all curves are normalized to $f = 33$ Hz, as shown in Fig. 3. The obtained values for k as a function of the DC bias are listed in Table 1.

Based on the above analysis of k, both α and β can be obtained from

$$\alpha(V_{ds}) = \frac{V_d}{p_0 s[Q_h + k] Q_b}, \tag{5}$$

where both V_d and p_0 are experimental data shown in Fig. 1(b). Bias-dependent parameters α and β are shown in Fig. 4 and Fig. 5, respectively. Thermal emission increases with applied DC bias and saturates above $V_{ds} \approx 9$ V, while THz emission efficiency decreases with DC bias and also saturates above $V_{ds} \approx 9$ V. It is noted that the ratio of Thz emission to thermal emission is pronounced in the bias range of 1–4 V (also clearly shown in Table 1.

In the above analysis, details on the spectra of thermal emission and THz emission are ignored. The specific spectra and the filters used in front of the bolometer will vary the numbers for parameter α and β. In the experiment, the filter chosen is of low-pass type and has a cut-off wavelength about 20 µm. In the future, emission spectrum will be measured by using a FTS system to reveal the physical nature of the extracted THz emission.

4. CONCLUSION

In conclusion, both a frequency-tuned detection technique and the corresponding quantitative analysis are applied to uncover the THz emission from a grating-coupled HEMT device at 18 K. The efficiencies for THz emission and thermal emission are extracted and exhibit strong DC bias dependence. High efficiency THz emission is observed at low DC bias in the range from 1 V to 4 V. This technique provides a simple yet quantitative way to evaluate the THz emission efficiencies in electrical powered solid-state devices. More detailed measurements on the emission spectrum are needed to reveal the physical nature of THz emission in grating-coupled HEMT devices.

ACKNOWLEDGMENT

This work was supported by the National Basic Research Program of China (973 Program) grant No. G2009CB929300, the Knowledge Innovation Program of the Chinese Academy of Sciences grant No. Y0BAQ31001 and the National Natural Science Foundation of China grant No. 60871077.

REFERENCES

1. Gornik, E. and D. C. Tsui, "Voltage-tunable far-infrared emission from Si inversion layers," *Phys. Rev. Lett.*, Vol. 37, No. 21, 1425–1428, 1976.
2. Allen, S. J., D. C. Tsui, and R. A. Logan, "Observation of the two-dimensional plasmon in sillicon inversion layers," *Phys. Rev. Lett.*, Vol. 38, No. 17, 980–983, 1977.
3. Tsui, D. C., E. Gornik, and R. A. Logan, "Far infrared emission from plasma osillation of Si inversion layers," *Solid State Commun.*, Vol. 35, 875–877, 1980.
4. Höpfel, R. A. and E. Gornik, "Two-dimensional plasmons and far infrared emission," *Surface Sci.*, Vol. 142, 412–422, 1984.
5. Hirakawa, K., K. Yamanaka, M. Grayson, and D. C. Tsui, "Far-infrared emission spectroscopy of hot two-dimensinal plasmons in $Al_{0.3}Ga_{0.7}As/GaAs$ heterojunctions," *Appl. Phys. Lett.*, Vol. 67, 2326–2328, 1995.
6. Onishi, T., T. Tanigawa, and S. Takigawa, "High power terahertz emission from a single gate AlGaN/GaN field effect transistor with periodic Ohmic contacts for plasmon coupling," *Appl. Phys. Lett.*, Vol. 97, 092117, 2010.
7. Mikhailov, S. A., "Plasma instability and amplification of electromagnetic waves in low-dimensional electron systems," *Phys. Rev. Lett.*, Vol. 8, No. 3, 1517–1532, 1998.
8. Zheng, L., W. L. Schaich, and A. H. MacDonald, "Theory of two-dimensional grating couplers," *Phys. Rev. B.*, Vol. 41, No.12, 8493–8499, 1990.

Terahertz Photocurrent in Point Contact Devices

J. D. Sun, D. M. Wu, B. S. Zhang, and H. Qin
Key Laboratory of Nanodevice and Application, Suzhou Institute of Nano-Tech and Nano-Bionics
Chinese Academy of Sciences, 398 Ruoshui Road, Industrial Park, Suzhou City, Jiangsu 215123, China

Abstract— Quantum point contacts (QPCs) are nanoscale constrictions for electron wave packets. QPCs are usually realized in a high-mobility two-dimensional electron gas (2DEG) by applying negative bias to split Schottky gates. We explored the photocurrent in point contact (PC) devices induced by terahertz (THz) electromagnetic wave in the frequency range from 850 GHz to 930 GHz. Directional photocurrent were observed by varying the conductance of the point contacts. Furthermore, photocurrent from two point contacts in series was measured and exhibited fairly independent THz responses. A model based on homodyne mixing of THz electric field was examined. The results suggest that voltage-controlled nonlinear point contact devices could be suitable for high sensitive THz detection above 1 THz.

1. INTRODUCTION

The terahertz or submillimeter-wave region of the electromagnetic spectrum, ranging from 300 GHz to 10 THz, has not been exploited for practical applications to the same degree as other frequency regimes. While its suitability for spectroscopy of low-energy excitations of matter has long been recognized (far-infrared spectroscopy) [1], this has only led to limited practical applications outside of research laboratories. In the past decade, THz detectors based on solid-state plasmons have been proposed and demonstrated both at cryogenic and room temperatures [2–5]. These plasmonic devices utilize the resonance between high density two dimensional [2–4] or three dimensional [5] electron gas and the incident THz wave. Due to the resonant nature, plasmonic detectors offer high sensitivity and possibly an ability to resolve the spectrum. Recently, subterahertz detectors and focal plane arrays based on complementary metal-oxide-semiconductor (CMOS) technology have been developed for room temperature operation [6–8]. A self-mixing model based on the resistive network of the field-effect transistor is found to be adequate for analyzing the devices operating in the non-resonant detection regime. In principle, any voltage controlled nonlinear resistor driven by THz electric field may exhibit a photocurrent or photovoltage. In this report, we provide evidences for possible THz detection (850–930 GHz) using a point-contact device based on GaAs/AlGaAs heterostructures. Furthermore, we attempted to study the effect of two point contacts connected to each other in series.

2. DEVICE FABRICATION AND THE EXPERIMENTAL SETUP

The device is fabricated from a GaAs/AlGaAs heterostructure, which provides a 2DEG about 90 nm below the surface. The 2DEG has an electron density of $8 \times 10^5\,\mathrm{cm}^2/\mathrm{Vs}$ and an electron mobility of $1.4 \times 10^{11}\,\mathrm{cm}^{-2}$ at 4.2 K. As shown in Fig. 1, five pairs of Schottky gates are fabricated using electron beam lithography and metal evaporation. The gate width is 200 nm. The distance between each two neighbouring Schottky gates is 150 nm. It has to be noted that the device was not deliberately designed for THz applications. Instead, the device was designed as a coupled double quantum dot for an experiment on photon-assisted tunneling in the microwave frequency range (3–50 GHz) [9]. Nevertheless, the bonding pads connecting to the Schottky gates are in a shape of bow-tie antennas.

The experiment setup is shown in Fig. 2(a), where the THz radiation from a backward wave oscillator (BWO) is chopped (f_c = 317 Hz), collected, collimated and focused onto the device located in a pulse-tube cooler. A 5 mm thick Polymethylpentene (TPX) disk is used as a window. Furthermore, a 2 mm thick high-resistivity-silicon wafer is used as a filter in front of the window in order to minimize the thermal radiation at room temperature and to block the visible light. For *in-situ* calibration, the THz beam is splitted ($T/R \approx 0.96$) by another high-resistivity-silicon wafer and guided to a pyroelectric (PE) detector (Model SPI-A-62THZ, from the *Spectrum Detector Inc.*). As shown in Fig. 2(b), the detector operates as a photocurrent sensor with zero source-drain bias. Only a small AC bias (f_m = 37 Hz, 20 μV) is applied to the drain. Both modulated AC source-drain current and the induced photocurrent are amplified by a DL1211 current preamplifier. Since the THz light and the source-drain bias are modulated at different frequencies (f_c, f_m), a

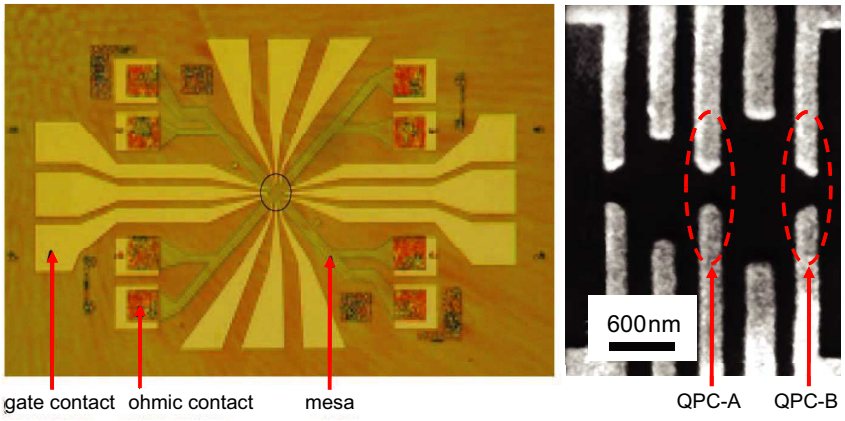

Figure 1: (a) The device layout. (b) A zoom-in view of the Schottky gates in the center of the device. The two point contacts labelled as QPC-A and QPC-B are about 900 nm apart.

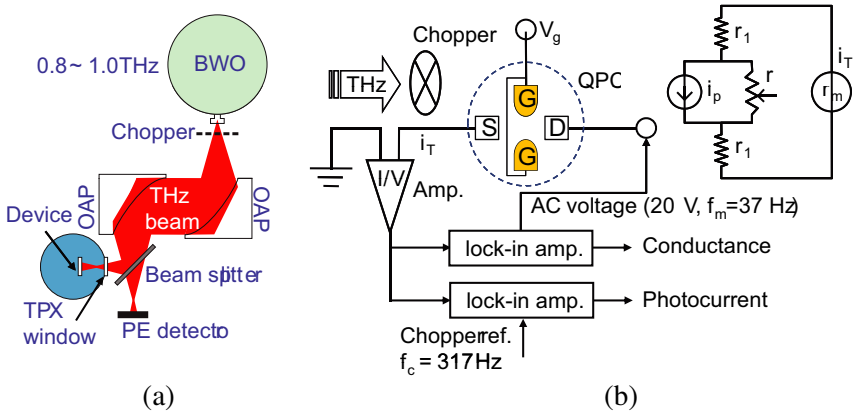

Figure 2: (a) The schematic of the experiment setup. (b) The scheme of dual lock-in technique to measure the differential conductance and photocurrent simultaneously. The inset is an equivalent circuit for the point contact device including the series lead resistance and the input resistance of the current preamplifier.

dual lock-in technique following the current amplifier is applied to extract the photocurrent (i_T) and the differential conductance ($G = \mathrm{d}I_{ds}/\mathrm{d}V_{ds}$) simultaneously.

3. RESULTS AND DISCUSSION

First, the gate-voltage controlled conductance of the device was characterized at 2.9 K, as shown in Fig. 3(a), (c). The electron channel can be pinched off completely at $V_{gA} \leq -0.5$ V for QPC-A and at $V_{gB} \leq -0.9$ V for QPC-B, respectively. Both point contacts can be fully opened when the corresponding gate voltage is greater than -0.2 V. It is clearly shown that both conductances have a transition around -0.3 V. This rapid decrease in conductance is due to the depletion of 2DEG under the large area of Schottky gates. When the gate voltage becomes more negative than -0.3 V, the constriction at the point contact begins to regulate the conductance. Before the pinch-off voltage is reached, steps of quantum conductance could appear. However, in our experiment we did not observe clear conductance steps mainly due to the temperature is relatively high. In Fig. 3(a), (c), the derivative ($\mathrm{d}G/\mathrm{d}V_g$) is plotted to reveal the rapid change in differential conductance.

In the second step, we rendered the device with a coherent THz irradiation from the BWO source. The frequency can be continuously tuned and is set between 850 GHz and 930 GHz. The induced photocurrent in the electron channel as a function of the gate voltage is shown in Fig. 3(b), (d). Under THz irradiation at 875 GHz, clearly shown is that strong photocurrent is induced when the conductance is varied by the gate voltage. According to the homodyne mixing of THz electric fields in the point contact, the induced photocurrent is in proportional to the derivative of the

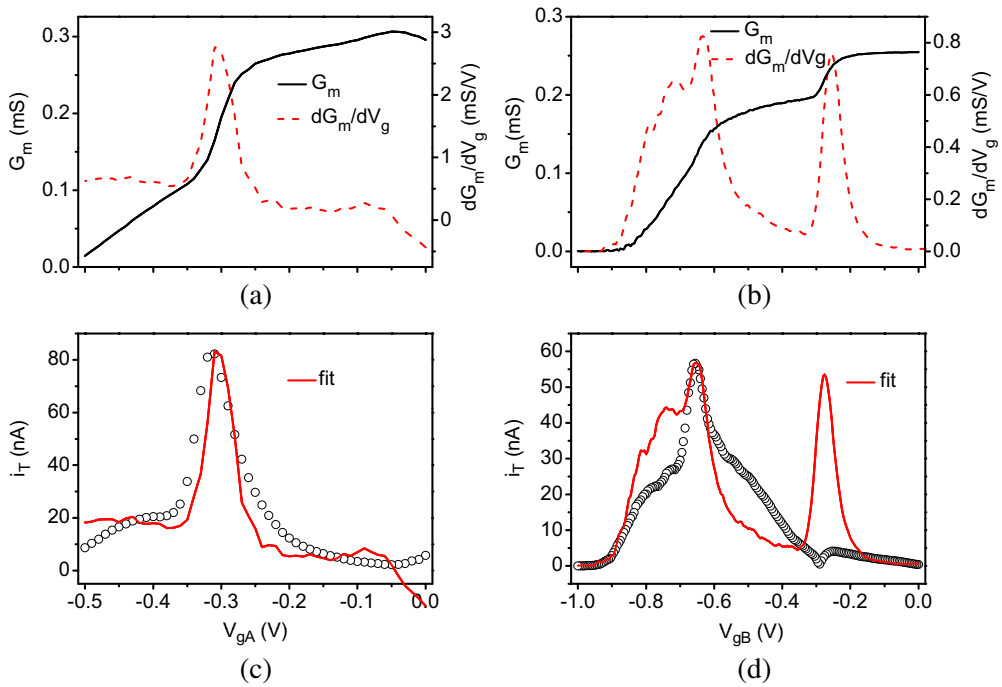

Figure 3: The (a) conductance and (b) photocurrent as a function of the gate voltage in point contact A. The (c) conductance and (d) photocurrent as a function of the gate voltage in point contact B. The data are taken at $T = 2.9\,\mathrm{K}$ and the THz frequency is 875 GHz. The solid curves in (b) and (d) are calculated photocurrent from measured conductance based on the model described by Eq. (1).

conductance

$$i_p = AP_0\xi \mathrm{d}G/\mathrm{d}V_g,$$

where, P_0 is the incident THz power, ξ is the coupling coefficient of the THz field at the point contact, A is a geometric factor. In the real device, there are parasitic resistances along the source and drain leads. An equivalent circuit is shown in the inset of Fig. 2(b), where the series resistance from the leads are marked as r_1, the input resistance of the current preamplifier is r_m, the gate voltage controlled resistance is $r = 1/G$. The measured photocurrent by the current preamplifier can be expressed as

$$i_T = AP_0 \frac{\xi}{1-(2r_1+r_m)G_m} \frac{\mathrm{d}G_m}{\mathrm{d}V_g}, \tag{1}$$

where $G_m = 1/(2r_1 + r_m + r)$ is the measured conductance as shown in Fig. 3(a), (c). Curve fitting based on Eq. (1) were taken to examine the mixing model, as shown in Fig. 3(b), (d). In the fitting, parameters are chosen as $r_m = 20\,\Omega$ and $r_1 = 100\,\Omega$. It is shown that the induce photocurrent can not be fully described by simple homodyne mixing. One of the possible causes of this deviation may comes from the fact that the above mixing model assumes that the coupling coefficient ξ is independent on the gate voltage. When varied by the gate voltage, the electron density near the point contact may change the effective THz electric fields. Other possible causes of the deviation include inhomogeneous heating of the 2DEG and nonlinear rectification of THz field across the point contact as has been discussed in Refs. [10–15].

In the third step, we studied the coupling effect between two point contacts in the neighbourhood, i.e., the induced photocurrent as a function of both gate voltages (V_{gA} and V_{gB}). The differential conductance and induced photocurrent are shown in Fig. 4(a) and (b) for direct comparison, respectively. Since the two point contacts are about 900 nm apart, fairly independent conductances were obtained. This decoupled feature is also clearly shown in the induced photocurrent. Clear correlations between the conductance change and the photocurrent can be seen and are marked by thin dashed lines in Fig. 4. When two point contacts get closer to each other, more complicated photocurrent patterns were observed (data not shown).

Finally, we studied the THz frequency response of the device. The power spectrum of the BWO source was monitored by a room-temperature pyroelectric detector, as shown in Fig. 5(a). The

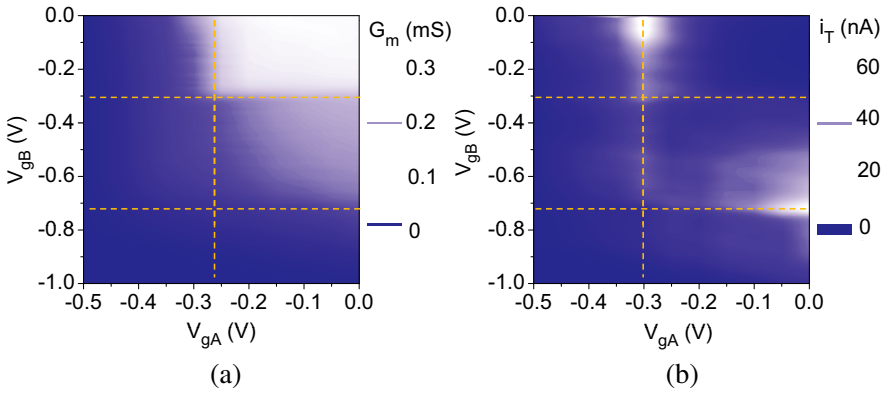

Figure 4: (a) The conductance of two point contacts in series. (b) The photocurrent as a function of the two gate voltages. The data were taken at $T = 2.9\,\mathrm{K}$ and the THz frequency was fixed at 875 GHz.

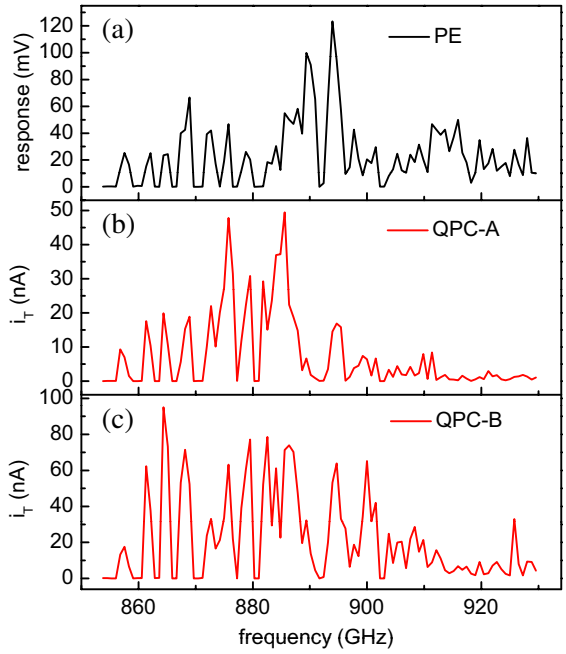

Figure 5: (a) The power spectrum of the BWO source measured by a pyroelectric detector at room temperature. (b) The photocurrent through point contact A at $V_{gA} = -0.3\,\mathrm{V}$ and $V_{gB} = 0\,\mathrm{V}$. (c) The photocurrent through point contact B at $V_{gB} = -0.66\,\mathrm{V}$ and $V_{gA} = 0\,\mathrm{V}$.

two point contacts have similar THz response in the frequency range from 850 GHz to 930 GHz. However, QPC-B has a relatively higher sensitivity, especially at the lower end of the frequency range. This is mainly due to the different shapes of gates/antennas.

4. CONCLUSION

In conclusion, we measured the THz photocurrent in point contacts at 2.9 K. Pronounced photocurrent were observed when the gate voltage strongly modulates the conductance. A model based on homodyne mixing of THz electric fields was applied to examine the induced photocurrent. Although the main feature in gate-controlled photocurrent can be recovered by the model, there are clear deviations between the model and the experiments. To uncover the physical nature of the induced photocurrent and its possible application in sensitive THz detection, more detailed experiments based on deliberately designed device structures have to be completed in the future.

ACKNOWLEDGMENT

This work was supported by the National Basic Research Program of China (973 Program) grant No. G2009CB929300, the Knowledge Innovation Program of the Chinese Academy of Sciences grant

No. Y0BAQ31001 and the National Natural Science Foundation of China grant No. 60871077.

REFERENCES

1. Huber, R., F. Tauser, A. Brodschelm, M. Bichler, G. Abstreiter, and A. Leitenstorfer, "How many-particle interactions develop after ultrafast excitation of an electron-hole plasma," *Nature*, Vol. 414, 286–289, 2001.
2. Dyakonov, M. and M. S. Shur, "Detection, mixing, and frequency multiplication of terahertz Radiation by two-Dimensional electronic fluid," *IEEE Trans. Electron Devices*, Vol. 43, No. 3, 380–387, 1996.
3. Knap, M., Y. Deng, S. Rumyantsev, and M. S. Shur, "Resonant detection of subterahertz and terahertz radiation by plasma waves in submicron field-effect transistors," *Appl. Phys. Lett.*, Vol. 81, No. 24, 4637–4639, 2002.
4. Veksler, D., F. Teppe, A. P. Dmitriev, V. Yu. Kachorovskii, W. Knap, and M. S. Shur, "Detection of terahertz radiation in gated two-dimensional structures governed by dc current," *Phys. Rev. B*, Vol. 73, No. 12, 125328–125337, 2008.
5. Kim, S. and J. D. Zimmerman, "Room temperature terahertz detection based on bulk plasmons in antenna-coupled GaAs field effect transistors," *Appl. Phys. Lett.*, Vol. 92, No. 25, 253508–253510, 2008.
6. Glaab, D., S. Boppel, and A. Lisauskas, "Terahertz heterodyne detection with silicon field-effect transistors," *Appl. Phys. Lett.*, Vol. 96, No. 4, 042106–042108, 2010.
7. Öjefors, E., A. Lisauskas, and D. Glaab, "Terahertz imaging detectors in CMOS technology," *J. Infrared Milli. Terahz. Waves*, Vol. 30, No. 12, 1269–1280, 2009.
8. Zhou, Y., J. D. Sun, Y. F. Sun, Z. P. Zhang, W. K. Lin, H. X. Liu, C. H. Zeng, M. Lu, Y. Cai, D. M. Wu, S. T. Lou, H. Qin, and B. S. Zhang, "Characterization of a room temperature terahertz detector," *Journal of Semiconductors*, Vol. 32, No. 6, 2011, in press.
9. Qin, H., A. W. Holleitner, K. Eberl, and R. H. Blick, "Coherent superposition of photon- and phonon-assisted tunneling in coupled quantum dots," *Phys. Rev. B*, Vol. 64, No. 24, 241302–241305, 2001.
10. Kouwenhoven, L. P., B. J. van Wees, C. J. P. M. Harmans, J. G. Williamson, and H. van Houten, "Nonlinear conductance of quantum point contacts," *Phys. Rev. B*, Vol. 39, No. 11, 8040–8043, 1989.
11. Wyss, R. A., C. C. Eugster, J. A. del Alamo, and Q. Hu, "Far-infrared photon-induced current in a quantum point contact," *Appl. Phys. Lett.*, Vol. 63, No. 11, 1522–1524, 1993.
12. Peralta, X. G., S. J. Allen, M. C. Wanke, N. E. Harff, J. A. Simmons, M. P. Lilly, J. L. Reno, P. J. Burke, and J. P. Eisenstein, "Terahertz photoconductivity and plasmon modes in double-quantum-well field-effect transistors," *Appl. Phys. Lett.*, Vol. 81, No. 9, 1627–1629, 2002.
13. Shaner, E. A., M. C. Wanke, A. D. Grine, S. K. Lyo, J. L. Reno, and S. J. Allen, "Enhanced responsivity in membrane isolated split-grating-gate plasmonic terahertz detectors," *Appl. Phys. Lett.*, Vol. 90, No. 18, 181127–181129, 2007.
14. Song, J. W., N. A. Kabir, Y. Kawano, K. Ishibashi, G. R. Aizin, L. Mourokh, J. L. Reno, A. G. Markelz, and J. P. Bird, "Terahertz response of quantum point contacts," *Appl. Phys. Lett.*, Vol. 92, No. 22, 223115–223117, 2008.
15. Song, J. W., G. Aizin, Y. Kawano, K. Ishibashi, N. Aoki, Y. Ochiai, J. L. Reno, and J. P. Bird, "Evaluating the performance of quantum point contacts as nanoscale terahertz sensors," *Optics Express*, Vol. 18, No. 5, 4609–4614, 2010.

Integrated UAVSAR Simulator and Processor Software (iSARX)

T. S. Lim, C. S. Lim, and V. C. Koo
Faculty of Engineering & Technology, Multimedia University
Jalan Ayer, Keroh Lama, Bukit Beruang, Melaka 75450, Malaysia

Abstract— Synthetic aperture radar (SAR) has been recognized as an essential component of future surveillance systems. One of the major challenges associated with SAR is image formation process. The generation of a two-dimensional image out of the SAR raw data is a computational intensive task. SAR sensors produce gigabytes of raw data that have to be processed into SAR image, thus the selection of the right SAR image algorithm for a particular system is very important to ensure time and cost efficiency without compromising the accuracy of the image. This is a time-consuming task without a reconfigurable and comprehensive software package. Thus, a new unmanned aerial vehicle (UAV) based SAR integrated simulator and processor software, called iSARX, is developed to aid the system designers in optimizing all the system parameters and performance. The iSARX is developed using Matlab platform, which is capable to perform mission planning, terrain modeling, autofocus and image processing algorithms evaluations as well as for understanding of SAR processes. Various plots are available for image quality analysis in iSARX software package. The design of iSARX is based on modular simulation and processing platform, which consists of various independent modules that share a pool of data files. Each module may be developed and executed separately, depending on individual applications. The data format of iSARX is a simplified version of the CEOS (Committee of Earth Observations Satellites) standard on SAR data set. The SAR data records will use the same data format for all SAR product types in iSARX. By having common formats, users from various working groups would be able to analyze and merge data from multiple resources. In the iSARX performance evaluation, simulated and actual SAR raw data were used for further analysis.

1. INTRODUCTION

One of the very important subsystems in SAR system is the ground-based SAR processing unit. The raw echoed signal received need to be processed in order to form a SAR imagery. Thus, a SAR integrated simulator and ground-based processing software is developed. The software package is known as integrated SAR simulator and processor (iSARX). A complete simulator would model end-to-end SAR process, including the sensor-target geometry, the operation of a signal processor and production of a radar image.

2. iSARX

The iSARX software is implemented by using Matlab® application software. The iSARX is capable of performing mission planning, terrain modeling and signal processing algorithms evaluations. The iSARX has been designed for the specification of unmanned aerial vehicle based synthetic aperture radar (UAVSAR). One of the enhancements of the iSARX is the development of UAVSAR specification simulator module. Apart from the SAR point target simulation, this simulation module is able to read and extract the SAR data from an existing SAR data which stored in CEOS (Committee of Earth Observations Satellites) format [3].

The structure of iSARX is a modular-based SAR simulation and processing platform as shown in Figure 1. It consists of various independent modules that share a pool of data files. Each module may be developed and executed separately, depending on individual applications. In order to exchange data resources, the iSARX requires an interpreter to convert their task-specific results to a common format. Besides, a common SAR data record format has been proposed. This data record format will be used in iSARX simulator module and processor module for further signal processing.

3. PERFORMANCE EVALUATION OF iSARX

Figure 2 shows the SAR processing program structure of the point target simulation. The SAR point target simulation module will first load the SAR system parameters and the point target's coordinate and radar cross section (RCS). With these parameters and information, the SAR point target simulation module will generate the SAR received signal and save the data into ".MAT" file for further processing. The generated data will then be loaded in the SAR processor module where

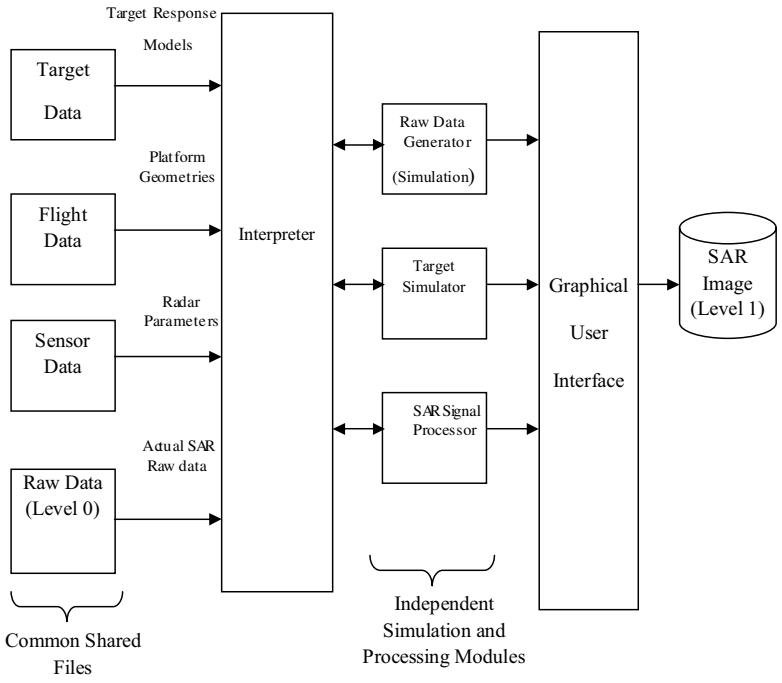

Figure 1: Structure of Modular-based iSARX.

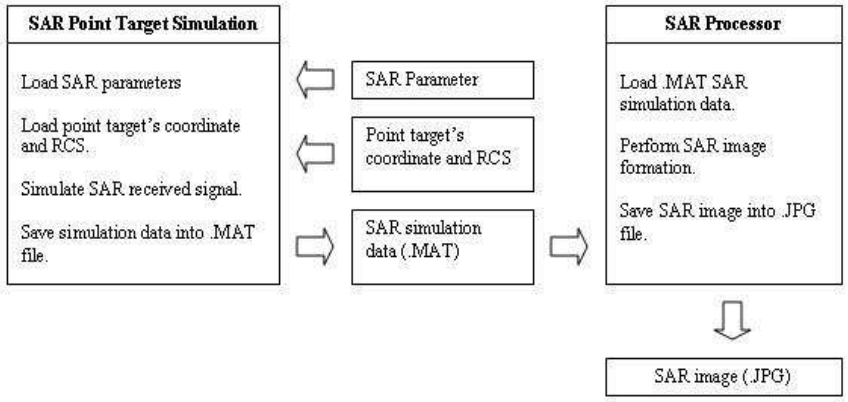

Figure 2: SAR point target simulation and processing program structure.

SAR image formation is performed. The output from the SAR processor module will be displayed on the module itself and the image can be saved into ".JPG" file format.

The first performance evaluation of the iSARX software will be a user-defined SAR point target simulation. The simulation raw data with three simulated point targets is generated using SAR Simulator module from iSARX. The reflectivity of the three simulated point targets is set at 1.0 (max), 0.8 and 0.6 respectively. Figure 3 shows the ideal 2D and 1D SAR images plots of the three simulated point targets using Range Doppler Algorithm from the SAR Processor Module.

Further verification of the performance of iSARX is conducted by using a selected set of actual SAR raw data extracted from Radarsat-1 SAR sensor [1, 2]. This set of Radarsat-1 SAR data which was acquired on June 16, 2002 covers the area of Vancouver, Canada. Radarsat-1 uses a SAR sensor to image the Earth at a single frequency of 5.3 GHz (C band) and its data are stored in CEOS format.

The selected portions (in circles) of the Radarsat-1 raw data employed in this evaluation are shown in Figure 4. The number of samples data extracted in this test for range and azimuth is 2048 by 2048 which will produce an image size of 2048×2048 pixels.

Figure 5 shows a processed SAR image of the selected portions of the Radarsat-1 SAR raw data by using RDA As illustrated in Figure 5, the iSARX has successfully processed the Radarsat-1 raw

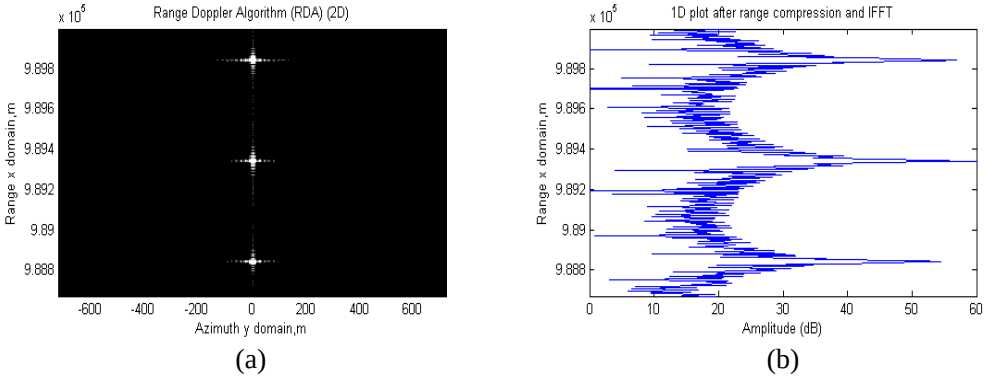

Figure 3: 2D and 1D SAR image of the three simulated point targets.

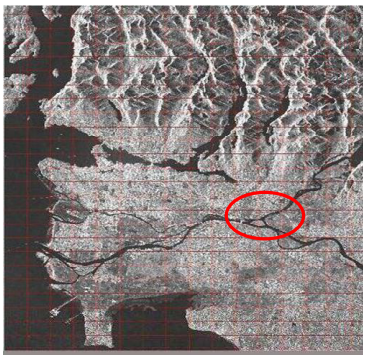

Figure 4: Selected portions of the Radarsat-1 SAR raw data.

Figure 5: SAR image from Radarsat-1 data (processed by iSARX).

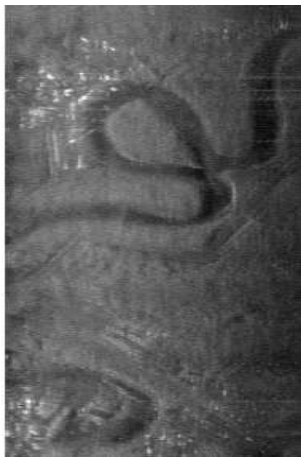

Figure 6: SAR image processed by iSARX of a Study Area at Mersing, Johor, Malaysia.

data. Similar SAR image can be produced by using chirp scaling algorithm (CSA) and Omega-K algorithm (ωKA) for the same set of Radarsat-1 raw data. In short, three precision image formation algorithms namely RDA, CSA and ωKA have been successfully implemented in iSARX software.

An airborne SAR flight test by using UAV has been conducted in December 2010 at Mersing, Johor, Malaysia. The primary objective of this flight test is to verify the capability of the developed UAVSAR sensor. During the Mersing flight test, 6 flight measurements were successfully conducted. Figure 6 shows one of the processed SAR image by iSARX. Clear signatures of river, roads, urban and forested areas are observed.

4. CONCLUSION

This paper introduces an integrated UAVSAR simulator and processor software package, called iSARX, which is developed to assist system designers and researchers in simulating and processing SAR data. This simulator is capable of generating raw SAR data based on user-defined system configurations. Three commonly used image formation algorithms (RDA, CSA and and ωKA) is also integrated in iSARX. Performance evaluations of iSARX are performed by using simulated and real UAVSAR data.

REFERENCES

1. Lim, T. S., C. S. Lim, V. C. Koo, H.-T. Ewe, and H.-T. Chuah, "Autofocus algorithms performance evaluations using an integrated sar product simulator and processor," *Progress In Electromagnetics Research B*, Vol. 3, 315–329, 2008.
2. Cumming, I. G. and F. H. Wong, *Digital Processing of Synthetic Aperture Radar Data*, Artech House Inc., 2005.
3. CEOS Working Group on Data, "Synthetic aperture radar data product format standards," CEOS-SAR-CCT, Issue/Rev: 2/0, 1989.

The Design and Development of Unmanned Aerial Vehicle Synthetic Aperture Radar

Yee Kit Chan and V. C. Koo
Faculty of Engineering & Technology, Multimedia University
Jalan Ayer Keroh Lama, Bukit Beruang, Melaka 75450, Malaysia

Abstract— An Unmanned Aerial Vehicle (UAV) airborne synthetic aperture radar (SAR) is being developed at Multimedia University, Malaysia with collaboration from Agency of Remote Sensing Malaysia (ARSM). The SAR system is a C-band, single polarization, linear FM pulse radar system. The system will be used for monitoring and management of earth resources such as paddy fields, oil palm plantation and soil surface. This paper describes the design and development of the UAVSAR.

1. INTRODUCTION

The principle of synthetic aperture radar (SAR) was discovered nearly 40 years ago [1–3]. It becomes a main tool of microwave remote sensing because of its capability to operate in nearly all weather condition and operates during day and night.

SAR is an imaging radar which uses signal processing to improve the resolution beyond the limitation of physical antenna aperture. As the radar platform flies over an observation area, the doppler spread of the echo signal can be processed using a digital signal processing method. This reduces the number of hardware components for doppler filtering as well as range gating [2].

Microwave remote sensing is one of the major research areas conducted by a research group in Multimedia University, Malaysia, for the past 10 years or so. Theoretical modelling and image processing technique on SAR images have been developed. However, the main limitation is the dependence on overseas institution to supply the measurement data and SAR images. For national monitoring and management of earth resources, limited number and timely supply of the required SAR images have been a major problem. Therefore, there is an urgent need to develop our own SAR sensor system.

In late 2007, the project to develop a UAVSAR system was initiated with joined collaboration with Agency Remote Sensing of Malaysia. The main objective of this project is to design and construct an imaging radar system with UAV as the platform. The proposed system is an single polarization, linear FM radar operating at C-band (5-cm wavelength). This SAR system is designed to operate at low altitudes with low transmit power and small swath width in order to optimize the development cost and operating cost.

This paper describes the design and development of the SAR sensor and current status of the development.

2. SYSTEM OUTLINE

System specifications of the UAVSAR system are summarized in Table 1. The development of UAVSAR system is presented in the subsequent section.

The UAVSAR Sensor can be functionally divided into a few assemblies: (i) RF section; (ii) Timing & Control Unit; (iii) Motion Sensor; (iv) Chirp Generator; (v) Data Recorder (vi) Real Time Processor and (vii) Antenna System. Each of these assemblies can be further divided into subassemblies and components.

Figure 1 shows the functional block diagram of the UAVSAR Sensor. The FPGA based Chirp generator produced the required LFM pulse signal and it will be upconverted and further amplified by the RF Section to the desired power level before transmitted via an antenna system. The light weight antenna system will be implemented by microstrip patch array antenna. The transmitted energy is intercepted by the target and reflected back to the same antenna system. The received echoes are amplified and down-converted to lower frequency in the RF section. Finally the intermediate frequency (IF) signals are digitised and stored in FPGA based data acquisition unit for future analysis. The IF signals is also feed into the real time processor to produce the low resolution image on the sport. The resultant image will transmitted to the ground station via the data downlink unit. Timing and Control Unit will provide the reference signal of 10 MHz to the RF section for synchronization purpose and acts as the signal and waveform manipulation device

Table 1: UAVSAR system parameter.

System Parameters	Specifications
Mode of Operation	Stripmap
Operating Frequency	5.3 GHz (C-band)
Bandwidth	80 MHz
Polarization Single	VV
Antenna Gain	18 dBi
Spatial Resolution	5 m × 5 m
RCS Dynamic Range 30 dB	(0 dB to −30 dB)
SNR	> 10 dB
Platform Height, h	2000 m
Swath Width	1000 m
Nominal Platform Speed	30 m/s
Data Take Duration	1 hour (10 min per scene)
SAR Processing	Off-line
Operating Platform	UAV, Aludra MK1
Overall Sensor Weight	< 20 kg
Overall Sensor Dimension	12" (L) × 9" (H) × 12" (W)

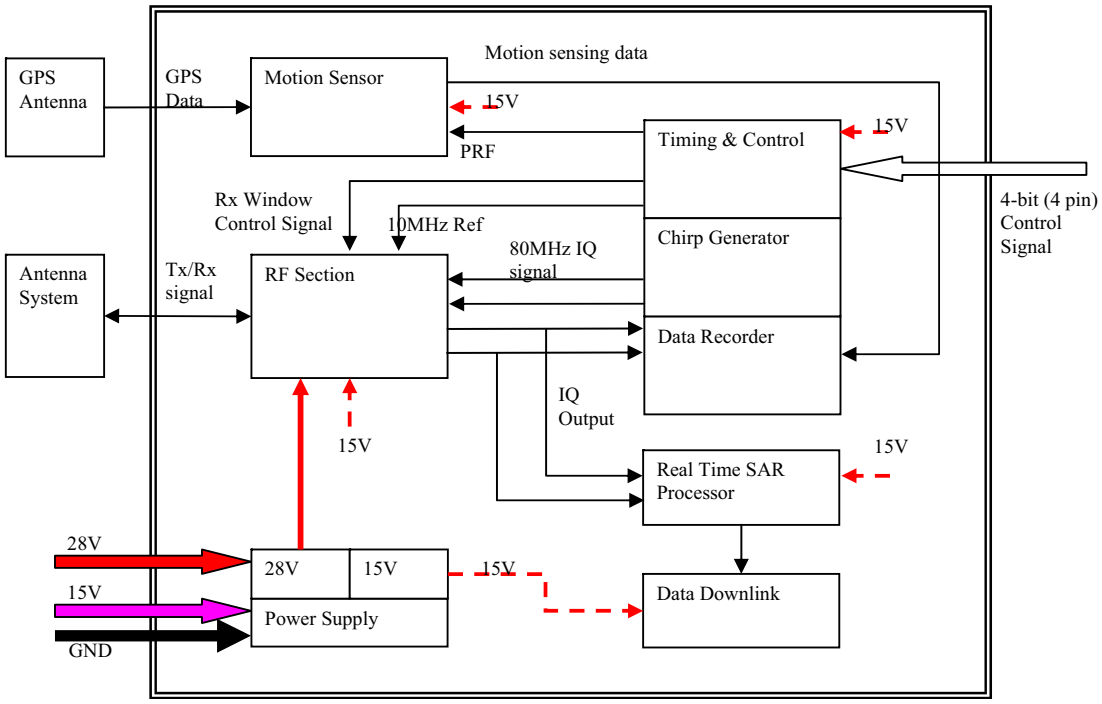

Figure 1: Block diagram of SAR sensor.

to supply appropriate and accurate signals or pulses. Besides, the motion sensor equipped with Inertial Measurement unit (IMU) and the Global Positioning System (GPS) receiver will provide the necessary real time motion information and this data will be recorded by the it's on board data recorder.

All the UAVSAR system except the SAR antenna system and GPS antenna will be sat inside the UAV compartment. The SAR platform has been identified as the Aludra MK1 from Unmanned System Technology (UST), Malaysia. Figure 2 shows the image of Aludra MK1 platform with optical sensor as payload.

An housing has to be design and constructed to host all the unit in a limited working space.

Figure 2: UAV.

Figure 3: SAR sensor.

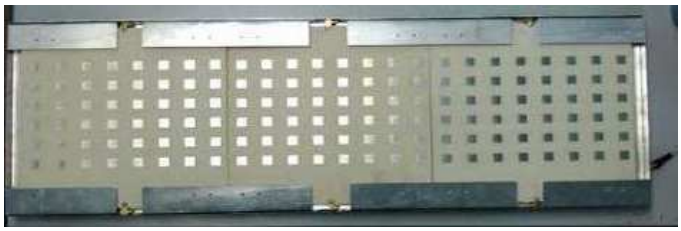

Figure 4: Antenna system.

Figure 5: SAR image of Mersing site.

Figure 3 shows the complete UAVSAR sensor and Figure 4 shows the microstrip antenna system employed in our UAVSAR system. In order to further reduce the hardware used in this system, a high performance FPGA board has been selected to perform the task of Chirp Generator, Timing and Control Unit, and Data Recorder.

3. FIELD MEASUREMENT

A series of field measurements have been successfully conducted end of 2010 at Mersing, Malaysia with primary objective is to verify the capability of UAVSAR system. During the Mersing Flight Mission, 6 flight measurements were successfully conducted. A total of about 200 sets of SAR raw data were collected. Figure 5 shows one of the samples of SAR images captured during the flight mission. Clear signatures of river, roads, urban and forested areas are observed.

4. CONCLUSION

In this research activity, a UAVSAR system has been successfully designed and developed based on the Aludra MK1 platform. A series of flight test has been conducted to verify the performance of UAVSAR sensor. A huge amount of SAR data was acquired during the flight test. Good quality SAR images with 3 m × 3 m resolutions were processed using this flight mission raw data.

ACKNOWLEDGMENT

This project is funded by Agency of Remote Sensing Malaysia under Ministry of Science, Technology and Innovation, Malaysia.

REFERENCES

1. Ulaby, F. T., R. K. Moore, and A. K. Fung, *Microwave Remote Sensing-Active and Passive*, Vol. 2, Addison Wesley, 1981.
2. Curlander, J. C. and R. N. McDonough, *Synthetic Aperture Radar: System and Signal Processing*, A Wiley Interscience Publication, 1991.
3. Wiley, C. A., "Synthetic aperture radar — A paradigm for technology evolution," *IEEE Trans. Aerosp. Electron. Syst.*, Vol. 21, 440–443, 1985.

A SIMO Step-frequency Radar Technology for Imaging and Reconstruction of a 3D Complex Target

Wei Li and Ya-Qiu Jin
Key Laboratory of Wave Scattering and Remote Sensing Information (MoE)
Fudan University, Shanghai 200433, China

Abstract— A SIMO-SF (single input and multiple output, step-frequency) radar system is presented for numerical simulations of electromagnetic scattering, imaging and reconstruction of a complex electric-large target.

The SIMO-SF system utilizes the linear SF radar array, working at $2 \sim 6$ GHz band in downward-looking spotlight mode and moving in transverse to form a 2-D (dimensional) synthetic array. The central radar of the array is used as both the transmitter and receiver, and the others are the receivers only. Suppose the radar number be N, the data acquisition time of the SIMO can be N times smaller than the SISO (single input and single output) model.

The FEKO codes are employed to calculate electromagnetic scattering from a complex electric-large target. An improved 3-D RMA (range migration algorithm) is then utilized to make the radar imaging. Finally, reconstruction of the 3-D PEC target, i.e., a tank-like, is presented and discussed.

1. INTRODUCTION

In recent years, ultra-wideband (UWB) imaging system has been applied to reconstruction of the reflectivity imaging of a complex scene. The migration algorithm is the most common approach, such as the range migration (RMA) and Kirchhoff migration (KMA), etc. [1]. The RMA can form a 3-D imaging by coherently integrating the backscattering data over the frequency band and 2-D synthetic aperture. It was further improved to cope with the signal-transmitting and multiple-receiving (SIMO) linear array antennas [2]. The RMA performs the image reconstruction in spatial Fourier domain with the advantage of fast Fourier transform (FFT). This algorithm can present good computational efficiency, much higher than other approaches of time domain integral. The Kirchhoff migration expresses the wave field at any point following the Kirchhoff integral theorem. It was modified to cope with multi-static data and sparse aperture [3]. The KMA can provide good image quality, while RMA's computation is more efficient. A comparison of the RMA and KMA can be found in [4].

The MIMO (multi-input and multi-output) system has been seen as a novel development of the UWB radar technology, which may simplify the RF front-end electronics and significantly increase the scanning speed. The MIMO system has been extensively applied to those imaging areas, such as ground penetrating radar (GPR), indoor/outdoor probing and positioning, and medical imaging, etc. The RMA of SIMO system has been described in [2] for imaging the point targets. However, its radiation pattern and operational process have not been well studied in those simulations. Actually, the imaging efficiency and quality are totally dependent on the complex system modeling with various antenna parameters. In this paper, numerical simulation of scattering, imaging and reconstruction using the SIMO system to observe a complex target is developed.

2. FORMULATION

Figure 1 shows a model of the SIMO system, where a 2-D synthetic array at the altitude h makes the measurements at the receiver grids with the spacing Δx_a and Δy_a. The central antenna (as both the transmitting and receiver) is denoted as TX at $(0, y_a, h)$, and other receiver antennas are RX at (x_a, y_a, h). The acquired backscattering data at each receiver is denoted as $S_0(x_a, y_a, f)$, where f is the frequency.

Suppose a point scatter P at (x_t, y_t, z_t) with the reflectivity $\sigma(x_t, y_t, z_t)$, the distance between P and TX is written as

$$R_T(x_a) = \sqrt{(x_a - x_t)^2 + y_t^2 + (h - z_t)^2} \tag{1}$$

And the distance between P and the n-th RX is

$$R_R(x_a, y_a) = \sqrt{(x_a - x_t)^2 + (y_a - y_t)^2 + (h - z_t)^2} \tag{2}$$

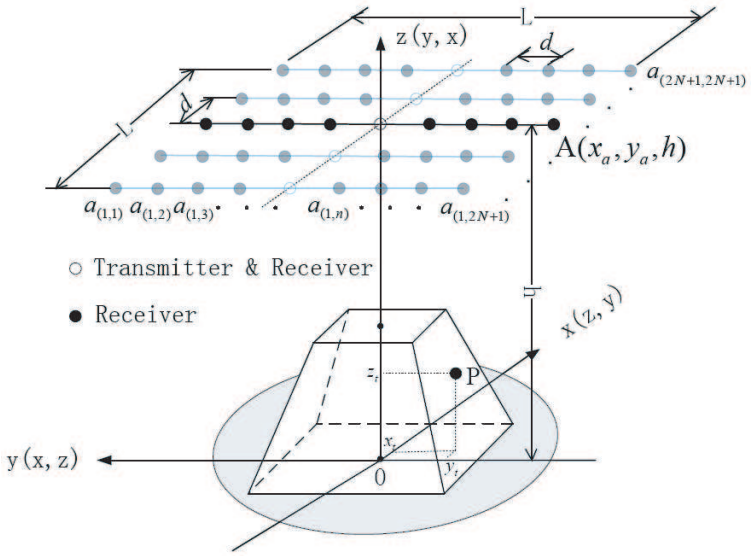

Figure 1: A SIMO-SF model for 3-D scattering, imaging and reconstruction of a complex electric-large target.

Thus, the round-trip range yields

$$R(x_a, y_a) = R_T(x_a) + R_R(x_a, y_a) \tag{3}$$

The receiving signal can be written as

$$S_0(x_a, y_a, f) = \iiint \sigma(x_t, y_t, z_t) \exp\left[-i\frac{2\pi f}{c} R(x_a, y_a)\right] dx_t dy_t dz_t \tag{4}$$

The 2-D FFT of the signal $S_0(x_a, y_a, f)$ with respect to (x_a, y_a) is written as

$$\begin{aligned} S_1(k_x, k_y, k) &= \iint S_0(x_a, y_a, f) \exp[-i(k_x x_a + k_y y_a)] dx_a dy_a \\ &= \iint \iiint \sigma(x_t, y_t, z_t) \exp\{-i[kR(x_a, y_a) + k_x x_a + k_y y_a]\} dx_t dy_t dz_t dx_a dy_a \end{aligned} \tag{5}$$

Making $X = x_a - x_t,\ Y = y_a - y_t$, Eq. (5) becomes

$$\begin{aligned} S_2(k_x, k_y, k) &= \iiint \sigma(x_t, y_t, z_t) \exp\left[-i(k_x x_a + k_y y_a)\right] \\ &\quad \iint \exp\left\{-i\left[kR(X, Y) + k_x X + k_y Y\right]\right\} dX dY dx_t dy_t dz_t \end{aligned} \tag{6}$$

Using the stationary phase method and the approximate signal spectrum [2], it gives

$$\Phi(X, Y) = kR(X, Y) + k_x X + k_y Y \tag{7}$$

$$\Phi_0(X, Y) = k_1(k_x, k_y, k) y_t + k_2(k_x, k_y, k) z_t \tag{8}$$

$$\begin{cases} k_1(k_x, k_y, k) = 0 \\ k_2(k_x, k_y, k) = -\sqrt{(k + \sqrt{k^2 - k_y^2})^2 - k_x^2} \end{cases} \tag{9}$$

Eq. (6) becomes

$$S_3(k_x, k_y, k_z) = \iiint \sigma(x_t, y_t, z_t) \exp\left[-i(k_x x_t + k_y y_t + k_z z_t)\right] dx_t dy_t dz_t \tag{10}$$

where $k_z = -\sqrt{(k + \sqrt{k^2 - k_y^2})^2 - k_x^2}$.

The algorithm is described in Fig. 2.

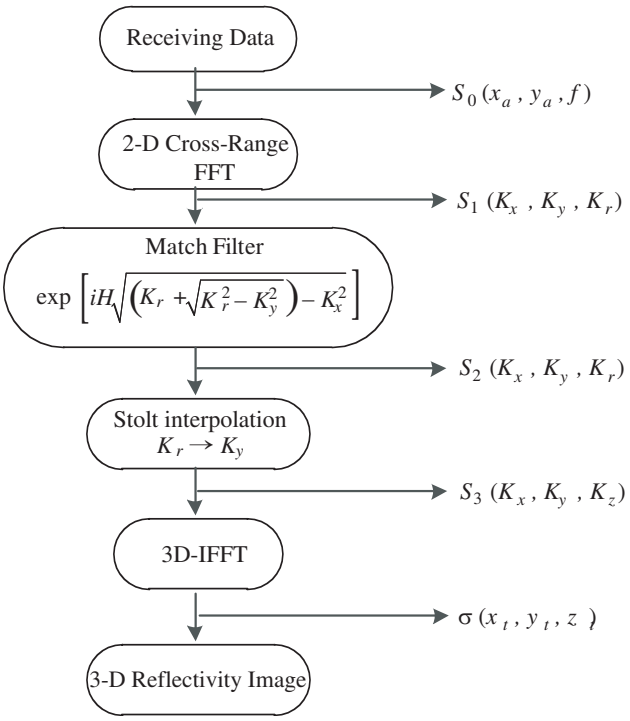

Figure 2: Block diagram of the 3-D SIMO RMA.

3. RESOLUTION AND SAMPLING CRITERIA

3.1. Resolutions

The resolution of a 3-D image resulting by the wideband radar depends on the operational bandwidth, the center frequency, the potential range distance of the target, and the dimensions of the synthetic array aperture. The down-range resolution is determined only by the bandwidth as $\delta_r = c/(2B)$, where B is the frequency bandwidth at -10-dB level and c denotes the speed of light [4]. The influence of the bandwidth on the cross-range resolution is very limited, even the target is supposed in the near field. In practice, the system bandwidth is about the same order of the central frequency in order to minimize influence on the cross-range resolution. Thus, the horizontal and vertical cross-range resolutions are estimated as $\delta_x \approx \lambda_c h/L_x^E$, $\delta_y \approx \lambda_c h/L_y^E$, where L_x^E and L_y^E are the lengths of the effective aperture of the 2-D synthetic/array aperture, h represents the range distance of the target, and λ_c is the wavelength at the center frequency f_c. For the synthetic aperture, the length of the effective aperture is twice the physical length LSAR of the synthetic aperture $L^E = 2L_{SAR}$.

3.2. Sampling Criteria

Suppose that a target is confined within a rectangular box with the dimensions $D_x \times D_y \times D_z$ centered at the coordinate origin. The Nyquist criteria should be satisfied in order to obtain a successful discretization. Specifically, the phase shift from one spatial sampling point to the next should be less than π rad. For distributing targets, the largest phase shift occurs at the farthest opposite edge of the target and the aperture. Thus, the Nyquist criterion for the spotlight model are given by [1]

$$\Delta_f \leq \frac{c}{2D_y} \tag{11}$$

$$\Delta_{x_a} \leq \frac{\lambda_{\min} h}{2\sqrt{D_x^2 + D_z^2}}, \quad \Delta_{y_a} \leq \frac{\lambda_{\min} h}{2\sqrt{D_y^2 + D_z^2}} \tag{12}$$

4. NUMERICAL RESULTS

Let the target be in a box with each size of 1 m. A system of SIMO TX/RX antenna synthesizes a linear radar array of 2 m located at $h = 2$ m from the target center. The number of RX antenna

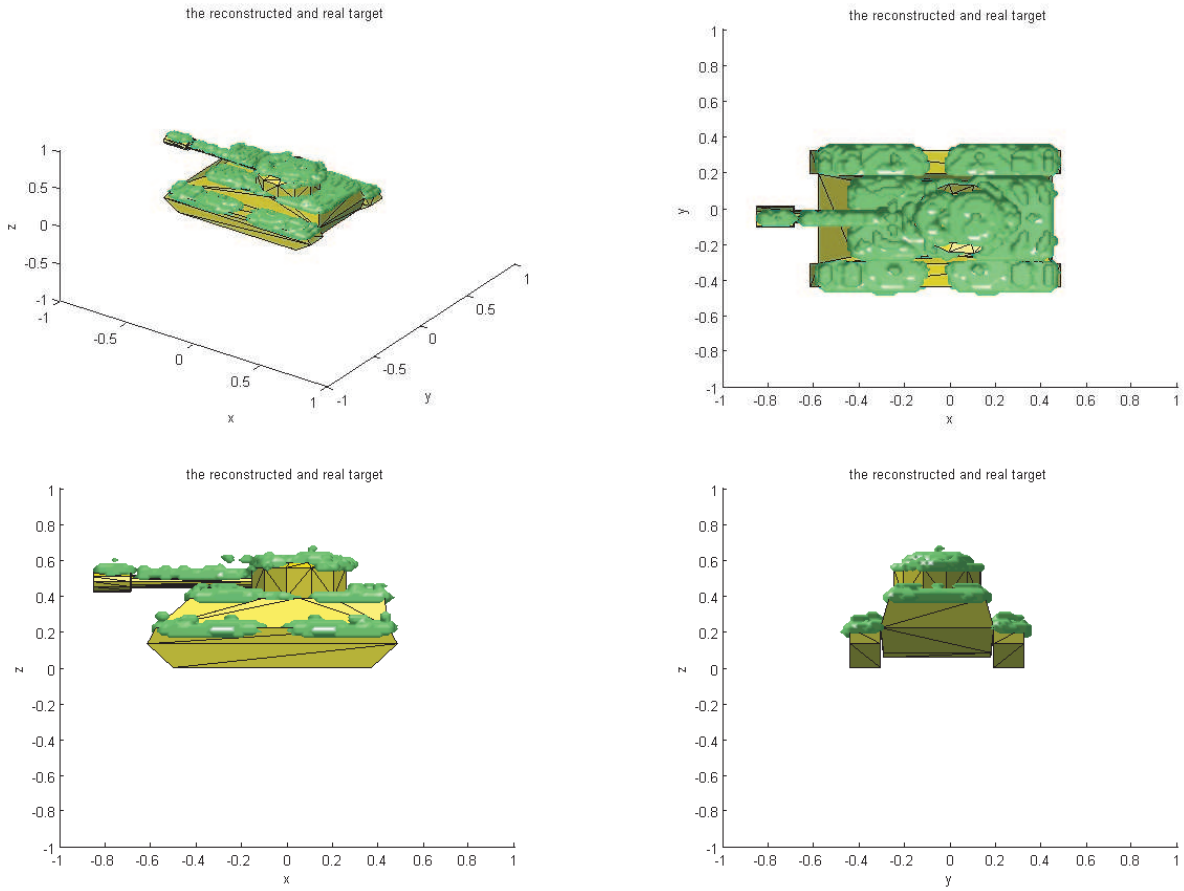

Figure 3: The imaging results of the complex target tank.

is 51 with each spacing 4 cm in the x-direction. The TX antenna working in the spotlight mode is in the center of the linear radar array. In this paper, the TX antenna is a magnetic dipole. The direction of the dipole is (θ, ϕ), where $\theta = \arctan(y_a/h)$, $\phi = 0$ when the dipole is positioned at $(0, y_a, h)$. The Frequency ranges from 2 to 6 GHz to make sampling 41points with a step of 100 MHz. The theoretical resolution is calculated as 3.75 cm.

The 3-D imaging of the reconstructed reflectivity (in green color) and an outline profile of the tank target (in yellow color) are overlapped as shown in Fig. 3.

REFERENCES

1. Lopez-Sanchez, J. M. and J. Fortuny-Guasch, "3-D radar imaging using range migration techniques," *IEEE Transactions on Antennas and Propagation,* Vol. 48, No. 5, 728–737, 2000.
2. Du, L., Y. Wang, W. Hong, W. Tan, and Y. Wu, "Three-dimensional range migration algorithm for downward-looking 3D-SAR with single-transmitting and multiple-receiving linear array antennas," *EURASIP Journal on Advances in Signal Processing*, Article ID 957916, 2010.
3. Zhuge, X., T. G. Savelyev, A. G. Yarovoy, L. P. Ligthart, and B. Levitas, "Comparison of different migration techniques for UWB short-range imaging," *Proceedings of the European Radar Conference*, Rome, Italy, September 30–October 2, 2009.
4. Zhuge, X. and A. G. Yarovoy, "A sparse aperture MIMO-SAR-based UWB imaging system for concealed weapon detection," *IEEE Transactions on Geoscience and Remote Sensing,* Vol. 49, No. 1, 509–518, 2011.

Circularly Polarized Array Antennas for Synthetic Aperture Radar

Yohandri[1,2], **J. T. Sri Sumantyo**[1], **and H. Kuze**[1]

[1]Josaphat Microwave Remote Sensing Laboratory, Center for Environmental Remote Sensing
Chiba University, 1-33 Yayoi-cho, Inage-ku, Chiba 263-8522, Japan
[2]Physics Department, State University of Padang, Kampus UNP
Jln. Prof. Hamka Air Tawar, Padang, Sumatera Barat 25131, Indonesia

Abstract— The L-band of LHCP and RHCP array antenna for circularly polarized synthetic aperture radar (CP-SAR) has been developed using simple corner-truncated square-patch elements. The corporate feed design concept is implemented by combining a split-T and a 3-way circular-sector-shape power divider to excite circularly polarized radiation. The fabrication of both antennas based on the simulation using the method of moment (MoM) gives a good circular polarization. Impedance bandwidth and 3-dB axial ratio bandwidth for LHCP are 6.1% and 1.0%, respectively, while for RHCP are 6.2% and 1.0%, respectively. The full antenna (four panels), will be installed on an Unmanned Aerial Vehicle (UAV) JX-1 in Center for Environmental Remote Sensing, Chiba University. In the future, CP-SAR is expected to improve the characteristics of conventional SAR system, especially to extract some new physical information on the earth surface.

1. INTRODUCTION

Currently, we are developing a Circularly Polarized Synthetic Aperture Radar (CP-SAR) sensor [1] for various applications such as land cover and snow cover mapping, oceanography, and disaster monitoring. To realize the circular polarization, the CP-SAR system is composed by Left Handed Circularly Polarized (LHCP) and Right Handed Circularly Polarized (RHCP) sub array antenna, where the transmission (Tx) is working in RHCP or LHCP, and reception (Rx) is working in both RHCP and LCHP. The main purpose of this sensor is to reduce the Faraday rotation effect when the microwave radiation propagates through the ionosphere and some other experiments for remote sensing field using circular polarization. This sensor is operated at L-Band frequency (1.27 GHz) and intended to install on a small satellite platform (μSAT CP-SAR) as illustrated in Figure 1. To verify the sensor performance, firstly, the sensor will be mounted a Josaphat experimental unmanned aerial vehicle (JX-1 UAV) in the Microwave Remote Sensing Laboratory (JMRSL), CEReS, Chiba University (Figure 2). In previous research [2], the LHCP array antenna has been reported and in this paper the comparison result of LHCP and RHCP array antenna will be discussed.

2. ARRAY ANTENNA DESIGN

The designing of circularly polarized array antenna for UAV and μSAT based on the essential parameters of CP-SAR as listed on Table 1 [3, 4]. The proposed antenna is developed using simple corner-truncated square-patch elements. In addition, a circular sector power divider [5] is adopted in feeding network, which is an improved version of the feeding method proposed in a literature [6]. The LHCP and RHCP array antennas are consisting of three blocks, each block having 2×2 element patches. Figure 3 shows the design and photograph of the antenna, made using a substrate with a permittivity $\varepsilon_r = 2.17$ and a loss tangent $\delta = 0.0005$. The length and width of the fabricated antenna are 810 mm and 325 mm, respectively.

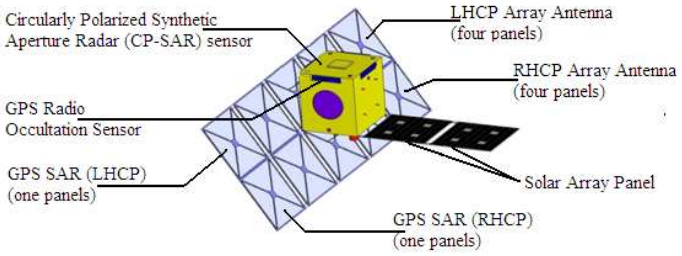

Figure 1: Circularly polarized synthetic aperture radar (CP-SAR) sensor onboard a small satellite (μSAT).

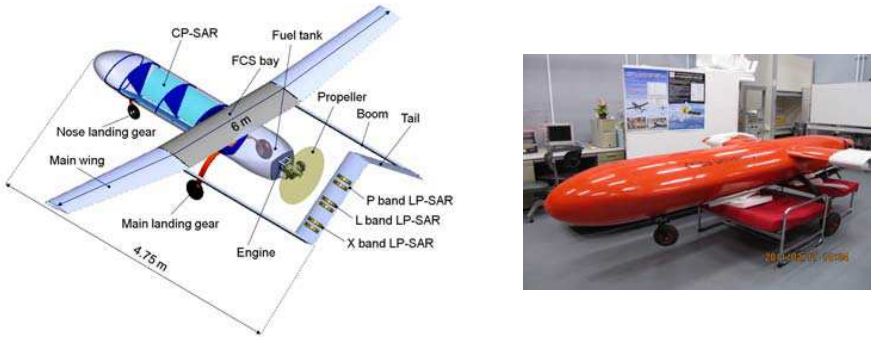

Figure 2: Josaphat experimental unmanned aerial vehicle (JX-1 UAV), (a) basic design, and (b) photograph.

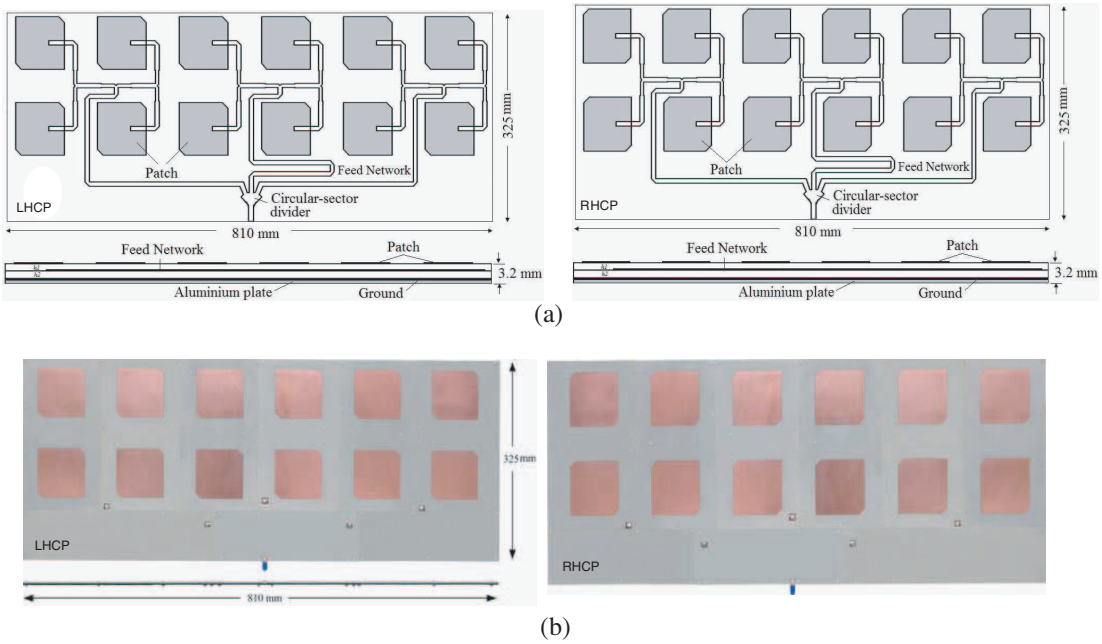

Figure 3: LHCP and RHCP array antennas, (a) configuration design, (b) photograph.

Table 1: The essential parameters of CP-SAR sensor.

Parameters	Specification	
	UAV	μSAT
Frequency center (GHz)	1.27	1.27
Pulse Bandwidth (MHz)	233.31	10
Axial ratio (dB)	≤ 3	≤ 3
Antenna efficiency	$> 80\%$	$> 80\%$
Antenna gain (dBic)	14.32	36.6
Azimuth beamwidth	6.77°	1.08°
Elevation beamwidth	$3.57° - 31.02°$	$\geq 2.16°$
Antenna size (m)	1.5×0.4	2×4
Polarization (Tx/Rx)	RHCP + LHCP	RHCP + LHCP

3. RESULTS AND DISCUSSION

In Figures 4 to 8, respectively, express the reflection coefficient (S_{11}), axial ratio (AR), gain (G) and radiation pattern of the both LHCP and RHCP array antenna. In general, good agreements are

shown between the simulated and measured results, indicating that the antenna properties mostly satisfy the target specification as a CP-SAR array antenna. Slight differences in comparisons are

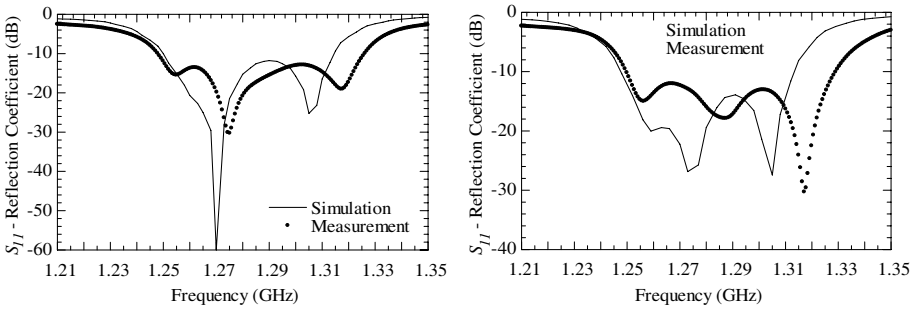

Figure 4: Simulated and measured reflection coefficient plotted as a function of frequency, (a) LHCP, and (b) RHCP.

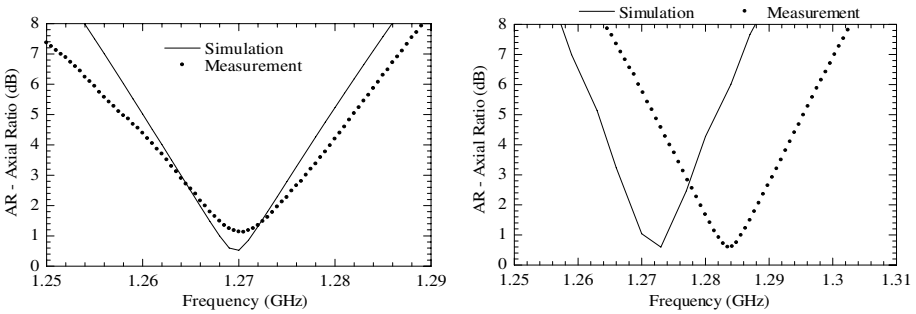

Figure 5: Simulated and measured axial ratio (AR) plotted as a function of frequency, (a) LHCP, and (b) RHCP.

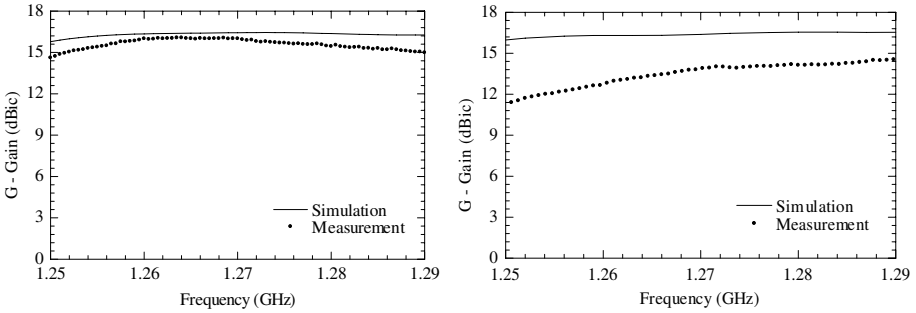

Figure 6: Relationship between antenna gain and frequency at θ angle $= 0°$, (a) LHCP, and (b) RHCP.

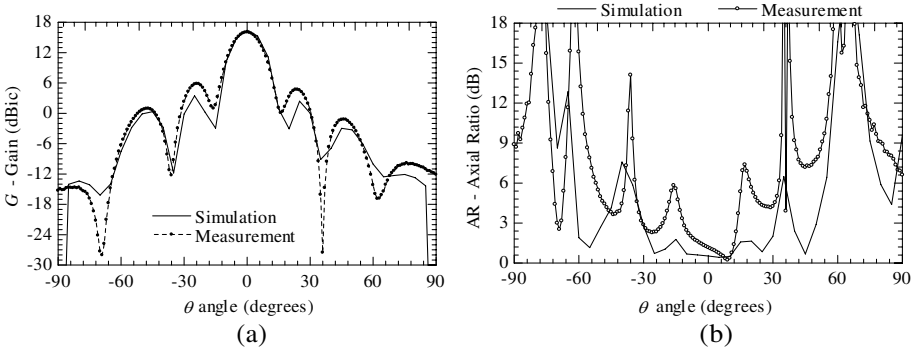

Figure 7: LHCP Array antenna characteristics in the theta plane (negative theta for $Az = 180°$ and positive for $Az = 0°$) (x-z plane), (a) gain versus theta angle, and (b) axial ratio versus theta angle.

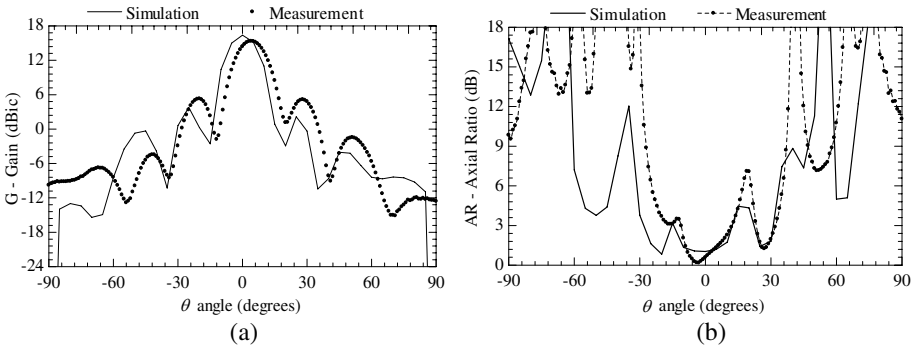

Figure 8: RHCP Array antenna characteristics in the theta plane (negative theta for $Az = 180°$ and positive for $Az = 0°$) (x-z plane), (a) gain versus theta angle, and (b) axial ratio versus theta angle.

probably derived from imperfections in the fabrication such as soldering, milling, and assembling the antenna segments.

4. CONCLUSION

The development of LHCP and RHCP array antennas for CP-SAR sensor system has been presented in this paper. The circular polarization for both array antennas has successfully been designed and constructed. The fabricated of proposed antenna has shown good performance in terms of return losses, axial ratio, gain, and radiation patterns. A good agreement has been obtained between the simulated and measured results, indicating that the antenna properties mostly satisfy the requirements for the CP-SAR sensor. In the future work, the performance of these array antennas will be enhanced and realized on synthetic aperture radar sensor.

ACKNOWLEDGMENT

The authors would like to thank National Institute of Information and Communication Technology (NICT) for International Research Collaboration Research Grant; Chiba University COE Start-up Programme "Small Satellite Institute for Earth Diagnosis"; and The Japan Society for The Promotion of Science (JSPS) Japan — East Network of Exchange for Students and Youths (JENESYS) Programme.

REFERENCES

1. Sri Sumantyo, J. T., H. Wakabayashi, A. Iwasaki, F. Takahashi, H. Ohmae, H. Watanabe, R. Tateishi, F. Nishio, M. Baharuddin, and P. Rizki Akbar, "Development of circularly polarized synthetic aperture radar onboard microsatellite," *PIERS Proceedings*, 382–385, Beijing, China, Mar. 23–27, 2009.
2. Yohandri, V. W., I. Firmansyah, P. Rizki Akbar, J. T. Sri Sumantyo, and H. Kuze, "Development of circularly polarized array antenna for synthetic aperture radar sensor installed on UAV," *Progress In Electromagnetics Research C*, Vol. 19, 119–133, Jan. 2011.
3. Rizki Akbar, P., J. T. Sri Sumantyo, and H. Kuze, "CP-SAR UAV development," *International Archives of the Photogrammetry, Remote Sensing and Spatial Information Science*, Vol. 38, Part 8, 203–208, Kyoto, Japan, 2010.
4. Rizki Akbar, P., S. S. J. Tetuko, and H. Kuze, "A novel circularly polarized synthetic aperture radar (CP-SAR) onboard spaceborne platform," *International Journal of Remote Sensing*, Vol. 31, No. 04, 1053–1060, 2010.
5. Abouzahra, M. D., "Multiport power divider-combiner circuits using circular-sector-shaped planar components," *IEEE Transactions on Microwave Theory and Techniques*, Vol. 36, No. 12, 1747–1752, Dec. 1988.
6. Rahim, M. K. A., T. Masri, O. Ayop, and H. A. Majid, "Circular polarization array antenna," *Asia-Pacific Microwave Conference*, 1–4, Hong Kong, Dec. 2008.

Design and Development of a Ground Based Frequency Modulated Continuous Wave Imaging Radar System

Y. K. Chan, C. Y. Ang, and V. C. Koo
Faculty of Engineering & Technology, Multimedia University
Jalan Ayer Keroh Lama, Bukit Beruang, Melaka 75450, Malaysia

Abstract— This paper describes the design and development of a ground based Frequency Modulated Continuous Wave (FMCW) radar system in Multimedia University (MMU), Malaysia. In this project, a ground-based fully polarometric, C-band, high bandwidth linear FM-CW imaging radar system is to be designed and constructed. The system should have the capability to measure the complex scattering return of distributed targets using FMCW system and obtained fully polarimetric signals which can be used to provide more accurate identification and classification of the geophysical media.

1. INTRODUCTION

When an earth terrain is illuminated by an electromagnetic wave, the characteristics of the scattered wave are found to be related to the physical properties of the terrain [1]. The wave received by a radar, commonly known as the backscattered signal, is therefore the information carrier from which the dielectric and geometrical properties of the terrain may be retrieved. In recent years, polarimetric technique has proven to be a promising tool for geophysical remote sensing [1–5]. Fully polarimetric radar signals carry additional phase information of the backscatterer and thereby provide more accurate identification and classification of terrain types [5–7].

In this project, a ground-based, full polarimetric C band imaging radar is constructed. FM-CW configuration is employed in this system due to its simplicity and constructions. The FM-CW also has added advantages in obtaining a high resolution image [8]. The main objectives of this project should cater the capability to measure the complex scattering matrices of distributed targets using FMCW system and produced a two dimensional image for the field measured. Based on the measurement results reported in numerous literatures, it is found that the typical value of scattering coefficients for various categories of terrain falls in the range from 0 dB to −30 dB. Therefore, a wide dynamic range (> 30 dB) is needed to accommodate the measurement of various types of terrain. A summary of the system specification is given in Table 1.

2. SYSTEM DESCRIPTION

In general, the this system can be subdivided into four major sections: Antenna System, Radio Frequency (RF) Section, Intermediate Frequency (IF) Section and Data Acquisition Unit (DAU).

Table 1: Summary of system specifications.

System Parameter	Selected Value
System configuration	FM-CW
Operating Frequency	6 GHz (C-band)
Transmit power, P_t	15 mW
Measurement range	20 m to 50 m
σ° dynamic range	+20 dB to −40 dB
Received power, P_r	−24 dBm to −122.6 dBm
IF bandwidth	100 kHz
Minimum signal-to-noise ratio	10 dB
Useful maximum signal level	+10 dBm
Narrowband noise level	−122 dBm

2.1. Antenna

The primary aspect in polarimetric radar is non other than the antenna. In this project, a quasi-static configuration is practised in this design. A total of four identical horn antennas were employed in this system, where two antennas are used for transmitting and the other two antennas are for receiving. Figure 1 shows the arrangement of antenna polarization.

2.2. RF Section

Figure 2 shows the RF section of the FMCW imaging radar. The required microwave signal is generated by a 15 mW voltage-controlled oscillator (VCO). The centre frequency of the VCO is fixed at 6 GHz, while the RF bandwidth is set to 400 MHz by a 60 Hz modulating signal. A fraction of the transmitted signal is used as the local oscillator (LO) signal for the quadrature mixer. The signal is then pass through the high-power amplifier which amplifies its signal to a range suitable

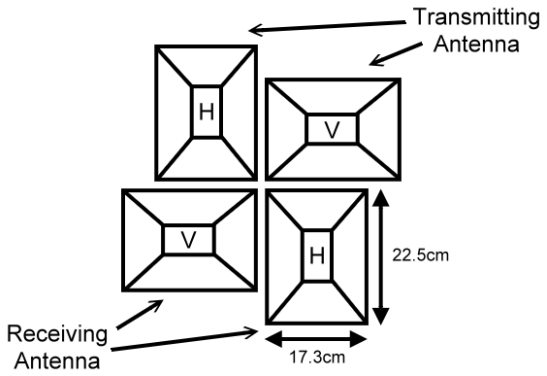

Figure 1: Arrangement of antenna polarization.

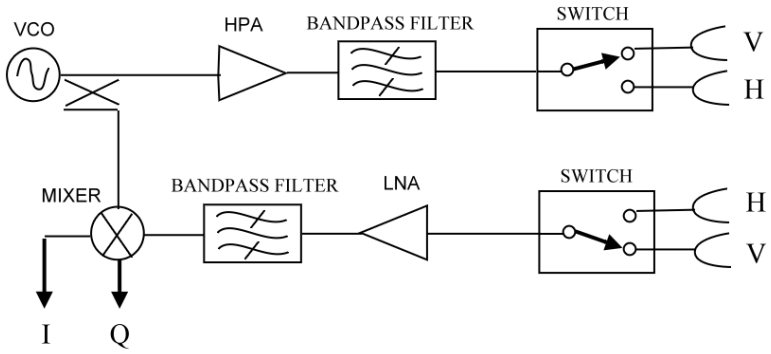

Figure 2: RF section.

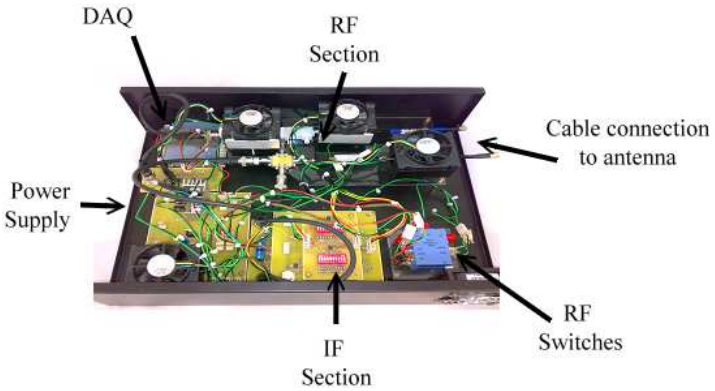

Figure 3: RF system.

for transmission. The polarisation states of the transmitted and received signals are selected using two mechanical switches. The received signal captured by antenna is amplified by a low noise amplifier. Finally the signal is fed to the quadrature mixer, where it is converted to form the full phase intermediate frequency signals (I and Q). Figure 3 shows the completed RF system.

2.3. Intermediate Frequency (IF) Section

The primary purpose of the IF section is to filter and amplify the full phase two-channel IF signals. At the input stage, to prevent the leakage signals from saturating the amplifier in the following stage, the 5th order Butterworth high-pass filter, cut-off at 5 kHz is used. To prevent the aliasing problem, a 5th order Butterworth low-pass filter, cutoff at 65 kHz, is used in the last stage of the IF section. After the signal is processed in this section, the output from the low-pass filter is then fed to the data acquisition unit for further processing.

2.4. Data Acquisition Unit (DAU)

Converting the analogue signals into strings of digital data is the responsibility of the data acquisition unit. It then stores them in a memory bank. In this project, a personal computer (PC) was used as the signal processor and storage device. The PC-based system is more flexible in handling various sources of data as compared to the network analyzer-based system. An 8-bit dual channel 100 kHz analogue-to-digital converter (ADC) has been used in this project to digitize the return radar echo into digital signals before stores them into high-density digital disk.

3. FIELD EXPERIMENTS

The FMCW imaging system was tested in outdoor environment with low reflection characteristics. The aptitude of the system as a useful tool to collect ground-truth measurement data is determined through the experiment. The outcomes of the experiment are reported in the following sections.

3.1. Measurement Setup

Several field experiments for the system have been carried out to verify functionality of the subsystems of FMCW imaging radar. This paper reported one of the experiments which took place at a car park. The measurement setup is shown in Figure 4.

3.2. Measurement Results

Figure 5 shows the polarimetric results with intensity of azimuth points vs range in meters. The difference in the color intensity of the results is the image location of the targets.

Base on the VV polarization result, the lamp posts is seen to be in the range of 30 m. The lamp post reflect strong horizontal components of the co-polarize image which produce a strong intensity of the target. The HV and VH polarization result show the lamp post can still slightly be seen in the range of 30 m. However the cross polarization did not produce a strong intensity in the image. It seen that the cross polarization of HV and VH have almost same magnitude. Base on the VV polarization result, the lamp post is seen to be in the range of 30 m. The targets reflect

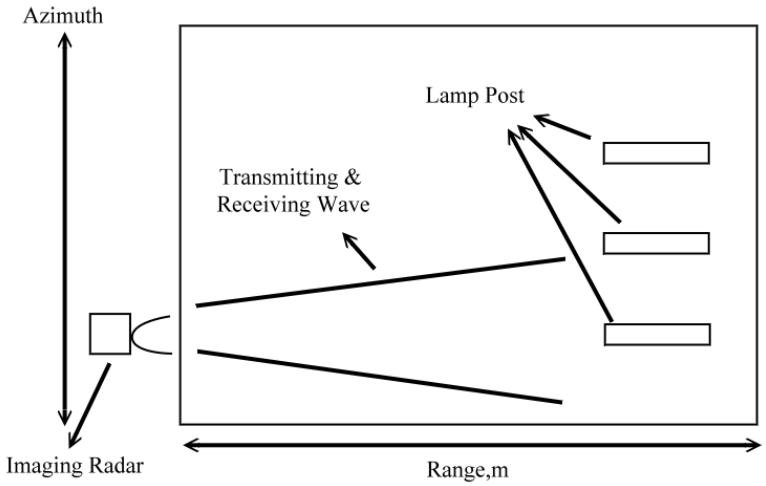

Figure 4: Experimental setup.

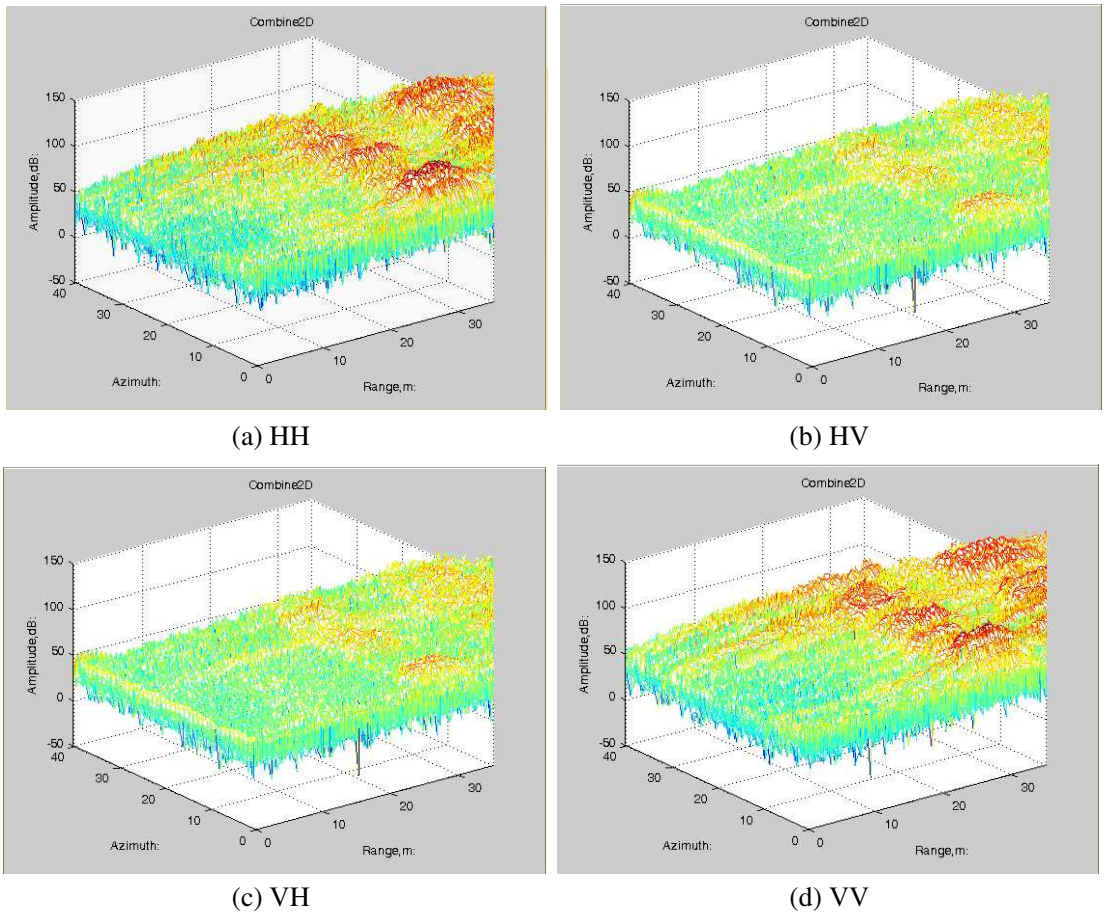

Figure 5: The polarimetric return of field experiment.

strong vertical components of the co-polarize image which produce a strong intensity of the return echo.

4. CONCLUSION

A FMCW imaging radar system has been successfully designed and constructed at the Multimedia University, Malaysia. Upon completion, a series of controlled testing and experiments have been conducted to verify the performance of the radar system. The validity of the imaging was confirmed by running tests in the laboratory which extended to the field measurements. The measured results gave good agreement with the field arrangement. This radar system may be useful and necessary for future sensor design and space technology development.

ACKNOWLEDGMENT

This project is funded by Science Fund under Ministry of Science, Technology and Innovation with project No: 04-02-01-SF0081.

REFERENCES

1. Ulaby, F. T., R. K. Moore, and A. K. Fung, *Microwave Remote Sensing: Active And Passive*, Vol. 2, Artech House, Norwood, 1982.
2. Yamaguchi, Y., T. Nishikawa, W.-M. Boernertt, M. Sengoku, and H. Joon, "On radar polarimetry in FM-CW radar," *IEEE Transactions Geoscience and Remote Sensing*, Vol. 2, 368–370, 1993.
3. Yamaguchi, Y., T. Nishikawa, M. Sengoku, and W.-M. Boernertt, "Two-dimensional and full polarimetric imaging by a synthetic aperture FM-CW radar," *IEEE Transactions Geoscience and Remote Sensing*, Vol. 2, 421–427, 1995.

4. Prescott, G., S. Gogineni, D. Depardo, H. Chakravarthula, and R. Hosseinmostafa, "MMIC-based FM-CW radar for multipolarization backscatter measurements," *IEEE Transactions Geoscience and Remote Sensing*, Vol. 3, 2273–2275, 1995.
5. S. V. Nghiem, M. Borgeaud, J. A. Kong, and R. T. Shin, "Polarimetric remote sensing of geophysical media with layer random medium model," *Progress In Electromagnetics Research*, Vol. 03, 1–73, 1990.
6. Ulaby, F. T. and C. Elachi, *Radar Polarimetry for Geoscience Applications*, Artech House, California, 1990.
7. Zebker, H. A., J. J. van Zyl, and D. Held, "Imaging radar polarimetry from wave synthesis," *Journal of Geophysical Research*, Vol. 92, No. B1, 683–701, 1987.
8. Boerner, W. M., M. B. El-Arini, C. Y. Chan, and P. M. Mastoris, "Polarization dependence in electromagnetic inverse problems," *IEEE Transactions on Antennas and Propagation*, Vol. 29, 262–271, 1981.

A GPS/SINU Design for Motion Sensing and Compensation Using Extended Kalman Filter for Airborne UAVSAR

C. H. Lim, C. S. Lim, W. Q. Tan, T. S. Lim, and V. C. Koo
Faculty of Engineering and Technology, Multimedia University
Jalan Ayer Keroh Lama, Melaka 75450, Malaysia

Abstract— Synthetic Aperture Radar (SAR) is classified as one of the high resolution imaging system in microwave remote sensing. The operational elements of SAR, unlike optical sensing, consist of a large number of frequency-modulated received echoes which must be acquired in real-time. Recently, airborne unmanned aerial vehicle (UAV) was commonly appeared in SAR applications for data acquisition purposes. Assumption was made on the nominal trajectory of the airborne UAV to be straight line path. In reality, however, such assumption will not hold due to atmosphere turbulence and UAV's motion error, which results in severe degradation in output images quality. In this paper, a global positioning system (GPS) aided strapdown inertial navigation unit (SINU) was used to sense and compensate the motion errors of the airborne UAVSAR. The GPS/SINU was mounted together with the airborne UAVSAR. The integration of GPS/SINU was modeled using extended Kalman filter. The results indicate the applicability and effectiveness of the proposed design.

1. INTRODUCTION

For many years, Synthetic Aperture Radar (SAR) has been a fascinating and efficient tool for microwave imaging of Earth's surface. Various applications such as imaging, guidance, and remote sensing were involved in the usage of SAR. Modern SAR system employed digital signal processing techniques to improve the imaging resolution with enhanced processing speed [1]. Recent trend in SAR sensor development turned the focuses on light weight, low cost systems such as airborne Unmanned Aerial Vehicle (UAV)-based SAR [2]. Airborne UAVSAR, which differs from spaceborne SAR, provides higher mobility and flexibility in geodetic imaging applications, which includes time critical missions such as earthquake assessment [3] and flood monitoring [4]. Like most SAR processing algorithms' assumption, the SAR raw data acquisition process assumed that the UAVSAR platform travelled in its nominal straight line path. However, such assumption doesn't hold for airborne UAVSAR. The atmosphere turbulence and deviations of UAV motion both contributes to the motion error of airborne UAVSAR which potentially jeopardized the output images.

Numbers of algorithms and methods were proposed in the last few decades to tackle the motion errors problem. John C. Kirk [5] proposed a generalized motion error compensation algorithm for SAR system. A detailed analysis on motion compensation was outlined in this paper. Joao R. Moreira [6] proposed a relatively unique method to achieve extraction of motion error from airborne SAR by combining the reflectivity displacement method (RDM) and the spectrum centroid method (SCM). The extracted errors were used for the real time motion compensation system. Gianfranco Fornaro et al. performed motion compensation errors analysis for airborne SAR images. Evan C. Zaugg et al. examined the theory and application of motion compensation for LFM-CW airborne UAVSAR.

Due to the effectiveness of SAR, the Multimedia University (MMU), in collaboration with Malaysian Remote Sensing Agency (ARSM) had developed a new C-band (5.3 GHz) UAVSAR for remote sensing applications. Two preliminary flight tests had been carried out in 2010. An onboard high performance single board computer is used to perform raw data storing, processing and motion sensing and compensation. A simplified SAR processing algorithm, based on the classical range-Doppler algorithm, is developed to enable image preview in real-time. It soon found out that one of the biggest challenges of this UAVSAR system is the degradation of image quality due to motion errors. Because of the size and the weight of the UAV, it is very difficult to maneuver steadily in cloudy and windy conditions. The flight path may have significant trajectory deviations from the ideal path and the variations of the UAV's forward velocity and attitude (yaw, pitch, and roll) further complicate the problem.

In this paper, a global positioning system (GPS) and a strapdown inertial navigation unit (SINU) are used for UAV's motion sensing. The SINU, which consists of three orthogonally arranged accelerometers and three orthogonally arranged gyroscopes, provides estimation of UAV's

accelerations and angular velocities in 167 Hz, which in turn provides estimation of position, velocity and orientation. Due to high accumulated errors that exist in SINU, a GPS with 5 Hz data rate is integrated to improve the position measurement accuracy. An extended Kalman filter is modeled and used for the GPS/SINU system, which in turn combining the merits of SINU in terms of short term accuracy and GPS in terms of no accumulated position errors.

This paper is organized as follow. Section 2 discussed the fundamental requirements and theories of motion sensing and compensation for SAR. Section 3 outlined the system specifications. Section 4 listed down the analysis and discussion of the experimental results using the designed system, and Section 5 concluded the findings in this paper.

2. MOTION SENSING AND COMPENSATION

This section discussed the theories and knowledge which were essential for motion sensing and compensation.

2.1. Motion Compensation Requirements

A successful SAR image processing depends on the returns of each image scatter's coherent phase history, which in turn provides a known phase relationship between successive radar returns. This knowledge is crucial for the relative phase of radar's returns adjustment. Consider a typical point scatter, the phase history can be described as:

$$\phi(t) = \phi_T(t) + \frac{4\pi}{\lambda} R(t) \tag{1}$$

where $\phi_T(t)$ is the transmitter's phase modulated signal, λ is the radar's wavelength, and $R(t)$ is the range from antenna phase center to the point scatter. In general case, both λ and $\phi_T(t)$ are known exactly. Thus it is the uncertainty in $R(t)$ that leads to massive image degradation in SAR system. The straight line path assumption is no longer hold, and a measurement on real $R(t)$ is required to estimate the phase history correctly.

From (1) it is easy to derive:

$$\phi(t) + \delta\phi(t) = \phi_T(t) + \frac{4\pi}{\lambda}\left(R(t) + \delta R(t)\right) \tag{2}$$

where $\delta\phi_T(t)$ is the residual phase distortion, and $\delta R(t)$ is the range deviation from the nominal path which is best estimated using a GPS/SINU integrated system.

2.2. Motion Sensing and Error Computation

The navigation equations (or motion equations) is a set of 1st order differential equations which describe the relationship of SINU outputs to the inputs in terms of accelerations and angular rates. Its derivation involved the usage of Newton's first law, and is best to be represented as follows:

$$\begin{bmatrix} \dot{r}^e \\ \dot{v}^e \\ \dot{R}_b^e \end{bmatrix} = \begin{bmatrix} v^e \\ R_b^e f^b + g^e - 2\Omega_{ie}^e v^e \\ R_b^e \Omega_{eb}^b \end{bmatrix} \tag{3}$$

where r^e, v^e are the position and velocity vectors in e-frame, g^e is the gravitational vector in e-frame, f^b is the b-frame's specific force vector measured by accelerometers, R_b^e is the direct cosine matrix (DCM) that transform coordinate from b-frame to e-frame, Ω_{ie}^e is the skew-symmetric matrix related to Earth's rotational rate $\omega_{ie} \approx 7.292115 * 10^{-5}$ rad/s, and Ω_{eb}^b is the skew-symmetric matrix which represent the rotation rates between e-frame and b-frame.

The navigation error equations can be derived from (3) by performing perturbations on the first order differential equations:

$$\begin{bmatrix} \delta\dot{r}^e \\ \delta\dot{v}^e \\ \dot{\varepsilon} \end{bmatrix} = \begin{bmatrix} \delta v^e \\ R_b^e \delta f^b - S_f^e \varepsilon + \delta g^e - 2\Omega_{ie}^e \delta v^e \\ R_b^e \delta\omega_{ib}^b - \Omega_{ie}^e \varepsilon \end{bmatrix} \tag{4}$$

where ε denotes the attitude error vector of the small angle rotations of the DCM R_b^e, and S_f^e is the skew-symmetric matrix of the specific force f^b.

As a conclusion (3) shows the system's navigation equations in terms of 1st order differential representation of position, velocity and orientation, while Equation (4) describes the erroneous of Equation (3) which are particularly important in performance analysis. It is of great desire to reduce, or eliminate, the errors and it can be accomplished by modeling and applying an extended Kalman filter.

2.3. Extended Kalman Filter

Due to the non-linear nature of the GPS/SINU system, an extended Kalman filter (EKF) is used to overcome the non-linearity problem. Figure 1 shows the EKF's recursive process in block diagram, with $\hat{x}_k^-$ and $\hat{x}_k$ denote as *a priori* and *a posteriori* state estimate respectively, u_k denotes the state input, P_k^- and P_k denote the *a priori* and *a posteriori* estimate error covariance respectively, A_k and W_k are the process Jacobians, Q_k is the process noise covariance, z_k is the measurement update, H_k and V_k are the measurement Jacobians, and R_k is the measurement noise covariance. The k indicates the current step of each variable.

3. SYSTEM SPECIFICATIONS

This section outlined the designed GPS/SINU system specification. A high precision GPS and a high precision inertial measurement unit (IMU) were incorporated in the system design, as shown in Figure 2(a). The IMU's gyroscopes and accelerometers were 14-bits resolution. The resolution of GPS, with at least 4 visible satellites, is 3 meters. Since the data rate of IMU is 167 Hz, while the data rate of GPS is 5 Hz, a process of linearization is required for the modeled EKF. Figure 2(b) visualized the overall system setup, including its operations, processing and expected outcomes. Both the GPS and IMU were communicated with a high performance computer (HPC) using serial communication. Data were recorded in MATLAB .mat format and processed using MATLAB.

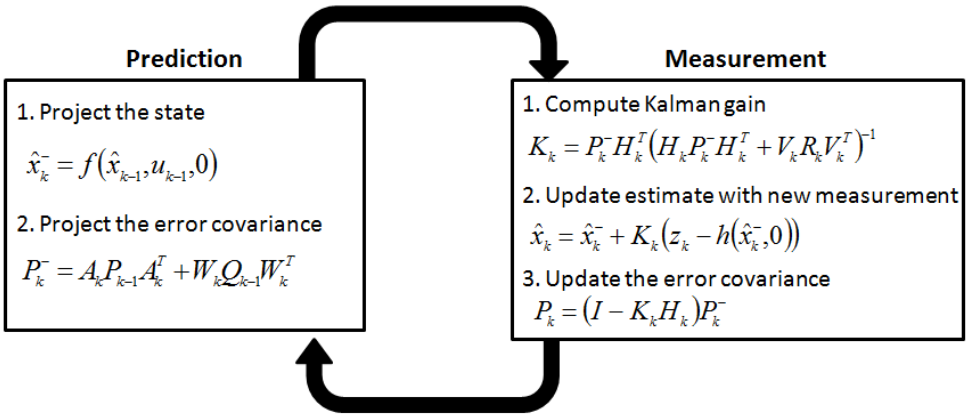

Figure 1: Operational descriptions of Extended Kalman filter with two stages of prediction and three stages of measurement that form the recursive loop. Zero initial condition is assumed.

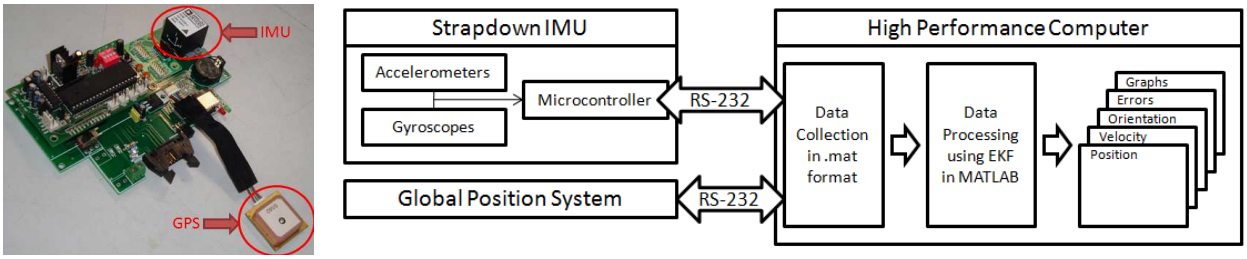

(a) (b)

Figure 2: (a) The designed GPS/SINU system. (b) Block diagram representation of overall system specification.

4. EXPERIMENTAL RESULTS

Experiments were carried out in Melaka International Trade Centre (MITC) on May 2011 using a car to validate the designed GPS/SINU system and the motion sensing & compensation algorithm using EKF. Calibration and Alignment were made before carried out any experiments. The initial b-frame was aligned to be in-conjunction with the NED frame. Since GPS data are represented in e-frame, it is best to transform the information obtained from the strapdown IMU into e-frame for the purpose of errors measurement:

$$z_k = \begin{pmatrix} r^e_{IMU} - r^e_{GPS} \\ v^e_{IMU} - v^e_{GPS} \end{pmatrix} \tag{5}$$

where r^e_{IMU} and v^e_{IMU} are the IMU's position and velocity respectively, and r^e_{GPS} and v^e_{GPS} are the GPS's position and velocity respectively. The errors measurement z_k is used in EKF for errors estimation.

Figure 3 shows graphs plotting of GPS data, uncompensated and compensated IMU data under

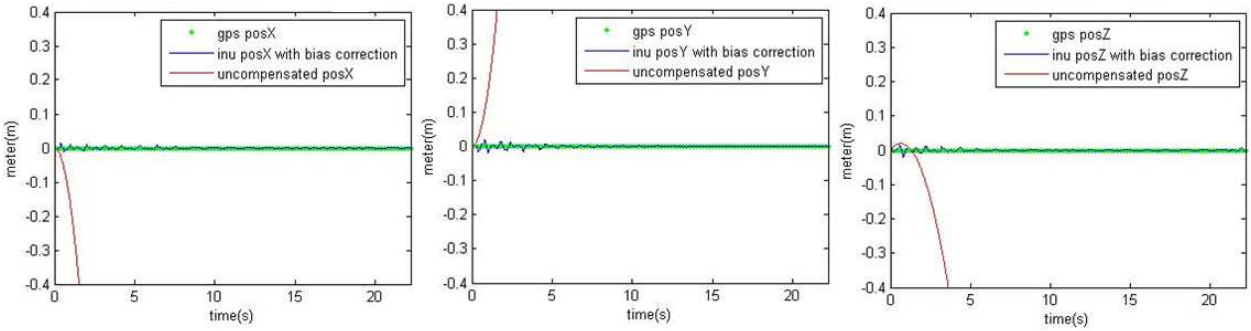

Figure 3: Static (no movement) data recorded of GPS, uncompensated and compensated IMU. (a) In X position, (b) in Y position, (c) in Z position.

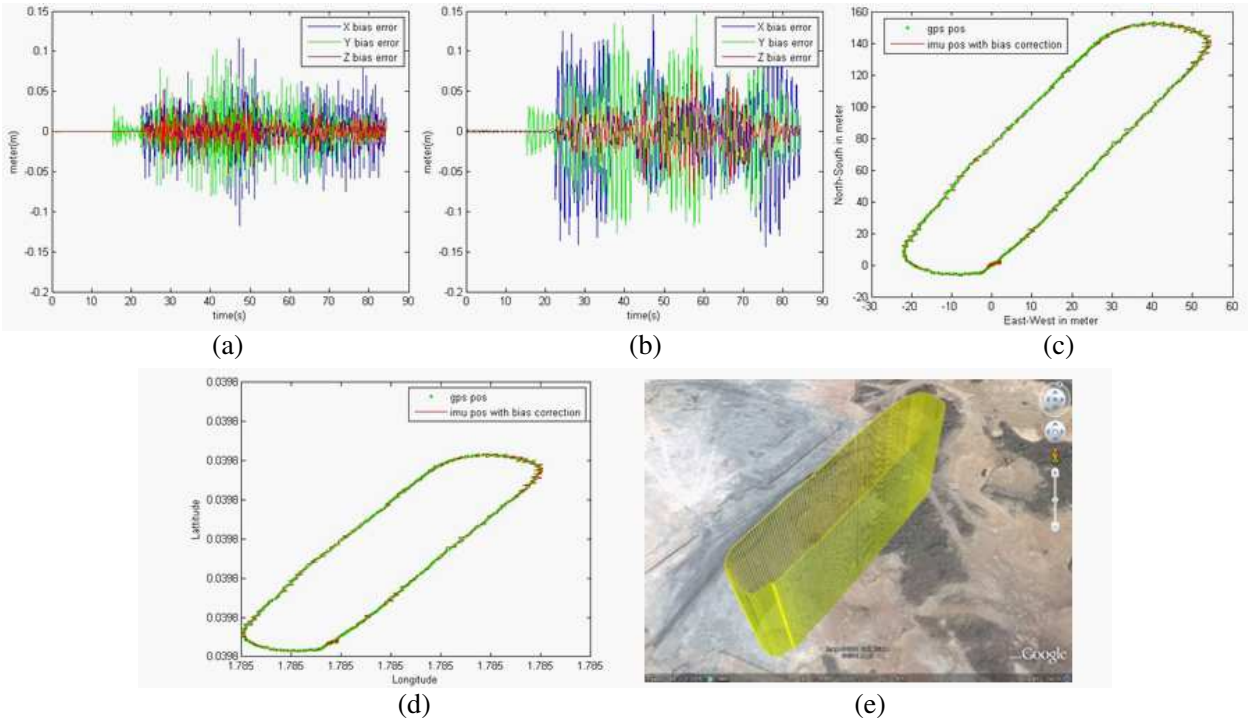

Figure 4: GPS/SINU recorded data with compensation for a round trip with (a) calculated position bias errors, (b) calculated velocity bias errors, (c) NED plot of GPS and SINU position, (d) e-frame plot of GPS and SINU position, (e) GPS plot using Google Earth.

static condition. All three axis results show exponential deviation of uncompensated IMU data from the GPS measurements, as compared to the compensated IMU data using EKF which kept its error to be within ± 0.02 m.

Figure 4 shows another set of GPS/SINU data record by taking a round trip, with Figures 5(a)–(c) show the position plots using EKF, Figures 5(d)–(e) show the position and velocity biases calculated from EKF, Figure 5(f) shows the round trip in NED frame, Figure 5(g) shows the same round trip in *e*-frame, and Figure 5(h) plots the GPS data in Google Earth to verify the results.

5. CONCLUSION

In this paper, a GPS/SINU system had been designed and developed to perform motion sensing and compensation using EKF algorithm. Experimental results indicate the applicability of such system for motion compensation applications, which is usable for UAVSAR applications.

REFERENCES

1. Chan, Y. K., V. C. Koo, B.-K. Chung, and H.-T. Chuah, "Modified algorithm for real time SAR signal processing," *Progress In Electromagnetics Research C*, Vol. 1, 159–168, 2008.
2. Rosen, P. A., S. Hensley, K. Wheeler, G. Sadowy, T. Miller, S. Shaffer, R. Muellerschoen, C. Jones, S. Madsen, and H. Zebker, "UAVSAR: New NASA airborne SAR system for research," *IEEE A&E System Magazine*, 21–28, November 2007.
3. Brunner, D., G. Lemoine, and L. Bruzzone, "Earthquake damage assessment of buildings using VHR optical and SAR imagery," *IEEE Trans. on Geoscience and Remote Sensing*, Vol. 48, No. 5, 2403–2420, May 2010.
4. Gebhardt, M., M. Warner, T. Bungey, A. Currie, and N. Holden, "Airborne SAR interferometry applied to flood modelling," *IEE Colloquium on Radar Interferometry*, April 11, 1997.
5. Kirk, J. C., "Motion compensation for synthetic aperture radar," *IEEE Trans. on Aerospace and Electronic Systems*, Vol. 11, No. 3, 338–348, May 1975.
6. Moreira, J. R., "A new method of aircraft motion error extraction from radar raw data for real time motion compensation," *IEEE Trans. ON Geoscience and Remote Sensing*, Vol. 28, No. 4, 620–626, July 1990.
7. Fornaro, G., G. Franceschetti, and S. Perna, "Motion compensation errors: Effects on the accuracy of airborne SAR images," *IEEE Trans. on Aerospace and Electronic System*, Vol. 41, No. 4, 1338–1352, October 2005.
8. Zaugg, E. C. and D. G. Long, "Theory and application of motion compensation for LFM-CW SAR," *IEEE Trans. on Geoscience and Remote Sensing*, Vol. 46, No. 10, 2990–2998, October 2008.

A New Dual Band E-shaped Slot Antenna Design for Wireless Applications

Jawad K. Ali
Department of Electrical and Electronic Engineering, University of Technology, Baghdad, Iraq

Abstract— An E-shaped printed slot antenna is presented as a candidate to cover dualband operation over the entire wireless local area network (WLAN) frequency bands of 2.4–2.5 GHz and 4.9–5.8 GHz. The E-shaped slot structure has been etched in the ground plane, and the 50 microstrip line feed is etched on the reverse side of the substrate. An additional trapezoidal slot has been etched attached to the slot structure on the feeding side to facilitate tuning and the dual-band operation. The antenna structure has been modeled and its performance has been evaluated using a method of moment based electromagnetic simulator, IE3D from Zeland Software Inc. Simulation results show that, the proposed antenna offers good return loss response (for S_{11} less than -10 dB) at the two bands. The ratio of the two resonating frequencies f_{02}/f_{01} could be varied in a considerable range, without changing the antenna external dimensions, making the antenna suitable for other dual band wireless applications.

1. INTRODUCTION

The application of the E-shaped structure in patch antenna design has been first presented in [1]; in an attempt to overcome the narrow band and the large size of the conventional microstrip patch antennas. Since then, this structure had attracted antenna designers in their efforts to produce antennas with reduced size and broadband performance for different applications. The conventional E-shaped patch antenna has been used to design wideband antennas [2–5]. Various E-shaped patch antennas with tapered, corrugated, and trapezoidal slots have been reported in the literature [6–8]. Many variants of the E-shaped patch structure have been proposed to produce reduced size and wide band antennas [9–12]. Patch antennas with half E-shaped and folded E-shaped structures have been also reported [9, 10, 13–15]. Moreover, the E-shaped structures have been used together with other slot structures to produce antennas with enhanced bandwidths [15–17]. For dual band antenna applications, E-shaped patch structures have been successfully verified as reported in [17, 18].

As a slot, the E-shaped structure has drawn less attention from antenna designers; to name a few [19, 20]. In [19], the E-shaped slot structure has been applied to build a complementary part of an ultrawideband (UWB) antenna to produce the 5 GHz/6 GHz band-notch. In the other work [20], two printed wide-slot antennas constituting of both E-shaped patch and E-shaped slot with rounded corners and fed by CPW and microstrip line have been presented. The presented antennas have been found to possess fractional bandwidths of about 146%.

In this paper, a printed microstrip slot antenna has been presented as a candidate for use in dual-band wireless applications. The slot structure is composed of a main E-shaped part and a small trapezoidal part for tuning purposes.

2. THE ANTENNA STRUCTURE

The geometry of the proposed E-shaped slot antenna structure is shown in Figure 1(a). The slot has been constructed, in the form of E-shape, on the ground plane side of a dielectric substrate. In order to achieve broadband operation, a small trapezoidal slot structure has been etched in the same plane and placed on the feed side of the rectangular E-shaped slot.The dielectric substrate is supposed to be the FR4 with a relative dielectric constant of 4.4 and thickness of 1.6 mm. For design convenience, the proposed antenna is fed by a 50 Ω microstrip line printed on the reverse side of the substrate. The microstrip line, with a width of 3.0 mm is placed on the centreline of the combined slot structure (x-axis). Figure 1(b) shows the antenna layout with respect to coordinate system.

3. ANTENNA DESIGN

The E-shaped printed slot antenna structure, depicted in Figure 1, has been modelled using the commercially available method of moments based EM simulator, IE3D, from Zeland Software Inc. [21]. The first design step is to make the modelled antenna resonating such that the lower resonant band

is located at 2.45 GHz. This design goal has been reached by suitable rescaling of the whole structure, varying the trapezoid dimensions, w_t and L_t, and varying the E-shape parameters, w_v and w_h. At this step, the proposed antenna has the following dimensions. The E-shaped slot dimensions are as follows: $L_h = 15.52\,\text{mm}$, $L_v = 23.38\,\text{mm}$, $w_h = 4.12\,\text{mm}$, and $w_v = 7.10\,\text{mm}$. The trapezoidal slot dimensions are: the central length, $L_t = 5.4\,\text{mm}$ the larger width, $w_t = 4.31\,\text{mm}$, and smaller width is equal to 3.00 mm, which is the same as that of the microstrip line. A parametric study has been carried out to demonstrate the effect of the slot internal dimensions, w_v and w_h on the antenna performance, such that the slot external dimensions are being held constant.

4. PERFORMANCE EVALUATION

Observing the influence of the various parameters on the dual band resonant behaviour of the modelled antenna, it has been found that the dominant factors in the antenna structure are the E-shaped slot parameters w_h and w_v, besides the slot external dimensions.

Figure 2 shows that the return loss response of the proposed antenna is highly affected by the variation of the value of w_h with constant value of $w_v = 7.0\,\text{mm}$. As the value of w_h has been increased, the antenna dual band behaviour is still maintained. However, the lower resonant frequency has been influenced more than the higher frequency because of the effect of change of w_h.

Variation of w_v has a little impact on both the lower and the upper resonant frequencies, as Figure 3 implies. Again the lower resonant frequency is relatively more affected than the higher one. Figure 4 shows the simulated the electric field radiation patterns E_θ, of the proposed E-shaped

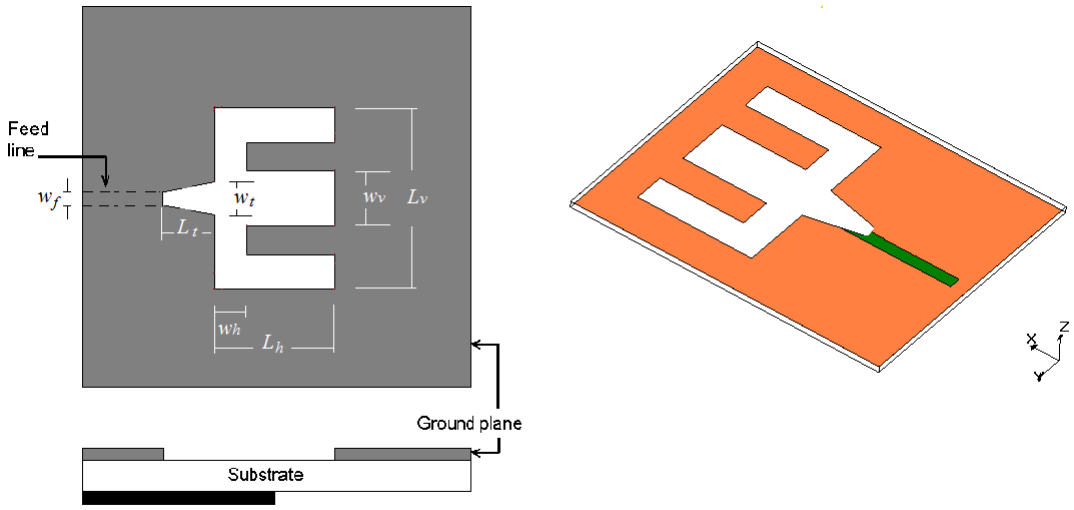

Figure 1: (a) The proposed antenna structure, and (b) its layout with respect to the coordinate system.

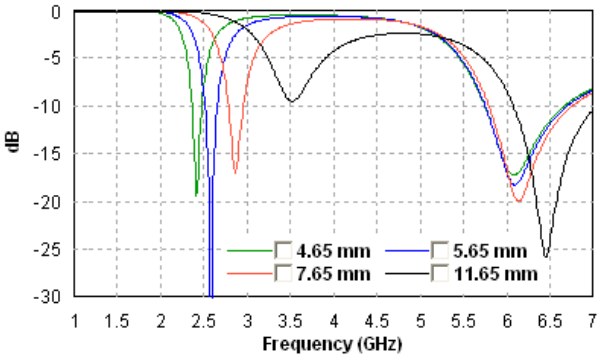

Figure 2: Simulated return loss responses of the proposed antenna for different values of $w_v = 7.0\,\text{mm}$ with w_h as a parameter.

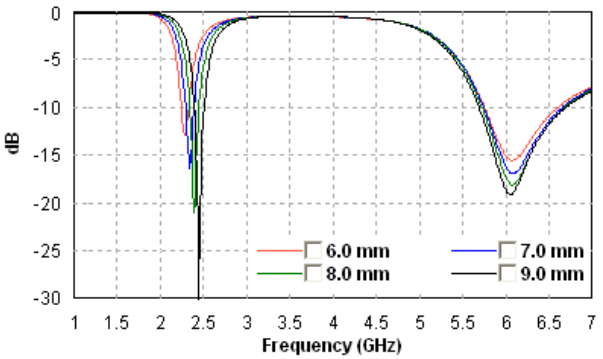

Figure 3: Simulated return loss responses of the proposed antenna for different values of $w_h = 4.12\,\text{mm}$ with w_v as a parameter.

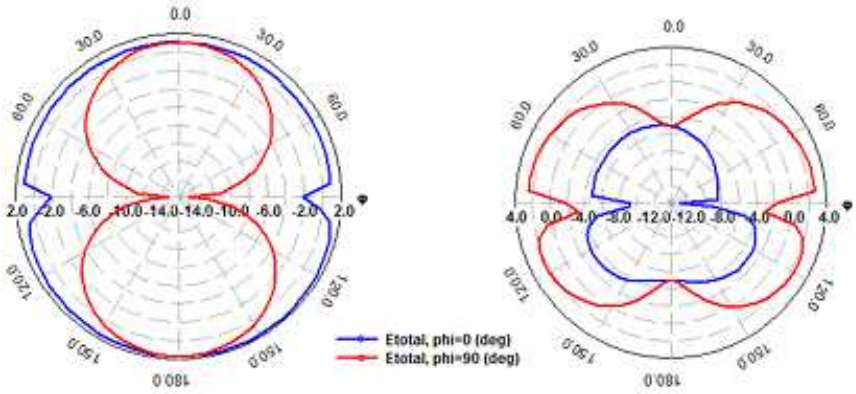

(a) (b)

Figure 4: Simulated electric field radiation patterns, E_θ, of the proposed E-shaped slot antenna for $\varphi = 0°$ and $\varphi = 90°$ at, (a) 2.45 GHz, and (b) 5.8 GHz. The antenna is printed on an FR-4 substrate. Other parameters are $w_h = 4.12$ mm and $w_v = 7.0$ mm.

slot antenna for $\varphi = 0°$ and $\varphi = 90°$ at: (a) 2.45 GHz, and (b) 5.8 GHz. The modeled antenna is with slot parameters of $w_h = 4.12$ mm and $w_v = 7.0$ mm.

5. CONCLUSIONS

A combined E-shaped microstrip printed slot antenna is presented in this paper, as a candidate for use for dual band wireless applications. The antenna has been modeled and its performance has been analyzed using a method of moment based software, IE3D. The proposed antenna shows an interesting dual band resonant behavior with a wide range of the two resonant frequency ratio without changing the external dimensions of the combined slot structure; providing the antenna designer with more degrees of freedom.

REFERENCES

1. Shen, Q., B. L. Qoi, and M. X. Leong, "A novel E-shaped broadband microstrip patch antenna," *Progress In Electromagnetic Research Symposium*, Boston, USA, Jul. 2000.
2. Yang, F., X. X. Zhang, and Y. Rahmat-Samii, "Wideband E-shaped patch antenna for wireless communications," *IEEE Trans. Antennas Propagat.*, Vol. 49, No. 7, 1094–1100, 2001.
3. Yu, A. and X. X. Zhang, "A method to enhance the bandwidth of microstrip antennas using a modified E-shaped patch," *Proceedings of Radio and Wireless Conference, RAWCON'03*, 2003.
4. Ge, Y., K. P. Essele, and T. S. Bird, "Compact diversity antenna for wireless devices," *Electronic Lett.*, Vol. 41, No. 2, 371–372, 2005.
5. Pramod, K. M., R. Jyoti, S. S. Kumar, and V. Reddy, "Simplified and efficient technique for designing of broadband patch antenna," *Proceedings of Applied Electromag. Conf., AEMC*, Dec. 2009.
6. Deshmukh, A. A. and G. Kumar, "Compact broadband E-shaped microstrip Antennas," *Electronic Lett.*, Vol. 41, No. 18, 2005.
7. Caratelli, D., R. Cicchetti, G. Bit-Babik, and A. Faraone, "A perturbed E-shaped patch antenna for wideband WLAN applications," *IEEE Trans. Antennas Propagat.*, Vol. 54, No. 6, 1871–1874, 2006.
8. Rao, Q. and T. A. Denidni, "Microstrip patch antennas with trapezoidal slots," *IEEE International Symposium on Antennas and Propagation and USNC/URSI National Radio Science Meeting*, New Mexico, USA, Jul. 2006.
9. Chiu, C. Y. and C. H. Chan, "A wideband antenna with a folded patch feed," *IEEE International Workshop on Antenna Technology Small Antennas and Novel Metamaterials*, Mar. 2005.
10. Chiu, C. Y., H. Wong, and C. H. Chan, "Study of small wideband folded-patch-feed antennas," *IET Microw. Antennas Propag.*, Vol. 1, No. 2, 501–505, 2007.
11. Matin, M. A., B. S. Sharif, and C. C. Tsimenidis, "Probe fed stacked patch antenna for wideband applications," *IEEE Trans. Antennas Propagat.*, Vol. 55, No. 8, 2385–2388, 2007.

12. Peng, L., C. Ruan, and Y. Zhang, "A novel compact broadband microstrip antenna," *Proceedings of Asia-Pacific Microwave Conference, APMC'07*, Bangkok, Dec. 2007.
13. Chair, R., C. Mak, K. Lee, K. Luk, and A. A. Kishk, "Miniature wide-band half U-slot and half E-shaped patch antennas," *IEEE Trans. Antennas Propagat.*, Vol. 53, No. 8, 2645–2652, 2005.
14. Sun, F., X. Ren, and H. He, "A compact half E-shaped patch antenna with a slotted U-shaped ground plane," *Proceedings of IEEE Global Symp. on Millimeter Waves, GSMM*, Nanjing, China, Apr. 2008.
15. Xiong, J., Z. Ying, and S. He, "A broadband E-shaped patch antenna of compact size and low profile," *IEEE Antennas and Propagation Society International Symposium*, 2008.
16. Kong, L., J. Pei, and X. Guo, "A new dual-frequency broadband L-slot mixed E-shaped patch antenna," *Global Symposium on Millimeter Waves Proceeding*, Nanjing, China, Apr. 2008.
17. Guterman, J., Y. Rahmat-Samii, A. A. Moreira, and C. Peixeiro, "Quasi-omnidirectional dual-band back to- back E-shaped patch antenna for laptop applications," *Electronic Lett.*, Vol. 42, No. 15, 2006.
18. Singh, A., "Dual band E-shaped patch antenna (ESPA) for ultra wide band applications," *Proceedings of 2009 Asia Pacific Microwave Conference, APMC*, Singapore, Dec. 2009.
19. Panda, J. R. and R. S. Kshetrimayum, "A compact CPW-fed monopole antenna with E-shaped slot for 5 GHz/6 GHz band-notched ultrawideband applications," *Proceedings of the Annual IEEE India Conf., INDICON*, India, Dec. 2009.
20. Dastranj, A. and H. Abiri, "Bandwidth enhancement of printed E-shaped slot antennas fed by CPW and microstrip line," *IEEE Trans. Antennas Propagat.*, Vol. 58, No. 4, 1402–1407, 2010.
21. *IE3D User's Manual*, Release 12.3, Zeland Software, Inc., Fremont, CA, 2007.

Combined Fractal Geometries for the Design of Wide Band Microstrip Antennas with Circular Polarization

Homayoon Oraizi and Shahram Hedayati
Department of Electrical Engineering, Iran University of Science and Technology
Narmak, Tehran 16846-13114, Iran

Abstract— In this paper, we propose the combination of several fractal geometries for microstrip patch antenna for the achievement of their miniaturization and multi banding characteristics. By placing air gaps under the microstrip patches (actually making suspended microstrips) the bandwidths of antennas are drastically improved. By cutting appropriate rectangular and triangular slits as perturbations on the edges of fractal geometries, circular polarizations may be realized in the radiation patterns.

1. INTRODUCTION

Antennas are mainly designed for narrow band applications and if their dimensions are smaller than a quarter wave length, they become impractical. Utilization of fractal antennas may extend their bandwidth. A few iterations of fractal geometries may make the antenna multiband. As the order of fractal iteration increases, the lowest resonance frequency decreases and additional frequencies appear in their frequency response. If the dimensions of an antenna become quite smaller than the wavelength of its operating frequency, then its efficiency drastically deteriorates, because its radiation resistance decreases and the reactive energy stored in its near field increases. Consequently, the impedance matching of the antenna with its feeding system becomes difficult and at best quite narrow band [1]. Consequently, the utilization of fractal geometries is one of the best methods for their miniaturization. Fractal antennas are design as monopoles, dipoles and as arrays with multi-band characteristics [2].

Common fractal antenna shapes (such as, Koch and Hilbert) have been used as shown in Fig. 1. Fractal antennas are based on self-similar geometries, which possess improved characteristics and some degree of miniaturization. They are used in integrated circuits, multi-band antennas and arrays [2]. Scale independent and frequency independent antennas were made possible by the introduction of fractal geometries, first proposed by Mandelbrot [1]. Then, they were used fractal for the design of multi-band antennas in 1993 [3].

The fractal dimension is defined as a fractional dimension, which may be considered as a criterion for the space filling potential of fractal geometries and also for the comparisons among fractals.

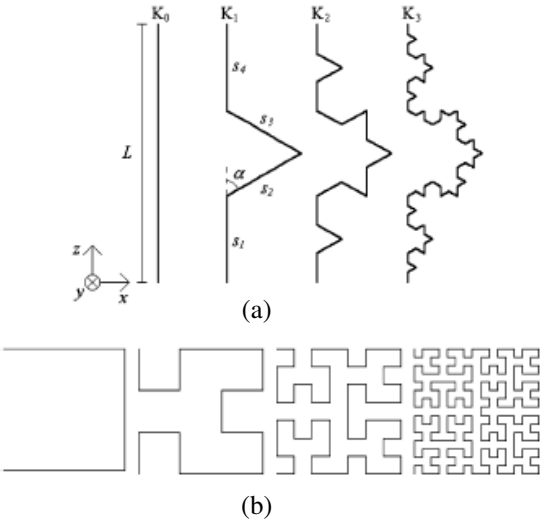

Figure 1: Ordinary fractals (a) Koch fractal (b) Hilbert fractal.

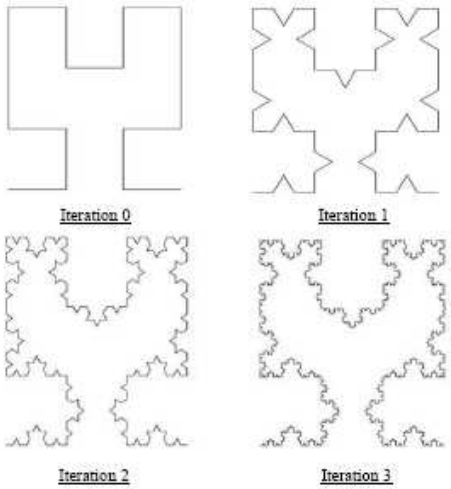

Figure 2: Geometries of combined fractals.

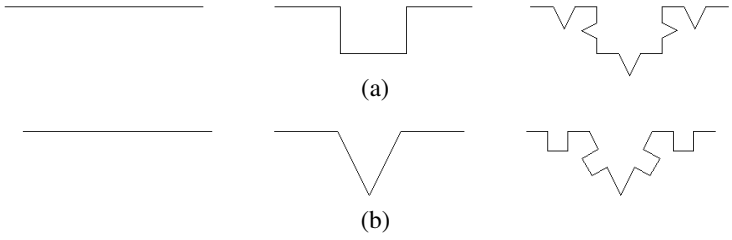

Figure 3: Procedure for the generation of fractals (a)Type I (b)Type II.

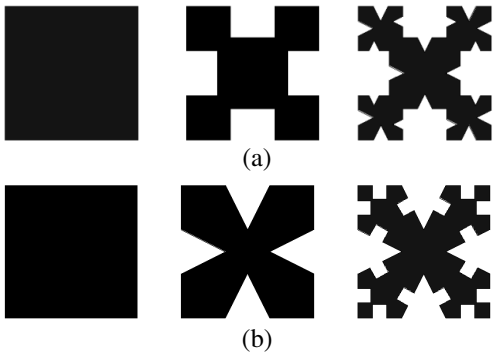

Figure 4: Combined fractal patch antennas.

Fractal geometries may be combined together to improve the characteristics, achieve their miniaturization and cause additional frequencies to appear in their bandwidths. For example we can combine Koch fractal and Hilbert fractal as shown in Fig. 2 [4].

In this paper, we apply the combination of triangular Koch and Minkowski fractal geometries on the sides of a square patch antenna. The fractal geometry is generated by an initiator and then generators are used for two types combinations [4]. Type I, uses first the Minkowski fractal then Koch triangular fractal as shown in Fig. 3(a). Type II, employs the reverse order as shown in Fig. 3(b). In both types, the scale factor is equal to 0.33. That is, in type I, the straight line is divided into three equal sections and a square is generated in the middle one. Then, each one of the four generated sections is divided into three equal sections and an equilateral triangular is generated in the middle one. This process may be continued. A similar procedure may be followed for the fractal type II .

Application of the fractal of types I and II to the edges of a square patch antenna for two iterations are shown in Figs. 4(a) and (b). We call them combined fractal patch antennas. It has

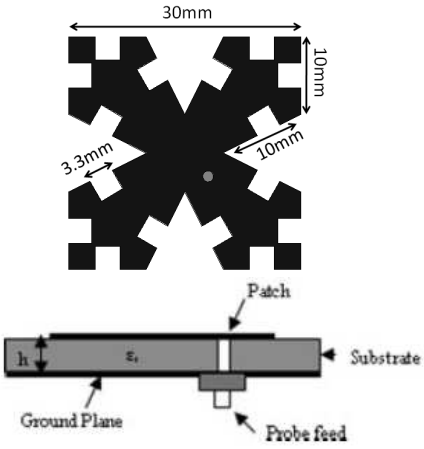

Figure 5: Structure of the proposed antenna.

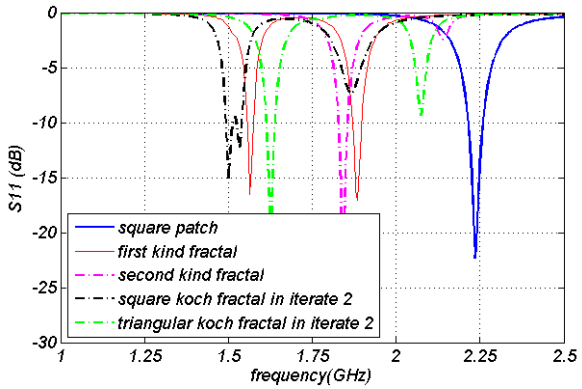

Figure 6: Comparison among S_{11} of proposed fractal antenna and common fractals.

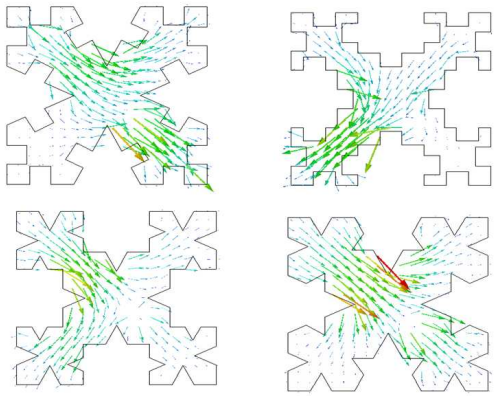

Figure 7: Current distribution on the antenna patches.

been shown that fractal iterations of more than two times do not have significant effect on the antenna characteristics [4].

2. COMPUTER SIMULATIONS

We use HFSS 12 software for the simulation of the designed fractal antennas. The substrate is FR4_epoxy with dielectric constant $\varepsilon_r = 4.4$, substrate thickness $h = 1.6\,\text{mm}$ and loss tangent $\tan\delta = 0.02$. The initial size of square patch is $a = 30\,\text{mm}$. The patch antenna feed is through a coaxial cable, which is positioned along its diagonal line at a distance of 4.2 mm from its center, as shown in Fig. 5. Both antenna types I and II are shown in Fig. 5.

2.1. Linear Polarization

The linear polarization of radiation is obtained by placing similar fractal shapes on the edges of square patch, so that their electrical lengths are identical. Fig. 6 shows the reflection coefficients (S_{11}) of the square patch fractal types I and II, with Minkowski and triangular Koch (with two iterations). Observe that the resonance frequencies of type I and II fractals are lower than that of the simple patch antenna by 600 MHz and 400 MHz, respectively. The reduction of the resonance frequency actually leads to the effective reduction of antenna size. Table 1 summarizes the resonance frequencies, band widths, areas and periphery lengths of square, Minkowski fractal, Koch fractal, combined fractal types I and II. Observe that by increasing the periphery of antennas, effective electrical length increases and the resonance frequency decreases [3]. The current distribution on the antenna patches is shown in Fig. 7. Observe that the length of current paths has increased, which leads to the reduction of resonance frequency.

Table 1.

Type of Antenna	F_r(GHz)	BW	Area mm^2	Periphery mm
Square patch	2.23	3%	900	120
Minkowski fractal	1.6	4%	464.4	268.99
Square koch	1.625	2%	624.9	225.04
Combined fractal 1	1.5	2%	533.8	243.4
Combined fractal 2	1.8	2%	549.8	257.6

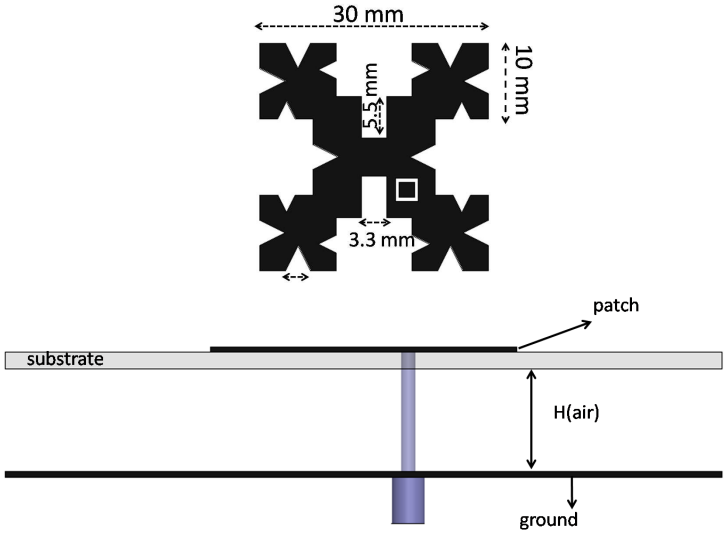

Figure 8. Combined fractal geometries for wide band antennas with circular polarization.

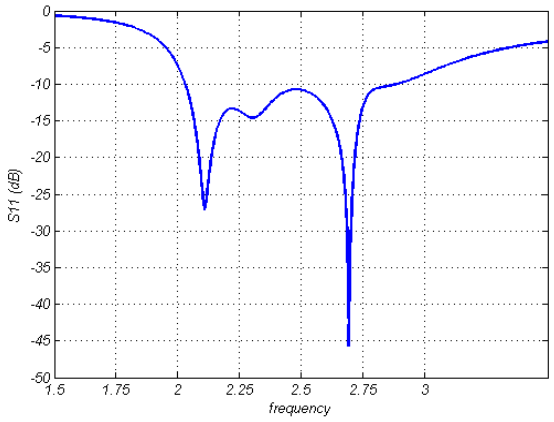

Figure 9. S_{11} for combined fractal geometries for wide band antennas with circular polarization.

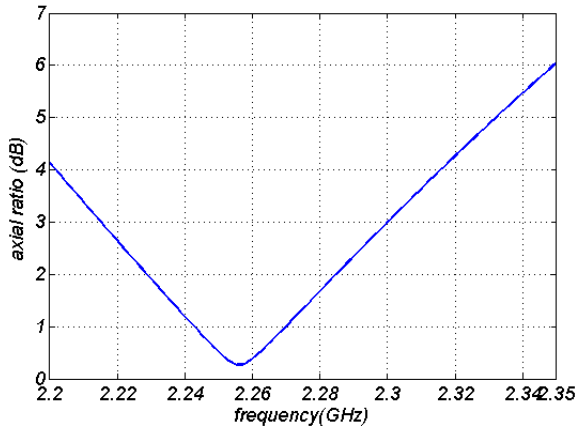

Figure 10. Axial ratio for combined fractal geometries for wide band antennas.

2.2. Bandwidth Extension and Circular Polarization

We place an air gap of height H between the dielectric substrate (FR4) and the ground plane , as shown in Fig. 8. The air gap decreases the effective dielectric constant of the antennas, leading to the reduction of quality factor and eventual increase of the antenna band-width. The combined fractal patch antenna and the 50 Ω coaxial feed are also shown in Fig. 8. However, the increase of length of the coaxial the impedance matching more difficult. In order to compensate for this effect, a square slot is cut around the feed point in the patch to produce to a capacitance effect and make the impedance matching possible [2]. For the achievement of circular polarization with maximum band-width, two orthogonal modes with 90 degrees phase shift are needed. For the excitation of two orthogonal modes with diagonal feed, the electrical length of patch edges should differ by about a quarter wavelength. Consequently, a rectangular slit is cut in an edge of the patch (see Fig. 8)in the

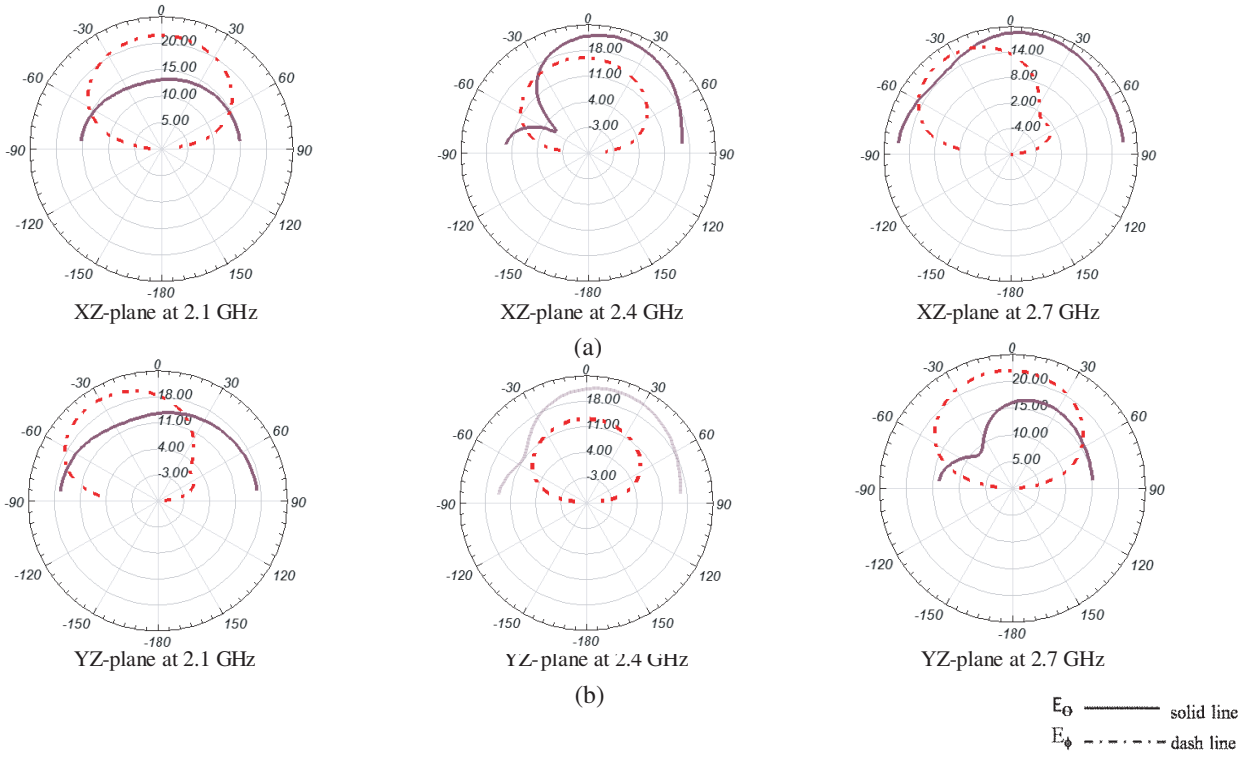

Figure 11. Computer simulated radiation patterns (a) simulated pattern in the XZ-plane (E-plane); (b) in the YZ-plane (H-plane).

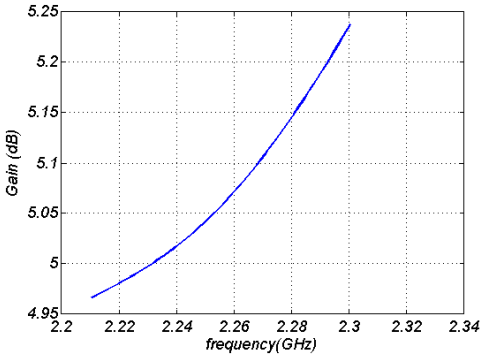

Figure 12. Radiation Gain in circular polarization band.

place of triangular slit as perturbation in antenna type II (see Fig. 5) [2, 3]. In order to maximize the frequency band-width, an optimization is performed by the HFSS12 on the square patch that exist on top of the feed point (L) and width of square slot cut around the feed point (W) and height of air gap under patch in suspended microstrip (H) (see Fig. 8). The optimum values are $L = 2\,\text{mm}$, $W = 0.25\,\text{mm}$ and $H = 10\,\text{mm}$. The return loss (S_{11}) of the proposed Combined Fractal patch Antenna With Circular Polarization is drawn in Fig. 9 and the axial ratio for this antenna is shown in Fig. 10. Figs. 9 and 10 show that the proposed antenna has a resonance frequency equal to 2.4 GHz and a band width ($S_{11} < -10\,\text{dB}$) equal to 890 MHZ or 36 percent. The bandwidth for circular polarization (axial ratio $< 3\,\text{dB}$) is 90 MHZ or 3 percent. The radiation patterns of the antenna are drawn in the xz-plane (E-plane) and yz-plane (H-plane) and is shown in Fig. 11. The diagram for the radiation gain of proposed antenna versus frequency is drawn in Fig. 12, which is about 5 dB.

3. CONCLUSIONS

We propose several combinations of fractal geometries for the design of microstrip patch antennas, which achieve some degree of antenna miniaturization, specifically reducing its resonant frequency. The perturbation of fractal geometries provides circular polarization of the radiation patterns. The

antenna bandwidth is also extended by cutting square slots around the feed point on patch. The optimization on the antenna geometrical configuration (namely, dimensions of slits on the patch edges, slots on the feed point, height of air gap) improve the antenna characteristics. It is shown that the combination of fractal geometries has improved the performance of antenna, relative to the application of single fractals.

REFERENCES

1. Werner, D. H. and R. Mittra, *Frontiers in Electromagnetics*, 48–81, IEEE Press, Piscataway, NJ, 2000.
2. Baliarda, C. P., J. Romeu, and A. Cardama, *The Koch Monopole: A Small Fractal Antenna & Propagation*, Vol. 48, No. 11, November 2000.
3. Baliaada, C. P., J. Romeu, and R. Cardama, "On the behavior of the Sierpinski multiband fractal antenna," *IEEE Transaction on Antenna And Propagation*, Vol. 46, No. 4, April 1998.
4. Mustafa Khalid.T, "Combined fractal dipole wire antenna," *IEEE Transaction on Antenna And Propagation*, Vol. 30, No. 6, November 2000.

Design of Internal Dual Band Printed Monopole Antenna Based on Peano-type Fractal Geometry for WLAN USB Dongle

Ali J. Salim and Jawad K. Ali
Department of Electrical and Electronic Engineering, University of Technology, Baghdad, Iraq

Abstract— This paper introduces the design of a new dual-band internal printed monopole antenna structure as a candidate for WLAN (wireless local area network) USB (universal serial bus) dongle applications. The proposed antenna structure is based on the second iteration of Peano- type space-filling geometry. The antenna has been printed on a substrate with relative permittivity of 2.33 and thickness of 0.8 mm, and fed with 50 Ω microstrip line. The resulting antenna has been found to possess a compact size of 15 mm × 5.6 mm, which is suitable for this application. Furthermore, the proposed antenna offers a dual resonant behavior with frequency ratio of about 2.41; resulting in bandwidths, for return loss ≤ −10 dB, covering the two WLAN band standards. Modeling and performance evaluation of the proposed antenna have been carried out using the CST Microwave Studio. Simulation results of return loss, radiation patterns, and gain verify that the presented antenna represents a good solution for dual-band WLAN USB dongle applications.

1. INTRODUCTION

Many USB dongle antennas for WLAN applications have been reported in the literature [1–8]. Beside the limited size constrains, these antennas must fight against other challenges such as the resulting gain, the radiation pattern, the bandwidth, and the ease of fabrication. In [1], a printed meander-line antenna has been proposed for WLAN/USB dongle; however this antenna can only operate at 2.4 GHz. Planar inverted-F antenna PIFA had been presented in [2] as a dual-band antenna for UTMS/WLAN applications. However, this antenna is considered more complex for fabrication, in spite of the compact size achieved. Another microstrip fed folded PIFA antenna has been presented in [3], but it only covers the lower WLAN band. A combined C-shaped strip and a straight strip of a compact printed monopole antenna provide two resonant paths to achieve 2.4, 5.2, and 5.8 GHz multiband operation [4]; the size of this antenna made it improper for USB dongle. A combination of meander line and Cohen-like fractal geometry has been suggested to construct a printed monopole antenna in [5]. This antenna has been found to possess suitable size and dual-band performance covering the required band for WLAN 802.1a/b/g standards; but it lacks from the relatively low gain. Another printed monopole antenna configuration for dual-WLAN USB dongle has been reported in [6]. The antenna consists of two parts; a circular hook-shaped patch resonating at 2.5 GHz ISM band, and a folded monopole stub, inserted in the hook-shaped patch to produce another resonant frequency at the upper frequency band near 5.5 GHz. On the other hand, a miniaturized internal antenna design covering the 2.4 GHz WLAN and UWB (ultra wideband) system bands, for USB dongle applications, has been reported in [7]. The antenna mainly consists of a folded metal plate with two sided beveled; supported by short circuited pin connected to the ground plane, and slots in the bevel sides of the folded metal plate. A coplanar printed loop antenna fed by a coupling-feed mechanism for 2.4-GHz WLAN applications has been proposed in [8]. The antenna has noticeable compact size; making the proposed design suitable for the use within wireless devices in the lower WLAN band environment. Except for the work reported in [5], fractal geometries have not been investigated in the design of dual-band antenna for WLAN USB dongle applications. However, these geometries have been successfully used to construct antenna structures for dual-band WLAN embedded in the laptop computers [9–11].

In this paper, a printed dual-band monopole antenna is proposed for use in the USB WLAN dongle applications covering the IEEE 802.11a/b standards. This antenna is combined of a transmission line structure, based on the 2nd iteration modified Peano fractal geometry, fed with a 50 Ω microstrip line, via a printed line used for allocating the two resonating WLAN bands.

2. THE PROPOSED ANTENNA STRUCTURE

The conventional Peano fractal curve has been widely used in the design of compact and multiband antennas, because of its space-filling and self-similarity properties it possesses [12–14]. Space-filling property leads to produce miniaturized antennas, while self-similarity results in antennas with

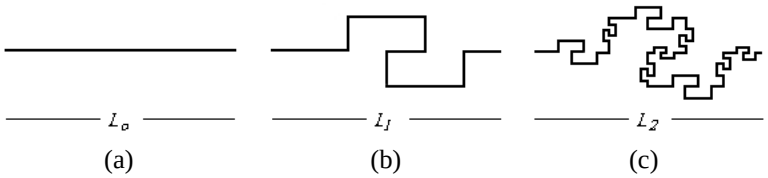

Figure 1: The generation process of the modified Peano pre-fractal curve up to the 2nd iteration.

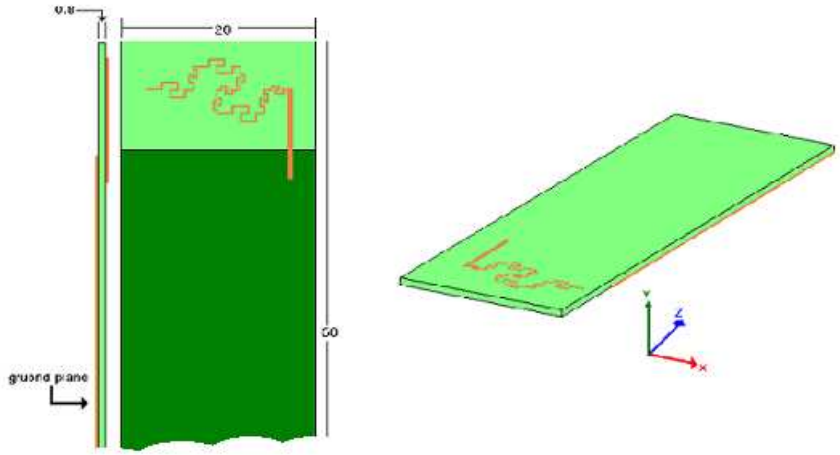

Figure 2: The layout of the proposed dual-band monopole antenna with respect to the coordinate system. All dimensions are in mm.

multi-resonant performance. However, this fractal curve fills the space, in such a way to form a square after infinite number of iterations. Taking into consideration the size constraints imposed on the antenna for USB dongle applications; this fractal geometry does not represent a proper choice.

Instead, a modified version of the conventional Peano fractal curve has been considered for this task. This Peano-type fractal geometry, as depicted in Figure 1, has been suggested to construct miniaturized microwave transmission lines, filters, capacitors, and many other passive components [15]. In this structure, the conventional Peano pre-fractal curve generator has been stretched by a factor of 0.5 in only one dimension, so the resulting fractal structure will no longer be with a square outline.

Figure 1 demonstrates the generation process of the modified Peano pre-fractal curve up to the 2nd iteration. The straight line in Figure 1(a), (the initiator), has been replaced by the nine segment structure in Figure 1(b), the generator. Then, in certain iteration n, each line segment has to be replaced by the whole structure of its preceding iteration, taking into account segment scaling and orientation.

Hence, the 1st iteration consists of 9 segments, and the 2nd iteration has 81 segments, and so on. If the length of the initiator line is L_o, the length enclosed by any pre-fractal structure at the nth iteration n, L_n is:

$$L_n = 2^n L_{n-1}, \quad \text{for } n \geq 1 \tag{1}$$

3. ANTENNA DESIGN

Figure 2 shows the layout of the proposed dual-band monopole antenna with respect of the coordinate system. A monopole antenna, in the form of the 2nd iteration modified pre-fractal geometry, has been printed on one side of a substrate with a relative dielectric constant of 2.33 and a substrate thickness of 0.8 mm. On the reverse side of the substrate, is the ground plane of the system which has the dimensions of $20 \times 50\,\text{mm}^2$.

The fractal part is combined with a small length of a printed transmission line, used for tuning purposes. A 50 Ω-microstrip line is used to feed the combined monopole antenna. It has been found that, the monopole antenna resonates near the standard dual WLAN bands when its length, L, of about 15 mm. In terms of the antenna parameters, the lower resonant frequency, f_L is calculated

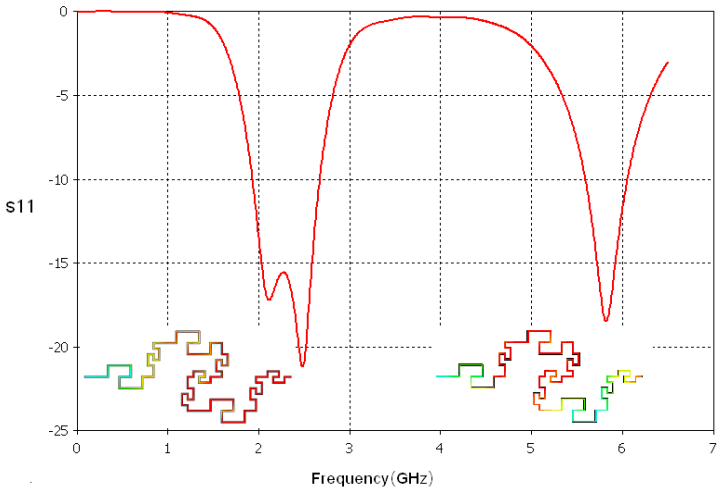

Figure 3: The simulated return loss response of the proposed antenna together with the current distributions at the two resonating bands.

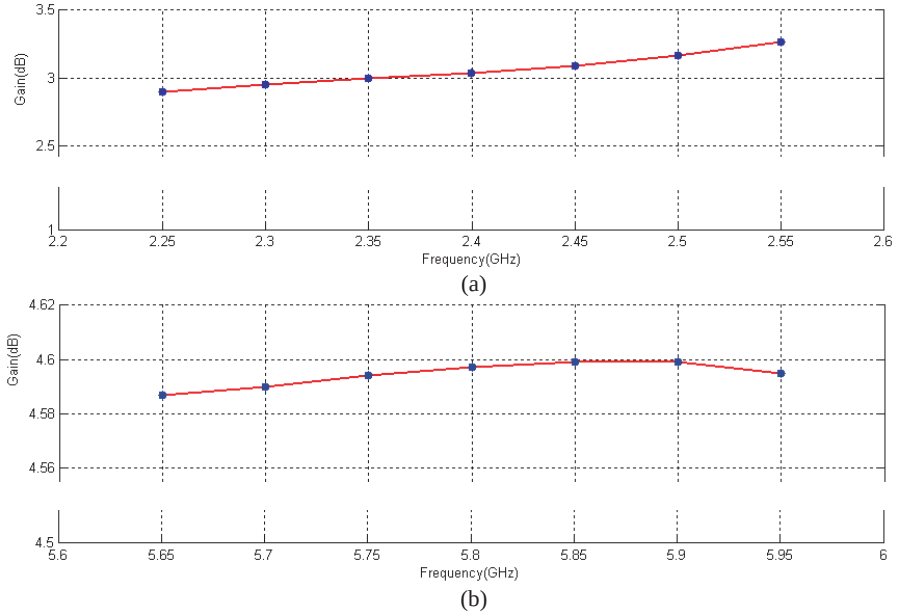

Figure 4: The simulated gain of the proposed antenna at: (a) the lower band, and (b) the upper band.

as

$$f_L = \frac{C_\circ}{6L\sqrt{\varepsilon_{re}}} \tag{2}$$

where C_o is the speed of light in free space, ε_{re} and is the relative effective permittivity of the substrate.

4. PERFORMANCE EVALUATION

The proposed antenna has been modeled, and its performance has been calculated using the CST Microwave Studio (MWS) simulation software. The simulated return loss has been depicted in Figure 3. The simulated return loss, for $S_{11} \leq -10$ dB, bandwidths range from 1.93–2.67 GHz and from 5.59 to 6.1 GHz with corresponding bandwidths of about 0.74 and 0.46 GHz respectively. Figure 3 also shows the simulated current distributions at the IEEE 802.11a and IEEE 802.11b/g bands, where the current distribution implies that the realization of the two bands is attributed by the corresponding antenna parts with reddish color.

The peak gain values in the two bands have been evaluated, as shown in Figure 4. In the lower frequency band, the peak gain plotted in Figure 4(a) is as large as 3.28 dBi, which is higher than

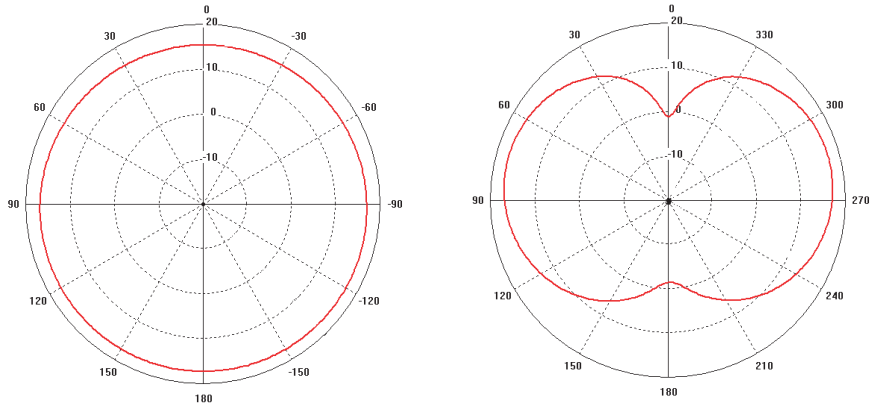

(a) 2.4 GHz

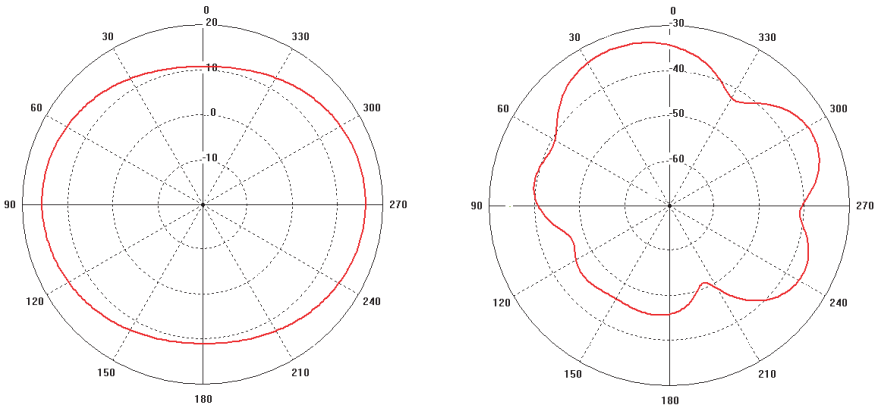

X-Y plane Y-Z plane

(b) 5.2 GHz

Figure 5: The simulated radiation patterns of the proposed antenna at: (a) the lower band, and (b) the upper band in the X-Y and Y-Z planes.

the gain values of reported antennas [5]. The gain versus frequency, for the upper band, is plotted in Figure 4(b), where the maximum gain of copolarization is found to be of about 4.6 dBi which is also higher than that reported in [5].

Curves in Figure 5 show the simulated radiation patterns in the X-Y plane and the Y-Z plane at the two bands. Like the conventional monopole antenna, the modeled antenna has an omnidirectional radiation patterns in the Y-Z plane at the two bands, while it has the two conventional minima in the X-Y plane radiation patterns.

5. CONCLUSION

In this paper, a new compact monopole dual-band antenna has been suggested to be a solution for the internal antenna for dual-band WLAN USB dongle. The proposed fractal shaped antenna has been found to offer acceptable dual-band behavior with nearly omnidirectional patterns at the two WLAN bands. In addition, the compact size of the proposed antenna makes it a good solution for the USB dongle applications. Beside the simple structure, the resulting antenna gain at the two bands is noticeably greater than what is published in the literature for other antennas of the same category. It is hopeful that this antenna finds its place for use in portable dual-band MIMO applications.

REFERENCES

1. Lin, C. C., S. W. Kuo, and H. R. Chang, "Internal PIFAs for UMTS/WLAN/WiMax multi-network operations for a USB dongle," *IEEE Microwave and Wireless Components Letters*, Vol. 15, No. 9, 546–548, 2005.
2. Su, W. C. and K. L. Wong, "Internal PIFAs for UMTS/WLAN/WiMax multi-network operations for a USB dongle," *Microwave and Optical Technology Letters*, Vol. 48, No. 11, 2249–2253, 2006.

3. Wei, J., L. Chen, X. W. Shi, and Y. W. Zhai, "Design and analysis of a folded printed inverted-F antenna for bluetooth applications," *2007 International Symposium on Microwave, Antenna, Propagation and EMC Technologies for Wireless Communications*, Beijing, China, 2009.
4. Song, Y., Y. C. Jiao, H. Zhao, Z. Zhang, Z. B. Weng, and F. S. Zhang, "Compact printed monopole antenna for multiband WLAN applications," *Microwave and Optical Technology Letters*, Vol. 50, No. 2, 365–367, 2008.
5. Luo, Q., J. R. Pereira, and H. M. Salgado "Fractal monopole antenna for WLAN USB dongle," *Proceedings of 2009 Loughborough Antenna and Propagation Conference*, UK, 2009.
6. Jeong, S. J. and K. C. Hwang, "Circular hook-shaped wireless USB dongle antenna with an open stub," *IEICE Electronic Express Journal*, Vol. 7, No. 18, 1370–1375, 2010.
7. Gong, J. G., Y. C. Jiao, Q. Li, J. Wang, and G. Zhao, "A miniaturized internal wideband antenna for wireless USB dongle applications," *Progress In Electromagnetic Research Letters*, Vol. 17, 67–74, 2010.
8. Su, S. W., T. C. Hong, and F. S. Chang, "Very compact coupled fed loop antenna for 2.4 GHz WLAN applications," *Microwave and Optical Technology Letters*, Vol. 52, No. 8, 1883–1887, 2010.
9. Bledowski, M. and M. Kitlinski, "Compact-planar monopole loop antennas for 802.11b/g WLAN systems," *Microwave and Optical Technology Letters*, Vol. 49, No. 9, 2299–2303, 2007.
10. Guterman, J., A. A. Moreira, C. Peixeiro, and Y. Rahmat-Samii, "Electromagnetic human interaction with ISM 2.4 GHz Laptop antennas," *Proceedings of the 2nd European Conference on Antenna and Propagation, EuCAP 2007*, Edinburgh, UK, 2007.
11. Krzysztofik, W. J., "Fractal antenna for WLAN/bluetooth multiple bands applications," *Proceedings of the 3rd European Conference on Antenna and Propagation, EuCAP 2009*, Berlin, Germany, 2009.
12. Zhu, J., A. Hoorfar, and N. Engheta, "Peano antennas," *Digest 2003 USNC/CNC/URSI North American Radio Science Meeting*, Columbus, OH, USA, 2003.
13. McVay, J. and A. Hoorfar, "Miniaturization of top-loaded monopole antennas using Peano-curves," *Proceedings of IEEE Radio and Wireless Symposium*, 2007.
14. Yu, Y. and W. Wu, "Miniaturized peano fractal loaded monopole antenna," *Proceedings of Asia Pacific Microwave Conference, APMC 2009*, Singapore, 2009.
15. Puente, C. B., "Fractal and space-filling transmission lines, resonators, filters and passive network elements," US Patent, No. 7, 538,641 B2, Apr. 2009.

A New Miniaturized E-shaped Printed Monopole Antenna for UWB Applications

Jawad K. Ali and Ahmad S. Hussain
Department of Electrical and Electronic Engineering, University of Technology, Baghdad, Iraq

Abstract— In this paper, a compact UWB printed monopole antenna design is proposed. The monopole antenna has the form of an E-shaped structure printed on a substrate with relative dielectric constant of 3.38, and thickness of 1.52 mm. The matching through the UWB response is satisfied using a reduced ground plane. The proposed antenna is fed by a 50 Ω unsymmetrical microstrip line. The ground plane is printed beneath the microstrip line. Modeling and performance evaluation of the proposed antenna have been carried out using the commercially available electromagnetic simulator, IE3D from Zeland Software Inc. A parametric study is performed to show the effects of the different antenna parameters on the overall antenna performance. The performance of the antenna is mainly affected by geometrical and electrical parameters, such as the width and length of the branches of the E-shape structure, feed gap as well as the ground plane. Simulation results show that the proposed antenna possesses an operating bandwidth, for return loss ≤ -10 dB, extending from approximately 2.93 GHz to about 14 GHz which covers the entire UWB band of 3.1 GHz to 10.6 GHz.

1. INTRODUCTION

The need of exchanging huge quantity of information at high transfer rates, in modern communication systems, tends toward the UWB systems. Multimedia contents as video data or high resolution ranging, are critical in hostile environment, such as underground communication for mines; hence, security issues and economic context leads to high demand of low-cost and reliable UWB systems for underground communication [1, 2]. The application of the E-shaped structure in patch antenna design has been first presented in [3]; in an attempt to overcome the narrow band and the large size of the conventional microstrip patch antennas. Since then, this structure had attracted antenna designers in their efforts to produce antennas with reduced size and broadband performance for different applications. The conventional E-shaped patch antenna has been used to design wideband antennas [4–6].

Various E-shaped patch antennas with tapered, corrugated, and trapezoidal slots have been reported in the literature [8–10]. Many variants of the E-shaped patch structure have been proposed to produce reduced size and wide band antennas [9–12]. Patch antennas with half E-shaped and folded E-shaped structures have been also reported [11, 12, 15–17]. Moreover, the E-shaped structures have been used together with other slot structures to produce antennas with enhanced bandwidths [17–19]. For dual band antenna applications, E-shaped patch structures have been successfully verified as reported in [19, 20].

The E-shaped slot structure has been applied to build a complementary part of an ultrawideband (UWB) antenna to produce the 5 GHz/6 GHz band-notch [21]. In [22], two printed wide-slot antennas constituting of both E-shaped patch and E-shaped slot with rounded corners and fed by CPW and microstrip line have been presented. The resulting antennas have been found to possess fractional bandwidths of about 146%.

In this paper, an E-shaped printed monopole antenna has been presented as a candidate for use ultrawideband applications. The influence of the antenna parameters on the ultrawideband resonating behavior has been investigated.

2. THE ANTENNA DESIGN

The geometry of the proposed E-shaped printed antenna structure is shown in Figure 1. The E-shaped radiating element has been printed on the upper side of a dielectric substrate, while a finite size ground plane is in the lower side, as shown in Figure 1(a). For design convenience, the proposed antenna is fed by a 50 Ω microstrip line printed on the radiator side of the substrate. The E-shaped structure is supposed to be printed on a substrate with relative dielectric constant of 3.38, and thickness of 1.52 mm. Figure 1(b) shows the antenna layout with respect to coordinate system. An initial design has been obtained to meet the ultrawideband bandwidth requirements. The resulting antenna structure has the following parameters; the E-shape length $L_E = 12.9$ mm,

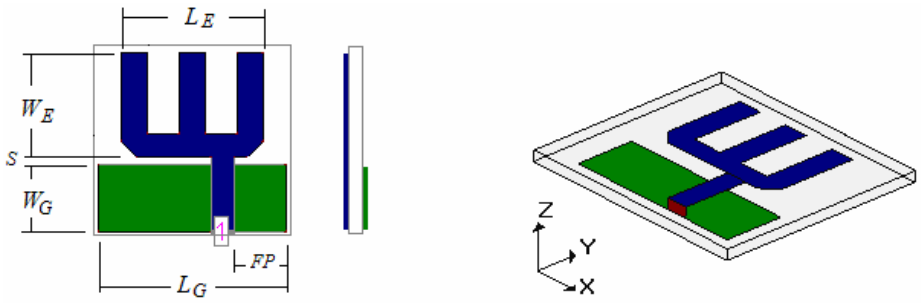

(a) (b)

Figure 1: (a) The proposed E-shaped printed monopole antenna structure, and (b) its layout with respect to the coordinate system.

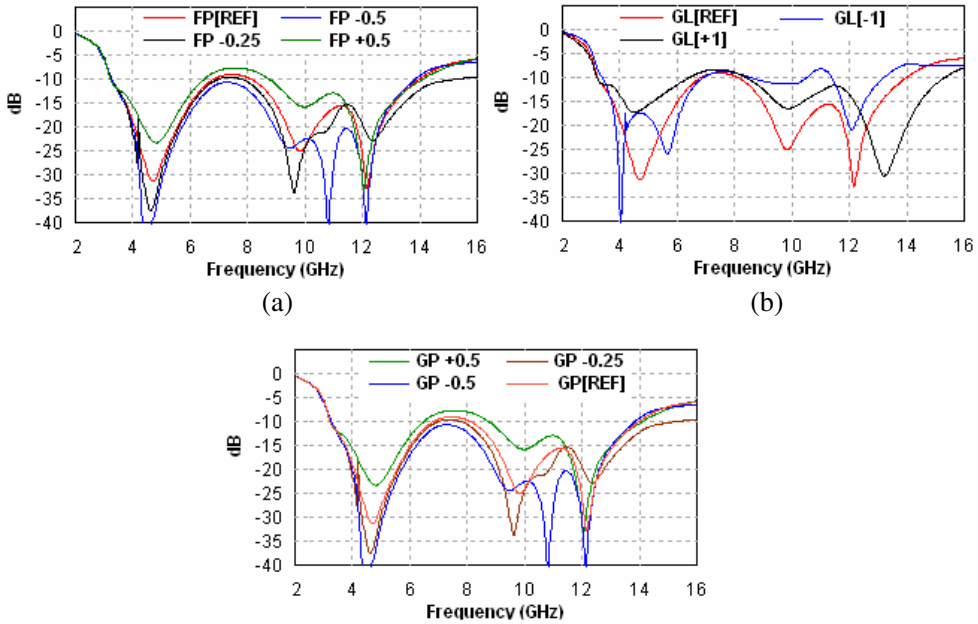

(a) (b)

(c)

Figure 2: The resulting E-shaped printed monopole antenna return loss responses corresponding to the variation of (a) the feed line position, (b) the size of the ground plane, and (c) the space width S.

and its width $W_E = 13.9\,\text{mm}$. The size of the ground plane has been found to be of $L_G = 25\,\text{mm}$ and $W_G = 8.9\,\text{mm}$. The feed line width is of about 3 mm, and its position, FP, is located at about 7 mm from right edge of the ground plane. The space width between the E-shaped structure and the ground plane is of about 1 mm. This antenna, with the depicted parameters, has been used as a reference in the parametric study later conducted.

The E-shaped printed monopole antenna structure, depicted in Figure 1, has been modelled using the commercially available method of moments based EM simulator, IE3D, from Zeland Software Inc. [23].

3. PERFORMANCE EVALUATION

Besides the E-shaped structure external dimensions, the influence of the various antenna parameters on the ultrawideband resonant behaviour have been observed. It has been found that the dominant parameters that have clear impact on the overall antenna performance are the unsymmetrical feed position, FP, the width of the space between the E-shaped radiator and the ground plane, S, and the size of the ground plane. Many antenna structures have been modelled to demonstrate the effects of these parameters on the resulting ultrawideband response. Figure 2 depicts the resulting return loss responses corresponding to variations of the related antenna parameters. The previously

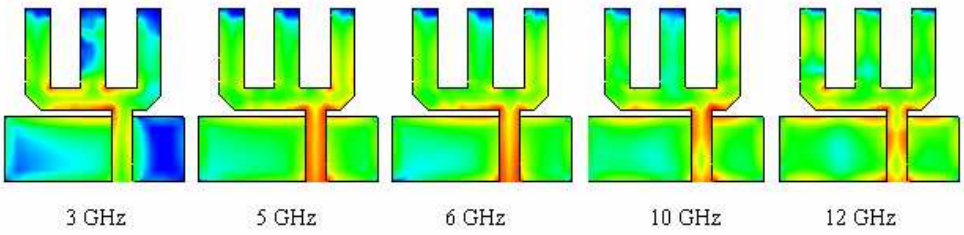

Figure 3: Simulated current distributions on the reference antenna at 3, 5, 6, 10, and 12 GHz.

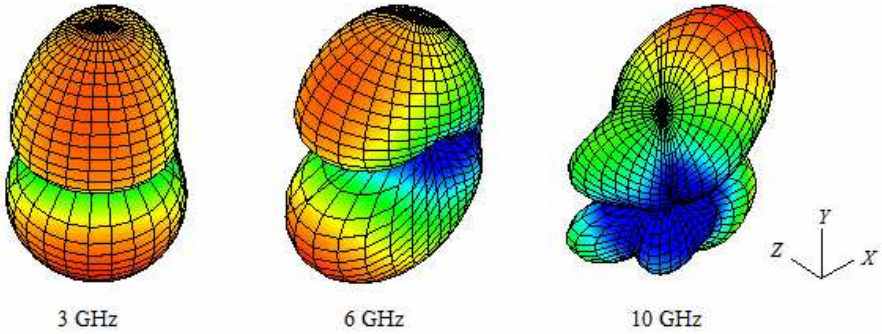

Figure 4: Simulated 3D total field radiation patterns of the reference antenna at 3, 6, and 10 GHz.

depicted antenna dimensions are used as a reference in this parametric study. Figure 2(a) shows the effect of the feed position on the resonant behaviour of the antenna, when all other parameters are kept constant. The change of the feed line location around the reference position makes the proposed antenna tending to have a dual-band response, for lower values of the feed position with respect to the right edge of the ground plane.

Results of the variation of the size of the ground plane, as Figure 2(b) implies, show that the ultrawideband response deteriorates for ground plane lengths other than the reference value. However, dual-band responses are obtained with increased or decreased higher resonating bands. The effect of the space width, S, has been demonstrated in Figure 2(c). For larger values of the space width, the antenna offers a dual-band resonant behavior, and the ultrawideband resonance occurs as the space width is made smaller and approaches that of the reference antenna. In addition, Figure 3 illustrates the electric current distributions on the surface of the reference antenna at frequencies of 3, 5, 6, 10, and 12 GHz. The contributions of the different antenna parameters on the related resonances are quite clear. In mobile applications, 3D radiation patterns are of greater interest than the 2D radiation patterns [24]. Figure 4 shows the simulated 3D radiation patterns for the total fields at 3, 6, and 10 GHz. The corresponding calculated average gains are 0.68, 2.47, and 2.76 dBi respectively. The radiation performance is almost stable across the operating bandwidth.

4. CONCLUSIONS

An E-shaped printed monopole antenna is presented in this paper, as a candidate for use for ultrawideband applications. The antenna has been modeled and its performance has been analyzed using a method of moment based software, IE3D. The proposed antenna has been found to possess a miniaturized size and a bandwidth making it suitable for compact size ultrawideband applications. The influence of the different antenna parameters on the ultrawideband resonant behavior has been demonstrated, providing the antenna designer with more degrees of freedom.

REFERENCES

1. Chehri, A., P. Fortier, and P.-M. Tardif, "Geolocation for UWB networks in underground mines," *Proceedings of IEEE Wirel. and Microw. Tech. Conf., WAMICON'06*, 1–4, December 2007.
2. Habib, M. A., A. Bostani, A. Djaiz, M. Nedil, M. C. E. Yagoub, and T. A. Denidni, "Ultra wideband CPW-FED aperture antenna with WLAN band rejection," *Progress In Electromagnetics Research*, Vol. 106, 17–31, 2010.

3. Shen, Q., B. L. Qoi, and M. X. Leong, "A novel E-shaped broadband microstrip patch antenna," *PIERS Proceedings*, Vol. 2000, Boston, USA, July 2000.
4. Yang, F., X. X. Zhang, and Y. Rahmat-Samii, "Wideband E-shaped patch antenna for wireless communications," *IEEE Trans. Antennas Propag.*, Vol. 49, No. 7, 1094–1100, 2001.
5. Yu, A. and X. X. Zhang, "A method to enhance the bandwidth of microstrip antennas using a modified E-shaped patch," *Proceedings of Radio and Wireless Conference, RAWCON'03*, 2003.
6. Ge, Y., K. P. Essele, and T. S. Bird, "Compact diversity antenna for wireless devices," *Electronic Lett.*, Vol. 41, No. 2, 371–372, 2005.
7. Pramod, K. M., R. Jyoti, S. S. Kumar, and V. Reddy, "Simplified and efficient technique for designing of broadband patch antenna," *Proceedings of Applied Electromag. Conf., AEMC2009*, December 2009.
8. Deshmukh, A. A. and G. Kumar, "Compact broadband E-shaped microstrip antennas," *Electronic Lett.*, Vol. 41, No. 18, 2005.
9. Caratelli, D., R. Cicchetti, G. Bit-Babik, and A. Faraone, "A perturbed E-shaped patch antenna for wideband WLAN applications," *IEEE Trans. Antennas Propag.*, Vol. 54, No. 6, 1871–1874, 2006.
10. Rao, Q. and T. A. Denidni, "Microstrip patch antennas with trapezoidal slots," *Proceedings of IEEE AP-S Int. Sym. on Antennas and Propag., and USNC/URSI National Radio Science Meeting*, New Mexico, USA, July 2006.
11. Chiu, C. Y. and C. H. Chan, "A wideband antenna with a folded patch feed," *Proceedings of IEEE Int. Workshop on Antenna Technology; Small Antenna and Novel Metamaterials, IWAT 2005*, March 2005.
12. Chiu, C. Y., H. Wong, and C. H. Chan, "Study of small wideband folded-patch-feed antennas," *IET Microw. Antennas Propag.*, Vol. 1, No. 2, 501–505, 2007.
13. Matin, M. A., B. S. Sharif, and C. C. Tsimenidis, "Probe fed stacked patch antenna for wideband applications," *IEEE Trans. Antennas Propag.*, Vol. 55, No. 8, 2385–2388, 2007.
14. Peng, L., C. Ruan, and Y. Zhang, "A novel compact broadband microstrip antenna," *Proceedings of 2007 Asia-Pacific Microwave Conference, APMC'07*, Bangkok, December 2007.
15. Chair, R., C. Mak, K. Lee, K. Luk, and A. A. Kishk, "Miniature wide-band half u-slot and half E-shaped patch antennas," *IEEE Trans. Antennas Propag.*, Vol. 53, No. 8, 2645–2652, 2005.
16. Sun, F., X. Ren, and H. He, "A compact half E-shaped patch antenna with a slotted U-shaped ground plane," *Proceedings of IEEE Global Symp. on Millimeter Waves, GSMM 2008*, Nanjing, China, April 2008.
17. Xiong, J., Z. Ying, and S. He, "A broadband E-shaped patch antenna of compact size and low profile," *Proceedings of IEEE Antenna and Propagation Society Int. Symp., AP-S 2008*, 2008.
18. Kong, L., J. Pei, and X. Guo, "A new dual-frequency broadband L-slot mixed E-shaped patch antenna," *Proceedings of IEEE Global Symp. on Millimeter Waves, GSMM 2008*, Nanjing, China, April 2008.
19. Guterman, J., Y. Rahmat-Samii, A. A. Moreira, and C. Peixeiro, "Quasi-omnidirectional dual-band back to- back E-shaped patch antenna for laptop applications," *Electronic Lett.*, Vol. 42, No. 15, 2006.
20. Singh, A., "Dual band E-shaped patch antenna (ESPA) for ultra wide band applications," *Proceedings of 2009 Asia Pacific Microwave Conference, APMC2009*, Singapore, December 2009.
21. Panda, J. R. and R. S. Kshetrimayum, "A compact CPW-FED monopole antenna with E-shaped slot for 5 GHz/6 GHz band-notched ultrawideband applications," *Proceedings of the Annual IEEE India Conf., INDICON 2009*, India, December 2009.
22. Dastranj, A. and H. Abiri, "Bandwidth enhancement of printed E-shaped slot antennas fed by CPW and microstrip line," *IEEE Trans. Antennas Propag.*, Vol. 58, No. 4, 1402–1407, 2010.
23. *IE3D User's Manual, Release 12.3*, Zeland Software, Inc., Fremont, CA, 2007.
24. Chen, Z. N., *Antennas for Portable Devices*, John Wiley & Sons Ltd., Chichester, England, 2007.

Miniaturized Surface Wave Dipole Antenna for Millimeter Wave Application

Zachariah C. Alex and G. Shrikanth Reddy
School of Electronics Engineering, Vellore Institute of Technology University
Vellore, Tamil Nadu 632014, India

Abstract— In the proposed paper a surface wave antenna is designed for millimeter wave application. We used a simple dipole structure whose length is optimized for millimeter wave (60 to 80 GHz) band. We introduced periodic patches with partial ground, which is responsible for guiding the surface wave along the partial ground and giving a directional radiation pattern as in case of monopole with reduction in magnitude of back lobe radiation. The proposed structure achieved a band width of ~ 20 GHz (-10 dB), i.e., 60.5 to 80 GHz. The maximum gain is around 8.32 dBi at 64 GHz and the average gain is of 7.5 dBi. The analyses of other antenna parameters like Co and cross polarization, gain, Radiation efficiency etc are also done.

1. INTRODUCTION

The concept of surface wave antenna was suggested in 1950 [1–3], and then many novel structure were reported. In surface wave antennas, surface waves are guided along the thin ground loaded with periodic patches resulting in non uniform input phase and low profile conformal geometry. Due to periodic patches the wave reflected back from the ground plane will be in phase to the radiated wave and results in constructive interference. Unlike conventional EBG structures, which involve via hole in the periodic patch and resulting in t band gap for certain frequencies, surface wave antennas do not contains via holes. In surface wave antennas in phase response is achieved through periodic patches but there won't be any band gap for any frequency or a band of frequencies. Through surface wave antennas the properties of basic antenna could be altered to achieve needed characteristics.

Through surface wave antennas, only narrow band width could be achieved, so for a wide band response a partial ground is added in place of conventional PEC. In the proposed structure the ground and the periodic patches are on same plane not like the conventional surface wave antenna. This structure Provides bandwidth of ~ 20 GHz with the maximum gain of 8.23 dB is at 64 GHz and with an average gain of 7.5 dB for the complete bandwidth.

The frequency at millimeter wave band, i.e., 60 to 80 GHz has a wide area of applications which includes high speed data communication, satellite to satellite link communication, astronomy and automotive radars systems etc. Band of 60 GHz i.e., 60 to 65 GHz is a good candidate for high speed data communication (up to Gbps range) [6] where as band of 70 to 80 GHz is utilize for automotive radar systems and astronomy. Even with such advantages millimeter wave faces a drawback, especially band of 60 GHz. At 60 GHz the attenuation rate of the frequency is very high, since resonant frequency of the oxygen is 60 GHz so this frequency has to face high free space absorption [6]. For this reason the applications of this frequency band are restricted to small distance only. But with proper design and frequency reuse criteria this deficiency could be overcome.

2. PROPOSED STRUCTURE

In the proposed structure the dimensional values are as follows: $a = 0.36\lambda$, $b = 0.7\lambda$, $c = 0.1\lambda$, $d = 1.2\lambda$, $e = 1.2\lambda$, $f = 0.22\lambda$, $g = 0.02\lambda$, $u = v = 1.2\lambda$, $y = .6\lambda$. Here w represents the feed width of the 50 Ω transmission line which is design according to the design equations given in [8]. Whereas the periodic patches in the ground were paced such that their center to center distance is less than the wave length. In the proposed structure we used FR4 substrate having dielectric permittivity of 4.4. The analysis of the antenna is done using the CST Microwave Studio simulator. The proposed structure was firstly designed as a complete dipole then the length a, is optimized for better result, using the optimizer provided in CST soft ware.

3. RESULT ANALYSIS

In this section the antenna parameters like return loss, radiation pattern, antenna gain and radiation efficiency were analyzed through simulation. During simulation the highest order of mesh limits

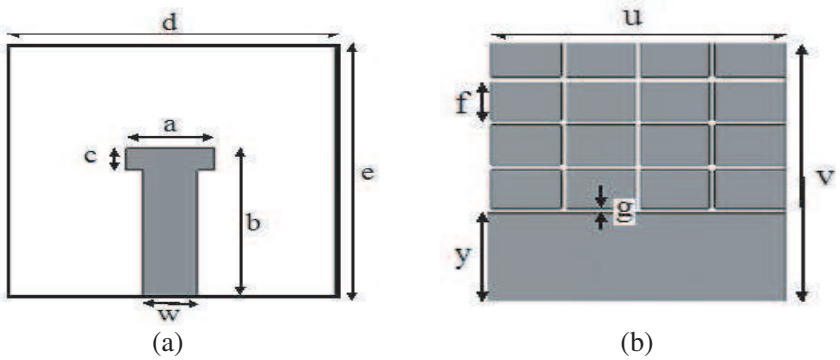

(a) (b)

Figure 1: (a) Proposed dipole structure with Microstrip feed. (b) Partial ground plane with periodic patches.

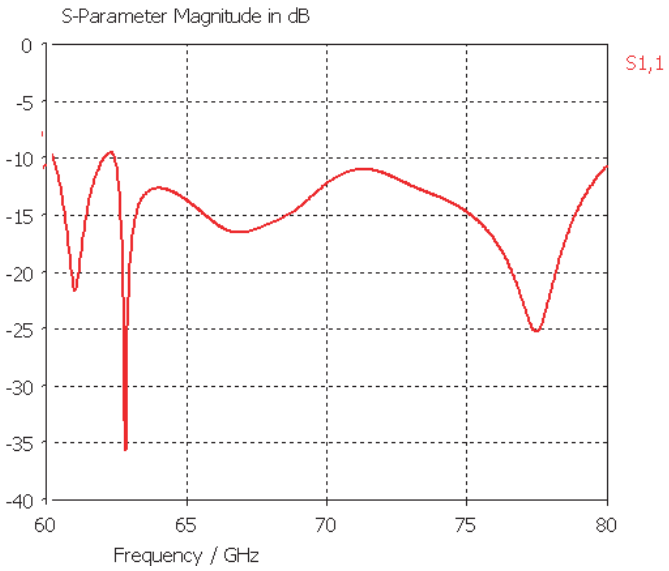

Figure 2: Return loss characteristic for the proposed structure.

were chosen so that high simulation accuracy could be maintained.

3.1. Return Loss Characteristic

From above graph it can be concluded that the proposed structure gives a wide band response. Though there is a small notch in the S_{11} response at the frequency 63.5 GHz and the value for return loss for this frequency in terms of dB is −9.89 dB. This notch was also reduced when the mesh cells for simulations were increased.

3.2. Radiation Pattern for Both *E* and *H* Plane

Figure 3 shows the radiation pattern characteristic for the proposed structure. Here the chosen frequency is 64 GHz. From above figure it is clear that the cross polarization level in both E and H plane are less than the co polarization level. Here, the obtained main lobes 3 dB beam width is around 80.3° and the direction for main lobe radiation pattern is around 64°.

The Gain and Radiation efficiency characteristic for complete band is given as in Fig. 4.

Since the gain required for the short distance data transmission at 60 GHz band especially for WPAN, WLAN application should be high and Figure 4 shows that the average gain given by the proposed structure is around 7.5 dB and highest of 8.25 dB at 64 GHz, thus it can be concluded that the proposed structure could be very well used for above mentioned applications. The total radiation efficiency for this structure is also in good terms with the required efficiency, needed for practical application.

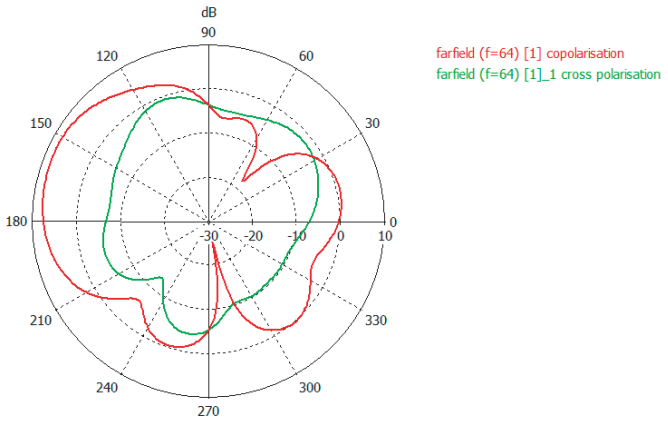

(a)

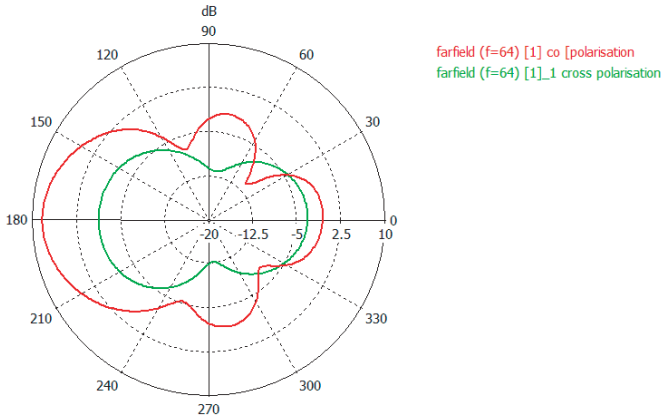

(b)

Figure 3: (a) Co-cross polarization characteristic for E Plane, (b) Co-cross polarization characteristic for H Plane.

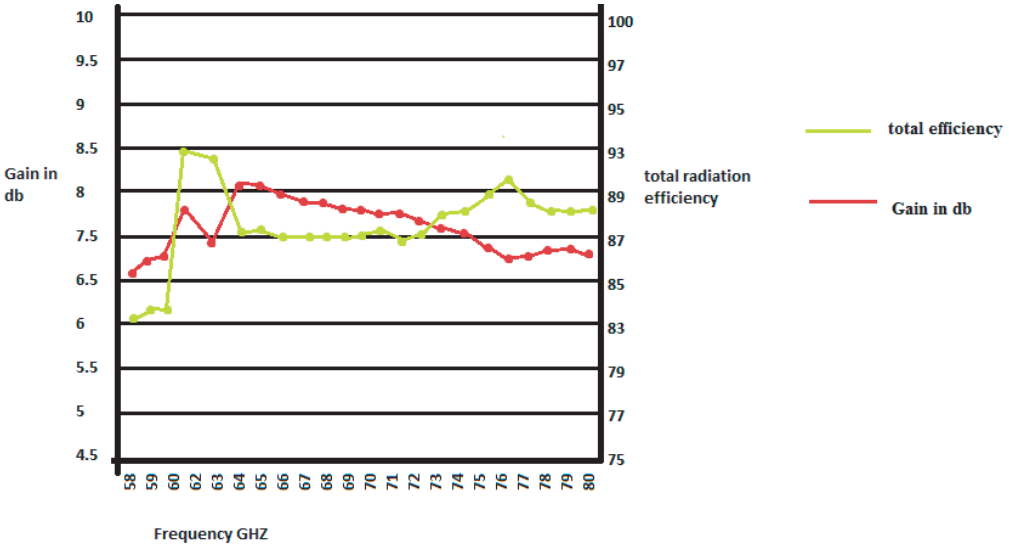

Figure 4: Gain and efficiency graph for proposed structure.

4. CONCLUSIONS AND FUTURE WORK

The proposed structure is showing a wide band width for complete 60 GHz and 70 GHz band, with an average gain and radiation efficiency of around 7.5 dB and 85% respectively. The proposed structure can also be used for band of 70–80 GHz which has a less attenuation level. Though the size of the antenna is reduced (i.e., from basic length of a dipole) it didn't affected the antenna

performance. Since the structure is drawn for higher frequency, similar concept can be used for designing the antenna at frequency of L-band with miniaturization technique.

ACKNOWLEDGMENT

The authors are thankful to Dr. G. Viswanathan, Chancellor VIT University, and the management of VIT University for their support and encouragement.

REFERENCES

1. Zucker, F. J., "Surface wave antenna," *Antenna Hand Book*, McGraw-Hill, Inc., 1993.
2. Schwering, F. and A. A. Oliner, *Millimeter Wave Antenna*, Edited by Y. T. Lo and S. W. Lee, New York, 1988.
3. R. Elliot, "Spherical surface wave antenna," *IRE Trans. Antenna Prop.*, Vol. 4, No. 3, 422–428, 1956.
4. Zoubi, A. A., F. Yang, and A. Kishik, "A low profile surface wave antenna for wireless comm.," *IET Proceeding Microwave Antenna & Prop.*, Vol. 1, No. 1, 261–266, Feb. 2007.
5. Yang, F., Y. R. Samii, and A. Kishik, "A low profile dual band surface wave antenna with a monopole like pattern," *IEEE Trans. & Antenna Prop.*, Vol. 55, No. 12, 3404–3412, Dec. 2007.
6. Chen, X. P., K. Wu, L. Hu, and F. He, "Low cost high gain planar antenna for 60 GHz band application," *IEEE Transaction on Antenna & Wire. Prop.*, Vol. 58, No. 6, 2126–2129, Jun. 2010.
7. Yang, F. and Y. R. Sami, "Application of electromagnetic band gap structures in microwave antenna design," *3rd International Conference, Microwave and Millimeter Wave Technology*, Dec. 2009.
8. Pozar, D. M., *Microstrip Transmission Line & Antenna Design*, 1995.
9. Balanis, C. A., *Antenna Theory & Analysis*, 3rd Edition, Wiley's Publication, 2005.

Extended Dipole Antenna with AMC Spiral Ground and Via Holes for Millimeter Wave Application

G. Shrikanth Reddy and Zachariah C. Alex
School of Electronic Engineering, Vellore Institute of Technology University
Vellore, Tamil Nadu 632014, India

Abstract— In the proposed paper Umbrella shaped Dipole antenna is chosen and its radius is optimized for Millimeter wave band, i.e., 60 GHz. The Extended dipole is given Microstrip feed and it is backed by Artificial Magnetic Conductor (AMC) ground added with closed cap via holes. In the proposed work the dimensions of Spiral ground and vias are optimized and their combine effects were used to suppress surface wave effect, which were responsible for decrement in the antenna performance in terms of antenna gain and efficiency. The proposed structure is drawn on RT Duriod having permittivity of 2.2 with substrate thickness of 0.45 mm. the results are based on simulation, done using IE3D simulator of Zeland Corporation.

1. INTRODUCTION

Monopole antenna being low profile, finds many application in different area. Their compatibility rate with MIC structures is very high, and their fabrication is also very easy, compared to other antenna structure. In this paper Millimeter wave is referred to unlicensed frequency band of 55 to 60 GHz. This band now a day's is seen as good candidate for high speed short distance data communication. The high free space attenuation rate for this band limits its application to short distance range only, and that makes it possible for using excellent frequency reuse criteria [1].

But when designing the antenna at such a high frequency it is seen that if the substrate thickness is less than quarter wavelength then, the radiated wave which impinges substrate and passes to ground layer will undergo two effects. Firstly some of the wave will get reflected back from ground layer with 180 degree phase shift (in order to maintain node and antinodes criteria of E and H field) and causes a destructive interference with the main radiation pattern. Secondly some wave will travel through the ground surface and get diffracted at the discontinuity, since ground used is finite in nature. This diffracted wave will again interfere with main radiating wave. Thus from both the effects the performance of the antenna in terms of Return loss, Gain and Efficiency will reduce.

For this reason, Antenna with Spiral AMC ground is proposed and further the performance of the proposed antenna is increased by introducing the vias to the structure [3–5], in following sections it will be explained that how surface wave effects are reduced and their by antenna performance is enhanced.

1.1. Semicircular Monopole Patch Antenna

The proposed antenna has a semicircular shape, and is designed on the RT Duriod substrate having relative permittivity of 2.2 with thickness of 0.45 mm. The semicircular patch is chosen because of the fact that, for increasing the band width of the simple monopole wire antenna, it has to be replaced with plate elements such as, elliptical, triangular, rectangular, circular or in this case a semicircular [3]. The semicircular shape of the proposed antenna is optimized, for getting the band width near 60 GHz frequency. The optimization is with respect to the cavity model of patch antenna and IE3D simulator optimizer, in which the semicircle part of the antenna is chosen and for needed frequency the limits of the dimension is given. For best optimized results the structure is finalized. After finalizing the design of the antenna the position of the vias was analyzed. Point of placing the vias at the lower end of semicircle and upper end of the Microstrip transmission line is to provide a path to surface wave and to seizes it in vias their by providing a high impedance surface and thus decreasing the effects of surface wave [5]. In following section it can be seen that through this process the radiation efficiency for the structure is also increased and is sufficient for Millimeter wave band. In Fig. 1 the semicircular monopole patch is shown, here $W = 0.26\lambda$, $L = 0.73\lambda$, and $r = 0.4\lambda$, here λ is free space wave length. The feed used is 50 Microstrip feed.

1.2. Spiral AMC Ground and Conventional PEC Ground

Artificial magnetic conductor (AMC) spiral geometry is often used, to reduce the antenna size and minimize the surface wave effect. There are several AMC structures like Hilbert Curve, Jerusalem

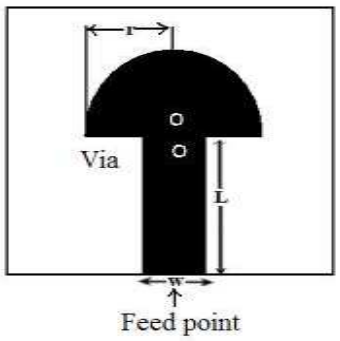

Figure 1: Semicircular monopole antenna with microstrip feed.

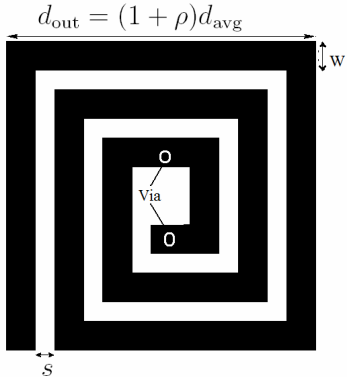

Figure 2: AMC ground with via holes.

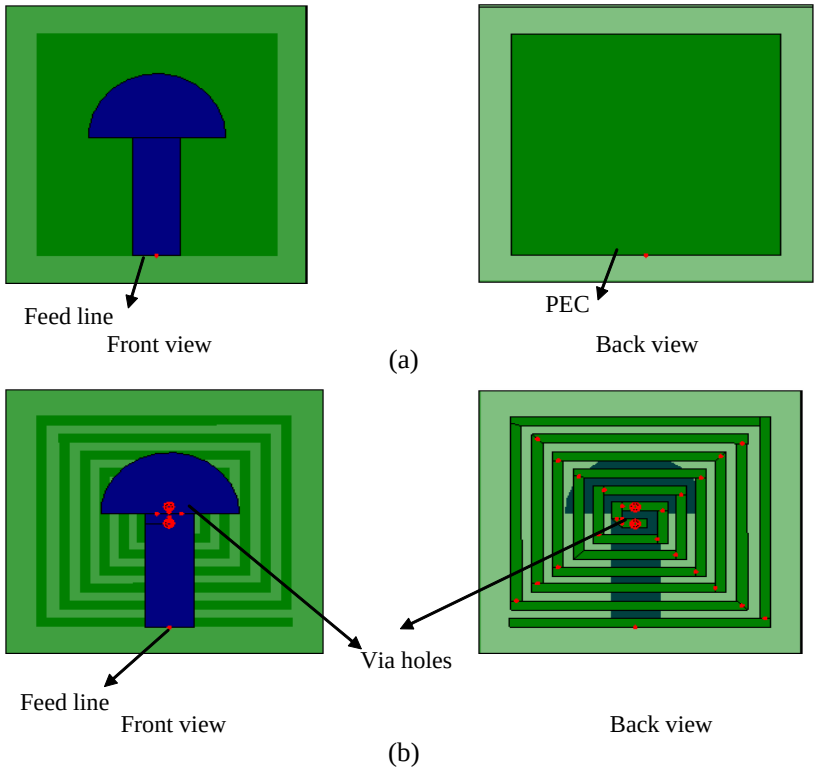

Figure 3: (a) Antenna on conventional PEC ground. (b) Antenna on AMC ground with via holes.

Cross, etc.. Hilbert curves are utilized for getting a variable resonance with respect to number of turns in spiral AMC. The dimensional analysis for the spiral is based on the equations [5],

$$d_{in} = d_{out} - 2n(w+s) + s \tag{1}$$

$$d_{avg} = \frac{d_{out} + d_{in}}{2} \tag{2}$$

$$l = 4n \times d_{avg} \tag{3}$$

Here d_{in} = inner diameter of the spiral structure, d_{avg} = average dia, d_{out} = distance (edge to edge of the spiral), n = no. of turns, W = width of the spiral, S = gap between the consecutive strips. Considering Fig. 2 the strip width of AMC ground, i.e., $W = 0.04\lambda$, $S = 0.06\lambda$ and total length and width of the Spiral square is 5.5–5.5 mm. the radius of both the vias are 0.5 mm. The structure was again optimized to get 60 GHz band as resonating frequency. In Fig. 3 semicircular monopole patch antenna is designed with various grounds. The conventional PEC ground is of 7×7 mm. In the proposed paper the monopole antenna is designed on conventional PEC ground, AMC with via hole. During simulation the structure without Via is also checked and its results

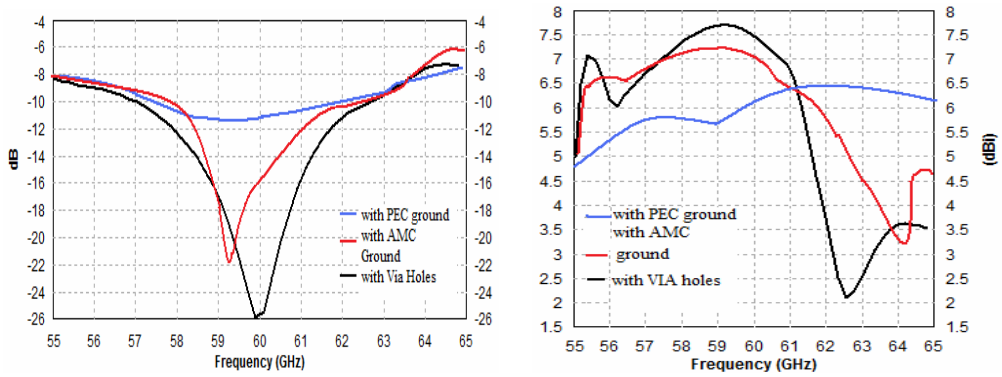

Figure 4: Return loss and gain characteristics of proposed structures.

were compared with proposed designs. Via holes in the proposed structure is closed cap and its radius is 0.5 mm. the whole ground is on finite dielectric substrate. The following figure shows the patch with different ground patterns, as stated above the feed point will remain same for all the structures.

2. RESULT ANALYSIS

2.1. Return Loss and Gain Characteristic

From Fig. 4 it is clear that the return loss in the case of AMC ground with via holes is less in comparison to AMC and PEC grounds. The bandwidth for the antenna in case of antenna with via holes is recorded as 6 GHz, i.e., from 57 GHZ to 63 GHz, where as in case of simple AMC the band width obtained is of 4 GHz. Thus from above figure it can be concluded that the antenna with via holes provide wider bandwidth. The gain across 60 GHz for the case of monopole antenna with AMC ground with via holes is around 7.7 dbi, whereas for simple AMC and PEC grounds the gain recorded is 7.3 dbi and 5.56 dbi respectively. For the short range Millimeter wave application the gain around 5 to 6 dbi is sufficient, only when a frequency reuse criterion is applied.

3. CONCLUSIONS

In this paper a novel design of semicircular monopole antenna with Microstrip feed is proposed, and it is integrated with AMC ground with via holes. All the antenna parameters are compared with respect to different structures. And it is found that, the performance of antenna with via holes gives good results as far as millimeter wave applications are concern. The achieved bandwidth is of 7 GHz with gain of 7.7 dbi at 59.6 GHz, with consistent radiation efficiency of 98% for whole bandwidth. Since the obtained gain is sufficient for short distance millimeter wave application, for long distance more gain is needed, and for this reason analysis for more sophisticated designs are going on. For this purpose investigation on surface wave antenna will be done in future.

ACKNOWLEDGMENT

The authors are thankful to Dr. G. Viswanathan, Chancellor VIT University and the management of VIT University for their support and encouragement.

REFERENCES

1. Daniels, R. C. and R. W. Health, "60 GHZ wireless communication emerging requirements & design recommendations," *Proceedings of Texas Conference*, Austin, 2008.
2. Alwis De, G. and M. Delahoy, "60 GHz band millimeter wave technology," *Document, Spectrum Planning and Engineering*, December 2004.
3. Elsheakh, D. N., H. Elsadek, E. A. AbdAllah, and M. F. Iskender, "Ulterawide band umberalla shaped monopole antenna using spiral artificial magnetic conductor," *IEEE Antenna & Wire. Prop. Letter*, Vol. 8, 1255–1258, 2009.
4. Yang, F. and Y. R. Sami, " Application of electromagnetic band gap structures in microwave antenna design," *3rd International Conference, Microwave and Millimeter Wave Technology*, December 2009.
5. Mohan, S. S., "Modelling and characterisation of on chip spiral inductors," *Center for Integrated Systems*, Stanford University, 1999.

6. Chen, X. P., K. Wu, L. Hu, and F. He, "Low cost high gain plannar antenna for 60 GHz band application," *IEEE Transaction on Antenna & Wire. Prop.*, Vol. 58, No. 6, 2126–2129, June 2010.
7. Li, L. W., W. Xu, and H. Y. Yao, "Design of left handed metamaterial using single resonant & double resonant structure," *International Journal of Microwave and Optics*, Vol. 1, No. 1, 10–14, June 2006.
8. Elsheakh, N., H. A. Elsadex, and E. A. Abdallah, " Enhancement of UWB antenna using metamaterial structure," *IEEE Trans. Antenna & Prop. Letter*, Vol. 8, 623–630, December 2009.
9. Sambhavi, K., Z. C. Alex, and T. P. Krishnan, "Patch array for 60 GHz application," *JATIT*, 2005.
10. Yang, F. and Y. Rahamat, *EBG Structure & Its Applications*, Cambridge University Press, 2008.
11. Pozar, D. M. and D. H. Schaubert, *Microstrip Antenna Design*, IEEE Press, 1995.
12. Balanis, C. A., *Antenna Theory Analysis and Design*, 3rd Edition, Wileys Publications, 2005.

Gain and Bandwidth Enhancement of a Microstrip Antenna Using Partial Substrate Removal in Multiple-layer Dielectric Substrate

Neeraj Rao and Dinesh Kumar V.
PDPM Indian Institute of Information Technology, Design & Manufacturing Jabalpur, India

Abstract— In this paper, a novel antenna design for simultaneous improvement of patch antenna gain and bandwidth has been proposed using partial substrate removal in a multiple-layer dielectric by suppression of surface wave losses beneath the substrate surface by embedding a low-dielectric (air) void. In this way, improvement in gain is achieved by fractional removal of substrate. Bandwidth of the patch antenna is increased by using multiple layer dielectric substrates. It is known that bandwidth of microstrip antenna is small and varies directly with the size of the patch, Increasing size of patch to improve bandwidth makes it large and bulky. Thus to overcome the bandwidth limitation without increasing size unacceptably, a patch on multiple-layer scheme has been designed to reduce the effective dielectric constant. This ensures that bandwidth increases greatly while size is nearly unaffected. Performance parameters like bandwidth and reflection loss have been evaluated and compared with that obtained from single layer dielectric substrates. Results suggest considerable improvement in bandwidth using the proposed patch antenna design on multi-layered dielectric substrate. The designed patch has a size of $12 \times 8\,\mathrm{mm}^2$ and gives a bandwidth and gain of 314 MHz and gain 4.035 dB at 6.479 GHz.

1. INTRODUCTION

A microstrip patch antenna is widely used in compact and portable communication devices due to its small size, thin profile configurations, conformity and low cost. In spite of these remarkable advantages, the patch suffers some serious drawbacks like low bandwidth (due to small size). Bandwidth can be increased but at the cost of size of the patch, making it large and bulky. To overcome this problem, a multiple-layer dielectric substrate has been used to improve bandwidth, in this paper [1]. There are different types of losses in antenna, one of which is surface wave loss due to of the permittivity of the material and thickness of the substrate [2–5]. Due to excitation of surface waves, patch antenna also suffers from reduced gain and efficiency as well as unacceptably high levels of cross-polarization and mutual coupling within an array environment at high frequencies. In this paper, parts of the substrate surrounding the patch have been strategically removed to suppress surface wave losses, and thereby increase gain [6–10]. It is known that for a particular resonant frequency, the bandwidth increases with increase in size of patch antenna for a high dielectric [11]. The patch antenna of low dielectric has a moderate bandwidth but large size [12]. Bandwidth decreases with increase in the dielectric value of the substrate. The two substrates have been combined so as to include the quality of both high and low dielectric, i.e., high bandwidth and low patch size respectively [1]. A microstrip patch antenna implemented on silicon ($\varepsilon_r = 11.9$) has moderate bandwidth with a small sized patch and that implemented on glass ($\varepsilon_r = 4.6$) has a high bandwidth. In this paper, a multiple-layer substrate is made by sandwiching one layer of glass ($\varepsilon_r = 4.6$) in between two layers of silicon ($\varepsilon_r = 11.9$) so as to reduce the antenna size as much as possible. Here, silicon ($\varepsilon_r = 11.9$) has been used directly below the patch so as to maximize the size reduction. As a result, the size is increased slightly, but the bandwidth is increased greatly. The method to improve the gain is to reduce the loss of the microstrip antenna. The gain of the antenna can be increased by reducing the loss due to surface wave propagation [13–17]. One method to do so is by replacing the substrate of patch with low dielectric values or with air ($\varepsilon_r = 1$). Periodic structures of electromagnetic band-gap (EBG) can be used to block the surface waves from propagating in a certain band of frequency. A common method to generate EBG structures is to drill holes in substrate to synthesize a lower dielectric constant substrate [18]. However, in this paper, a rather simpler version of EBG structure approach has been used by partially removing the substrate surrounding the patch instead of drilling periodic holes. Removing the substrate partially stops the propagation of surface wave in the substrate, which reduces the power coupled in backward direction and enhances the forward coupled power [6]. As a result the gain increases.

2. SIGNIFICANCE OF A MULTIPLE-LAYER SUBSTRATE

The wavelength of an EM wave at 5 GHz is about 6 cm in air [1]. The size of the antenna at 5 GHz is typically in the order of centimeters, which take a lot of area in wireless devices. To address

the issue of narrow bandwidth, many methods can be found in literature, typical methods being E-patch and U slot, aperture coupling [19]. These approaches enable broadband characteristics using air or low dielectric constant substrates, but at the cost of large volume and need of a large ground plane. For small-size compact antenna, the requirement is not only the smaller size but also a smaller ground plane. A compact rectangular patch microstrip antenna with small volume has been proposed in [20]. It has broadband characteristics due to multiple layer substrates. The dielectric constant of the substrate is closely related to the size and the bandwidth of the microstrip antenna. A trade-off relationship exists between antenna size and bandwidth [21]. But if we use multiple-layer substrates of different materials, the effect of trade-off relationship can be reduced. The use of high and low dielectric constant materials for multiple layer substrates puts effective dielectric constant to a value at the centre of both high and low dielectric constant materials [20]. HRS (High Resistivity Silicon) was chosen as a substrate. An antenna fabricated on HRS substrate had small patch size but it also had narrow bandwidth. However, a glass substrate in the middle of silicon substrates lowered the effective dielectric constant. By using a Si/Glass/Si multi layer substrate, the bandwidth is increased greatly while the size is increased slightly. In this paper we have designed the antenna which has a broad bandwidth and a higher gain [22].

3. PROPOSED ANTENNA DESIGN

It is known that for a particular resonant frequency, the bandwidth increases with increase in size of patch antenna for a high dielectric [6]. The patch antenna of low dielectric has a moderate bandwidth but large size. Bandwidth decreases with increase in the dielectric value of the substrate [6]. The two substrates have been combined so as to include the quality of both high and low dielectric, i.e., high bandwidth and low patch size respectively. Figure 1 shows the proposed antenna design for a circular patch antenna on multiple-layer dielectric. A microstrip patch antenna implemented on silicon ($\varepsilon_r = 11.9$) has moderate bandwidth with a small sized patch and that implemented on glass ($\varepsilon_r = 4.6$) has a high bandwidth. In this paper, a multiple-layer substrate is made by sandwiching one layer of glass ($\varepsilon_r = 4.6$) in between two layers of silicon ($\varepsilon_r = 11.9$) so as to reduce the antenna size as much as possible. Here, silicon ($\varepsilon_r = 11.9$) has been strategically used directly below the patch so as to maximize the size reduction. As a result, the size is increased slightly, but the bandwidth is increased greatly. The proposed fractional substrate removal design consists of replacing certain fractions of the patch substrate by air in certain configurations. It has been tested for fractional substrate removal in various configurations like-along radiating and non-radiating edges, making trenches of different widths all-around the patch, below the patch and on all its sides. Figure 1 shows the design using removal of a fraction of substrate from the substrate surrounding the patch. The performance metrics — gain (dB), half power Beam Width (E plane) and half power Beam Width (H plane) in degrees has been computed and analyzed for the proposed structure.

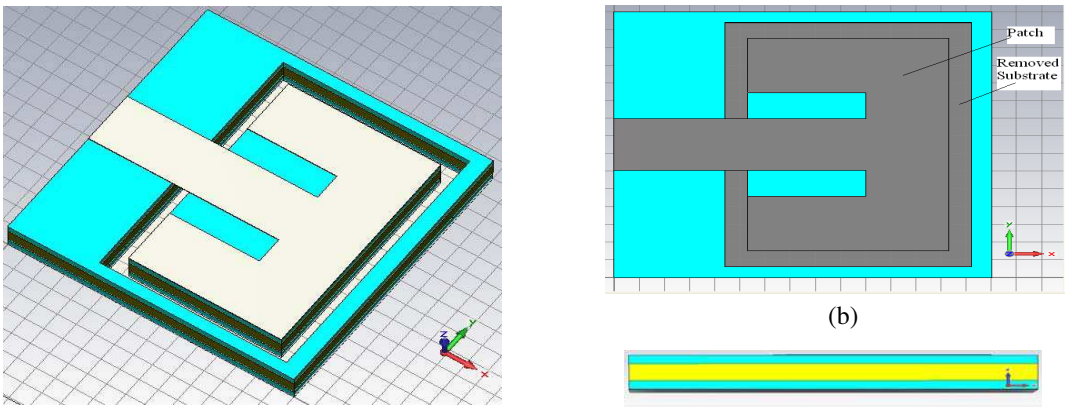

Figure 1: Proposed antenna design — Patch on multiple-layer dielectric. (a) Isometric view. (b) Top view. (c) Side view.

4. SIMULATION RESULTS

The advantages of the proposed multi-layer substrate for a rectangular patch were verified using the Computer Simulation Technology Studio Suite^{TM} 2011 simulation tool. Simulation results and performance parameter bandwidth has been calculated using the proposed multilayer dielectric and were compared with that obtained from single-layer silicon and single-layer glass substrate. Table 1 shows the dimensions and the simulation results of the tested microstrip antenna designs.

The parametric description of the multiple-layer substrate is as follows:

- Glass substrate ($\varepsilon_r = 4.6$) of 1 mm is sandwiched between two silicon layers ($\varepsilon_r = 11.9$) of thickness 0.5 mm each.
- The rectangular patch has size $12 \times 8\,\text{mm}^2$ and has been fed using microstrip feed.
- All of the designed microstrip antenna have $15 \times 15\,\text{mm}^2$ ground plane.

5. OBSERVATIONS

Performance metric — bandwidth — has been analyzed and observations regarding the radiation pattern and reflection loss obtained using the proposed patch antennas have been discussed in this section.

5.1. Bandwidth and Patch Size

Figure 2 shows reflection loss (in dB) for different dielectric substrates.

- Best bandwidth-size trade-off was observed using the proposed multiple-layer dielectric substrate (Si/Glass/Si) giving a bandwidth of 314 MHz (reflection loss: −9.5014 dB) at patch size $8 \times 12\,\text{mm}^2$.

Table 1: Comparison of simulation results on rectangular patch antenna using different types of substrates.

Dielectric	**Dielectric constant**	**Thickness (mm)**	**Bandwidth (MHz)**	**Size of rectangular patch**	**Gain**	**Directivity**
Silicon (single layer)	11.9	2	72.7	8×6	2.490	4.728
Glass (single layer)	4.6	2	86.4	12×13	2.326	4.528
Silicon/ Glass/Silicon (Multiple-layer)	**11.9/4.6/11/9**	**0.5/1/0.5**	**314**	8×12	**4.035**	**6.646**

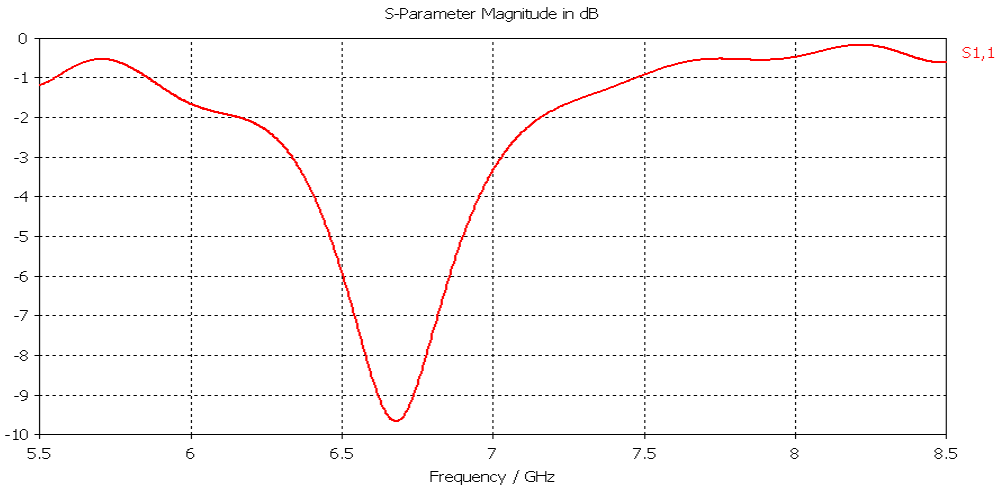

Figure 2: Reflection loss (in dB) for Multiple layer Dielectric with partial substrate removal. Reflection loss for the proposed antenna reaches −9.5014 dB, it has the highest 3 dB bandwidth of 314 MHz.

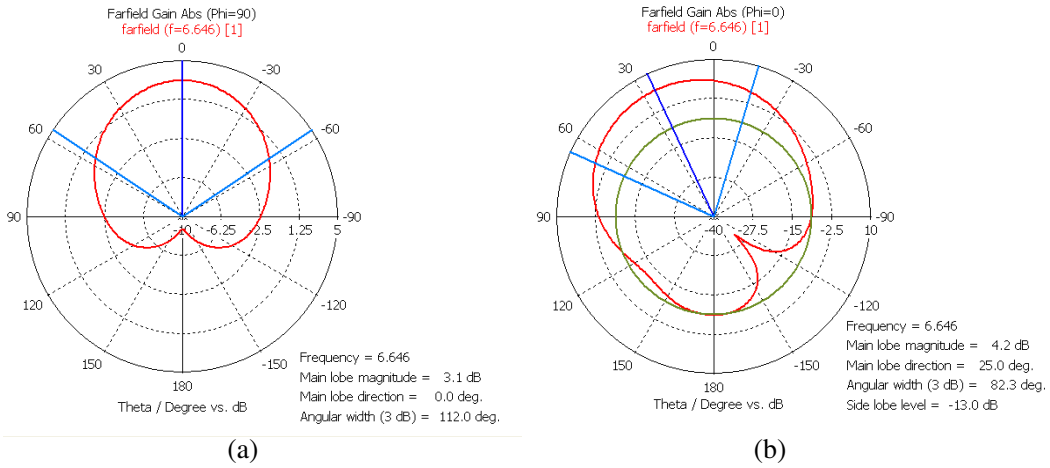

Figure 3: Radiation pattern for patch antenna on multiple-layer dielectric with partial substrate removal in (a) E plane, $\varphi = 90$. (b) H-plane, $\varphi = 0$. The main lobe magnitude (gain) is found to be 4.035 dB.

- The smallest patch on single-layer silicon substrate was found to be $8 \times 6\,\text{mm}^2$ and very low reflection loss of $-19.246\,\text{dB}$ but the bandwidth was only 72.7 MHz.
- The rectangular patch on single-layer glass substrate was found to give a bandwidth of 86.4 MHz (reflection loss: $-7.8\,\text{dB}$) but at a size of $12 \times 13\,\text{mm}^2$.

When compared with bandwidth of single-layer substrate the bandwidth was found to increase remarkably using the proposed multiple-layer substrate. Bandwidth using multiple-layer dielectric is greater than that obtained using single-layer Si substrate by while the size (patch area) was increased.

On comparison with bandwidth of single-layer glass substrate, multiple-layer dielectric substrate gives 260% increase in bandwidth while the size is reduced by 38%.

5.2. Radiation Pattern

- Figure 3 shows the simulation results of the radiation patterns for the proposed patch on multiple-layer substrate along E and H-planes. The microstrip antennas on glass and Si/glass-/Si substrate were found to have similar radiation patterns.
- The gain of the proposed multiple-layer with partial substrate removal patch was found to be 4.035 dB. This is acceptable value gain for a microstrip antenna.
- Also back lobe of the radiation pattern is quite large due to small ground planes. These can be improved by increasing the area of the ground plane.

6. CONCLUSION

The proposed antenna design using multiple-layer dielectric with partial substrate removal has been found to give a bandwidth of 314 MHz with a gain of 4.035 dB at an operating frequency of 6.646 GHz. This is a noteworthy improvement in bandwidth over that obtained using microstrip antenna over single-layer silicon or single-layer glass substrate. These broadband characteristics can be attributed to the multiple-layer dielectric substrate that lowers the effective dielectric value while reducing the size as much as possible. The proposed antenna has a gain of 4.035 dB. This approach can be extended further to improve gain and bandwidth simultaneously by incorporating various electromagnetic band-gap structures in a multiple-layer configuration.

REFERENCES

1. Kim, J., H. Kim, and K. Chun, "Performance enhancements of a microstrip antenna with multiple layer substrates," *International Symposium on Signals, Systems and Electronics 2007 (ISSSE '07)*, 319–322, 2007.
2. Rojas, R. G. and K. W. Lee, "Surface wave control using nonperiodic parasitic strips in printed antennas," *Proc. Inst. Elect. Eng. — Microw. Antennas Propag.*, Vol. 148, 25–28, Feb. 2001.
3. Bhattacharayya, A. K., "Characteristics of space and surface-waves in a multilayered structure," *IEEE Transactions on Antennas and Propagation*, Vol. 38, 1231–1238, Aug. 1990.

4. Jakson, D. R., J. T. Williams, A. K. Bhattacharayya, R. L. Smith, J. Buchleit, and S. A. Long, "Microstrip patch designs that do not excite surface waves," *IEEE Transactions on Antennas and Propagation*, Vol. 41, 1026–1037, Aug. 1993.
5. Khayat, M., J. T.Williams, D. R. Jakson, and S. A. Long, "Mutual coupling between reduced surface-wave microstrip antennas," *IEEE Transactions on Antennas and Propagation*, Vol. 48, 1581–1593, Oct. 2000.
6. Yeap, S. B. and Z. N. Chen, "Microstrip patch antennas with enhanced gain by partial substrate removal," *IEEE Transactions on Antennas and Propagation*, Vol. 58, No. 9, Sept. 2010.
7. Jackson, D. R., J. T. Williams, A. K. Bhattacharyya, R. L. Smith, S. J. Buchheit, and S. A. Long, "Microstrip patch designs that do not excite surface waves," *IEEE Transactions on Antennas and Propagation*, Vol. 41, No. 8, 1026–1037, Aug. 1993.
8. Gonzalo, R., P. de Maagt, and M. Sorolla, "Enhanced patch-antenna performance by suppressing surface waves using photonic-bandgap substrates," *IEEE Transactions on Microwave Theory and Techniques*, Vol. 47, No. 11, 2131–2138, Nov. 1999.
9. Boutayeb, H. and T. A. Denidni, "Gain enhancement of a microstrip patch antenna using a cylindrical electromagnetic crystal substrate," *IEEE Transactions on Antennas and Propagation*, Vol. 55, No. 11, 3140–3145, Nov. 2007.
10. Llombart, N., A. Neto, G. Gerini, and P. de Maagt, "Planar circularly symmetric EBG structures for reducing surface waves in printed antennas," *IEEE Transactions on Antennas and Propagation*, Vol. 53, No. 10, 3210–3218, Oct. 2005.
11. Gauthier, G. P., A. Courtay, and G. H. Rebeiz, "Microstrip antennas on synthesized low dilectric-constant substrate," *IEEE Transactions on Microwave Theory and Techniques*, Vol. 45, 1310–1314, Aug. 1997.
12. Colburn, J. S. and Y. Rahmat-Sammii, "Patch antennas on externally perforated high dilectric constant substrate," *IEEE Transactions on Microwave Theory and Techniques*, Vol. 47, 1785–1794, Dec. 1999.
13. Park, Y. J., A. Herchlein, and W. Wiesbeck, "A photonic band-gap (PBG) structure for guiding and suppressing surface waves in millimeter-wave antennas," *IEEE Transactions on Antennas and Propagation*, Vol. 49, 1854–1857, Oct. 2001.
14. Agi, K., M. Mojahedi, B. Minhas, E. Schamilogu, and K. J. Malloy, "The effects of an electromagnetic crystal substrate on a microstrip patch antenna," *IEEE Transactions on Antennas and Propagation*, Vol. 50, 451–456, Apr. 2002.
15. Yang, F. and Y. Rahmat-Samii, "Microstrip antennas integrated with electromagnetic bandgap (EBG) structures: A low mutual coupling design for array applications," *IEEE Transactions on Antennas and Propagation*, Vol. 51, 2936–2946, Oct. 2003.
16. Neto, A., N. Llombart, G. Gerini, and P. de Maagt, "On the optimal radiation bandwidth of printed slot antennas surrounded by EBGs," *IEEE Transactions on Antennas and Propagation*, Vol. 543, 1074–1083, Apr. 2006.
17. Boutayeb, H. and T. A. Denidni, "Gain enhancement of a microstrip patch antenna using a cylindrical electromagnetic crystal substrate," *IEEE Transactions on Antennas and Propagation*, Vol. 55, No. 11, Nov. 2007.
18. Zhou, Y., F. Yu, T. Shen, P. Ji, J. Ge, J. Gen, and J. Len, "Investigation of patch antennas based on embedded multiple PBG structure," *IEEE Photonics Technology Letters*, Vol. 20, No. 20, 1685, Oct. 15, 2008.
19. Chen, Q., V. F. Fusco, M. Zheng, and P. S. Hall, "Silicon active slot loop antenna with micromachined trenches," *IEE National Conf. on Antennas and Propagation*, No. 461, 253–255, Apr. 1999.
20. Shen, L. C., S. A. Long, M. R. Allerding, and M. D. Walton, "Resonant frequency of a circular disc, printed-circuit antenna," *IEEE Transactions on Antennas and Propagation*, Vol. 25, No. 4, 595–596, 1977.
21. Collin, R., *Field Theory of Guided Waves*, 2nd Edition, IEEE Press, New York, 1991.
22. Balanis, C. A., *Antenna Theory — Analysis and Design*, 3rd Edition, John Wiley & Sons, 2005.

Non-spatial Filtering for Laser Beams with Volume Bragg Grating in Photo-Thermo-Refractive Glass

Xiang Zhang[1], **Jiansheng Feng**[1], **Shang Wu**[2], **Baoxing Xiong**[2], **and Keming Jiang**[2]

[1]Wuhan National Laboratory for Optoelectronics, School of Optoelectronic Science and Engineering
Huazhong University of Science and Technology, Wuhan 430074, China
[2]Key Lab of Modern Optical Technologies of Jiangsu Province, Institute of Modern Optical Technologies
Soochow University, Suzhou, Jiangsu 215006, China

Abstract— A non-spatial filter based on the angular selectivity of volume Bragg grating (VBGs) is described for laser beam cleanup. The diffraction characteristics of VBGs are discussed with coupled wave theory. The angle selectivity of VBGs is markedly influenced by tiny deviation of thickness and refractive index modulation. Two VBGs with period of 0.96 μm and the thickness of 2.5 mm and 2.9 mm in Photo-Thermo-Refractive (PTR) Glass are used for non-spatial filtering. The filtering effect is exhibited with divergent beams.

1. INTRODUCTION

In high-power or high-energy laser system, the load capacity is limited by the small-scale self-focusing in laser beams [1]. The spatial filtering has been used for more than 30 years to combat with the nonlinear effects [2]. The traditional spatial filter consists of a pair of lenses that focus and recollimate a beam, with a pinhole in the transform plane. The pinhole acts as a low-pass filter for the spatial modulation in the input laser beam, allowing only the lower spatial frequencies to be transmitted [3]. This eliminates the need for laser beam focusing, which is the source of many inherent defects of traditional spatial filters, such as "pinhole closure" [4].

The non-spatial filter which is developed by Ludman et al is a practicable way to overcome the inherent defects of traditional spatial filters [5]. Unlike traditional spatial filters, they operate directly on the laser beam [6]. Therefore, they are aligned more easily, may be used with high-power or high-energy lasers, and are cheaper in manufacturing. The non-spatial filters are based on the angular selectivity of thick holograms [5]. Initial holographic materials are not suitable for this application because differential shrinkage during holographic processing limits the maximum Bragg angle selectivity attainable by affecting the Bragg angle in a nonuniform manner [6], and their optical damage threshold is low [7]. Photo-Thermo-Refractive (PTR) glasses developed by Glebov possess linear transfer characteristics, high resolution and high optical damage threshold [8].

In this paper, we theoretical and experimental research the non-spatial filter on the basis transmission Volume Bragg gratings (TBGs) in PTR glass. The simulation of angular selectivity of TBGs with coupled wave theory is discussed, and the angular selectivity of TBGs is experimentally measured. The divergent laser beams are used to evaluate the filtering ability of non-spatial filters.

2. SIMULATION

According to the coupled wave theory [9], the diffraction efficiency of lossless transmission volume Bragg grating can be expressed as follow:

$$\eta = \sin^2(\upsilon^2 + \xi^2)^{1/2} \Big/ 1 + (\xi/\upsilon)^2 \tag{1}$$

$$\begin{cases} \upsilon = \pi n_1 d/\lambda(\cos\theta(\cos\theta - K\cos\phi/\beta))^{1/2} \\ \xi = \Delta\theta K d\sin(\phi - \theta_0)/2(\cos\theta - K\cos\phi/\beta) \\ K = 2\pi/\Lambda, \beta = 2\pi n_0/\lambda \end{cases} \tag{2}$$

where n_1 is refractive index modulation, n_0 is average refractive index of recording material, d is the effective thickness of the gratings, Λ is the gratings period, ϕ is the tilt angle of grating vector, λ is the wavelength of incident beam, is incidence angle in medium. As shown in this Fig. 1, The peak diffraction efficiency of VBG is 96% and the Half Width at First Zero (HWFZ) is ~ 0.45 mrad.

The desired non-spatial filters could be achieved with selection of structural parameters of VBGs, such as thickness, period, refractive index modulation or tilt angle of grating vector. The target wavelength is 532 nm, 632.8 nm and 1064 nm. The diffraction characteristic of VBGs varies with one of the above grating parameters, and the others are determinate.

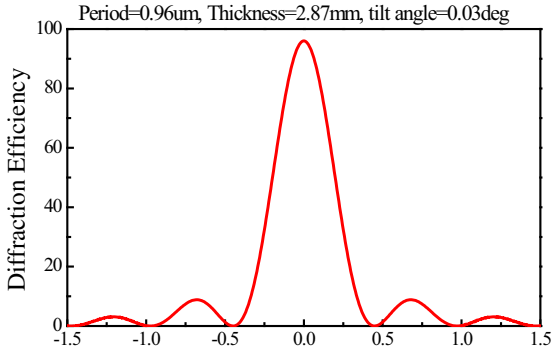

Figure 1: The angular selectivity of volume Bragg gratings (Theoretically).

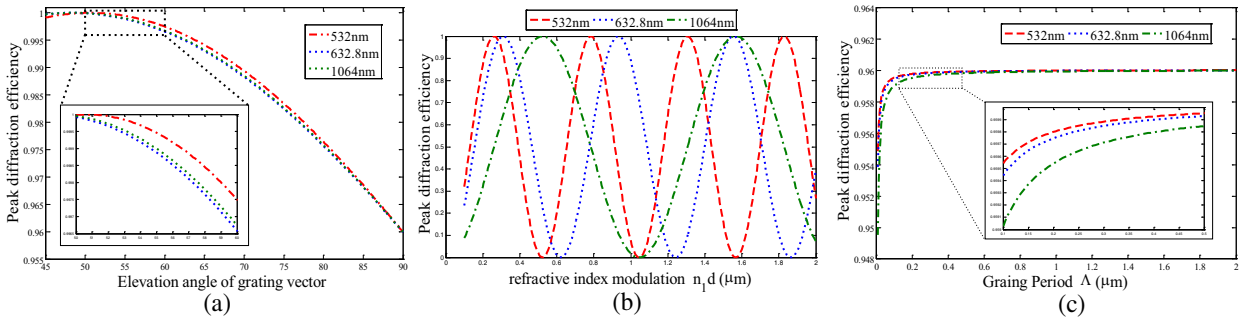

Figure 2: The dependence of peak diffraction efficiency of angular filter with tile angle of grating vector for (a), the product of refractive index modulation and thickness for (b), grating period for (c).

2.1. Peak Diffraction Efficiency

The VBGs have maximum peak diffraction efficiency when the beam is incident on the VBGs at Bragg angle. Meanwhile, the VBGs operate on Bragg condition, and $\theta = \theta_B$, $\lambda = \lambda_B$.

$$\eta_{MAX} = \sin^2\left[\frac{\pi n_1 d}{\lambda_B(\cos\theta_0(\cos\theta_0 - \lambda_B\cos\varphi/n_0\Lambda)^{1/2})}\right] \tag{3}$$

As known from Eq. (3), each structural parameter of VBGs reacts on the peak diffraction efficiency of non-spatial filters. Besides, the effect of refractive index modulation and the grating thickness is equivalent, thus, we investigate the product of refractive index modulation and the grating thickness on the peak diffraction efficiency. The analysis results are shown in Fig. 2.

As shown in Fig. 2(a), the peak diffraction efficiency reaches maximum value as tilt angle of grating vector of ~ 45 deg, approach to 100%. As shown in Fig. 2(b), the product of thickness and refractive index modulation makes the periodic variation of peak diffraction efficiency. The period is 0.52 μm, 0.63 μm and 1.04 μm with respond to wavelength of 532 nm, 632.8 nm and 1064 nm, respectively. As shown in Fig. 2(c), when the grating period is larger than a specific value of ~ 0.2 μm, the variation of peak diffraction is not obviously. Once the grating period is less than ~ 0.2 μm, the peak diffraction efficiency reduced sharply.

2.2. FWFZ

ull Width at First Zero (FWFZ) of VBGs directly limits the filtering ability of non-spatial filters. When the diffraction efficiency of VBGs is zero, according to Eq. (1)

$$\sin^2\left(\upsilon^2 + \xi^2\right)^{1/2} = 0 \tag{4}$$

and

$$(\nu^2 + \xi^2)^{1/2} = \pm k\pi, \quad k = \pm 1, \pm 2, \pm 3 \ldots \tag{5}$$

where υ and ξ is shown in Eq. (2). A series of k value is corresponding to zero value at all levels on the angular selectivity curve. When the each grating parameter is determined, υ and ξ is a function of one variable on divergence angle of $\Delta\theta$. The exponential increase of $\upsilon^2 + \xi^2$ is caused

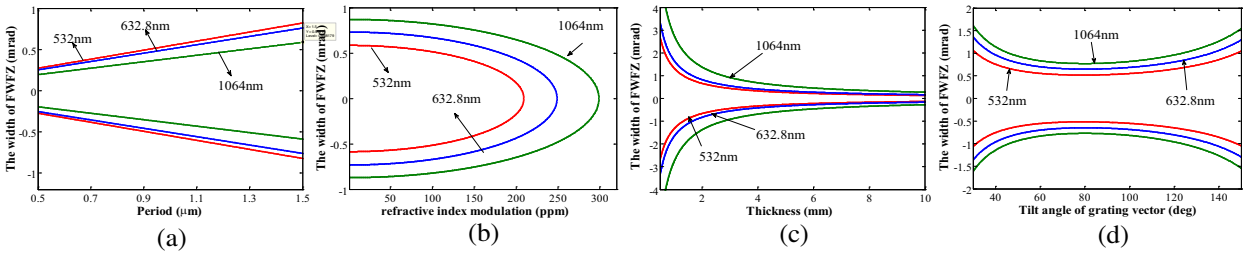

Figure 3: The dependence of FWFZ of VBGs with grating period (a), thickness (b), tile angle of grating vector (c) and refractive index modulation (d).

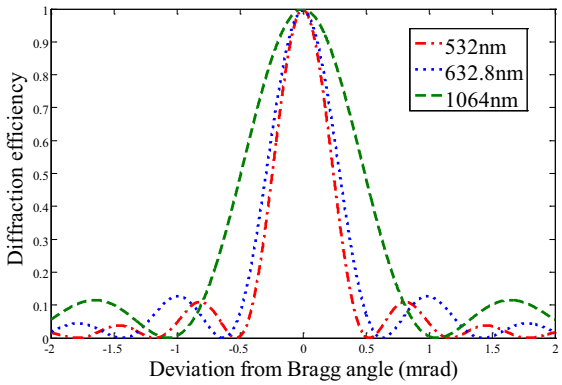

Figure 4: The angular selectivity of designed VBGs.

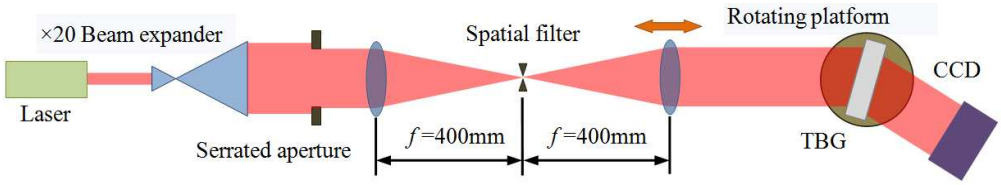

Figure 5: The schematic diagram of non-spatial filtering with VBGs in PTR glass. The beam is incident on the VBGs at Bragg angle.

by addition of $\Delta\theta$. Therefore, the first-order and m-order zero is corresponding to $k = \pm 1$ and $k = \pm m$, respectively. The analysis results are shown in Fig. 3.

As shown in Figs. 3(a) and (b), the FWFZ increases linearly with the addition of grating period, but reduces with the addition of grating thickness. The FWFZ approximately increase 1.12 mrad (532 nm), 1.0 mrad (632.8 nm) and 0.8 mrad (1064 nm) when the grating period raise 1 μm. With the increase of thickness, FWFZ be reduced sharply and tend to smooth at a specific value which is about 2 mm, 3 mm and 4 mm with the incident wavelength of 532 nm, 632.8 nm and 1064 nm, respectively. As shown in Fig. 3(c), the FWFZ reaches minimum value as tilt angle of grating vector of 90 deg. It means that the grooves of VBGs are perpendicular to grating surface. When the tilt angle of grating vector gradually deviates from 90 deg, the FWFZ raises slowly. As shown in Fig. 3(d). The refractive index modulation only chooses in a certain interval. When the wavelength is 532 nm, the upper limit is 200 ppm.

2.3. Results and Error Tolerance Analysis

The designed angular selectivity of VBGs for different wavelength (532 nm, 632.8 nm, 1064 nm) is shown in Fig. 4. Obviously, peak diffraction efficiency of VBGs is all greater than 99%.

Results of error tolerance analysis are shown in Table 1. It was demonstrated that the diffraction characteristic of VBGs is little affected by the deviation of grating period and tilt angle of grating vector. Otherwise, the deviation of grating thickness and the refractive index modulation cannot be ignored. The diffraction characteristic of VBGs is weakened observably by the small deviation of grating thickness and refractive index modulation.

Table 1: Results of error tolerance analysis. η_{MAX} is the peak diffraction efficiency, $\eta_s$is the sidelobes diffraction efficiency, λ is the wavelength of incident beam.

λ	Grating ability	Λ(lp/mm)		ϕ (deg)		d (mm)		n_1 (ppm)	
		+10	−10	+0.1	−0.1	+0.1	−0.1	+10	−10
532 nm	η_{MAX}	0	0	0	0	+1.8%	−1.1%	−0.6%	−3.2%
	η_s	−0.9%	−0.1%	0	0	+8.9%	−8.5%	+19%	−17.4%
	FWFZ	−2.6%	+5.2%	+1.2%	+1%	−4.1%	+5.7%	−2.8%	+2.9%
632.8 nm	η_{MAX}	0	0	0	0	−1.3%	+0.5%	−3.3%	+0.12%
	η_s	0	0	0	0	+8.1%	−7.8%	+15.7%	−14.9%
	FWFZ	−1.2%	+1.2%	0	0	−5.3%	+5.7%	-3%	+2.7%
1064 nm	η_{MAX}	0	0	0	0	−0.12%	−0.3%	−0.9%	−1.2%
	η_s	0	0	0	0	+5.8%	−5.6%	+12.1%	−12.8%
	FWFZ	−2.8%	+2.8%	0	0	−3.8%	+3.8%	−2.3%	+2%

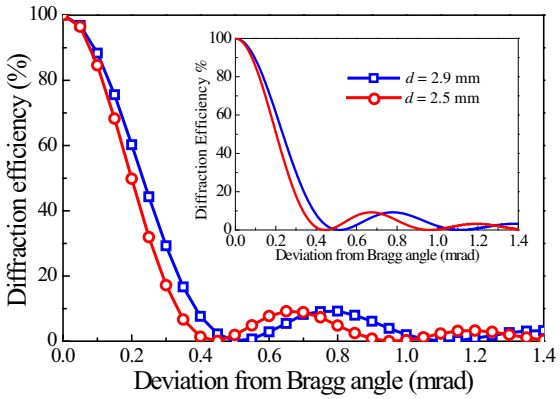

Figure 6: Contours of angular selectivity for VBGs. Both VBGs have the same period (0.96 µm) and the same tilt angle of grating vector (0.03 deg). Illustration theoretical contour calculated for the same parameters of the VBGs.

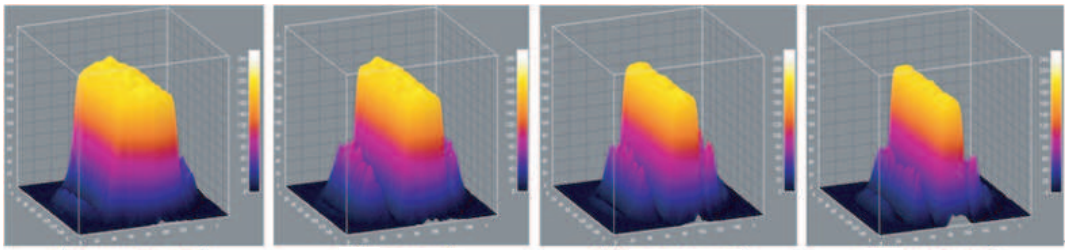

(a) 1.16 mrad (b) 2 mrad (c) 2.95 mrad (d) 3.6 mrad

Figure 7: The beam profile of different divergence angle from the non-spatial filter.

3. EXPERIMENT

The equipment of measuring the angular selectivity of VBGs borrows ideas from Ref. [10]. The schematic diagram of non-spatial filtering was shown in Fig. 5. The laser is a CW frequency-doubled YAG laser with the wavelength of 532 nm and output power of 2 W. The near field beam profile was shaped with a serrated aperture. Different beam divergence angles are obtained by adjusting the second mirror in the spatial filter. After shaped, the laser beam is incident on the VBGs at the Bragg angle of 16.2 degree. The 12 bit CCD camera is used to monitor the diffracted beams through the VBGs.

FIgure 6 presents the measured contours of angular selectivity for these two VBGs. Illustration displays the theoretical angular selectivity contour for these VBGs. One can see that the experimental contours of angular selectivity of the VBGs are good, but it is somewhat greater than

the theory. The first diffraction zero of the theoretical contour is 0.44 mrad and 0.5 mrad that of experimental contour are 0.44 mrad and 0.52 mrad. The experimental peak diffraction efficiency is in line with the theoretical value.

The incident beams with different divergence angle are used to evaluate the filtering ability of non-spatial filtering. As shown in Fig. 7. The width of main maximum diffraction is 4.84 mm, 4.71 mm, 3.6 mm and 2.44 mm with respect to the divergence angle of 1.16 mrad, 2 mrad, 2.95 mrad and 3.6 mrad respectively. Meanwhile, the height of first sidelobe is 8.73%, 8.3%, 7.95% and 7.56% respectively.

4. CONCLUSION

Practical mathematical model on the basis of coupled wave theory is developed for laser beam clean-up with efficient VBGs. The experimental data coincides with simulation results. VBGs possess high diffraction efficiency of 96% and angular selectivity of 0.44 mrad and 0.52 mrad. With the increasing of divergence angle of incident beams, the width of central peak narrows and the height of sidelobes reduce. The nonspatial filtering may has potential applications in laser beam clean-up.

ACKNOWLEDGMENT

This work is supported by NSAF and NSFC under the contract Nos. of 10806011 and 91023009, Natural Science Foundation of Jiangsu Higher Education Institutions under the contract No. of 10KJA140045, the Priority Academic Program Development of Jiangsu Higher Education Institutions, and the national High-Tech 863 program of China.

REFERENCES

1. Bespalov, V. I. and V. I. Talanov, "Filamentary structure of light beams in nonlinear liquids," *J. ETP Lett.*, Vol. 3, No. 12, 307–310, 1966.
2. Hunt, J. T., J. A. Glaze, W. W. Simmons, and P. A. Renard, "Suppression of self-focusing through low-pass spatial filtering and relay imaging," *Appl. Opt.*, Vol. 17, No. 13, 2053–2057, 1978.
3. Murray, J. E, D. Milam, C. D. Boley, K. G. Estabrook, and J. A. Caird, "Spatial filter pinhole development for the National Ignition Facility," *Appl. Opt.*, Vol. 39, No. 9, 1405–1420, 2000.
4. Auerbach, J. M., N. C. Holmes, J. T. Hunt, and G. J. Linford, "Closure phenomena in pinholes irradiated by Nd laser pulses," *Appl. Opt.*, Vol. 18, No. 14, 2495–2499, 1979.
5. Ludman, J. E., J. R. Riccobono, H. J Caulfield, J. M Fournier, I. V. Semenova, N. O. Reinhand, P. R. Hemmer, and S. M Shahriar, "Porous-matrix holography for nonspatial filtering of lasers," *SPIE*, Vol. 2406, 76–85, April 1995.
6. Ludman, J. E, J. R. Riccobono, N. O. Reinhand, I. V. Semenova, Y. L. Korzinin, S. M. Shahriar, H. J. Caulfield, J. M. R. Fournier, and P. Hemmer, "Very thick holographic nonspatial filtering of laser beams," *Opt. Eng.*, Vol. 36, No. 6, 1700–1705, 1997.
7. Efimov, O. M., L. B Glebov, S. Papernov, and A. W. Schmid, "Laser-induced damage of photo-thermo-refractive glasses for optical holographic element writing," *SPIE*, Vol. 3578, 564–575, April 1999.
8. Efimov, O. M., L. B. Glebov, L. N. Glebova, K. C. Richardson, and V. I. Smirnov, "High-efficiency bragg gratings in photothermorefractive glass," *Appl. Opt.*, Vol. 38, No. 4, 619–627, 1999.
9. Kogelnik, H., "Coupled wave theory for thick hologram gratings," *Bell Syst. Tech. J.*, Vol. 48, 2909, 1969.
10. Zheng, H. B., Y. L. He, J. C. Tan, G. W. Zheng, X. Wang, X. D. Wang, and D. Y. Ding, "Spatial filtering for high power laser beam by volume Bragg grating," *SPIE*, Vol. 7506, November 2009.

Simulation of Chirped Volume Bragg Grating with a Partition-integration Method

Jiansheng Feng[1], **Xiao Yuan**[1, 2], **Xiang Zhang**[1], **Shang Wu**[2], **Kuaisheng Zou**[2], **and Guiju Zhang**[2]

[1]Wuhan National Laboratory for Optoelectronics, School of Optoelectronic Science and Engineering
Huazhong University of Science and Technology, Wuhan, Hubei 430074, China
[2]Institute of Modern Optical Technologies and Key Lab of Modern Optical Technologies of Jiangsu
Province, Soochow University, Suzhou, Jiangsu 215006, China

Abstract— A partition-integration method is proposed and used to study the dispersion property and the frequency response for chirped volume Bragg gratings (CVBGs). The CVBG is divided into short segments, in which each segment is assumed to be uniform and characterized with a matrix. The frequency responses and dispersion properties of CVBGs are simulated. The frequency response is a gate-like function, and the group delay shows linearity with a few ripples.

1. INTRODUCTION

Ultrashort laser pulses with high peak power and short duration have been widely used in various fields of science, medicine and engineering such as spectroscopy, optoelectronics, communication and material processing [1–4]. As one of the technologies in high power laser facilities, chirped pulse amplification (CPA) has been the most effective approach to purchase ultrashort pulses since its development by Gerard Mourou and Donna Strickland [5] in the mid 1980s. The indispensable devices in CPA are the dispersion elements, which are used as the stretchers and compressors, such as surface gratings [6–8], prism pairs [9, 10] and single mode fibers [11, 12], etc.. The widely used surface grating is not of an ideal laser damage threshold, and improving the laser beam power requires the increase of the grating size. Petawatt-class systems would require gratings exhibiting ruled areas of approximately 1 m × 1 m [13], and such a huge aperture of surface grating orders extreme fabrication. Chirped volume Bragg gratings (CVBGs) may be the potential dispersion elements for CPA due to the high laser damage threshold, simple configuration and easy alignment.

In 1998, A. Galvanauskas presented an experimental demonstration of using a 200 µm × 300 µm × 5 mm CVBG for ultrashort pulse stretching and recompression in a compact CPA arrangement, and a 500 nJ pulse was obtained [14]. In 2005, researchers in University of Michigan and University of Central Florida employed a 5 mm × 5 mm × 10 mm CVBG recorded in the photo-thermal-refractive glass for a fiber CPA system [15]. The stretcher and compressor are realized in the same CVBG. Specially, such grating has a pretty high laser damage threshold of about 20 J/cm^2 for 1-ns pulse duration at 1054-nm [16], and it would be adapted to high power laser facilities. These researchers subsequently made a series of experimental investigations on CPA systems with photo-thermal-refractive glass based CVBGs at different central wavelengths, original pulses' durations and bandwidths [17–20]. The analytic theory for CVBGs in Ref. [21], to our knowledge, is derived from Shapiro's theory [22] which is based on the coupled mode analysis and proposed for the chirped fiber gratings. Transfer matrix approach for volume Bragg gratings discussed by B. Y. Zeldovich [23] has the potential to characterize CVBGs. In this paper, we describe the detailed derivation of a partition-integration method which is easy and simple and could characterize the CVBGs as well.

2. PRINCIPLE

Since the grating period of CVBGs varies with the location in the gratings, the wave equation in such a configuration is not a Mathieu function, thus the coupled wave theory [24] and rigorous coupled wave theory [25] are not suitable for characterizing CVBGs. While dividing CVBGs into N short segments shown in Fig. 1, the variation of refractive index in each part can be taken as uniform. The CVBG is considered the congregation of all these uniform parts.

The CVBG is assumed to operate at normal incidence and be an unslanted reflective one, so the index modulation varies along z-axis. The basic cell in this partition-integration method is a uniform part with constant permittivity and predetermined thicknesses. The propagation of the TE mode ($\mathbf{E} = E_y$; $E_x = E_z = B_y = 0$) during the j-th uniform part ($z_j \leq z \leq z_{j+1}$) in Ref. [26]

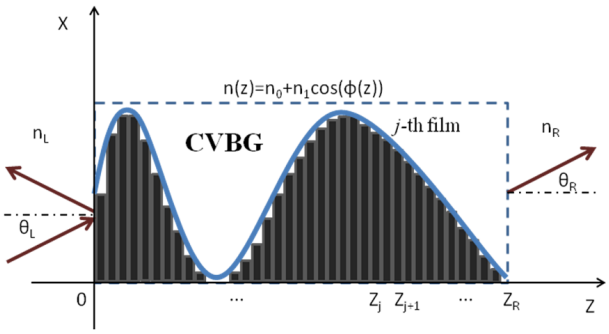

Figure 1: Uniform decomposition of chirped volume Bragg grating.

could be characterized with a matrix

$$\begin{pmatrix} E_y^{(j)}(z_{j+1}) \\ cB_x^{(j)}(z_{j+1}) \end{pmatrix} = M_j \begin{pmatrix} E_y^{(j)}(z_j) \\ cB_x^{(j)}(z_j) \end{pmatrix}. \tag{1}$$

where $E_y^{(j)}$ and $B_x^{(j)}$ are the tangential components in TE mode, and c is the light speed in vacuum. The transfer matrix M_j is given below

$$M_j = \begin{pmatrix} \cos(k_j L_j) & \frac{i}{n_j}\sin(k_j L_j) \\ in_j \sin(k_j L_j) & \cos(k_j L_j) \end{pmatrix}, \tag{2}$$

where k_j is the propagation constant in the j-th part. L_j and n_j are the thickness and refractive index of the j-th part. With the continuity of the electromagnetic field's tangential components $(E_y^{(j)}(z_{j+1}) = E_y^{(j+1)}(z_{j+1})$, and $(B_x^{(j)}(z_{j+1}) = B_x^{(j+1)}(z_{j+1}))$, the relationship between the input and output fields is obtained

$$\begin{pmatrix} E_y^R(z_R) \\ cB_x^R(z_R) \end{pmatrix} = M \begin{pmatrix} E_y^L(0) \\ cB_x^L(0) \end{pmatrix}. \tag{3}$$

where z_R is the thickness of CVBG. M is the transfer matrix of the CVBG, and it is the product of all the N small parts' matrix

$$M = \begin{pmatrix} M_{11} & M_{12} \\ M_{21} & M_{22} \end{pmatrix} = M_N M_{N-1} \cdots M_i \cdots M_2 M_1. \tag{4}$$

Assuming that the electric reflective coefficient and electric transmitted coefficient are r and t, the fields' distribution in the left and right region out of the CVBG is obtained

$$\begin{cases} E_y^L(z,t) = (E_0 \exp(ik_L z) + rE_0 \exp(-ik_L z)) \exp(-i\omega t), & z \le 0 \\ E_y^R(z,t) = tE_0 \exp(ik_R z) \exp(-i\omega t), & z \ge z_R \end{cases}. \tag{5}$$

where E_0 is the amplitude of the incident field, and ω is the angular frequency in vacuum. $k_L = n_L\omega/c$ and $k_R = n_R\omega/c$ are the propagation constants in the left and right region out of the CVBG, respectively. n_L and n_R are the refractive indexes. The magnetic field B_x could be obtained with the relation $\mathbf{B} = (1/i\omega)\nabla \times \mathbf{E}$. Inserting the fields into Eq. (3), the electric reflective coefficient is

$$r = \frac{(n_L M_{22} - n_R M_{11}) - (n_L \rho_R M_{12} - M_{21})}{(n_L M_{22} + n_R M_{11}) - (n_L n_R M_{12} + M_{21})}. \tag{6}$$

The diffraction efficiency of the CVBG is

$$R = |r|^2, \tag{7}$$

and the group delay is

$$f = \frac{d\arg(r)}{d\omega} = -\frac{\lambda^2}{2\pi c} \cdot \frac{d\mathrm{Im}(\ln r)}{d\lambda}, \tag{8}$$

where λ is wavelength of the incident field in vacuum.

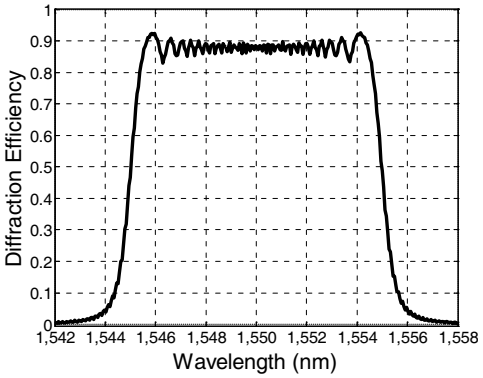

Figure 2: Frequency response of a chirped volume Bragg grating.

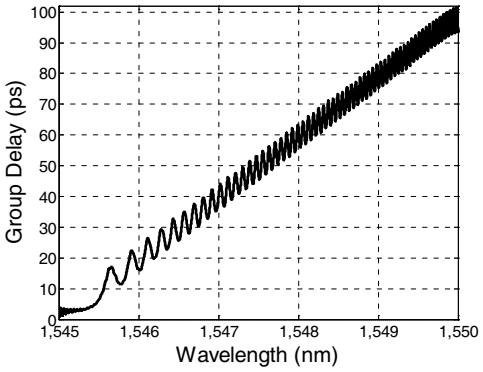

Figure 3: Group delay of a chirped volume Bragg grating.

3. SIMULATION

With this partition-integration method, the diffraction efficiencies and the group delays of arbitrary CVBGs could be obtained. For a pure reflective CVBG, the most important parameters are the thickness and the refraction index modulation. If the parameters are well designed, the gratings would show satisfactory diffraction efficiency, considering that the inherent absorption of recording material is negligible.

Figure 2 shows the frequency response of a linear chirped CVBG with the partition-integration method in which the number of points per period of spatial modulation is fixed at $N = 30$, then the step varies along the grating. The central wavelength of this CVBG is about 1550 nm, the bandwidth is 10 nm, the thickness is 10 mm and the refraction index modulation is about 800 ppm ($n_1 = 8 \times 10^{-4}$). The diffraction efficiency at the pass band from 1545nm to 1555 nm is about 88%, but some ripples exist especially at the two ends of the band. Fig. 3 shows the group delay of the same CVBG as in Fig. 2. In the predetermined band of the CVBG, the group delay is almost a linear function with respect to the incident wavelength, and there are a few dispersion ripples.

4. CONCLUSION

The partition-integration method describing the frequency responses and dispersion properties of CVBGs is given in this paper. The numerical analysis shows the frequency response is almost a gate-shaped function with some ripples especially at the two ends of the band, and the group delay is linear and with a few dispersion ripples in the bandwidth.

ACKNOWLEDGMENT

This work is supported by NSAF and NSFC under the contract Nos. of 10806011 and 91023009, Natural Science Foundation of Jiangsu Higher Education Institutions under the contract No. of 10KJA140045, the Priority Academic Program Development of Jiangsu Higher Education Institutions, and the national High-Tech 863 program of China.

REFERENCES

1. Sawa, M., K. Awazu, T. Takahashi, H. Sakaguchi, H. Horiike, M. Ohji, and Y. Tano, "Application of femtosecond ultrashort pulse laser to photodynamic therapy mediated by indocyanine green," *British Journal of Ophthalmology*, Vol. 88, No. 6, 826–831, 2004.
2. Da Silva, L. B., B. M. Kim, M. D. Feit, and A. M. Rubenchik, "Use of ultrashort pulse lasers in medicine," *Lasers and Electro-optics Society Annual Meeting, 1998 LEOS '98 IEEE*, 443–444, Orlando, USA, Dec. 1998.
3. Heilweil, E. J., "Ultrashort-pulse multichannel infrared spectroscopy using broadband frequency conversion in $LiIO_3$," *Opt. Lett.*, Vol. 14, No. 11, 551–553, 1989.
4. Salehi, J. A., A. M. Weiner, and J. P. Heritage, "Coherent ultrashort light pulse code-division multiple access communication systems," *Journal of Lightwave Technology*, Vol. 8, No. 3, 478–491, 1990.
5. Strickland, D. and G. Mourou, "Compression of amplified chirped optical pulses," *Optics Communications*, Vol. 56, No. 3, 219–221, 1985.

6. Treacy, E., "Optical pulse compression with diffraction gratings," *IEEE Journal of Quantum Electronics*, Vol. 5, No. 9, 454–458, 1969.
7. Maine, P., D. Strickland, P. Bado, M. Pessot, and G. Mourou, "Generation of ultrahigh peak power pulses by chirped pulse amplification," *IEEE Journal of Quantum Electronics*, Vol. 24, No. 2, 398–403, 1988.
8. Squier, J., C. P. J. Barty, F. Salin, C. L. Blanc, and S. Kane, "Use of mismatched grating pairs in chirped-pulse amplification systems," *Appl. Opt.*, Vol. 37, No. 9, 1638–1641, 1998.
9. Fork, R. L., O. E. Martinez, and J. P. Gordon, "Negative dispersion using pairs of prisms," *Opt. Lett.*, Vol. 9, No. 5, 150–152, 1984.
10. Nisoli, M., S. de Silvestri, and O. Svelto, "Generation of high energy 10 fs pulses by a new pulse compression technique," *Applied Physics Letters*, Vol. 68, No. 20, 2793–2795, 1996.
11. Jens, L., A. Liem, S. Höfer, S. Nolte, H. Zellmer, A. Tünnermann, V. Reichel, S. Unger, S. Jetschke, and H. R. Müller, "High average power femtosecond fiber CPA system," *Advanced Solid-state Lasers, Optical Society of America*, MC4, Québec City, Canada, 2002.
12. Chen, C. M. and P. L. Kelley, "Nonlinear pulse compression in optical fibers: Scaling laws and numerical analysis," *J. Opt. Soc. Am. B*, Vol. 19, No. 9, 1961–1967, 2002.
13. Perry, M. D. and G. Mourou, "Terawatt to petawatt subpicosecond lasers," *Science*, Vol. 264, No. 5161, 917–924, 1994.
14. Galvanauskas, A., A. Heaney, T. Erdogan, and D. Harter, "Use of volume chirped Bragg gratings for compact high-energy chirped pulse amplification circuits," *Lasers and Electro-optics, CLEO 98 Technical Digest Summaries*, 362, San Francisco, USA, 1998.
15. Kai-Hsiu, L., C.-H. Liu, G. Almantas, F. Emilie, I. S. Vadim, and B. G. Leonid, "A novel chirped pulse amplification system based on a monolithic large aperture bulk-Bragg-grating stretcher/compressor," *Advanced Solid-state Photonics*, 768, Vienna, Austria, 2005.
16. Glebov, L. B., L. N. Glebova, V. I. Smirnov, M. Dubinskii, L. D. Merkle, S. Papernov, and A. W. Schmid, "Laser damage resistance of photo-thermo-refractive glass bragg gratings," *Proceedings of Solid State and Diode Lasers Technical Review*, 2004.
17. Liao, K. H., M. Y. Cheng, E. Flecher, V. I. Smirnov, L. B. Glebov, and A. Galvanauskas, "Large-aperture chirped volume Bragg grating based fiber CPA system," *Opt. Express*, Vol. 15, No. 8, 4876–4882, 2007.
18. Chang, G., C.-H. Liu, K.-H. Liao, V. Smirnov, L. Glebov, and A. Galvanauskas, "50-W chirped-volume-bragg-grating based fiber CPA at 1055-nm," *Conference on Lasers and Electro-optics/Quantum Electronics and Laser Science Conference and Photonic Applications Systems Technologies*, 1–2, Baltimore, Maryland, May, 2007.
19. Chang, G. Q., M. Rever, V. Smirnov, L. Glebov, and A. Galvanauskas, "32 W Femtosecond Yb-fiber CPA system based on chirped-volume-bragg-gratings," *Conference on Lasers and Electro-optics*, CThB3, May 2008.
20. Chang, G. Q., M. Rever, V. Smirnov, L. Glebov, and A. Galvanauskas, "Femtosecond Yb-fiber CPA system based on chirped-volume-bragg-gratings," *Advanced Solid-state Photonics*, MD4, Nara, Japan, Jan. 2008.
21. Glebov, L. B., S. V. Mokhov, V. I. Smirnov, and B. Y. Zeldovich, "Analytic theory of light reflection from a chirped volume bragg grating," *Frontiers in Optics*, San Jose, Oct. 2009.
22. Belai, O. V., E. V. Podivilov, and D. A. Shapiro, "Group delay in Bragg grating with linear chirp," *Optics Communications*, Vol. 266, No. 2, 512–520, 2006.
23. Glebov, L. B., J. Lumeau, S. Mokhov, V. Smirnov, and B. Y. Zeldovich, "Reflection of light by composite volume holograms: Fresnel corrections and Fabry-Perot spectral filtering," *J. Opt. Soc. Am. A*, Vol. 25, No. 3, 751–764, 2008.
24. Kogelnik, H., "coupled wave theory for thick hologram gratings," *The Bell System Technical Journal*, Vol. 48, No. 9, 2909–2947, 1969.
25. Moharam, M. G. and T. K. Gaylord, "Rigorous coupled-wave analysis of planar-grating diffraction," *J. Opt. Soc. Am.*, Vol. 71, No. 7, 811–818, 1981.
26. Wang, L. G., N. H. Liu, L. Qiang, and S. Y. Zhu, "Propagation of coherent and partially coherent pulses through one-dimensional photonic crystals," *Physical Review E*, Vol. 70, No. 1, 016601, 2004.

Anomalous Transmission Properties of epsilon-near-zero Metamaterials

Jie Luo, **Huanyang Chen**, **Yun Lai**, **Ping Xu**, **and Lei Gao**
Jiangsu Key Laboratory of Thin Films, Department of Physics
Soochow University, Suzhou 215006, China

Abstract— We present a semi-analytical model to investigate the optical properties of the metal grating which is transparent for white light. At a balanced angle the Fabry-Perot effect is absent and the transmission curve becomes nearly flat in a long wavelength range. This phenomenon can be explained by spoof surface plasmons (SSPs). Our numerical calculations show that by modifying the refractive index of the substrate the phenomenon of non-degeneracy of the Wood's anomalies appears. As a consequence, more long-wavelength ranges in which the transmission curve is nearly flat appear. At the same time, as the increase of the refractive index the transmittance decreases. Moreover, we can tune the balanced angle by varying the refractive index of the material filling the slits in the grating.

1. INTRODUCTION

Since the experiments of Ebbesen, et al. [1] showed extraordinary transmission through two-dimensional (2D) arrays of holes in metallic films, the goal of theoretical research in this area has been to achieve an understanding of the transmission mechanism in one-dimensional (1D) and 2D configurations [2–4]. In many cases, the enhanced transmission of holes or slit arrays has been explained in terms of the excitation of surface plasmons on the metal film, but the explanation was challenged. It has been shown that for slit arrays Fabry-Perot-type waveguide resonances can also give rise to a considerably enhanced transmission [2, 5, 6]. In 2004, Pendry et al. proposed the concept of spoof or structured surface plasmons for perfectly conducting structures [7]. The effective permittivity of the SSP has the same form as classic surface plasmons. Recently Huang et al. have presented a concrete picture of SPP combined with cavity resonance to clarify the basic mechanism underlying extraordinary light transmission through metal films with subwavelength silts [8–10]. They find that when light incidents on a highly conducting surface, it can drive free surface electrons to move. The moving electrons can be impeded by grooves, holes, or particles on the surface to form charge patterns. The oscillating charges and dipoles then emit new wavelets and the interference between the new wavelets may give rise to anomalous transmission, reflection, or scattering. Interestingly, at oblique incidence the incident wave can drive free electrons on the conducting surfaces and part of the slit walls to form spoof surface plasmons. As a consequence, at a balanced angle the metallic gratings consisting of narrow slits may become transparent for extremely board bandwidths.

In this letter, we investigate the optical properties of the metallic grating transparent for white light. Our numerical calculations show that by modifying the refractive index of the substrate the phenomenon of non-degeneracy of the Wood's anomalies appears. And as the increase of the refractive index the transmittance decreases. Furthermore, the balanced angle can be tuned through adjusting the refractive index of the material filling the silts in the grating.

2. THEORETICAL AND NUMERICAL ANALYSIS

Figure 1 shows a schematic view of the structures under study with the definition of the different parameters: the period of the grating $d = 3.5\,\mu\text{m}$, the width $a = 0.5\,\mu\text{m}$, and height $h = 4\,\mu\text{m}$ of the slits. The grating is sandwiched between air and substrate with refractive index n_1. The silts are filled with dielectric with refractive index n_2. A transverse magnetic (TM) polarized wave with incident angle of θ_i and wavelength λ_0 is considered.

As depicted in Fig. 2, at oblique incidence the incident light can illuminate part of the slit wall BP, providing a vertical driving force F_V on the electrons on the wall. On the top surface, the electrons can move continuously around corner B because of the vertical driving force F_V. However, charge discontinuity occurs at corner A since the incident wave provides no driving force on wall AD, resulting in the charge accumulation at the corner A. The charges near corner A oscillate with the incident wave and emit new wavelets. For a subwavelength grating, only along the specular reflection direction R_0 are the wavelets emitted from adjacent slits in phase, which

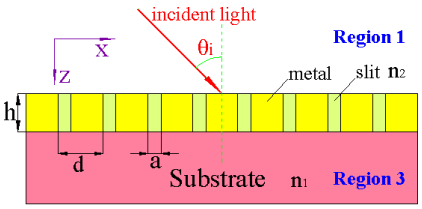

Figure 1: Schematic view of the metallic grating.

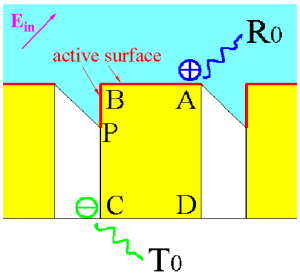

Figure 2: Light transmission through the metal grating at oblique incidence.

form the propagating reflected wave. Wavelets along other directions are always out of phase and form evanescent waves.

The charge waves formed on the active surfaces AB and BP then continuously propagate on the wall PC as an SSP. The moving charges are stopped and accumulated at corner C. The wavelets emitting from corners C form the transmitted wave along the transmission direction T_0. The SSPs on the slit walls are bounced back from C. The forward and backward SSPs then form standing charge waves on the walls, resulting in the Fabry-Perot resonance transmission peaks [11, 12].

In order to achieve flat transmission spectra, we should eliminate the backward SPP. The tendency for the SSP to be bounced back is suppressed by the vertical force F_V. Similarly, the force F_H on AB suppresses the tendency for the charge waves to be bounced back from A. Note that the magnitudes of both forces depend on the incident angle, and the vertical force depends on the refractive index of the material filling the silts. We can find a balanced angle θ_B, near which the two forces completely suppress the bouncing-back tendency of the moving electrons at both A and C. The balanced angle can be approximately expressed as

$$\theta_B = \arctan\left(n_2 d/a - 1\right) \tag{1}$$

The balanced angle can be tuned by changing the refractive index of the material filling the silts, as predicted by Eq. (1). At the balanced angle, the transmission is maximized and flat, as shown in Fig. 3(a). The numerical calculations are performed by the means of a semi-analytical model which can quantitatively predict the transmission [6, 13]. The zero-order transmittance can be calculated by

$$T_0 = \frac{4p_2^{(1)} p_3 u / \left(1+\beta_3\right)}{\left(p_3 + p_2^{(3)}\right)\left(p_1 + p_2^{(1)}\right) + \left(p_3 - p_2^{(3)}\right)\left(p_2^{(1)} - p_1\right) u^2} \tag{2}$$

where $u = \exp\left(-jn_{eff} k_0 h\right)$ with $k_0 = 2\pi/\lambda_0$. n_{eff} is the effective mode index [11]. $p_1 = 1/\cos\theta_i$, $p_3 = n_1/\cos\theta_t$, $p_2^{(l)} = n_2^2/\left[n_{eff} f g_0^2 \left(1+\beta_l\right)\right]$ ($l = 1$ or 3) with $f = a/d$ and $\beta_l = \sum_{s\neq 0}\left(g_s^2 \cos\theta_i\right)/\left(g_0^2 \gamma_{l,s}\right)$, s is the relative integer. $\gamma_{l,s} = \left[1 - \left(\sin\theta_i + s\mathrm{K}/k_0^2\right)/n_l^2\right]^{1/2}$, $\mathrm{K} = 2\pi/d$, and $g_s = \left(k_0 \sin\theta_i + s\mathrm{K}\right) a/2$.

Figure 3(a) shows the transmission spectral of the grating with different substrates. The refractive indices of the substrate are 1.0 (green), 1.05 (red) and 1.1 (blue), respectively. In the Fig. 3(a), the transmission dips attribute to Wood's anomalies occurring at [14]

$$\lambda = \frac{nd}{m}\left(1 + \sin\theta\right) \quad (m = 1, 2, 3, \ldots) \tag{3}$$

where n is the refractive index of the material in region 1 or 3. θ is the incident angle or the refractive angle.

When the wavelength λ is smaller than $d\left(1+\sin\theta\right)$, the grating is no longer a subwavelength grating. So the non-evanescent wave diffraction appears, resulting in low transmission in the short wavelength range, as presented in Fig. 3(a).

From Fig. 3, one can see that as the increase of the substrate's refractive index, the transmittance drops evidently and the Wood's anomaly becomes non-degenerate. The decrease of the

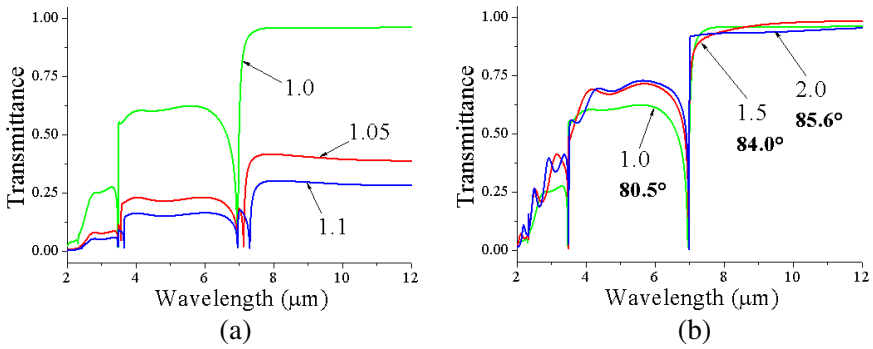

Figure 3: Transmission spectral of a gold grating with slits of depth $h = 4\,\mu\text{m}$, period $d = 3.5\,\mu\text{m}$, and width $a = 0.5\,\mu\text{m}$. (a) The refractive indices of the substrate are 1.0 (green), 1.05 (red) and 1.1 (blue), respectively. Small variation of the refractive index results in great change of the transmission spectral. (b) The refractive indices of the material filling the slits in the grating are 1.0 (green), 1.5 (red) and 2.0 (blue), respectively. As the increase of the refractive index, the balanced angle increases.

transmittance results from the mismatch of the impedances. Equation (2) indicates that the wavelength position of Wood's anomaly depends on the substrate's refractive index. Because the space above the grating is air, the wavelength position of Wood's anomaly at the upper surface of the grating is $d\,(1 + \sin\theta_i)\,/m$ $(m = 1, 2, 3, \ldots)$. However, the wavelength position of Wood's anomaly at the lower surface of the grating is $n_1 d\,(1 + \sin\theta_t)\,/m$ $(m = 1, 2, 3, \ldots)$. Consequently, the previous degenerate Wood's anomaly splits, as depicted in Fig. 3(a). One can see that small variation of the refractive index of the substrate may result in great change of the transmission spectral. So one may expect the optical properties may be helpful for the design of biosensors.

Figure 3(b) presents the transmission spectral with different material filling the slits. The refractive indices of the material filling the slits in the grating are 1.0 (green), 1.5 (red) and 2.0 (blue), respectively. Equation (1) predicts that the balanced angle depends on the refractive index of the material filling the silts of the grating. So when the increase of the filling material's refractive index, the balanced angle increases. Note that the transmittance is not evidently disturbed. And the wavelength position of Wood's anomaly is independent of the filling material's refractive index, as predicted by Equation (3).

3. CONCLUSION

We have studied the optical properties of the metal grating which is transparent for white light. At a balanced angle the Fabry-Perot effect is absent and the transmission curve becomes nearly flat in a long wavelength range. By modifying the refractive index of the substrate the phenomenon of non-degeneracy of the Wood's anomalies appears. As a consequence, more long-wavelength ranges in which the transmission curve is nearly flat appear. Moreover, the transmittance decreases with the increase of the refractive index of the substrate. In addition, the balanced angle can be tuned by modifying the refractive index of the material filling the slits in the grating. And the wavelength position of Wood's anomalies is independent of the refractive index of the material filling the slits.

ACKNOWLEDGMENT

This work was supported by the National Science Foundation of Jiangsu Education Committee of China under Grant No. 10KJB14007, the National Natural Science Foundation of China under Grant No. 11074183, the key project in Natural Science Foundation of Jiangsu Education Committee of China under the Grant No. 10KJA140044, the key project in Science and Technology Innovation Cultivation Program and the plan of Dongwu Scholar Soochow University, and the Project Funded by the Priority Academic Program Development of Jiangsu Higher Education Institutions.

REFERENCES

1. Ebbesen, T. W., H. J. Lezec, H. F. Ghaemi, T. Thio, and P. A. Wolff, "Extraordinary optical transmission through sub-wavelength hole arrays," *Nature*, Vol. 391, 667–669, London, 1998.
2. Porto, J. A., F. J. Garcıa-Vidal, and J. B. Pendry, "Transmission resonances on metallic gratings with very narrow slits," *Phys. Rev. Lett.*, Vol. 83, 2845–2848, 1999.

3. Ung, B. and Y. Sheng, "Interference of surface waves in a metallic nanoslit," *Opt. Express*, Vol. 15, 1182–1190, 2007.
4. Steele, J. M., C. E. Moran, A. Lee, C. M. Aguirre, and N. J. Halas, "Metallodielectric gratings with subwavelength slots: Optical properties," *Phys. Rev. B*, Vol. 68, 205103, 2003.
5. Treacy, M. M. J., "Dynamical diffraction explanation of the anomalous transmission of light through metallic gratings," *Phys. Rev. B*, Vol. 66, 195105, 2002.
6. Cao, Q. and P. Lalanne, "Negative role of surface plasmons in the transmission of metallic gratings with very narrow slits," *Phys. Rev. Lett.*, Vol. 88, 057403, 2002.
7. Pendry, J. B., L. Martın-Moreno, and F. J. Garcia-Vidal, "Mimicking surface plasmons with structured surfaces," *Science*, Vol. 305, 847–848, 2004.
8. Huang, X. R., R. W. Peng, Z. Wang, F. Gao, and S. S. Jiang, "Charge-oscillation-induced light transmission through subwavelength slits and holes," *Phys. Rev. A*, Vol. 76, 035802, 2007.
9. Huang, X. R. and R. W. Peng, "General mechanism involved in subwavelength optics of conducting microstructures: Charge-oscillation-induced light emission and interference," *J. Opt. Soc. Am. A*, Vol. 27, 718–729, 2010.
10. Huang, X. R., R. W. Peng, and R. H. Fan, "Making metals transparent for white light by spoof surface plasmons," *Phys. Rev. Lett.*, Vol. 105, 243901, 2010.
11. Takakura, Y., "Optical resonance in a narrow slit in a thick metallic screen," *Phys. Rev. Lett.*, Vol. 86, 5601–5603, 2001.
12. Suckling, J. R., A. P. Hibbins, M. J. Lockyear, T. W. Preist, and J. R. Sambles, "Finite conductance governs the resonance transmission of thin metal slits at microwave frequencies," *Phys. Rev. Lett.*, Vol. 92, 147401, 2004.
13. Lalanne, P., J. P. Hugonin, S. Astilean, M. Palamaru, and K. D. Moller, "One-mode model and Airy-like formulae for one-dimensional metallic gratings," *J. Opt. A: Pure Appl. Opt.*, Vol. 2, 48–51, 2000.
14. Wood, R. W., "On a remarkable case of uneven distribution of light in a diffraction grating spectrum," *Philos. Mag.*, Vol. 4, 396, 1902.

Extrahigh Color Rendering Color Temperature Tunable White Light LED Cluster with Warm-white Red Green Blue LEDs

G. X. He[1], **J. Xu**[1], **and H. F. Yan**[2]

[1]Department of Applied Physics, Dong Hua University, 1882 Yan'an Road (W), Shanghai 200051, China
[2]Shanghai Yaming Lighting Co., Ltd., 1001 Jiaxin Road, Jiading District, Shanghai 201801, China

Abstract— The realization of correlated color temerature (CCT) tunable white sources with a combination of high color rendering index (CRI) and the special CRI of R9 for strong red is an important challenge in the field of solid-state lighting. The CCT tunable WW/R/G/B LED cluster with extrehigh color rendering property has been found by simulation and fabricated, which consists of three WW LEDs (excited wavelengh $\lambda_o = 450.5\,\text{nm}$, CCT = 3183 K, $\Phi = 62.1\,\text{lm}$, $P_{in} = 1.15\,\text{W}$, and $\eta = 53.9\,\text{lm/W}$ at $I_F = 350\,\text{mA}$), one red LED ($\lambda_o = 634.1\,\text{nm}$, $\Phi = 34.4\,\text{lm}$, and $P_{in} = 0.83\,\text{W}$ at $I_F = 350\,\text{mA}$), one green LED ($\lambda_o = 513.9\,\text{nm}$, $\Phi = 41.0\,\text{lm}$, and $P_{in} = 1.24\,\text{W}$ at $I_F = 350\,\text{mA}$), and one blue LED ($\lambda_o = 456.2\,\text{nm}$, $\Phi = 10.2\,\text{lm}$, and $P_{in} = 1.18\,\text{W}$ at $I_F = 350\,\text{mA}$). The experimental results show that the WW/R/G/B LED cluster can realize the CCT tunable white lights with CRIs of 93 $\sim$ 95, R9s of 90 $\sim$ 96, averages of the special CRIs R9 to R12 of 83 $\sim$ 85, as well as luminous efficacies of 46.8 $\sim$ 56.8 lm/W at CCTs of 2719 K to 6497 K.

1. INTRODUCTION

Semiconductor white light-emitting diodes (LEDs) have attracted a great deal of attention in solid-state lighting applications. Due to their potential for substantial energy savings, high efficiency, small size, and long lifetime, it has been projected that LEDs will broadly replace conventional incandescent and fluorescent lamps for general lighting in the future [1]. An important factor is how well a light source renders the true colors of objects. This factor is known as color rendering index (CRI) [2]. Another important aspect to consider is luminous efficacy (lumens per watt). The term luminous efficacy is normally used as the conversion efficiency from the input electrical power (watt) to the output luminous flux (lumin) and is hereinafter denoted as LE. The challenge in the design of white light LED clusters with correlated tunable color temperatures (CCTs) consists of achieving high CRIs over a reasonable range of color temperatures, while at the same time maximizing LEs. To create CCT tunable LED white lights, many approaches using of three or four LEDs have been adopted. A warm-white/cool-white (WW/CW) cluster, a red/green/blue (R/G/B) cluster, a R/G/B/amber (R/G/B/A) cluster, a WW/G/B cluster and R/G/B/CW cluster have been discussed [3]. Their performance of WW/CW and R/G/B clusters was suboptimal for architectural lighting applications. The R/G/B/A cluster could achieve high CRIs, but the LEs were lower due to the low LEs of red, green, blue and amber LEDs. In addition, the primary disadvantage of this approach was the strong temperature dependency of the amber LED for both wavelength shift and luminous flux. The WW/G/B cluster could achieve the highest CRI (above 90), but LEs was lower duo to low LE of WW LED. The R/G/B/CW cluster could achieve the higher LEs, but CRIs were not good (about 60–70). A 3-color RpcGB system with phosphor-converted red (Rpc) and a 4-color RAGB system were investigated [4]. With both systems, a CRI of at least 80 can be maintained over the relevant color temperature range of approximately 2700 K to 6500 K. It was reported that the apparent emission colors of InGaN-based LEDs using micro-structured multifacet quantum wells as active layers can externally be controlled over a wide spectral range that encompasses green to blue or white at a color temperature of 4000 K to blue along the Planckian locus [5]. A sunlight-style color temperature tunable as well as color temperature span tunable OLED was achieved by employing daylight-complementary emissive constituents with the use of a hole-modulating layer to regulate the distribution of holes [6, 7], however, the CRI was not reported. A CCT tunable phosphor-coated white LED with an omni-directional reflector (ODR) was proposed [8]. The optimum color properties of the resulting white light are (0.3347, 0.3384), 5398 K, 81, 3137 $\sim$ 8746 K for color coordinates, CCT, CRI and CCT tuning range, respectively. In order to analyze numerous designs of white light LED clusters, the model for LED spectra at different drive currents and the simulation program were developed [9]. It was reported that the WW/R/G/B cluster could achieve CRIs above 91.6, but LEs below 64.4 lm/W, that the CW/R/A/G cluster could achieve CRIs above 84.6, but LEs below 52.8 lm/W, that the neutral-white/R/G/B (NW/R/G/B) cluster

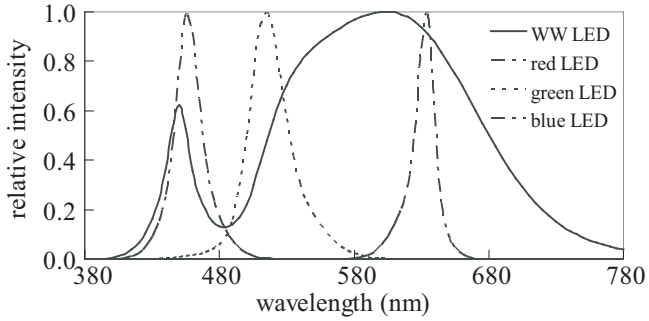

Figure 1: The relative SPDs of WW, red, green and blue LEDs.

Table 1: The predicted and measured results of the WW/R/G/B LED cluster at $T_a = 45°C$.

Predicted results									
	CCT (K)	2703	2952	3431	3922	4490	4976	5715	6547
WW LED	I_F (mA)	273	268	260	250	239	229	214	203
red LED	I_F (mA)	156	126	87	60	44	34	20	10
green LED	I_F (mA)	27	56	88	115	140	160	198	213
blue LED	I_F (mA)	0	12	53	90	129	154	179	210
	dC $\times 10^{-3}$	+1.2	+1.6	−0.9	−2.6	−4.9	−5.2	−3.0	−3.3
	CRI	93	93	94	95	96	96	96	95
	R9	94	88	90	93	98	98	94	91
	R(9-12)	85	82	84	84	86	85	86	85
	R13	98	96	97	98	99	100	97	96
	R15	99	97	98	99	97	97	95	94
	Φ (lm)	173.7	173.5	172.2	169.2	166.4	163.3	159.2	155.0
	η (lm/W)	57.9	57.9	56.2	54.4	52.4	50.9	48.9	47.1
	Measured results								
	CCT (K)	2719	3028	3458	3983	4537	5008	5723	6497
	dC $\times 10^{-3}$	−1.1	−2.6	−3.6	−4.5	−4.7	−5.4	−4.6	−4.9
	CRI	93	93	94	94	95	94	94	94
	R9	90	94	92	95	96	95	96	93
	R(9-12)	84	85	83	84	85	85	84	83
	R13	97	98	98	98	97	98	97	97
	R15	98	99	99	99	95	95	95	94
	Φ (lm)	170.5	166.3	174.8	169.5	163.0	162.7	156.0	151.9
	η (lm/W)	56.8	55.8	56.9	56.4	51.9	50.9	48.5	46.8

could achieve CRIs above 86.2, as well as LEs above 64.4 lm/W [9], and that the NW/R/B cluster could achieve CRIs above 85.7, as well as LEs above 67.4 lm/W [10].

The realization of CCT tunable white sources with a combination of high CRI and special CR R9 for strong red is an important challenge in the field of solid-state lighting (such as art objects, shop window displays, and medical applications). The high R9 have to be considered as requirement for general lighting due to the red-green contrast is very important for color rendering property [11, 12], and red tends to be problematic. Lack of red component shrinks the reproducible color gamut and makes the illuminated scene look dull. In this paper, a CCT tunable WW/R/G/B LED cluster with extrahigh color rendering (CRI > 93 and R9 > 90) at CCTs of 2700 K to 6500 K is found by simulation. The predicted and measured results are presented.

2. SIMULATION AND REALIZATION OF THE WW/R/G/B LED CLUSTER

A model for spectra of single color LED as well as phosphor-coated white LED at different drive currents was developed [9]. To analyze the possible performance of the CCT tunable white light LED cluster, the simulation program has been developed according to the principle of additive color mixture [9]. The simulation program can predict not only the relative SPD, chromaticity

coordinates, but also numbers of LED (N), drive currents (I_F), the input power (P_{in}), the luminous flux (Φ) and the luminous efficacy (LE) according to requirements of CRI, R9, CCT, and the distance from the Planckian locus on the CIE 1960 uv chromaticity diagram (dC), with polarity, plus (above the Planckian locus) or minus (below the Planckian locus) [1]. The CCT tunable WW/R/G/B LED cluster with extrahigh color rendering has been found by simulation analysis, which consists of three WW LEDs (excited wavelengh $\lambda_o = 450.5\,\text{nm}$, CCT = 3183 K, $\Phi = 62.1\,\text{lm}$, $P_{in} = 1.15\,\text{W}$, and $\eta = 53.9\,\text{lm/W}$ at $I_F = 350\,\text{mA}$), one red LED ($\lambda_o = 634.1\,\text{nm}$, $\Phi = 34.4\,\text{lm}$, and $P_{in} = 0.83\,\text{W}$ at $I_F = 350\,\text{mA}$), one green LED ($\lambda_o = 513.9\,\text{nm}$, $\Phi = 41.0\,\text{lm}$, and $P_{in} = 1.24\,\text{W}$ at $I_F = 350\,\text{mA}$), and one blue LED ($\lambda_o = 456.2\,\text{nm}$, $\Phi = 10.2\,\text{lm}$, and $P_{in} = 1.18\,\text{W}$ at $I_F = 350\,\text{mA}$).

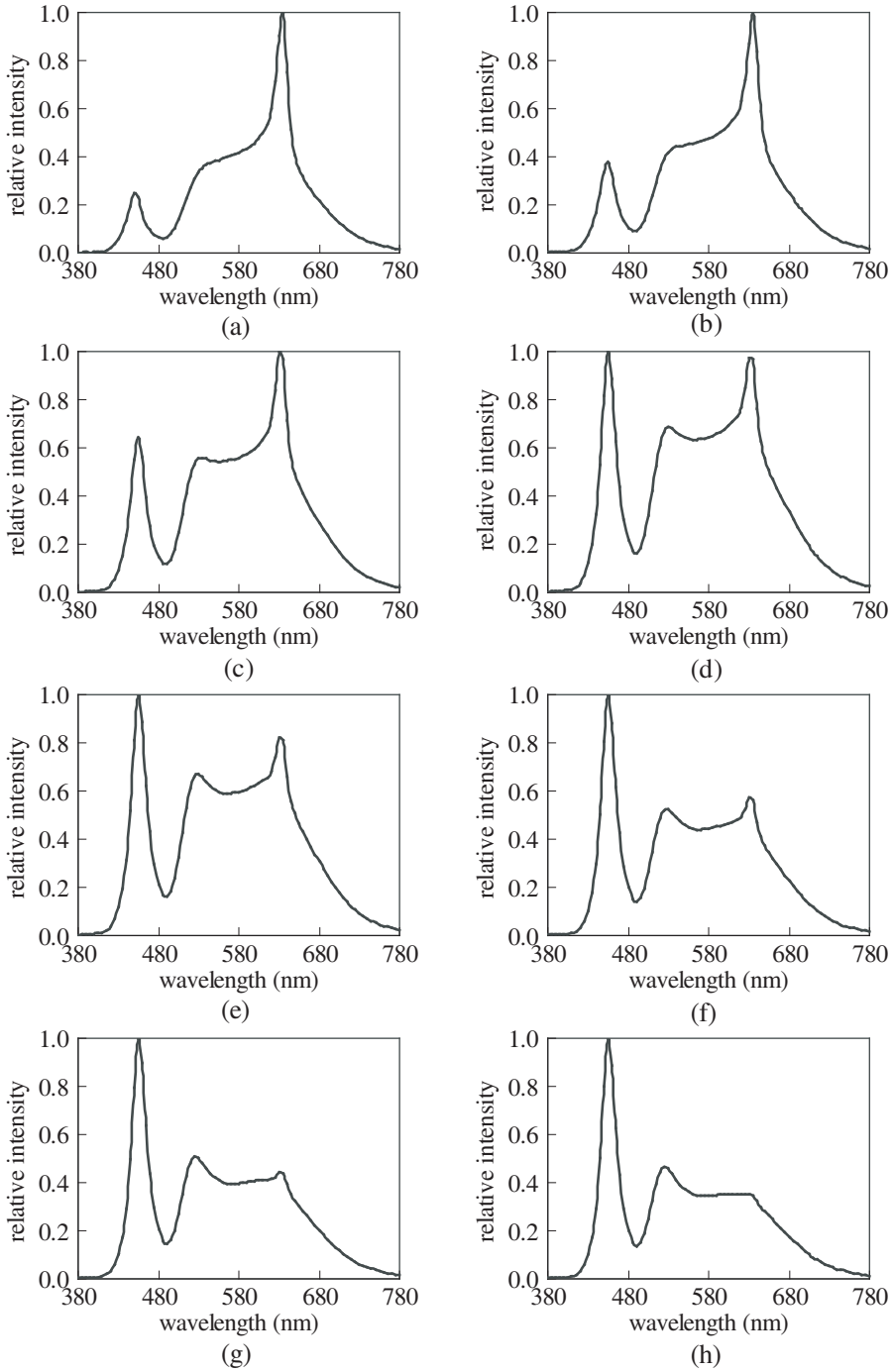

Figure 2: The measured SPDs of the WW/R/G/B LED cluster at different CCTs: (a) CCT = 2719 K; (b) CCT = 3028 K; (c) CCT = 3458 K; (d) CCT = 3983 K; (e) CCT = 4537 K; (f) CCT = 5008 K; (g) CCT = 5727 K; (h) CCT = 6497 K.

The relative SPDs of WW, red, green and blue LEDs are shown in Fig. 1. The predicted and measured results of WW/R/G/B LED cluster at an ambient temperature (T_a) of 45°C are shown in Table 1. The SPD and luminous flux of the cluster are measured by using the spectroradiometer with an integrating sphere. R(9–12) in the Table 1 is the average of the special CRIs R9 to R12 of the four saturated colors (red, yellow, green, and blue). The Table 1 indicates that the predicted results are very close to the measured values. The measured SPDs of the WW/R/G/B LED cluster at different CCTs are show in Fig. 2. The experimental results show that this cluster can realize CCT tunable white lights with CRIs of 93 $\sim$ 95, R9s of 90 $\sim$ 96, R(9–12)s of 83 $\sim$ 85, as well as a LEs of 46.8 $\sim$ 56.8 lm/W at CCTs of 2719 K to 6497 K. Furthermore, its special CRIs of R13 and R15 corresponding to the colors of the skin on the face of European and Chinese women are also very high (R13 $>$ 97 and R15 $>$ 94). R13 and R15 are especially important for interior lighting.

3. CONCLUSIONS

The WW/R/G/B LED cluster consisting of three WW LEDs (excited wavelengh $\lambda_o = 450.5$ nm, CCT = 3183 K, $\Phi = 62.1$ lm, $P_{in} = 1.15$ W, and $\eta = 53.9$ lm/W at $I_F = 350$ mA), one red LED ($\lambda_o = 634.1$ nm, $\Phi = 34.4$ lm, and $P_{in} = 0.83$ W at $I_F = 350$ mA), one green LED ($\lambda_o = 513.9$ nm, $\Phi = 41.0$ lm, and $P_{in} = 1.24$ W at $I_F = 350$ mA), and one blue LED ($\lambda_o = 456.2$ nm, $\Phi = 10.2$ lm, and $P_{in} = 1.18$ W at $I_F = 350$ mA) can realize the CCT tunable white lights with CRIs of 93 $\sim$ 95, R9s of 90 $\sim$ 96, R(9–12)s of 83 $\sim$ 85, as well as a LEs of 46.8 $\sim$ 56.8 lm/W at CCTs of 2719 K to 6497 K.

ACKNOWLEDGMENT

This work was supported by Shanghai Science and Technology Committee (No.09DZ1141100) and the National "ITER" Project of Ministry of Science and technology of P. R. China (No. 2009GB107006 and No. 2010GB107003).

REFERENCES

1. Schubert, E. F. and J. K. Kim, "Solid-state light sources getting smart," *Science*, Vol. 308, No. 5726, 1274–1278, 2005.
2. International Commission on Illumination, "Method of measuring and specifying colour rendering properties of light sources," 1995, ISBN 978–3900734572.
3. Speier, I. and M. Salsbury, "Color temperature tunable white light LED system," *Proc. SPIE*, Vol. 6337, 63371F, 2006.
4. Hoelen, C., J. Ansems, P. Deurenberg, W. van Duijneveldt, M. Peeters, G. Steenbruggen, T. Treurniet, A. Valster, and J. W. ter Weeme, "Color-tunable LED spot lighting," *Proc. SPIE*, Vol. 6337, 63370Q, 2006.
5. Funato, M., K. Hayashi, M. Ueda, Y. Kawakami, Y. Narukawa, and T. Mukai, "Emission color tunable light-emitting diodes composed of InGaN multifacet quantum wells," *Appl. Phys. Lett.*, Vol. 93, No. 22, 021126, 2008.
6. Jou, J. H., C. J. Wang, Y. P. Lin, P. H. Chiang, M. H. Wu, C. P. Wang, C. L. Lai, and C. Chang, "Color-stable, efficient fluorescent pure-white organic light-emitting diodes with device architecture preventing excessive exciton formation on guest," *Appl. Phys. Lett.*, Vol. 92, No. 22, 223504, 2008.
7. Jou, J. H., M. H. Wu, S. M. Shen, H. C. Wang, S. Z. Chen, S. H. Chen, C. R. Lin, and Y. L. Hsieh, "Sunlight-style color-temperature tunable organic light-emitting diode," *Appl. Phys. Lett.*, Vol. 95, No. 1, 013307, 2009.
8. Su, J. C. and C. L. Lu, "Color temperature tunable white light emitting diodes packaged with an omni-directional reflector," *Optics Express*, Vol. 17, No. 24, 21408–21413, 2009.
9. He, G. X. and L. H. Zheng, "Color temperature tunable white-light light-emitting diode clusters with high color rendering index," *Applied Optics*, Vol. 49, No. 24, 4670–4676, 2010.
10. He, G. X. and L. H. Zheng, "White light LED clusters with high color rendering," *Optics Letters*, Vol. 35, No. 17, 2955–2957, 2010.
11. Worthey, J., "Color rendering: Asking the questions," *Color Res. Appl.*, Vol. 28, No. 6, 403–412, 2003.
12. Hashimoto, K. and Y. Nayatani, "Visual clarity and feeling of contrast," *Color Res. Appl.*, Vol. 19, No. 3, 171–185, 1994.

Spectral Optimization of Warm-white LED with Red LED Instead of Red Phosphor under Conditions of CRI $\geqslant$ 90 and R9 $\geqslant$ 90

G. X. He[1], **J. Xu**[1], **and H. F. Yan**[2]

[1]Department of Applied Physics, Dong Hua University, 1882 Yan'an Road (W), Shanghai 200051, China
[2]Shanghai Yaming Lighting Co., Ltd., 1001 Jiaxin Road, Jiading District, Shanghai 201801, China

Abstract— The realization of correlated color temerature (CCT) tunable white sources with a combination of high color rendering index (CRI) and the special CRI of R9 for strong red is an important challenge in the field of solid-state lighting. The CCT tunable WW/R/G/B LED cluster with extrehigh color rendering property has been found by simulation and fabricated, which consists of three WW LEDs (excited wavelengh λ_o = 450.5 nm, CCT = 3183 K, Φ = 62.1 lm, P_{in} = 1.15 W, and η = 53.9 lm/W at I_F = 350 mA), one red LED (λ_o = 634.1 nm, Φ = 34.4 lm, and P_{in} = 0.83 W at I_F = 350 mA), one green LED (λ_o = 513.9 nm, Φ = 41.0 lm, and P_{in} = 1.24 W at I_F = 350 mA), and one blue LED (λ_o = 456.2 nm, Φ = 10.2 lm, and P_{in} = 1.18 W at I_F = 350 mA). The experimental results show that the WW/R/G/B LED cluster can realize the CCT tunable white lights with CRIs of 93 $\sim$ 95, R9s of 90 $\sim$ 96, averages of the special CRIs R9 to R12 of 83 $\sim$ 85, as well as luminous efficacies of 46.8 $\sim$ 56.8 lm/W at CCTs of 2719 K to 6497 K.

1. INTRODUCTION

White LED lamps have promising features such as small size, safety, long lifetime, and are mercury-free, so they are expected to replace conventional incandescent and fluorescent lamps for general lighting applications in the near future [1]. The luminous efficacy (LE) of white LED lamp now exceeds not only to that of conventional incandescent lamps but also to that of fluorescent lamps. With the luminous efficacy of white LEDs progressing steadily, however, their color rendering properties cannot fully meet the requirements for general lighting applications, and are needed to be improved greatly. Different from an incandescent lamp or a fluorescent lamp, the phosphor-coated white LED (p-W LED) do not cause the damage to the illuminated body, because they do not give infrared ray and ultraviolet (UV) ray. Therefore, they are considered to be very suitable for lighting for art objects, shop window displays, and medical applications, but these purposes require much higher color rendering properties. However, the p-W LED suffers from low luminous efficacy due to down-conversion and relatively broad emission spectra [2, 3]. A solution for producing white-light LED cluster using the red LED and the p-W LED with green and orange phosphors excited by blue LED die was proposed in order to overcome the low conversion efficiency of red phosphor [4, 5]. It has been reported that the W/R LED cluster consisting of the red LED and p-W LED had achieved warm-wihte light with high color rendering properties and and high luminous efficacy. However, the spectral power distribution (SPD) of p-W LED is not optimal. To determine optimized peak wavelengths of red LED, blue LED die, green and yellow phosphors for maximizing the LER while the CRI and the special CRI of R9 for strong red above 90, a model for spectra of the white-light LED with p-W LED and red LED is presented. In this paper, the optimal spectra of the p-W LED and the red LED in the warm-white W/R LED cluster (WWLED) with CCT = 2700 K have been found by nonlinear program for maximizing the luminous efficacy of radiation (LER) while both color rendering index (CRI) and special CRI R9 for strong red above 90. The real WWLED is fabricated and measured at an ambient temperature (Ta) of 45°C. Optimal wavelength combinations and experimental results are presented.

2. SPECTRAL OPTIMIZATION OF THE WWLED

A WWLED consists of the red LED and p-W LED with blue LED die, green and orange phosphors. The relative SPD of WWLED, $S_{WW}(\lambda)$, is given by,

$$S_{WW}(\lambda) = q_b S_b(\lambda) + q_g S_g(\lambda) + q_{or} S_{or}(\lambda) + q_R S_R(\lambda) \tag{1}$$

where $S_b(\lambda)$ refers to relative SPD of the blue spectrum transmitted through the phosphors, $S_g(\lambda)$ and $S_{or}(\lambda)$ refer to the relative emission spectra of green and orange phosphors respectively, $S_R(\lambda)$ refers to the relative SPD of red LED, q_b, q_g, q_{or} and q_R are proportions of the relative spectra of

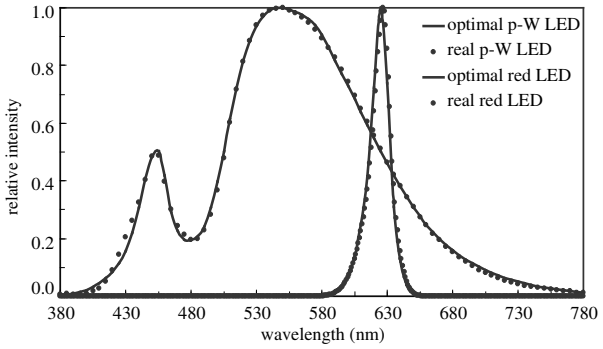

Figure 1: Optimal and real SPDs of the p-W LED and the red LED.

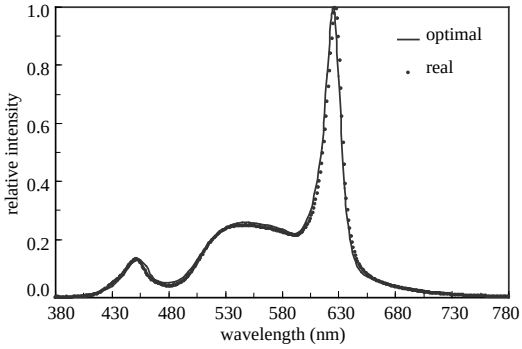

Figure 2: SPDs of the optimal and real WWLEDs.

Table 1: Optimal proportions, relative luminous and radation fluxs of $S_b(\lambda)$, $S_g(\lambda)$, $S_{or}(\lambda)$ and $S_R(\lambda)$.

	$S_b(\lambda)$	$S_g(\lambda)$	$S_{or}(\lambda)$	$S_R(\lambda)$
q	0.1295	0.2233	0.1368	0.8708
$\Phi(\%)$	1.5	49.7	27.2	21.6
$\Phi_e(\%)$	9.7	33.4	26.1	30.8

$S_b(\lambda)$, $S_g(\lambda)$, $S_{or}(\lambda)$ and $S_R(\lambda)$ respectively. The relative SPD of the single color LED, $S(\lambda)$, was given as [6],

$$S(\lambda) = \left\{\exp\left[-(\lambda-\lambda_0)^2/(\Delta\lambda)^2\right] + k_1 \exp\left[-k_2(\lambda-\lambda_0)^2/(\Delta\lambda)^2\right]\right\}/(1+k_1) \tag{2}$$

where $\Delta\lambda = \begin{cases} \Delta\lambda_1, (\lambda < \lambda_o) \\ \Delta\lambda_2, (\lambda \geqslant \lambda_o) \end{cases}$, $k_i = \begin{cases} k_i^1, & (\lambda < \lambda_o) \\ k_i^2, & (\lambda \geqslant \lambda_o) \end{cases}$ $(i = 1, 2,)$, λ_o refers to peak wavelength, $\Delta\lambda_1$ refers to the left half-spectral-width (HSW) which is $2\int_{380\,\mathrm{nm}}^{\lambda_o} S(\lambda)d\lambda$, $\Delta\lambda_2$ refers to the right HSW which is $2\int_{\lambda_o}^{780\,\mathrm{nm}} S(\lambda)d\lambda$, and $\Delta\lambda_o$ refers to the HSW which is $(\Delta\lambda_1 + \Delta\lambda_2)/2$, $k_i\,(i = 1, 2)$ refers to characteristic parameters of spectral shape. The units of peak wavelength and HSW are nm. Also $S_g(\lambda)$ and $S_{or}(\lambda)$ can be expressed by Eq. (2).

Consider a SPD that contains emission spectrum from AlGaInP red LED as well as p-W LED with a InGaN blue LED die, silicate green and silicate orange phosphors of the WWLED. We employ model SPD of Eq. (2) for AlGaInP red LED, InGaN blue LED die and silicate phosphors. Since photon energy linewidths of InGaN blue and AlGaInP red LEDs about 5 kT and 2 kT respectively, HSW of $S_R(\lambda)$ is assumed to 20 nm, and HSW of $S_b(\lambda)$ is assumed to be 32 nm duo to broadening blue spectra transmitted through the phosphors. Subjecting the 8-dimensional parameter space to three color-mixing constrains results in the location of the feasible vectors on the hypersurface with 5 dimensionality [7]. It was found that the high CRI is not good color rendering for white LED sources [8–10]. Poor color rendering of white LED with high CRI is duo to low special CRIs of R9 to R12 for the four saturated colors (red, yellow, green, and blue) [11, 12]. The special CRI R9 is very important to visual color rendering so that CRI and R9 are considered in optimization of WWLED. In order to optimize spectra of the WWLED lamp, we introduce an objective function

$$F(\lambda_R, \lambda_b, \lambda_g, \lambda_{or}, q_R) = \mathrm{LER} \quad (\text{under conditions of CRI} \geqslant 90 \text{ and } R9 \geqslant 90) \tag{3}$$

where λ_R, λ_b, λ_g and λ_{or} refer to peak wavelengths of $S_R(\lambda)$, $S_b(\lambda)$, $S_g(\lambda)$ and $S_{or}(\lambda)$, respectively. Hence the optimization problem reduces to finding maxima of the objective function under conditions of CRI $\geqslant$ 90 and R9 $\geqslant$ 90. Nine silicate green (510 nm $\sim$ 546 nm) phosphors and five silicate orange (580 nm $\sim$ 606 nm) phosphors are used in optimization.

The WWLED with extrahigh CRI and R9 as well as high LER at CCT of 2700 K, which consists of p-W LED and red LED, has been obtained by nonlinear program for maximizing the objective function F while both CRI and R9 above 90 at CCT of 2700 K. Optimal peak wavelengths of red LED, blue LED die, silicate green and orange phosphors are 626 nm, 454 nm, 535 nm and 584 nm, respectively. The optimal proportions, relative luminous fluxs ($\Phi\%$) and relative radation fluxs ($\Phi_e\%$) of $S_b(\lambda)$, $S_g(\lambda)$, $S_{or}(\lambda)$ and $S_R(\lambda)$ are shown in Table 1. The CCT and chromaticity coordinates (u, v) of the p-W LED are 4599 K and (0.1854, 0.3593), respectively. The optimal

Table 2: Color redering properties and luminous efficacy (of radiation) of optimal and real WWLED.

WWLED lamp	CCT (K)	dC	CRI	R9	R(9–12)	R13	R15	LER (lm/W)	LE (lm/W)
optimal	2700	0.0007	92.5	90.4	88.5	92.2	94.4	343.6	
real	2653	0.0001	90.4	93.7	88.3	91.1	91.5	340.7	80.2

Table 3: The CCTs, chromaticity coordinates, color rendering properties, luminous fluxs and luminous efficacies of the real WWLED at different drive currents of the red LED.

red LED: I_F (mA)	350	330	310	290	270	250	230	210
CCT (K)	2392	2448	2511	2578	2653	2817	2910	3014
u	0.2787	0.2755	0.2720	0.2684	0.2645	0.2567	0.2525	0.2480
v	0.3520	0.3520	0.3521	0.3522	0.3522	0.3523	0.3524	0.3525
dC	0.0034	0.0027	0.0019	0.0010	0.0001	0.0024	0.0038	0.0055
CRI	86	87	88	89	90	92	93	93
R9	86	88	89	91	94	95	92	86
R(9–12)	87	89	89	89	88	86	84	81
R13	84	85	87	89	91	96	98	98
R15	86	87	89	90	92	95	98	99
Φ (lm)	516.7	508.9	501.2	493.2	485.4	469.5	461.7	453.6
LE (lm/W)	78.2	78.5	79.2	79.7	80.2	79.4	79.9	80.3

SPDs of the p-W LED and the red LED are shown in Fig. 1. The SPD of the optimal WWLED is shown in Fig. 2. The color rendering properties and LER of optimal WWLED are shown in Table 2. R(9–12) in the Table 2 is the average of the special CRIs R9 to R12. The results show that the optimal WWLED could realize white-light with CRI = 92, R9 = 90, R(9–12) = 88 as well as LER = 343.6 lm/W at CCT of 2700 K. The p-W LED with the spectra shown in Fig. 1 could be realize white-light with high luminous efficacy, and the relative luminous flux of the p-W LED in the WWLED lamp is 78.4%, therefore the WWLED could realize warm-white-light with extrahigh color rendering properties as well as high luminous efficacy.

3. REALIZATION OF THE WWLED

The p-W LED (CCT = 4579 K, Φ = 96.5 lm, P_{in} = 1.10 W, and LE = 87.7 lm/W at I_F = 350 mA) with a InGaN blue LED die (451.6 nm), 56% silicate green (535 nm) and 44% orange (584 nm) phosphors, and the AlGaInP red LED (627.2 nm, Φ = 44.2 lm, and P_{in} = 0.74 W at I_F = 350 mA) are fabricated and measured at an ambient temperature (T_a) of 45°C. The real SPDs of the p-W LED (4579 K) and red LED (627.2 nm) are shown in Fig. 2. The numbers of LED (N), drive currents (I_F) according to requirements of CCT, CRI, R9 and input power (P_{in}) of the WWLED can be predicted by using He-Zheng model [6]. The real WWLED consists of four p-W LEDs and three red LEDs. The drive currents of p-W LED and red LED are 350 mA and 270 mA, respectively. The SPD of the real WWLED is shown in Fig. 2. The color redering properties and luminous efficacy of the real WWLED at an ambient temperature (T_a) of 45°C are shown in Table 2. The experimental results show that the real WWLED can realize the warm-white-light with CCT = 2653 K, CRI = 90.4, R9 = 93.7 and R(9–12) = 88.3, as well as LE = 80.2 lm/W. Furthermore, their special CRIs of R13 and R15 corresponding to the colors of the skin on the face of European and Chinese women are also very high. Both R13 and R15 are especially important for interior lighting.

The AlInGaP red LED and p-W LED with InGaN LED die as well as phosphors and exhibit different the long term degradation and aging characteristics. Both CCT and CRI of the WWLED will be changed duo to different the long term degradation and aging characteristics. To simulate the influence of relative intensity of red LED on CCT as well as CRI, the WWLEDs at different drive currents of the red LED are measured. The CCTs, chromaticity coordinates, color rendering properties, luminous fluxs and luminous efficacies of the real WWLED at different drive currents of red LED are shown in Table 3. The experimental results show that the WWLED keep high color rendering properties and luminous efficacy in despite of decreasring or inreasing the relative luminous flux of the red LED. Therefor, the WWLED can relized CCT tunable warm-white-lights with CRIs of 86 $\sim$ 93, R9s of 86 $\sim$ 95, R(9–12) s of 81 $\sim$ 89 and LEs of 78.2 $\sim$ 80.3 lm/W at CCTs of 2392 K to 3014 K by adjusting drive current of the red LED.

4. DISCUSSION

The luminous efficacy of WWLED with extrahigh color rendering properties is dependence on that of p-W LED and is about 91% of p-W LED. The luminous efficacy of p-W LED in our experiment is only 87.7 lm/W duo to lower radiant efficiency blue LED die (about 350 mW/W). If the blue LED die with radiant efficiency of 500 mW/W is applied to the p-W LED, The luminous efficacy of the p-W LED will attain to about 125 lm/W, and the luminous efficacy of the WWLED will rise to about 114 lm/W. The p-W LED and red LED will exhibit different long-term degradation rates that will change the resulting spectral distribution of the WWLED. This could be solved by adjusting drive currents of LEDs according to the ratio of their light intensity, which could be measured by an auxiliary detector in the WWLED. Detailed solutions need to be further explored.

5. CONCLUSIONS

The optimal WWLED consists of AlGaInP red LED ($\lambda_o = 626$ nm), and the p-W LED (4599 K) packaged by combining silicate green (535 nm) and orange (584 nm) phosphors with a InGaN blue LED die (454 nm). It could realize warm-white-light with CRI = 92, R9 = 90, R(9–12) = 88, as well as LER = 343.6 lm/W. The real WWLED with CCT = 2653 K, CRI = 90, R9 = 94 and R(9–12) = 88, as well as LE = 80.2 lm/W is fabricated. The experimental results show that the WWLED keep high color rendering properties and luminous efficacy in despite of decreasring or inreasing relative luminous flux of the red LED. Furthermore, it has been found that the WWLED lamp can relized CCT tunable warm-white-light with CRIs of 86 $\sim$ 93, R9s of 86 $\sim$ 95, R(9–12)s of 81 $\sim$ 89 and LEs of 78.2 $\sim$ 80.3 lm/W at CCTs of 2392 K to 3014 K by adjusting drive current of the red LED. The luminous efficacy of the WWLED could rise to about 114 lm/W if the p-W LED with LE of 125 lm/W is used.

ACKNOWLEDGMENT

This work was supported by Shanghai Science and Technology Committee (No. 09DZ1141100) and the National "ITER" Project of Ministry of Science and technology of P. R. China (No. 2009GB1070-06 and No. 2010GB107003).

REFERENCES

1. Schubert, E. F. and J. K. Kim, "Solid-state light sources getting smart," *Science*, Vol. 308, No. 5726, 1274–1278, 2005.
2. Kimura, N., K. Sakuma, S. Hirafune, K. Asano, N. Hirosaki, and R. J. Xie, "Extrahigh color rendering white light-emitting diode lamps using oxynitride and nitride phosphors excited by blue light-emitting diode," *Appl. Phys. Lett.*, Vol. 90, No. 5, 051109, 2007.
3. Wu, H., C. Wang, and S. He, "Research of color rendering of white LED based on red and green phosphors," *Acta Optica Sinica*, Vol. 28, No. 9, 1777–1782, 2008.
4. He, G. X. and L. H. Zheng, "White light LED clusters with high color rendering," *Optics Letters*, Vol. 35, No. 17, 2955–2957, 2010.
5. He, G. X. and H. F. Yan, "Optimal spectra of the phosphor-coated white LEDs with excellent color rendering property and high luminous efficacy of radiation," *Optics Express*, Vol. 19, No. 3, 2519–2529, 2011.
6. He, G. X. and L. H. Zheng, "Color temperature tunable white-light light-emitting diode clusters with high color rendering index," *Applied Optics*, Vol. 49, No. 24, 4670–4676, 2010.
7. Mereno, J. I. and U. Contreras, "Color distribution from muticolor LED arrays," *Optics Express*, Vol. 15, No. 6, 3607–3618, 2007.
8. Narendran, N. and L. Deng, "Color rendering properties of LED light sources," *Proc. SPIE*, Vol. 4776, 61–67, 2002.
9. Sándor, N., P. Csuti, P. Bodrogi, and J. Schanda, "Visual observation of colour rendering," *Proc. CIE Symposium'04 on "LED Light Sources"*, Tokyo, Japan, Jun. 16–19, 2004.
10. Sándor, N. and J. Schanda, "Visual colour rendering based on colour difference evaluations," *Light. Res. Technol.*, Vol. 38, No. 3, 225–239, 2006.
11. Worthey, J., "Color rendering: Asking the questions," *Color Res. Appl.*, Vol. 28, No. 6, 403–412, 2003.
12. Hashimoto, K. and Y. Nayatani, "Visual clarity and feeling of contrast," *Color Res. Appl.*, Vol. 19, No. 3, 171–185, 1994.

Design of an All-optical Controllable Switch Using Dipole Induced Transparency (DIT)

K. Abbasian[1], **K. Eftekhari**[2], **and A. Rostami**[1]

[1]School of Engineering-Emerging Technologies, University of Tabriz, Tabriz 51666, Iran
[2]Technical & Engineering University of Bonab, Province of East Azarbaijan, Iran

Abstract— In this paper, we have proposed an all-optical controllable switch with ultrahigh speed by using dipole induced transparency effect applied on 5-level nanocrystal doped in photonic crystal (PC) cavity. By applying the third control field the PC cavity, comprising 5-level nanocrystal, has been converted to transparent one and switching operation has been occurred. Then by applying the second or first control field, the transparent PC cavity has been changed to opaque one again. However,applying both of the second and the first control field simultaneously can change the opaque PC cavity to transparent medium again. Analytical relation of this all optical switch has been presented and investigated in different situations of parameters on switching characteristics.

1. INTRODUCTION

Many theoretical and experimental works has been done on Quantum information processing or all-optical communication as one of all-optical discipline, recently. So in recent years, many valuable works has been done on EIT specially on solid state atomic systems with few photon level, where multilevel nanocrystals are realized by quantum dots (QD) [1, 2]. Theoretical and experimental research on QDs and multilevel atomic systems is on the frontier of research, which has seen rapid progress.

All-optical switching (AOS) is one of the main building blocks of quantum information processing and all-optical communication. So, study of AOS is very interested to many scientists. In some of researches, all-optical switch is based on nonlinear optics and Nonlinear phase shift, which requires strength optical intensity, so it is difficult and expensive.

In this paper, we have suggested doping a single multilevel atomic system in a PC cavity, which is coupled to input and output waveguides. By using DIT, where perpendicular applied control fields to the cavity is strong enough, we have got strong Purcell regime ($g^2/\kappa\gamma > 1$). Where γ is the QD decay into modes other than the cavity mode, κ is the cavity field decay rate and g is the coupling between the cavity and the QD [2, 3].

2. THEORY BACKGROUND

In this paper, we have proposed an all-optical controllable normal on or off switch, illustrated in Fig. 1. Including two coupled waveguides a, b by using a two dimensional photonic crystal cavity doped with a 5-level nanocrystal (QD). In this configuration input signal propagates in waveguide a, and three control fields are applied in perpendicular dimension to the PC cavity. In the absent of control fields, waveguides are transparent and PC cavity is opaque, so the input signal field propagates in waveguide a. While in presence of E_{c3} control field, the cavity becomes transparent to the input signal. Then the input signal is switched to the waveguide b via PC cavity. By applying one of the Ec1 or Ec2 control fields, the PC cavity becomes opaque again. But by applying both of Ec1 and Ec2 the PC cavity becomes transparent again. To illustrate these processes, we consider 5-level atomic system that can be realized using suitable QDs structures. In absent of control fields, the nanocrystal has $|1>, |2>, |3>, |4>$ and $|5>$ bare states [2–5].

Now, we can observe that how the PC cavity changes from an opaque case to a transparent one and vice versa, which is in result of shifted nanocrystal states by applying strong control fields. Thereby after shifting the probe signal resonant with transition energy between excited and ground states. Then the input field transmits from original waveguide into another through the cavity.

The Hamiltonian of the 5-level system, by using Rotating wave approximation, can be written as [4].

Based on the considered Hamiltonian, dynamics of the annihilation operator, $\hat{c}$, transition operators of σ_-^{15}, σ_-^{24}, σ_-^{34} and σ_-^{45} are obtained by using the Heisenberg equations.

By using Fourier transformation with some approximations and mathematical manipulations, the following relations are given for output modes of the waveguides. Where, we have assumed

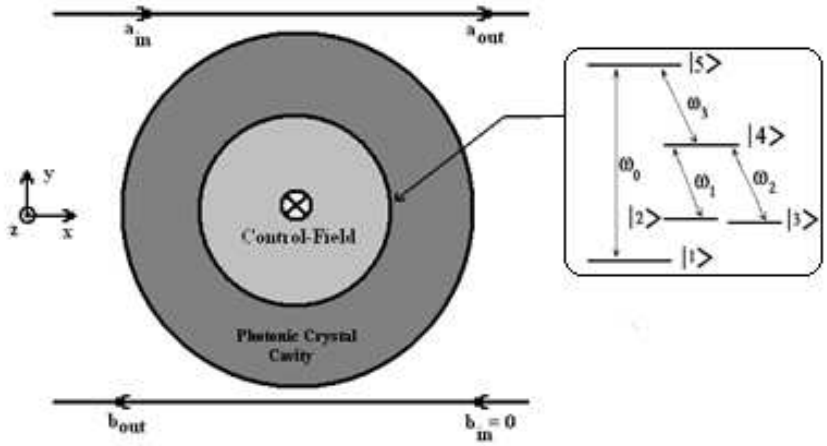

Figure 1: Proposed PC cavity-waveguide switch system, including schematic of 5-level nanocrystal doped in PC cavity.

that the optical signal is very weak to transit electrons from the bottom state to the upper state and the control field is sufficiently far from resonant, so population transition by control field is neglected too [1, 7]. If we start simplifying of the dynamics equations by inserting σ_{-}^{24} in σ_{-}^{34} after some mathematical manipulation, the outputs of waveguides are calculated as following equations

$$\begin{aligned} a_{out} &= \frac{-\gamma b_{in} + \left(i\delta_0 + \kappa/2 + \frac{g^2}{-i\delta_{15}+\Gamma/2-S_3}\right) a_{in}}{\left(-i\delta_0 + \gamma + \kappa/2 + \frac{g^2}{-i\delta_{15}+\Gamma/2-S_3}\right)}, \\ b_{out} &= \frac{-\gamma b_{in} + \left(i\delta_0 + \kappa/2 + \frac{g^2}{-i\delta_{15}+\Gamma/2-S_3}\right) a_{in}}{\left(-i\delta_0 + \gamma + \kappa/2 + \frac{g^2}{-i\delta_{15}+\Gamma/2-S_3}\right)}, \end{aligned} \tag{1}$$

where, dependency of output fields to the control fields are given by the following equations,

$$S_1 = \frac{\Omega_1^2}{-i\delta_{24} + \Gamma/2}, \qquad S_2 = \frac{\Omega_2^2}{-i\delta_{34} + \Gamma/2 - S_1}, \qquad S_3 = \frac{\Omega_3^2}{i\delta_{45} + \Gamma/2 - S_1 + \frac{\Omega_2^2}{-i\delta_{34}+\Gamma/2-S_1}}, \tag{2}$$

However, if we start simplifying of the dynamics equations by inserting σ_{-}^{34} in σ_{-}^{24} after some mathematical manipulation, the outputs of waveguides are given by the following equations

$$\begin{aligned} a_{out} &= \frac{-\gamma b_{in} + \left(-i\delta_0 + (\kappa/2) + \frac{g^2}{-i\delta_{15}+(\Gamma/2)-S_3'}\right) a_{in}}{\left(-i\delta_0 + \gamma + (\kappa/2) + \frac{g^2}{-i\delta_{15}+(\Gamma/2)-S_3'}\right)}, \\ b_{out} &= \frac{-\gamma b_{in} + \left(-i\delta_0 + (\kappa/2) + \frac{g^2}{-i\delta_{15}+(\Gamma/2)-S_3'}\right) a_{in}}{\left(-i\delta_0 + \gamma + (\kappa/2) + \frac{g^2}{-i\delta_{15}+(\Gamma/2)-S_3'}\right)}, \end{aligned} \tag{3}$$

where, dependency of outputs to the control fields are obtained by

$$S_2' = \frac{\Omega_2^2}{-i\delta_{34} + \Gamma/2}, \quad S_1' = \frac{\Omega_1^2}{-i\delta_{24} + (\Gamma/2) - S_2}, \quad S_3' = \frac{\Omega_3^2}{i\delta_{45} + (\Gamma/2) - S_2' + \frac{\Omega_1^2}{-i\delta_{24}+(\Gamma/2)-S_2}}, \tag{4}$$

where detuning of the cavity mode, the probe and control fields' frequencies from the corresponding resonant frequencies are defined by

$$\delta_0 = \omega_c - \omega_0, \quad \delta_{15} = \omega - \omega_{15}, \quad \delta_{34} = \omega_2 - \omega_{34}, \quad \delta_{24} = \omega_1 - \omega_{24}, \quad \delta_{45} = \omega_3 - \omega_{45} \tag{5}$$

Now, we can calculate the transmission coefficients of the waveguides by following equations

$$T_a = \frac{\langle a_{out}^{\dagger} a_{out} \rangle}{\langle a_{in}^{\dagger} a_{in} \rangle}, \quad T_b = \frac{\langle b_{out}^{\dagger} b_{out} \rangle}{\langle a_{in}^{\dagger} a_{in} \rangle}, \tag{6}$$

3. SIMULATION RESULTS

In Figs. 2, 3 and 4 transmission coefficient of PC cavity-waveguide switch system doped with 5-level nanocrystal is represented. Fig. 2 shows the transmission coefficient versus the Rabi frequency of Ω_3 with constant values of $\Omega_1 = \Omega_2 = 1\,\mathrm{GHz}$. We can see that for $\Omega_3 = 0$ the input optical field transmits directly without coupling with the PC cavity, i.e., $T_a \approx 1$. By increasing the Rabi frequency of Ω_3, input optical field couples to the PC cavity and therefore T_a decreases and T_b increases continuously, because of the destructive interference of the $|2>-|4>$ and $|3>-|4>$

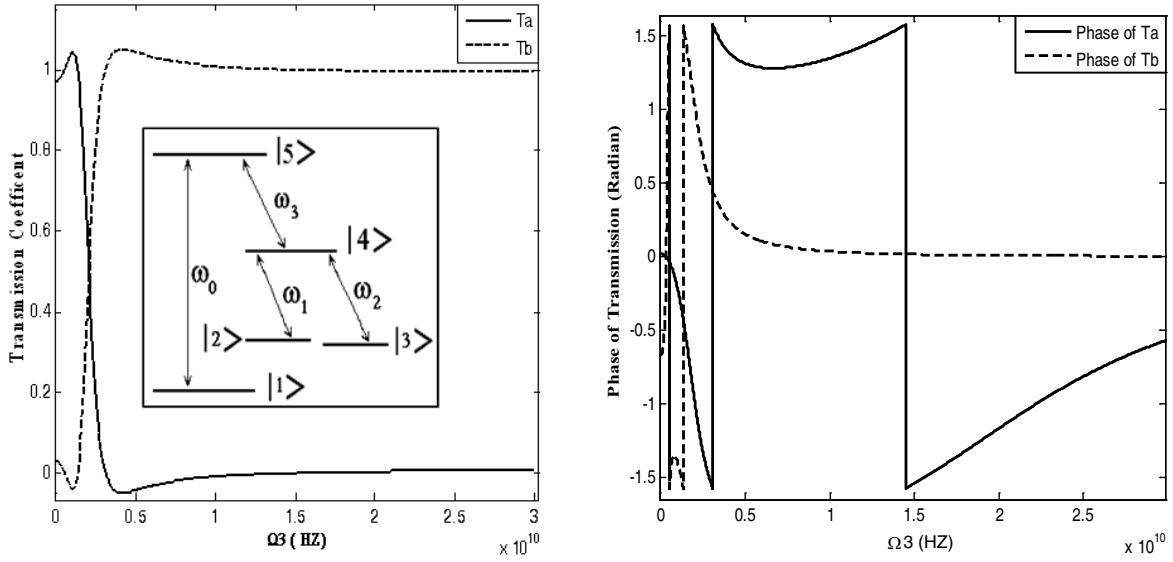

Figure 2: Transmission Coefficient vs. Rabi frequency of the third control field to 5-level nanocrystal. $\delta_0 = 0$, $\delta_{15} = 0$, $\delta_{24} = 1\,\mathrm{GHz}$, $\delta_{34} = 1\,\mathrm{GHz}$, $\delta_{45} = 1\,\mathrm{GHz}$, $k = 100\,\mathrm{GHz}$, $g = 330\,\mathrm{GHz}$, $\gamma = 6\,\mathrm{THz}$, $\Gamma = 1\,\mathrm{GHz}$, $\Omega_2 = 1\,\mathrm{GHz}$,$\Omega_1 = 1\,\mathrm{GHz}$.

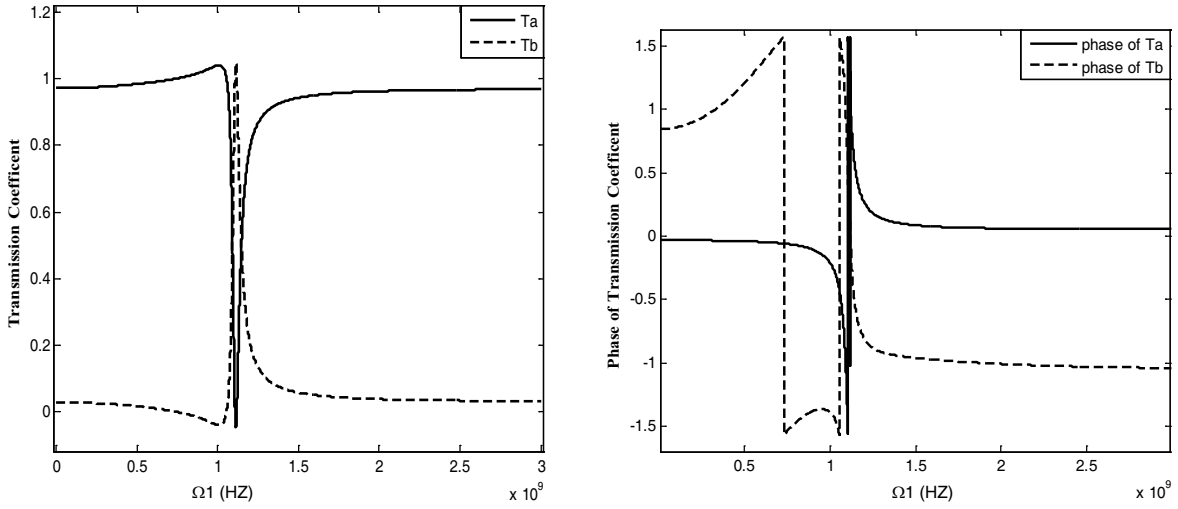

Figure 3: (a) Transmission coefficient. (b) Transmission coefficient phase, vs. Rabi frequency of the first control field to 5-level nanocrystal. $\delta_0 = 0$, $\delta_{15} = 0$, $\delta_{24} = 1\,\mathrm{GHz}$, $\delta_{34} = 1\mathrm{GHz}$, $\delta_{45} = 1\,\mathrm{GHz}$, $k = 100\,\mathrm{GHz}$, $g = 330\,\mathrm{GHz}$, $\gamma = 6\mathrm{THz}$, $\Gamma = 1\,\mathrm{GHz}$, $\Omega_3 = 1\,\mathrm{GHz}$, $\Omega_2 = 1\,\mathrm{GHz}$.

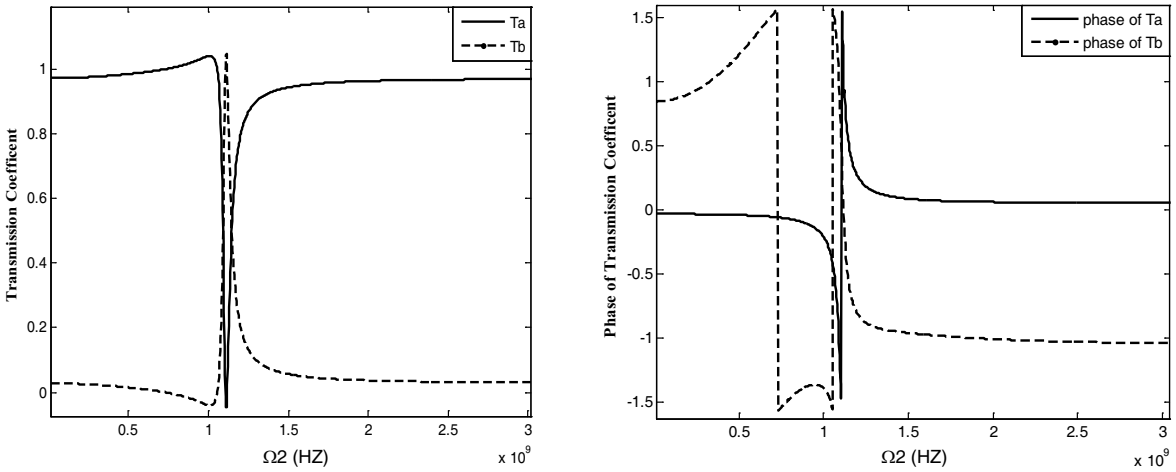

Figure 4: (a) Transmission coefficient. (b) Transmission coefficient phase, vs. Rabi frequency of the second control field ($\Omega 2$) of 5-level nanocrystal doped in PC cavity. $\delta_0 = 0$, $\delta_{15} = 0$, $\delta_{24} = 1\,\text{GHz}$, $\delta_{34} = 1\,\text{GHz}$, $\delta_{45} = 1\,\text{GHz}$, $k = 100\,\text{GHz}$, $g = 330\,\text{GHz}$, $\gamma = 6\,\text{THz}$, $\Gamma = 1\,\text{GHz}$, $\Omega_3 = 1\,\text{GHz}$, $\Omega_1 = 1\,\text{GHz}$.

transitions. With the value of $\Omega_3 = 2.046\,\text{GHz}$, we can get $T_a = T_b = 0.5$. When the Rabi frequency reaches to $\Omega_3 = 3.021\,\text{GHz}$, T_b increases to 0.988 and T_a decreases to 0.012, i.e., Switching occurs.

Figure 3 shows advantage of the PC cavity-waveguide switch system doped with a 5-level nanocrystal. Fig. 3(a) represents the transmission coefficient versus the Rabi frequency of Ω_1 while $\Omega_2 = \Omega_3 = 1\,\text{GHz}$. By increasing the Ω_1 to $1.111\,\text{GHz}$, both of T_a and T_b oscillate. So, with the value of $\Omega_1 = 1.106\,\text{GHz}$ T_a becomes 0.988 and T_b becomes 0.012 but by increasing of the Ω_1, T_a returns to 0.1 and T_b becomes 0.9. This oscillation of data between two outputs is occured in result of destructive interference of $|2> - |4>$ and $|3> - |4>$ transitions. In this case, T_a and T_b can be used as drop and band pass filters, respectively. In this situation 5-level nanocrystal acts as two isolated 3-level Λ type nanocrystals, $|1> - |5> - |4>$ and $|2> - |4> - |3>$. Fig. 3(b) shows the phase of transmission coefficient, where both phases of T_a and T_b oscillate in $\Omega_1 = 1.111\,\text{GHz}$. In out of oscillation region, phase of T_a is less than phase of T_b, so the most of input signal transmits to a_{out}.

Figure 4(a) represents the transmission coefficient of 5-level nanocrystal doped PC cavity-waveguide switch system versus the Rabi frequency of Ω_2 with constant values of $\Omega_3 = 1\,\text{GHz}$ and $\Omega_1 = 1\,\text{GHz}$. It is seen that transmission coefficient and phase versus Ω_1 in Fig. 3 and versus Ω_2 in Fig. 4 are the same corresponding to symmetric transitions $|2> - |4>$ and $|3> - |4>$.

4. CONCLUSION

We have proposed an all-optical DIT based switch using cavity-QED effects, which can act as an all-optical controllable normal on or off low-power switch. We demonstrate that doping 5 level atomic systems not only increases transmission coefficient but also decreases its required power. Also, one can control the normal case of switch and it's controlling by the applied control fields.

REFERENCES

1. Lai, W.-X., H.-C. Li, and R.-C. Yang, "Controlled optical switching based on DIT in a cavity-waveguide system," *Optics Communications*, Vol. 281, 4048–4053, 2008.
2. Eftekhari, K., K. Abbasian, and A. Rostami, "Proposal for all-optical controllable switch using DIT," *Optics Communications*, Vol. 283, 1817–1825, 2010.
3. Abbasian, K., A. Rostami, and Z. D. Koozehkanani, "All-optical tunable mirror design using electromagnetically induced transparency," *Progress In Electromagnetics Research M*, Vol. 5, 25–41, 2008.
4. Fleischhauer, M., "Electromagnetically induced transparency and coherent-state preparation in optically thick media," *Optics Express*, Vol. 4, No. 2, 107, January 1999.
5. Fleischhauer, M., A. Imamoglu, and J. P. Marangos, "EIT: Optics in coherent media," *Rev. Mod. Phys.*, Vol. 77, 633, 2005.

System-level Susceptibility Analysis for Intentional EMI Based on Bayesian Networks

Congguang Mao, Hui Zhou, Zhitong Cui, Aibin Zhai, and Beiyun Sun
Northwest Institute of Nuclear Technology, Xi'an 710024, China

Abstract— The Bayesian Networks (BN) is applied to the system-level susceptibility analysis for the intentional EMI. Based on the Bayesian Networks model the structural function characterizing the electronic system reliability can be obtained. The physical meanings of the formulation are illuminated further. Then several helpful concepts, such as the EM sensitivity, probability importance and criticality importance, are defined and analyzed, which are of great engineering senses in the practical protective design and effect tests of the systems.

1. INTRODUCTION

With the remarkable progress of the high-power electromagnetic (HPEM) technologies, the susceptibility problem of the electronic systems and the civilian infrastructures has abstracted increasing attentions [1]. The term of the intentional EMI (IEMI) mainly refers to the activities that utilizing the HPEM energy to interfere the normal operation of the electronics. Generally the HPEM environments mean the amplitude of the electric field greater than 100 V/m, such as the electromagnetic pulse (EMP), high-power microwave (HPM), intense radio frequency (RF), lightning EMP (LEMP), and so on. The American EMP Commission has assessed the threat to the United States from EMP attack, and concluded that "the electromagnetic pulse generated by a high altitude nuclear explosion is one of a small number of threats that can hold our society at risk of catastrophic consequences", and it further pointed out that "the increasingly pervasive use of electronics of all forms represents the greatest source of vulnerability to attack by EMP" [2].

The purpose of the system-level susceptibility assessment and analysis is to quantify the adverse impact of the electromagnetic (EM) environment on the electronics, and ultimately improve and ensure their survivability and functional safety. The fundamental concepts of the system-level susceptibility assessment are illuminated in [3]. And a special standard focusing on the tests techniques in the assessment has been developed by International Electrotechnical Commission (IEC) [4]. Because the assessment procedure involves several subprograms, i.e., the response analyses, tests, protection designs, nonlinear effect characterizations, and so on, an appropriate methodology or framework to unify all sides of activities is badly necessary.

With respect to the susceptibility analysis method, the Bayesian Networks (BN) has been introduced and the BN model is built based on the electromagnetic topology (EMT) and fault tree (FT) [5]. Thus the structural function characterizing the reliability of the system in the rigorous environments can be obtained. In this paper the physical meanings of the formulation are further expounded. And several helpful concepts, such as the EM sensitivity, probability importance and criticality importance, are defined and analyzed, which are of great engineering senses in the practical protective design and effect tests of the systems.

2. BAYESIAN NETWORKS MODEL OF SYSTEM RELIABILITY

The structural and functional diagrams of a typical system are presented respectively in Figs. 1 and 2. In Fig. 2, V_2 and V_3 denote respectively the exterior conductors and antenna; V_6, V_7 and V_8 the three assistant subsystems of the core equipment, V_9. On the branches of V_2-V_6 and V_3-V_8 there are conducted protective devices, P_3 and P_4. V_7 and V_8 are redundantly designed, i.e., they are of the same function and can replace each other. Moreover, V_8 is protected by V_3-P_4, which is similar with V_6.

The Bayesian Networks (BN) model of the system is built in Fig. 3 [5]. The upper part represents the functional structure and the lower describes the physical composition and the EM energy propagation scenarios. The nodes and rows stand respectively for the components of the system and EM propagating paths and logical depending relations. V_1 is the outer space; V_4 and V_5 denote the slots and diffusion. The shields, P_1 and P_2, are placed on the branches of V_1-V_4 and V_1-V_5. The abbreviation, EMS, indicates the EM stress on the particular element coupling from the outer EM environments and through all kinds of routes. The interference or damage threshold (IT) of the

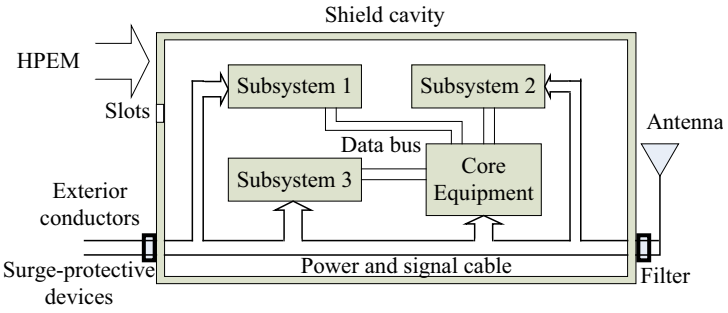

Figure 1: Physical structural diagram of electronic system.

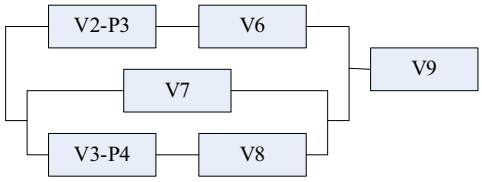

Figure 2: Functional logic relation of subsystem and equipment.

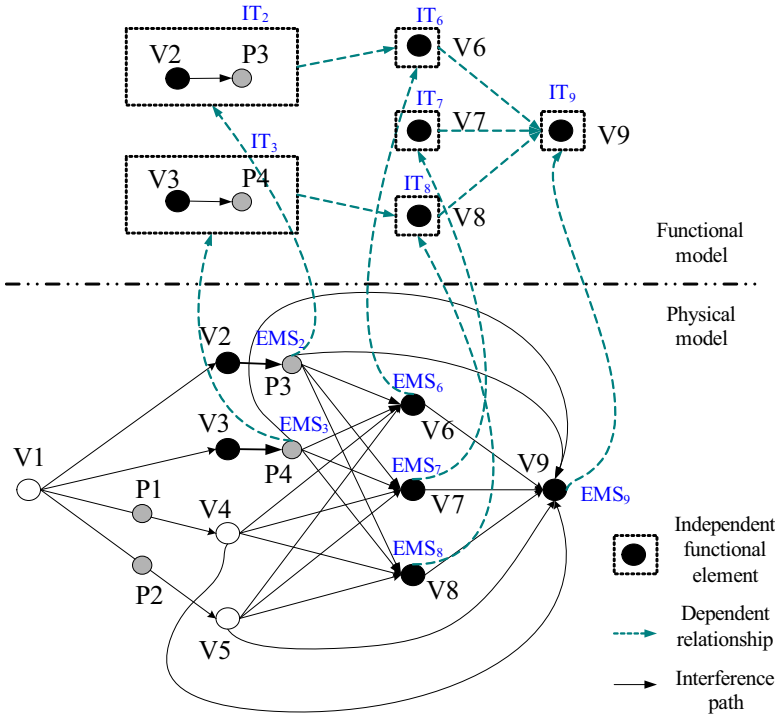

Figure 3: Bayesian Networks (BN) model.

element means the inherent strength of the element itself tolerating the EMS. All these factors in the BN model can be unified into one formulation (1), named as the structural function,

$$
\begin{aligned}
P(V_{sys}) &= P(V_9|V_8,V_7,V_6,\mathrm{EMS}_9) && (1)\\
&= P(V_9|V_8,V_7,V_6)\times[P(V_6)+P(V_7)P(V_8)]+P(V_9|\mathrm{EMS}_9) && (2)\\
&= P(V_9|V_8,V_7,V_6)\times\{[P(V_6|V_2)\cdot FP_2\cdot P(\mathrm{EMS}_2)+FP_6\cdot P(\mathrm{EMS}_6)] && (3)\\
&\quad +[FP_7\cdot P(\mathrm{EMS}_7)]\times[P(V_8|V_3)\cdot FP_3\cdot P(\mathrm{EMS}_3)+FP_8\cdot P(\mathrm{EMS}_8)]\}+FP_9\cdot P(\mathrm{EMS}_9) && (4)
\end{aligned}
$$

where, given i, $j=2,3,6,7,8$ or 9, $P(V_{sys})$ stands for the failure probability of the whole system; $P(V_i|V_j)$ means the V_i failure probability under the conditions of the V_j failure, which represents the functional dependent relationship of the subsystems; $FP_i=P(V_i|\mathrm{IT}_i,\mathrm{EMS}_i)$ refers to the failure probability of the element under the condition of the interfering threshold (IT_i) of itself and the corresponding EMS_i, which quantifies the effect of the EMI on the component; $P(\mathrm{EMS}_i)$ is the probability of the EMS greater than some level, which describes the responses of the system to the environment; and $P(V_9|V_6,\ V_7,\ V_8)$ depicts the V_9 failure possibility with the operation statuses of $V_6\sim V_8$.

All of the parameters in (1) need to be iteratively updated in the cycle of the analysis, design, manufactures and tests until the system reliability satisfies the specifications of the contracts. The

primary data generally comes from the computation and the small size of sampling tests. With the progress of the system design and test the data will get more and more precise.

Beside the algebraic operation, the symbols "×" and "+" in (1) respectively denote the logical relationship "AND" and "OR", which conforms to the principles of the Boolean algebra. For example, only when V_7 and V_8 failed simultaneously, V_{sys} would fail; however, the breakdown of V_{sys} only needs one element of V_6 OR V_9. The building of the logical relationship of the elements is completed during the system partition. The dividing of a complex system into the tractable subsystems is a critical idea in the system-level susceptibility assessment, which is one of the tasks of the BN model to fulfill.

3. SUSCETPTIBILITY ANALYSIS OF SYSTEM

With the BN model and structural function, we can analyze the sensitivity and reliability of the system in the HPEM environment, and applies the analysis results to the protective designs and tests of the system.

3.1. System-level Electromagnetic Sensitivity Analysis

The sensitivity analysis aims at the investigation the physical meanings and influences of the value varying of the elements to the failure probability of the overall system. According to the BN model and EM interfering mechanism, the failure causes of elements can be mainly divided into two classes: one is the EMS from the exterior environment; the other is the dependency between the elements.

When $P\ (\mathrm{EMS}_i) = 1$, the ith element of the system is suffered from the highest level of EMS, i.e., the most rigorous EM environment or the rated EMS level, and $P(V_{sys})$ becomes the maximal failure probability under the EMS_i. At the extreme circumstance if all $P\ (\mathrm{EMS}_i) = 1\ (i = 2, 3, \ldots, 9)$, all the elements are exposed to the highest level of EMS, thus $P(V_{sys})$ reaches the lowest survival probability. Actually the structural function (1) under this condition is just as the same as that of the fault tree (FT).

Otherwise, if $P\ (\mathrm{EMS}_i) = 0$, $FP_i \cdot P\,(\mathrm{EMS}_i) = 0$, this means that the EMS_i on the element V_i cannot reach the lowest rated level or just not exist. So the failure of the subsystem V_i caused by the EM interference need not to be considered, then this item can be deleted from formulation (1). Similar to the circumstance forenamed, if all $P\ (\mathrm{EMS}_i) = 0\ (i = 2, 3, \ldots, 9)$, then $P(V_{sys}) = 0$. Thus the reliability of the system $R(V_{sys}) = 1 - P(V_{sys}) = 1$, it means that the system is absolutely safe in the EM environment, which just is the aim of the protective design.

Now we take the parameter FP_i into account. If $P(V_i|\mathrm{IT}_i, \mathrm{EMS}_i) = 0$, the level of EMS_i cannot reach that threshold, IT_i, so cannot cause the element V_i to fail. Thus this item can also be removed from (1). After some elements are ignored in the analysis phase, the complexity of the assessment can be reduced and the remainder items or factors can be emphasized in the following design and test procedure.

As for the factors $P(V_i|V_j)$ and $P(V_9|V_8,\ V_7,\ V_6)$, they represent the element fault possibility caused by the other components, which reflects the functional structure and logical relationship. This property of BN model is identified with the other reliability tool, such as Fault Tree Analysis (FTA) [6].

3.2. Probability Importance Analysis

For the system composed with many elements or subsystems, what we want to know firstly is which one failure has the great contribution to the fault of the whole system. The quantity characterizing this property is called the probability importance, i.e., the varying extent of the failure probability of the overall system induced by the changing of that of the elements, that can be formulated as (5)

$$\Delta P_i = \frac{\partial P(V_{sys})}{\partial P_i}. \tag{5}$$

For instance,

$$\Delta P_{V_6} = \frac{\partial P(V_{sys})}{\partial P(V_6)} = P(V_9|V_8, V_7, V_6) \cdot P(\mathrm{EMS}_6). \tag{6}$$

This formulation (6) shows that the importance of V_6 to the system depends on both the environment stress EMS_6 and the relevancy of $V_6 \sim V_8$ to V_9. Obviously if the latter two values are great,

V_6 is the component needed to be carefully protected. For another instance,

$$\Delta P_{\mathrm{EMS}_6} = \frac{\partial P(V_{sys})}{\partial P(\mathrm{EMS}_6)} = P(V_9|V_8, V_7, V_6) \cdot FP_6. \tag{7}$$

It indicates that the importance of EMS_6 to the system rests with both the failure probability $FP(V_6)$ and the relevancy of $V_6 \sim V_8$ to V_9. If the latter two values are great, EMS_6 should be measured and investigated in the effect tests.

3.3. Criticality Importance Analysis [6, 7]

In the practical applications the important element must be well strengthened, so the failure probability of the element itself would be very low and little margin could be achieved. It reveals such a fact that improving a robust component will be more expensive and difficult. And this character can be described by the concept of the criticality importance, which is defined as following:

$$I_i^{CR} = \frac{P(V_i)}{P(V_{sys})} \cdot \frac{\partial P(V_{sys})}{\partial P(V_i)} = \frac{P(V_i)}{P(V_{sys})} \cdot \Delta P_i. \tag{8}$$

It can be seen that for the given $P(V_{sys})$ the probability importance ΔP_i and the failure probability of the component itself $P(V_i)$ are directly proportional with each other, however, only one value great cannot always increase the product $P(V_i) \cdot \Delta P_{V_i}$. So the criticality importance is a more comprehensive measurement. If this weight value is high, the component should be carefully considered.

Take the element V_6 and its EM stress as an example,

$$I_{V_6}^{CR} = \frac{P(V_6)}{P(V_{sys})} \cdot \frac{\partial P(V_{sys})}{\partial P(V_6)} = \frac{P(V_6)}{P(V_{sys})} \cdot \Delta P_6 = \frac{FP_6}{P(V_{sys})} P(V_9|V_8, V_7, V_6) \cdot P(\mathrm{EMS}_6). \tag{9}$$

$$I_{\mathrm{EMS}_6}^{CR} = \frac{P(\mathrm{EMS}_6)}{P(V_{sys})} \cdot \frac{\partial P(V_{sys})}{\partial P(\mathrm{EMS}_6)} = \frac{P(\mathrm{EMS}_6)}{P(V_{sys})} \cdot \Delta P_6 = \frac{P(\mathrm{EMS}_6)}{P(V_{sys})} P(V_9|V_8, V_7, V_6) \cdot FP_6. \tag{10}$$

Formula (9) and (10) indicate that FP_6 and EMS_6 are at the same consequence. Both improving the strength of V_6 and depressing the EM stress EMS_6 can enhance the survivability of the overall system, which just identifies with that in the practice. Similarlybecause of the redundancy design the criticality importance of the subsystem composed by V_7 and V_8 will be reduced greatly.

4. CONCLUSION AND COMMENT

Based on the idea of the Bayesian Networks (BN), the reliability model of the system interacting with the HPEM environments has been built. All of the parameters in the structural function are of definite physical meanings. Furthermore the concepts of the sensitivity and importance of the subsystems or elements are defined and analyzed, which can be utilized in the system-level effect tests and protective design. All these characters shows that BN method can present a more clear view of the complex behaviors of the system in IEMI, and can play an important role in the system-level susceptibility/vulnerability assessment. The assessment test of a typical electronic system guided by the BN model and definitions is now ongoing, which will further examine the validity of the method.

REFERENCES

1. Radasky, W. A., C. E. Baum, and M. W. Wik, "Introduction to the special issue on high-power electromagnetics (HPEM) and intentional electromagnetic interference (IEMI)", *IEEE Trans. on Electromagn. Compat.*, Vol. 46, 314–321, August 2004.
2. Report of the commission to assess the threat to the United States from electromagnetic pulse (EMP) attack — critical national infrastructures, 2008.04. Online: http://armedservices.house.gov/ comdocs/openingstatementsandpressreleases/108thcongress/04-07-22emp.pdf.
3. Mao, C., H. Zhou, J. Fu, B. Sun, and H. Yu, "Introduction to the system-level susceptibility assessments for HEMP and HPEM," *PIERS Proceedings*, 1746–1750, Beijing, China, March 23–27, 2009.
4. IEC/TS 61000-5-9 System-level susceptibility assessments for HEMP and HPEM, July 2009.

5. Mao, C. and H. Zhou, "Bayesian network modeling in system-level susceptibility assessment for intentional EMI," *Proceedings of the Ninth International Symposium on EMC*, 502–505, Wroclaw, Poland, September 2010.
6. Zeng, S., T. Zhao, J. Zhang, et al., *System Reliability Design and Analysis*, Publish House of Beijing Avigation and Spaceflight University, April 2004.
7. Evgeni, G., M. Mleczko, and H. Garbe, "Importance analysis to describe reliability of systems," *Proceedings of the Ninth International Symposium on EMC*, 290–293, Wroclaw, Poland, September 2010.

Time Domain Analysis of Nonlinear Load Terminated in Shielded Cable

Yinghui Zhou, **Lihua Shi**, **and Liyuan Su**
EMC Lab, PLA University of Science and Technology, China

Abstract— Aimed to verify the proposed time domain calculation model is fit for analyzing and estimating the protective effectiveness of the nonlinear loads against EMP (Electromagnetic Pulse), the nonlinear device of SPD (Surge Protection Device) is researched in this paper. The SPD test system is built and the response character of the under tested SPD is obtained by this system. Introducing the obtained U-R relation to the time domain calculation, result shows that this time domain calculation is fit for forecasting and analyzing the protective effectiveness to EMP.

1. INTRODUCTION

When the non plane wave act on the shielded cable or shield enclosure, the research in time domain plays very important role. The authors have created a model to analyze the induced current and induced voltage in the shielded cable in time domain. In this built model, the digital filtering technique is combined with the FDTD method and the induced voltage and induced current in the shielded layer have been obtained under the external electromagnetic field [1, 2]. Then, the authors designed a transfer impedance test system and the transfer impedance of shielded cable can be measured and the induced voltage and induced current in the core line can be calculated by the established system and model [3].

However, how to protect the devices and equipments terminated in the shielded cable or other shielded enclosure is a problem valuable to research. We know nonlinear load SPD can suppress surge overvoltage in the power line or signal transmission line to the immunity limit. As a kind of protective device it has nonlinear response character. This kind of device is generally used to protect devices connected in cables against lightning surge overvoltage [4]. Whether it has protective effectiveness against EMP still hasn't certain convolution. Thus, according to the relative international standard, the nonlinear device testing system is built in this paper and its response characters can be measured. Introducing the nonlinear device response character (U-R relation) to the proposed time domain calculation model, the induced voltage and induced current in the nonlinear load will be obtained under the external injected electromagnetic field. By the proposed calculation and measurement system, the induced voltage and induced current can be acquired respectively. Then, combining the measured data, the protection effect of the nonlinear load to device terminated in shielded cable against the external electromagnetic field can be analyzed validly.

2. SPD TEST AND CALCULATION

To accurately assess the protective effectiveness of SPD to the terminated device against the EMP, test systematically is necessary to obtain its response character to injected EMP, on the other hand, the model is require to introduce test result of SPD to the domain calculation equations. Owing to the practical protective effectiveness is related to its install location in the whole test system and the relevant electromagnetic environment, the test to SPD should coincide with its actual service condition and take measures to deduce noises. According to [5], the test fixture is designed by the 5.7 mm aluminum sheet and with the following features:

(1). It can fix the device under tested and its cavity is applicable to the usual SPD;
(2). It is designed with standard joint and matched with frequent-use test instruments (generally is 50 Ω);
(3). It has certain shielding efficiency to insulate the instant pulse radiation;
(4). It has adequate strength to protect the tester from sudden burst.

This established test system is shown as Figure 1. It is composed by the pulse generator, current probe, SPD test fixture, attenuators and the oscilloscope. Here the current probe is adopt

to measure the injected voltage and current through the SPD in the meantime, and then the V-I relation of the under tested SPD can be acquired by data fitting technique.

By this test system, the response character of frequent-used SPD and different signal protection device has been tested and researched. Here the TVS tube is taken as an example to explain the analysis process and principle. The TVS tube suppresses transient voltage by means of the PN junction avalanche effect. If the transient disturbance has not appeared, the TVS tube doesn't work. Once the transient over voltage coming, the TVS tube will limit the peak voltage to immunity limit for protecting the terminated device.

Injecting a wide pulse to the TVS tube, the response voltage and current through this TVS tube is shown as Figure 2. It can be seen from this figure that the protection device can limit the

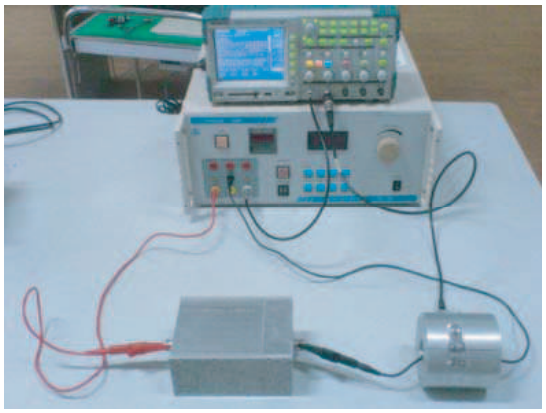

Figure 1: Photo of the SPD test system.

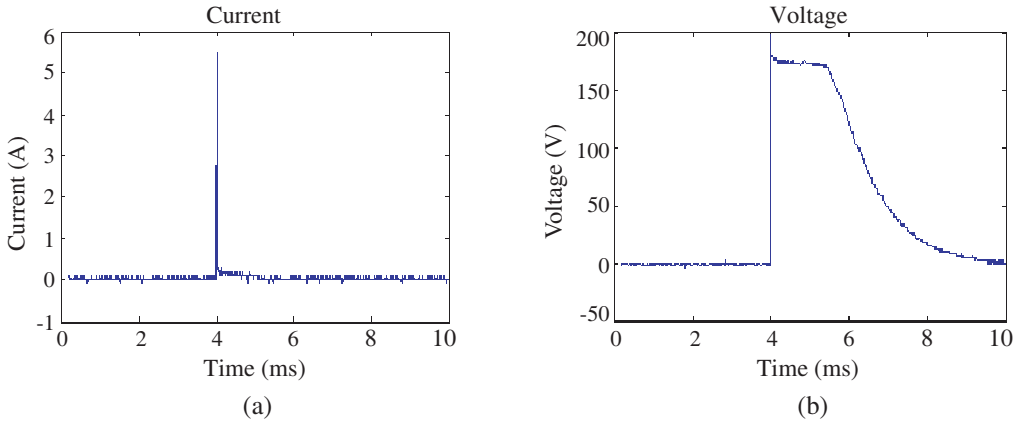

Figure 2: Response waveform of the TVS tube to injected wide pulse: (a) current through the TVS tube; (b) response voltage in the TVS tube.

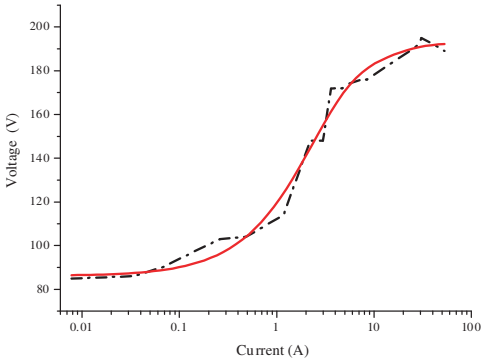

Figure 3: V-I character of the certain type TVS tube.

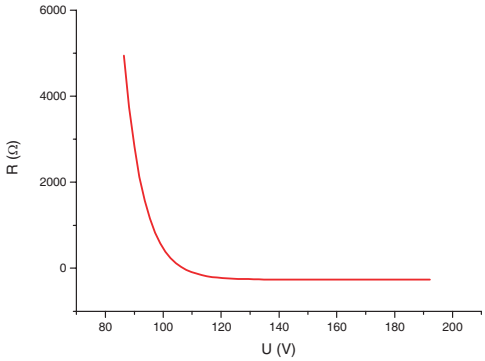

Figure 4: Relationship of the injected voltage U and the equivalent resistance R.

voltage under about 200 V and enlarge the pulse wide obviously.

Applying the repetitious testing result, the V-I character of this TVS tube can be described as Figure 3. Aimed to get the relationship of its voltage and current, the 3rd exp fit is used here. Figure 3 is the TVS tube V-I character, in this figure, the dashed line and solid line are the actual measurement value and fitted value, respectively. The fitted relationship of voltage and current is shown as Equation (1).

$$U = 43.75 \times \exp\left(-\frac{I}{2.18}\right) - 20.12 \times \exp\left(-\frac{I}{11.57}\right) - 42.59 \times \exp\left(-\frac{I}{2.17}\right) + 192.39 \quad (1)$$

3. SPD PROTECTION EFFECTIVENESS ANALYZING

According to the TVS voltage and current character, the curve of injected voltage U and its equivalent resistance R can be obtained, and exp fitted it we can get relationship of U-R as Equation (2).

$$R = 14740559.96 \times \exp\left(-\frac{U}{10.74}\right) - 321.89 \quad (2)$$

Calculation of EMP coupled to SPD devices in time will be processed as the following steps:

Firstly, by the proposed DF-FDTD time domain calculation model [1], coupled voltage and current in the outer layer of the shielded cable can be obtained;

Then, using the designed transfer impedance test system, transform the current in the outer layer to the source voltage of the inner conductor and obtained the coupled voltage and current in the inner conductor;

Nest, introducing the nonlinear device (TVS tube here) as a terminated load and calculate the coupled voltage between it;

Finally, analyzing the protective effectiveness of this nonlinear device and estimating whether it can be choose to protect the device or equipment connected in this shielded cable.

According to above method, the calculation process can be expressed as the following model:

$$\frac{\partial[v_T(z,t)]}{\partial z} + L_T\frac{\partial[i_T(z,t)]}{\partial t} + R_T i_T(z,t) = \rho(t) \otimes i(z,t) \quad (3)$$

$$\frac{\partial[i_T(z,t)]}{\partial z} + C_T\frac{\partial[v_T(z,t)]}{\partial t} + G_T v_T(z,t) = 0 \quad (4)$$

where: $\rho(t)\otimes i(z,t)$ denotes the convolution of the transfer impedance with the current in the shielding layer; $\rho(t) = F^{-1}(Z_T)$; $F^{-1}(\cdot)$ denotes the inverse Fourier transform; Z_T denotes the transfer impedance; L_T, R_T, C_T and G_T denotes the inductance, impedance, capacitance and conductance in unit length, respectively. v_T, i_T denotes the coupled voltage and current in the core line of the shielded cable.

By the 1st center difference method, the iterative relationship of coupled current in the inner conductor can be obtained as:

$$I_{Tk}^n = \left(\frac{L_T}{\Delta t} + \frac{R_T}{2}\right)^{-1} \left\{\sum_{i=1}^{M} T_{ki}^n - \frac{V_{Tk+1}^n - V_{Tk}^n}{\Delta z} + \left(\frac{L_T}{\Delta t} - \frac{R_T}{2}\right) I_{Tk}^{n-1}\right\} \quad (5)$$

Similar method can be adopted for the coupled voltage.

$$V_{Tk}^n = \left(\frac{C_T}{\Delta t} + \frac{G_T}{2}\right)^{-1} \left\{-\frac{I_{Tk}^{n-1} - V_{Tk-1}^{n-1}}{\Delta z} + \left(\frac{C_T}{\Delta t} - \frac{G_T}{2}\right) V_{Tk}^{n-1}\right\} \quad (6)$$

We introducing the SPD expressed as Equation (2) to the calculation model, then, the coupled voltage and current of the core line can be calculated. Here we must attention the boundary

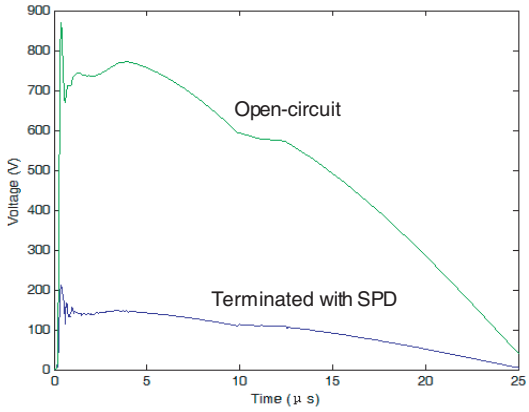

Figure 5: Comparison of the coupled voltage open-circuit and terminated with the TVS tube.

conditions (Equations (7), (8)) is different under different calculation circumstances).

$$\begin{aligned} I_{T1}^n &= \left(\frac{L_T}{\Delta t}+\frac{R_T}{2}+\frac{3Z_0}{2\Delta z}\right)^{-1}\left\{\sum_{i=1}^{M}T_{1i}^n-\frac{V_{T2}^n}{\Delta z}+\frac{Z_0}{2\Delta z}I_{T2}^n+\left(\frac{L_T}{\Delta t}-\frac{R_T}{2}\right)I_{T1}^{n-1}\right\}, \\ V_{T1}^n &= -Z_0\frac{3I_{T1}^n-I_{T2}^n}{2} \end{aligned} \tag{7}$$

$$\begin{aligned} I_{TN}^n &= \left(\frac{L_T}{\Delta t}+\frac{R_T}{2}+\frac{3Z_L}{2\Delta z}\right)^{-1}\left\{\sum_{i=1}^{M}T_{1i}^n+\frac{V_{TN}^n}{\Delta z}+\frac{Z_L}{2\Delta z}I_{T(N-1)}^n+\left(\frac{L_T}{\Delta t}-\frac{R_T}{2}\right)I_{TN}^{n-1}\right\}, \\ V_{T(N+1)}^n &= Z_L\frac{3I_{TN}^n-I_{T(N-1)}^n}{2} \end{aligned} \tag{8}$$

where, Z_0 is the character impedance of the shielded cable, when the end is open-circuit Z_L is ∞, while the end is terminated with the nonlinear load TVS tube, introducing Equation (2) to Z_L.

In the above equations, Δz and Δt are space-step and time-step, respectively. The relationship of every item in the difference equation is shown as following:

$$\begin{aligned} z_V^k &= (k-1)\Delta z \quad & t_v^n &= n\Delta t & I_{Tk}^n &= i_T\left(z_I^k, t_I^n\right) \\ z_I^k &= (k-1/2)\Delta z & t_i^n &= (n+1/2)\Delta t & V_{Tk}^n &= v_T\left(z_V^k, t_V^n\right) \end{aligned}$$

The voltage between this nonlinear device can be calculate. Figure 5 gives the comparison of the coupled voltage when the end is open and terminated with the TVS tube. In order to facilitate observing, the coupled voltage between the TVS is enlarged 10 times shown. It can be seen from the figure, before connected the nonlinear device, peak voltage coupled in the core line is about 871 V. After connected this device, the coupled voltage is about 208 V. This is accordance with the rule reflected by Figure 2.

4. CONCLUSIONS

In this paper, the SPD test system is built and by this test system the response character of nonlinear device has be measured. Using the tested result and adopted the exp fit method, the U-R relationship can be acquired. Introducing this relationship to the time domain calculation simplified by the authors, the voltage between the terminated equipment after connected the nonlinear device can be calculated. The calculation result shows that this model can be used to forecast and analyze the protective effectiveness to EMP.

ACKNOWLEDGMENT

This work was supported by the National Science Foundation of China under Grants No. 51077133 and the NCTE.

REFERENCES

1. Zhou, Y.-H., L.-H. Shi, C. Gao, et al., "Combination of FDTD method with digital filter in analyzing the field-to-transmission line coupling," *IEEE Trans. on EMC*, Vol. 50 No. 4, 1003–1007, 2008.
2. Zhou, Y.-H., L.-H. Shi, B. H. Zhou, et al., "Calculation of the induced current of a shielded inner conductor coupled by an EMP field," *International Symposium on EMC Proceedings 2007*, 194–197, Qingdao, China, October 2007.
3. Zhou, Y.-H., L.-H. Shi, B. H. Zhou, et al., "Comparison of the measurement method for surface transfer impedance in frequency-domain and time-domain," *Proceedings CEEM'2009*, 54–57, Xi'an, China, September 2009.
4. He, J. L., Z. Y. Yuan, S. C. Wang, et al., "Effective protection distances of low-voltage SPD with different voltage protection levels," *IEEE Trans. on Power Delivery*, Vol. 25, No. 1, 187–195, 2010.
5. IEC 61000-4-24, *Testing and Measurement Techniques-test Methods for Protective Devices for HEMP Conducted Disturbance*, 1997.

Research on High Voltage Electrostatic Discharge to EED and Fuze

Tuan Zhao, **Lixia Wang**, **Qingmei Feng**, **Hongzhi Yao**, **and Xiangfei Ji**
State key Laboratory of Applied Physics-Chemistry
Shaanxi Applied Physics-Chemistry Research Institute, Xi'an 710061,China

Abstract— In this the paper, by setting up the high voltage electrostatic discharge systems composed of 300 kV, 1000 pF, 1 Ω and so on, that the simulating test about electrostatic discharge of helicopter air supplying is mainly discussed. In this system, it is six levels of electrostatic sensitivity for fuse (which do not bear passing-explode tubes and expanding drug) and for EED (electro-explosive devices), with charging voltage from 50 kV to 300 kV including positive polarity and negative polarity that may be tested. At present, the related testing research on calibrated resistance of 100 Ω has been made.

1. INTRODUCTION

EEDs are not only absolutely necessary igniting and blasting components in special power, but also the most dangerous and susceptive subsystems in weapon systems. They are widely used not only in the fuse of engine of rocket, missile and roll booster impetus but in spreading of two-double's wing, self-damage setting and explosive bolt and so on. The safety and reliability of whole weapon's system are directly decided by the safety and the reliability of EED. The research on anti-electrostatic technology of EED is in the demand of development of science and technology of military affairs, and is the important part of improving safety and the reliability of weapon system. So it is attached important to home and abroad.

With the development of science of military affairs, in the future, the war will be in the capacious field of solid. Because electron antagonism, electromagnetic interference, microwave weapon etc will make the electromagnetic field of astrospace become more and more strong. At the same time, with the change appearance of the transportation and the logistic safeguard of weapon [1], the highly insulted materials and the costume of chemical fiber are also indispensable for the weapon equipment and the persons attending a war. In order to ensure that the EED are immune to danger of electromagnetic and to avoid invalidation and improper action, the simulative test of EED against electromagnetic environment hazard is of importance, of which, the simulative electrostatic sensitivity test for EED is more vital, which insure the safety and the reliability of EED against electromagnetic environment hazard.

In our nation, since seventies' of last century, such special apparatuses as instrument of electrostatic sensitivity of EED, instrument of electrostatic sensitivity of powder and instrument of electrostatic accumulating of powder have been completely manufactured. At the same time, the test of electrostatic sensitivity of EED has been developed, the test with the capacitance of 500 ± 25 pF having voltage charged of 2500 kV, the serial resistance of $5000 \pm 250\,\Omega$. In the test, the electrostatic sensitivity of EED's leg-leg or leg-shell may be tested by Bruceton method. Then, according to the result of test, the electrostatic sensitivity of EED, namely the firing average voltage and criterion may be calculated. In later of eighties' of last century, GJB736.11-90 [5] (method of EED test, EED determining electrostatic sensitivity), WJ1869-89 (method of EED test, powder determining electrostatic sensitivity), JGB737.3-89 (method of EED test, column of powder and surface resistance determining electrostatic sensitivity) and WJ2018-91 (method of EED test, powder accumulating electrostatic sensitivity) are successfully set down. Such methods have met the demand of hazard of electrostatic from human body to EED but not in the demand of hazard of electrostatic from aerial supply to EED.

In the nineties' of last century, the test simulating electrostatic discharge of helicopter was brought forward, because of the change appearance of transportation and logistic safeguard of weapon, the test of electrostatic sensitivity confined to simulating static of human body does not meet the demand of actual war, especially, in aerial transportation of weapon. With the speed of transportation growing up, and the conveyances charged up by atmosphere or thundercloud in interspaces, the new hazard of electrostatic power to EED appears. So, the test that simulate electrostatic of aerial transportation of weapon will be new one subject. So, the electrostatic discharge test technique simulated aerial supply have been studied since 2003 in our research institute.

2. ELECTROSTATIC DISCHARGE TEST OF AERIAL SUPPLY TO FUSE'S SYSTEM

In the nineties' of last century, the test simulating electrostatic discharge of helicopter was brought forward, whose character with capacitance of 1000 pF, discharging resistance of 1 Ω, maximal inductance of 20 μH and maximal testing voltage charged of 300 kV. If packed fuse under the test, its electrostatic sensitivity is tested. Then the safety of fuse against electrostatic discharge is further assessed. If bare fuse under the test, the reliability may be evaluated

According to above figure, the testing equipment of 300 kV electrostatic discharge of aerial supply to fuse's system including EED, with maximal Voltage of 300 kV, Capacitance of 1000 pF and Maximal resistance of 1 Ω, was successfully manufactured by us. As is shown in following Fig. 1.

In the simulating circuit, the capacitance of capacitor is 1000 pF, and other parameters are referred to Table 1. When tested, rising maximal voltage, rising time and pulse width passing calibrated resistance will be gotten. By comparing the result of test with indexes of MIL-STD-331B, as is shown in Table 1, we can come to conclusion that, given the same rising maximal voltage, rising time and pulse width (half-height width of pulse) passing the calibrated resistance in MIL-STD-331B is respectively 180 ns and 300 ns, but in our test, which is respectively 50ns and 150ns. At the same time, the dissipation of energy in calibrated resistance in MIL-STD-331B accounts for 88.8 percent of total energy of capacitor but in our test 95.9 percent. The waveform of test result is shown in Fig. 2.

3. TEST

When testing, to ensure that the selected test point in fuse surface is the worst case, especially, the test point can be selected which the electromagnetic energy can be transferred, such as, contact point, lead, pinhole, aperture and so on. The test result on high voltage electrostatic discharge to

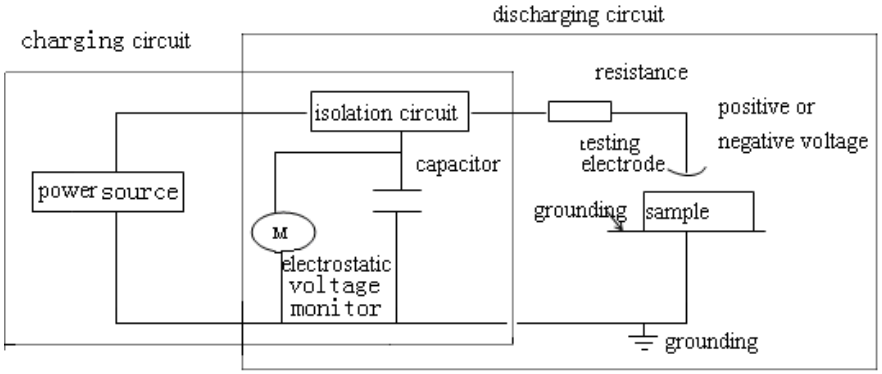

Figure 1: The configuration of high voltage electrostatic discharge test system on EED and fuze.

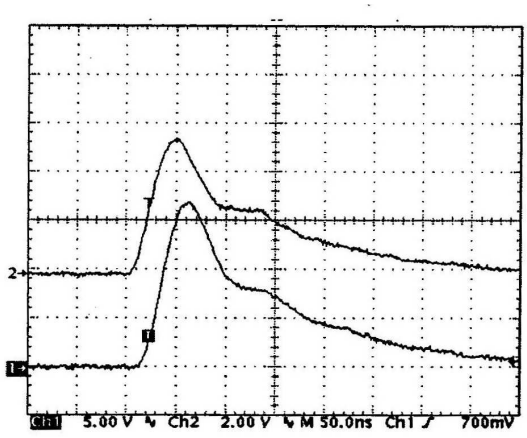

Figure 2: Current and voltage waveforms of calibrated resistance with capacitor charged voltage of 300 kV, channel 1 is current waveform; channel 2 is voltage waveform.

EED and Fuze is shown as followed:

(1) Detonators are placed with one pin contacted to the ground and another pin contacted to the discharge electrode, the ten detonators are random took from one set of detonators, then the voltage of high voltage electrostatic discharge test system is adjusted to 50 kV, the all testers are fired.

(2) Ten detonators are random took from one set of detonators, detonators are placed with two wringing pins contacted to the ground and the case contacted to the discharge electrode, The

Table 1: The voltage peak, rise time, pulse width in 100 Ω calibrated resistance through simulated calculation and actual testing.

Parameters of circuit / voltage	Parameters in MIL-STD-331B $R = 1\,\Omega$, $R_s = 100\,\Omega$, $L < 20\,\mu H$			Parameters in our test $R = 4\,\Omega$, $R_s = 100\,\Omega$, $L = 3.0\,\mu H$		
	U_s /kV	T_r /ns	pulse width /ns	U_s /kV	T_r /ns	pulse width /ns
50 kV	22.3	180	300	40.70	50	100
100 kV	44.7	180	300	81.70	50	100
150 kV	67.0	180	300	122.5	50	100
200 kV	89.0	180	300	163.4	50	100
250 kV	112.0	180	300	204.2	50	100
300 kV	134.0	180	300	245.1	50	100
Parameters of circuit / voltage	Actual testing result (calibrated resistance of 100 Ω is linked)					
	U_s /kV	T_r /ns	pulse width /ns			
50 kV	40.2	50	150			
100 kV	81.6	50	150			
150 kV	121.7	50	150			
200 kV	161.9	50	150			
250 kV	205.0	50	150			
300 kV	252.0	50	150			

Table 2: The test results of EED of pin-case.

Tester	The quantity of tester	The voltage of charge /kV	Test result	remark
1#detonators	1	50	0	
		100	0	
		200	0	
	1	50	0	
		200	0	
		250	0	
	1	200	0	
		225	1	
	1	150	0	
		300	1	
	1	300	1	
	1	275	0	
		300	1	
	1	150	0	
		200	1	
	1	150	0	
	1	200	0	
	1	300	1	

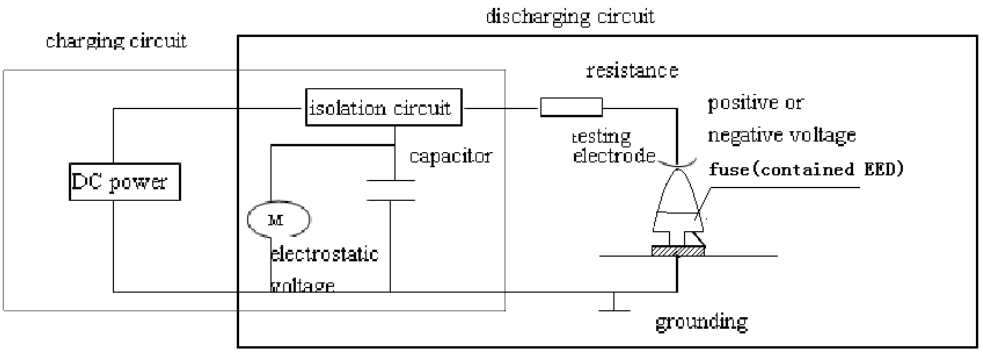

Figure 3: The figure of electrostatic discharge test system on fuse (contained EED).

test results of detonators are shown in Table 2.

(3) The fuse(contained EED)is selected, the voltage of high voltage electrostatic discharge test system is adjusted to 50 kV, 100 kV, 200 kV, 300 kV, the EED in fuse is not fired, the figure of test with fuse is shown in Fig. 3.

4. CONCLUSION

According to above analyzing, the testing performance of electrostatic discharge of aerial supply to fuse's system manufactured by us is superior to that of MIL-STD-331B. For example, the 95.9 percent of energy dissipation in calibrated resistance in our test is higher than that of MIL-STD-331B

In above 300 kV electrostatic discharge testing system for EED, there is a isolated circuit, which has following function: when the capacitor is charged by power of high voltage, the discharge circuit will be isolated; in turn, when the capacitor is discharged toward sample, the charge circuit will be isolated. Most of all, in this systems, six levels of electrostatic discharge for fuse or for EED, with charging voltage from 50 kV to 300 kV including positive polarity and negative polarity, may be tested. So this testing systems supply a gap in our nation.

REFERENCES

1. Liu, S., G. Wei, and Z. Liu, *The Theory and Safety of Electrostatic*, Beijing Publishing House of Ordnance Industry, 1999.
2. MIL-STD-1512, Electroexplosive Subsystems, Electrically Initiated, Design Requirements and Test Methods, 1976.
3. MIL-STD-1576, Electroexplosive Subsystems Safety Requirements and Test Methods for Space Systems, 1984.
4. MIL-STD-331B, Fuze and Fuze Components Environment and Performance Test, 1989.2.
5. GJB736. 11-90, Test Method of Initiating Explosive Device, Electrostatic Sensitivity Test for Electric Initiating Explosive Device, 1991.6.

A Method for Assessing EED against HPEM

Hong-Zhi Yao[1, 2], **Qing-Mei Feng**[1, 2], **Tuan Zhao**[1, 2], **and Xiang-Fei Ji**[1, 2]

[1]Science and Technology on Applied Physical Chemistry Laboratory, Xi'an 710061, China
[2]Shaanxi Applied Physics-Chemistry Research Institute, Xi'an 710061, China

Abstract— The methods used for assessing HERO(hazards of electromagnetic radiation to ordnance) and the measurement for the induced energy or current about EED which located in special electromagnetic radiation environment were discussed in this paper. The infrared fiber temperature sensor is suitable for the measurement of induced current caused by high power electromagnetic radiation on electro-explosive device (EED) since the transmission link of the sensor is infrared optical fiber which is immune to electromagnetic radiation. This paper investigates the application of an infrared mercury-cadmium-telluride (MCT) based on radiation thermometer within a high-power electromagnetic (HPEM) environment in order to measure induced energy and to determine EED's safety. According to the test requirement, the temperature range of the senor should be between 0°C to 2000°C. The response time of the MCT detector should be less than 1ms. The InSb detector is even faster because of its smaller edge length of 100 mm compared to 250 mm for the MCT detector. However, the MCT is the preferable detector because its maximum spectral response is shifted to higher wavelengths. This makes the detector more sensitive for lower temperature. The experimental results using the infrared sensor suggest that the measurement of bridge-wire temperature caused by induced current is satisfactory, which would be a reliable and improved method for evaluating the safety of EED against HPEM.

1. INSTRUCTION

The problem of HERO (hazards of electromagnetic radiation to ordnance) that was widely considered since from 1950s, and the quantitative assessment techniques for HERO have been pressing to solve. With the development of science technology, HERO testing technology has gone through the process of qualitative to quantitative. Initially, the researchers use wax or paper sensitive of temperature to monitor the induced energy that used for early safety assessment of ordnance which has large error and difficult to quantify the HERO. Then, the researchers used a thermocouple to test the induced energy of ordnance which is susceptible to electromagnetic radiation environment should be resulting in distorted measurement [1]. And then, the researchers used current probe with fast response time and stable result to test the induced current directly on the bridge-wire of EED, but it is limit to it's frequency range. Finally, temperature measurement gradually applied to the HERO test with the development of optical fiber technology with fast response time and free from the influence of electromagnetic radiation characteristics solve all the problem very well [2]. Test method described in this paper is based on principle and method of infrared temperature measurement technology.

2. INFRARED TEMPERATURE MEASUREMENT

Non-contact infrared temperature measurement is a method of temperature measurement, temperature measurement devices and measured object without contact, through the principle of thermal radiation to measure temperature. Theoretical and experimental studies have shown that: Any object above absolute zero temperature, and the radiation energy of the vast majority objects are in the infrared region. The method of infrared temperature measurement using the characteristics by measuring the infrared radiation of an object [3].

Characteristic of hot wire EED is presented as a temperature response on the bridge wire when the current flowed through the bridge wire. So we can establish the relationship between the temperature and the current of EED in EME.

By Stefan-Boltzmann thermal radiation principle, the bridge wire current density of spectral radiation:

$$\Phi = \int_0^\infty r d\lambda = \int_0^\infty \frac{\varepsilon 2\pi c^2 h}{\lambda^5 (e^{hc/(\lambda kT)} - 1)} d\lambda = \varepsilon \sigma T^4$$

where h is Planck's constant, C is the speed of light, k is the Boltzmann factor, ε is the bridge wire radiation coefficient, T — the absolute temperature of the bridge wire, σ is the Stefan-Boltzmann

constant. For a given spectral range λ_1 to λ_2 ($\lambda_1 < \lambda_2$), the

$$\Phi_{\lambda_1-\lambda_2} = \int_{\lambda_1}^{\lambda_2} r d\lambda = \int_0^{\lambda_2} r d\lambda - \int_0^{\lambda_1} r d\lambda$$

Then, light voltage of the detector:

$$V_{\lambda_1-\lambda_2} = R_T P$$

where R_T is the detector responsivity, P is the radiation optical power of bridge wire

$$P = A\Phi_{\lambda_1-\lambda_2}$$

A is the radiated area

$$V_{\lambda_1-\lambda_2} = R_T A\Phi_{\lambda_1-\lambda_2}$$

Then another wavelength range λ_3 to λ_4 ($\lambda_2 < \lambda_3 < \lambda_4$) optical response voltage $V_{\lambda 3-\lambda 4}$, the ratio of

$$q = \frac{V_{\lambda_3-\lambda_4}}{V_{\lambda_1-\lambda_2}} = t\frac{\Phi_{\lambda_3-\lambda_4}}{\Phi_{\lambda_1-\lambda_2}}$$

where t is the response of two detectors the ratio of degrees

According to the analysis above, the corresponding relationship between voltage and current, is carried out the induced current measurement.

It is a complex process of thermoelectric response of EED in the electromagnetic environment, the mathematical model is difficult to solve. After it made a lot of evolution of a simplified mathematical model, the most famous is the Rosenthol energy equation, and has been widely used, the core consideration is to ignore the explosive chemical reaction before ignition.

$$C\frac{d\tilde{T}(t)}{dt} = P(t) - G\cdot\tilde{T}(t)$$

where: $\tilde{T}(t)$is temperature of change; $P(t)$ is induced power; C is thermal capacitance; G is thermal conductivity;

When temperature of EED arrive a steady situation. the equation must be a simple format [4]:

$$\tilde{T}(t) = \frac{P(t)}{G}$$

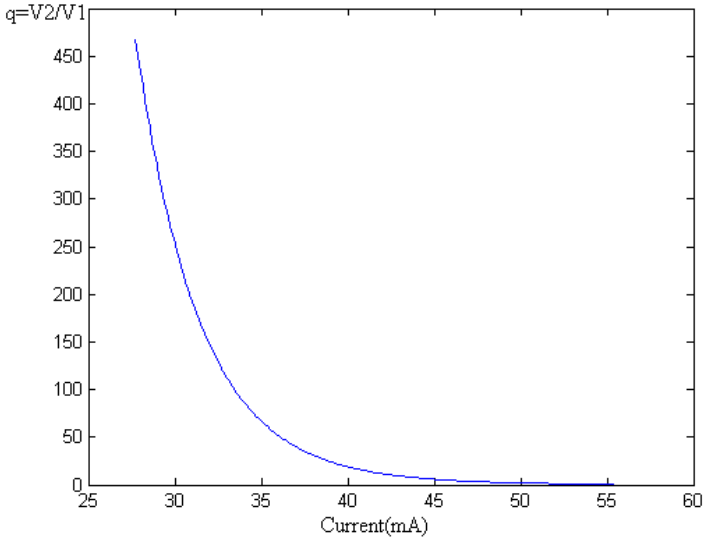

Figure 1: Relationship between light voltage ratio of mid and far infrared and current.

3. INDUCED ENERGY TEST

The test method of EED induced energy which pick up from the electromagnetic environment based on infrared optical approach to establish the relationship between temperature and induced current. Using the result to assess the safety of EED in the electromagnetic environment.

The Fig. 2 describe the test principle of infrared optical fiber temperature system.

The infrared temperature measurement system consists of lenses, infrared fiber, infrared spectroscopy, infrared detectors, fiber, signal amplifier,and so on. Infrared signal is generated from bridge wire coupling through infrared lens, go through the infrared spectroscopy, separate the signal to the mid-infrared and far infrared signal and sent separately, and then photoelectric detector will transform infrared signal as a weak signal which will magnify by the signal amplifier, sampling and analysis the data into the signal processing device for reading the temperature [5].

The main parameters of infrared temperature measurement system are as follows:

(1) Temperature Dynamic Range: $0 \sim 2000°C$.
(2) Response time: 1 ms.
(3) Temperature accuracy: $\pm 0.5°C$.

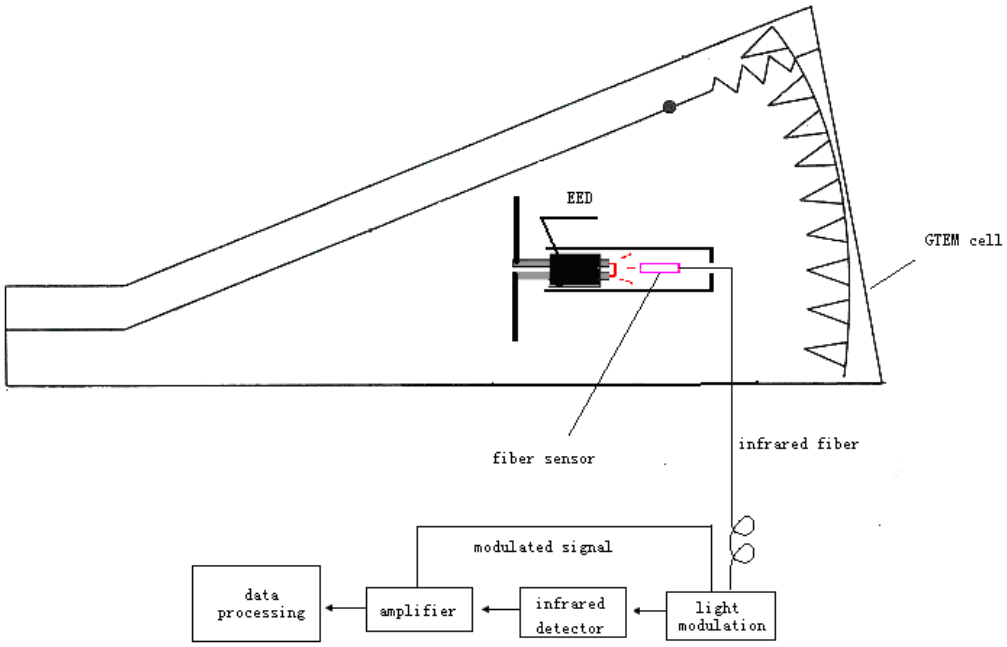

Figure 2: Induced current test in EME.

Figure 3: Infrared detector and system.

In this paper, we used a typical bridge-wire EED to test the temperature and induced current and assess the safety of the EED.

According to the parameters of this typical hot wire EED, the no-fire current is 600 mA; To assess the safety of EED in the electromagnetic environment using the induced current that mentioned in MIL-STD-464A and GJB786; In order to ensure the safety of ordnance, the induced current of EED should not exceed 16.5 dB of the no-fire current; In another words, the induced current can not exceed 15% of no-fire current. Fig. 6 describe the relation between induced current and safety margin.

According to Fig. 6, when the induced current more than 90 mA (temperature exceed 80°C) of the typical EED in the electromagnetic environment, there will be a potential safety hazards of the EED(in this case the electric field Strength of about 150 V/m, frequency: 190 MHz).

Table 1: Data for temperature and current of a typical bridge-wire.

number	temperature°C	current mA	number	temperature °C	current mA
1	10	35	11	110	104
2	20	50	12	120	106
3	30	62	13	130	110
4	40	70	14	140	111
5	50	77	15	150	114
6	60	82			
7	70	88			
8	80	91.5			
9	90	93			
10	100	100			

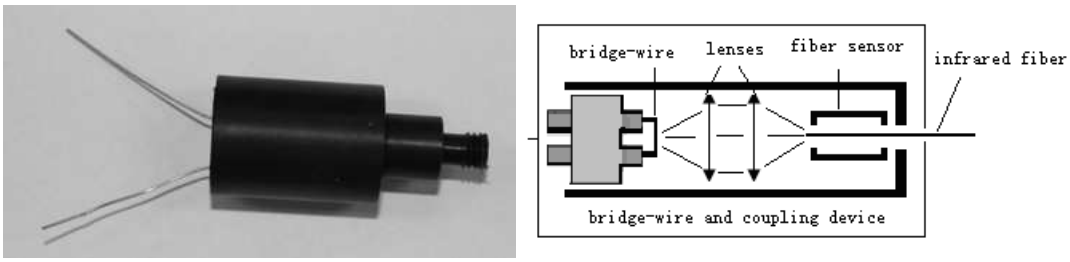

Figure 4: Coupling device between bridge-wire and fiber.

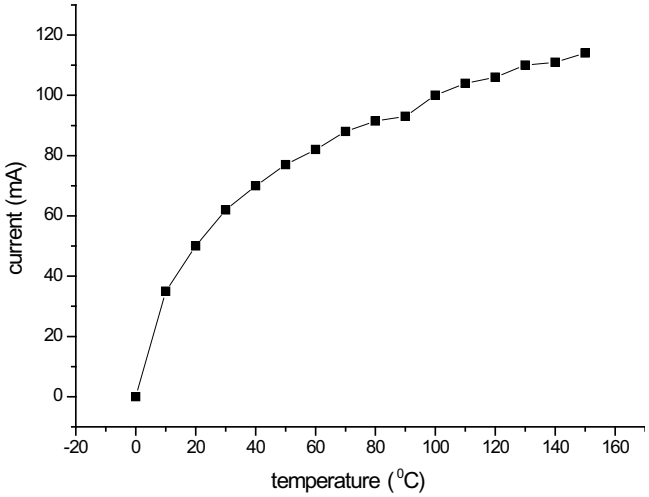

Figure 5: Temperature and current of typical bridge-wire.

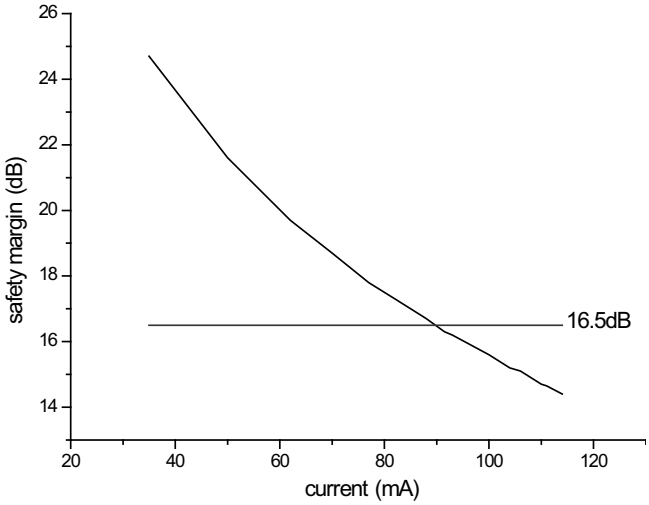

Figure 6: Relation between current and safety margin.

4. CONCLUSION

Based on the principle of infrared fiber temperature measurement that is not only solve the other test systems vulnerable to electromagnetic radiation shadow of the shortcomings, but also solve the other measurement system is attached to the introduction of human error.

ACKNOWLEDGMENT

Support by foundation: 9140c3703020905.

REFERENCES

1. Qi, X.-L., S.-G. Wang, and L.-R. Shi, "Safety measurement of electric ignition in EMR [J]," *Initiators & Pyrotechnics*, No. 4, 2004 (in Chinese).
2. Luo, X.-Q., "Security measurement of EED in strong electromagnetic field [J]," *Safety and EMC*, No. 4, 2002 (in Chinese).
3. Lee, K. R., J. E. Bennett, W. H. Pinkston, and J. E. Bryant, "New method for assessing EED susceptibility to electromagnetic radiation [J]," *IEEE Transactions on Electromagnetic Compatibility*, Vol. 33, No. 4, 1991.
4. Cai, R.-J., *Design Principle for EED [M]*, Beijing Institute of Technology Press, 1999 (in Chinese).
5. Sonnemann, F. and M. Hahn, "Determination of EID safety distance in pulsed electromagnetic environments [J]," *2010 Asia-Pacific International Symposium on Electromagnetic Compatibility*, No. 4, 2010.

Measurement of the Shielding Effectiveness of Connector by Improved Triaxial Method

Qi Zhang, **Li-Hua Shi**, **Ying Hui Zhou**, **Cheng Gao**, **and Yong Chao Guo**
Engineering Institute of Engineering Corps, PLA, University of Science & Technology
Nanjing, Jiangsu 210007, China

Abstract— Protection of electronic system from high intensity radio field (HIRF) receives more and more attention in avionic systems. Shielding effectiveness (SE) and transfer impedance are important parameters that describes the electromagnetic protection ability of cable systems. In the design of electronic system in flights, it is required to compare the shielding property of different kinds of cable connectors. A triaxial test fixture for measuring SE of cable connectors is designed according to IEC 62153-4-7. Compared to the most commonly used test fixtures, this fixture is designed to eliminate the influence of cable shields and bonding condition at cable ends. Therefore the material property and the manufacturing quality of the connector itself can be evaluated. Two kinds of connectors made of aluminum alloy and carbon-fiber composite, respectively, are tested and compared.

1. INTRODUCTION

Electromagnetic fields from distant sources such as high intensity radiate field (HIRF), lightning, high electromagnetic pulse (HEMP), as well as nearby interference sources can induce undesired signals at the endpoints of transmission lines and connectors and therefore disturbs those termination systems. Besides cable shields, connectors of cables also have electromagntic leakage and its value may be higher than cable shields if the connector is not properly selected or not imperfectly bonded [1]. Susceptibility measurement and analysis of connectors to electromagnetic interference (EMI) are becoming a key requirement in design of modern electronic systems.

Field coupling to connectors has been widely addressed in the literatures [2–5]. Because the connectors are electrical small, the testing results were transfer impedance of assembles including additional cables and connectors, the impact of additional cables was not eliminated. A triaxial test fixture for measuring SE of cable connectors is designed according to IEC 62153-4-7 in this paper. Compared to the most commonly used test fixtures, this fixture is designed to eliminate the influence of cable shields and bonding condition at cable ends on SE of the connector under test. Therefore the material property and the manufacturing quality of the connector itself can be evaluated. Two kinds of connectors made of aluminum alloy and carbon-fiber composite, respectively, are tested and compare by using the established triaxial test fixture.

This paper is organized as follows. Section 2 presents the design method of the triaxial test fixture applying for the avionic connectors. Data processing and measurement results analyzing in Section 3. The conclusions are given in Section 4.

2. DESIGN OF THE TRIAXIAL FIXTURE

The connector test method of IEC 62153-4-7 is an extended triaxial method, also named screening shielding method, or tube in tube method. The complete measurement setup is shown as Figure 1. The connector is electrical small, this method for testing connector has some advantages as follows:

1) an apparatus of a triple coaxial form with a length sufficient to produce a superimposition of waves in narrow frequency bands which enable the envelope curve to be drawn.

2) variable length of the tube, e.g., by different parts of the tube and/or by a movable tube in tube. Both transfer impedance and screening attenuation are measured with this method.

3) a RF-tight extension tube, variable in length, which should have preferably a diameter such that the characteristic impedance to the outer tube is 50 Ohm respectively the nominal impedance of the network analyser or generator and receiver.

4) the material of the extension tube shall be non ferromagnetic and well conductive (copper or brass) and shall have a thickness ≥ 1 mm such that the transfer impedance is negligible compared to the transfer impedance of the device under test.

2.1. Design the Diameter Size and Length of the Outer Tube and Extension Tube

In order to avoiding the resonance, the tube length must consider the following condition in terms of transmission lines theory [6]:

$$\frac{4L}{\lambda} = 2n - 1, \quad (n = 1, 2, 3, \ldots) \tag{1}$$

where, L is the tube length, $\lambda = c/f$ is the wavelength, c, f are light speed and frequency, respectively.

Simultaneity, the higher mode of TEM wave must be restrained with the ratio of the diameter of the outer tube and extension tube:

$$\pi \left(D_{\text{in}} + D_{\text{out}} \right) < 2\lambda \tag{2}$$

Considering the characteristic impedance of connectors, the ratio is

$$Z_{\text{C}} = \frac{60}{\sqrt{\varepsilon_{\text{r}}}} \ln \left(\frac{D_{\text{in}}}{D_{\text{out}}} \right) \tag{3}$$

where, Z_C is the characteristic impedance of connectors, ε_r is relative permittivity, D_{in}, D_{out} are the diameter of the outer tube and the extension tube, respectively.

2.2. Impedance Matching Circuit

It is very important that the inner circuit should be matched. If not matching, the input current cannot be injected into the inner circuit; and the receiver cannot gain the maximal coupling voltage of the outer circuit, which conspicuously degrade the precision of the test setup. However, the outer circuit may not be matched. The likely voltage peaks at the far end are not dependant on the input impedance of the receiver, provided that it is lower than the characteristic impedance of the secondary circuit. However, it is an advantage to have a low mismatch, for example, by selecting a range of tube diameters for several sizes of coaxial cables [1].

If the impedance of the connector under test Z_C is not equal to the generator output resistance (commonly 50 Ω), then an impedance matching circuit is needed. It shall be implemented as a two resistor circuit with one series resistor, R_S and one parallel resistor R_P [1]. If the impedance of the

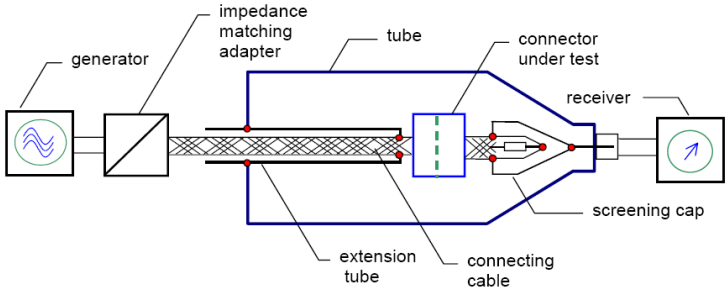

Figure 1: The complete measurement scheme.

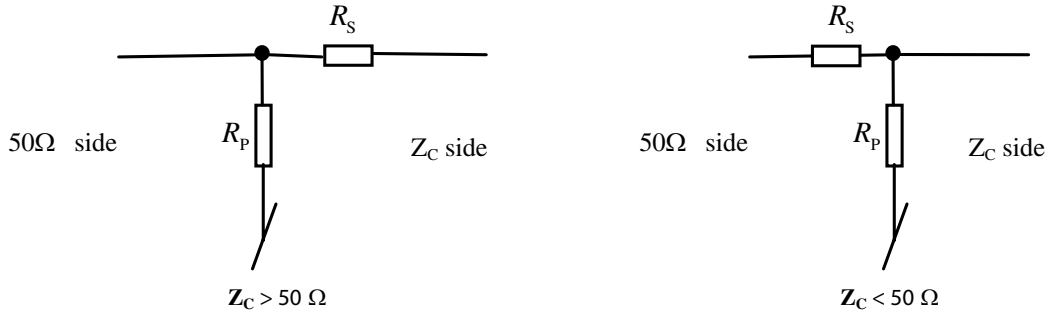

Figure 2: Impedance matching.

Figure 3: The outer tube.

Figure 4: The extension tube.

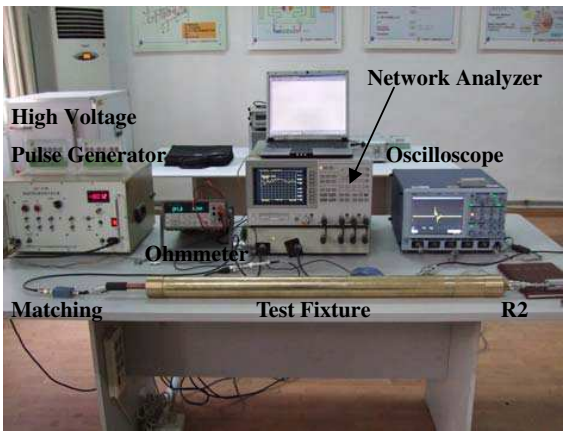

Figure 5: The complete testing setup.

inner system is greater than 50 Ω, the formulas below are used:

$$R_{\mathrm{S}} = Z_C\sqrt{1-\frac{50}{Z_C}}, \qquad R_P = 50\Big/\sqrt{1-\frac{50}{Z_C}} \tag{4}$$

The configuration is depicted in Fig. 2.

If the impedance of the inner system Z_C is less than 50 Ω, the formulas below are used:

$$R_S = 50\sqrt{1-\frac{Z_C}{50}}, \qquad R_P = Z_C\Big/\sqrt{1-\frac{50}{Z_C}} \tag{5}$$

The feed resistor R_2 is related to the outer circuital characteristic impedance. It has an important impact on the cut-off frequency of the test setup, so impacts also on the precision of the higher frequency. R_2 is

$$R_2 = 1.4 \times Z_{\mathrm{Out}} - 50 \tag{6}$$

The Photo of the outer tube, the extension tube, and the complete test system are shown as Fig. 3, Fig. 4, and Fig. 5, respectively.

3. MEASUREMENT RESULT ANALYZING

3.1. Screening Attenuation

By extending the electrically length of the RF-connector by a RF-tight closed metallic extension tube (tube in tube), the tested combination becomes electrically long and the cutoff frequency is moved towards the lower frequency range. In this way, also in the lower frequency range, the screening attenuation may be measured and the effective transfer impedance calculated of electrical short devices.

$$As = A_{B,\min} - A_{z,\min} + 10\log_{10}\left|\frac{Z_{\mathrm{out}}}{Z_{\mathrm{in}}}\right| \tag{7}$$

where, As is the screening attenuation related to an outer circuit (radiating) impedance of Z_{out} in dB; $A_{B,\min}$ is the operational attenuation recorded as minimum envelope curve of the measured values in dB; A_Z is the additional operational attenuation of an eventually inserted adapter, if

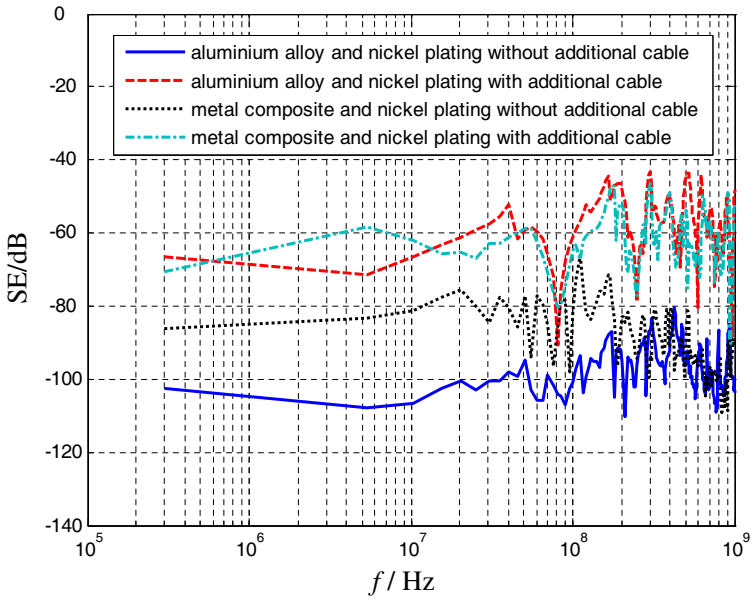

Figure 6: Screening efficiency of two kinds of connectors.

Figure 7: The improved method compared with Fig. 4.

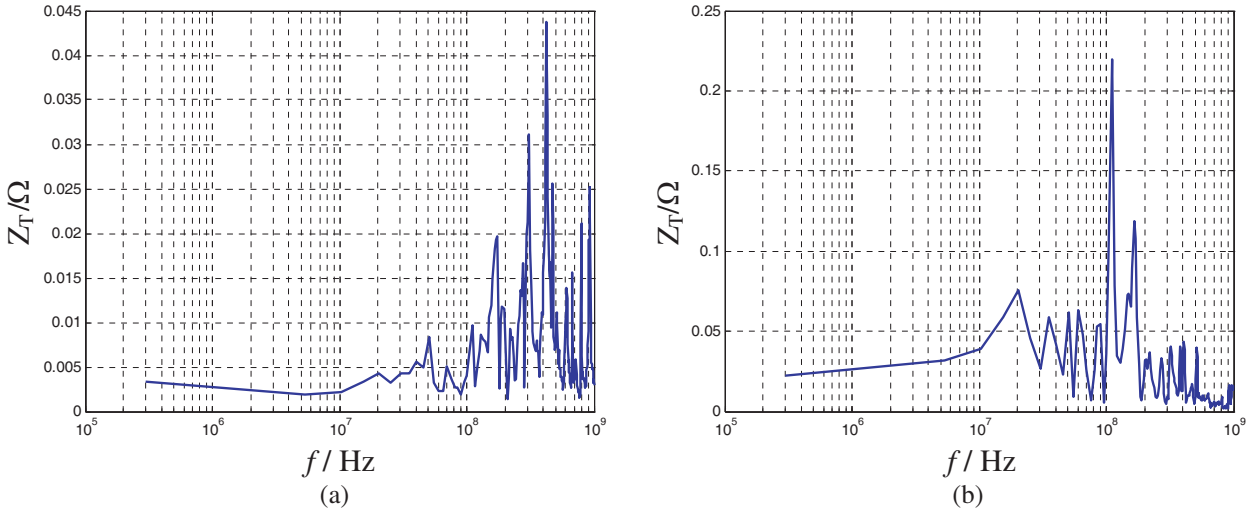

Figure 8: Effective transfer impedance of aluminium alloy-nickel plating connector (a) and carbon-fiber composite-nickel plating connector (b).

not otherwise eliminated, e.g., by the calibration, in dB. Z_{in} is the characteristic impedance of the feeding cable and the DUT, in Ohms.

Two kinds of connectors are tested, which are aluminium alloy-nickel plating and carbon-fiber composite-nickel plating connectors, respectively. Test results shown as Fig. 6. show that the SE curve of the two connectors are very close to each other (the red and light blue ones) if the additional cable influence is not eliminated, and the quality of connectors can not be identified clearly. By using the newly designed test fixture, shown as Fig. 7, the difference of the connector can be found (the blue and black ones). It is proved that the test fixture designed in this paper can be used as a good approach for selection of cable connectors.

3.2. Effective Transfer Impedance

Contrary to the measurement of the transfer impedance of cable screens, the transfer impedance of the connector is not related to length.

$$Z_T = \sqrt{Z_1 Z_2} \cdot 10^{-\frac{A_B}{20}}, \text{ or, } Z_T \text{dB}(\Omega) = 20 \cdot \log\left(\frac{|Z_T|}{1\Omega}\right) \tag{8}$$

where, Z_1 and Z_2 are the characteristic impedance of inner circuit and outer circuit. A_B is the results of network analyzer.

The results of effective transfer impedance are shown as Fig. 8 with the neglect of the transfer impedance of the extension brass tube. In addition, the low frequency data of transfer impedance is in accord with the resistor $r_{dc} = 3\,\text{m}\Omega$, which is one of the characteristic parameters of connector.

4. CONCLUSION

The connector measurement is very complicated due to the multi-materials, multi-conductors and complex structure. An improved triaxial method has been proposed in this paper. The testing setup can measure both screening attenuation and the effective transfer impedance. Two kinds of different material connectors for the avionic connectors are tested, these connectors are distinguished successfully.

REFERENCES

1. IEC 62153-4-7: Metallic communication cable test methods — Part 4-7: Electro Magnetic Compatibility (EMC) — Shielded screening attenuation, test method for measuring the transfer impedance ZT, the screening attenuation as and the coupling attenuation ac of RF-Connectors up to and above 3 GHz; Tube in Tube method.
2. Fowler, E. P., "Screening of multipin connectors — Suggested measuring techniques," *10th International Conference Electromagnetic Compatibility, IEE*, September 1–3, 1997.
3. Hoeft, L. O. and J. S. Hofstra, "Measured electromagnetic shielding performance of commonly used cables and connectors," *IEEE Transactions on Electromagnetic Compatibility*, Vol. 30, No. 3, August 1988.
4. Bluhm, M. and E. Peroglio, "Measurements of transfer impedance with the line injection method on cables and connectors," *IEEE*, 2000.
5. Van Horck, F. B. M. and A. P. J. van Deursen, "A rapid method for measuring the transfer impedance of connectors," *IEEE Transactions on Electromagnetic Compatibility*, Vol. 40, No. 3, August 1998.
6. Gu, R. and M. Sheng, *Microwave Technique and Antenna*, National Defence Industry Press, 1980.

A Small-sized Fast Rise Time HEMP Simulator

Yanxin Li, **Qiwu Wang**, **Lihua Shi**, **Cheng Gao**, **Feng Lu**, **and Bihua Zhou**
Nanjing Engineering Institute, No. 1 Haifuxiang, Nanjing, Jiangsu 210007, China

Abstract— A small-sized fast rise time HEMP simulator is designed. The structure of the small-sized fast rise time HEMP simulator is made of four components, including automatic high voltage source, pusle generator, antenna and match load. The automatic high voltage source produces high direct current voltage for the pulse generator automatically. Through replacing the traditional gas by refined rapeseed oil in the pulse generator, a moving electrode reduces the inductance of the discharge circuit. Therefore, the rise time of the pulse is more fast, up to 2 ns. A microcomputer (MPU) controls the charge procedure and monitors the charge voltage. To measure the electronic field a fiber optic measurement device is used. An application on measurement of shielding body's pulse electric field shielding effectiveness shows that the simulator is suitable for fieldwork.

1. INTRODUCTION

Nowadays, EMP simulator is widely studied [1, 2]. In Reference [2], a portable pulse electric field shielding effectiveness measurement device, which can be used in fieldwork, is designed. But the pulse electric field simulator of the device can not meet the requirement of the MIL-STD-461E [3] or IEC61000-2-9 [4] specification. Because the rise time of the device is 4 ns, slower than 2.5 ns of the specifications. In this paper, a small-sized fast rise time HEMP simulator is designed.

2. HEMP SIMULATOR

2.1. The Structure of the Simulator

The structure of the small-sized fast rise time HEMP simulator is made of four components, including automatic high voltage source, pulse generator, antenna and match load, showed in Fig. 1. The automatic high voltage source produces high direct current voltage for the pulse generator automatically, and can control the discharge procedure. The structure of the pulse generator is showed in Fig. 2.

The circuit diagram of the simulator is showed in Fig. 3. To charge high voltage pulse capacitor Cm, A microcomputer (MPU) controls a MOS FET T1 to swith on and off alternatively. The charge procedure and charge voltage are also monitored by the MPU. If the voltage reachs the preseted level, the MPU instructs the electromagnet to move through the transistor T2, and then the upper electrode is pushed to the nether electrode in Fig. 2, so the high voltage pulse capacitor Cm discharges. Because no gas control circuit is need, the structure of the simulator is simpled.

2.2. Oil Isolation Fast Discharge Switch

The discharge switch is made of two electrodes, one electromagnet and one isolation stick, showed as Fig. 2. When the electromagnet is power on by the transistor T2, the isolation stick is pushed,

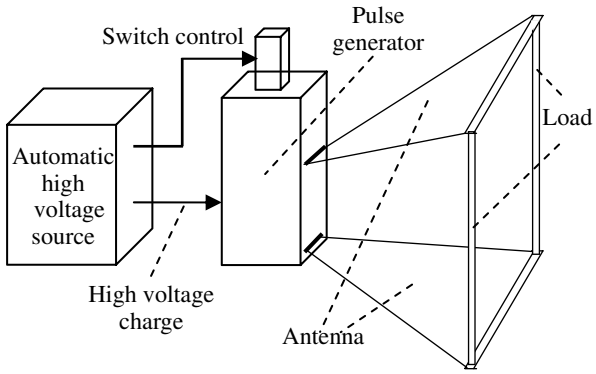

Figure 1: The structure of the small-sized fast rise time HEMP simulator.

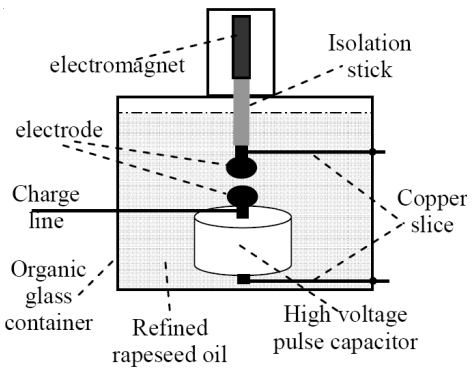

Figure 2: The structure of the pulse generator.

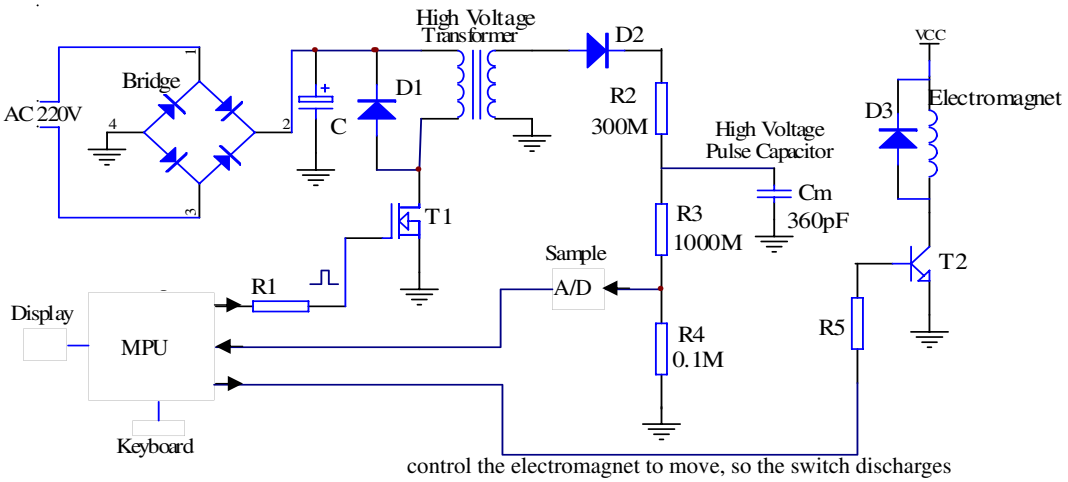

Figure 3: The circuit diagram of the simulator.

therefore the upper electrode move to the other the capacitor Cm is discharged. To reduce the rise time of the simulator, optimizing the parameter of the discharge switch is very important. The relationship between the inductance of the discharge circuit and the rise-time of the double-exponential wave produced by the HEMP stimulator is as follows:

$$t_r \approx 2.2L/R \tag{1}$$

in formula (1), L is the distribution inductance in the discharge circuit, which plays a key role in deciding the rise-time of the pulse. However the switch inductance $L1$ is one important part of L. According to reference [5] there is the follow formula:

$$L_1 \approx 14dnH \tag{2}$$

in formula (2), d is the distance of the spark channel whose unit is cm. Therefore, if the switch is small and compacted, that is to say the distance of the spark channel is more short, the switch inductance $L1$ is more low. The discharge switch gap is filled with innocuous, fully biodegradable, and well insulating refined rap oil. Through replacing the traditional gas by the refined rapeseed oil in the discharge switch, when one electrode moving to the other the discharge spark channel is very short, and the rise time of the radiating electric field is very short, as fast as 2 ns.

3. FIBER OPTIC TRANSMISSION MEASUREMENT DEVICE

In measurement of strong electromagnetic field, a fiber optic transmission device is usually used to pass the measured quantity of the field to a recording and analyzing system [6]. Because the rise time of HEMP electric field is about 2 ns, the frequency bandwide must be broad enough. To expand the bandwide of the fiber optic transmission device in referance [6], a frequency compensation module is added. The structure is showed in Fig. 4. The electric field is firstly changed to electric signal, and then be amplified and compensated. At last,it is turn into the optical signal in a light emission device. The modulation is amplitude modulation. The transmission fiber is multi-mode. At the receiving end, the optical signal is turn into electric signal within the range of ± 1 V. Both the emission device and receiving device are respectively fixed in a metal box which protects the circuits from outside interference. Especially, the emission device metal box has more than 100 dB electromagnetic shielding effectiveness.

The fiber optic transmission device bandwide can be sweeped by Agilent 4396B network. The bandwide is showed in Fig. 5. It can be found in Fig. 5 that the bandwide is expanded up to 200 MHz. By adding a electrically small monopole antenna, the fiber optic transmission device can measure the HEMP simulator's electric field. Fig. 6 shows the measurement result. The rise time of the measurement wave is 2 ns.

4. APPLICATION

The simulator can be used to measure pulse electric field shielding effectiveness of a shielding body. The setup of the measurement is showed in Fig. 7.

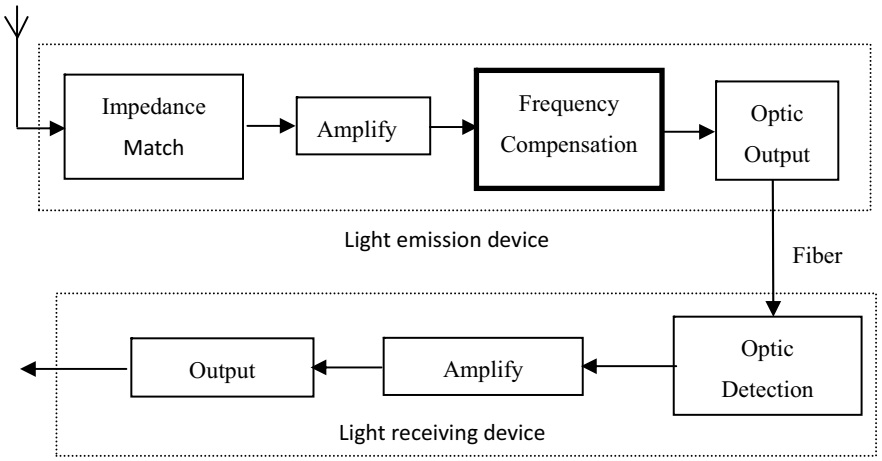

Figure 4: Fiber optic transmission device.

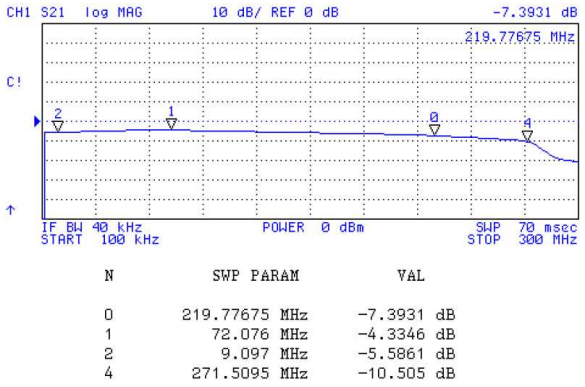

Figure 5: The fiber optic transmission device bandwide.

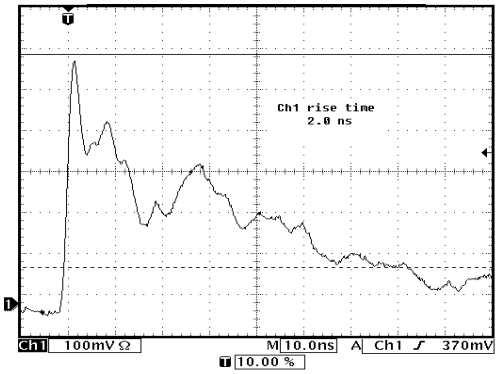

Figure 6: The radiation wave measured by the device.

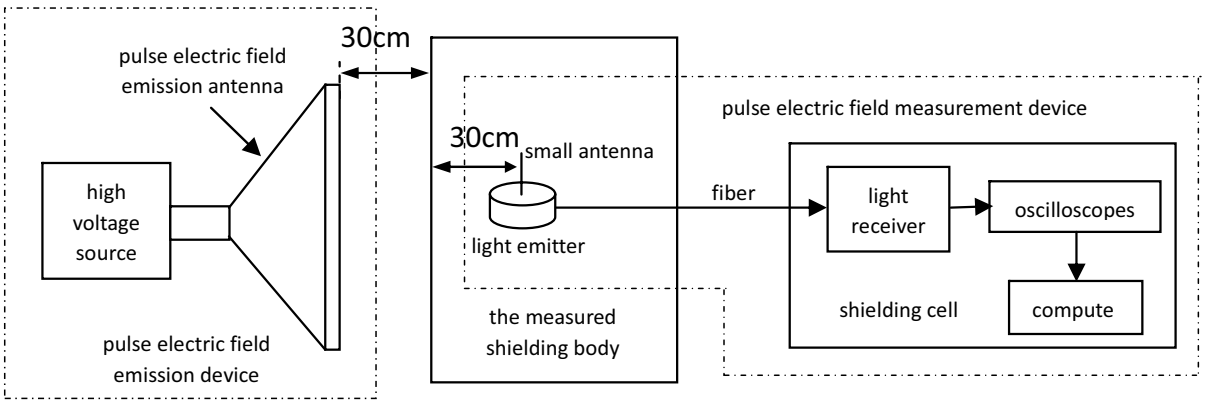

Figure 7: Diagram of pulse electric field shielding effectiveness measurement.

Shielding effectiveness of pulse electric field of shielding body is defined as the ratio of peak (E_{op}, E_{ip}) value of the electric field of one point non-shielded and shielded, that is,

$$SE_{MP} = 20 \log \frac{E_{op}}{E_{ip}} \text{ (dB)} \tag{3}$$

By measuring the two peaks of E_{op} and E_{ip}, the shielding effectiveness can be calculated.

5. CONCLUSIONS

Analyze the measurement results, some conclusions can be obtained as following:

(1) Through replacing the traditional gas by refined rapeseed oil in the discharge switch, a moving electrode can reduce the inductance of the discharge circuit. Therefore, the rise time of the pulse is more fast, up to 2 ns.

(2) The simulator is convenient for using because of its automation and its small size.

(3) By adding a frequency compensation module, 100 MHz bandwide fiber optic transmission device can be expanded to 200 MHz bandwide, suitable for HEMP measurement.

ACKNOWLEDGMENT

This work was supported by the National Nature Science Foundation of China under Grants 51077133 and the NCET.

REFERENCES

1. Zhou, B.-H., B. Chen, and L.-H. Shi, *EMP and EMP Protection*, National Defense Industry Press, Beijing, 2003.
2. Lu, F., B. Chen, H. Wan, et al., "Portable electric field shielding effectiveness measurement device," *High Voltage Technology*, Vol. 32, No. 8, 49–51, 87, 2006.
3. IEC 61000-2-9, *Description of HEMP Environment Radiated Disturbance*, 1996.
4. MIL-STD-461E, "Requirements for the control of electromagnetic interference characteristics of subsystems and equipment," 1999.
5. Zeng, Z.-Z., "Introduction to practical pulsed power technique," Shanxi Technology Press, Xi'an, 2003.
6. Li, Y., L. Shi, C. Gao, et al., "Measurement of pulse electromagnetic field using wide band fiber optic analogue transmission system," *High Voltage Engineering*, Vol. 32, No. 2, 34–36, 2006.

Coupling Energy Analysis and Calculation of HEMP on EED

Xiangfei Ji, **Qingmei Feng**, **Tuan Zhao**, **and Hongzhi Yao**
Science and Technology on Applied Physical Chemistry Laboratory
Shaanxi Applied Physics-Chemistry Research Institute, Xi'an, Shannxi 710061, China

Abstract— In order to analyze the impact of HEMP on EED, the energy distribution of HEMP at different frequency bands and the coupling energy of HEMP on EED should be studied firstly. This paper analyzed the coupling energy of high altitude nuclear electromagnetic pulse (HEMP) on EED by the methods of effective aperture of the antenna and electromagnetic hazards analysis, established the quantitative calculation model of coupling energy and proposed the preliminary verification method. Test the induced current of HEMP radiating on EED by the current monitor, calculate the coupling energy, and compare with the theoretical results. The test results and calculated results are at the same magnitude, which indicated that the theoretical analysis model is relatively reasonable.

1. INTRODUCTION

The vast majority of currently used EED are hot bridge wire type, and the initiation is achieved by the heated bridge wire buried in detonator. When the EED is in the nuclear electromagnetic pulse radiation field, its foot line is able to receive electromagnetic pulse energy to make the foot line generate induced current, which lead to EED initiation or degradation in performance.

High-altitude nuclear electromagnetic pulse (HEMP) is the single pulse wave. It's often represented by double exponential function. The action time is from tens to hundreds nanoseconds, peak power is up to MW, and the power of each point in the pulse duration is different. From the frequency domain analysis, frequency band is wider, different energy densities of different frequency bands, so the effects research of HEMP on EED should analyze the energy distribution of various frequency bands and the energy of HEMP coupling into EED.

2. HEMP ENVIRONMENT

High-altitude electromagnetic pulse (HEMP) is generally expressed as a double exponential function [1, 2],

$$E(t) = E_0 k(e^{-\alpha t} - e^{-\beta t}) \tag{1}$$

where: E_0 is the peak electric field strength, k is the correction factor, α, β are the parameter of the pulse trailing edge and the pulse leading edge.

At present, in HEMP effect test, typical waveform standards applied are primarily Bell Laboratory and MIL-STD-461E waveform standards. The waveform of Bell Lab is shown in Fig. 1; the waveform of MIL-STD-461E is shown in Fig. 2.

Waveform parameters of Bell Lab are as follows:

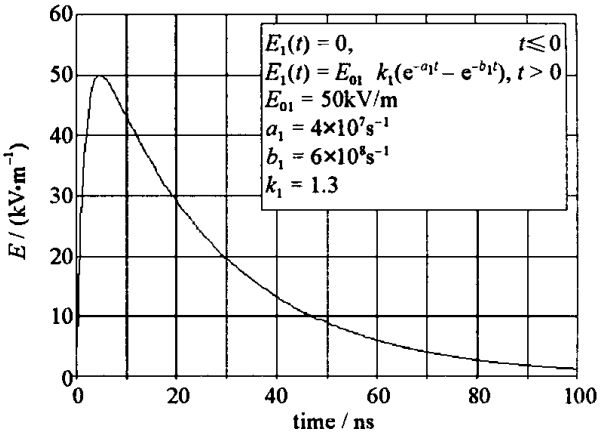

Figure 1: Bell Lab waveform.

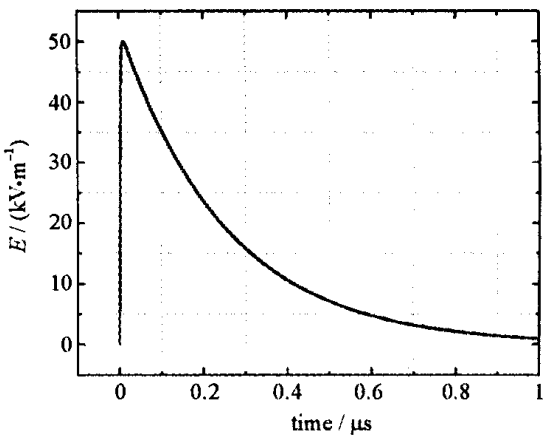

Figure 2: MIL-STD-461E waveform.

- rise time (between 10% and 90% points) about equal to 5 ns,
- full width half maximum (FWHM) pulse width equal to 184 ns,
- parameters: $\alpha = 4 \times 10^6\,\mathrm{s}^{-1}$, $\beta = 4.76 \times 10^8\,\mathrm{s}^{-1}$, $k = 1.05$, $E_0 = 50\,\mathrm{kV/m}$.

MIL-STD-461E standard waveform parameters are as follows:

- rise time between 1.8 ns and 2.8 ns,
- FWHM pulse width equal to $23\,\mathrm{ns} \pm 5\,\mathrm{ns}$,
- parameters: $\alpha = 4 \times 10^6\,\mathrm{s}^{-1}$, $\beta = 6 \times 10^8\,\mathrm{s}^{-1}$, $k = 1.3$, $E_0 = 50\,\mathrm{kV/m}$.

From the time domain analysis, the rising time of MIL-STD-461E Waveform is faster than Bell Lab waveform (the latter is about 2 times of the former), and half width of MIL-STD-461E Waveform is more narrow than Bell Lab waveform (the latter is about 8 times of the former). From the frequency domain analysis, 96% energy flow of MIL-STD-461E waveform distribute between $100\,\mathrm{kHz} \sim 100\,\mathrm{MHz}$; and the energy flow of Bell Lab waveform distribute between $10\,\mathrm{kHz} \sim 30\,\mathrm{MHz}$. By calculating the energy density, the energy density of Bell Lab waveform is larger, which is about $0.891\,\mathrm{J/m^2}$; and the energy density of MIL-STD-461E is smaller, which is only $0.114\,\mathrm{J/m^2}$.

3. COUPLING ENERGY ANALYSIS MODEL OF HEMP ON EED

The EED foot line which is expanded to 180° in the nuclear electromagnetic pulse field, can be calculated coupling energy as the equivalent dipole. The coupling energy of HEMP on EED has prodigious relation with the foot line length. The operating frequency of equivalent antenna with the different length of foot line is different. HEMP frequency bandwidth is wider, then the distribution of energy in each band is also smaller under the same total energy. The more narrow bandwidth is, the smaller the probability covering the equivalent antenna bandwidth will, and the greater the average power of distribution in each band is. Under normal circumstances, HEMP bandwidth is wider than the bandwidth of equivalent antenna, which can completely cover the work bandwidth of the equivalent antenna.

This paper approximately calculated the coupling energy of HEMP on EED by the methods of effective aperture of the antenna and electromagnetic hazards analysis. In free field, the effective aperture of the dipole antenna is A_e, which like this [3].

$$A_e = \frac{1.64\lambda^2}{4\pi} = \frac{1.64c^2}{4\pi f^2} \quad f > f_c \tag{2}$$

$$A_e = \frac{1.64c^2 f^2}{4\pi f_c^4} \quad f \le f_c \tag{3}$$

Make Fourier Transform for the field expressions of High-altitude nuclear electromagnetic pulse. $E_{(f)}$ can be obtained.

$$E_{(f)} = kE_0 \left(\frac{1}{\alpha + j2\pi f} - \frac{1}{\beta + j2\pi f} \right) \tag{4}$$

Energy spectral density can be calculated by the equation:

$$S_{(f)} = \frac{2\left|E_{(f)}\right|^2}{Z_0}\,(\mathrm{W/m^2 \cdot Hz}), \quad Z_0 = 120\pi\,\Omega \tag{5}$$

The feet line of EED starting can be equivalent to the dipole antenna. The foot length is l m. Effective length of dipole antenna $l = \lambda/4$, the resonant frequency $f_0 = c/\lambda$, the antenna bandwidth $\Delta f = f_2 - f_1$. Dipole antenna bandwidth is currently 10% of resonant frequency typically. The lower limit of antenna bandwidth is $f_1 = (1 - 5\%)f_c$, and the upper limit of antenna bandwidth is $f_2 = (1 + 5\%)f_c$. The energy of HEMP coupling into EED can be calculated:

$$\mathrm{d}W = S_{(f)} \cdot A_e \mathrm{d}f \tag{6}$$

$$W = \int_{f_1}^{f_2} S_{(f)} A_e \mathrm{d}f = \frac{2}{Z_0} \int_{f_1}^{f_2} \left|E_{(f)}\right|^2 A_e \mathrm{d}f \tag{7}$$

where:

W — coupling energy of HEMP on EED (J);
A_e — antenna effective aperture (m^2);
c — the speed of light, 3×10^8 m/s;
Z_0 — free space wave impedance, $Z_0 = 120\pi = 377\,\Omega$;
f_1 — the lower limit antenna bandwidth (Hz);
f_2 — the upper limit antenna bandwidth (Hz).

Calculate the coupling energy of HEMP on EED with different foot line length by using the above method. In the test, measure the induced current of EED, which is $I_{(t)}$, and calculate the coupling energy HEMP on EED with the formula $W = \int I_{(t)}^2 R\mathrm{d}\,t$. Where: R is the EED resistance; t is the ignition time of EED. The ignition time of EED is greater than the pulse width of HEMP waveform, and there is the heat accumulated in the process, so t is taken as the pulse width of HEMP waveform in the calculation.

4. COMPARATIVE ANALYSIS OF TEST RESULTS AND THEORETICAL CALCULATION RESULTS

Calculate the energy of HEMP coupling into EED by using the effective aperture of equivalent antenna and electromagnetic hazard analysis methods. The calculation results record as the theoretical value. Use current monitor to test the induced current of EED which in the nuclear electromagnetic pulse field, and calculate the coupling energy through integral. The test results record as the test value.

Such as the foot-line length of the EED is 90 cm. Vertically place in the MIL-STD-461E standard environment, and the theoretical value of coupling energy is W_1, the test value of coupling energy by using current monitor is W_2.

1) The coupling energy W_1 of MIL-STD-461E standard environment (the theoretical value).

The effective length of dipole antenna is $l = \lambda/4 = 90$ cm. The resonant frequency is $f_c = c/\lambda = 3 \times 10^8/\lambda$. Antenna effective aperture: when $f \le f_c$, $A_{e1} = \frac{1.64c^2 f^2}{4\pi f_c^4}$; when $f \ge f_c$, $A_{e2} = \frac{1.64\lambda^2}{4\pi} = \frac{1.64c^2}{4\pi f^2}$. Peak field strength is $E_1 = 47$ kV/m, and the frequency domain expression for electric field is $E_{(f)} = E_1(\frac{1}{\alpha+j2\pi f} - \frac{1}{\beta+j2\pi f})$, $\alpha = 4.0 \times 10^7\,\mathrm{s}^{-1}\beta = 6 \times 10^8\,\mathrm{s}^{-1}$.

In accordance with the above mestord and data, W_1 is gained.

$$W_1 == \frac{2}{Z_0}\int_{f_1}^{fc} \left|E_{(f)}\right|^2 A_{e1}\mathrm{d}f + \frac{2}{Z_0}\int_{f_c}^{f2} \left|E_{(f)}\right|^2 A_{e2}\mathrm{d}f = 5.1 \times 10^{-4}\,\mathrm{J}.$$

2) The energy through integral W_2 by using the current monitor (the test value).

When peak field strength is $E_1 = 47$ kV/m, measure the induced current of EED foot-line by using the current monitor. Electric the resistance of the EED $R = 10\,\Omega$, the time is $t = 50$ ns.

Calculate the energy of HEMP coupling into EED. $W_2 = \int I_{(t)}^2 R\mathrm{d}t = 4 \times 10^{-4}$ J.

The data can be gained by the above method. The calculation data is shown in Table 1.

The test value is gained by using current monitor to measure the induced current, through integral in the whole pulse width (10% to 10% of the time). The theoretical value is obtained as the calculation result through the whole bandwidth with 100% coupling. From the table analysis, it

Table 1: The test value compare with the theoretical calculation.

EED foot-line length(cm)	Bell waveform			MIL-STD-461E waveform		
	Electric field strength (V/m)	coupling energy (J)		Electric field strength (V/m)	coupling energy (J)	
		Test value	Theoretical value		Test value	Theoretical value
90	4×10^4 4.7×10^4	$10^{-6} \sim 10^{-5}$	1.3×10^{-5} 9.6×10^{-6}	4×10^4 4.7×10^4	$10^{-6} \sim 10^{-5}$	1.9×10^{-5} 2.6×10^{-5}
200	4×10^4 4.7×10^4	10^{-4}	3.1×10^{-4} 4.3×10^{-4}	4×10^4 4.7×10^4	10^{-4}	5.1×10^{-4} 7.3×10^{-4}

is known that the test results and calculated results are at the same magnitude, which indicated that the theoretical analysis model is relatively reasonable. We can carry out approximate calculation on the energy of HEMP coupling into EED by using the effective aperture of equivalent antenna and electromagnetic hazard analysis methods, and estimate the effect of EED in different nuclear electromagnetic pulse field.

5. CONCLUSIONS

In this stage the effects research of nuclear electromagnetic pulse, study on inspecting the state changes by making products test in the nuclear electromagnetic pulse radiation. Such as whether the computer crashes, whether digital display is wrong, whether EED is ignition and so on, all these are qualitative judgments.

This paper analyzed the coupling energy of high altitude nuclear electromagnetic pulse (HEMP) on EED, make the quantitative calculation model of coupling energy and propose the preliminary verification method. Test the induced current of HEMP radiating on EED by the current loop, calculate the coupling energy, and compare with the theoretical results. The test results and calculated results are the same magnitude, indicating that the theoretical analysis model is more reasonable.

The theoretical and experimental results are compared to verify the theoretical calculation. Currently, the dipole antenna bandwidth is generally taken 10% of the resonant frequency to calculate. In the future studies we will study and determine the equivalent bandwidth of the antenna with the different length of EED foot-line, so that the calculation results are more fit with the theoretical results. The coupling energy of HEMP on EED in HEMP radiation field can be theoretically calculated by using the analysis model. All the studies can provide theoretical guidance for the effect test of HEMP on EED to improve the pertinence and validity of testing.

REFERENCES

1. Xie, Y., Z. Wang, and Q. Wang, "Standards and characteristics of high-altitude nuclear electromagnetic pulse waveform [J]," *High Power Laser and Particle Beams*, Vol. 15, No. 6, 781–787, 2003-8 (in Chinese).
2. Ji, X., Q. Feng, J. Li, T. Zhao, and H. Yao, "Research on anti nuclear electromagnetic pulse technology of EED [J]," *Defense Technology Foundation*, No. 3, 21–24, 2008-3 (in Chinese).
3. Yao, H., "Electromagnetic compatibility and safety study on industrial electric detonators," Graduate Dissertations (in Chinese).

A Multi-step Electromagnetic Topology Method to Compute the Coupling of External Electromagnetic Fields and Inner Wires of a Cavity through Apertures

Guyan Ni, **Ying Li**, **and Jianshu Luo**
Department of Mathematics and System Science, College of Science
National University of Defense Technology, Changsha, Hunan 410073, China

Abstract— In this paper, we introduce a multi-step electromagnetic topology (EMT) method to analyze interactions of external EM fields and inner wires of a cavity through apertures. The method involves three basic steps. The first step obtains an interaction sequence diagram to analyze the interaction processes for the electromagnetic coupling. The second step obtains different models to compute parameters of each junction in the diagram. For instance, based on the equivalence principle, we will use a semi-analytical approach based on the Modal Green Function and the method of moment (MoM) to compute an equivalent source for the aperture and employe Baum-Liu-Tesche (BLT) equations and Agrawal's or Taylor's formulations to calculate the coupling of field-to-wire. The last step calculates all junctions' parameters. We use above models to compute each junction's parameters from one junction to the next according the interaction sequence diagram. By multi-step iteration the coupling computation is finished. Compared with the traditional EMT theory, the new method has a remarkable change that is not need to compute a scattering supermatrix. Numeric results confirm the validity of the method.

1. INTRODUCTION

The Electromagnetic Topology (EMT) is first proposed by Baum and Tesche during the 70's ([1–3]), which is a method to analyze and calculate the coupling problems of a complex electromagnetic system. The main idea of this theory is to break down the complex system into elementary subsystems, in order to find proper rules for the design of hardened structures [4–6].

The traditional EMT includes three main steps. The first step is to build an interaction sequence diagram of a system. The outer surfaces of the system is assumed to behave as an EM shield, the system is broken up into independent volumes which are bounded by these surfaces that define the so-called "shielding levels". The propagation of EM signals moving within the system can be realized by the topological shielding diagram, as depicted in Fig. 1. An appropriate labeling of volumes and surfaces allows the diagram to define the relative shielding levels between each volume. The EM interaction in the system can be summarized in an interaction sequence diagram (Fig. 2). This contains information on the signal flow within the system, in that sense that the directed branches represent the flux of interference from the outside to the inside.

The second step is to build the Baum-Liu-Tesche (BLT) equation. The BLT equation is used to determine the signals in any point of the network by grouping the propagation and distribution equations.

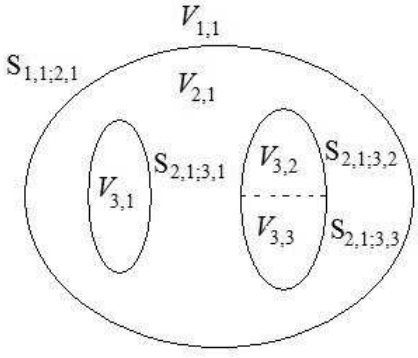

Figure 1: Topological shielding diagram.

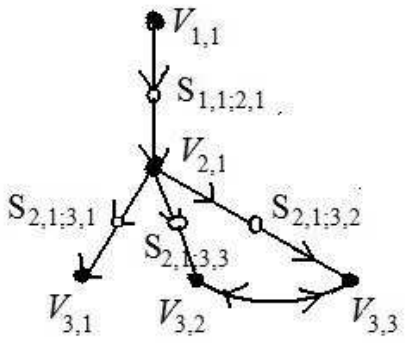

Figure 2: Interaction sequence diagram.

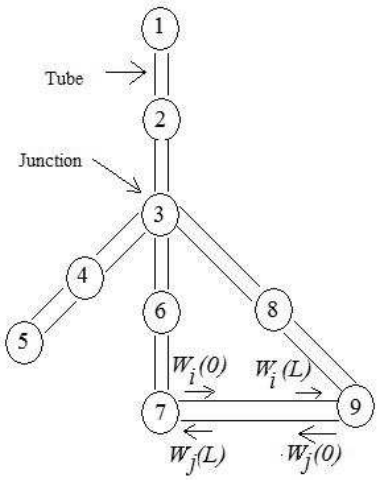

Figure 3: Topological network.

On each tube, define two independent opposite directions waves, outgoing wave, $W_i(0)$, $W_i(L)$, and incoming wave, $W_j(0), W_j(L)$, and define equivalent combined excitation source W_{s_i} (see Fig. 3). Where L is the real length of a cable section. Introducing a propagation matrix, Γ_i, [7, 10] shows that the equation on a tube supporting a wave W_i can be written as

$$W_i(L) = \Gamma_i \cdot W_i(0) + W_{s_i}$$

At each junction, a scattering equation provides the relation between each outgoing wave, W_i, and incoming wave, W_j, by introducing a S_{ij} scattering matrix. The junction scattering relationship is thereby defined as

$$W_i(0) = S_{ij} \cdot W_j(L)$$

By collecting all the incoming wave, outgoing wave, and source-wave vectors in wave supervectors, respectively, $[W(0)]$, $W(L)$, and $[W_s]$, a propagation equation and a scattering equation for the entire network can be defined as

$$[W(L)] = [\Gamma] \cdot [W(0)] + [W_s] \quad (1)$$

$$[W(0)] = [S] \cdot [W(L)] \quad (2)$$

where $[\Gamma]$ and $[S]$ are the propagation and scattering supermatrices of the network, respectively. By eliminating the incoming wave vector in (1) and (2), the BLT equation is as follows

$$\{[1] - [S][\Gamma]\}[W(0)] = [S][W_s] \quad (3)$$

where [1] is the unit matrix.

The last step is to calculate the supermatrix $[S]$ and $[\Gamma]$, and solve the BLT equation. The concept of supermatrix means that all the calculations of Equation (3) can be made by blocks. However, the supermatrix $[S]$ is hard to be obtained. For an aperture junction, the supermatrix is obtained by electric fields probed at the distance of 1 unit on both sides as the expressions are given by [8]

$$S_{11}^{ap}(\omega) = S_{22}^{ap}(\omega) = \frac{E_{xref}(\omega)}{E_{xinc}(\omega)}$$

$$S_{21}^{ap}(\omega) = S_{12}^{ap}(\omega) = \frac{E_{xtrans}(\omega)}{E_{xinc}(\omega)}$$

where $E_{xref}(\omega)$ is the reflected field, $E_{xinc}(\omega)$ is the incident field, and $E_{xtrans}(\omega)$ is the transmitted field.

This paper proposes a multi-step EMT method which need not to compute the scattering supermatrix $[S]$. It also has three basic steps. The first step is to obtain an interaction sequence diagram to analyze the interaction processes for the electromagnetic coupling similar to the traditional EMT. The second step is to select a proper method to compute parameters of each junction in the diagram. The last step calculates coupling of the system applying a multi-step iteration method from one junction to the next according the interaction sequence diagram.

2. THE MULTI-STEP ELECTROMAGNETIC TOPOLOGY METHOD

Consider a rectangular cavity with 2 energy penetration paths (apertures) illuminated by a harmonic plane wave, see Fig. 4. We first analyze the electromagnetic interaction process as Fig. 5 and Fig. 6.

Figure 5 shows the topological structure model associated to Fig. 4. V_1 and V_2 denote subvolumes, $ap1$ and $ap2$ denote two apertures. Fig. 6 shows the electromagnetic interaction sequence network diagram.

The next step is to select a proper method for each junction. For the junction "$ap1$", coupling roads "$V_1 \longrightarrow ap1 \longrightarrow V_2$" and "$V_2 \longrightarrow ap1 \longrightarrow V_1$" are aperture coupling, the exterior (inner) fields are coupled to the inner (exterior) fields. We employ dyadic Greens functions and the method of moments to determine the electromagnetic coupling fields inside (outside) the cavity, the detail to see Ref. [11, 12]. For the junction "tube", the coupling road "$V_2 \longrightarrow tube$" is a coupling of fields to lines. We apply the BLT equation to obtain the induced voltage and current. Another road "tube $\longrightarrow V_2$" is a coupling of lines to fields, only to compute scattering fields.

The last step is a multi-step iteration algorithm to compute the induced voltage and current on the tube. Assume the exterior incident field (E^i, H^i).

The first-road iteration is to compute the coupling alon the road

$$V_1 \longrightarrow (ap1,\ ap2) \longrightarrow V_2 \longrightarrow tube.$$

Denote $(E^1_{V1},\ H^1_{V1}) = (E^i, H^i)$. Compute (E^1_{ap1}, H^1_{ap1}), (E^1_{ap2}, H^1_{ap2}), (E^1_{V2}, H^1_{V2}) and (I^1_{tube}, V^1_{tube}) in turn. Here I^1_{tube} and V^1_{tube} are the induced voltage and current of the tube.

The second-road iteration is to compute the added coupling alon the road

$$V_1 \longleftarrow (ap1,\ ap2) \longleftarrow V_2 \longleftarrow tube.$$

Denote $(\Delta I^1_{tube}, \Delta V^1_{tube}) = (I^1_{tube}, V^1_{tube})$ as input. Compute $(\Delta E^1_{V2}, \Delta H^1_{V2})$, $(\Delta E^1_{ap2}, \Delta H^1_{ap2})$, $(\Delta E^1_{ap1},\ \Delta H^1_{ap1})$, $(\Delta E^1_{V1},\ \Delta H^1_{V1})$ in turn. Here Δ denotes the added coupling. Then

$$\begin{aligned}
\left(E^2_{V1}, H^2_{V1}\right) &= \left(E^1_{V1}, H^1_{V1}\right) + \left(\Delta E^1_{V1}, \Delta H^1_{V1}\right) \\
\left(E^2_{ap1}, H^2_{ap1}\right) &= \left(E^1_{ap1}, H^1_{ap1}\right) + \left(\Delta E^1_{ap1}, \Delta H^1_{ap1}\right) \\
\left(E^2_{ap2}, H^2_{ap2}\right) &= \left(E^1_{ap2}, H^1_{ap2}\right) + \left(\Delta E^1_{ap2}, \Delta H^1_{ap2}\right) \\
\left(E^2_{V2}, H^2_{V2}\right) &= \left(E^1_{V2}, H^1_{V2}\right) + \left(\Delta E^1_{V2}, \Delta H^1_{V2}\right) \\
\left(I^2_{tube}, V^2_{tube}\right) &= \left(I^1_{tube}, V^1_{tube}\right)
\end{aligned}$$

The third-road iteration is to compute the added coupling alon the road

$$V_1 \longrightarrow (ap1,\ ap2) \longrightarrow V_2 \longrightarrow tube.$$

Denote $(\Delta E^2_{V1},\ \Delta H^2_{V1}) = (\Delta E^1_{V1},\ \Delta H^1_{V1})$ as input. Compute $(\Delta E^2_{ap1},\ \Delta H^2_{ap1})$, $(\Delta E^2_{ap2},\ \Delta H^2_{ap2})$,

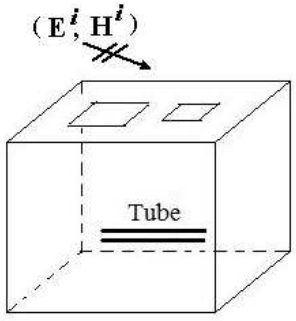

Figure 4: Rectangular cavity with apertures.

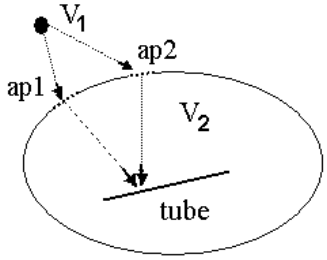

Figure 5: Topological shielding diagram.

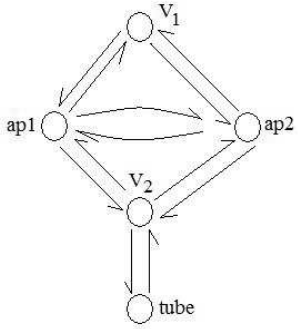

Figure 6: Interaction sequence diagram.

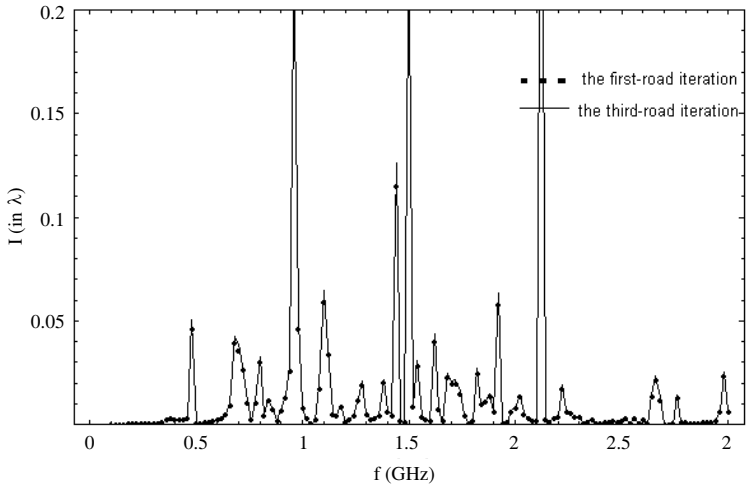

Figure 7: Return loss of a circular corrugated horn.

$(\Delta E_{V2}^2, \Delta H_{V2}^2)$ and $(\Delta I_{tube}^2, \Delta V_{tube}^2)$ in turn. Then

$$\begin{aligned}
\left(E_{V1}^3, H_{V1}^3\right) &= \left(E_{V1}^2, H_{V1}^2\right) \\
\left(E_{ap1}^3, H_{ap1}^3\right) &= \left(E_{ap1}^2, H_{ap1}^2\right) + \left(\Delta E_{ap1}^2, \Delta H_{ap1}^2\right) \\
\left(E_{ap2}^3, H_{ap2}^3\right) &= \left(E_{ap2}^2, H_{ap2}^2\right) + \left(\Delta E_{ap2}^2, \Delta H_{ap2}^2\right) \\
\left(E_{V2}^3, H_{V2}^3\right) &= \left(E_{V2}^2, H_{V2}^2\right) + \left(\Delta E_{V2}^2, \Delta H_{V2}^2\right) \\
\left(I_{tube}^3, V_{tube}^3\right) &= \left(I_{tube}^2, V_{tube}^2\right) + \left(\Delta I_{tube}^2, \Delta V_{tube}^2\right)
\end{aligned}$$

And so on, till the algorithm is ended.

3. NUMERICAL COMPUTATION

We compute the coupling of a rectangular cavity with two rectangular apertures on a surface and a two-wire transmission line in it, which is illuminated by a harmonic plane wave. The parameters of the cavity is as follows: the cavity's size $0.5\,\mathrm{m} \times 0.4\,\mathrm{m} \times 0.3\,\mathrm{m}$, two identical apertures's size $0.1\,\mathrm{m} \times 0.04\,\mathrm{m}$, the wire radius $0.0003\,\mathrm{m}$, the wire length $0.4\,\mathrm{m}$, the wire separation distance $0.02\,\mathrm{m}$, the load resistance $Z_1 = Z_2 = 50\,\Omega$. Fig. 7 shows that the induced current of the wire at the load obtained by the first-road iteration is less than that of by the third-road step iteration.

4. CONCLUSION

In this paper, A multistep electromagnetic topology method is introduced to analysis and calculate the coupling EM fields of a complex system. The method inherits the topology interaction sequence diagram and abandons the computation of the scattering supermatrix of the traditional EMT. The method makes our computation easy and convenient.

ACKNOWLEDGMENT

This work was supported by China Postdoctoral Special Science Foundation (No. 200902662), the National Natural Science Foundation of China (No. 10871231), and Pre-research Foundation of Weapon and Equipment (No. 9140A31020609KG0170).

REFERENCES

1. Tesche, F. M., "Topological concepts for internal EMP interaction," *IEEE Trans. Antennas Propagat.*, Vol. 26, 60–64, February 1978.
2. Baum, C. E., "The theory of the electromagnetic interference and reference data," Interaction Notes, 478, December 1989.
3. Baum, C. E., "The Theory of electromagnetic Interference control," *Modern Radio Science*, Oxford University Press, 87–101, 1990.
4. Baum, C. E., "Sublayers sets and relative shielding order in electromagnetic topology," *Electromagnetics*, Vol. 2, 335–354, 1982.

5. Baum, C. E., T. K. Liu, and F. M. Tesche, "On the analysis of general multi-conductor transmission-line networks," Interaction Notes, 350, November 1978.
6. Parmantier, J. P., J. C. Alliot, G. Labaune, and P. Degauque, "Electromagnetic coupling on complex systems: Topology approach," Interaction Notes, 488, 1990.
7. Baum, C. E., "Electromagnetic topology for the analysis and design of complex electromagnetic systems," *Fast Electrical and Optical Measurements*, J. E. Thomson and H. Leussen, (Eds). Vol. 1, 467C-547, Martinus Nijoff, Dordrecht, The Netherlands, 1986.
8. Kirawanich, P., J. R. Wilson, S. J. Yakura, and N. E. Islam, "A generic topological simulation scheme for studying aperture electromagnetic field interactions and cable couplings," *J. Appl. Phys.*, Vol. 102, 024902, 2007.
9. Yang, F. C. and C. E. Baum, "Electromagnetic topology measurements and norms of scattering parameters of subshields," *Electromagnetics*, Vol. 6, 47–59, 1986.
10. Parmantier, J.-P., "Numerical coupling models for complex systems and results," *IEEE Trans. Electromagnetic Compatibility*, Vol. 46, 359–367, 2004.
11. Li, Y., G. Y. Ni, J. S. Luo, et al., "Coupling onto the two-wire transmission line enclosed in cavities with apertures," *PIERS Proceedings*, 682–633, Moscow, Russia, August 18–21, 2009.
12. Li, Y., J. S. Luo, and G. Y. Ni, "The terminal responses of the two-wire line in multiaperture cavities based on electromagnetic topology and method of moments," *Mathematical Problems in Engineering*, accepted January 7, 2011.

Equivalent Circuit Model for Two Layer Dumbbell Type Defected Ground Structures

D. Baatarkhuu[1], Y. S. Choi[1], S. T. Yu[1], T. Tharoeun[1], H. Liu[2], and D. Ahn[1]

[1]Soonchunhyang University, Republic of Korea
[2]East China Jiaotong University, China

Abstract— A new equivalent circuit model for a two-layer dumbbell-type defected ground structure (DGS) is proposed. Many papers on defected ground structures have been published over the past ten years. However, the majority have focused on microstrip structures. In this paper, we introduce a two-layer dumbbell-type DGS, and derive an equivalent circuit model. The structure is designed for increased equivalent capacitance. To confirm the validity of the equivalent circuit model, several EM simulation and measurement results for two-layer dumbbell type DGS circuits are compared with the corresponding simulated results for the equivalent circuits.

1. INTRODUCTION

A defected ground structure (DGS) allows a circuit to be inserted readily into the ground plane. These structures are used in the RF/microwave/millimeter-wave frequency bands, and many research papers in this area have been published and presented at conferences [1–11]. The etched defect in the ground plane of a DGS offers the advantages of increased effective inductance and capacitance, giving rise to high impedance transmission lines and facilitating size reduction and/or improved performance of RF/microwave circuits [1–4]. Furthermore, lumped elements and transmission line equivalent circuit modeling can be achieved with DGS circuits, enabling the development of low-pass and band-pass filters, couplers, power dividers, antennas, amplifiers, and other such devices. [4–11] In wireless communication devices, the effective application of DGS requires an exact equivalent circuit modeling method.

We propose an exact equivalent circuit model for increasing the equivalent capacitance of a two-layer dumbbell-type DGS until transmission line loss occurs (Fig. 1). The validity of the modeling technique for the new equivalent circuit and two-layer dumbbell-type DGS is verified by comparing measurement results, circuit simulation results, and electromagnetic (EM) simulation results.

2. EQUIVALENT CIRCUIT AND MODELING METHOD

Figure 1 shows a schematic of a two-layer dumbbell-type DGS. The microstrip transmission line width (w) is chosen for a characteristic impedance (Z_0) of 50 ohm. The dimensions shown in Fig. 1 are $a = 5$ mm, $b = 1.4$ mm, $g = s = 0.2$ mm, $w = 1.84$ mm, $w_1 = 1$ mm, and $l = 5.8$ mm. The substrate used for the simulations and measurements has a dielectric constant (ε_r) of 3.2 and a thickness of 32 mil. The characteristic DGS parameters are extracted from Fig. 1 via the de-embedding technique.

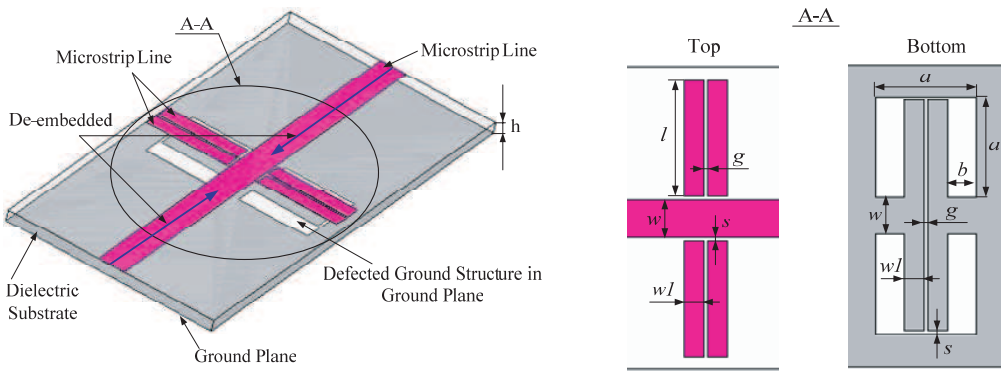

Figure 1. Schematic of a two-layer dumbbell type DGS.

Figure 2 shows the results of the EM simulation of a two-layer dumbbell-type DGS microstrip line, using ANSYS HFSS (ver. 12.1). A 3-dB cutoff frequency (f_C) and an attenuation pole at frequency (f_0) are seen in the figure. Because of the etched defect in the ground, the current flow is interrupted, creating an inductance and giving rise to the cutoff frequency. The gap distance creates a capacitance and causes LC resonance to be achieved, leading to the appearance of the attenuation pole. Thus, by manipulating the characteristics of the cutoff frequency and attenuation pole, the parallel capacitance of the DGS circuit can be used to develop the attenuation pole as a one-pole low-pass filter with series inductance. The capacitance and inductance in the parallel LC circuit can be obtained from the following equations [1, 2]:

$$C = \frac{f_C}{4\pi Z_0 \left(f_0^2 - f_C^2\right)} \tag{1}$$

where f_C is the cutoff frequency, f_0 is the resonant frequency and Z_0 is the impedance of the in/out terminated port.

Figure 3 shows the proposed equivalent circuit model of the two-layer dumbbell-type DGS. In Fig. 3, the DGS losses in the ground plane and microstrip line are regarded as resistance (R) components. The 50-ohm fixed-length (P) microstrip line on the right and left sides of the circuit is included in the equivalent circuit model, and calculated as a phase characteristic of the equivalent circuit.

The resistance can be calculated from the transmission coefficient (S_{21}) at the attenuation pole (i.e., at the resonant frequency (f_0)):

$$R = \frac{2Z_0\left(1 - |S_{21}|\right)}{|S_{21}|} \tag{2}$$

The total length of the microstrip line can be calculated from the dimensional parameters of the DGS:

$$P = b + w_1 \tag{3}$$

where P is the physical length in Fig. 3, and b, w_1 are the physical lengths in Fig. 1.

Using Equations (1)–(4), we can determine the component values of the equivalent circuit for the two-layer dumbbell-type DGS.

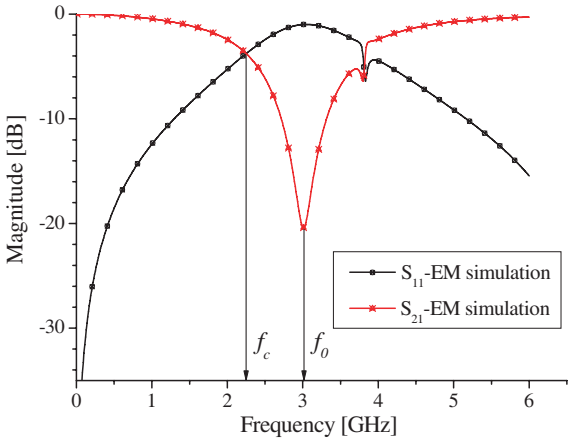

Figure 2. EM simulation result of the two-layer dumbbell type DGS.

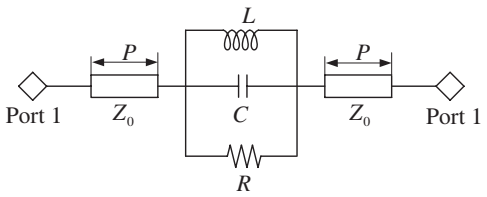

Figure 3. Equivalent circuit model for two-layer dumbbell type DGS.

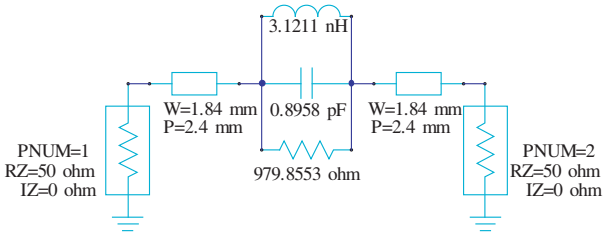

Figure 4. The equivalent circuit structure from ANSYS Designer V.6.0.

3. SIMULATION AND MEASUREMENT

To design the equivalent circuit for the two-layer dumbbell-type DGS, the circuit simulation conditions are: cutoff frequency $f_C = 2.25\,\text{GHz}$, resonant frequency $f_0 = 3.01\,\text{GHz}$, prototype element value of the Butterworth-type one-pole filter $g_1 = 2$, characteristic impedance of the microstrip line $Z_0 = 50\,\text{ohms}$, total microstrip line length $P = 2.4\,\text{mm}$. The component values of the equivalent circuit are those shown in Fig. 4. Fig. 5 presents the circuit simulation results for the S-parameters of the equivalent circuit, using ANSYS Designer (ver. 6.0).

The EM and circuit simulations of the S-parameter magnitudes and phase characteristics (shown in Figs. 5(a) and 5(b), respectively) are in excellent agreement with each other. Fig. 6 shows photographs of the two-layer dumbbell-type DGS. Fig. 7 compares the results obtained by circuit simulation, EM simulation and measurement. The observed agreement between the simulations and experimental results validates the accuracy of new equivalent circuit.

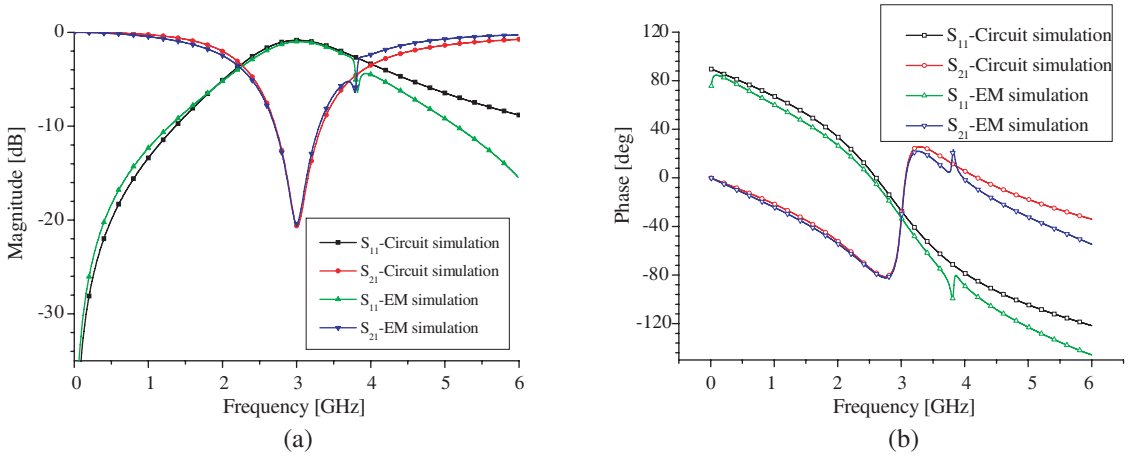

Figure 5. Simulated magnitude and phase result of a two-layer dumbbell type DGS.

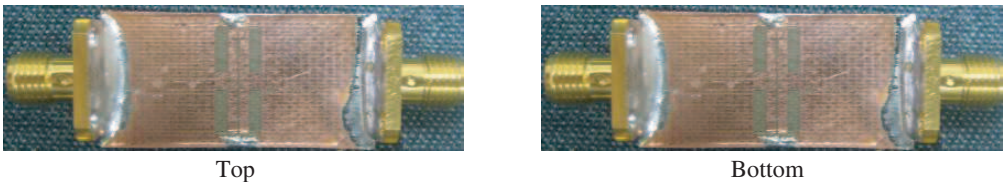

Figure 6. Photograph of a two-layer dumbbell type DGS.

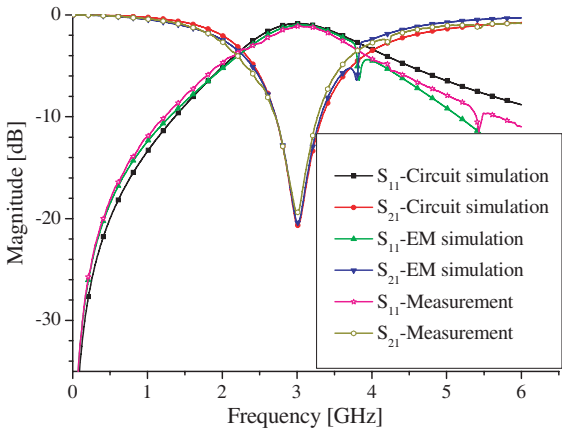

Figure 7. Measured result of a two-layer dumbbell type DGS and the simulation results.

4. CONCLUSIONS

This paper introduced a new two-layer dumbbell-type DGS circuit and its equivalent circuit model. The component values of the equivalent circuit can be found by using resonant frequency conditions and EM simulation results for the proposed circuit. The equivalent circuit simply consists of a parallel RLC circuit and series transmission line. The results of circuit simulations, EM simulations, and experimental measurements were in excellent agreement, and confirmed the validity of the equivalent circuit. It is anticipated that the new two-layer dumbbell-type DGS equivalent circuit could be useful in wireless communication devices.

REFERENCES

1. Ahn, D., J. S. Park, C. S. Kim, J. Kim, Y. Dian, and T. Itoh, "A design of the low-pass filter using the novel microstrip defected ground structure," *IEEE Trans. on MT Ts.*, Vol. 49, No. 1, 86–93, 2001.
2. Kim, C. S., J. S. Park, D. Ahn, and L. B. Lim, "A novel 1-D periodic defected ground structure for planar circuits," *IEEE Microwave Guide Wave Lett.*, Vol. 10, No. 4, 131–133, 2000.
3. Kim, C. S., J. S. Lim, S. Nam, K. Y. Kang, and D. Ahn, "Equivalent circuit modelling of spiral defected ground structure for microstrip line," *Electronics Letters 12th*, Vol. 38, No. 19. 1109–1110, 2002.
4. Lim, J. S., J. S. Park, Y. T. Lee, D. Ahn, and S. Nam, "Application of defected ground structure in reducing the size of amplifiers," *IEEE Microwave and Wireless Components Lett.*, Vol. 12, No. 7, 261–263, 2002.
5. Lim, J. S., C. S. Kim, J. S. Park, D. Ahn, and S. Nam, "Design of 10 dB 90° branch line coupler using microstrip line with defected ground structure," *IEE Electronics Lett.*, Vol. 36, No. 21, 1784–1785, 2000.
6. Lim, J. S., S. W. Lee, C. S. Kim, J. S. Park, D. Ahn, and S. Nam, "A 4 : 1 unequal wilkinson power divider," *IEEE Microwave and Wireless Components Lett.*, Vol. 11, No. 3, 124–126, 2001.
7. Park, J. S., J. S. Yun, and D. Ahn, "A design of the novel coupler-line bandpass filter using defected ground structure with wide stopband performance," *IEEE Trans. on MT Ts.*, Vol. 50, No. 9, 2037–2043, 2002.
8. Chung, Y. K., S. S. Jeon, D. Ahn, and T. Itoh, "High isolation dual-polarized patch antenna using integrated defected ground structure," *IEEE Microwave and Wireless Components Lett.*, Vol. 14, No. 1, 4–6, 2004.
9. Lim, J. S., C. S. Kim, D. Ahn, Y. C. Jeong, and S. Nam, "Design of low-pass filters using defected ground structure," *IEEE Trans. on MT Ts.*, Vol. 53, No. 8, 2539–2545, 2005.
10. Park, J. S., C. S. Kim, H. T. Kang, and D. Ahn, "A novel resonnat microstrip RF phase shiffer using defected ground structure," *30th European Microwave Conference*, Vol. 53, 72–75, October 2000.
11. Koo, J. J., S. M. Oh, M. S. Hwang, C. S. Park, Y. C. Jeong, K. S. Choi, J. S. Lim, and D. Ahn, "An unequal wilkinson power divider without packaging problem of defected ground structure," *Mediterranean Microwave Symposium*, 249–252, Hungary, May 2007.

Triple Mode Resonator Bandpass Filters with Source-load Coupling

K. C. Lee, H. T. Su, and M. K. Haldar
School of Engineering, Computing and Science, Swinburne University of Technology (Sarawak Campus)
Jalan Simpang Tiga, Kuching 93350, Sarawak, Malaysia

Abstract— This paper presents an analytical technique for the study of transmission zeros, which appeared close to the passband edges of a microstrip bandpass filter. The bandpass filter uses a published triple mode resonator, which exhibits two transmission zeros close to the passband and odd resonance suppression in its wideband response. Source-load coupling is introduced to produce an additional transmission zero located to the right of the passband. The stopband response is further improved by this transmission zero. These filters demonstrate good selectivity, compact size, and predictable transmission zeros.

1. INTRODUCTION

Triple-mode resonator structures for microstrip filter are rarely reported in literature. Research work on the triple-mode resonator refers to those using stepped-impedance resonator and ring resonator with incorporated branch-lines as reported in [1–3]. The designs of higher order filters are also demonstrated in [1, 2]. In [3], the desired resonant frequencies of a triple-mode resonator using a ring resonator with two branch-lines can be adjusted by varying the distance between two branch-lines. In a later research [4], a novel hexagonal loop triple-mode resonator reported, with the basic structure using a conventional hexagonal loop dual-mode resonator together with three radial-line stubs.

In this paper, a triple mode resonator consisting of a square open loop resonator and a stepped impedance resonator, as shown in Figure 1(a), is investigated. The stepped impedance resonator is connected to the mid-point of the open loop structure where a grounding via is located. The via which is in the symmetry plane of the square open-loop structure effectively splits the resonator into two quarter-wavelength resonators. Using odd and even mode analysis, the triple mode-resonator structure has one odd mode and two even mode resonant frequencies. Further to our previous work in [5], the existence of the two transmission zeros due to the triple-mode resonator are analyzed. In addition, source-load coupling is introduced by feed structures, which produce an additional transmission zero to the right side of the passband. The effects of the source-load coupling on these transmission zeros, are then investigated and analysed.

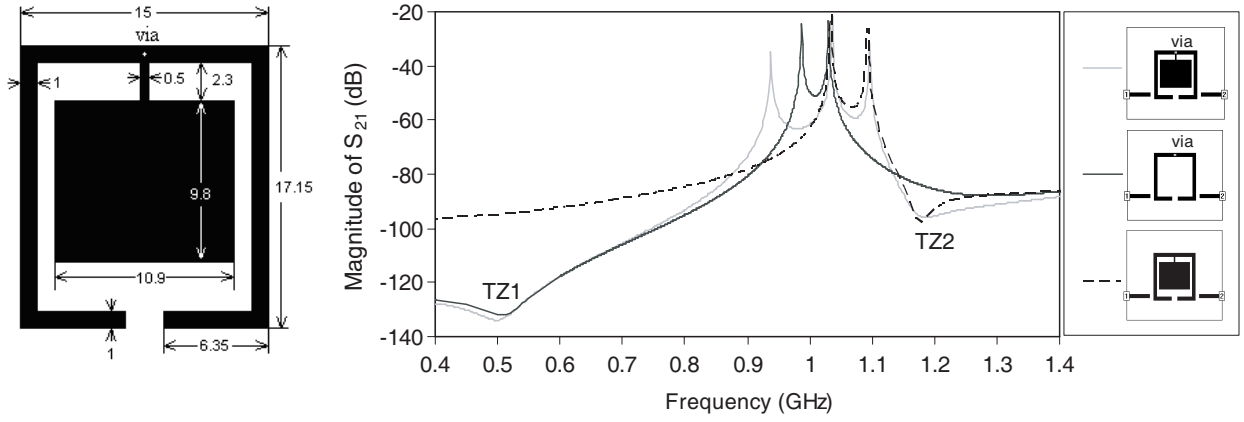

(a) (b)

Figure 1: (a) Compact triple-mode square ring-like resonator (Dimension in millimeters). (b) Simulated responses of various weakly coupled resonators to observe the appearance of transmission zeros. (Top diagram) Triple-mode resonator, (Middle diagram) open-loop resonator with a grounding via in the middle of the structure, and (Bottom diagram) triple-mode resonator without a grounding via.

2. TRANSMISSION ZERO ANALYSIS ON TRIPLE MODE RESONATOR

The triple-mode resonator (Figure 1(a)) is designed using Roger Duroid 6010 substrate with a dielectric constant of 10.2, a substrate thickness of 1.27 mm and a copper thickness of 0.017 mm. It is designed and simulated using Sonnet EM simulator [6]. This resonator is designed for a three-pole bandpass filter with a passband ripple of 0.5 dB, a fractional bandwidth of 15.0% and at the operating center frequency of 1.0 GHz.

When the triple-mode resonator is weakly coupled to the input and output ports, three resonant frequencies and transmission zeros, TZ1 and TZ2, on each side of the passband edge are obtained, as shown in Figure 1(b). Another transmission zero TZ4, not shown in the figure, is located about three times the center frequency of the passband. This transmission zero is not significant in this paper because it is not near the required operating frequency. From simulation, it is found that the stepped impedance resonator can be omitted to obtain TZ1 appearing on the left side of the resonances. The equivalent circuit of the resonator without the stepped impedance resonator is shown in Figure 2(a). $ABCD$ matrix for the equivalent circuit in Figure 2(a) is given as

$$\begin{bmatrix} A & B \\ C & D \end{bmatrix} = \begin{bmatrix} \cos(2\beta_1\ell_1) + \frac{Z_1}{\omega L_{via}}\frac{1}{2}\sin(2\beta_1\ell_1) & jZ_1\sin(2\beta_1\ell_1) + j\frac{Z_1^2}{\omega L_{via}}\sin^2(\beta_1\ell_1) \\ j\frac{1}{Z_1}\sin(2\beta_1\ell_1) - j\frac{1}{\omega L_{via}}\cos^2(\beta_1\ell_1) & \cos(2\beta_1\ell_1) + \frac{Z_1}{\omega L_{via}}\frac{1}{2}\sin(2\beta_1\ell_1) \end{bmatrix} \quad (1)$$

where β_1, ℓ_1 and Z_1 are the propagation constant, the length and the characteristic impedance of the microstrip line, respectively. L_{via} is the inductance value of the grounding via. ω is the angular frequency of the desired passband center frequency. The matrix element B must be infinite to produce a transmission zero. This is not possible as B in (1) consists of two sine functions. TZ1 can be explained using the coupling scheme [7] as discussed in the next section.

The transmission zero on the right side of the resonances (TZ2) can be modeled using the triple-mode resonator structure without the grounding via in Figure 1(b) (the bottom diagram). The stepped-impedance resonator in this resonator produces second transmission zero, which is an added advantage to achieve compact design. The frequency of the second transmission zero, f_{TZ2}, can be estimated using the equivalent circuit in Figure 2(b) and the following equations [8] that present the inductive (L_{zero}) and capacitive (C_{zero}) elements on the stepped impedance line,

$$\begin{aligned} L_{zero} &= \frac{1}{2\pi f_c}\left[Z_{0L}\sin\left(\frac{2\pi\ell_L}{\lambda_{gL}}\right) + Z_{0C}\tan\left(\frac{\pi\ell_C}{\lambda_{gC}}\right)\right] \\ C_{zero} &= \frac{1}{2\pi f_c}\left[\frac{1}{Z_{0C}}\sin\left(\frac{2\pi\ell_C}{\lambda_{gC}}\right) + \frac{1}{Z_{0L}}\tan\left(\frac{\pi\ell_L}{\lambda_{gL}}\right)\right] \\ f_{TZ2} &= \frac{1}{2\pi\sqrt{L_{zero}C_{zero}}} \end{aligned} \quad (2)$$

where ℓ, Z_0, λ_g are the length, impedance and guided wavelength of the inductive (L) or capacitive (C) element, respectively. In this analysis, any capacitive coupling between the two open ends of the two quarter-wavelength lines is neglected. Using the average length of the inductive element to compute (2), the calculated higher transmission zero, f_{TZ2}, is at 1.192 GHz compared to the simulated transmission zeros for the resonator without the grounding via and the triple mode resonator at 1.195 GHz.

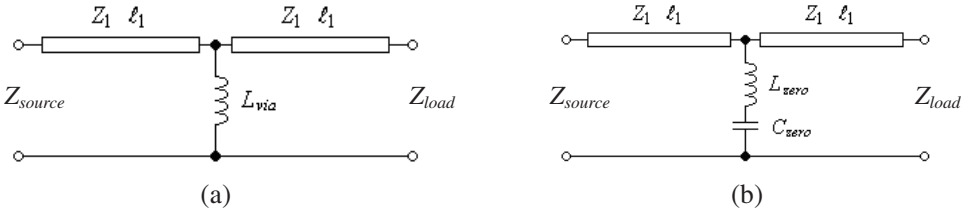

Figure 2: (a) Equivalent circuit of the open-loop resonator with a grounding via in the middle of the structure for the analysis of the lower frequency transmission zero. (b) Equivalent circuit of the triple-mode square ring like resonator without a grounding via for the estimation of the higher frequency transmission zero.

3. TRANSMISSION ZERO CONTRIBUTED BY SOURCE-LOAD COUPLING

The triple mode resonator filter with source-load coupling can be modeled using the coupling scheme shown in Figure 3(a) [7]. The transmission zero TZ1 can result only from unequal coupling of the source-load to the odd and even modes. Since two transmission zeros are produced by such unequal coupling [7, 9], TZ4 represents the other transmission zero.

The design of the triple mode resonator filter is shown in Figure 3(b), where the gap between the two feedlines is kept at 1.2 mm to introduce source-load coupling. This introduces a transmission zero, TZ3, on the right of TZ2. The coupling can be increased by extending the feed structure (segments ℓ_g and ℓ_b) as shown in Figure 3(c). The increase in coupling moves TZ3 towards the passband edge as in [7].

Figure 4(a) shows that increase in length ℓ_g pushes TZ1 from 0.5 GHz towards 0.7 GHz. It also pushes TZ3 closer to TZ2. TZ3 merges with TZ2 when ℓ_g equals to 4.00 mm. The extra segment ℓ_b is added to the feed structures to move TZ3 away from TZ2, as shown in Figure 4(b).

The following are two applications of this triple-mode resonator with the required feed structures as shown in Figures 5(a) and 5(b). Figure 5(a) shows the frequency response of the filter without the extended segment, it shows its TZ1, TZ2 and TZ3 at 0.500 GHz, 1.195 GHz and 1.930 GHz, respectively. The simulated and measured responses are very close to each other. In Figure 5(b) when the extended segment, ℓ_g is 4.00 mm, the simulated TZ3 merges with TZ2 and the measured results for TZ3 is very close to TZ2. TZ1 and TZ3 of the measured results are 0.700 GHz and 1.235 GHz, respectively, compared to the simulated values at 0.700 GHz and 1.245 GHz, respectively.

When ℓ_g is 4.00 mm, the segment ℓ_b with the length of 1.00 mm is added as shown in the inset of Figure 6. This additional segment on the feed structure moves TZ3 away from TZ2 while maintaining the frequency of TZ1 and TZ2. The simulated results are 0.705 GHz, 1.205 GHz and 1.275 GHz compared to the measured results 0.700 GHz, 1.195 GHz, and 1.295 GHz.

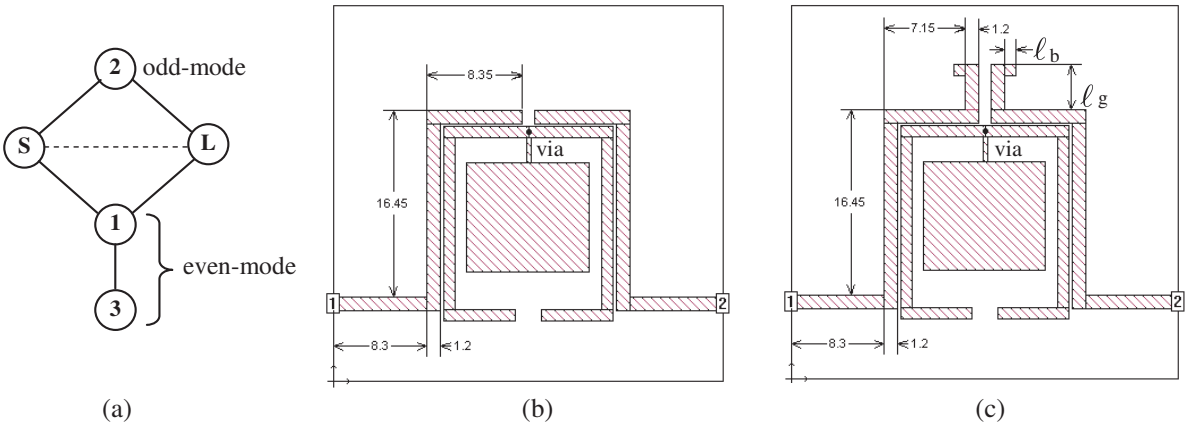

Figure 3: (a) Coupling scheme of the filter, S is the source and L is the load. (b) Layout of the filter with the required feed structure. (c) Layout of the filter with improved passband response. ℓ_g is the extended source-load coupling segment on the feed structure. ℓ_b is the additional segment on the extended segment.

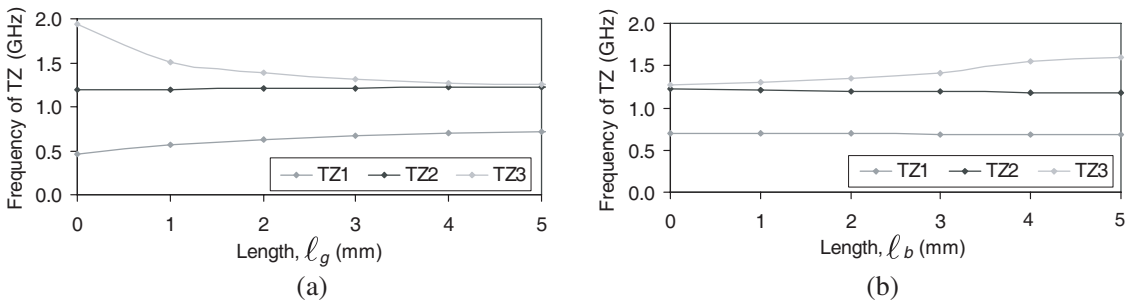

Figure 4: (a) Variation of the frequencies of the transmission zeros (TZ) due to ℓ_g. (b) Variation of the frequency of the transmission zeros due to ℓ_b, when ℓ_g equals to 4.00 mm.

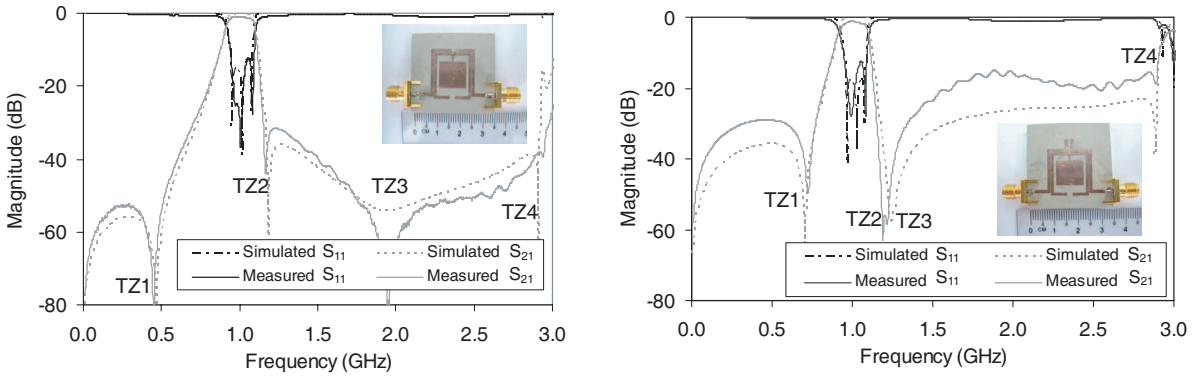

Figure 5: (a) Frequency response of the triple mode resonator filter. The inset shows the filter structure. (b) Frequency response of the triple mode resonator filter with extended segment, ℓ_g, ℓ_g equals to 4.00 mm. The inset shows the filter structure.

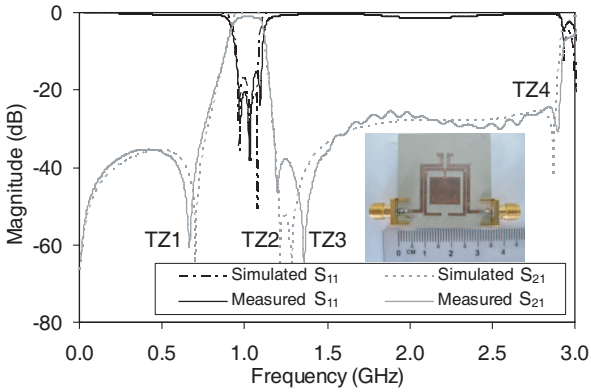

Figure 6: Frequency response of the triple mode resonator filter with extended segment ℓ_g of 4.00 mm and an additional ℓ_b segment with the length of 1.00 mm.

4. CONCLUSIONS

The appearance of transmission zeros associated with the triple mode resonator filter design has been studied. Source-load coupling was introduced and further enhanced by the extended portion of the feed structures. Passband edge and stopband response of the filter are improved.

REFERENCES

1. Chiou, Y.-C., J.-T. Kuo, and E. Cheng, "Broadband quasi-Chebyshev bandpass filters with multimode stepped-impedance resonators (SIRs)," *IEEE Trans. Microwave Theory Tech.*, Vol. 54, No. 8, 3352–3358, Aug. 2006.
2. Zhu, L., S. Sun, and W. Menzel, "Ultra-wideband (UWB) bandpass filters using multiple-mode resonator," *IEEE Trans. Microwave Wireless Component Lett.*, Vol. 15, No. 11, 796–798, Nov. 2005.
3. Cho, C. S., J. W. Lee, and J. Kim, "Dual- and triple-mode branch-line ring resonators and harmonic suppressed half-ring resonators," *IEEE Trans. Microwave Theory Tech.*, Vol. 54, No. 11, 3968–3974, Nov. 2006.
4. Mo, S.-G., Z.-Y. Yu, and L. Zhang, "Design of triple-mode bandpass filter using improved hexagonal loop resonator," *Progress In Electromagnetics Research*, Vol. 96, 117–125, 2009.
5. Lee, K. C., H. T. Su, and M. K. Haldar, "A novel compact triple-mode resonator for microstrip bandpass filter design," *Proceedings of Asia-Pacific Microwave Conference*, 1871–1874, Yokohama, Japan, Dec. 2010.
6. *Sonnet User's Manual*, Version 10, Sonnet Software Inc., Syracuse, New York, 2005.

7. Zhou, M., X. Tang, and F. Xiao, "Miniature microstrip bandpass filter using resonator-embedded dual-mode resonator based on source-load coupling," *IEEE Trans. Microwave Wireless Component Lett.*, Vol. 20, No. 3, 139–141, Mar. 2010.
8. Hong, J.-S. and M. J. Lancaster, *Microstrip Filter for RF/Microwave Applications*, Wiley-Interscience, New York, 2001.
9. Liao, C.-K., P.-L. Chi, and C.-Y. Chang, "Microstrip realization of generalized Chebyshev filters with box-like coupling schemes," *IEEE Trans. Microwave Theory Tech.*, Vol. 55, No. 1, 147–153, Jan. 2007.

A Conjunct Analysis for Breast Cancer Detection by Volume Rendering of Low Dosage Three Dimensional Mammogram

R. Dharanija and T. Rajalakshmi
Electronics & Instrumentation Engineering Department, Panimalar Engineering College
Anna University, India

Abstract— Breast cancer is the fifth most common cause of cancer death after lung cancer, stomach cancer, liver cancer, and colon cancer. Breast cancer is the most common cause of cancer in women and the second most common cause of cancer death in women. The earlier the breast cancer is detected the more the chances of treatment and even cure. If detected early, the five-year survival rate exceeds 95%.

A majority of breast cancers are diagnosed as a result of an abnormality seen on a mammogram. A mammogram is actually a 2-D x-ray image of the breast. The radiologist, who specializes in reading x-ray images, can identify differences between a normal breast and one that may show signs of cancer. Mammography is a test that allows the doctor to look at images of the inside of the breasts.

However, it is possible for a 2D mammogram to look normal even though a breast cancer is actually present. This is more common in patients of younger age where the breast tissues are denser and thus spotting an abnormality becomes difficult. Also, it is possible for a 2D mammogram to look abnormal when there is actually no cancer and in this case additional testing is required. To overcome limitations of these kinds in breast cancer detection, the patient had to undergo additional testing procedures. One such additional procedure is the recently developed 3-D (Tomosynthesis) technology which allows us to see cancers that might be hidden and using a three-dimensional image along with a 2-D mammogram provided a clearer picture.

Despite the fact that 3D mammography eliminates overlapping of tissue that is seen in conventional 2-D mammograms, it was noted that using 3-D mammography technique as an adjunct with 2-D mammograms doubled the radiation dose the patient received, increasing cancer risk.

This paper gives an idea of how 2D image can be obtained from the 3D mammogram data without the need to take 2-D slices additionally and hence avoiding issues related to over dose of radiation. Volume rendering technique is proposed which displays a 2D projection of a 3D discretely sampled data set.

1. INTRODUCTION

Mammography can detect very early breast tumors, when they are too small to be felt. In fact, most of the breast cancers detected by screening at this very early stage are relatively easy to cure. The treatment for breast cancer has been improving for the last twenty years. In the early 1970's, only half of all women diagnosed with the disease survived for five years. Now, over three quarters survive for that long and most of them will live for very much longer. Studies have shown that women who take part in screening are more likely to have breast cancer diagnosed early and more likely to have it cured and, as a result, are less likely to die from it, than women who do not take part in mammography screening. Hence early detection is the most important. It is extremely important to catch breast cancer at an early stage.

The advantage of screening at an early stage is a significant reduction in false positive test results. Conventional mammography produces two-dimensional imaging, but identyfing cancer was not so accurate especially at the earlier stages.

The 3-D mammography exceeded the limitations of conventional 2-D mammograms when used parallelly. This will give radiologists and doctors the chance to compare a patient's previous standard 2-D mammogram side-by-side, as well as provide more thorough information in a 3-D format. At the same time, the combination of 2-D and 3-D images approximately doubled the radiation dose the patient received; however, it improved the accuracy with which radiologists detected cancers, decreasing the number of women recalled for a diagnostic workup. However, safety of the patient is of atmost importance. The paper gives an algorithm that can be used to convert the 3D mammogram obtained into a 2D image that avoids additional scanning and hence does not expose the patient to X-ray dose that exceeds the prescribed levels in the medical field. Volume rendering techniques are used for this purpose.

2. 3D MAMMOGRAPHY

A new three-dimensional mammography system (also known as tomosynthesis) for use in screening patients for breast cancer provides a clearer picture and eliminates overlapping of tissue that is seen in conventional mammograms. Reviewing an additional 3-D image helped doctors find more cancers than with 2-D images alone. Approximately 10 percent of women undergo additional testing after the initial screening exam for abnormalities that are later determined to be noncancerous.

Tomosynthesis takes digital mammography to the next level. It is a modification of a standard digital mammography unit. The breast is held the same way, but the test requires only one compression of each breast rather than the two as currently required by standard mammography. The X-ray tube moves in a 50-degree arc around the breast while 11 number of low-dose images are taken during a 7-second examination. A computer then assembles the information to provide high-resolution cross-section and three-dimensional images that can be reviewed by the radiologist at a computer workstation. **These 3-D mammograms had to be used along with 2-D mammograms for more clarity sacrificing on the dosage factor.**

So, for obtaining a combination of both 2D and 3D images frequent exposure to radiations becomes unavoidable. The Food and Drug Administration(FDA) of the U.S has voiced concerns regarding patient radiation exposure from diagnostic devices. This paper looks at the volume rendering technique as a promising tool to eliminate this overdose of radiation by converting 3-D mammograms to 2-D mammograms.

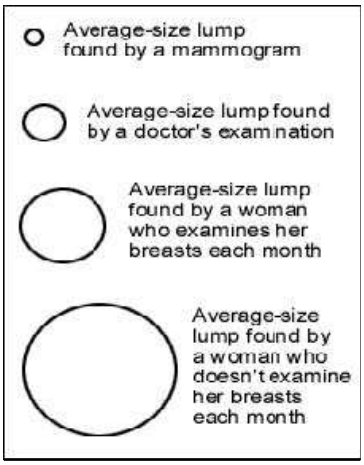

Figure 1: Illustration of importance of mammogram in breast cancer detection.

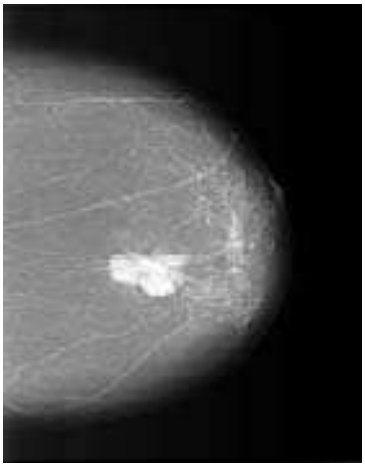

Figure 2: A 2-D mammogram.

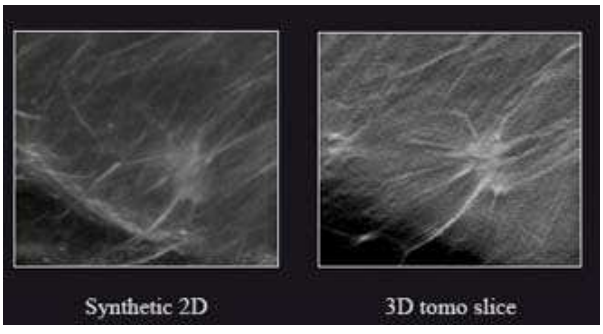

Figure 3: 2-D mammogram versus 3-D mammogram.

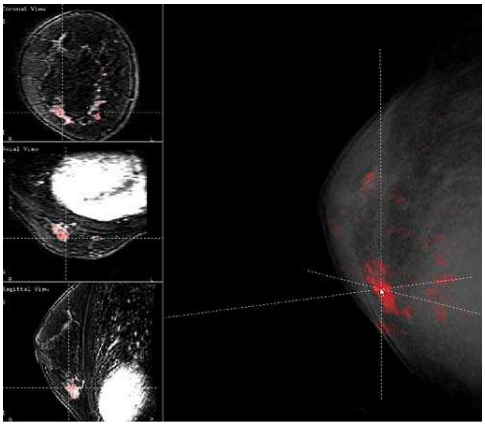

Figure 4: Volume rendered 2-D mammogram.

3. VOLUME RENDERING

3D rendering is the 3D computer graphics process of automatically converting 3D wire frame models into 2D images with 3D photorealistic effects on a computer. Among the rendering techniques available, surface rendering and volume rendering are commonly used in the medical field. In surface rendering a complex surface extraction must be done as a preprocessing step, and only a fraction of the data is retained in the final image.

In contrast to surface rendering, volume rendering is done by considering the imaging volume to be a translucent gelatin whose optical density and opacity are mapped to each voxel (Volume Element) intensity through user-adjustable transfer functions.

Volume rendering technique is used to display a 2D projection of a 3D discretely sampled data set. Volume visualization is used to create images from scalar and vector datasets defined on multiple dimensional grids, i.e., it is the process of projecting a multidimensional (usually 3D) dataset onto a 2D image plane to gain an understanding of the structure contained within the data.

A typical 3D data set is a group of 2D slice images acquired by a CT, MRI, or MicroCT scanner. Usually these are acquired in a regular pattern (e.g., one slice every millimeter) and usually have a regular number of image pixels in a regular pattern. This is an example of a regular volumetric grid, with each volume element, or voxel represented by a single value that is obtained by sampling the immediate area surrounding the voxel. A volume may be viewed by extracting surfaces of equal values from the volume and rendering them as polygonal meshes or by rendering the volume directly as a block of data. The marching cubes algorithm is a common technique for extracting a surface from volume data.

4. ALGORITHM

4.1. Marching Cubes Algorithm

In a 3D space 256 different situations are enumerated for the marching cubes representation. All these cases can be generalized in 15 families by rotations and symetries.

Complementary cubes are created and this allows to give an orientation to the surface. Since the early work on the Marching Cubes algorithm by Lorensen and Cline [1], successive authors have

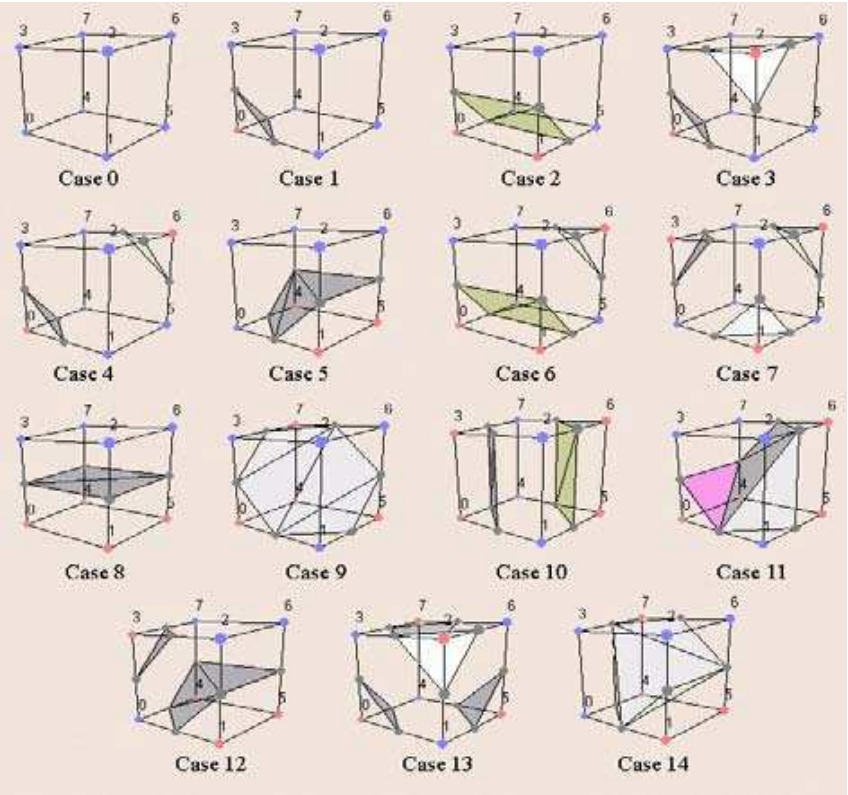

Figure 5: Generalized representation of marching cubes.

sought to improve the topological correctness and accuracy of the surface representation. Nielson and Hamann [2] point out that there is an ambiguity in the face of a cube when all four edges of the face are intersected. The triangulation has to choose which pairs of intersections to connect. An inconsistent strategy can lead to "holes" when surfaces in adjacent cells use different connections on the common face.

4.2. Marching Tetrahedra Algorithm

Marching tetrahedra algorithm is closely related to the so called "marching cube" algorithm except in that case the fundamental sampling structure is a cube while here it is a tetrahedron.

It was developed to circumvent a patent on the marching cubes algorithm. It also clarifies a minor ambiguity problem of marching cubes with some cube configurations.

Six tetrahedra are grouped together at a time to form a solid cube, this could have been done with only five tetrahedra, but by using six there is no need to reorient them between cubes.

It is important to have coherence between cubes, so that all the tetrahedra in the entire grid share edges, so when a certain edge is found to have the surface going through it that surface point is used for multiple tetrahedral [4]. If the edges of the different tetrahedra were not the same there would be holes in the final mesh where the edges did not line up properly.

When dividing a single tetrahedron there are eight possible split cases, enumerated. Through symmetry though these can be reduced to only three cases, all four vertices are either in or out, one vertex is different than the other three, or there are two

vertices in and two out. When all four are on the same side nothing need to be done, when one

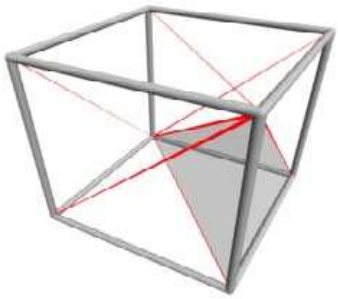

Figure 6: Basic sampling structure of marching Tetrahedra algorithm.

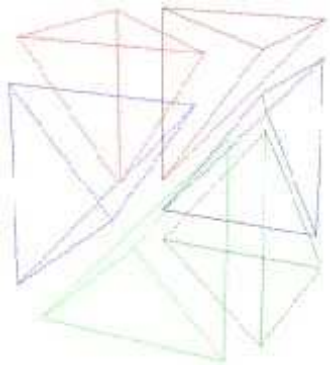

Figure 7: Six Tetrahedra to forms a solid cube.

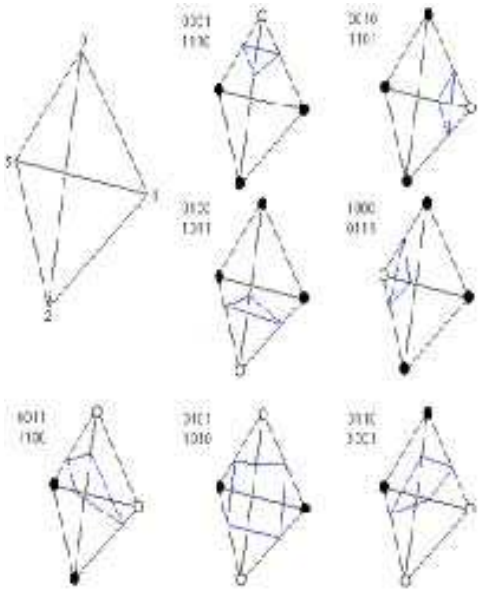

Figure 8: Different cases of iso-surface vertices in marching Tetrahedra algorithm.

is different then the three edges are splitted leading to that vertex, and a single triangle created, and when there are two, four edges are splitted, and two triangles are made from those four points.

When splitting an edge it is important to create the vertex for the surface as near as possible to where the field evaluates to the cutoff strength. Using the midpoint or some other static split results in very strange, blocky looking results. By simply doing a linear interpolation between the strengths at the two endpoints nice looking results are achieved.

The advantage of the coherence between different tetrahedra is taken to make a single mesh of triangles that share vertices, rather than individual triangles with vertices at the same points [3]. This allowed to do per vertex smooth shading which greatly improved the look of the surfaces.

There are several advantages to this approach:

1. It avoids the patent that covered the Marching Cubes algorithm, which has since expired.
2. It could work on unstructured meshes as well as structured meshes (which could be split into six tetrahedra). In fact, it has been proven that any geometric cell can be deconstructed into a series of tetrahedra, making Marching Tetrahedra a generic solution for isosurface extraction on all grid types.
3. A final advantage is that it avoided certain ambiguous cases of the Marching Cubes algorithm.

The Marching Tetrahedra algorithm is also significantly simpler than the Marching Cubes algorithm. Having only 4 points in a cell leads to merely 8 cases to consider, which can be reduced down to 3 with symmetry (No cross, 3 crosses = 1 point in, 2 crosses = 1 edge in). Because of the simplicity and that it is essentially a triangle-driven algorithm, the Marching Tetrahedra algorithm has enjoyed a lot of research by GPGPU groups on accelerating it in hardware.

Marching cube algorithm is a classical 3D reconstruction method, while topological ambiguity exists. Marching tetrahedra algorithms can solve the problem of topological ambiguity, but there are too many triangle patches. However research is going on to combine the MC method with a new decomposing method which could avoid topological ambiguity and the number of triangle patches with better efficiency.

5. CONCLUSION

Analysis and confirmation of cancer in 2-D mammography is possible only with more number of follow-up screening tests. 3-D mammography being the latest technology for detection of breast cancer aids in effective diagnosis and picks up additional cancerous points which are not picked up by any other method at an earlier stage. It enables precise charaterisation of suspicious lesions with just 11 number of low dose images. For the radiologist or the doctor to compare a patient's previous conventional 2-D mammogram side-by-side with 3-D mammogram, it is necessary to have 2-D mammograms also. Using volume rendering techniques like Marching Cubes Algorithm and Marching Tetrahedra Algorithm, a 3-D image can be volume rendered to 2-D thus confining to radiation regulations of medical field.

REFERENCES

1. Lorensen, W. and H. Cline, "Marching cubes: A high resolution 3D surface reconstruction algorithm," *Computer Graphics*, Vol. 21, No. 4, 163–169, 1987.
2. Nielson, G. and B. Hamann, "The asymptotic decider: Resolving the ambiguity in marching cubes," *Proc. IEEE Visualization '92*, 83–91, 1992.
3. Cignoni, P., C. Montani, and R. Scopigno, "A comparison of mesh simplification algo-rithms," *Computers and Graphics*, Vol. 22, No. 1, 37–54, 1998.
4. Guéziec, A. and R. Hummel, "Exploiting triangulated surface extraction using tetrahedral decomposition," *IEEE Transactions on Visualization and Computer Graphics*, Vol. 1, No. 4, 328–342, December 1995.
5. Jiang, H., R. Zhang, H. Liu, B. Wang, and Y. Li, "An improved 3D reconstruction method," *International Conference on Multimedia Information Networking and Security, MINES '09*, Multimedia Med. Inf. Technol. Lab., Northeastern Univ., Shenyang, China, 2009.
6. DICOM, http://medical.nema.org/.
7. VOREEN, http://www.voreen.org/.
8. Jain, A. K., *Fundamentals of Digital Image Processing*, Prentice Hall, 1988.
9. Alvarez, R. E. and A. Macovski, "Energy-selective reconstruction in X-ray computerised tomography," *Phys. Med. Biol.*, Vol. 21, 733–744, 1976.

Scattering from Periodic Cone Structure Array

M. Jin[1], M. Bai[1], W. Y. Chen[2], J. K. He[2], and J. G. Miao[1]

[1]Microwave Engineering Lab, Beihang University, Beijing 100191, China
[2]Shanghai Aerospace Electronic Technology Institute, Shanghai 201109, China

Abstract— The scattering patterns of cone array structures with absorbing material, commonly used for calibration targets of microwave radiometers are numerically studied using the finite-finite difference time domain (FDTD) method. The bi-static scattering far-field patterns are calculated and integrated to obtain the reflectivity of the structures, which provide the emissivity information of the corresponding structures. The scattering patterns from different cone structures made by PEC, absorbing material coated PEC and absorbing bulk material are simulated with irradiating sources of plane wave and Gaussian beam. A method of calibration target performance measurement is designed based on the analysis of the simulation results.

1. INTRODUCTION

Periodic cone structure array is the common shape of low reflection walls in microwave chambers, and the calibration targets used for satellite board microwave radiometer (MWR). For the two kind of usage, the low reflectivity property is required. The low reflection walls are made of absorbing foam (or other material) cones, and the calibration targets are usually made of metallic cones, which are coated with high emissivity (or absorbing) material. These metal cones are built to heat the coating material uniformly, thus the targets can provide a standard brightness temperature for the MWR.

For analyzing or evaluating performance of calibration target, one commonly comes to the Kirchhoff's law of thermal radiation: at thermal equilibrium, the emissivity and reflectivity of an object satisfies the equation, $e = 1 - r$. As a result, the numerical (experimental) evaluation of emissivity is usually conducted by scattering computation (measurement) [1].

Taking use of the period property of the array, one can do numerical simulations efficiently to obtain significant information for the design, parameter optimization, and evaluation [2–4]. For experimental reflectivity (or emissivity) evaluation, numerical simulations are still useful by offering information about bi-static scattering patterns. In the former works, scattering from an infinite size or a finite size array of coated cones were studied, with normally plan-wave incident [5, 6]. Those results provided meaningful information for the scattering measurement. However, simulations using incident beams with an incline incident direction may offer more. As an irradiating beam with an incident angle $\theta > 0$ make it more convenient to capture the forward scattering lobe in the bi-static scattering measurement.

In this paper, the FDTD method is used, to calculate the scattering from a cone array irradiated by a beam, which is generally the case of the bi-static measurement of a calibration target or a piece of low reflection wall. We made 2 comparisons in this paper, one is about the difference of scattering patterns with plane-wave incident and Gaussian-beam incident, the other is about scattering from the array consisting of different type of cones. Those results help to develop an evaluating method of reflectivity measurements.

2. GEOMETRY AND CALCULATION DOMAIN

In Fig. 1, the geometry of the considered cone array is shown. It consists of round cones (top-angle $\alpha = 17.5°$) periodically placed along X and Y directions with the period 17.5 mm. We considered three type of unit cone, one is treated as PEC, another one is modeled as coated cone, which is the shape of general calibration target units, and the last one is a cone made of absorbing material bulk directly. The frequencies in the simulation are 18.7 GHz and 23.8 GHz, those two are the important frequencies used in remote sensing.

The calculation domain of simulation carried out in this paper is shown in Fig. 2. It seems no difference with the traditional scattering field/total field (SF/TF) boundaries treatment used in general scattering calculation in the FDTD scheme. As discussed in [6], in the traditional SF/TF model with plane-wave incident, it is hard to evaluate the ratio of scattering power and irradiating power. However, when the incident wave is in form of Gaussian beam with a low edge-level of irradiating power on the array (scattering object), it is much more convenient to take count of the

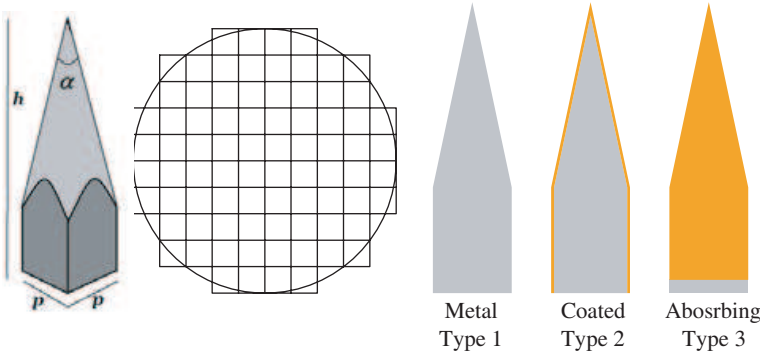

Figure 1: Calibration target geometry.

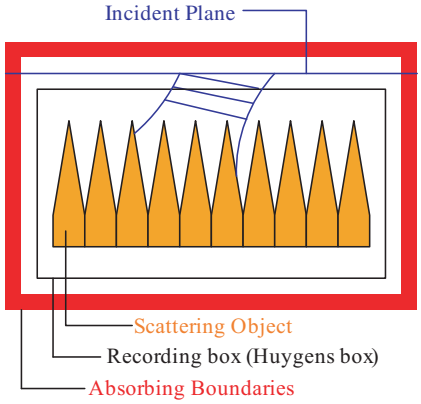

Figure 2: Simulation domain.

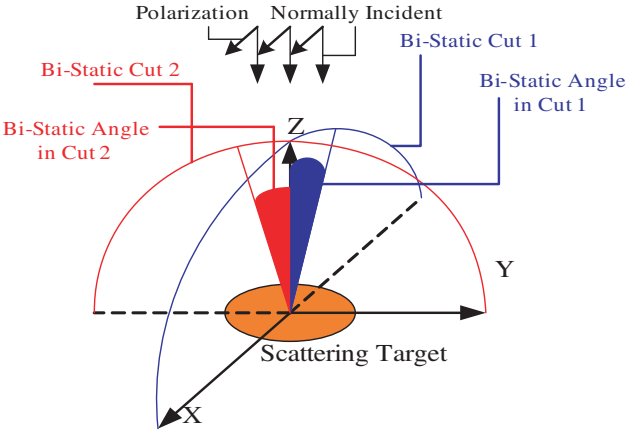

Figure 3: Bi-static geometry in Comparison 1.

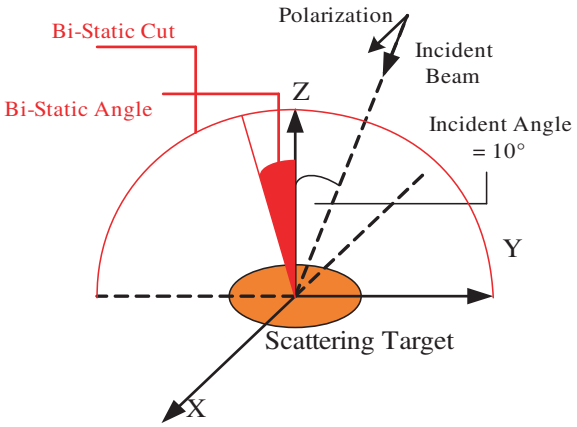

Figure 4: Bi-static geometry in Comparison 2.

scattering power and incident power, as in Fig. 2. The total field contains incident field only on the plane $XOY1$, and on other recording planes the total fields can be considered as consisting only of scattering field.

3. NUMERICAL RESULTS AND DISCUSSION

The simulations are done for providing information for the bi-static scattering measurement of the cone array. Specifically, we've made two pair of comparisons. The first one is made between scattering far-field patterns from PEC-cones array with normally plane-wave incident and Gaussian-beam incident, as in Fig. 3. The other one is also about far-field patterns, that is the scattering from arrays of different type of cones, with the same Gaussian-beam incident, as in Fig. 4.

The far-field results presented in this paper is shown in form of differential scattering coefficient, which is defined as $\gamma = 4\pi R^2 S_s / S_i A \cos\theta_i$, where $S_i A \cos\theta_i$ can be considered as incident power intercepted by scattering target, and the S_s is the far-field scattering power density.

Comparison 1:

When the Gaussian beam is selected as irradiating wave, the edge level of incident on the cone array is lower than -40 dB. As we can see from the results shown above, when the irradiating wave switches from plane-wave to Gaussian beam, the bi-static far-field distribution changes dramatically. First, the forward (also the backward in this case) scattering lobe and second scattering lobe is obvious wider with Gaussian beam incident. Second, the gap between main scattering lobe and second scattering lope gets deeper with Gaussian beam incident.

Comparison 2:

For the comparison 2, as shown in Fig. 7 and Fig. 8, the unit made of absorbing material scatters least energy. And the outlines of differential scattering coefficient curves versus bi-static angle are closing to each others with some local differences. This fact can be explained. For the scattering from periodic structure, the angle positions of strongly scattering lobes are mainly related to the

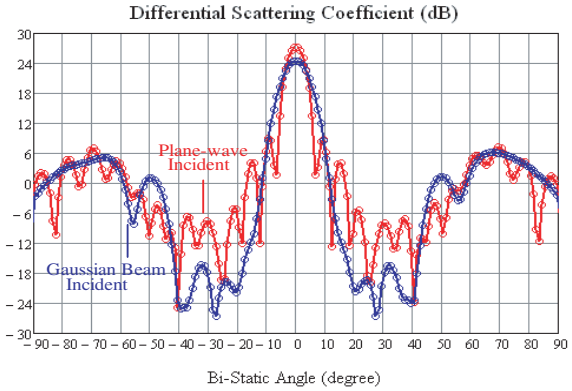

Figure 5: Far-field distribution in bi-static cut 1 (18.7 GHz).

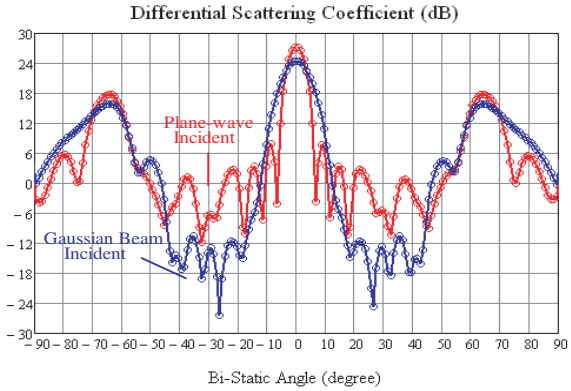

Figure 6: Far-field distribution in bi-static cut 2 (18.7 GHz).

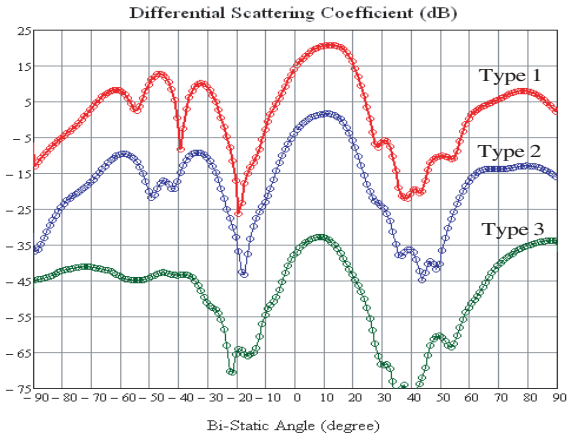

Figure 7: Far-field results in comparison 2 (18.7 GHz).

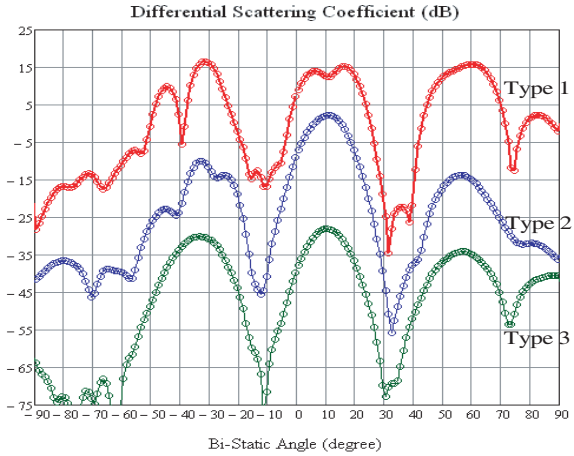

Figure 8: Far-field results in comparison 2 (23.8 GHz).

Table 1: Calculation results (reflectivity) with incident angle theta = 10 degree.

Frequency GHz/Unit type	Type 1 (Metal)	Type 2 (Coating)	Type 3 (Absorbing)
18.7	1.004	0.0143	0.0000162
23.8	0.996	0.00791	0.0000161

incident angle of irradiating source and the periodic parameters. It is interesting that, with the frequency of 23.8 GHz, the magnitudes of second scattering lobe from type 1 array are even slightly bigger than that of forward lobe. But for the type 2 array, the strongest scattering direction remains at the forward direction. Meanwhile, one can arrive at another conclusion that, the reflectivity of absorbing bulk cones is much lower than coated cones, if the same absorbing material is used.

4. CONCLUSIONS

These simulations are done in order to provide information for reflectivity or scattering measurement of periodic cone array. With these results, we can arrive at several conclusions:

1. For the measurements of scattering pattern, it is vital for simulations or theoretical analysis to use the practical irradiating source or an approximate source rather than plane-wave.

2. For the measurements of reflectivity of absorbing cone arrays, an evaluating method can be derived. First of all, using the measurement and simulation results of metal cone arrays, considering the noise-bar of measurement system, one can get the lowest reflectivity detection level the specific measurement system can achieve. Secondly, for an array with reflectivity level higher than the lowest detection bar, it is vital to capture the scattering magnitude on the forward direction. And

it is convenient to evaluate the reflectivity, using the scattering power flow density on the forward direction measured, from a calibrating metal cone array (Mm) and the specific array (Ms), and a correcting coefficient obtained by simulations, which is defined as below:

$$c = \left(Ps_{sim}^{All} \cdot Mm_{sim}^{forward}\right) / \left(Pm_{sim}^{All} \cdot Ms_{sim}^{foward}\right)$$

where Ps_{sim}^{All}, Pm_{sim}^{All} refer to the total scattering power from the specific array and the calibrating metal array obtained by simulation, respectively. And Ms_{sim}^{All}, Mm_{sim}^{All} are the scattering power flow density on the forward direction from the specific array and the metal array obtained by simulation, respectively. Finally the reflectivity can be evaluated: $reflec = c \cdot (Ms/Mm)$.

ACKNOWLEDGMENT

This work is supported by the National Natural Science Foundation of China (Project 60771012).

REFERENCES

1. Pigeat, P., D. Rouxel, and B. Weber, "Calculation of thermal emissivity for thin films by a direct method," *Phy. Rev. B: Cond. Matter*, Vol. 57, No. 15, 9293–9300, 1998.
2. Yang, C. F., W. D. Burnside, and R. C. Rudduck, "A doubly periodic moment method solution for the analysis and design of an absorber covered wall," *IEEE Trans. Antennas Propag.*, Vol. 41, No. 5, 600–609, 1993.
3. Li, Z. P., Y. Peng, J. G. Miao, and Z. Y. Wang, "Evaluation of disturbance in the antenna calibration of the microwave radiometer," *ICMMT2008 Proceedings*, 810–813, April 2008.
4. Nian, F. and W. Wang, "The optimization design for microwave wide band blackbody calibration target," *ICMMT2008 Proceedings*, 1695, April 2008.
5. Wang, J. H., J. G. Miao, Y. J. Yang, and Y. M. Chen, "Scattering property and emissivity of a periodic pyramid array covered with absorbing material," *IEEE Trans. Antennas Propag.*, Vol. 56, No. 8, 2656–2663, 2008.
6. Wang, J. H., Y. J. Yang, J. G. Miao, and Y. M. Chen, "Emissivity calculation for a finite circular array of pyramidal absorbers based on Kirchhoff's law of thermal radiation," *IEEE Trans. Antennas Propag.*, Vol. 58, No. 4, 1173–1180, 2010.

Cylindrical Slot Antennas for Monitoring the Quality of Milled Rice

K. Y. You[1], **J. Salleh**[1], **Z. Abbas**[2], **and L. L. You**[3]

[1]Radio Communication Engineering Department, University Teknologi Malaysia
UTM Skudai 81310, Malaysia
[2]Department of Physics, University Putra Malaysia, UPM Serdang 43400, Malaysia
[3]Department of Human Biology, School of Medicine and Health Sciences
International Medical University, Kuala Lumpur 57000, Malaysia

Abstract— This paper presents the use of a cylindrical slot antenna sensor to determine the quality of rice based on the percentage of moisture content and percentage of broken rice. The reflection coefficient of rice were measured using both single and parallel slot sensors of infinite ground plane in the frequency range from DC to 6 GHz using a Vector Network Analyzer (VNA). Five varieties of rice with moisture content between 13% and 16% were tested in this work. Calibration equations were established to relate the measured reflection coefficient to moisture content which in turn allows prediction of the percentages of broken rice. From the measurement results, the parallel two slot sensor showed the high sensitivity of reflection coefficient to the moisture content in the rice grain, as well as the percentage of cracked rice in the samples.

1. INTRODUCTION

There are many brands and grades of rice in the market. Thus, these give raise on the need to determine and characterize the quality of rice properly to ensure that all types of rice can be priced accordingly. One of the important physical quality is the moisture content, $m.c$ inside the rice grain [1–5]. In manufacturing, the rice grain is dried to below 14% moisture content, $m.c$ to prevent storage deterioration. Nevertheless, when grains are over dried to lower moisture content, $m.c$ the producers also will lose their money from excessive weight loss [1]. Besides moisture content, the grade and price of the rice grain are also depending on the percentage of broken grain. The broken rice grain has a length less than three quarters but more than one quarter of the average normal grain length. In this paper, microwave techniques were proposed to monitor the moisture content, $m.c$ in rice grain as well as the fraction of broken rice grain.

2. PRINCIPLE OF RICE GRAINS MEASUREMENT USING SLOT ANTENNAS

The slot antennas concept was implemented in rice quality processing by instead the free space with thousand of rice grain samples. The rice sample is composed of a mixture of air and rice grains. The radiated waves from slot antenna spread around the mixed sample, thus the long wavelength radiated waves (low frequency) is required to reduce the sensitivity of wave to the air gap between the rice grains. In addition, the low frequency fields can also conduct electric currents in the rice grains. Different moisture in the rice grain will give a change of reflected signal when it is measured using Vector Network Analyzer. In contrast, the short wavelength signal (high frequency) is required to enhance the air gap sensitivity for broken rice measurement and reduces the penetration of energy into the rice grains. The air gap between the broken grains is smaller as compared to the normal rice gains. Thus, the density of rice grains in the mixed sample is high. In measurements, the measured reflection coefficient will vary with changes in the density of rice grains in the sample.

3. METHODOLOGY

A single and coupling slots sensor with one input signal were fabricated. The slot sensors were constructed using commercial SMA stub panel with radius of slot, $a = 0.65$ mm and length of slot, $h = 16$ mm. The slots were driven from aluminum ground and covered by acrylic as shown in Figure 1. For coupling slots sensor, the separate distance between the coupling slots is 9 mm and one of the slot was terminated. The density of sensing field was strengthened using coupling slots sensor.

The reflection coefficient, Γ of the mixed rice gain-air filled in acrylic casing was measured using the E5071C Network Analyzer at frequency 1 GHz and 13.5 GHz as shown in Figure 2. Before taking the measurements, the one-port calibration at the both ends of coaxial cable was carried out

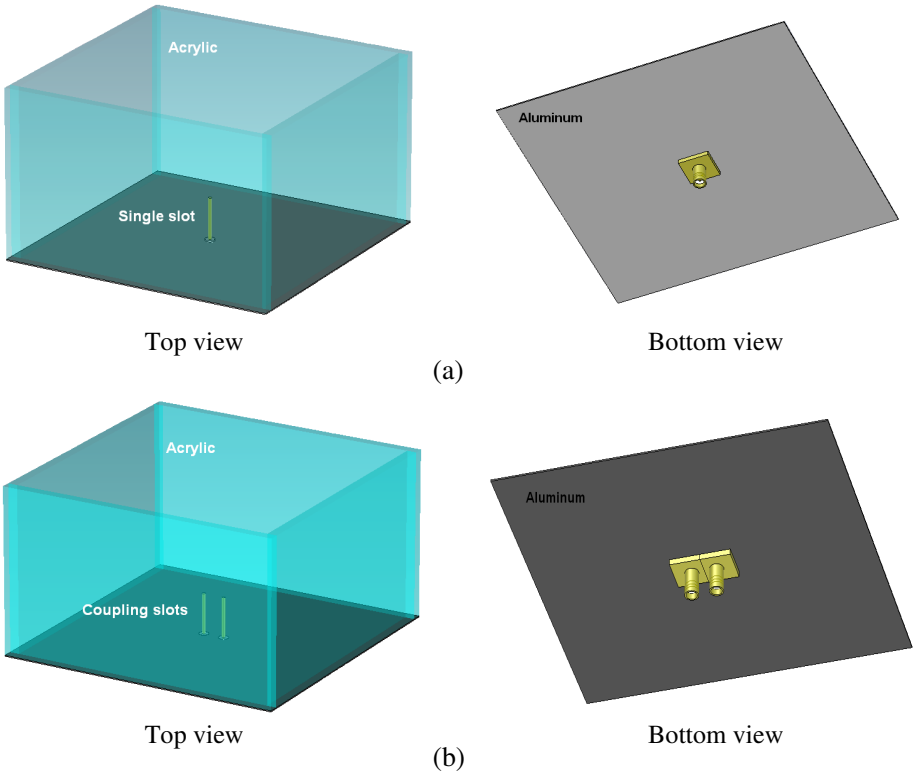

Figure 1: (a) Configuration of single slot sensor. (b) Configuration of coupling slots sensor.

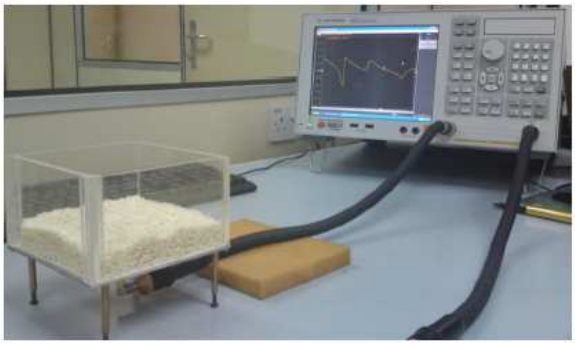

Figure 2: Experimental setup.

using calibration kits (open, short and load). The rice samples were placed over the acrylic holder sensor with a height of 30 mm.

The relative moisture content, $m.c(\%)$ in rice gain was obtained by drying the rice gain for 6 hours at 130°C and following by wet basic calculation [1]

$$m.c = \frac{m_{Before\_Dry} - m_{After\_Dry}}{m_{Before\_Dry}} \times 100\% \quad (1)$$

where m_{Before_Dry} and m_{After_Dry} are the weighs of mixed rice-air sample before and after drying, respectively.

4. RESULTS AND DISCUSSION

The moisture measurement for rice grain samples is challenging because all types of rice has a distinctive dimension and the differential moisture is normally only in the range of $\sim 8\%$ to $\sim 16\%$. Dimensions and moisture content, $m.c$ for 5 kinds of rice under test were listed in Table 1. To avoid the moisture measurement is influenced by the air gap between the rice grains, the measurements were done at low frequency (1 GHz) in order to reduce air gap sensitivity. Figure 3 shows the

measured reflection coefficient, $|\Gamma|$ of the rice grain vary with the moisture content, $m.c$. From the measurement, both sensors show that moisture content, $m.c$ had directly proportional relationship with reflection coefficient, Γ. In this study, the relationship between the magnitude reflection coefficient, $|\Gamma|$ and moisture content, $m.c$ (in unit %) at 1 GHz were represented in linear equations as

$$|\Gamma| = 0.012937m.c + 0.72464 \quad \pm 0.0062258 \quad \text{for single slot sensor}$$
$$|\Gamma| = 0.032956m.c + 0.44156 \quad \pm 0.028114 \quad \text{for coupling slots sensor}$$

Figure 4 shows the measured reflection coefficient, $|\Gamma|$ of the rice grain vary with the percentage of broken rice in the samples at 13.5 GHz. Similarly, the correlation between magnitude reflection coefficient, $|\Gamma|$ and percentage of broken rice (in unit %) in grain sample at 13.5 GHz were also

Table 1: Moisture content, $m.c$ (%) and average dimensions for various rice gain.

Rice Sample	$m.c$ (%)	Rice length, L (mm)	Rice width, W(mm)	L/W
Sakura Super Basmathi Pakistan Rice	15.99	7.52	1.76	4.27
Bird of Paradise Thai Fragrant Rice	15.14	7.18	1.86	3.86
Jasmine Nutri Rice	14.79	7.29	2.04	3.57
Floral Glutinous Rice	14.42	7.06	1.95	3.62
Maharaja Basmathi Rice	13.38	6.79	1.52	4.47

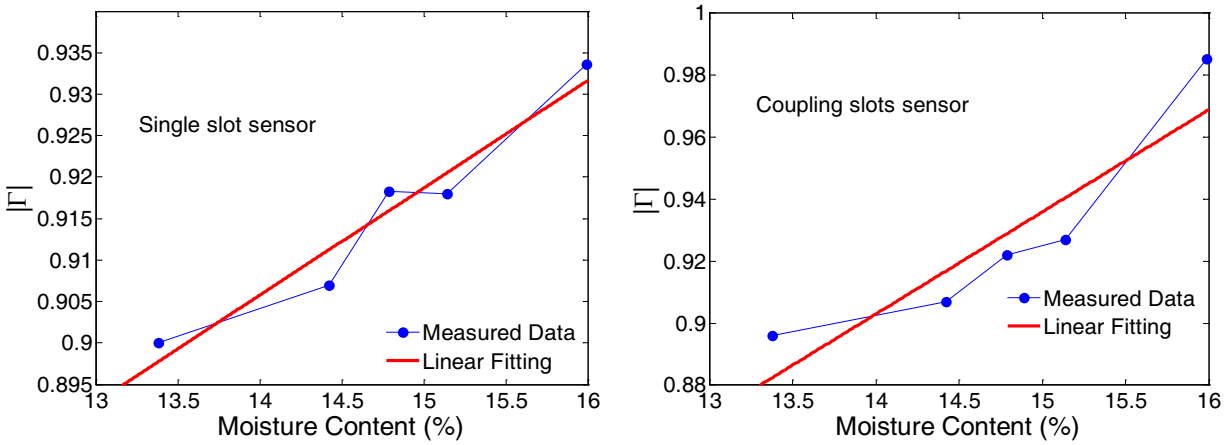

Figure 3: Variation in magnitude reflection coefficient, $|\Gamma|$ with percentage of moisture content, $m.c$ in the rice grain at 1 GHz at room temperature 25°C.

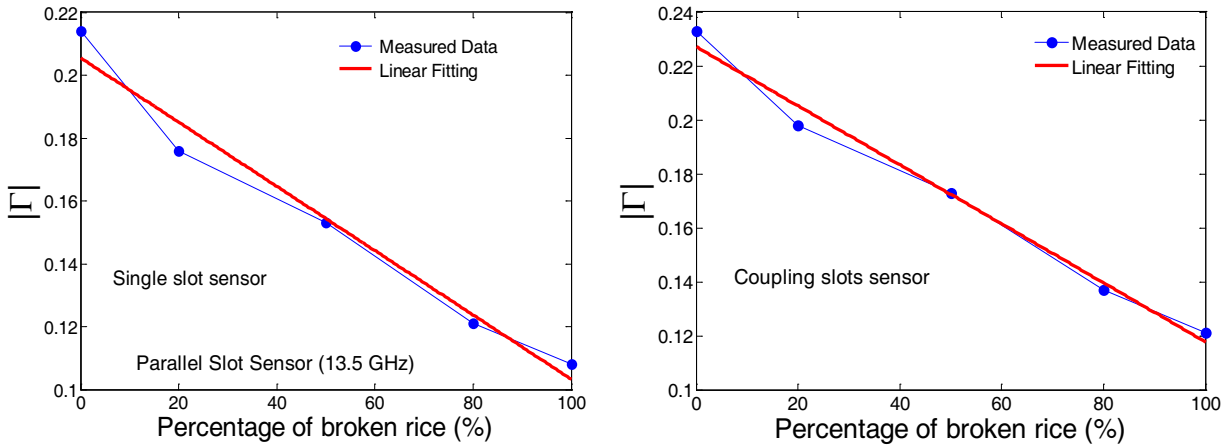

Figure 4: Variation in magnitude reflection coefficient, $|\Gamma|$ with percentage of broken grain in the rice sample at 13.5 GHz at room temperature 25°C.

represented in linear equations as

$$|\Gamma| = -0.0010221\ (\textit{Broken Rice}) + 0.20550 \quad \pm 0.013630 \quad \text{for single slot sensor}$$
$$|\Gamma| = -0.0010926\ (\textit{Broken Rice}) + 0.22703 \quad \pm 0.010239 \quad \text{for coupling slots sensor}$$

5. CONCLUSIONS

In this study, the single and coupling slots sensors have been developed for moisture and broken rice grain measurement. This work provides a simple and sensitive of microwave sensors for testing and monitoring of packaging in rice industry in order to minimize the human effort in manufacturing.

ACKNOWLEDGMENT

This study was supported by the Ministry of Science, and Environment of Malaysia under project number 03-01-06-SF0599.

REFERENCES

1. You, K. Y., S. N. A. Jalani, Z. Abbas, and L. L. You, "Application of bandpass filter as a sensor for rice characterization," *International Conference on Computer Applications and Industrial Electronics (ICCAIE 2010)*, 570–573, Kuala Lumpur, Malaysia, December 2010.
2. Jafari, F., K. Khalid, W. M. D. W. Yusoff, and J. Hassan, "The analysis and design of multilayer microstrip moisture sensor for rice grain," *Biosystems Engineering*, Vol. 106, No. 3, 324–331, 2010.
3. You, T. S. and S. O. Nelson, "Microwave dielectric properties of rice kernels," *Journal of Microwave Power*, Vol. 23, No. 3, 150–159, 1988.
4. Yagihara, S., O. Oyama, A. Inoue, M. Asano, S. Sudo, and N. Shinyashiki, "Dielectric relaxation measurement and analysis of restricted water structure in rice kernels," *Meas. Sci. Technol.*, Vol. 18, 983–990, 2007.
5. Kaatze, U., *Electromagnetic Aquametry*, K. Kupfer, Ed., Springer, New York, 2005.
6. Nyfors, N. and P. Vainikainen, *Industrial Microwave Sensors*, Artech House, Norwood, MA, 1989.
7. You, K. Y., J. Salleh, Z. Abbas, and L. L. You, "A rectangular patch antenna technique for the determination of moisture content in soil," *PIERS Proceedings*, 850–854, Cambridge, USA, July 5–8, 2010.

Leaf Area Index Inversion Based on Ground Passive Microwave Measurement Experiment

Jianli Shuang[1], **Shanjun Liu**[1], **Lixin Wu**[1, 2], **Qi Li**[1], **and Jianying Zhuo**[1]

[1]Institute for Geo-informatics & Digital Mine Research, Northeastern University, Shenyang 110819, China
[2]Academe of Disaster Reduction and Emergency Management, Beijing Normal University
Beijing 100875, China

Abstract— The passive microwave sensor can provide significant information compared with optical and infrared sensors due to its penetrating property. It plays an important role in the detection of growth vigour of corps. In this paper, consecutive passive microwave detection experiments were conducted considering row direction effect. The result showed that a well negative exponential relationship exists between normalized MPDI and LAI for frequencies 6.6 and 18.7 GHz. With the increase of measurement angle, the negative exponential relationship is more obvious. When observation is parallel to the row, two MPDIs at 6.6 and 18.7 GHz at same observation angle have a good linear relationship, but when observation is vertical to the row or cross 45° with the row the linear relationship becomes weak.

1. INTRODUCTION

In the 1970s, experimental and theoretical investigations showed that the microwave radiation from fields covered with canopy were different from bare soil. In order to study the effect of vegetation on soil microwave radiation, ground and airborne passive microwave measurement experiment were conducted. Ulaby [1] and Wang [2] etc measured bare fields and fields covered with grass, soybean, corn, and alfalfa by 1.4 GHz and 5 GHz microwave radiometers. They discovered that the brightness temperature affected by the vegetation biomass, water content, observation angle and the frequency. During the 1980s Pampaloni [3], Ulaby [4], Brunfeldt [5] and Macelloni [6] etc evaluated the importance of different canopy constituents (such as heads, leaves, and stalks etc.) to the total canopy microwave radiation. Their studies established that vegetation microwave radiation were non-uniform and anisotropic, and was highly related to their constituents. From the later 1990s to now, scientists have been studying the effects of vegetation parameter (such as vegetation biomass, water content, soil moisture, LAI) to the vegetation index which is used to derive vegetation information from passive microwave instruments For example, Simonetta [7], Paloscia [8], Macellon [9], Jen [10] and Huhui [11] etc analyzed qualitatively the relationships between vegetation indices and vegetation biomass, water content and so on.

One commonly used tool in microwave vegetation monitoring is microwave polarization difference temperatures (MPDT):

$$\mathbf{MPDT} = T_{fV} - T_{fH} \tag{1}$$

Here, T_{fH} and T_{fV} are respectively the brightness temperature for horizontal and vertical polarizations. From microwave radiation transfer theory and field measurements we know that MPDT is not only affected by vegetation properties but also by effective surface reflectivity (related to soil moisture and roughness) and the physical temperature [12].

In order to minimize the physical temperature effects, Becker and Choudhury [13] proposed microwave polarization difference index (MPDI):

$$\mathbf{MPDI} = \frac{(T_{fV} - T_{fH})}{(T_{fV} + T_{fH})} \tag{2}$$

MPDI can minimize physical temperature effects for a given frequency, but also affected by surface effective reflectivity. It is also referred to as the normalized polarization index (PI) [8].

A new index based on the difference in normalized brightness temperature at two frequencies was explored:

$$\Delta T = T_{f1} - T_{f2} \tag{3}$$

Here, T_{f1} and T_{f2} are respectively the brightness temperature for f_1 and f_2 frequencies. This approach derives the impact of physical temperature on vegetation properties that it is used for detecting biomass and water conditions of agricultural crops [14–16].

A new technique for deriving Microwave Vegetation Indices (MVIs) was demonstrated by jiancheng Shi. This method is independent of soil surface emission signals, and depend only on vegetation properties when the microwave sensor can "see" the ground surface [17–19].

Those observations contributed greatly to the development of microwave remote sensing. However, past passive microwave detection experiments concentrated mainly on the observation of corps in one growth season, less on the consecutive detection. Moreover, the effect of row direction on microwave brightness temperature was less considered. Against such weakness, we conducted consecutive passive microwave detection experiments considering the row direction effect, and the index MPDI is selected as the tool to detect the growth vigour of the corn.

2. MICROWAVE MEASUREMENT EXPERIMENT

2.1. Experimental Design

The measurements were carried out in Huailai county of Hebei province of China from August to September in 2010. The observed area was 10 m × 10 m (see Fig. 1). Two passive microwave radiometers (6.7 GHz and 18.7 GHz) were installed in two-dimensional turntable to measure the brightness temperature variation of corn both horizontal and vertical polarizations in different growth stages. The turntable was hanged on an elevated tower which could move in three directions. With the help of two-dimensional turntable and three-dimensional elevated tower, the measurement angle can vary from 0° to 60° at interval of 5° and the measurement direction can vary respectively in parallel, vertical to the row and cross 45° with the row. Because the observation region changes at different observation angles we made the observation area always at same center point. The detection periods included eight stages of corn growth. During the experiment, some ground parameters were measured, such as environment temperature, soil temperature and moisture, vegetation height, density, thickness, LAI, water content etc. During whole growing process the soil roughness and moisture were made to be same in order to avoid their influence to the measurement.

2.2. Experimental Result

Table 1 shows LAI measurement result at different stages.

2.2.1. Relationship between MPDI and LAI

Figures 2 and 3 illustrate the relationship between MPDI and LAI respectively at 6.6 GHz and 18.7 GHz, in three measurement direction (parallel (a), vertical (b) and cross 45° with the row (c))

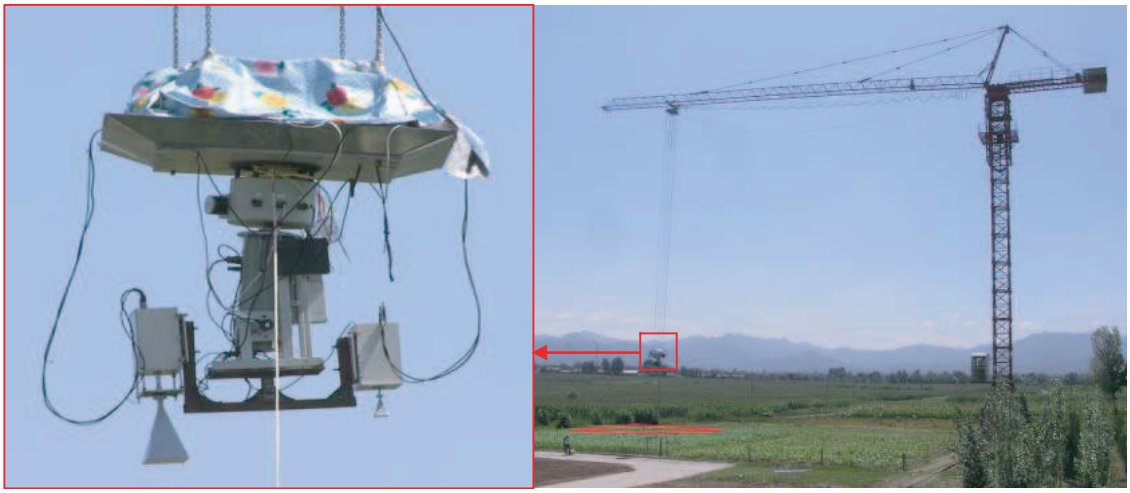

Figure 1: The scene of ground passive microwave measurement experiment.

Table 1: The result of LAI during corn's growth.

Days	10	15	19	25	31	**34**	40	45
LAI	0.16	0.39	0.68	1.28	2.15	**2.54**	3.28	3.58

and at four measurement angle 30°, 40°, 50°, 60°. Curves are the fitting results between MPDI and LAI, and the fitting equation and correlation coefficient are showed in Table 2 and Table 3.

The fitting results show a negative exponential function relationship exists between MPDI and LAI, which indicates that MPDI decreases with LAI increase. Table 2 shows that almost correlation coefficients are more than 0.80 except that at observation angle 30° in vertical direction to the row. Meanwhile the correlation coefficients in the Parallel direction to the row and Cross 45° with the row are higher than that in the vertical direction to the row, and the fitting relationships between MPDI and LAI at 18.7 GHz are not as good as at 6.6 GHz. With the increase of measurement angle, the exponential relationship is more obvious. The figure shows also that MPDI and LAI are affected by measurement direction and angle, as well as frequency of radiometer.

2.2.2. Relationship between Two MPDIs at 6.6 and 18.7 GHz

Table 4 shows fitting equation and correlation coefficient of liner relationships between two MPDIs at 6.6 and 18.7 GHz in different measurement directions during whole corn's growth stage.

From Table 4 we know that the linear relationship between MPDIs at frequencies of 6.6 and 18.7 GHz at same observation angle is well when observation direction is parallel to the row, and the correlation coefficient decrease with the increase of LAI. But when observation is vertical to the row or cross 45° with the row the linear relationship becomes weak.

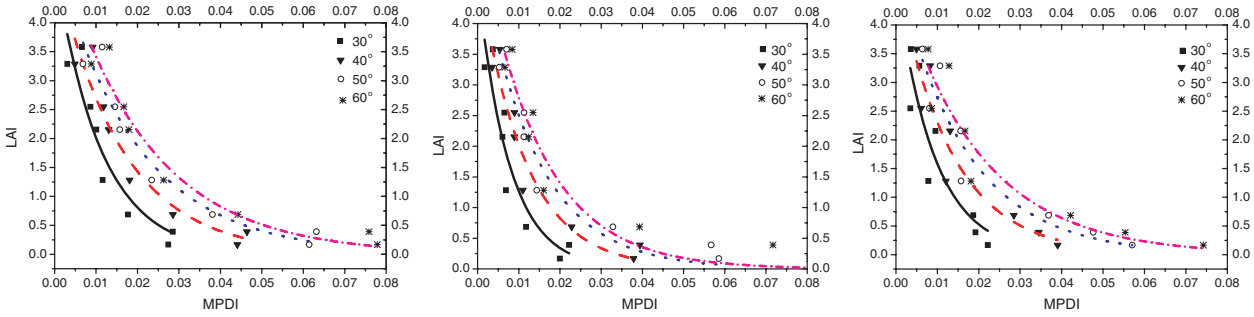

Figure 2: Experiment relationship of MPDI and LAI at 6.6 GHz.

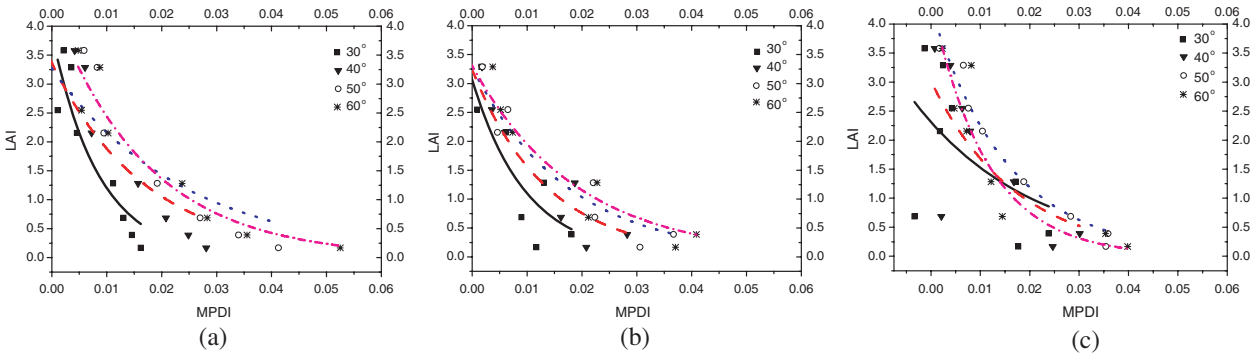

Figure 3: Experiment relationship of MPDI and LAI at 18.7 GHz.

Table 2: Fitting equation and correlation coefficient of MPDI and LAI at 6.6 GHz*.

Angle	Parallel to the row		Vertical to the row		Cross 45° with the row	
	Fitting equation	R^2	Fitting equation	R^2	Fitting equation	R^2
30°	$y = 4.02e^{-95.35x}$	0.95	$y = 2.76e^{-86.64x}$	0.50	$y = 4.53e^{-117.3x}$	0.84
40°	$y = 4.14e^{-59.79x}$	0.94	$y = 4.17e^{-67.52x}$	0.81	$y = 4.58e^{-72.4x}$	0.91
50°	$y = 3.95e^{-43.55x}$	0.93	$y = 3.92e^{-46.54x}$	0.89	$y = 4.16e^{-53.18x}$	0.95
60°	$y = 3.98e^{-36.04x}$	0.95	$y = 3.67e^{-36.19x}$	0.92	$y = 4.10e^{-42.21x}$	0.95

*y represents MPDI, x represents LAI

Table 3: Fitting equation and correlation coefficient of MPDI and LAI at 18.7 GHz*.

Angle	Parallel to the row		Vertical to the row		Cross 45° with the row	
	Fitting equation	R^2	Fitting equation	R^2	Fitting equation	R^2
30°	$y = 3.29e^{-132.8x}$	0.42	$y = 5.10e^{-152.2x}$	0.76	$y = 2.06e^{-71.78x}$	0.43
40°	$y = 3.51e^{-91.75x}$	0.76	$y = 5.28e^{-108x}$	0.88	$y = 2.92e^{-78.41x}$	0.60
50°	$y = 3.73e^{-68.66x}$	0.88	$y = 5.23e^{-83.07x}$	0.91	$y = 3.71e^{-73.71x}$	0.78
60°	$y = 4.26e^{-65.78x}$	0.96	$y = 4.84e^{-70.85x}$	0.87	$y = 3.72e^{-74.11x}$	0.90

*y represents MPDI, x represents LAI

Table 4: Liner relationship between MPDIs at frequencies of 6.6 and 18.7 GHz.

LAI	Parallel to the row		Vertical to the row		Cross 45° with the row	
	Fitting equation	R^2	Fitting equation	R^2	Fitting equation	R^2
0.1641	$y = 0.5040x + 0.0072$	0.99	$y = 0.4674x + 0.0113$	0.99	$y = 0.5243x + 0.0032$	0.99
0.3903	$y = 0.6622x - 0.0004$	0.98	$y = 0.5873x - 0.0012$	0.98	$y = 0.3437x + 0.0163$	0.71
0.6862	$y = 0.6886x - 0.0124$	0.99	$y = 0.5745x + 0.0026$	0.98	$y = 0.6521x - 0.0082$	0.98
1.2829	$y = 0.7947x - 0.0015$	0.98	$y = 1.4177x - 0.0155$	0.94	$y = 4.5127x - 0.0117$	0.89
2.1537	$y = 0.6561x + 0.0014$	0.97	$y = 0.4124x + 0.0009$	0.46	$y = 0.2052x + 0.0060$	0.89
3.2874	$y = 1.1049x - 0.0044$	0.96	$y = 0.3210x - 0.0005$	0.45	$y = 0.8754x - 0.0021$	0.97
3.5806	$y = 0.4961x + 0.0017$	0.91	$y = -0.3243x + 0.0063$	0.56	$y = 0.3139x - 0.0018$	0.36

y represents MPDI at 18.7 GHz, x represents MPDI at 6.6 GHz

3. CONCLUSIONS

Based on ground passive microwave measurement experiments we analyzed the relationship between MPDI and LAI, considering the measurement direction's influence to the radiation of vegetation. The result showed that a well negative exponential relationship exists between MPDI and LAI for 6.6 and 18.7 GHz frequencies. With the increase of measurement angle, the exponential relationship is more obvious. When observation is parallel to the row, two MPDIs at 6.6 and 18.7 GHz at same observation angle have a good linear relationship, but when observation is vertical to the row or cross 45° with the row the linear relationship becomes weak. In addition, with the increase of LAI, the linear relationship become weak in both parallel and vertical to the row. The experimental result shows that passive microwave remote sensing can detect the growth vigour of corps, and the observing angle and direction are very important for detection.

REFERENCES

1. Ulaby, F. T., M. Razani, and M. C. Dobson, "Microwave attenuation properties of vegetation canopies," *Transactions on Geoscience and Remote Sensing*, Vol. 21, No. 1, 746–753, 1983.
2. Wang, J. R., J. C. Shiue, et al., "Thermal microwave emission from vegetated fields: A comparison between theory and experiment," *Transactions on Geoscience and Remote Sensing*, Vol. 22, No. 2, 143–150, 1984.
3. Pampaloni, P. and S. Paloscia, "Microwave emission and plant water content: A comparison between field measurements and theory," *Transactions on Geoscience and Remote Sensing*, Vol. 24, No. 6, 900–905, 1986.
4. Ulaby, F. T. and E. A. Wilson, "Microwave attenuation properties of vegetation canopies," *Transactions on Geoscience and Remote Sensing*, Vol. 23, No. 5, 746–753, 1985.
5. Brunfeldt, D. R. and F. T. Ulaby, "Microwave emission from row crops," *Transactions on Geoscience and Remote Sensing*, Vol. 24, No. 3, 353–359, 1986.
6. Macelloni, G., S. Paloscia, P. Pampaloni, et al., "Microwave emission features of crops with vertical stems," *Transactions on Geoscience and Remote Sensing*, Vol. 36, No. 1, 332–337, 1998.

7. Paloscia, S. and P. Pampaloni, "Microwave polarization index for monitoring vegetation growth," *Transactions on Geoscience and Remote Sensing*, Vol. 26, No. 5, 617–621, 1988.
8. Paloscia, S. and P. Pampaloni, "Microwave vegetation indexes for detecting biomass and water conditions of agricultural crops," *Remote Sens. Environ.*, Vol. 40, 15–26, 1992.
9. Macelloni, G., S. Paloscia, and P. Pampaloni, "Airborne multifrequency L- to Ka-band radiometric measurements over forests," *Transactions on Geoscience and Remote Sensing*, Vol. 39, No. 11, 300–307, 2001.
10. Tien, K.-J. C. and J. Judge, "Passive microwave remote sensing of soil moisture, evapotranspiration, and vegetation properties during a growing season of cotton," *IGARSS*, 2795–2798, 2004.
11. Lu, H., K. Toshio, T. Hiroyuki, et al., "Moritoring wingter wheat growth with grand based microwave radiometers (GBMR)," *IGARSS*, 2008.
12. Pampaloni, P., S. Paloscia, and G. Zipoli, "Microwave emission of soil and vegetation at X and Ka bands," *IGARSS*, 1983.
13. Becker, F. and B. J. Choudhury, "Relative sensitivity of normalized difference vegetation index (NDVI) and microwave polarization difference index (MPDI) for vegetation and desertification monitoring," *Remote Sensing of Environment*, Vol. 24, 297–311, 1988.
14. Paloscia, S. and P. Pampaloni, "Microwave vegetation indexes for detecting biomass and water conditions of agricultural crops," *Remote Sensing of Environment*, Vol. 40, 15–26, 1992.
15. Justice, C. O., J. R. G. Townshend, and B. J. Choudhury, "Comparision of AVHRR and SMMR data for monitoring vegetation phenology on a continental scale," *International Journal of Remote Sensing*, Vol. 10, No. 10, 1607–1632, 1989.
16. Njoku, E. G. and T. K. Chan, "Vegetation and surface roughness effects on AMSR-E land observations," *Remote Sensing of Environment*, Vol. 100, 190–199, 2006.
17. Shi, J., "Microwave vegetation indices for short vegetation covers from satellite passive microwave sensor AMSR-E," *Remote Sensing of Environment*, Vol. 112, 4285–4300, 2008.
18. Chen, L., J. Shi, and Y. Jin, "Microwave vegetation index derived from multi-angular passive microwave observations at L-band," *IGARSS*, 396–399, 2008.
19. Chen, L. and J. Shi, "The development of microwave vegetation index for future SMOS applications," *IGARSS*, 89–92, 2009.

Three Dimensional Visualization of Pol-InSAR Image

Guangyi Zhou[1], **Tao Xiong**[1, 2], **and Jian Yang**[1]

[1]Department of Electronic Engineering, Tsinghua University, Beijing 100084, China
[2]Nokia Research Center, Beijing 100176, China

Abstract— Visual interpretation of Synthetic Aperture Radar (SAR) images plays a critical role in remote sensing applications. This paper will propose a framework of SAR image visualization, from the single channel SAR image to Polarimetric Interferometric SAR image. Single channel SAR image can be visualized as a grey image which is suitable for human observation. Polarimetric SAR (Pol-SAR) image can be visualized as a color image based on the Pauli decomposition. Since interferometric SAR (InSAR) can provide the elevation information, InSAR data can be visualized as a three-dimensional (3-D) scene. Especially, Polarimetric Interferometric SAR (Pol-InSAR) data can be visualized as a color 3-D scene. The 3-D visualization is implemented using Pol-InSAR data of PISAR, SIR-C/X-SAR, and ESAR systems.

1. INTRODUCTION

Synthetic Aperture Radar (SAR) is a kind of imaging radar with all weather, all time working capabilities [1]. Visual interpretation plays an important role in remote sensing applications, in particular for the surveillance of natural disasters, such as earthquake, debris flow and so on. With resolution improvement, it becomes easier to perform the visual interpretation on the SAR images. Naturally, the original SAR data should be visualized as an image suitable for the human observation ahead of visual interpretation.

Using the intensity of each resolution element, single channel SAR image can be visualized as a grey image. Polarimetric SAR (Pol-SAR) measures the target's reflectivity in four polarization channel combinations (HH, HV, VH and VV) [2]. This capability makes it possible to visualize the Pol-SAR data as a color image. The visualization to a grey or color image is called two-dimensional (2-D) visualization.

SAR interferometry is an important technique [3] which can be used to obtain elevation information from the interferometric phase. Combining the 2-D visualization result of the SAR image above, we can realize three-dimensional (3-D) visualization of the interferometric SAR (InSAR) data. Polarimetric interferometric SAR (Pol-InSAR) [4] measures for each resolution element in the scene from two slightly different look angles and provides both polarimetric and interferometric information simultaneously. Pol-InSAR system is just like human eyes, which have the capability to observe 3-D color scene. So the Pol-InSAR data can be used to realize 3-D color visualization.

In this paper, the visualization methods of SAR image and Pol-SAR image are proposed, and finally the Pol-InSAR data are visualized as a 3-D color scene. The other sections of this paper are organized as follows: in Section 2, a visualization method of the single channel SAR image is proposed based on the statistic of the data; the visualization method of the Pol-SAR image is proposed in Section 3; 3-D visualization of the InSAR data or Pol-InSAR data can be realized based on the theory of the elevation information extraction from the InSAR data which is reviewed in Section 4; in Section 5, the effectiveness of the framework is demonstrated with the PISAR, SIC-C/X-SAR and ESAR data.

2. VISUALIZATION OF SINGLE CHANNEL SAR IMAGES

2.1. SAR Data Statistic

In SAR images, the reflectivity of each scattering element or pixel, i.e.,

$$s = a + \mathrm{j}b, \tag{1}$$

can be regarded as a complex random variable, where a and b are the real and imaginary parts of s respectively. Considering the very large number of small scattering elements in a resolution element, we invoke the central limit theorem to assume that the probability densities of the real and imaginary parts of s are Gaussian [5]. We are mainly interested in the statistics of its intensity, i.e.,

$$I = |s|^2, \tag{2}$$

which represents the "pixel value" of the image. If we assume that a and b are independent with zero mean and equal variances σ^2, i.e.,

$$P(a,b) = \frac{1}{2\pi\sigma^2} \exp\left[-\frac{(a^2+b^2)}{2\sigma^2}\right], \tag{3}$$

then I follows exponential distribution,

$$P(I) = \frac{1}{R} \exp\left(-\frac{I}{R}\right), \tag{4}$$

where $R = 2\sigma^2$, which is the mean and standard deviation of the intensity.

For purposes of fading reduction, the multi-look data are usually generated by the multi-look processing with independent measurements which often correspond to different sub-bands in Doppler domain, or by averaging the values of neighboring pixels. The multi-look data conform to Gamma distribution,

$$P(I) = \left(\frac{L}{R}\right)^L \frac{1}{\Gamma(L)} \exp\left(-\frac{LI}{R}\right) I^{L-1}, \tag{5}$$

where L is the number of looks and $\Gamma(\cdot)$ is the Gamma function.

2.2. Gray Image Formation

With the above analysis, the number of pixels with high intensity is very small, and most of the pixels are with low intensities. In a high contrast visual image, the components of the histogram cover a broad range of gray scales and further, that the Probability Density Function (PDF) of the intensity levels is not too far from uniform distribution. Therefore, uniform distribution should be the target distribution of the transformed image. Performing a transform with the form of the Cumulative Distribution Function (CDF) of the distribution on the variables, this distribution can be transformed to a uniform distribution. The CDF of the distribution in formula (4) and (5) can be obtained as follows.

For the single channel SAR data, in the single look case, the CDF of the pixel's intensity is

$$C(I) = 1 - \exp\left(-\frac{I}{R}\right), \tag{6}$$

while in the multi-look case, the CDF of the intensity is

$$C(I) = \frac{\gamma\left(L, \frac{LI}{R}\right)}{\Gamma(L)}, \tag{7}$$

where $\gamma\ (s,\ x)$ is the lower incomplete Gamma function.

The parameter R can be obtained by Maximum Likelihood Estimation (MLE) based on the real SAR data [6, 7].

3. VISUALIZATION OF POL-SAR IMAGES

3.1. Polarimetric SAR Data

Pol-SAR is used to measure the target's reflectivity with four polarization combinations, which can be expressed as a complex scattering matrix. The scattering matrix in the linear horizontal and vertical polarization base can be expressed as

$$\mathbf{S} = \begin{bmatrix} S_{\mathrm{HH}} & S_{\mathrm{HV}} \\ S_{\mathrm{VH}} & S_{\mathrm{VV}} \end{bmatrix}, \tag{8}$$

where S_{pq} is the scattering element of q-transmitting and p-receiving polarizations. For the reciprocal backscattering case, $S_{\mathrm{HV}} = S_{\mathrm{VH}}$. The polarimetric scattering information of a pixel i can be represented by a complex vector, called the Pauli vector,

$$\mathbf{k}_i = \frac{1}{\sqrt{2}} \begin{bmatrix} S_{\mathrm{HH}} + S_{\mathrm{VV}} \\ S_{\mathrm{HH}} - S_{\mathrm{VV}} \\ 2S_{\mathrm{HV}} \end{bmatrix} \quad \text{and} \quad \mathbf{T}_i = \mathbf{k}_i \mathbf{k}_i^{\mathrm{H}}, \tag{9}$$

where $\mathbf{T}_{\mathrm{i}}$ is the coherency matrix in the single-look case. The equivalent multi-look coherency matrix can be obtained by averaging n neighboring pixels, i.e.,

$$\langle \mathbf{T} \rangle = \frac{1}{n} \sum_{i=1}^{n} \mathbf{k}_i \mathbf{k}_i^{\mathrm{H}} \tag{10}$$

The same as the single channel data, the intensity of each element in the Pauli vector and every diagonal element in the coherency matrix conforms to exponential distribution or gamma distribution as formula (4) or formula (5), respectively, but with the different parameters. So the data of each polarization channel can be transformed to the values between 0 and 1 which conform to uniform distribution.

3.2. Colorization Based on the Pauli Decomposition

As shown in Formula (9), the polarimetric SAR data are represented as a Pauli vector, which is based on the linear combinations arising from a complete orthogonal set of $2 * 2$ complex basis matrices, i.e., the Pauli spin matrix basis set $\{\mathbf{\Psi}_{\mathrm{P}}\}$ [2],

$$\{\mathbf{\Psi}_{\mathrm{P}}\} = \left\{ \sqrt{2} \begin{bmatrix} 1 & 0 \\ 0 & 1 \end{bmatrix} \quad \sqrt{2} \begin{bmatrix} 1 & 0 \\ 0 & -1 \end{bmatrix} \quad \sqrt{2} \begin{bmatrix} 0 & 1 \\ 1 & 0 \end{bmatrix} \right\}. \tag{11}$$

This representation is also called the Pauli decomposition. The elements in the Pauli vector or the diagonal elements in the coherency matrix relate to the surface scattering, double-bounce scattering and cross-polarization channel, respectively.

The typical terrains underlying the surface scattering are the physical surfaces, such as ground, water and sea-ice. Some manmade targets and the ground form a double-bounce scattering, such as the buildings and bridges. The primary component of the scattering from the vegetation is volume scattering, which has a relatively high response in the cross-polarization channel. Therefore, three channels in the Pauli vector can be assigned to three color channels, R, G, and B, respectively. The surface scattering corresponds to the B (blue) channel, since the color of the sea is blue. The double-bounce scattering corresponds to the R (red) channel, and then the manmade targets can be highlighted. The cross-polarization channel corresponds to the G (green) channel, and then the vegetation can be colorized by green.

4. VISUALIZATION OF POL-INSAR IMAGES

4.1. Topography Retrieval

The single channel SAR or the polarimetric SAR discussed in Sections 2 and 3 only measures the location of a target in a two-dimensional coordinate system, with the along-track direction and the cross-track direction. The Interferometric SAR system observes the same scene from two slightly different angles by two imaging sensors or two repeat passes of a single imaging sensor. Topography information can be obtained from the actual phase between two SAR images. But the phase of the interferogram is restricted in $[-\pi, \pi)$. Therefore, phase unwrapping is the most important technique for topography retrieval in InSAR data processing. Many phase unwrapping methods have been proposed in the past 20 years. One typical method is the branch-cut method proposed by Goldstein [8]. In this work, this method will be employed for phase unwrapping.

4.2. Tree and Building Height Inversion

According to the theory of SAR imaging, the backscattering of a tree or building can be modeled by the sum of two dominant scattering centers located on the ground and in the canopy or on the roof of the building, as the cases from 1 to 4 in the Figs. 1(a) and (b).

Assuming that the InSAR data are obtained from the repeat-pass observation, the received signals in two orbits may be written by

$$S_1 = \sum_{m=1}^{2} \sigma_m e^{-\mathrm{j}\frac{4\pi}{\lambda}R} + n_1 \tag{12}$$

and

$$S_2 = \sum_{m=1}^{2} \sigma_m e^{-\mathrm{j}\frac{4\pi}{\lambda}(R+\Delta R_m)} + n_2 \tag{13}$$

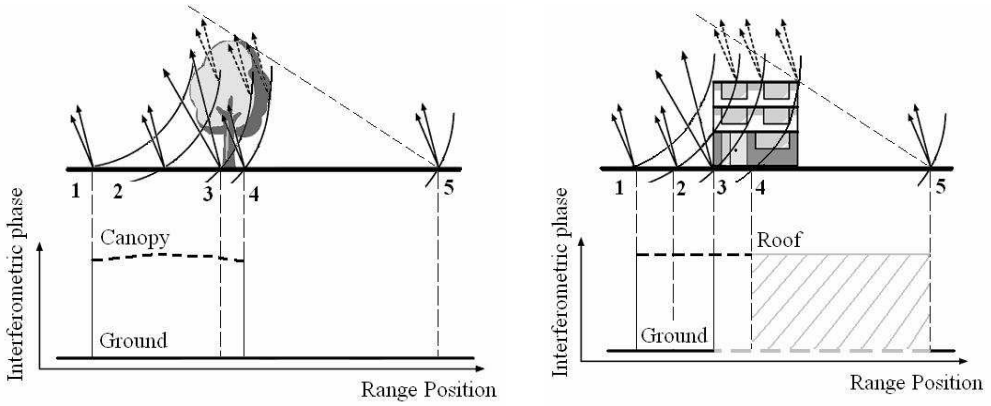

Figure 1: Imaging mechanisms of the tree and building.

λ is the wavelength of the electromagnetic wave. σ_m is the scattering coefficient of the m-th scattering center. n_1 and n_2 are the additive noises in orbit 1 and 2, respectively. R is the slant-range distance from the target to orbit 1. ΔR_m is the slant-range difference of the m-th scattering center. So the interferometric phase of each scattering center is $\Delta\psi_m = -4\pi\Delta R_m/\lambda$. The relationship between the interferometric phase and the height difference of two scattering centers is as follows.

$$\Delta\varphi = \Delta\psi_1 - \Delta\psi_2 = \frac{4\pi Bh\cos(\theta-\alpha)}{\lambda R\sin\theta}. \tag{14}$$

h is the height from the first scattering center to the second one, and that is the height of the tree or building. B is the baseline between two orbits. θ is the look-angle and α is the angle that the baseline makes with respect to a referenced horizontal plane.

Pol-InSAR system works with four polarization channels. The received signals in formula (12) and (13) can be rewritten in vector notation as follows.

$$\begin{aligned}\mathbf{S}_1 &= \mathbf{A}\sigma + \mathbf{n}_1\\ \mathbf{S}_2 &= \mathbf{A}\mathbf{\Phi}\sigma + \mathbf{n}_2\end{aligned}, \tag{15}$$

where

$$\begin{aligned}&\mathbf{S}_i = \begin{bmatrix} S_i^{\mathrm{HH}} \\ S_i^{\mathrm{HV}} \\ S_i^{\mathrm{VV}}, \end{bmatrix} \quad \mathbf{n}_i = \begin{bmatrix} n_i^{\mathrm{HH}} \\ n_i^{\mathrm{HV}} \\ n_i^{\mathrm{VV}} \end{bmatrix}, \quad i = 1,2 \quad \mathbf{A} = e^{-\mathrm{j}\frac{4\pi}{\lambda}R}\begin{bmatrix} \zeta_1^{\mathrm{HH}} & \zeta_2^{\mathrm{HH}} \\ \zeta_1^{\mathrm{HV}} & \zeta_2^{\mathrm{HV}} \\ \zeta_1^{\mathrm{VV}} & \zeta_2^{\mathrm{VV}} \end{bmatrix}, \quad \sigma = \begin{bmatrix} \sigma_1 \\ \sigma_2 \end{bmatrix},\\ &\mathbf{\Phi} = \begin{bmatrix} e^{\mathrm{j}\Delta\psi_1} & \\ & e^{\mathrm{j}\Delta\psi_2} \end{bmatrix}.\end{aligned} \tag{16}$$

ζ_m^{pq} represents the amplitude difference between the scattering intensities of the different polarization channels.

The interferometric phases of two scattering centers can be obtained from formula (15) by ESPRIT algorithm [9]. Then using the formula (14), the height of the tree or building can be retrieved.

4.3. 3-D Visualization for the InSAR Data

As the discussion above, InSAR data provide the elevation information of the scene, the topography or the height of the trees and buildings. For the InSAR or Pol-InSAR data of mountainous regions, the topography information can be obtained through phase unwrapping technique. For the Pol-InSAR data of the flat terrain, especially the areas of the countryside or town, the height of the trees and buildings can be retrieved using the ESPRIT algorithm.

Combining the elevation information extracted from the InSAR data and the 2-D visualization result, the InSAR data can be visualized as a 3-D scene.

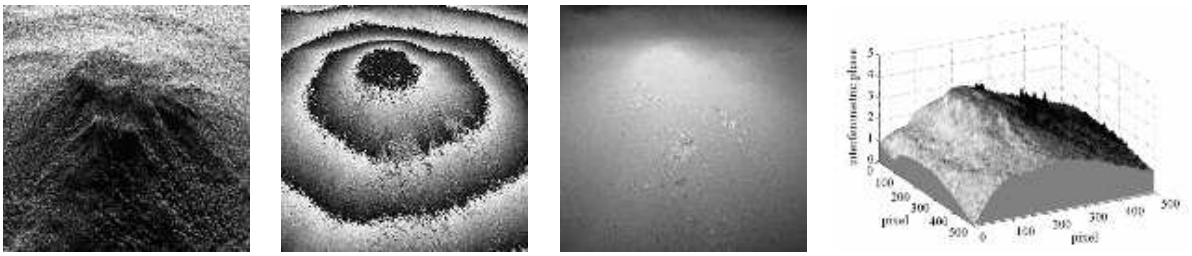

(a) (b) (c) (d)

Figure 2: The visualization results of the Kaimon volcano: (a) 2-D visualization result; (b) wrapped phase; (c) unwrapped phase; (d) 3-D visualization result.

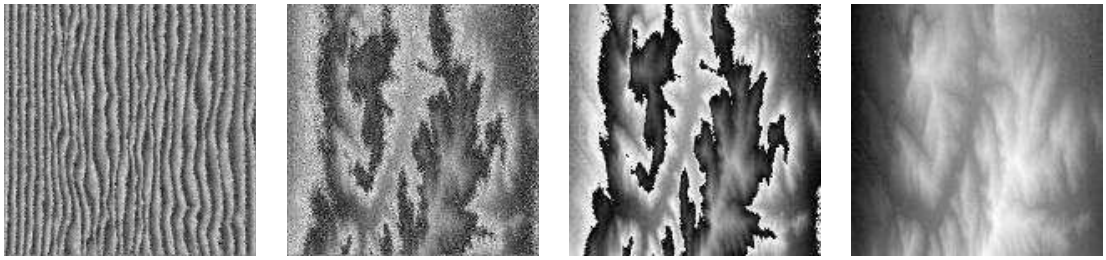

(a) (b) (c) (d)

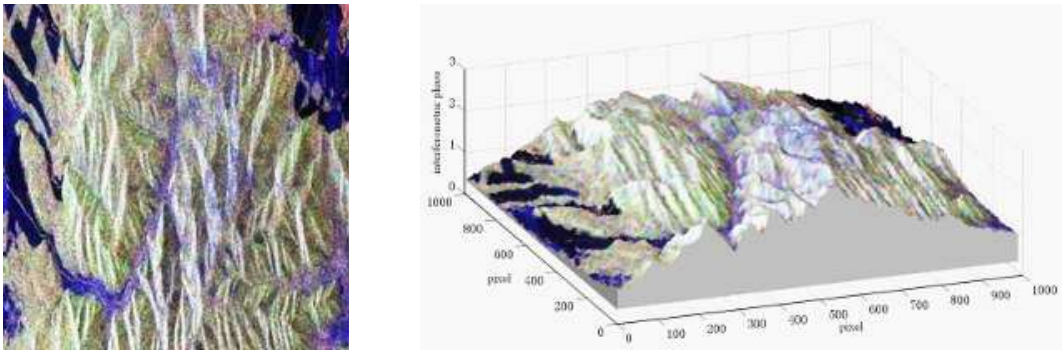

(e) (f)

Figure 3: The visualization results of Tienshan area: (a) wrapped phase; (b) wrapped phase after removal of the flat earth phase; (c) filtered wrapped phase; (d) unwrapped phase; (e) 2-D visualization result; (f) 3-D visualization result.

5. EXPERIMENTAL RESULTS

The experimental data are composed of InSAR data of Kaimon Volcano, Japan, acquired by PISAR system, Pol-SAR data of Tienshan area, acquired by SIR-C/X-SAR system, and Pol-InSAR data of Oberpfaffenhofen, Germany, acquired by ESAR system.

The grey visualization result of Kaimon volcano is shown in Fig. 2(a). The altitude-dependent distortion of the targets, such as foreshorten and shadow, can be seen in the scene. The interferogram of the volcano is shown in Fig. 2(b). The result of phase unwrapping based on the branch-cut algorithm is shown in Fig. 2(c). The brighter pixel corresponds to the higher region. Combining the results in Figs. 2(a) and (c), the 3-D visualization result can be obtained, as shown in Fig. 2(d).

The interferometric phase of Tienshan data is shown in Fig. 3(a). In order to thin out the fringes in the interferogram, the phase contribution of the flat earth should be removed first. The wrapped phase after that is shown in Fig. 3(b). Then the phase should be filtered to reduce the phase noise, as shown in Fig. 3(c). The phase unwrapping result is shown in Fig. 3(d). The colorization result of Tienshan area based on Pauli decomposition is shown in Fig. 3(e). The trees on the mountains are colorized as green due to their high intensity in cross-polarization channel. The river among the mountains is blue due to its surface scattering mechanism. The 3-D visualization result is shown in Fig. 3(f).

The 2-D visualization result of Oberpfaffenhofen is shown in Fig. 4(a). The houses in the

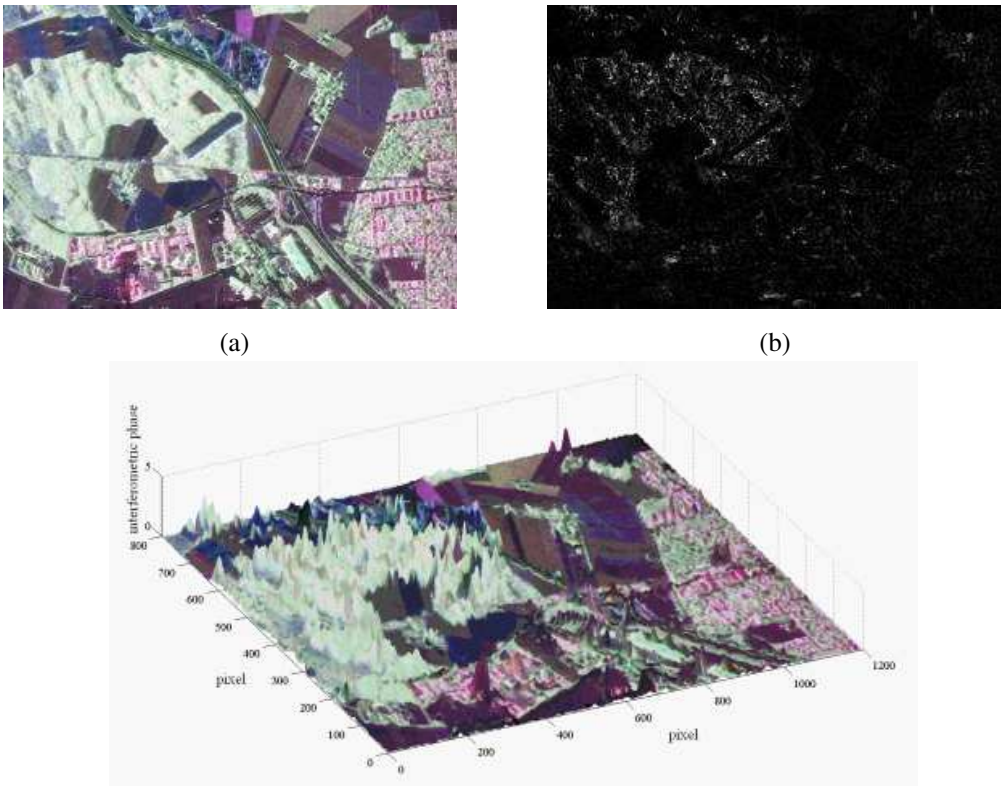

Figure 4: The visualization results of Oberpfaffenhofen: (a) 2-D visualization result; (b) interferometric phase difference obtained by ESPRIT algorithm; (c) 3-D visualization result.

town are red due to their double-bounce scattering mechanism, and the trees are green as well. Formula (14) indicates that the height of the tree or building is proportional to the interferometric phase difference of two scattering centers, which are obtained by the ESPRIT algorithm. As shown in Fig. 4(b), the brighter pixel corresponds to the higher target. Combining Figs. 4(a) and (b), 3-D visualization result can be obtained, as shown in Fig. 4(c).

6. CONCLUSIONS

In this paper, a framework of SAR image visualization is proposed, from single channel SAR to Pol-InSAR, from grey to color, from 2-D visualization to 3-D visualization. 2-D visualization methods of single channel SAR image and Pol-SAR image are first proposed. Combining the elevation information extracted from the InSAR data and 2-D visualization results, 3-D visualization of InSAR or Pol-InSAR data can be realized. The effectiveness of the proposed visualization methods have been demonstrated by PISAR data, SIR-C/X-SAR data, and ESAR data, respectively.

ACKNOWLEDGMENT

This work was supported partially by the National Natural Science Foundation of China (40871157) and the Foundation of Advanced Research for National Defense.

REFERENCES

1. Franceschetti, G. and R. Lanari, *Synthetic Aperture Radar Processing*, CRC Press, 1999.
2. Lee, J. S. and E. Pottier, *Polarimetric Radar Imaging, from Basics to Applications*, CRC Press, Boca Raton, 2009.
3. Graham, L. C., "Synthetic interferometric radar for topographic mapping," *Proc. IEEE*, Vol. 62, 763–768, June 1974.
4. Cloude, S. R. and K. P. Papathanassiou, "Polarimetric SAR interferometry," *IEEE Trans. on Geoscience and Remote Sensing*, Vol. 36, 1551–1565, 1998.

5. Curlander, J. and R. Mcdonough, *Synthetic Aperture Radar Systems and Signal Processing*, John Wiley & Sons Inc., 1991.
6. Kay, S., *Fundamentals of Statistical Signal Processing, Volume I: Estimation Theory*, Pearson Education, 1993.
7. Zhou, G., H. Zhong, and J. Yang, "A novel method of visualization for SAR images," *International Conference on Digital Signal Processing and Communications Engineering*, 2011.
8. Goldstein, R. M., H. A. Zebker, and C. L. Werner, "Satellite radar interferometry: Two dimensional phase unwrapping," *Radio Sci.*, Vol. 23, 713–720, 1988.
9. Yamada, H., Y. Yamaguchi, E. Rodriquez, et al., "Polarimetric SAR interferometry for forest canopy analysis by using the super-resolution method," *Geoscience and Remote Sensing Symposium*, Vol. 3, 1101–1103, 2001.

H-α Decomposition and Alternative Parameters for Dual Polarization SAR Data

Zili Shan[1, 2], **Chao Wang**[1], **Hong Zhang**[1], **and Jiehong Chen**[1, 2]

[1]Center for Earth Observation and Digital Earth, Chinese Academy of Science, Beijing 100094, China
[2]Graduate University of Chinese Academy of Science, Beijing, China

Abstract— In order to exploit the dual polarization data more efficiently, the H-α decomposition in the HH-VV polarization mode is investigated in this paper. Experiment results indicate that different types of scattering mechanisms can still be separated in the H-α space of the HH-VV polarization mode, although some ambiguities of classes are observed. Moreover, as the scattering angle α has an obscure physical meaning, alternatives such as E and ρ are proposed for both the H and α parameter in this paper. The parameter E, derived from the rotation invariants of the Hermitian matrix, has the same maximum and minimum property as the entropy H, and meanwhile the parameter ρ has an explicit physical meaning as the proportion of the non-surface scattering powers in the total power. Another advantage of the parameters E and ρ is that they can be derived quite simply and efficiently. Further experiment results indicate that the alternative parameters E and ρ possess similar characteristics corresponding to the scattering mechanisms as that of the H and α parameters under the dual polarization mode.

1. INTRODUCTION

Incoherent polarimetric target decomposition theories lay particular emphasis on separating the target scattering coherency matrix into a weighted sum of several basic scattering mechanisms [1], depending on the target polarization information. Cloude and Pottier [2] have proposed an entropy based decomposition method for quad polarization data, based on the assumption that the polarization scattering characteristics can be represented by the space of the entropy H and the averaged scattering angle α. Their method is based on the eigenvalue analysis of Hermitian matrices. The H-α decomposition has such good properties as rotation invariance, irrelevance to specific probability density distributions, and covering the whole scattering mechanism space. There are two basic polarization modes, namely the quad polarization mode, and the dual polarization mode. Although the quad polarization data are superior in the extraction of scattering mechanisms, they are not always available, due to various practical limitations. For instance, they are too expensive for some certain applications. Therefore, when quad polarization data are un-available, we usually have to reduce to exploitation of dual polarization data in particular applications [3, 4]. Moreover, the data of Envisat, PALSAR or Terra-SAR are usually provided in dual polarization mode.

In this paper, we will take the HH-VV dual polarization mode as an example for analysis. In Section 2, the feasibility of the H-α decomposition is investigated in the dual polarization mode, compared to that in the quad polarization mode. Comparative evaluations have been carried out in both of the polarization modes. However, the derivation of the entropy H and the scattering angle α involves in eigenvalue decompositions of Hermitian matrices, which is not quick enough in computation. Additionally, the scattering angle α does not have a clear physical meaning when the entropy is high. Therefore, two alternative parameters are proposed in Section 3. After analyzing the relationships between these parameters, we will find that the alternative parameters have similar characteristics with the entropy and α in analyzing the scattering mechanisms. They only require some simple computations, besides the alternative parameter of α has an unambiguous physical meaning. The classification results in terms of the alternative parameters based on the ESAR dual polarimetric data are provided in Section 4. Finally, the paper is summarized in Section 5.

2. TARGET DECOMPOSITION BASED ON THE COHERENCY MATRIX FOR DUAL-POL DATA

In this section, the theories of the H-α decomposition in both the quad polarization mode and the dual polarization mode are briefly summarized. Subsequently, the feasibility of the H-α decomposition in the HH-VV dual polarization mode is analyzed, using the ESAR polarimetric image acquired over the Oberpfaffenhofen area in Germany.

2.1. H-α Decomposition in the Quad Polarization Mode

For a quad polarization SAR image, each pixel is represented by a 3×3 coherency matrix T_{quad}, which is nonnegative definite and Hermitian. The matrix T_{quad} is decomposed as shown in (1) and (2).

$$T_{quad} = \begin{bmatrix} T_{11} & T_{12} & T_{13} \\ T_{12}^* & T_{22} & T_{23} \\ T_{13}^* & T_{23}^* & T_{33} \end{bmatrix} = U \begin{bmatrix} \lambda_1 & & \\ & \lambda_2 & \\ & & \lambda_3 \end{bmatrix} U^H = \lambda_1 u_1 u_1^H + \lambda_2 u_2 u_2^H + \lambda_3 u_3 u_3^H \tag{1}$$

where

$$\begin{gathered} U = \begin{bmatrix} u_{11} & u_{12} & u_{13} \\ u_{21} & u_{22} & u_{23} \\ u_{31} & u_{32} & u_{33} \end{bmatrix} = \begin{bmatrix} u_1 & u_2 & u_3 \end{bmatrix} \\ \text{and } u_i = e^{j\phi_i} \begin{bmatrix} \cos\alpha_i & \sin\alpha_i \cos\beta_i e^{j\delta_i} & \sin\alpha_i \sin\beta_i e^{j\gamma_i} \end{bmatrix}^T, \quad i = 1, 2, 3 \end{gathered} \tag{2}$$

The superscript H denotes the conjugate transpose, and $*$ denotes the conjugate. The polarimetric entropy H and the scattering angle α are defined by (3) and (4).

$$H = \sum_{i=1}^{3} -P_i \log_3 P_i \text{ and } \alpha = \sum_{i=1}^{3} P_i \cos^{-1}(|u_{1i}|) \tag{3}$$

where

$$P_i = \lambda_i \Big/ \sum_{j=1}^{3} \lambda_j, \quad i = 1, 2, 3 \tag{4}$$

2.2. H-α Decomposition in the Dual Polarization Mode

For a dual polarization SAR image, each pixel is represented by a 2×2 coherency matrix T_{dual}, which is nonnegative definite and Hermitian. The eigenvalue decomposition of T_{dual} is shown in (5) and (6).

$$T_{dual} = \begin{bmatrix} T_{11} & T_{12} \\ T_{12}^* & T_{22} \end{bmatrix} = U \begin{bmatrix} \lambda_1 & \\ & \lambda_2 \end{bmatrix} U^H = \lambda_1 u_1 u_1^H + \lambda_2 u_2 u_2^H \tag{5}$$

where

$$U = \begin{bmatrix} u_{11} & u_{12} \\ u_{21} & u_{22} \end{bmatrix} = \begin{bmatrix} u_1 & u_2 \end{bmatrix} \quad \text{and} \quad u_i = e^{j\phi_i} \begin{bmatrix} \cos\alpha_i & \sin\alpha_i e^{j\delta_i} \end{bmatrix}^T \tag{6}$$

The superscript H denotes the conjugate transpose, and $*$ denotes the conjugate. The polarimetric entropy H and the scattering angle α are defined by (7) and (8).

$$H = \sum_{i=1}^{2} -P_i \log_2 P_i \quad \text{and} \quad \alpha = \sum_{i=1}^{2} P_i \cos^{-1}(|u_{1i}|) \tag{7}$$

where

$$P_i = \lambda_i \Big/ \sum_{j=1}^{2} \lambda_j, \quad i = 1, 2 \tag{8}$$

Let us take three classical scattering mechanisms as examples, namely the surface, the double bounce, and the dipole scattering. Their coherency matrices are shown in (9). And the corresponding parameters H and α are as (10) shows. From (10), we can find that although the entropies of the scattering mechanisms are the same, the scattering angles are different, i.e., these three basic scattering mechanisms are still distinguishable in the H-α space in the dual polarization mode.

$$T_{surface} = \begin{bmatrix} 2 & 0 \\ 0 & 0 \end{bmatrix}, \quad T_{double\text{-}bounce} = \begin{bmatrix} 0 & 0 \\ 0 & 2 \end{bmatrix}, \quad T_{dipole} = \begin{bmatrix} \frac{1}{2} & \frac{1}{2} \\ \frac{1}{2} & \frac{1}{2} \end{bmatrix} \tag{9}$$

$$\begin{cases} H_{surface} = 0 \\ \alpha_{surface} = 0^\circ \end{cases}, \quad \begin{cases} H_{double\text{-}bounce} = 0 \\ \alpha_{double\text{-}bounce} = 90^\circ \end{cases}, \quad \begin{cases} H_{dipole} = 0 \\ \alpha_{dipole} = 45^\circ \end{cases} \tag{10}$$

2.3. Experimental Results of H-α Decomposition in Both Polarization Modes

To evaluate the performance of the H-α decomposition in the dual polarization mode, an polarimetric image acquired over the Oberpfaffenhofen area in Germany is applied for demonstration. Both the decomposition results are shown in Fig. 1. It can be seen from Figs. 1(c) and (d) that the entropy increases in some farmlands, because it lacks the HV scattering channel, and the remainder scattering mechanisms powers are close to each other. However, the α values in both polarization modes are similar. Therefore, the scattering mechanisms are still distinguishable in the dual polarization mode, thus the H-α decomposition in the dual polarization mode is workable.

3. H-α ALTERNATIVE PARAMETERS FOR DUAL POLARIZATION DATA

Despite the advantages of the H and α parameters, some drawbacks exist in the definition of these parameters. The definition of α, i.e., a weighted eigenvector angles in the complex spherical coordinate makes its physical significance inexplicit, particularly when the entropy is close to 1. In addition, the computation of H and α is time-consuming, which is unfavorable for high resolution images. Therefore, we propose two alternative parameters, which possess explicit physical meanings and require less time for computation as well. The alternative parameters of H-α are E-ρ, as is shown in (11). The parameters E and ρ are respectively defined by the Frobenius norm and the first element of the normalized coherency matrix T. It is easy to find that the computation

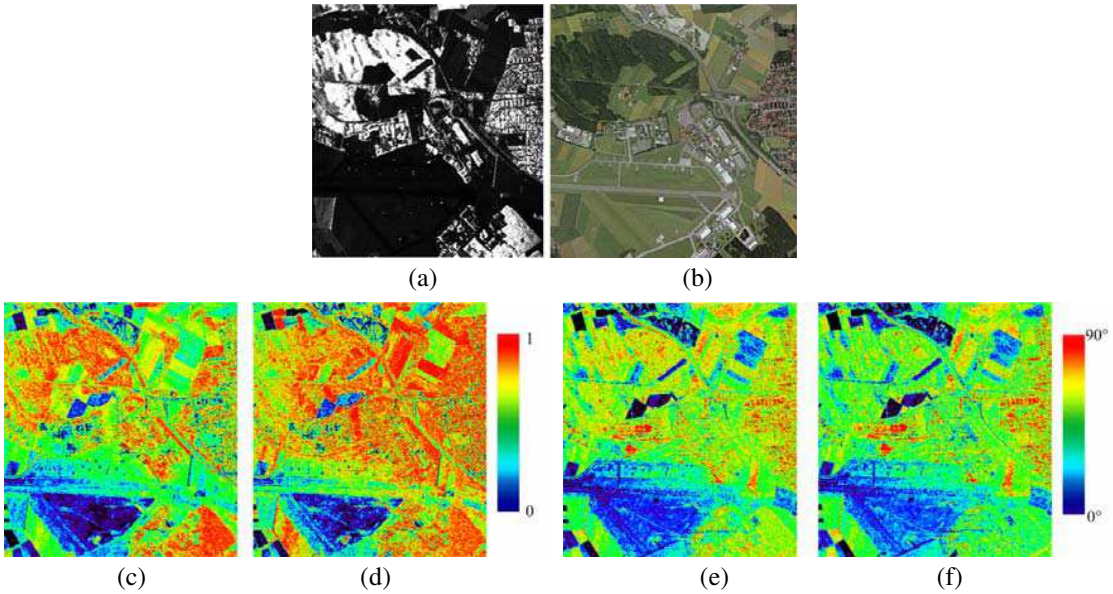

Figure 1: Decomposition results in both polarization modes (a) the span image, (b) the optical image © 2011 Europa techniques, 2011 GeoContent, and 2011 Tele Atlas, (c) H values of the quad polarization image, (d) H values of the dual polarization image, (e) α values of the quad polarization image, (f) α values of the dual polarization image.

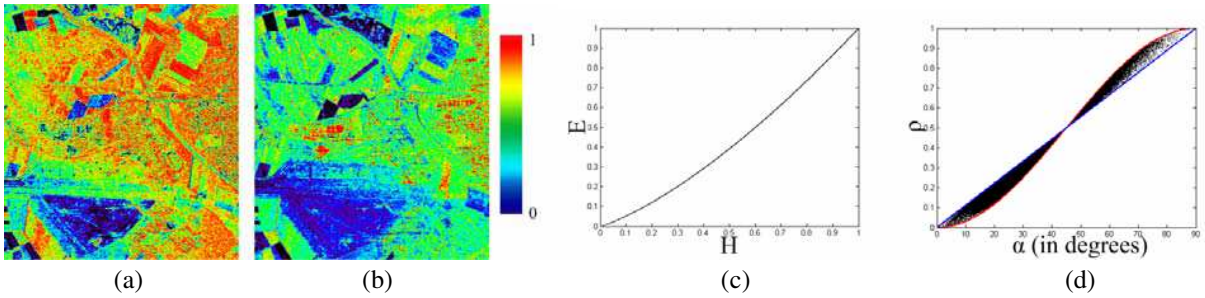

Figure 2: Decomposition results of the alternative parameters (a) values of E, (b) values of ρ, (c) correlation between H and E, (d) correlation between α and ρ.

load is lower in (11), compared to that in (7). Both of the alternative parameters are rotation invariant. Another advantage of ρ is that it has a distinct physical meaning, i.e., the power ratio of the scattering mechanisms exclusive of the double bounce. As shown in Figs. 2(a) and (b), the alternative parameters have similar characteristics with H and α in relation to the scattering mechanisms. Both parameters range from 0 to 1. Fig. 2(c) shows that the correlation between H and E is nearly linear, and all of the pixels in the image in Fig. 1 are overlapped on the curve, which corresponds to (12a). The correlation between α and ρ, characterized by (12b), is shown in Fig. 2(d). All pixels lie between the two theoretical correlation curves.

$$E=2\left(1-\left\|\frac{T}{span}\right\|_F^2\right) \quad \rho=1-\frac{T_{11}}{span}=1-\frac{|S_{HH}+S_{VV}|^2}{span}=1-\left(\frac{\lambda_1}{\lambda_1+\lambda_2}\cos\alpha_1+\frac{\lambda_2}{\lambda_1+\lambda_2}\cos\alpha_2\right) \quad (11)$$

$$\begin{cases} T_1=\begin{bmatrix} p & 0 \\ 0 & 1-p \end{bmatrix} & 0\le p \le \frac{1}{2} \\ T_2=\begin{bmatrix} 1-p & 0 \\ 0 & p \end{bmatrix} & \frac{1}{2}\le p \le 1 \end{cases} \quad (12a)$$

$$\begin{cases} \rho_1=\sin^2\left(\frac{\pi\alpha}{180}\right) & 0\le\alpha\le 90 \\ \rho_2=\frac{\alpha}{90} & 0\le\alpha\le 90 \end{cases} \quad (12b)$$

4. CLASSIFICATION BASED ON THE ALTERNATIVE PARAMETERS

As shown in Fig. 3(a), the H-α space of the dual polarization image is partitioned into 9 regions, which are identical to those in [2]. Region 3 does not correspond to any pixel in theory, so it is excluded from analysis. Fig. 3(b) is the corresponding classification result. Fig. 3(c) exhibits the pixels' distribution for the dual polarization image in the H-α space, which is partitioned in the same way as Fig. 3(a). From Fig. 3(c), it can be found that without revisions of the region borders in the H-α space, some certain pixels with different scattering mechanisms will mix up. Therefore, corresponding revisions have been carried out according to Table 1. The revised regions

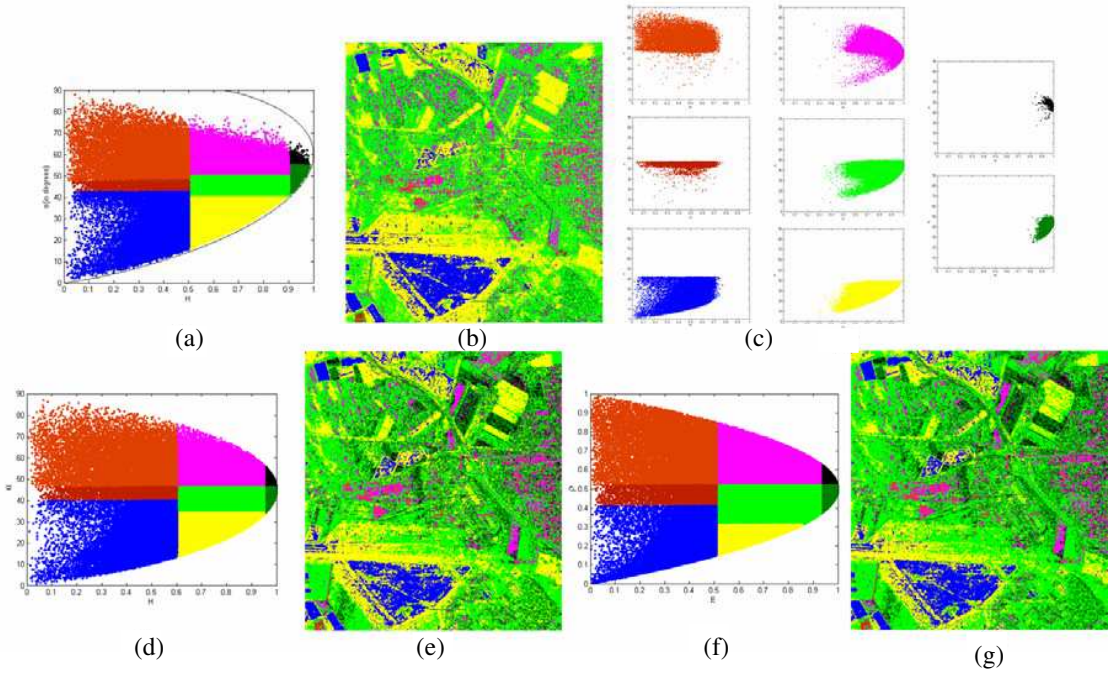

Figure 3: Decomposition results in both polarization modes (a) pixel distribution for the quad polarization image, (b) classification result for the quad polarization image, (c) pixel distribution corresponding to the same partition method as in (a), (d) pixel distribution for the dual polarization image, (e) classification result for the dual polarization image, (f) pixel distribution corresponding to the alternative parameters, (g) classification result corresponding to the alternative parameters.

Table 1: Scattering regions for classification.

	Region 1	Region 2	Region 4	Region 5	Region 6	Region 7	Region 8	Region 9
H	[0.95, 1]	[0.95, 1]	[0.6, 0.95)	[0.6, 0. 95)	[0.6, 0.95)	[0, 0.6)	[0, 0.6)	[0, 0.6)
g	[46, 90]	[0, 46]	[46, 90]	[34, 46)	[0, 34)	[46, 90]	[40, 46)	[0, 40)
E	[0.93, 1]	[0.93, 1]	[0.51, 0.93)	[0.51, 0.93)	[0.51, 0.93)	[0, 0.51)	[0, 0.51)	[0, 0.51)
ρ	[0.52, 1]	[0, 0.52]	[0.52, 1]	[0.31, 0.52)	[0, 0.31)	[0.52, 1]	[0.41, 0.52)	[0, 0.41)

and the corresponding classification result are shown in Figs. 3(d) and (e). Similarly, the space of the alternative parameters E and ρ is also divided into 9 regions in accordance with Table 1. The values of ρ are the corresponding sine values of α. Figs. 3(f) and (g) are the pixel distribution and the classification image. The classification results in Figs. 3(e) to (g) are almost identical, which indicates that the alternative parameters have similar characteristics in term of scattering mechanisms. Therefore, the parameter set E-ρ is a good option for replacing the parameters H and α.

5. CONCLUSION

The H-α decomposition method in dual polarization mode is investigated in this paper. Then, two alternative parameters are proposed in order to reduce the computation load in the derivation of the entropy and the averaged scattering angle. Moreover, the alternative parameters have an explicit physical meaning. Experimental results show that the H-α decomposition is applicable in the dual polarization mode, and that the alternative parameters E and ρ are viable to act as a good substitute for the previous H and α.

ACKNOWLEDGMENT

This work was supported in part by the National Natural Science Foundation of China under Grant 40971198 and 40871191, and by the National High-Tech Research and Development Program of China under Grant 2009AA12Z118.

REFERENCES

1. Cloude, S. R., *Polarisation Applications in Remote Sensing*, Oxford University Press, Oxford, UK, 2010.
2. Cloude, S. R. and E. Pottier, "An entropy based classification scheme for land applications of polarimetric SAR," *IEEE Trans. Geosci. Remote Sens.*, Vol. 35, No. 1, 68–78, 1997.
3. Camilla, B. and S. N. Anfinsen, "Ship detection in ice-infested waters based on dual-polarization SAR imagery," *IEEE Geosci. Remote Sens. Lett.*, Vol. 8, No. 3, 391–395, 2011.
4. Cedric, L., P.-L. Frison, C. Tison, J.-C. Souyris, B. Stoll, B. Fruneau, and J.-P. Rudant, "Classification of tropical vegetation using multifrequency partial SAR polarimetry," *IEEE Geosci. Remote Sens. Lett.*, Vol. 8, No. 1, 133–137, 2011.

Forest Model for Height Estimation Using POLinSAR Data

Jiehong Chen[1, 2], **Hong Zhang**[1], **Chao Wang**[1], **and Yixian Tang**[1]

[1]Key Laboratory of Digital Earth, Center for Earth Observation and Digital Earth, CAS, Beijing 100094, China

[2]Graduate University of Chinese Academy of Sciences, Beijing 100049, China

Abstract— The Random Volume over Ground (RVoG) model has been widely applied to polarimetric synthetic aperture radar interferometry (POLinSAR) data for forest height inversion. The model assumes forest as a homogeneous volume of randomly oriented particles characterized by a constant extinction, over an impenetrable ground layer, which doesn't take into account the ground decorrelation. In order to integrate the ground decorrelation, two models taking into consideration the ground decorrelation will be investigated. The first model uses Gaussian function instead of Delta function to describe the response of electromagnetic wave interacting with ground; and the second model considers the ground coherence not equaling one anymore because of the change of the dielectric properties, even the deformation of ground. The influence of the complementary forest models on topography related phase is investigated. Finally we will discuss the method of these two models to invert forest height.

1. INTRODUCTION

Forest canopy height is an important parameter that is strongly correlated with timber volume, biomass, carbon stocks and ecological values such as habitat quality, as well as key to the terrestrial carbon cycle, biomass models and in forest inventory. Forest canopy height, together with other forest parameter, can be retrieved via POLinSAR technique. POLinSAR technique [1] is sensitive to the shape, the dielectric constants and orientation of the scatterers, and spatial distribution of distributed scatterers. Therefore POLinSAR technique is an important tool to estimate forest parameters, and has been widely applied to Geoscience.

In order to invert vegetation height and other parameters, it is necessary to build a simple geophysical model under some assumptions to relate geophysical parameters to POLinSAR observables. The vegetated area is always modeled in a simple way by a set of possible overlapping volume layer over ground. In the most simple case forest model is consisting of a single homogeneous canopy layer above the impenetrate ground, known as Random Volume over Ground (RVoG) [2–4], as displayed in Fig. 1. The whole coherence can be expressed as

$$\gamma(z) = e^{i\phi_0}\left(\frac{\gamma_{tv}\gamma_v + \mu(\omega)\gamma_g}{1+\mu(\omega)}\right) \tag{1}$$

For the case of RVoG model, volume temporal decorrelation γ_{tv} and ground coherence γ_g are 1.

Due to forest height are mostly determined by forest canopy [5–7], the effect of ground coherence on forest height inversion is often ignored except ground topography phase (actually it is just a reference phase, not carrying the ground's information), so that the ground coherence always is set to 1. Considering the ground response effected by many factors, for example the moisture of ground, in fact the ground coherence isn't always unit. Therefore we will investigate two ground decorrelation models with respect to the canopy only with pure volume decorrelation caused by the looking angle difference between interferometers in this paper.

The first model, in which ground is assumed penetrable and a Gaussian response is assumed, referred as the Random volume over Penetrable Ground (RVoPG) model in the following. In the

Figure 1: Two layer model for forest: ground and canopy.

second model the underlying surface coherence is assumed as a scalar and smaller than 1, referred as the Random Volume over Ground with Ground Temporal Decorrelation (RVoG + GTD) model in the following. As a result, the ground coherence of both models are not unit any more.

In this paper, Section 2 will propose RVoPG model, and Section 3 will introduce the RVoG + GTD model. Section 4 will discuss the topography bias, and Section 5 will discuss the inversion steps on vegetation height estimation in the context of two complementary models.

2. RVOPG MODEL

We consider the ground is penetrable with penetrated depth χ and independent on polarization. Due to the unfitness of Delta function, Gaussian function which is a vertically linear varying extinction exponent function is chose to describe the ground response. The schematic diagram of the vertical structure are shown in Fig. 2. In this case, the whole coherence can be characterized as

$$\gamma(z,\chi) = e^{i\phi_0}\left(\frac{\gamma_v + \mu(\omega)\gamma_g}{1+\mu(\omega)}\right) \tag{2}$$

with

$$\begin{cases} \gamma_v = \dfrac{2\sigma_z}{2\sigma_z + jk_z}\dfrac{e^{(2\sigma_z+jk_z)hv}-1}{e^{2\sigma_z hv}-1} \\ \gamma_g = \exp\left(-\dfrac{k_z^2\chi^2}{4}\right)\dfrac{\mathrm{erf}\left(1+i\dfrac{k_z\chi}{2}\right)-\mathrm{erf}\left(i\dfrac{k_z\chi}{2}\right)}{\mathrm{erf}(1)} \end{cases} \tag{3}$$

where γ_v, γ_g stand for pure volume and ground coherence, respectively. k_z denotes the vertical wavenumber of the interferometer, hv denotes the depth of the volume, σ_z is the volume extinction. Function erf$(\cdot)$ is the Gaussian error function.

Figure 3 shows the amplitude (a) and interferometric phase (c) of the ground coherence γ_g in RVoPG model with $kz * \chi$ ranging from $-\pi$ to π. Note the γ_g is complex, with a none-zero phase determined by $k_z\chi$, and its interferometric phase decreases linearly with the increase in $kz * \chi$. For a small penetrable depth for example $kz * \chi \in [-0.4, 0.4]$, the ground coherence amplitude almost equal to unit, shown in Fig. 4.

3. RVOG + GTD MODEL

Because of the change in the dielectric properties of ground, as for example due to a change in soil moisture or the roughness of the groundground will decorrelate. In this case ground coherence is always very difficult to be estimated but closed to 1, so in most papers ground coherence is assigned to 1. As a consequence of the change of effective scatterers within the scene leads the ground coherence no longer to be 1, the whole coherence within a resolution cell becomes

$$\gamma(z) = e^{i\phi_0}\left(\frac{\gamma_v + m(\omega)\gamma_g}{1+m(\omega)}\right), \quad \text{with } \gamma_g < 1 \tag{4}$$

Here γ_g is a real scalar and smaller than 1.

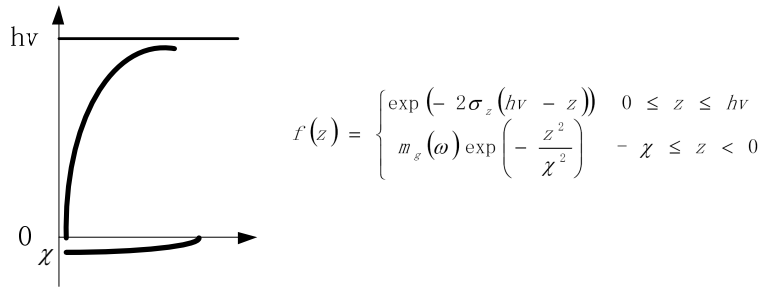

Figure 2: The schematic diagram for effective vertical ditribution of sactterers for RVoPG.

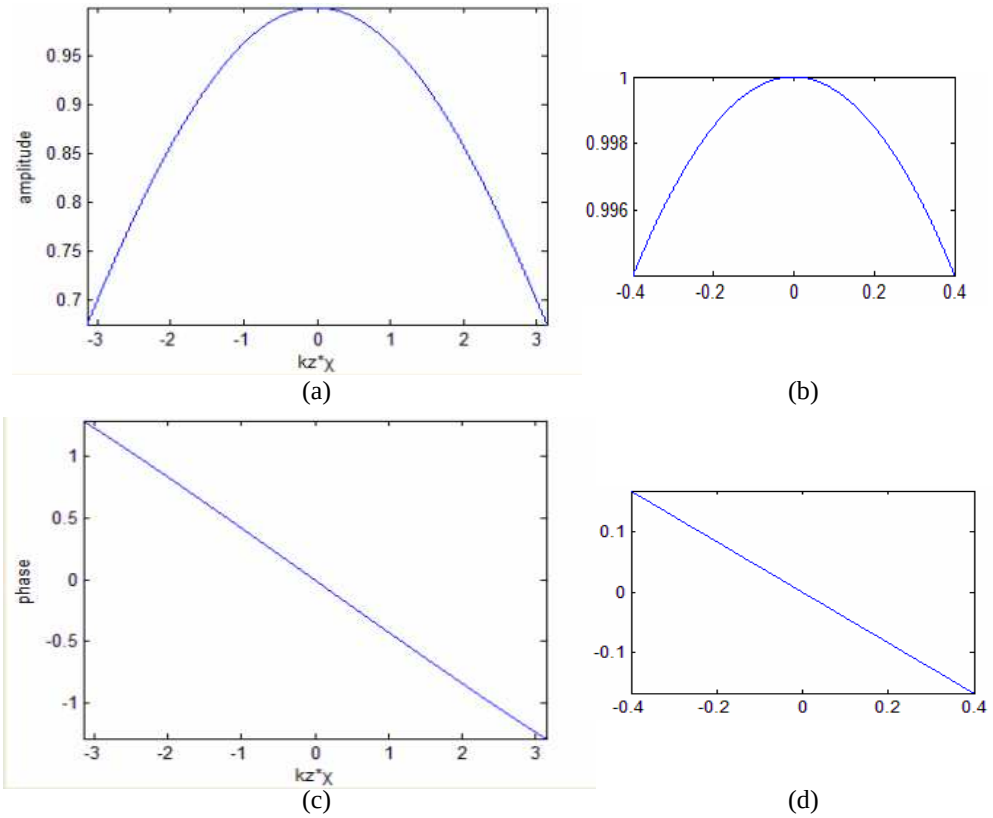

Figure 3: The amplitude (a) and interferometric phase (c) of the ground coherence γ_g in RVoPG model with $kz * \chi$ ranging from $-\pi$ to π. The zoomed pictures are shown on their right for $kz * \chi$ ranging from -0.4 to 0.4.

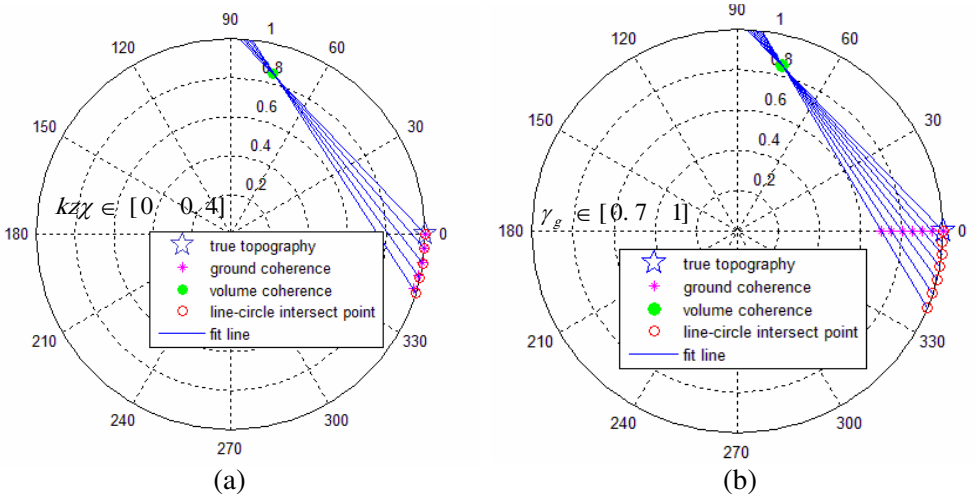

Figure 4: The effect of the ground decorrelation γ_g on topography.

4. THE EFFECTION ON TOPOGRAPHY ESTIMATION

Rewrite Eq. (2) and Eq. (4) as

$$\gamma(z) = e^{i\phi_0}\left(\gamma_v + \frac{m(\omega)}{1+m(\omega)}(\gamma_g - \gamma_v)\right) \tag{5}$$

it can be concluded that the coherences generate a line going through the point γ_v with direction $(\gamma_g - \gamma_v)$ in the complex plane. The line will intersect the circle at two points. The point nearer to topography phase point will only be consider and indicated by red circle in Fig. 4, although none of

them are the underlying topography related phase ($e^{i\phi_0}$). Fig. 4 shows the effect of ground coherence decorrelation on topography estimation with the volume coherence as $0.85\exp(i\frac{5\pi}{12})$ denotes by green dot, the true topography is indicated by blue pentagram, ground coherences are indicated by maroon star. By varying $kz * \chi$ or γ_g the fitting line is rotated about the volume coherence point. In Fig. 4(a) is for RVoPG model and right is for RVoG + GTD model. We find in the ground decorrelation case, if using RVoG model to invert parameters, the topography related phase will be biased, result in an overestimated forest height.

The inversion process also can be break into three stages like classical three-stage inversion process, least squares line fit, vegetation bias removal and height and extinction estimation; the difference is in stage 2: vegetation bias removal. Line-circle intersection points is not the topography point anymore. In order to estimate topography phase, the ground coherence γ_g should be known in priori.

5. CONCLUSION

In this paper, in order to integrate the ground decorrelation, we have discussed two models, one is RVoPG model, the other is RVoG + GTD model, and analyze their influence on topography phase and forest height estimation. The analysis result show that if the ground coherence is small than 1, it will bias the topography phase, and lead to forest height overestimation.

ACKNOWLEDGMENT

This work was supported in part by the National Natural Science Foundation of China under Grant 40971198 and 40871191, and by the National High-Tech Research and Development Program of China under Grant 2009AA12Z118.

REFERENCES

1. Cloude, S. R. and K. P. Papathanassiou, "Polarimetric SAR interferometry," *IEEE Transactions on Geoscience and Remote Sensing*, Vol. 36, No. 5, 1551–1565, 1998.
2. Treuhaft, R. N., S. N. madsen, M. Moghaddam, and J. J. van Zyl, "Vegetation characterics and underlying topography from interferometric radar," *Radio Science*, Vol. 31, 1449–1485, 1996.
3. Treuhaft, R. N. and P. R. Siqueira, "The vertical structure of vegetated land surfaces from interferometric and polarimetric radar," *Radio Science*, Vol. 35, 141–177, 2000.
4. Papathanassiou, K. P. and S. R. Cloude, "Single baseline polarimetric SAR interferometry," *IEEE Transactions on Geoscience and Remote Sensing*, Vol. 35, No. 1, 141–177, 2001.
5. Cloude, S. R. and K. P. Papathanassiou, "Three-stage inversion process for polarimetric SAR interferometry," *IEE Proceedings on Radar Sonar & Navigation*, Vol. 15, 125–134, 2003.
6. Garestier, F. and T. L. Toan, "Forest modeling for height inversion using single-baseline InSAR/Pol-insar data," *IEEE Transactions on Geoscience and Remote Sensing*, Vol. 48, No. 3, Mar. 2010.
7. Ballester-Berman, J. D. and J. M. Lopez-Sanchez, "Coherence Loci for a homogeneous volume over a double-bounce ground return," *IEEE Geoscience and Remote Sensing Letters*, Vol. 4, No. 2, 317–321, 2007.

Improved Sigma Filter for Speckle Filtering of PolinSAR Imagery

Hong Zhang[1], **Wuping Lu**[1], **Chao Wang**[1], **Jiehong Chen**[1,2], **and Bo Zhang**[1]

[1]Key Laboratory of Digital Earth, Center for Earth Observation and Digital Earth, CAS, Beijing 100094, China

[2]Graduate University of Chinese Academy of Sciences, Beijing, China

Abstract— The authors propose an improved sigma filter for the speckle filtering of polarimetric interferometry data. The Lee sigma filter was developed in 1983 based on the simple concept of two-sigma probability, and it was reasonably effective in speckle filtering. However the speckle model used in Lee sigma filter is the negative exponential model, which is only suitable for uniform regions. For the texture and very uneven regional areas, the effectiveness of this filter is to be questioned. In this paper, we extend and improve the Lee sigma filter by introducing generalized Gamma model, which can be applied to a variety of areas. In addition, we incorporate the phase processing to improve the interferometric coherence. The proposed algorithm is applied to Chinese airborne SAR data to demonstrate its overall speckle filtering characteristics as compared with other algorithms.

1. INTRODUCTION

Speckle noise is a common phenomena in all coherent imaging systems like laser, acoustic and Synthetic Aperture Radar (SAR) imagery. SAR data are subjected to the speckle effect that degrades the SAR information content and complicates image interpretation and terrain classification. In general, speckle reduction techniques are applied before information extraction.

Speckle filtering has been an active research area for more than 20 years, and many algorithms have been proposed [1–10]. Among them, The sigma filter was introduced by Lee in 1983 [1, 2], and In 2009, Lee extended the Lee sigma filter and developed the improved sigma filter [10]. The Lee sigma filter has widely applied because of its simplicity, its effectiveness in speckle reduction, and its computational efficiency.

In this paper, we propose an improved POLinSAR speckle filtering algorithm based on Lee sigma filter and the generalized gamma distribution model. Compared to the Lee-Sigma filter, the proposed filter uses a more accurate clutter model which can estimate the local distributions of different parts of the image. Therefore, it can get better estimated of filtering parameters, which result in reducing more speckles while preserving edges. The effectiveness of this proposed method is demonstrated using Chinese airborne X-band polarimetric interferometric SAR data.

2. LEE SIGMA FILTER

2.1. Lee Sigma Filter

The Lee sigma filter is based on the concept that 95.5% of pixels are distributed within the two-sigma range from its mean. The main steps of this algorithm is as follows,

Step 1): The pixels with two percents of the Maximum DN in the whole image are as strong pixels. If more than Tk pixels (usually Tk = 5) (including the center pixel) exist in the 3×3 neighboring window, these pixels are point targets without filter.

Step 2): The MMSE filter is applied in the 3×3 window for image I, the result $\hat{I}$ will be the basis for determining the threshold.

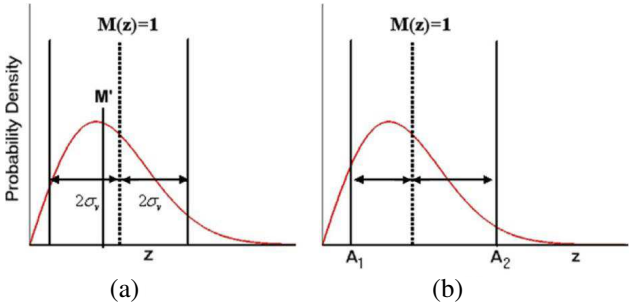

Figure 1: The basic principle of the Lee Sigma filter.

Step 3): The MMSE filter is applied in the 9×9 window for image Z, only the pixels with DN in the defined neighborhood of $\hat{I}$ is calculated. The neighborhood is defined as $(\hat{I} * a_1,\ \hat{I} * a_2)$, where a_1 and a_2 are given in advance.

2.2. Deficiencies of the Lee Sigma Filter

One of the theoretical foundation of the Lee sigma filter is that the probability distribution of the single-look intensity SAR image is the exponential distribution, and the probability distribution of the multi-look intensity SAR image is the Rayleigh distribution, shown as follows,

$$p_1(I) = \frac{1}{\bar{I}} \exp\left(-\frac{I}{\bar{I}}\right), \quad I \geq 0 \qquad p_N(I) = \frac{N^N I^{N-1}}{(N-1)!\bar{I}^N} \exp\left(-\frac{NI}{\bar{I}}\right), \quad I \geq 0 \tag{1}$$

The clutter model used by Lee-Sigma filter is the simplest model and is only suitable for homogeneous areas, no longer applicable for the general area and uneven areas. If the image does not meet the Rayleigh distribution, the confidence interval $[I_1,\ I_2]$ of the Rayleigh distribution of cannot guarantee the basic principle that the mean of SAR image remains unchanged; and the confidence interval must be re-estimated. If different distribution types of surface features should be filtered using Sigma filter, at first the different distribution model must be estimated.

3. THE IMPROVED LEE-SIGMA FILTER BASED ON GENERALIZED GAMMA DISTRIBUTION

We proposed a 3-parameter generalized gamma distribution to achieve the statistical modeling of SAR image. The probability density function of Generalized Gamma distribution,

$$f_{G\Gamma-pdf}(x;\rho,\beta,\delta) = \frac{\delta}{\beta\Gamma(\rho)} \left(\frac{x}{\beta}\right)^{\rho\delta-1} \exp\left[-\left(\frac{x}{\beta}\right)^{\delta}\right] \tag{2}$$

where, ρ is a shape parameter, β is a scale parameter, δ is an energy parameter.

By parameter estimation, the corresponding probability density function of SAR image is fitted, shown in Fig. 2. Figs. 2(a)–(c) are three different surface features in Chinese airborne 4-look polarimetric SAR data. Figs. 2(d)–(f) represent the histogram and the fitting function of the box area of the image, respectively.

From Fig. 2, we can see that, the distribution function of different surface feature is different, the fitting parameters are not the same. Therefore, we need to use the different probability density

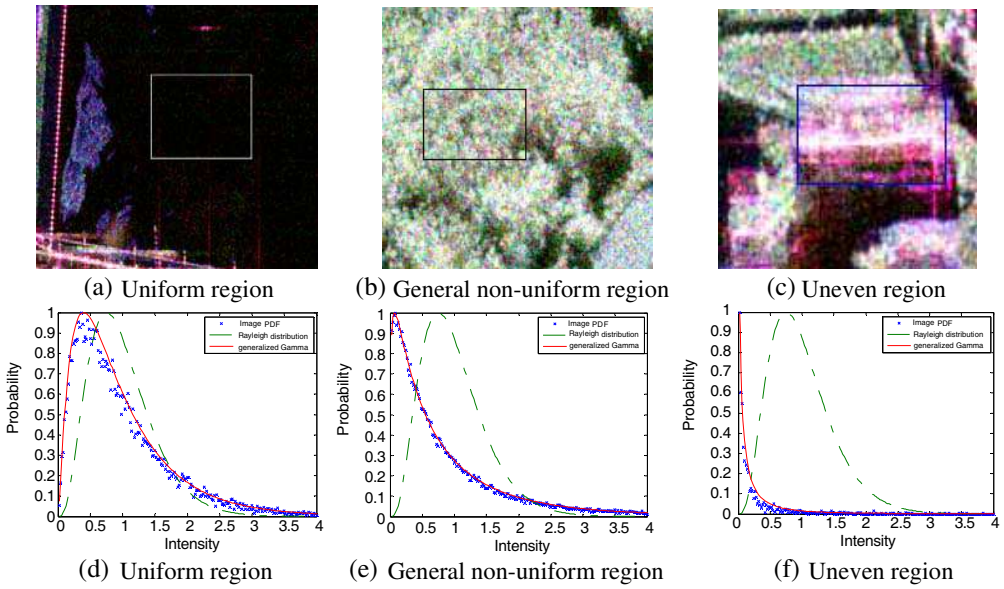

Figure 2: (a)–(c) are three different surface features in Chinese airborne 4-look polarimetric SAR data. (d)–(f) represent the histogram and the fitting function of the box area of the image, respectively. Where, the blue curve represents the image histogram, the green curve represents the Rayleigh distribution, the red curve represents the fitting of generalized Gamma probability density function.

functions for different regions. In this paper, we propose a PolinSAR filter based on Lee-sigma filter and model based on generalized Gamma model. The flowchart of this algorithm is shown in Fig. 3.

4. EXPERIMENTAL RESULTS

To illustrate the performances of the proposed filtering method presented in Section 3, results obtained with real airborne polarimetric interferometric SLC images are reported. The Chinese PolinSAR flight took place on January 8, 2010. It is the first dual-antenna polarimetric data in China. The instrument developed by East China Research Institute of Electronic Engineering, CETC, collected quad-pol images at X-band. The incidence angle was about 50°. The resolution of pixel is one meter. The test site is located in Lingshui Li Minority Autonomous County with a geographical position at 18°22′–18°47′ North and 109°45′–110°08′ East, Hainan province, China. Fig. 4 shows the comparison of different filters.

Table 1 shows the comparison of coherence before and after phase filtering. Compared to the coherences of three channels, before phase filtering, the coherences of three channels decreased slightly, and after phase filtering, the coherences have been improved.

In order to verify the filter method applied to PolinSAR, the paper use the data before and after filter to optimize the coherence by CP algorithm [11], the results is shown in Table 2. It is shown

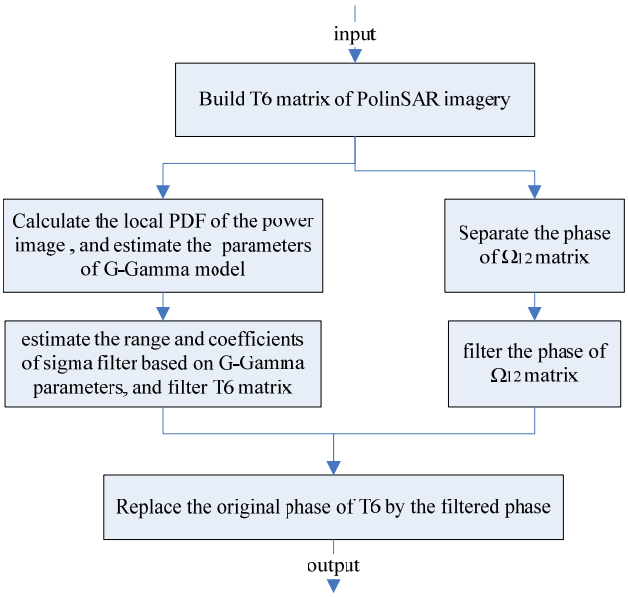

Figure 3: The flowchart of the improved algorithm.

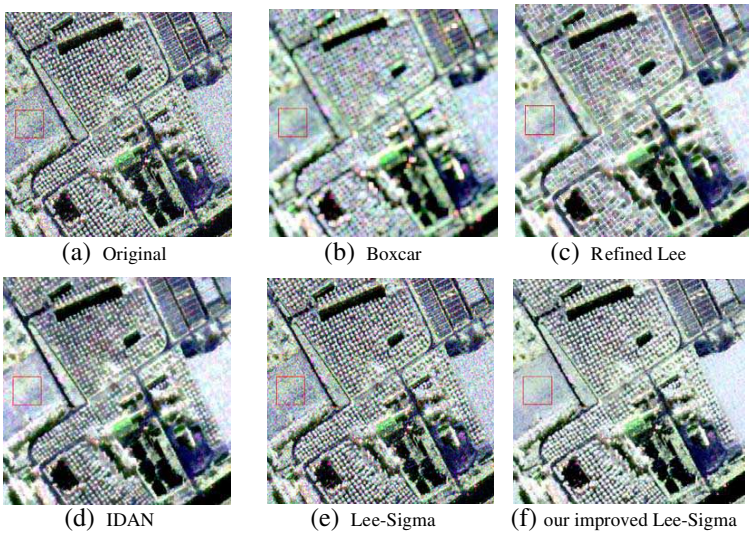

Figure 4: Comparison of filtered results using Chinese airborne SAR data.

Table 1: Quantitative comparison of coherence before and after phase filtering.

		Original image	Without phase filter	After phase filter
mean	$HH+VV$	0.804	0.798	0.871
	$HH-VV$	0.698	0.688	0.817
	$HV+VH$	0.793	0.785	0.864
Standard deviation	$HH+VV$	0.116	0.112	0.060
	$HH-VV$	0.144	0.138	0.072
	$HV+VH$	0.126	0.123	0.067

Table 2: Comparison of the optimal coherence before and after filter.

	Opt 1		Opt 2		Opt 3	
	Mean	Std	Mean	Std	Mean	Std
Original image	0.916	0.046	0.810	0.091	0.599	0.161
Boxcar	0.886	0.053	0.796	0.087	0.643	0.135
Our method	0.920	0.050	0.813	0.095	0.598	0.163

that Boxcar filter reduces the optimal coherence.

5. CONCLUSION

In this paper, the authors propose an improved sigma filter for the speckle filtering of polarimetric interferometry data. Experimental results using airborne SAR data demonstrate its effectiveness.

ACKNOWLEDGMENT

This work was supported in part by the National Natural Science Foundation of China under Grant 40971198 and 40871191, and by the National High-Tech Research and Development Program of China under Grant 2009AA12Z118.

REFERENCES

1. Lee, J. S., "Digital image smoothing and the sigma filter," *Comput. Vis. Graph. Image Process.*, Vol. 24, No. 2, 255–269, Nov. 1983.
2. Lee, J. S., "A simple speckle smoothing algorithm for synthetic aperture radar images," *IEEE Trans. Syst., Man, Cybern.*, Vol. 13, No. 1, 85–89, Jan.–Feb. 1983
3. Lee, J. S., "Speckle suppression and analysis for synthetic aperture radar images," *Opt. Eng.*, Vol. 25, No. 5, 636–643, May 1986.
4. Lee, J. S., P. Dewaele, P. Wambacq, A. Oosterlinck, and I. Jurkevich, "Speckle filtering of synthetic aperture radar images — A review," *Remote Sens. Rev.*, Vol. 8, 313–340, 1994.
5. Alparone, L., S. Baronti, and A. Garzelli, "A hybrid sigma filter for unbiased and edge-preserving speckle reduction," *Proc. IGARSS*, 1409–1411, Florence, Italy, Jul. 1995.
6. Lee, J. S., et al., "Speckle filtering of polarimetric SAR interferometry data," *Proc. IGARSS*, 2002.
7. Lee, J. S., et al., "Speckle filtering and coherence estimation of polarimetric SAR interferometry data for forest applications," *IEEE Transactions on Geoscience and Remote Sensing*, Vol. 41, No. 10, 2254–2263, 2003.
8. Lee, J. S., et al., "Scattering-model-based spekle filtering of polarimetric SAR data," *IEEE Transactions on Geoscience and Remote Sensing*, Vol. 44, No. 1, 176–187, 2006.
9. Lee, J. S., "Speckle filtering of dual-polarization and polarimetric SAR data based on improved sigma filter," *Proc. IGARSS*, 2008.
10. Lee, J. S., "Improved sigma filter for speckle filtering of SAR imagery," *IEEE Transcations on Geoscience and Remote Sensing*, Vol. 47, No. 1, 202–213, Jan. 2009.
11. Cloude, S. R. and K. P. Papathanassiou, "Polarimetric SAR interferometry," *IEEE Transactions on Geoscience and Remote Sensing*, Vol. 36, No. 5, 1551–1565, 1998.

An Analysis Method on Scattering Characteristics of Finite Periodic Array

Zhiping Li[1], **Xuan Li**[2], **Jungang Miao**[1,2], **Dawei Liu**[1], **and Wenle Liang**[1]

[1]Electromagnetics Laboratory, Beihang University, Beijing, China
[2]Science and Technology on Space Microwave Laboratory, Xi'an, China

Abstract— The structure with periodic array structure is a common structure in electromagnetic fields. In general, the periodic array with electrically large size or complex electromagnetic parameters etc., the scattering characteristics of this structure is difficult to obtaine. A novel and simple analysis method on the scattering characteristics of the finite periodic array is proposed in this paper, taking advantage of this periodic array structure, and regardless of the unit material. The effect of the array arrangement and the unit structure on the scattering distribution of the finite periodic array is derived. The novel method can be used to analyze the lobe position conveniently, and the angle error is less than 1 degree based on the verification with the Finite Difference Time Domain (FDTD) method combined by perfect material layer (PML).

1. INTRODUCTION

The structure with periodic array structure is a common structure in electromagnetic fields, for example, the array antennas, the frequency selective surface, the absorbing materials, etc.. Especially, the calibration load used in the microwave radiometer calibration system is often made of this periodic array, which is constructed by a metal base coated with absorbing materials or made from certain absorbing materials directly such as ferrite, crystalline silicon. In general, the absorbing materials are the magnetic materials, whose electromagnetic parameters are difficult to be obtained. However, the electromagnetic parameters are the key elements in analyzing the scattering characteristics of the target. A novel and simple analysis method on the scattering characteristics of the finite periodic array is proposed in this paper, taking advantage of this periodic array structure, and regardless of the unit material. In this paper, the effect of the array arrangement and the unit structure on the scattering distribution of the finite periodic array is derived, and the array lobe factor theory is obtained. It may be adopted to estimate the lobe position conveniently.

2. BASIC THEORY

When the uniform plane wave impinges upon a finite periodic array, as shown in the Fig. 1, the incident direction is negative Z axis.

The incident plane wave is reflected by the finite periodic array, and then the scattering far field can be expressed by

$$E(r,\theta,\varphi) = \sum_m \sum_n \left(\sum_p \sum_q e^{jkz(x_p,y_q)} \frac{e^{-jkR}}{R} \right) \tag{1}$$

where m, n represent the pyramids whose center are at x_0^m, y_0^n. p, q represent the distance to the center position (x_0^m, y_0^n). x_p, y_q, and $z(x_p, y_q)$ are the coordinate of the point at the pyramid surface. R is the distance from the point at the pyramid surface to the observing point in the far field.

Where,

$$R = \sqrt{(r\sin\theta\cos\varphi - x_{mp})^2 + (r\sin\theta\sin\varphi - y_{nq})^2 + [r\cos\theta - z(x_p, y_q)]^2} \tag{2}$$

On the condition of far field approximation, the small amount is ignored, and the approximation is taken as

$$\sqrt{1-x} \approx 1 - \frac{1}{2}x, \quad |x| \le 1 \tag{3}$$

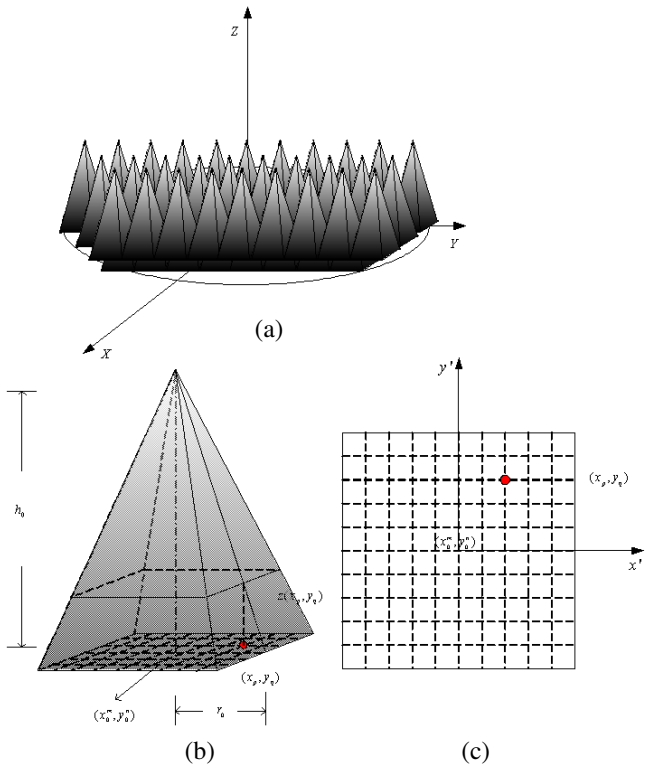

Figure 1: Schematic diagram of the finite periodic array for far field analysis. (a) Structure of the finite periodic array. (b) Structure of the unit pyramid. (c) Equivalent plan graph.

Then,

$$E(r,\theta,\varphi) \approx \sum_m \sum_n \left(\sum_p \sum_q e^{jkz(x_p,y_q)} \frac{e^{-jk\{r-[\sin\theta\cos\varphi x_{mp}+\sin\theta\sin\varphi y_{nq}+\cos\theta z(x_p,y_q)]\}}}{r} \right)$$

$$= \frac{e^{-jkr}}{r} \left[\sum_m \sum_n e^{jk(\sin\theta\cos\varphi x_0^m+\sin\theta\sin\varphi y_0^n)} \right] \times \left[\sum_p \sum_q e^{jkz(x_p,y_q)(1+\cos\theta)} e^{jk(\sin\theta\cos\varphi x_p+\sin\theta\sin\varphi y_q)} \right]$$

$$= \frac{e^{-jkr}}{r} \mathbf{AF}(\theta,\varphi) \times \mathbf{f}(\theta,\varphi) \tag{4}$$

where, $\mathbf{AF}(\theta,\varphi)$ is the lobe factor of the array, and $f(\theta,\varphi)$ is the scattering lobe factor of the unit. Then,

$$\mathbf{AF}(\theta,\varphi) = \sum_m \sum_n e^{jk(\sin\theta\cos\varphi x_0^m+\sin\theta\sin\varphi y_0^n)} \tag{5}$$

$$f(\theta,\varphi) = \sum_p \sum_q e^{jkz(x_p,y_q)(1+\cos\theta)} e^{jk(\sin\theta\cos\varphi x_p+\sin\theta\sin\varphi y_q)} \tag{6}$$

It can be seen that under the approximation condition, the scattering interaction among the units is ignored, and the total scattering field of the finite periodic array approximately equals to the lobe factor of the array multiplied by the scattering lobe factor of the unit. This is similar to the multiplication principle of lobe pattern, and it's the field lobe pattern of the point sources array which is the product of the lobe pattern of the unit $f(\theta,\varphi)$ and the lobe of the point sources array.

The lobe factor of the array $\mathbf{AF}(\theta,\varphi)$ presents the scattering lobe distribution of the finite periodic array, and the scattering lobe factor of the unit $f(\theta,\varphi)$ presents the weighting of the scattering lobe distribution at different lobe. The Equation (5) shows that the only lobe factor of the array $\mathbf{AF}(\theta,\varphi)$ has relation to the structure parameters in the periodic direction. The Equation (6) shows that the scattering lobe factor of the unit $f(\theta,\varphi)$ has relation to all of the structure parameters of the unit, which contains the size parameters in the periodic and non-periodic direction, but has no relation to the array arrangement of the units. Therefore, the finite

periodic array arrangement of the units influences the scattering lobe distribution of the array, and the scattering distribution of the unit is the weight of the every scattering lobe determined by the array arrangement. We can take advantage of the lobe factor of the array to estimate the lobe position conveniently, regardless of the parameters of the unit such as the size and material parameters.

3. SIMULATION RESULTS

The calibration load used in the microwave radiometer calibration system is often made of this periodic array. In this section, a type of calibration load is taken as the analysis target, whose structure is shown as Fig. 1.

The calibration load is constructed by a metal base coated with absorbing materials or made from certain absorbing materials directly such as ferrite, crystalline silicon. In general, the absorbing materials are the magnetic materials, whose electromagnetic parameters are difficult to be obtained. However, the electromagnetic parameters are the key elements in analyzing the scattering characteristics of the target. The precise scattering distribution is simulated based on FDTD method combined by perfect material layer (PML), shown by dotted line in Fig. 2. The simple lobe distribution is simulated by array factor, shown by solid line in Fig. 2.

Figures 2(a), (b), (c), (d) show that the scattering distribution of the periodic array simulated by FDTD and array factor at 36.5 GHz, 23.8 GHz, 18.7 GHz, 10.7 GHz, respectively. From 10.7–36.5 GHz, the angle difference of the lobe position simulated by FDTD and array factor is less than 1 degree. The angle error is less than 1 degree when the scattering lobe factor theory is adopted to estimate the scattering distribution of the finite periodic array. For example, when the calibration load is performed spherical scanning, the scattering distribution can be estimated simply used by array factor before scanning, then the scanning should be seriously at the lobe position, therefore it can avoid missing the point at the lobe position effectively.

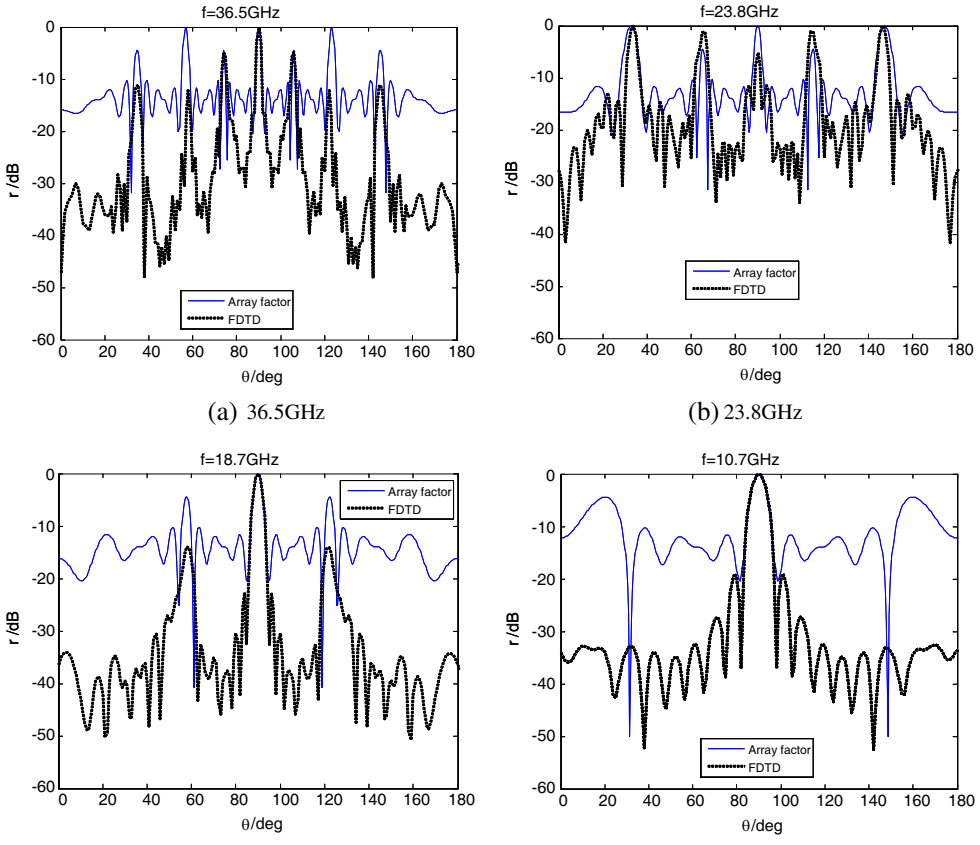

(a) 36.5GHz (b) 23.8GHz

(c) 18.7GHz (d) 10.7GHz

Figure 2: The scattering distribution of the periodic array.

4. CONCLUSION

In this paper, the effect of the array arrangement and the unit structure on the scattering distribution of the finite periodic array is derived, and the array lobe factor theory is obtained. Under the premise that the interaction among the scattering from the units is neglected, the total scattering field is approximately equal to lobe factor of unit by lobe factor of array. Then, the verification for the array lobe factor theory is performed based on FDTD method combined by perfect material layer (PML), and the results show that the angle error is less than 1 degree when the scattering lobe factor theory is adopted to estimate the scattering distribution of the finite periodic array, thus the scattering lobe factor theory may be adopted to estimate the lobe position conveniently.

ACKNOWLEDGMENT

This work is supported by National Key Laboratory Foundation of China (No. 9140c5305021005).

REFERENCES

1. Nian, F., Y. J. Yang, and W. Wang, "Research of optimizing the microwave wide band blackbody calibration target," *Journal of Systems Engineering and Electronics*, Vol. 20, No. 1, 6–12, 2009.
2. Wang, J. H., J. G. Miao, Y. J. Yang, and Y. M. Chen, "Scattering property and emissivity of a periodic pyramid array covered with absorbing material," *IEEE Transactions Antennas and Propagation*, Vol. 56, No. 8, 2656–2663, 2008.
3. Cronin, N. J., N. Athamena, and D. Tinkler, "Design of millimeter wave grooved targets," *IEE PROCEEDINGS-F*, Vol. 138, No. 6, 576–580, 1991.
4. Yang, C. F., W. D. Burnside, and R. C. Rudduck, "A doubly periodic moment method solution for the analysis and design of an absorber covered wall," *IEEE Transactions Antennas and Propagation*, Vol. 41, No. 5, 600–609, 1993.

The Simulation and Measurement of Scattering Property and Emissivity of the Microwave Radiometer Calibrator

Wenle Liang[1], **Xuan Li**[2], **Jungang Miao**[1, 2], **and Dawei Liu**[1]

[1]Electromagnetics Laboratory, Beihang University, Beijing 100191, China
[2]Science and Technology on Space Microwave Laboratory, Xi'an 710100, China

Abstract— The accuracy of measurement of calibrator emissivity is necessary for calibration of microwave radiometer. In this paper, the optimization of calibration source is presented, and the method of bistatic measurement system was chosen to measure the emissivity of calibration source, which is periodic cone array. The scattering property is measured and the emissivity of the calibrator is evaluated using bistatic measurement. The measurement is used to analyze scattering field of the calibrator as well as obtain the emissivity by integrating the differential scattering coefficient of the backscattered field.

1. INTRODUCTION

With the development of quantitive microwave remote sensing technology, the higher accuracy of data measured by remote sensor is required including the microwave radiometer. However for microwave radiometer, the accuracy of calibration directly affects the absolute accuracy of microwave radiometry.

The emissivity of calibrator is an important indicator for accuracy of calibration. In this paper, finite periodic cone array is taken as a unit of calibration source, which is simulated to test and confirm the theory and to compare with the experiment [1, 2].

2. SIMULATION

The reflection of single cone is simulated and observed so as to optimize the cone, including its dimensions, the shape of top and thickness of absorbing material. In the process of the optimization, the parameters are changed one by one to view the results and compare with the theoretical value, so as to optimize system working parameters and get the best design scheme. Also the effect from the parameters on the emissivity can be observed.

The periodic boundary conditions are adopted to simulate the finite periodic array. The corn with a bottom side length of 10 mm and a height of 40 mm is taken as the reference. Periodic boundary is considered as to optimize the cone. The absorbing material used in this simulation is CR112.

Figure 1 shows how the emissivity varies with thickness of the coat changed. As seen from this figure, emissivity increases with coat of the cone comes thicker. When the thickness of the coat reaches 1.5 mm, the emissivity stays stable at 0.9999, although the coat gets thicker. Fig. 2 shows

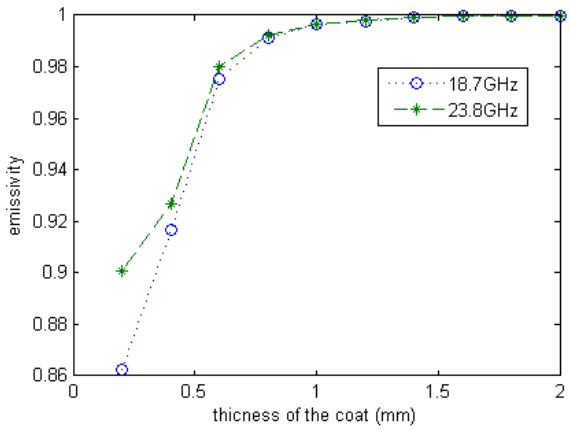

Figure 1: The emissivity as a function of thickness of the coat.

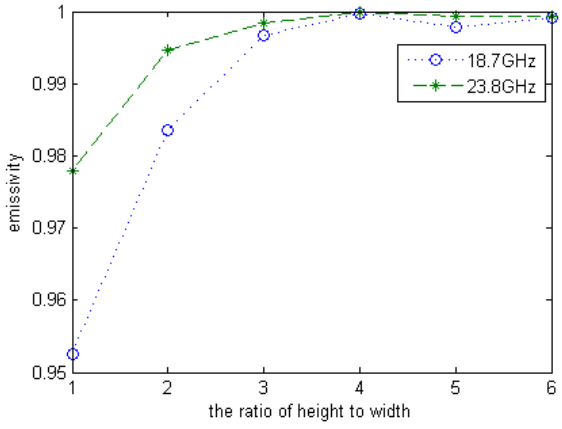

Figure 2: The emissivity as a function of the ratio of height to width.

variations of emissivity with the changing ratio of height to width. With the ratio of height to width increasing, the emissivity rises. When the height is four times of the bottom side length, the emissivity reaches the maximum value.

Table 1 shows the effect of the shape of the cone top on the reflection of calibration source. From this table, it's can be seen that the shape with sharp top has the minimum reflection compared with the other shapes, while the shape of flat top has the maximum one. From the kirchhoff's law, it can be known that the smaller the reflection is, the bigger the emissivity. So we will try to use the top of cone with the sharp shape.

We attend to analyze the scattering properties to obtain the most suitable way of bistatic measurement. In this situation, we can obtain the scattering field distribution and the differential scattering coefficient in every direction.

To get the absolute reflection of calibration source, we have to use the calibration target to calibrate the calibration source. The calibration target includes the metallic flat plate, the metallic sphere. Here we use the metallic cone arrays with the same shape of calibration source. Fig. 3 and Fig. 4 are consequences solved out by simulation of calibration source and calibration target. There are 14 corns in diameter location, arranged in 8 rows. And the number decreases to 8 on the edge of each column (the reduction of two per line in equal difference) as shown in Fig. 5. The height of one cone is 94 mm while the bottom diameter is 18 mm. The arrays are illuminated by plane wave. Frequency is 18.7 GHz.

As seen from Fig. 3 and Fig. 4, the reflected power concentrates on the backward direction. From the two scattering lobes, it can be seen that the arrays with the same arrange have the similar scattering properties, but the voltage reflected by calibration source is about 30 dB lower than the calibration target. The emissivity of calibration is 0.9955 by calibration target, which is an ideal value.

Since the scattering characteristics are supposed to be measured in a two-dimensional device and thus calculate the emissivity, we draw the line of reflected voltages at the azimuth angle $\varphi(\text{phi}) = 0°$. The x axis represents the elevation angle $\theta(\text{theta})$, which is from $-90°$ to $90°$, while $0°$ is the position of vertical to the array.

In Fig. 6, the left y-axis shows the reflection by calibration target in unit of dB, while the right y-axis shows reflection by calibration source. Compared with the three-dimensional result, the shape of two curves are similar but there is 30 dB gap between the two curves. The plane chosen is appropriate for the scattering voltages of calibration source and target. The emissivity of calibration is 0.9973 by calibration target, close to the result obtained by three-dimensional integration.

Table 1: The reflection of periodic cones with different top shape.

The shape of top	flat	round	sharp
reflection at 18.7 GHz	−20.7 dB	−28.9 dB	−32.8 dB
reflection at 23.8 GHz	−21.3 dB	−29.3 dB	−34.3 dB

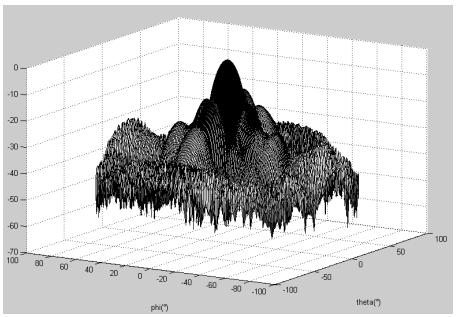

Figure 3: The scattering image by calibration target of metal corn array.

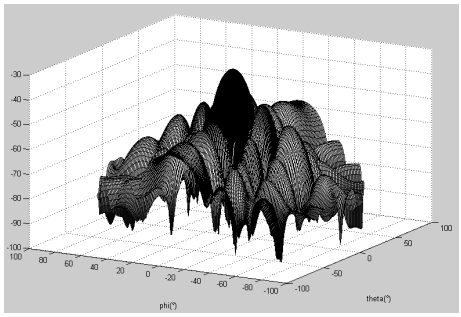

Figure 4: The scattering image by calibration source of ferrite corn array.

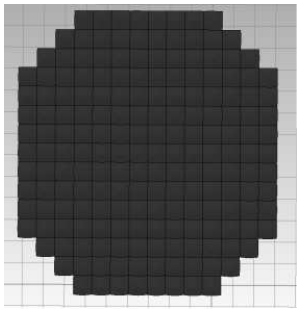

Figure 5: The top view of calibration load.

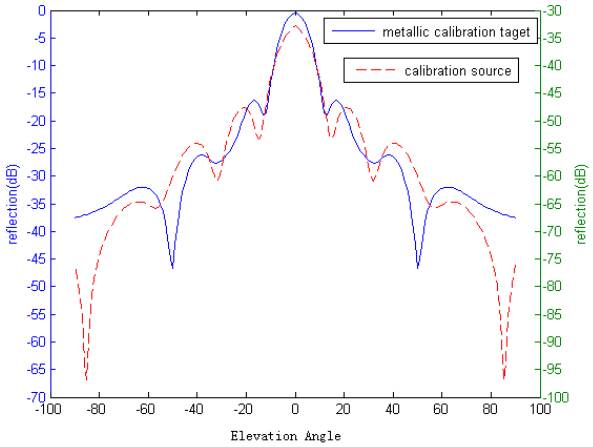

Figure 6: The two-dimensional simulation result.

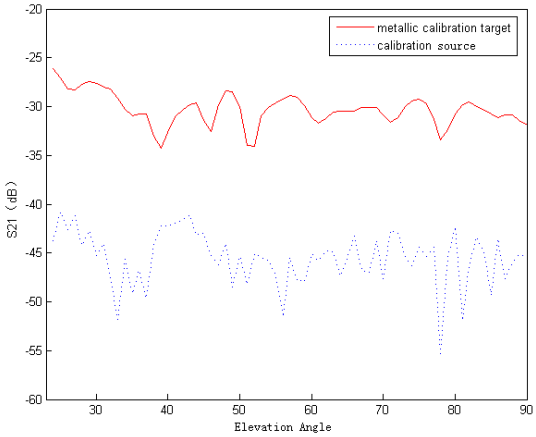

Figure 7: The scattering lobe from 23° to 90° at frequency of 18.7 GHz.

3. MEASUREMENT

All the experiments performed are conducted in the microwave anechoic chamber. Different from the monostatic measurement, two antennas are adopted, one for the transmitting, the other for the receiving. The ultimate goal of the measurement is to analyze the scattering field of the calibration source as well as obtained the reflectivity and emissivity by integrating the differential scattering coefficient of the backscattered field.

Target is illuminated by the fixed transmitting system and the scattering of target are received by the receiving antenna point by point guided by a circular slippery path. The array structures are the same with finite arrays stated in the last section. The following is the scattering lobe of metallic calibration target and calibration source at 18.7GHz. Due to the space taken by the transmitting and receiving antennas, scattering can only be received from angle of 23° to 90°.

In Fig. 7, lobes are not obvious at the observing angles because the backward scattering cannot be detected in a bistatic system. The basic configurations of scattering signal are similar. The emissivity calculated from this data is 0.9745, which is lower than the simulation result, because the main backscattering lobe is missing. This result also further proves that calibration target of the same structure as the calibration source has a similar scattering distribution. The backscattering energy needs to be obtained in the future work.

4. CONCLUSION

For single cone, the result is better that the height to width aspect ratio is about 4 and the shape of top of the cone is sharp. When the frequency and polarization of incident wave is determined, the quantity and position of the scattering lobe of the finite periodic array is only related to the array configuration, unrelated to the size at the non-periodic direction and the material of the array. The emissivity of the calibration source is calculated by integration of the voltage along the single plane.

In the measurement, two-dimensional results are attained and then emissivity is gained. Since the main lobe is at the backward direction, it is difficult to receive it. So it may take oblique incident into consideration in later research.

ACKNOWLEDGMENT

This work is supported by National Key Laboratory Foundation of China (No.: 9140c5305021005).

REFERENCES

1. Hauck, B., F. Ulaby, and R. DeRoo, "Polarimetric bistatic-measurement facility for point and distributed targets," *IEEE Antennas and Propagation Magazine*, Vol. 40, No. 1, 31–41, 1998.
2. Jackson, D. M., "Calibration of millimeter-wave radiometers with application to clear-air remote sensing of the atmosphere," Ph.D. Dissertation, 36–40, 1999.

Electromagnetic Simulation of a Bulk Current Injection Test Setup for Automotive Applications

F. Grassi and S. A. Pignari
Department of Electrical Engineering, Politecnico di Milano
P.za Leonardo da Vinci, 32, I-20133-Milano, Italy

Abstract— In this paper, electromagnetic (EM) simulation is used to predict the radio-frequency noise induced by Bulk Current Injection (BCI) in the terminations of a CAN-bus. In the analysis, a typical setup for automotive applications is considered and common mode (CM) and differential mode (DM) noise voltages induced across the bus terminations are evaluated by combining EM simulation of the setup with mixed-mode scattering parameter representation of the simulation outputs, and suitable circuit models of the bus terminal networks. The proposed approach can be used to analyze setups with different terminal networks, and allows to quantify the severity of the BCI test by correlating CM-to-DM conversion to the degree of unbalance of the CAN-bus terminal networks.

1. INTRODUCTION

Electromagnetic Compatibility (EMC) test procedures based on the Bulk Current Injection (BCI) technique are widely diffused in the automotive sector for immunity assessment of equipments interconnected by wiring harnesses. The procedure is cost-effective and not time-consuming. Additionally, it allows for onboard testing as well as for pre-compliance verifications at the early design-stage. However a difficulty is expressed for the shortage of reasonably accurate methods to predict the noise levels actually injected into the terminal units. This is particularly true in the practical case of multi-wire bundles, since the fixture for probe-calibration foreseen by the Standards (i.e., the so-called jig) is designed to reproduce the external characteristics of a bunch of wires (as an ideal single-ended interconnection), but it is inherently unable to account for its transmission characteristics, involving different propagation modes. Particularly, differential lines used for data communication [e.g., bus lines used to implement the controller area network (CAN) technology] represent simple but relevant examples of cable harnesses for which standard calibration procedures do not provide accurate indication on the actual noise levels entering the terminal units. As a consequence, consistent correlation between immunity levels obtained by the BCI technique and by other testing methods foreseen by automotive Standards [1, 2] is also not straightforward. For instance, in [3] the higher severity of the BCI test with respect to the transverse electromagnetic (TEM) cell method was proven by measurements.

Particularly, it was shown that CAN-bus sensitivity to the BCI test is mainly to be ascribed to the susceptibility of the bus terminal-networks rather than to the susceptibility of the CAN-bus nodes. As a matter of fact, while the nodes are designed to exhibit high impedance levels, CAN-bus terminations are matched to the line characteristic impedance. Accordingly, assessment of the severity of the BCI technique for conducted susceptibility testing of CAN-bus lines requires to verify whether CAN-bus terminations may withstand the high levels of common-mode (CM) voltages induced by BCI.

In line with this need, in this paper common mode (CM) and differential mode (DM) voltages induced by BCI across the terminations of the CAN-bus are investigated by resorting to electromagnetic (EM) simulation of a typical automotive setup for BCI testing. Particularly, FIT-based EM modeling [4, 5], of the BCI probe mounted onto a differential line above ground is used to obtain a Scattering Parameter (SP) representation of the structure which does not depend on the bus terminal networks. Effects due to line terminations are subsequently included into the model by off-line post-processing of simulation results, exploiting mixed-mode SP theory [6] and suitable representations of the CAN-bus terminal networks. This approach yields prediction of the CM and DM-noise levels as function of the simulated SPs and of the terminal networks, whose electromagnetic compatibility (EMC) behavior could be eventually characterized by measurements. Additionally, it allows to interpret the injected DM-noise voltages as a result of CM-to-DM conversion, and to correlate them to the degree of unbalance of the CAN-bus terminal networks.

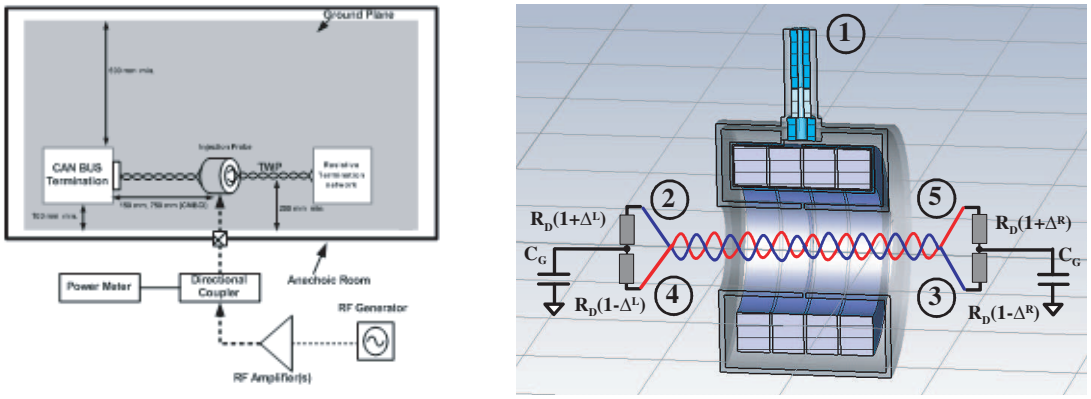

(a) (b)

Figure 1: BCI setup for CAN-bus testing: (a) principle drawing of the test setup [1]; (b) EM model and port-numbering adopted for numerical simulation.

2. DESCRIPTION OF THE BCI SETUP

A principle drawing of the BCI test setup under investigation is shown in Fig. 1(a). The setup is composed of a pair of twisted wires running above ground (standard physical medium for CAN-bus lines onboard cars) with end-points connected to suitable terminal networks [7]. High-speed CAN-bus terminations are here considered [see Fig. 1(b)]. In these terminations, the matching resistor — designed to match the differential impedance, $Z_{diff} \cong 124\,\Omega$, of the TWP so to optimize DM signaling — is split into two equal parts (i.e, $R_D \cong 62\,\Omega$), in order to reduce bus susceptibility to external disturbances. The center-tap is grounded by means of a capacitor C_G, with typical capacitance values on the order of $10\,\text{nF} \div 100\,\text{nF}$ [3].

3. EM SIMULATION OF THE BCI SETUP

EM modeling of the BCI test setup in Fig. 1(a) was achieved by the FIT-based numerical code CST Microwave Studio (MWS) [5]. To this end, an EM model of injection probe FCC-F130A [8] was developed, validated versus input impedance measurement [4], and mounted onto a two-wire cable harness. For simplicity, the TWP is approximated via an ideally-balanced differential interconnection composed of a pair of 25 cm-long straight wires, with the injection device mounted at midpoint. The structure was characterized numerically at the five output ports in terms of SPs, according to the port numbering fixed in Fig. 1(b). To this end, each setup port was excited by a wave-guide port through an SMA coaxial connector, and the obtained SPs were normalized to the reference impedance $R_0 \cong 50\,\Omega$. EM simulation in the frequency range $1 \div 400\,\text{MHz}$ led to a 5×5 SP matrix,

$$\mathbf{S}_{5\times5} = \begin{bmatrix} S_{11} & S_{12} & S_{13} & S_{14} & S_{15} \\ S_{12} & S_{22} & S_{23} & S_{24} & S_{25} \\ S_{13} & S_{23} & S_{33} & S_{34} & S_{35} \\ S_{14} & S_{24} & S_{34} & S_{44} & S_{45} \\ S_{15} & S_{25} & S_{35} & S_{45} & S_{55} \end{bmatrix}, \tag{1}$$

exhibiting the following symmetries: $S_{12} = S_{14} = -S_{13} = -S_{15}$; $S_{24} = S_{35} = S_c$; $S_{23} = S_{45} = S_b$; $S_{25} = S_{34} = S_d$; $S_{22} = S_{33} = S_{44} = S_{55} = S_a$, as long as probe positioning is symmetric with respect to the harness end-points.

4. CM AND DM-NOISE PREDICTION

To simplify the system in (1), port-reduction is exploited. Namely, the input port of the probe [i.e., port 1 in Fig. 1(b)] is eliminated by port-connection to a non-ideal voltage source with internal parameters V_{RF}, $R_0 \cong 50\,\Omega$. This reduces the passive five-port network in (1) in an active four port, with the following port-constraints:

$$\begin{pmatrix} b_2 \\ b_3 \\ b_4 \\ b_5 \end{pmatrix} = \begin{bmatrix} S_a & S_b & S_c & S_d \\ S_b & S_a & S_d & S_c \\ S_c & S_d & S_a & S_b \\ S_d & S_c & S_b & S_a \end{bmatrix} \cdot \begin{pmatrix} a_2 \\ a_3 \\ a_4 \\ a_5 \end{pmatrix} + \begin{pmatrix} b_S \\ -b_S \\ b_S \\ -b_S \end{pmatrix}, \tag{2}$$

where $b_S = S_{12}V_{RF}/(2\sqrt{R_0})$.

Mixed-mode SPs are then introduced by decomposition of the power waves at left (i.e., power waves associated with ports 2, 4) and at the right (i.e., power waves associated with ports 3, 5) sides of the probe into their CM and DM components as:

$$\mathbf{a}_m^{(L)} = \begin{pmatrix} a_{DM}^{(L)} \\ a_{CM}^{(L)} \end{pmatrix} = \underbrace{\begin{bmatrix} 1 & -1 \\ 1/2 & 1/2 \end{bmatrix}}_{\mathbf{M}} \cdot \begin{pmatrix} a_2 \\ a_4 \end{pmatrix}; \quad \mathbf{b}_m^{(L)} = \begin{pmatrix} b_{DM}^{(L)} \\ b_{CM}^{(L)} \end{pmatrix} = \mathbf{M} \cdot \begin{pmatrix} b_2 \\ b_4 \end{pmatrix};$$

$$\mathbf{a}_m^{(R)} = \mathbf{M} \cdot \begin{pmatrix} a_3 \\ a_5 \end{pmatrix}; \quad \mathbf{b}_m^{(R)} = \mathbf{M} \cdot \begin{pmatrix} b_3 \\ b_5 \end{pmatrix}, \tag{3}$$

where apexes L and R denote the pair of ports lying by the left and right side of the probe, respectively.

Use of the above similarity transformation and subsequent conversion into scattering transfer parameters (T-parameters) notation allow to re-write the port-constraints in (2) as:

$$\begin{pmatrix} \mathbf{a}_m^{(R)} \\ \mathbf{b}_m^{(R)} \end{pmatrix} = \begin{bmatrix} \mathbf{T}_{11m} & \mathbf{T}_{12m} \\ \mathbf{T}_{21m} & -\mathbf{T}_{11m} \end{bmatrix} \cdot \begin{pmatrix} \mathbf{a}_m^{(L)} \\ \mathbf{b}_m^{(L)} \end{pmatrix} - \begin{pmatrix} \mathbf{B}_{1Sm} \\ \mathbf{B}_{2Sm} \end{pmatrix} \cdot b_S \tag{4}$$

$$\mathbf{T}_{11m} = \mathrm{diag}\left\{ \frac{S_c - S_a}{S_b - S_d}; \; -\frac{S_c + S_a}{S_b + S_d} \right\}; \quad \mathbf{T}_{12m} = \mathrm{diag}\left\{ \frac{1}{S_b - S_d}; \; \frac{1}{S_b + S_d} \right\} \tag{5}$$

$$\mathbf{T}_{21m} = \mathrm{diag}\left\{ \frac{S_b^2 + S_d^2 - S_a^2 - S_c^2 - 2(S_b S_d - S_a S_c)}{S_b - S_d}; \; \frac{S_b^2 + S_d^2 - S_a^2 - S_c^2 + 2(S_b S_d - S_a S_c)}{S_b + S_d} \right\} \tag{6}$$

$$\mathbf{B}_{1Sm} = \frac{1}{S_b + S_d} \begin{pmatrix} 0 \\ 1 \end{pmatrix}; \qquad \mathbf{B}_{2Sm} = \frac{S_a + S_b + S_c + S_d}{S_b + S_d} \begin{pmatrix} 0 \\ 1 \end{pmatrix} \tag{7}$$

Finally, the system in (4)–(7) is solved with respect to the modal power-wave vectors in (3), by enforcing the additional port-constraints imposed by the bus terminal networks, that is

$$\mathbf{a}_m^{(L)} = \left(\mathbf{S}_m^{(L)} \right) \cdot \mathbf{b}_m^{(L)}; \quad \mathbf{a}_m^{(R)} = \left(\mathbf{S}_m^{(R)} \right) \cdot \mathbf{b}_m^{(R)}. \tag{8}$$

Assuming bus terminations modeled by the lumped-parameter circuits in Fig. 1(b), the SP matrices, $\mathbf{S}^{(X)}$, at the left (apex $X = L$) and right (apex $X = R$) termination of the bus take the general expression:

$$\mathbf{S}_m^{(X)} \cong \begin{bmatrix} -\frac{1 - r_D^2 + 2z_G(1 - r_D)}{(1 + r_D)^2 + 2z_G(1 + r_D)} & \frac{4r_D \Delta^{(X)}}{(1 + r_D)^2 + 2z_G(1 + r_D)} \\ \frac{r_D \Delta^{(X)}}{(1 + r_D)^2 + 2z_G(1 + r_D)} & -\frac{1 - r_D^2 - 2z_G(1 + r_D)}{(1 + r_D)^2 + 2z_G(1 + r_D)} \end{bmatrix} = \begin{bmatrix} S_{DM} & 4S_\Delta^{(X)} \\ S_\Delta^{(X)} & S_{CM} \end{bmatrix}, \tag{9}$$

where $r_D = R_R/R_0$, $z_G = Z_G/R_0 = -j/(\omega C_G R_0)$, and coefficients $0 \leq \Delta^{(L)}, \Delta^{(R)} \ll 1$ are used to denote the degree of unbalance of the left and right termination of the bus. In the ideal case of absence of unbalance (i.e., $\Delta^{(L)} = \Delta^{(R)} = 0$), DM-noise levels are null, while CM-noise voltages induced across bus terminations are cast by the expression:

$$\frac{V_{CM}^{(L)}}{V_{RF}} = -\frac{V_{CM}^{(R)}}{V_{RF}} = -\frac{S_{12}}{2} \cdot \frac{1 + S_{CM}}{S_{CM}(S_c + S_a - S_b - S_d) - 1}. \tag{10}$$

Conversely, if one or both of the bus terminations are unbalanced with respect to ground, both CM and DM disturbances are induced. However, while CM-noise levels are still predicted by (10), DM-noise voltages strongly depend on termination unbalance. In particular, if both the terminal networks are affected by the same degree of unbalance (i.e., $\Delta^{(L)} = \Delta^{(R)} = \Delta$), DM-noise voltages are proportional to Δ, according to the expression:

$$\frac{V_{DM}^{(L)}}{V_{RF}} = -\frac{V_{DM}^{(R)}}{V_{RF}} \cong -\frac{4S_\Delta}{1 + S_{CM}} \cdot \frac{S_b + S_c - S_a - S_d - 1}{S_{DM}(S_b + S_c - S_a - S_d) + 1} \cdot \frac{V_{CM}^{(L)}}{V_{RF}}. \tag{11}$$

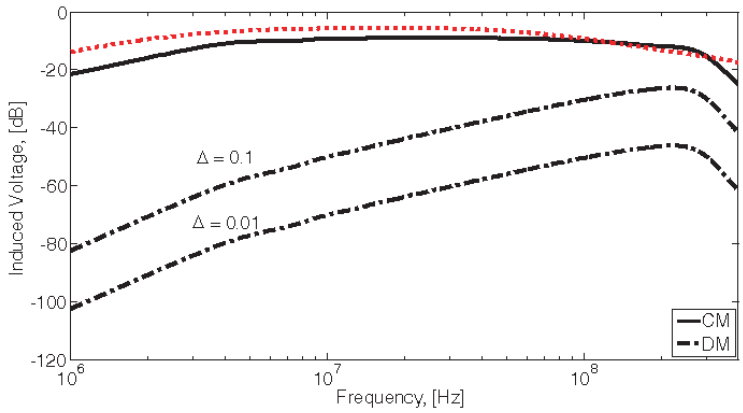

Figure 2: Example of CM (solid) and DM (dashed) noise levels induced by BCI at the terminations [see Fig. 1(b)] of the CAN-bus. Comparison versus the voltage level measured across the 50-Ω termination of a single-ended interconnection [4].

5. SIMULATION EXAMPLE

As a specific simulation example, prediction of the CM and DM-noise voltages induced by BCI across the CAN-bus terminal networks in Fig. 1(b) [the capacitance value $C_G = 10\,\text{nF}$ is adopted for the grounding capacitor] are plotted in Fig. 2 by solid and dashed lines, respectively, for different degrees of unbalance of bus terminations. In the same figure, the voltage levels measured across the 50-Ω termination of a single-ended BCI setup of equal length are also shown (red-dotted curve) [4], for comparison.

REFERENCES

1. ISO 11452-4, *Road Vehicles-component Test Methods for Electrical Disturbances from Narrow-band Radiated Electromagnetic Energy — Part 4: Bulk Current Injection (BCI)*, Apr. 2005.
2. SAE J1113-4, *Immunity to Radiated Electromagnetic Fields — Bulk Current Injection (BCI) Method*, Feb. 1998.
3. Rostamzadeh, C. and S. A. Pignari, "Test procedure for CAN bus susceptibility evaluation based on the use of radio frequency detectors," *Proceedings XIXth General Assembly of International Union of Radio Science (U.R.S.I.)*, Commission AE, Paper AE.2, Chicago, IL, USA, Aug. 2008.
4. Di Rienzo, L., F. Grassi, and S. A. Pignari, "FIT modeling of injection probes for bulk current injection," *Proceedings 23rd Annual Review of Progress in Applied Computational Electromagnetics, ACES 2007*, 782–787, Verona, Italy, Mar. 19–23, 2007.
5. CST Studio Suite, 2011, www.cst.com.
6. Bockelman, D. and W. R. Einsenstadt, "Combined differential and common-mode scattering parameters: Theory and simulation," *IEEE Trans. Microw. Theory Tech.*, Vol. 43, No. 7, 1530–1539, Jul. 1995.
7. ISO 11898-2: 2003, *Road Vehicles — Controller Area Network (CAN) — Part 2: High-speed Medium Access Unit*, Jan. 12, 2003.
8. Fischer Custom Communications, Inc., 2004, www.fischercc.com.

Analysis and Simulation for RF Interconnect

Jian-Fei Xu and Na Yan
ASIC & System State Key Laboratory, Fudan University, China

Abstract— A RF interconnect system consists of RF transmitters, microwave transmission lines or antennas, and RF receivers. In this work, the concept and characteristics of RF interconnect are introduced. Then a RF interconnect system is analyzed and simulated by system model in ADS environment. A FDMA (frequency division multiple access) transceiver system with carrier frequencies at 25 GHz, 45 GHz and 65 GHz is designed. Baseband signal is modulated and transmitted through a common microwave transmission line. The date rate of each RF band is 4 Gb/s, so the total date rate is 12 Gb/s.

1. INTRODUCTION

As the development of the speed and scale of ULSI, date rate between different cores becomes higher and higher. For the past years, people have focused on the traditional date communication methods by reducing the resistivity of the connection wires (using copper) and reducing the dielectric constant of interlayer dielectric materials (using low-k polymers). But these methods may meet fundamental material limits [1]. Researchers are looking for new means to achieve high date rate and low energy. RF interconnect is introduced to overcome the difficulties in 2001 [2]. A RF interconnect system includes RF transmitters, microwave transmission lines or antennas and RF receivers. The baseband signal is modulated by a high frequency signal such as 50GHz, then the RF signal is transmitted through transmission line or antenna; at the other terminal, the signal is amplified and demodulated. RF interconnect has a great development in the past years. In 2009, a FDMA interconnect on chip communication system with 10 Gb/s was realized [3]; and in ISSCC 2011, a mobile memory I/O interface using simultaneous bidirectional dual (base + RF) band signaling is published [4]. The interface operates at 8.4 Gb/s (quicker than current DDR memory I/O (5 Gb/s)) and with a power efficiency of 2.5 pJ/b (also less than DDR (17.4 pJ/b)).

The block of a RF interconnect system with multiple channels is illustrated in Fig. 1. The Baseband signals from the digital processor or the memory core are modulated by carriers at 25 GHz, 45 GHz and 65 GHz. Then, the three RF signals are added to a transmission line, as the frequencies of the carriers are different, the interference of the different signals can be filtered. The transmission line can be intra or inter chips; it depends on whether the baseband signal will be transferred in the chip or among the chips. Three receivers are added at the other terminal of the transmission line to demodulate the RF signal to baseband.

2. ANALYSIS AND SIMULATION OF THE COMMUNICATION CHANNEL

Figure 2 illustrates a capacitive coupled RF interconnect module. To minimize the reflection from the terminals, a resister equals to the characteristic impedance of the transmission line is connected to each terminal of the line. The RF signals are uplinked to CPW (coplanar waveguide) or MTL (microwave transmission line) and down linked to receivers through capacitors.

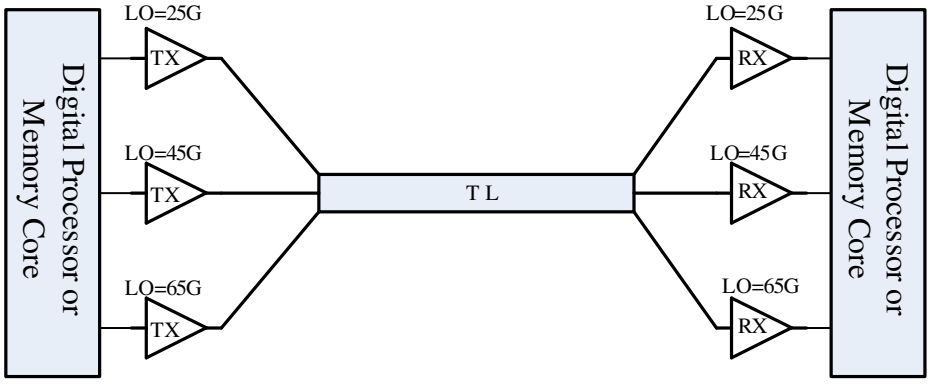

Figure 1: The architecture of RF interconnect system.

Figure 3 is the simplified module of the communication channel in Fig. 2. Rt represents the output impedance of the transmitter; Rr represents the input impedance of the receiver; Ct equals to the capacitor between the transmitter and the CPW or MTL; Cr equals to the capacitor between the receiver and the CPW or MTL; and Vrec equals to the voltage transferred from the transmitter to the receiver. The value of Rt and Rr, Ct and Cr are chosen to be equal to each other; and to preserve the characteristic impedance, Rt and Rc should be greater than Zc [5]. So in the module

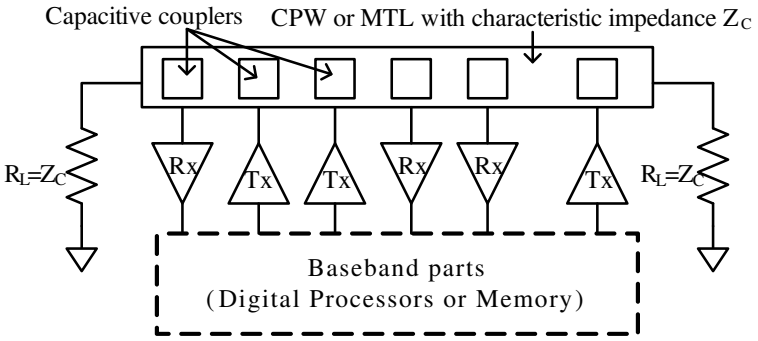

Figure 2: Channel of the RF interconnect system with multiple I/Os.

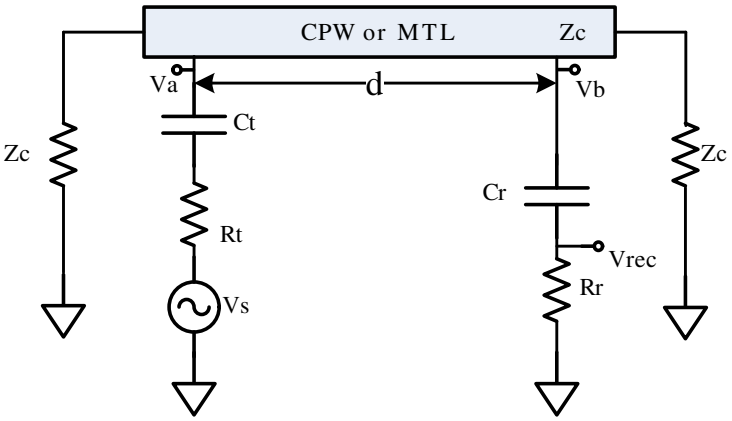

Figure 3: Simplified module of the channel in Fig. 2.

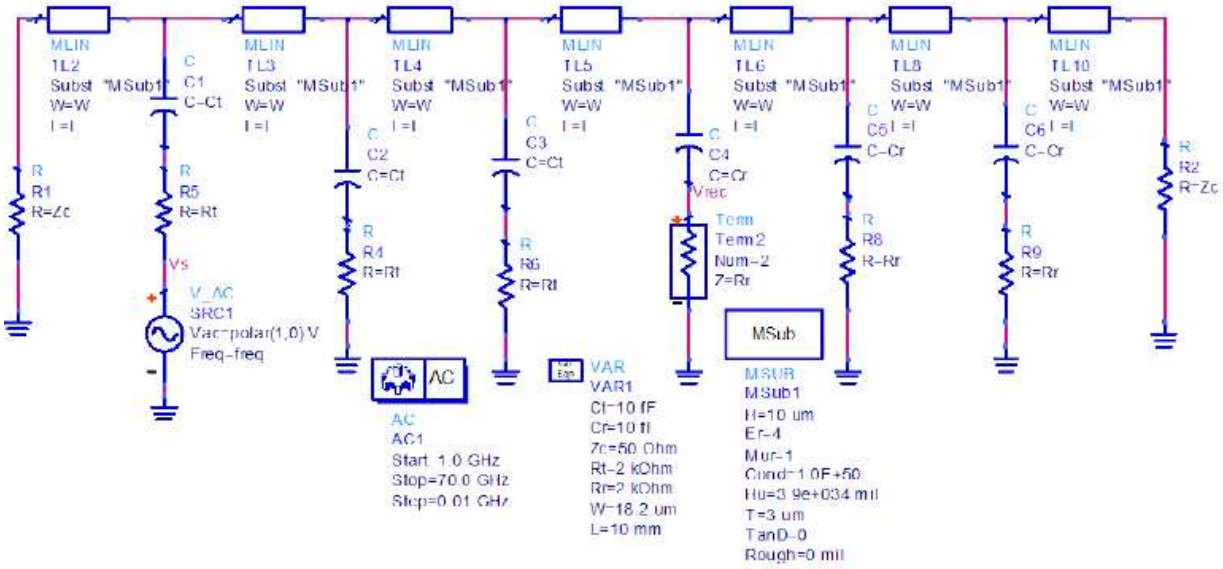

Figure 4: ADS simulation module of the communication channel.

of Fig. 3, the other pairs of Rt, Rc, Ct, Cr in Fig. 2 can be neglected and only one pair of Rt, Rc, Ct, Cr is considered. The voltage received at the receiver can be calculated as

$$V_{rec} = \frac{Rt}{Rt - j\frac{1}{\omega c}} Vb \tag{1}$$

The impedance from point a is expressed as $Za = Zb\exp(-j\beta d)//Zc$; β is propagation constant which is related to the frequency of the signal and the dielectric coefficient ε_r of the CPW. Neglect the attenuation of the transmission line, then

$$Vb = Va = \frac{Za}{Za + Rt - j\frac{1}{\omega c}} \tag{2}$$

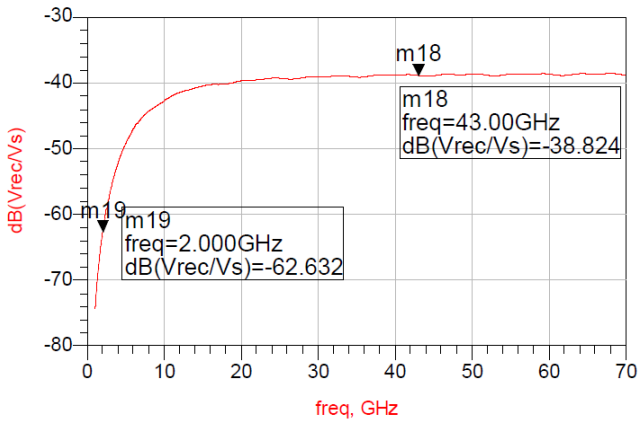

Figure 5: ADS simulation result of the communication channel.

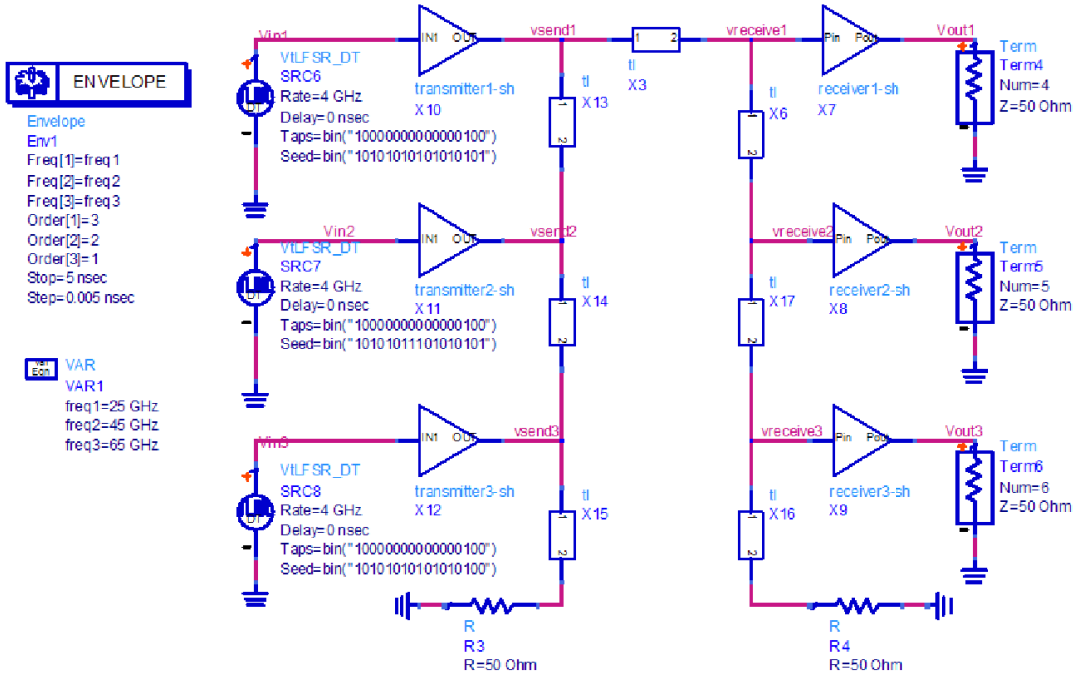

Figure 6: ADS simulation module of the system.

Then V_{rec} can be derived according to (1), (2)

$$V_{rec} = \frac{\frac{ZcRr}{2}}{\left(\frac{Zc}{2} + Rt - j\frac{1}{\omega Ct}\right)\left(\frac{Zc}{2} + Rr - j\frac{1}{\omega Cr}\right)} V_{se}^{-j\beta d} \tag{3}$$

It is clearly from (3) that Rt and Rr should be much greater than $1/(j\omega Ct)$ and $1/(j\omega Cr)$ to obtain dispersion free V_{rec}. Fig. 3 shows that Rt and Ct compose a high pass filter, so are Rr and Cr. The cut off frequency of the filter can be chosen to be higher than the baseband frequency to minimize the interference of the switch noise at baseband. The module of communication channel of the FDMA RF interconnect system is simulated by ADS in Fig. 4. In this module, $Rt = Rr = 2\,\mathrm{k\Omega}$, $Ct = Cr = 10\,\mathrm{fF}$, $Zc = 50\,\Omega$, and on chip micro strip is used as transmission line with dielectric

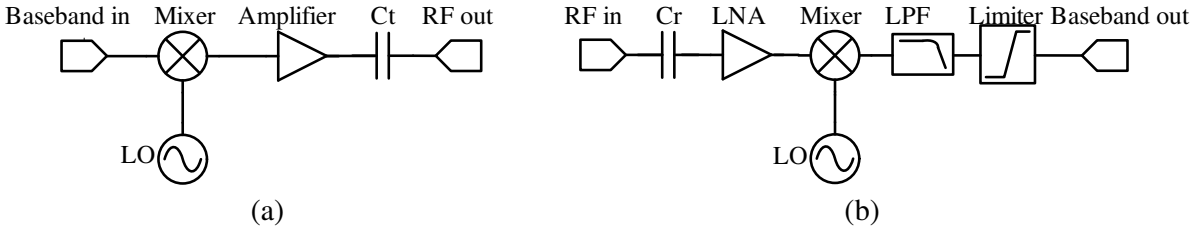

Figure 7: (a) Block of the transmitter; (b) Block of the receiver.

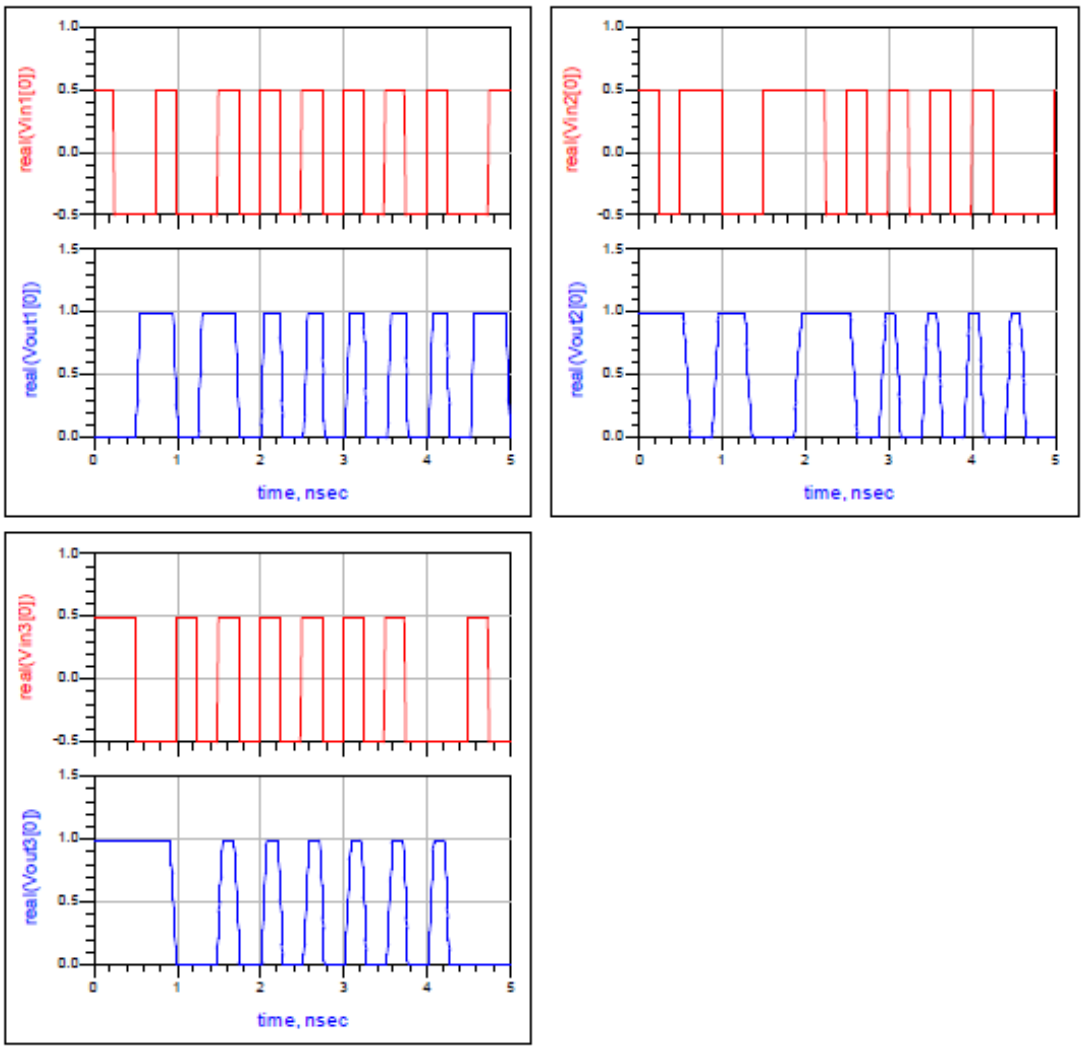

Figure 8: Simulation results of the FDMA RF interconnect.

coefficient $\varepsilon_r = 4$, substrate thickness $H = 10\,\mu\text{m}$. It is calculated that when the width of the micro strip is 18.2 μm, the characteristic impedance of the MTL is 50 Ω. The length of each micro strip is 10 mm. Simulation result of the module is illustrated in Fig. 5. The attenuation of the channel is 38.8 dB at 43 GHz, and 62.6 dB at 2 GHz, so the attenuation of the switch noise at baseband is 23.8 dB.

3. ANALYSIS AND SIMULATION OF A FDMA INTERCONNECT SYSTEM

The simulation module of the whole system is shown in Fig. 6. Three carrier frequencies are 25 GHz, 45 GHz, and 65 GHz.The length of each MTL is 10 mm. Linear feedback shift registers with rate at 4 Gb/s are used to generate the baseband signal. Fig. 7 is the block of the transmitter (TX) and the receiver (RX). As the RF interconnect system is used for intra or inter chips communication instead of passive lines, the chip size of the system should be as small as possible and it should cost less energy. So the structure of the transceivers should be as simple as possible. Direct conversion transceivers are most popular used in recent design of RF interconnect system. Baseband signal is modulated with LO by mixer; then the signal is amplified and transmitted to the MTL through a coupling capacitor ($Ct = 10\,\text{fF}$). In the receiver side, the RF signal is coupled from the MTL through a capacitor ($Cr = 10\,\text{fF}$), amplified by a LNA and down converted by a mixer, then a low pass filter is used to filter out the high frequency. At last, the baseband signal is amplified by a limiter. The output impedance of the amplifier in the transmitter equals to $Rt = 2\,\text{k}\Omega$ and the input impedance of the LNA equals to $Rr = 2\,\text{k}\Omega$, as illustrated in Section 2. The time domain signals are shown in Fig. 8.

4. CONCLUSIONS

This work presents a FDMA RF interconnect system used for intra or inter chips communication. Total date rate of the system is 12 Gb/s. The simulation result can be used to guide the design implemented with deep sub micrometer IC. This is what we will focus on in the future research.

REFERENCES

1. Meindl, J. D., IEEE Interconnect Tech. Conf. Short Course, May 1998
2. Chang, M. C. F., "RF/wireless interconnect for inter- and intra-chip communications," *Proc. IEEE*, 456466, 2001.
3. Tam, S.-W. and M. C. F. Chang, "A simultaneous tri-band on-chip RF-interconnect for future network-on-chip," *Symposium on VLSI Circuits Digest of Technical Papers*, 90–91, 2009.
4. Byun, G.-S. and M.-C. F. Chang, "An 8.4 Gb/s 2.5 pJ/b mobile memory I/O interface using simultaneous bidirectional dual (base + RF) band signaling," *ISSCC*, February 2011.
5. Chang, M. C. F., "RF/Wireless interconnect for inter- and intra-chip communications," *Proceeding of the IEEE*, Vol. 89, No. 4, April 2001.

Studies of Planar Antennas with Different Radiator Shapes for Ultra-wideband Body-centric Wireless Communications

Y. Y. Sun, S. W. Cheung, and T. I. Yuk
Department of Electrical and Electronic Engineering,
The University of Hong Kong, Pokfulam Road, Hong Kong, China

Abstract— This paper studies the performances of planar UWB monopole antennas using a radiator of different shapes including triangle, rectangle, square, annual ring, circle, vertical ellipse, ellipse, pentagon and hexagon for body-centric wireless communications. The planar antennas consist of a radiator and a microstrip-feed line on one side of the substrate and a ground plane on the other side. Results of simulation studies show that the antenna using an elliptical radiator appears to have a better overall performance in terms of bandwidth, gain, efficiency and radiation pattern, among the antennas studied. The antenna achieves a wide impedance bandwidth of 3.1–12 GHz, an average peak gain of nearly 3.5 dBi and good radiation patterns, making it a good candidate for UWB body-centric wireless communications.

1. INTRODUCTION

Ultra-wideband (UWB) technology, due to the advantages of low cost, low complexity, low spectral power density, high precision ranging, low interferences and extremely high data rates, has attracted much attention Since the Federal Communications Commission (FCC) allocated 7.5 GHz spectrum from 3.1 to 10.6 GHz for UWB radio applications in 2002 [1] UWB antennas as a key component in UWB systems have been widely investigated by many researchers [2–9]. One of the most promising areas in UWB applications is body-centric wireless communications where various sensors are connected together by UWB antennas which have to be low power, low-profile and unobtrusive to the human body [10, 11].

Due to the presence of the human body the design of UWB antennas for body-centric communications is complicated Several fundamental requirements such as wide impedance bandwidth, small size and low profile, good on-body propagation and radiation characteristics in the proximity of the body are needed to be fulfilled [10–15].

In this paper, planar UWB monopole antennas using a radiator of different shapes for body-centric wireless communications are studied by computer simulation. Results show that the antenna with an elliptical radiator appears to be the best choice for UWB body-centric wireless communications.

2. ANTENNA STRUCTURE

2.1. Structure of Planar Antennas with Different Radiators

The proposed UWB monopole antennas with radiators of different shapes, including triangle, rectangle, square, annual ring, circle, ellipse, pentagon and hexagon for studies are shown in Fig. 1. Each antenna consists of a radiator fed by a microstrip line, with a width of w_m to achieve 50 Ω characteristics impedance, printed on one side of the substrate and a rectangular ground plane on the other side of the substrate. The antennas are designed on lowcost FR4-substrates with a thickness of 1.6 mm, a relative permittivity of 4.6 and a total size of $W \times L$ optimised in terms of impedance bandwidth ($S_{11} < -10$ dB) using computer simulation and having the following parameters: $W = 30$ mm, $L = 35$ mm, $w_f = 3$ mm and $h_g = 12$ mm. Other parameters for these antennas are listed in Table 1.

Table 1: Dimensions of different radiators of antennas.

	Rectangle	Triangle	Square	Circle	Annual ring	Ellipse	Ellipse h	Pentagon	Hexagon
h_f (mm)	13.65	14	13.7	13	13	13.1	13	13.1	13.2
a (mm)	16	16	13	16	16	16	16	10.4	9.24
b (mm)	12.88	12	13		6	12	12		

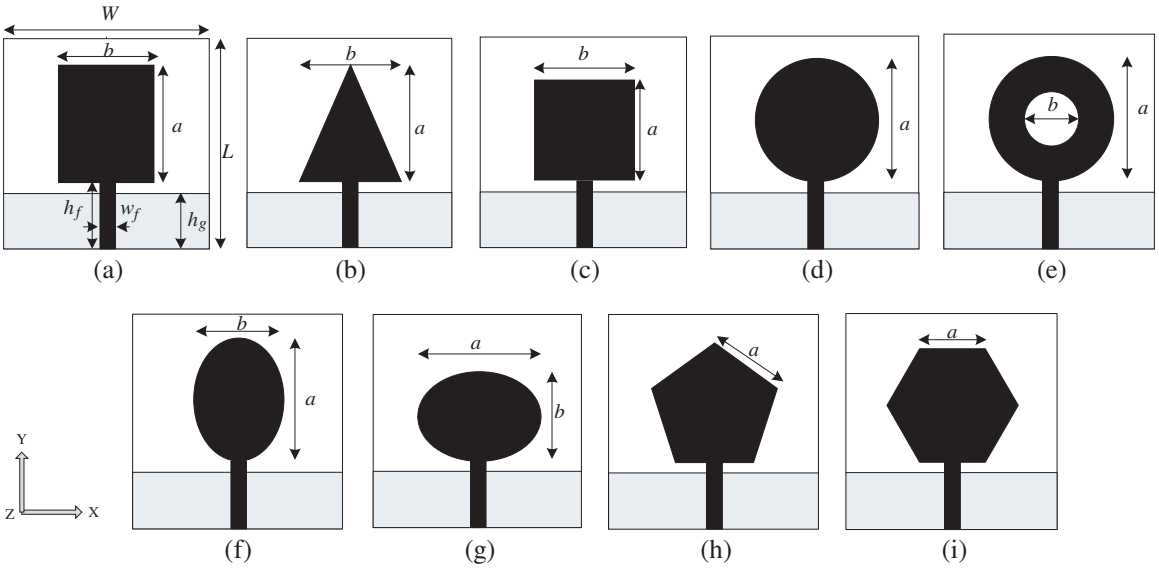

Figure 1: Geometries of antennas : (a) Rectangle, (b) triangle, (c) square, (d) circle, (e) annual ring, (f) ellipse (vertical), (g) ellipse, (h) pentagon and (i) hexagon.

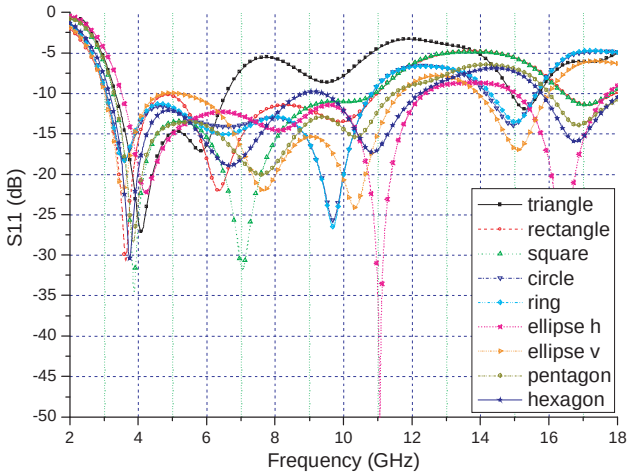

Figure 2: Reflection coefficient of antennas.

2.2. Body Model

Human body has a significant influence on the antenna characteristics, so it is important to include the human-body model in the antenna design process. Two types of human-body models are often used One type is the three-tissue model consisting of skin, fat and muscle tissue, while the other type is a homogeneous model composing of muscle tissue only [10]. In this paper, the homogeneous model is used due to its simpler structure and shorter simulation time compared to the three-tissue model. Simulation results have shown that there are only slight differences between them. In our simulation studies, the dimension used for the body model is $100 \times 100 \times 30\,\mathrm{mm}^3$ with a relative permittivity of 53.58 and a loss tangent 0.2.

3. RESULTS AND DISCUSSIONS

3.1. Antennas in Free Space

The simulated reflection coefficients S_{11} peak gains and radiation efficiencies of the antennas are shown in Figs. 2, 3 and 4, respectively. It can be seen in Fig. 2 that the elliptical antenna has the widest impedance bandwidth (for $S_{11} < 10\,\mathrm{dB}$) of 3.112 GHz and the triangular antenna has the narrowest bandwidth. The simulated results show that the hexagonal antenna has an average peak gain of about 3.82 dBi and an average efficiency of about 80% throughout the whole UWB bandwidth which are the best among all antennas studied The elliptical antenna has an average

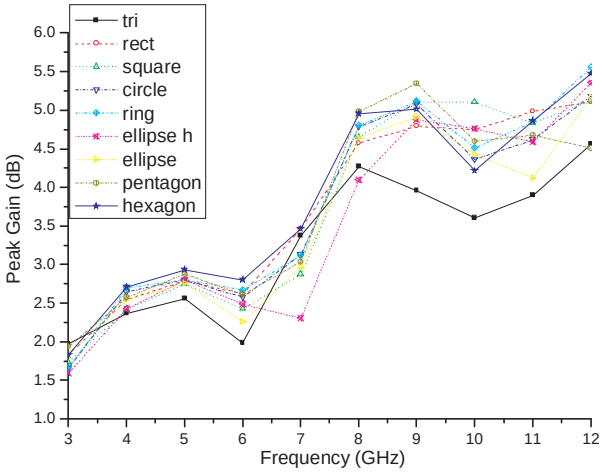

Figure 3: Peak gain.

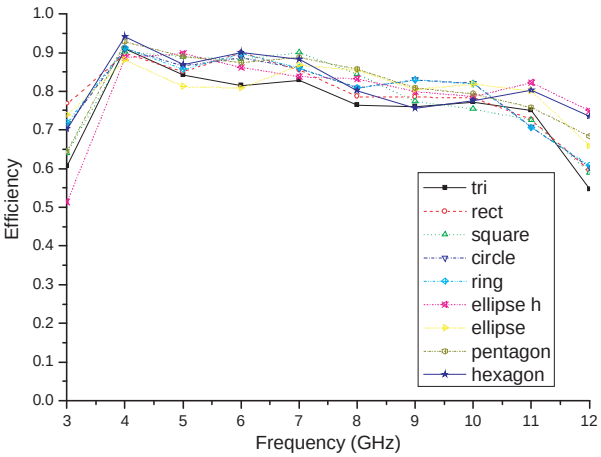

Figure 4: Radiation efficiency.

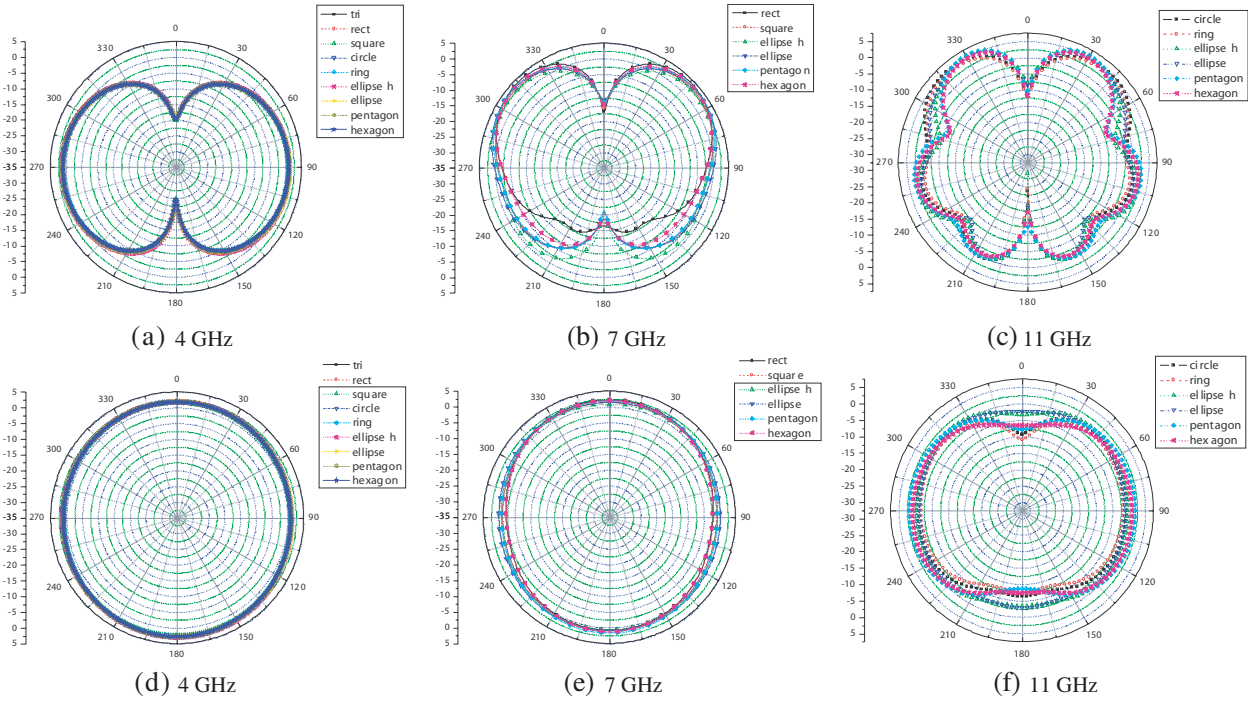

Figure 5: Radiation patterns of (a), (b) & (c) E-plane and (d), (e) & (f) H-plane.

peak gain of about 3.78 dBi and an average efficiency of 80%, which is quite close to the hexagon one. Fig. 5 shows the radiation patterns of the antennas at the frequencies of 4, 7 and 11 GHz are quite similar. The radiation patterns of all the antennas in the H-plane are almost omnidirectional and in the E-plane have obvious nulls which are typical for monopole antennas For body-centric communications, the radiation in the E-plane plays a more important role. Fig. 5 shows that all of these antennas perform about the same in this sense.

3.2. Antennas on Body

Figures 6 & 7 show the peak gains and radiation efficiencies of the antennas (except the triangular antenna which has a bandwidth narrower than the UWB), respectively, on body from 3 to 12 GHz. In these studies, the distance between the antenna and the body model is 5 mm. It can be seen that the hexagon antenna also is the best in terms of average peak gain and efficiency. However, compared with the results in free space the average efficiency drops from about 80% to 30% and the average peak gain increases a little to 4.18 dBi which is due to reflections of the body. The elliptical antenna has an average peak gain of 4.15 dBi and an average efficiency of 31%. The

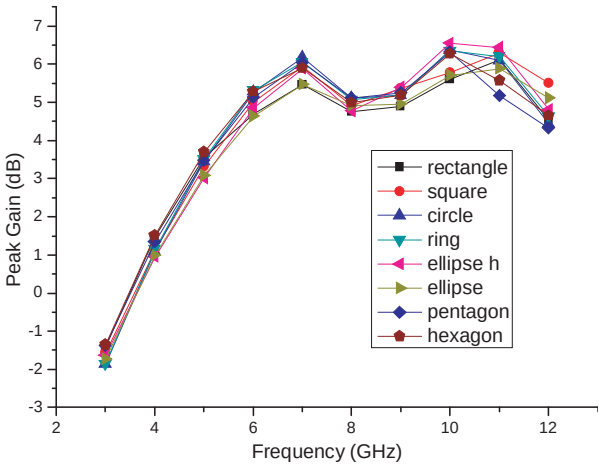

Figure 6: Peak gain on body.

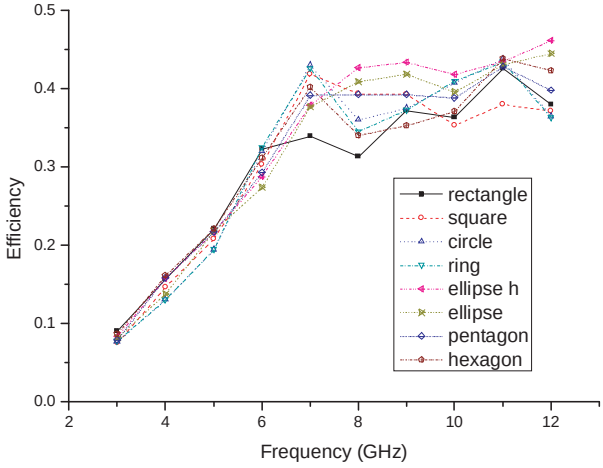

Figure 7: Radiation efficiency on body.

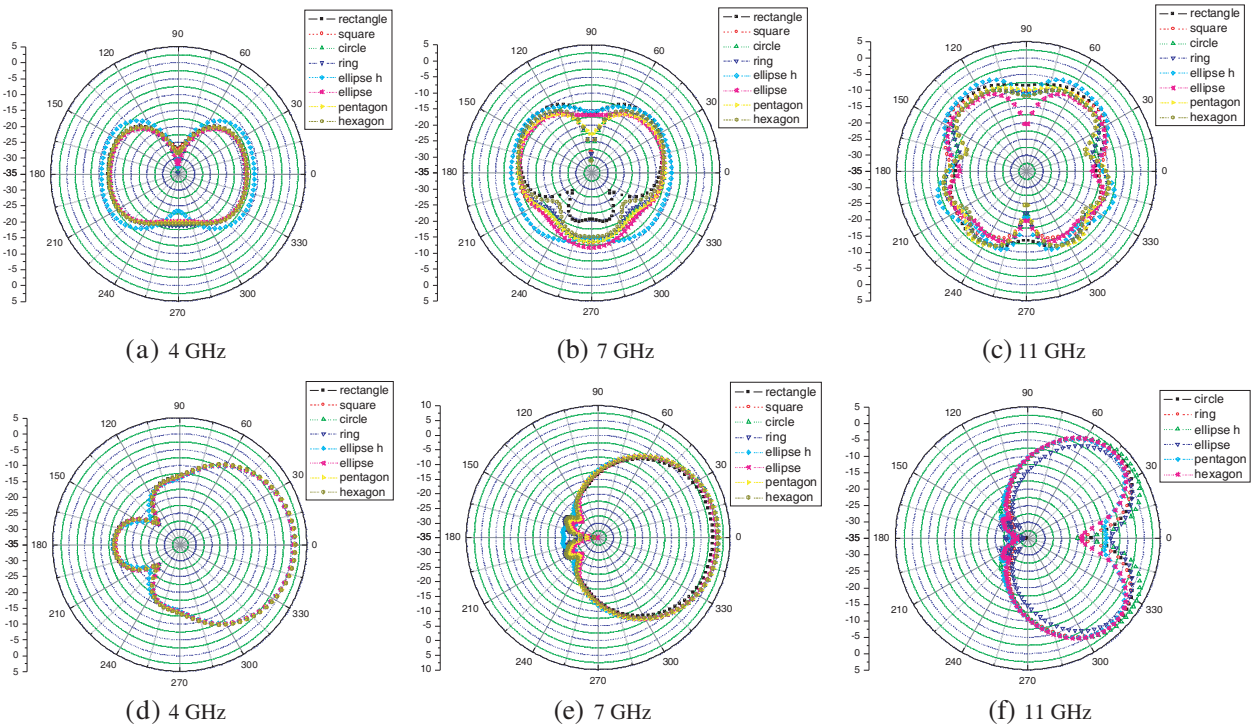

(a) 4 GHz (b) 7 GHz (c) 11 GHz

(d) 4 GHz (e) 7 GHz (f) 11 GHz

Figure 8: On-body radiation pattern (a), (b) & (c) E-plane and (d), (e) & (f) H-plane.

radiation patterns at 4, 7 and 11 GHz are shown in Fig. 8. It can be seen that the radiations are directional, with the front-to-back ratios of about 20–30 dB. Since the radiation in the E-plane plays an important role in body-centric communications, the results in Fig. 8 show that the elliptical antenna has the slightly larger radiation patterns in the E-plane at all these frequencies and so appears to be better than the other antennas.

4. CONCLUSION

The performances of using different shapes including triangle, rectangle, square, annual ring, circle, ellipse, pentagon and hexagon, as the radiator of a planar UWB antenna for body-centric wireless communications have been studied. Results of the simulation study have showed that the antenna with an elliptical radiator has a better overall performance in terms of bandwidth, gain and radiation pattern, both in free space and on body. The antenna can achieve a bandwidth from 3.1 to 12 GHz, an average peak gain of about 3.5 dBi, an average efficiency of 80% and good radiation patterns in the E-plane, making it a good candidate for UWB body-centric wireless communications.

REFERENCES

1. Federal Communications Commission, "Revision of Part 15 of the commission's rules regarding ultra-wideband transmission system from 3.1 to 10.6 GHz," Federal Communications Commission, 98–153, ET-Docket, Washington, DC, 2002.
2. Lin, D. B., I. T. Tang, and M. Y. Tsou, "A compact UWB antenna with CPW-fed," *Microw. Opt. Technol. Lett.,* Vol. 49, 372–375, 2007.
3. Ren, Y. J. and K. Chang, "Ultra-wideband planar elliptical ring antenna," *Electron. Lett.*, Vol. 42, No. 8, 447–449, 2006.
4. Liang, J., C. C. Chiau, X. Chen, and C. G. Parini, "Printed circular ring monopole antennas," *Microw. Opt. Technol. Lett.,* Vol. 45, 372–375, 2005.
5. Ren, Y. J. and K. Chang, "An annual ring antenna for UWB communications," *IEEE Antennas Wireless Propag. Lett.*, Vol. 5, No. 1, 274–276, 2006.
6. Xiao, J. X., M. F. Wang, and G. J. Li, "A ring monopole antenna for UWB application," *Microw. Opt. Technol. Lett.*, Vol. 48, No. 1, 179–182, 2010.
7. Jung, J., W. Choi, and J. Choi, "A small wideband microstrip-fed monopole antenna," *IEEE Microw. Wireless Compon. Lett.,* Vol. 15, No. 10, 703–705, 2005.
8. Zhang, J. S. and F. J. Wang, "Study of a double printed UWB dipole antenna," *Microw. Opt. Technol. Lett.,* Vol. 50, 3179–3181, 2008.
9. Kiminami, K., A. Hirata, and T. Shiozawa, "Double-sided printed bow-tie antenna for UWB communications," *IEEE Antennas Wireless Propag. Lett.,* Vol. 3, No. 1, 152–153, 2004.
10. Hall, P. S. and Y. Hao, *Antennas and Propagation for Body-centric Wireless Communications*, Artech House, Norwood, MA, 2006.
11. Alomainy, A., A. Sani, Y. Hao, et al., "Transient characteristics of wearable antennas and radio propagation channels for ultrawideband body-centric wireless communications," *IEEE Trans. Antennas Propag.,* Vol. 57, No. 4, 875–883, 2009.
12. Low, X. N., Z. N. Chen, and T. S. P. See, "A UWB dipole antenna with enhanced impedance and gain performance," *IEEE Trans. Antennas Propag.,* Vol. 57, No. 10, 2959–2966, 2009.
13. Alomainy, A., Y. Hao, P. S. Hall, et al., "Comparison between two different antennas for UWB on-body propagation measurements," *IEEE Antennas Wirel. Propag. Lett.,* Vol. 4, No. 1, 31–34, 2005.
14. Cai, A., T. S. P. See, and Z. N. Chen, "Study of human head effects on UWB antenna," *IEEE International Workshop on Antenna Technology: Small Antennas and Novel Metamaterials*, 310–313, Mar. 7–9, 2005.
15. Chen, Z. N., A. Cai, T. S. P. See, and M. Y. W. Chia, "Small planar UWB antennas in proximity of the human head," *IEEE Trans. Microw. Theory Tech.*, Vol. 54, No. 4, 1846–1857, 2006.

Bandwidth Improvements Using Ground Slots for Compact UWB Microstrip-fed Antennas

L. Liu, S. W. Cheung, and T. I. Yuk
Department of Electrical and Electronic Engineering, The University of Hong Kong, Hong Kong, China

Abstract— The paper studies the method of using a ground slot for bandwidth improvement of compact ultra-wide band (UWB) antennas with microstrip line feed. Slots of different shapes such as triangular, rectangular, partially circular and hexagonal, placed on the ground plane under the feed line of the radiator are studied for impedance matching. The effects of the slots on the performances of the antennas, in terms of impedance bandwidth, radiation pattern, gain, and efficiency, are studied. Results of simulation tests show that a ground slot with proper dimensions placed under the feed line can improve the impedance matching and hence increase the bandwidth without affecting much the performance of the antenna. Results of studies also show that, by using a hexagonal slot on the ground plane under the feed line, a patch antenna with a compact size of 35 mm × 23 mm can achieve a bandwidth of 3.1–16.3 GHz for $S_{11} < -10$ dB. Moreover, it has a stable omnidirectional radiation pattern across the whole bandwidth and achieves an average gain of 2.8 dBi and an average efficiency of about 88% across the UWB.

1. INTRODUCTION

The planar-monopole antenna, due to its compact size, ease of fabrication and low cost, is one of the most popular structures for the design of UWB antennas [1]. In the designs of microstrip-fed monopole antennas, some strategies such as tapered or stepped feed lines have been used to enhance the impedance matching [2–4]. However, these methods make the calculations of the feed-line dimensions very complicated. A simpler and effective method by cutting a slot on the ground plane under the feed line has been proposed and studied [5–11]. In these studies, rectangular slots were most often used [5–8]. Other shapes such as triangular [9, 10], trapezoidal [11] and "T-Shape" [12] have been also studied. In these studies, different shapes of radiators were used, so it is difficult to say which slot shape is the best choice for UWB antennas. In this paper, attempts are made to find out the best slot shape for the UWB antenna. We present the results of a study on the effects of using different slot shapes on the performance of an UWB antenna, in terms of impedance bandwidth, radiation pattern, gain and efficiency. A compact microstrip-fed monopole antenna with a square radiator and a partial-ground plane is used in our study.

2. ANTENNA DESIGN

The geometry of the microstrip-fed UWB monopole antenna without slot is shown in Fig. 1, which is used as a reference antenna in our study. The antenna is designed on a FR4 substrate with a thickness of 1.6 mm, a dielectric constant of 4.2 and a loss tangent of 0.02. The square radiator printed on one side of the substrate has a length of L_p and is fed by a microstrip line with a length of L_f and a width of W_f. A partial-ground plane with the dimension $L_G \times W$ is printed on the

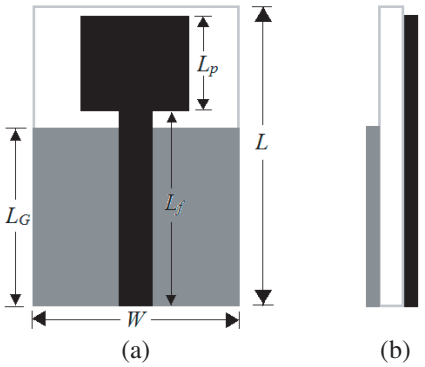

Figure 1: Geometry of reference UWB antenna without slot: (a) front view, (b) side view.

other side of the substrate. The overall antenna occupies an area of $L \times W$. The performance of the antenna is optimized, in terms of maximizing the bandwidth (for $S_{11} < -10\,\text{dB}$) and stabilizing the radiation pattern (omnidirectional radiation pattern), using the EM simulation tool CST. The optimized dimensions are: $L_p = 10\,\text{mm}$, $L_f = 22\,\text{mm}$, $W_f = 3\,\text{mm}$, $L_G = 20\,\text{mm}$, $W = 23\,\text{mm}$ and $L = 35\,\text{mm}$.

To improve the impedance matching of the antenna throughout the UWB, a small slot is cut on the upper edge of the ground plane under the feed line as shown in Fig. 2. Slots of different shapes including: (a) triangular, (b) rectangular, (c) partially circular, and (d) hexagonal shapes, are used in our studies.

3. RESULTS AND DISCUSSIONS

An extensive-simulation study has been carried out to determine the optimal dimensions of the triangular, rectangular, partially circular and hexagonal slots in the antenna of Fig. 2, by maximizing the bandwidth and results are shown in Table 1. With the uses of these dimensions, the simulated $S_{11}$of the antenna without a slot and with different slots are shown in Fig. 3. It can be seen that, without a slot, the antenna has a bandwidth of 3.3–10.3 GHz (a relative bandwidth of 103%) for $S_{11} < -10\,\text{dB}$. However, with the use of a slot, the antenna can have a remarkable increase in bandwidth. The largest improvement is provided by the hexagonal slot, with which the antenna can extend the bandwidth to 3.1–16.3 GHz (136%). The antennas using the circular, rectangular, and triangular slots can also extend the bandwidths to 3.1–15.4 GHz (133%), 3.1–14.9 GHz (131%), and 3.1–14 GHz (127%), respectively. Thus, among the slots studied, the hexagonal slot provides the best impedance matching and the maximum bandwidth.

The influences of the slots on the radiation patterns have also been investigated. Fig. 4 shows the co-polarization radiation patterns of the antennas at 3, 8.5, 10 and 15 GHz in the E- and H-planes. It can be seen that all the antennas have stable omnidirectional radiation patterns in the H-plane throughout the operation band, indicating that adding a slot under the feed line does not affect the radiation patterns in the H-plane. Thus, in applying this method for bandwidth

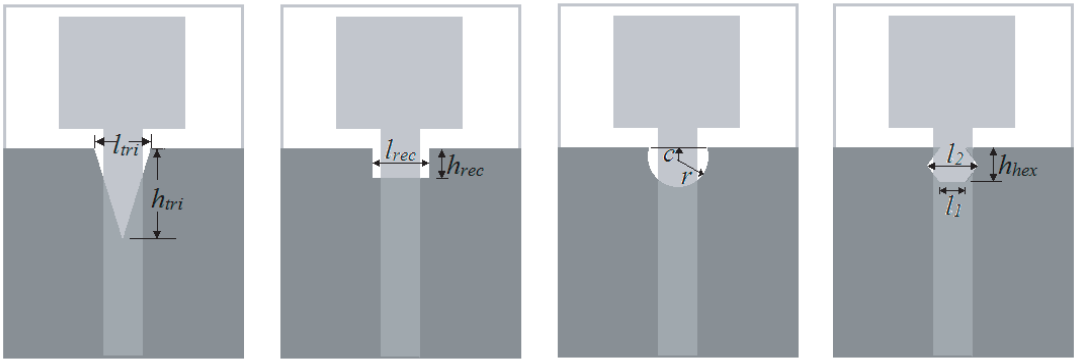

Figure 2: Antennas with different slot shapes: (a) triangular slot, (b) rectangular slot, (c) partial circular slot and (d) hexagonal slot.

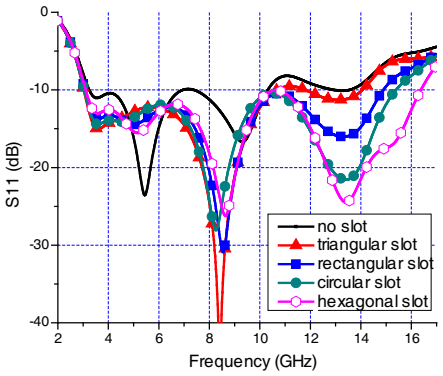

Figure 3: Simulated S_{11} of antennas without slot and with different shapes of slots.

Table 1: Optimized dimension of different slots.

parameter	Triangular slot		Rectangular slot		Partially circular slot		Hexagonal slot		
	l_{tri}	h_{tri}	l_{rec}	h_{rec}	r	C	l_1	l_2	h_{hex}
value (mm)	4	8	3	3.2	2	1.5	1.8	6	2

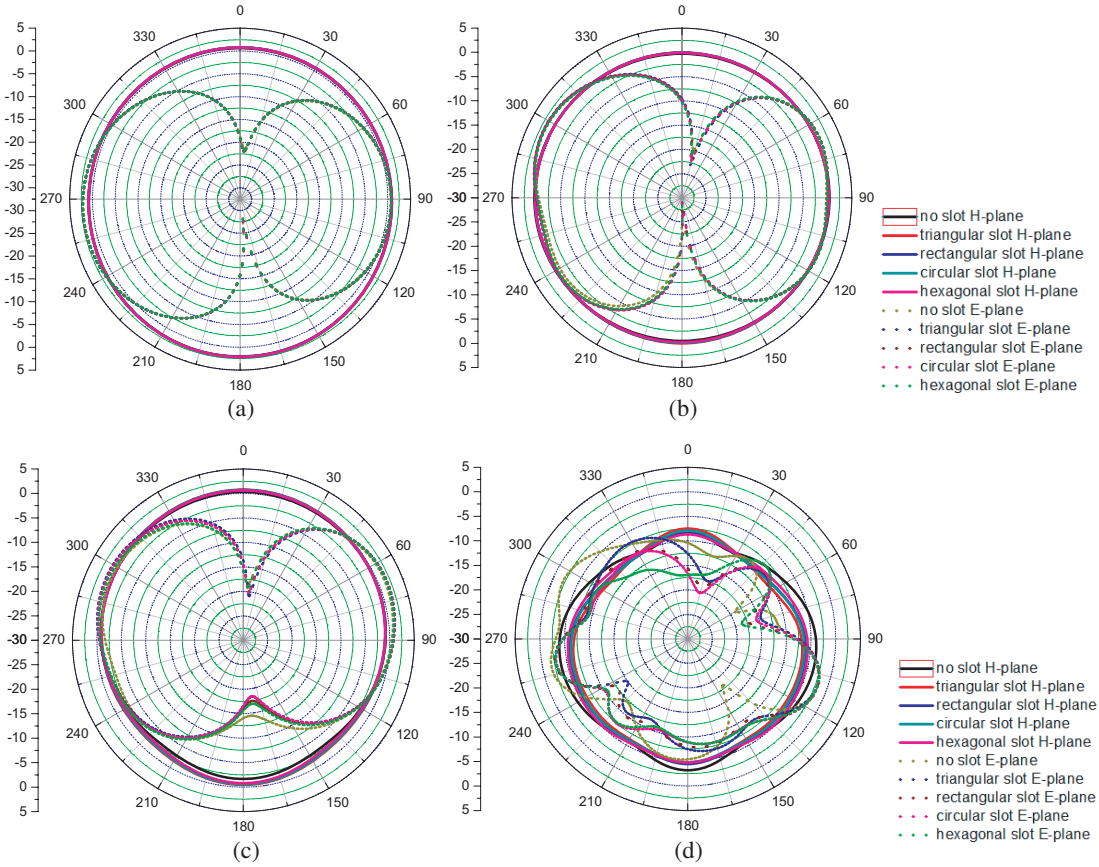

Figure 4: Co-polarization in H- and E-planes: (a) 3 GHz, (b) 8.5 GHz, (c) 10 GHz and (d) 15 GHz.

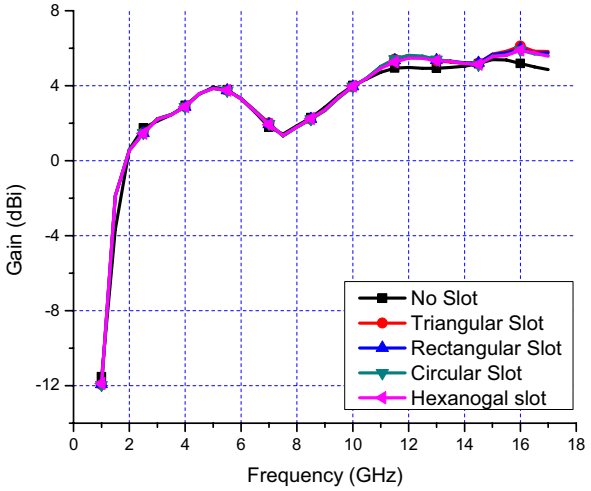

Figure 5: Peak gain of antennas.

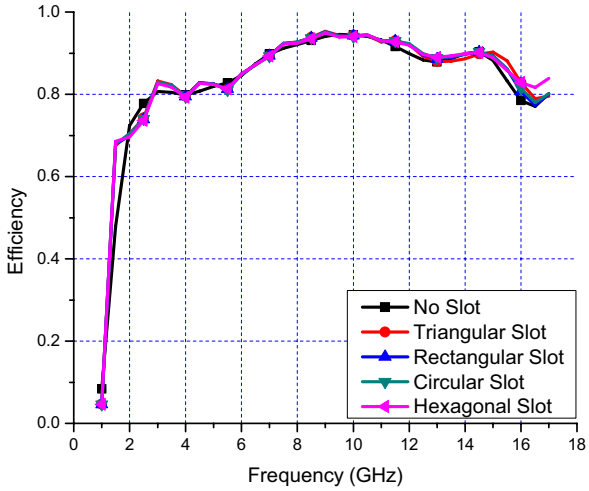

Figure 6: Efficiency of antennas.

improvement, we could firstly design an UWB antenna with a stable omnidirectional pattern and then add a hexagonal slot to improve the impedance matching. This gives antenna designers an

additional and independent way to increase the bandwidth of their monopole antennas.

The simulated peak gains and efficiencies of the antennas from 1 to 17 GHz are shown in Figs. 5 and 6, respectively. It can be seen that all of the antennas have almost the same gain and efficiency, so again the slots do not have much effects on the performances throughout the entire operation band. The average gains of these antennas from 3.1to 10.6 GHz are about 2.8 dBi and the average efficiencies are about 0.88.

4. CONCLUSIONS

The method of using a ground slot for bandwidth improvement of a compact UWB planar monopole antenna has been studied. The antenna has a compact size of 35 mm × 23 mm and the small ground slot is placed under the feed line on the ground plane. Triangular, rectangular, partially circular and hexagonal slots have been used for studies by simulation. Results have shown that the slots can improve impedance matching of the antenna with little effect on the radiation characteristics. Among these slots investigated, the hexagonal slot provides the largest impedance bandwidth of 3.1–16.3 GHz for $S_{11} < -10$ dB, with an average gain of about 2.8 dBi and an average efficiency of about 88%.

REFERENCES

1. Chen, Z. N., M. J. Ammann, X. Qing, X. H. Wu, T. S. P. See, and A. Cai, "Planar antennas," *IEEE Microwave Magazine*, Vol. 7, 63–73, 2006.
2. Lin, S., W. Wang, Y. Liu, L. J. Chen, C. T. Yang, J. H. Qiu, and J. X. Wang, "Planar composite triangle monopole UWB antenna," *2010 IEEE International Conference on Ultra-Wideband (ICUWB)*, 1–3, Nanjing, China, September 2010.
3. Qu, S. W., J. L. Li, and Q. Xue, "A band-notched ultrawideband printed monopole antenna," *IEEE Antennas and Wireless Propagation Letters*, Vol. 5, 495–498, 2006.
4. Nagalingam, M., "Circular patch UWB antenna with time domain analysis," *2010 IEEE Region 8 International Conference on Computational Technologies in Electrical and Electronics Engineering (SIBIRCON)*, 251–256, 2010.
5. Azim, R., M. T. Islam, N. Misran, S. W. Cheung, and Y. Yamada, "Planar UWB antenna with multi-slotted ground plane," *Microwave and Optical Technology Letters*, Vol. 53, No. 5, 966–968, 2011.
6. Zaker, R. and A. Abdipour, "A very compact ultrawideband printed omnidirectional monopole antenna," *IEEE Antennas and Wireless Propagation Letters*, Vol. 9, 471–473, 2010.
7. Bao, X. L. and M. J. Ammann, "Printed band-rejection UWB antenna with H-shaped slot," *International Workshop on Antenna Technology: Small and Smart Antennas Metamaterials and Applications 2007*, 319–322, Cambridge, UK, March 2007.
8. Chayono, R., M. Haneishi, and Y. Kimura, "Inverted triangle printed monopole antenna with halfdisk for UWB applications," *Asia-Pacific Microwave Conference 2006*, 1994–1997, Yokohama, Japan, December 2006.
9. Naser-Moghadasi, M., H. Rousta, and B. S. Virdee, "Compact UWB planar monopole antenna," *IEEE Antennas and Wireless Propagation Letters*, Vol. 8, 1382–1385, 2009.
10. Guo, L., S. Wang, X. Chen, and C. G. Parini, "A miniature quasi-self-complementary antenna for UWB applications," *Asia-Pacific Microwave Conference 2008*, 1–4, Hong Kong, China, December 2008.
11. Ojaroudi, M., G. Kohneshahri, and J. Noory, "Small modified monopole antenna for UWB application," *IET Microwaves, Antennas & Propagation*, Vol. 3, No. 5, 863–869, 2009.
12. Ojaroudi, M., C. Ghobadi, and J. Nourinia, "Small square monopole antenna with inverted T-shaped notch in the ground plane for UWB application," *IEEE Antennas and Wireless Propagation Letters*, Vol. 8, 728–731, 2009.

Band-notch Patch Ultra-wide Band Antenna

Ayman A. R. Saad[1], **Deena A. Salem**[2], **and Elsayed E. M. Khaled**[3]

[1]Kosseir Radio, Telecom Egypt, Kosseir, Egypt
[2]Microstrip Department, Electronics Research Institute, Giza, Egypt
[3]Electrical Engineering Department, Assiut University, Assiut, Egypt

Abstract— This paper presents a new design of a compact band-notched planar antenna for ultra-wide band (UWB) applications. By properly incorporating a slotted patch electromagnetic band gap (spEBG) element in the design of the antenna a wide operating bandwidth from 3.7 to 11.4 GHz can be obtained with a frequency rejection band from 5.29 to 5.96 GHz. A parametric study for the proposed antenna is presented. The proposed antenna is simulated, using Zeland IE3D software. Also the antenna is fabricated. The measured data are highly agreed with the simulated results. The proposed antenna has good gain flatness and high efficiency over its whole frequency band excluding the rejected band.

1. INTRODUCTION

High data rate transmission with high efficiency and minimum distortion in the received signal are crucial requirements for ultra-wide band (UWB) wireless communication systems (frequency band of 3.1–10.6 GHz). These requirements are involved with UWB planar antennas design. Many of these antennas configurations have been proposed and developed [1, 2]. However, these antennas need a band rejection filter to maintain the coexistence of the narrow band applications which sharing part of the same spectrum such as WLAN in USA (5.15–5.35 GHz, 5.725–5.825 GHz) and HIPERLAN/2 in Europe (5.15–5.35 GHz, 5.47–5.725 GHz). A simple method to achieve this band-rejection property is by loading the radiator with a slot. This slotted radiator resonates at the central frequency of the stop band in which the antenna does not radiate [3–6]. Furthermore, using planar antenna to obtain ultra-wide band characteristics is easy to incorporate with electromagnetic band gap (EBG) structures to improve antenna's performance such as increasing the antenna efficiency, enhancing its gain, and minimizing the side and back lobe levels in the radiation patterns. These enhancements for the antenna performance can be obtained due to the ability of such antennas to suppress the surface wave propagation in a specific frequency band [7].

In this paper, unlike usual method of slotted patch antennas we proposed a new UWB planar antenna that employs a spEBG element coplanar with the ground plane of the structure beneath the radiating element to obtain and control the rejected frequency band at 5 GHz for UWB applications. The design process involves two phases; the first phase is to design a new shape of UWB planar antenna. The second phase is to incorporate the designed antenna with a single spEBG element to achieve the required frequency band-notched characteristic for the UWB applications. The simulated results and the measured data elucidate that the spEBG element exhibit well-behaved band stop characteristics required for UWB applications.

2. ANTENNA CONFIGURATION

The geometry of the proposed band-notched UWB antenna is illustrated in Figure 1. The antenna is etched on FR-4 substrate of dimensions $L_{Sub} \times W_{Sub} = 20 \times 56\,\text{mm}^2$ and a thickness $h = 1.6\,\text{mm}$. The relative permittivity of the substrate is $\varepsilon_r = 4.2$ and its loss tangent is $\tan(\delta) = 0.01$. The substrate is partially backed by a ground plane with $L_g = 10\,\text{mm}$. The patch has a dimension of $L_p = 6\,\text{mm}$ and $W_p = 8\,\text{mm}$. The antenna is fed by a 50-microstrip line of width $W_f = 3\,\text{mm}$, and length $L_f = 7\,\text{mm}$ printed on the top surface of the substrate. The feed gap (g) can be used to adjust the impedance matching. The optimal chosen value of the gap width is 2 mm.

After optimizing the shape and size of the UWB antenna, a single spEBG element is added beneath the patch at the opposite side of the substrate The spEBG element consists of rectangular metallic patch, identical to the radiating patch, loaded with a resonant U-shaped slot. The slot dimensions are selected to optimize the band-rejection performance with a center frequency of 5.5 GHz. The slot has a uniform width of 1 mm, the two vertical lengths are $l_1 = l_2 = 5\,\text{mm}$ and the horizontal length is $l_3 = 7\,\text{mm}$. The slot is placed 0.5 mm away from the edge of the spEBG element.

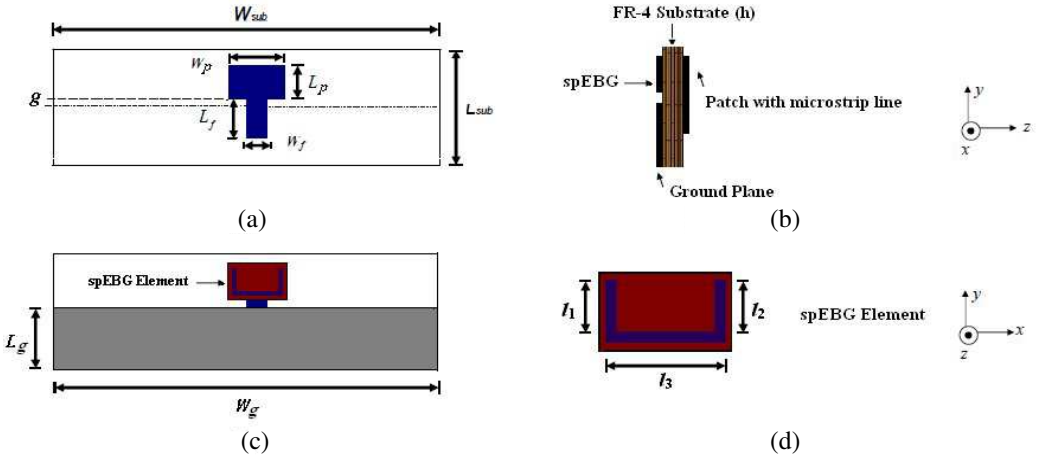

Figure 1: Geometry of the proposed band-notched UWB antenna. (a) Top-view, (b) side-view, (c) bottom-view, (d) spEBG element.

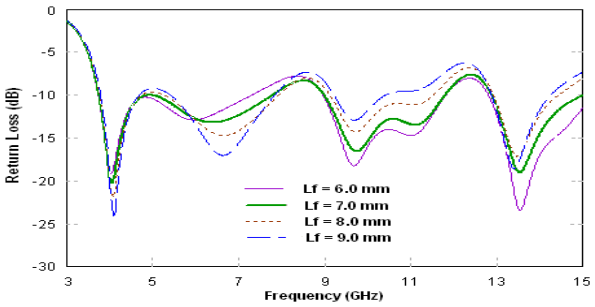

Figure 2: Simulated return loss versus frequency of the proposed antenna for different feed line length, L_f with $g = 2\,\text{mm}$, $L_g = 10\,\text{mm}$, $W_f = 3\,\text{mm}$, $W_p = 8\,\text{mm}$, and $L_p = 6\,\text{mm}$.

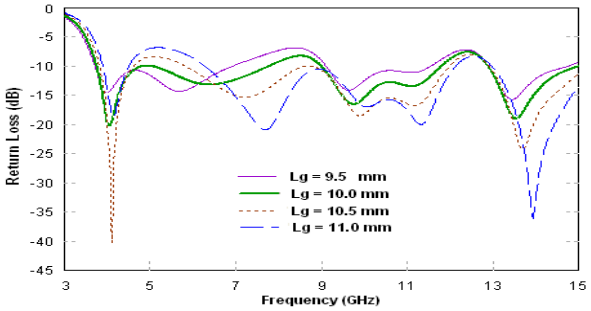

Figure 3: Simulated return loss versus frequency of the proposed antenna for different value of the ground plane length, L_g with $g = 2\,\text{mm}$, $L_f = 7\,\text{mm}$, $W_f = 3\,\text{mm}$, $W_p = 8\,\text{mm}$, and $L_p = 6\,\text{mm}$.

3. RESULTS AND DISCUSSIONS

A full wave analysis of the proposed antenna is obtained by using the ready-made software, Zeland IE3D which is based on the method of moment (MoM) numerical technique. Parametric analysis was adopted to optimize the proposed design. Figure 2 shows the effect of the feed line length, L_f on the return loss, RL, as a function of frequency. Four different lengths were considered with the same dimensions of $g = 2\,\text{mm}$, $L_g = 10\,\text{mm}$, $W_f = 3\,\text{mm}$, $W_p = 8\,\text{mm}$, and $L_p = 6\,\text{mm}$. The length L_f =7 mm provided the widest bandwidth.

Variations of RL as a function of frequency for different values of ground plane length, L_g are depicted in Figure 3. Four different lengths were investigated with the same dimensions of $g = 2\,\text{mm}$, $L_f = 7\,\text{mm}$, $W_f = 3\,\text{mm}$, $W_p = 8\,\text{mm}$, and $L_p = 6\,\text{mm}$. It is observed that as L_g increases, the antenna bandwidth extends to higher frequency ranges. The optimum value of L_g is 10 mm.

The effect of the separation between the radiating patch and the ground plane, g on the performance of the antenna was investigated. Results of the simulated RL as a function of frequency for different values of g with $L_g = 10\,\text{mm}$, $L_f = 7\,\text{mm}$, $W_f = 3\,\text{mm}$, $W_p = 8\,\text{mm}$, and $L_p = 6\,\text{mm}$, are shown in Figure 4. It was found that, by increasing g the antenna shows a wider bandwidth, which may be attributed to reduced coupling between the patch and the ground plane. The optimum value of g is 2 mm at which the widest bandwidth is obtained. Moreover the dimensions of the rectangular patch to maximize the bandwidth were obtained by a parametric analysis. Figure 5 shows the RL as a function of frequency for different patch width, W_p. The other parameters are $g = 2\,\text{mm}$, $L_g = 10\,\text{mm}$, $L_f = 7\,\text{mm}$, $W_f = 3\,\text{mm}$, and $L_p = 6\,\text{mm}$. The $W_p = 8\,\text{mm}$ achieves the widest bandwidth for an acceptable RL throughout the band. Finally, the behavior of the simulated return loss with various values of W_g and with $g = 2\,\text{mm}$, $L_g = 10\,\text{mm}$, $L_f = 7\,\text{mm}$, $W_f = 3\,\text{mm}$,

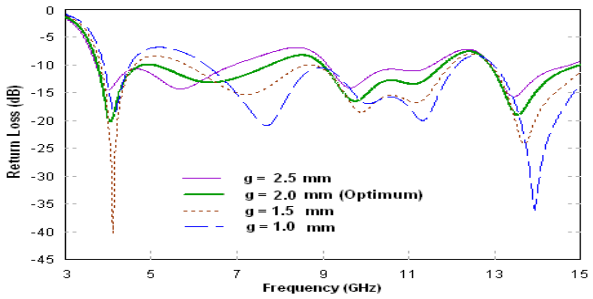

Figure 4: Simulated return loss versus frequency for different values of the feed gap (g) of the proposed antenna. The results are obtained with $L_g = 10\,\text{mm}$, $L_f = 7\,\text{mm}$, $W_f = 3\,\text{mm}$, $W_p = 8\,\text{mm}$, and $L_p = 6\,\text{mm}$.

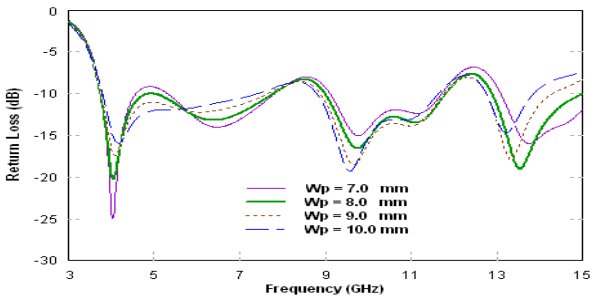

Figure 5: Simulated return loss versus frequency of the proposed antenna for different patch widths, W_p. The other parameters are $g = 2\,\text{mm}$, $L_g = 10\,\text{mm}$, $L_f = 7\,\text{mm}$, $W_f = 3\,\text{mm}$, and $L_p = 6\,\text{mm}$.

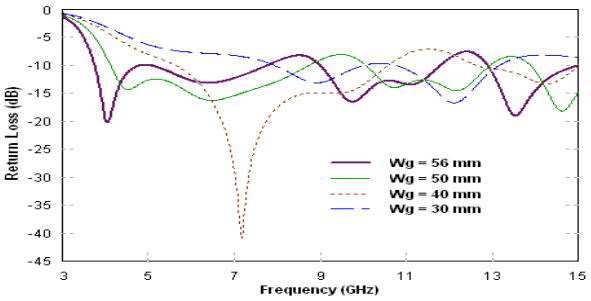

Figure 6: Simulated return loss versus frequency of the proposed antenna for different ground plane widths, W_g with $g = 2\,\text{mm}$, $L_g = 10\,\text{mm}$, $L_f = 7\,\text{mm}$, $W_f = 3\,\text{mm}$, $W_p = 8\,\text{mm}$, and $L_p = 6\,\text{mm}$.

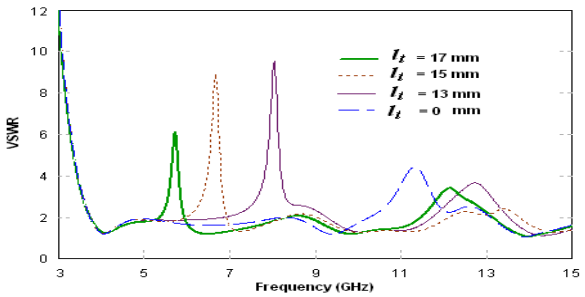

Figure 7: Effect of the total length of the slot l_t on the VSWR of proposed antenna with spEBG element.

$W_p = 8\,\text{mm}$, and $L_p = 6\,\text{mm}$ is illustrated in Figure 6. It was observed that the proposed antenna is sensitive to the width of the ground plane. As the lower limit of operational frequency band increases the W_g increases, and thus the bandwidth of the antenna increases. The optimum value of W_g was found to be 56 mm, beyond which the effect is negligible.

By varying the parameters of the spEBG element, the frequency notch is controlled. It is observed that by adjusting the position of the slot and selecting the length of the spEBG element of about one-half of the wavelength of the center frequency of the desired rejected band, destructive interference is maximized at that frequency which causes the antenna to be non-responsive. The notched frequency f_r can be empirically approximated by [6]:

$$f_r \approx \frac{c}{2l_t\sqrt{\frac{\varepsilon_r+1}{2}}} \tag{1}$$

where l_t is the total length of the U-shaped slot and c is the speed of light. Figure 7 shows the simulated VSWR of the proposed UWB antenna with the spEBG element for different values of l_t. As shown in the figure by increasing l_t, the notch frequency is shifted towards lower frequencies. To achieve frequency rejection from 5.29 to 5.96 GHz, the slot was chosen to be of total length 17 mm and width 1 mm.

The antenna is fabricated using photolithographic technique and illustrated in Figure 8. The RL behavior as a function of frequency is measured for the fabricated antenna with the spEBG element. Figure 9 shows the simulated results and the measured data of the RL. It is apparent that the proposed antenna with spEBG element covers the frequency band from 3.7 to 11.4 GHz with a sharp band rejection from 5.29 to 5.96 GHz. The measured data shows fairly good agreement with the simulated results.

For further insight of the band-notch property, the excited surface current distribution of the antenna at the center-rejected frequency 5.745 GHz and at a frequency 9.765 GHz which is out of

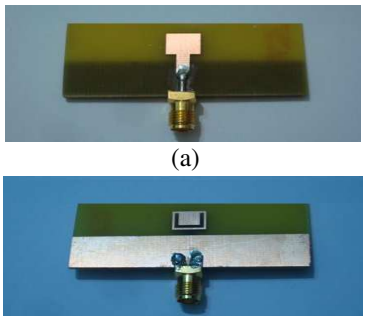

Figure 8: Photograph of the fabricated antenna. (a) Top-view, (b) bottom-view.

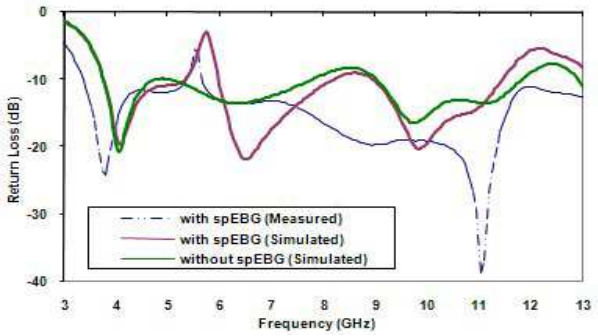

Figure 9: Simulated and measured return losses versus frequency of the proposed UWB antenna with and without spEBG element.

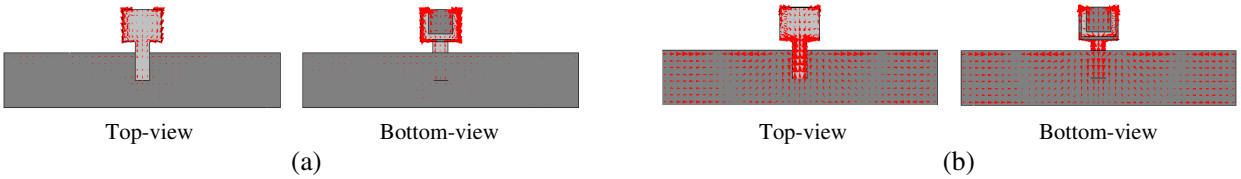

Figure 10: Simulated surface current distribution of the proposed antenna at the top and bottom view for, (a) center-rejected frequency of 5.745 GHz, (b) out of rejected-band of 9.765 GHz.

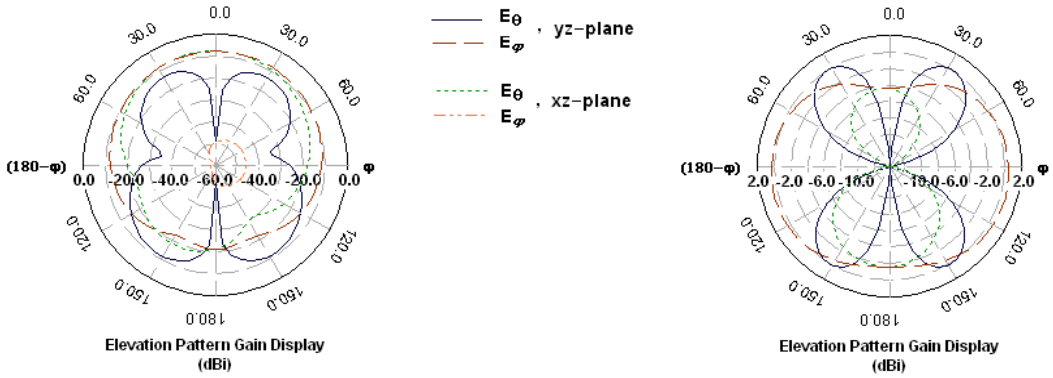

Figure 11: Simulated radiation patterns of E_θ and E_φ in the yz and xz planes of the proposed band-notched UWB antenna at 5.745 GHz: (a) with spEBG element, (b) without spEBG element.

the rejected band are illustrated in Figures 10(a) and 10(b), respectively. Figure 10(a) shows that the spEBG element blocked the propagation of surface current at the band stop frequency due to its high impedance property. Large surface current distribution is observed on the edges of spEBG element along the strip around the slots. The current at the frequency of 9.765 GHz which is out of the stop band is distributed along the radiating patch and along the spEBG element as well. Figure 10 illustrates different diffusion of the current distribution which is sensitive to the frequency of operation.

Figure 11 shows the simulated far-field radiation patterns of E_θ and E_φ in the yz and xz planes for the proposed antenna with and without spEBG element at the frequency 5.745 GHz. Nearly omnidirectional patterns are observed in the yz plane (E-plane). The patterns in the xz plane (H-plane) are similar to bidirectional. The radiating signal operating in the frequency band gap of the antenna with the spEBG element is suppressed which reduce the antenna gain and radiation efficiency than those of the antenna without the spEBG element. Simulated results of the antenna peak gain and radiation efficiency versus frequencies are shown in Figure 12. The gain varies from -3.18 dBi to 5.55 dBi over the operating frequency range of 3.1–10.6 GHz while at the notched

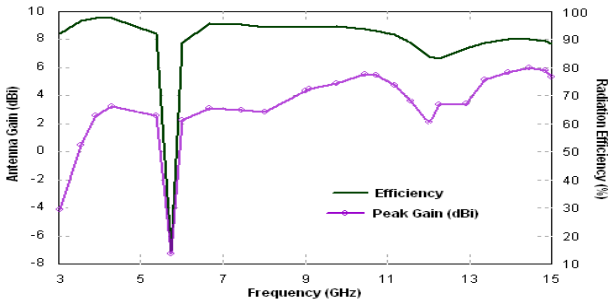

Figure 12: Simulated peak gain and radiation efficiency versus frequency of the proposed band-notched UWB antenna.

band, the antenna gain sharply reduced to nearly −7.5 dBi due to the frequency rejection property. Also, the radiation efficiency is larger than 90% overall the whole frequency band excluding the rejected band.

4. CONCLUSION

A novel design of a compact planar antenna with a frequency band-notched characteristic for UWB applications is proposed and investigated. The design depends on adding a single spEBG element, on the opposite side of the substrate under the radiating patch. The designed antenna satisfies the voltage standing wave ratio (VSWR) requirement that is less than 2.0 in the frequency band between 3.7 and 11.4 GHz, and shows band rejection properties in the frequency band from 5.29 to 5.96 GHz. This rejected frequency band depends on the dimension and location of the spEBG element. In this research the rejected frequency band is required to avoid interference with the existing HIPERLAN/2 and WLAN communication systems, which operate at this range of frequencies. The proposed antenna has a simple-shape and provides a good radiation pattern, relatively flat gain, and high efficiency over the entire frequency band excluding the rejected band. The antenna is fabricated and the return loss versus frequency is measured The measured data show good agreement with those obtained by simulations.

REFERENCES

1. Jafari, H. M., M. J. Deen, S. Hranilovic, and N. K. Nikolova, "Slot antenna for ultra-wideband applications," *IEEE AP-S Int. Symp.*, 1107–1110, Albuquerque, 2006.
2. Danideh, A., R. Sadeghi-Fakhr, and H. R. Hassani, "Wideband co-planar microstrip patch antenna," *Progress In Electromagnetics Research Letters*, Vol. 4, 81–89, 2008.
3. Yoon, H., H. Kim, K. Chang, Y. J. Yoon, and Y. H. Kim, " A study on the UWB antenna with band-rejection characteristic," *IEEE AP-S Int. Symp.*, Vol. 2, 1784–1787, Monterey, CA, 2004.
4. Choi, S. H., H. J. Lee, and J. K. Kim, "Design of an ultra-wideband antenna with band notch characteristic," *IEEE AP-S Int. Symp.,* 1–4, San Diego, USA, 2008.
5. Liu, H.-W., C.-H. Ku, T.-S. Wang, and C.-F. Yang, "Compact monopole antenna with band-notched characteristic for UWB applications," *IEEE Antenna and Wireless Propagation*, Vol. 9, 397–400, 2010.
6. Gofsheh, R. A. S. S., M. A. Honarvar, and A. R. Eskandari, "Coplanar-fed UWB elliptical patch antenna with notched band characteristics," *PIERS Proceedings,* 1225–1228, Xi'an, China, Mar. 22–26, 2010.
7. Coccioli, R., W. R. Deal, and T. Itoh, "Radiation characteristics of a patch antenna on a thin PBG substrate," *IEEE AP-S Int. Symp.*, Vol. 2, 656–659, 1998.

Novel Design of Proximity-fed Ultra-wide Band Annular Slot Antenna

Ayman A. R. Saad[1], **Elsayed E. M. Khaled**[2], **and Deena A. Salem**[3]

[1]Kosseir Radio, Telecom Egypt, Kosseir, Egypt
[2]Electrical Engineering Department, Assiut University, Assiut, Egypt
[3]Microstrip Department, Electronics Research Institute, Giza, Egypt

Abstract— A novel design of a proximity-fed annular slot antenna for UWB operation is presented. Different techniques are used to introduce a band rejection to the operated frequency band of the proposed prototype antenna. The antenna consists of a circular radiating patch placed non-concentrically inside a circular ground plane aperture. The patch is proximity-fed by a microstrip line on the other side of the substrate. This configuration provides an UWB performance in the frequency range of 2.85 to 7.95 GHz with relatively stable radiation parameters. Three different techniques to construct a resonant circuit are investigated to achieve the band-notch property in the 5.0–6.0 GHz band corresponding to the existing WLAN and HIPERLAN/2 networks. In the first technique, a single complementary split ring resonator (CSRR) and in the second technique, a complementary spiral loop resonator (CSLR) is etched off the circular patch. Whereas, in the third technique, a U-shaped slot is etched off the microstrip line. These resonators provide the band-notch property without degrading the UWB performance of the prototype antenna. Furthermore, the band-notched resonance frequency and the bandwidth can be easily controlled by adjusting the dimensions of the slots. The proposed antenna is simulated, using Zeland IE3D. The prototype antenna is fabricated and the measured data of the return loss versus frequency show very good agreement with the simulated results. The performance of the antenna is analyzed using parametric study to investigate the tuning effects of the resonator parameters on the impedance matching. The proposed antenna has a simple shape and provides almost omnidirectional field patterns, relatively flat gain and high radiation efficiency over the entire operated UWB frequency band excluding the rejected band. Satisfactory antenna performance with a simple structure and small size makes the proposed proximity-feed antenna a good candidate for UWB.

1. INTRODUCTION

Since the Federal Communications Commission (FCC) in USA released the unlicensed commercial use of ultra-wide band (UWB) radio system (3.1–10.6 GHz) in 2002, various types of planar UWB antennas with band-notch property has been proposed and developed for wireless communication systems Such types of antennas are important to maintain the coexistence of the narrow band services such as WLAN in USA (5.15–5.35 GHz, 5.725–5.825 GHz) and HIPERLAN/2 in Europe (5.15–5.35 GHz, 5.47–5.725 GHz) [1]. The most often used methods to design planar UWB antennas with band-notch property are etching different shapes of slots on the patch or on the ground plane of the antennas [2–4]. Other methods include adding parasitic elements or using folded strips to the antennas [5]. Recently, several research groups have attempted to reject certain frequency bands using the metamaterial resonators such as the split ring resonator (SRR), or its negative image which is the complementary split ring resonator (CSRR) [6, 7], and the spiral loop resonator (SLR) [8].

Most of the available researches in the literature focused on designing planar band-notched UWB antennas with microstrip line-feed technique. In this work, a different feeding technique which is the proximity-feed is adopted. Moreover, new techniques are applied to acquire the band-notch property, in which a circular patch is placed non-concentrically in a ground plane aperture (GPA), with a microstrip line on the other side of the substrate. The band-notch property is obtained by using three different techniques. The first technique uses a single complementary split ring resonator (CSRR) etched off the circular patch. In the second technique, a complementary spiral loop resonator (CSLR) is etched off the circular patch. In the third technique, a U-shaped slot is etched off the microstrip line. The main idea of these techniques is to adjust the resonant frequency of the etched slots with the required rejected band, to provide the band-notch property over the desired frequency range. The proposed prototype antenna is fabricated. Simulated results and measured data are presented.

2. DESIGN PROCESS

A parametric study of the proposed antenna is carried out to optimize the design of the antenna using the commercially available Zeland IE3D software that is based on method of moments (MoM). Based on several parametric studies, the optimized UWB prototype antenna is designed with the following dimensions: A circular radiating patch of radius $r = 6.0\,\text{mm}$ is placed non-concentrically inside a circular slot of radius $R = 12.0\,\text{mm}$ etched off the ground plane This circular slot represents a ground plane aperture (GPA). The distance between the lower edge of the circular patch and the lower edge of the circular slot is 1.0 mm. The circular patch is excited using a $50\,\Omega$ proximity-feed microstrip line placed on the other side of the substrate, with width $w_f = 3.0\,\text{mm}$ and length $l_f = 11.5\,\text{mm}$ as illustrated in Figures 1(a) and 1(b). The antenna is etched on a $30 \times 30\,\text{mm}^2$ FR4 substrate with relative permittivity of 4.7 of a loss tangent $\tan\delta = 0.02$ and a thickness $h = 1.5\,\text{mm}$.

In order to obtain the band-notch property either one of three methods are implemented, one uses a single CSRR (Figure 1(c)), the other uses a CSLR (Figure 1(d)) which are etched off the circular patch, and a third method is implementing a U-shaped slot etched off the microstrip feed-line (Figure 1(e)).

The external radius of the single CSRR element is $r_{ext} = 3.0\,\text{mm}$, its gap is $g = 1.5\,\text{mm}$. The ring is of uniform width 0.5 mm. The unit cell of the CSLR element has the following dimensions: the outer length $L = 3.2\,\text{mm}$, spiral loop line width $w = 0.4\,\text{mm}$, and the other dimensions are $c = 0.4\,\text{mm}$, $d = 1.2\,\text{mm}$. The three sides of the U-shaped slot are L_1, L_2, and L_3. These lengths are optimized to control the band-notch performance. The U-shaped slot is of a uniform width 0.25 mm and of dimensions of $L_1 = L_2 = 7.5\,\text{mm}$, and $L_3 = 1.5\,\text{mm}$.

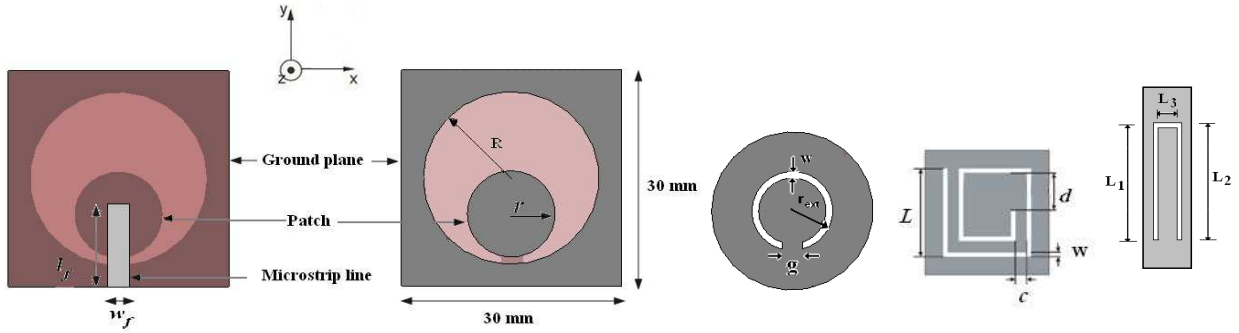

Figure 1: Geometry of the proposed band-notched UWB antenna. (a) Top view. (b) Bottom view. (c) Single CSRR etched off the circular patch. (d) CSLR unit cell. (e) Microstrip-feed line integrated with U-shaped slot.

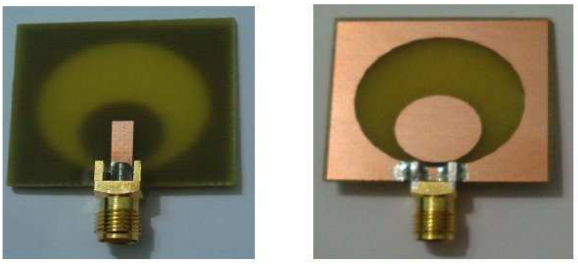

Figure 2: Photograph of the proposed prototype UWB antenna. (a) Top-view. (b) Bottom-view.

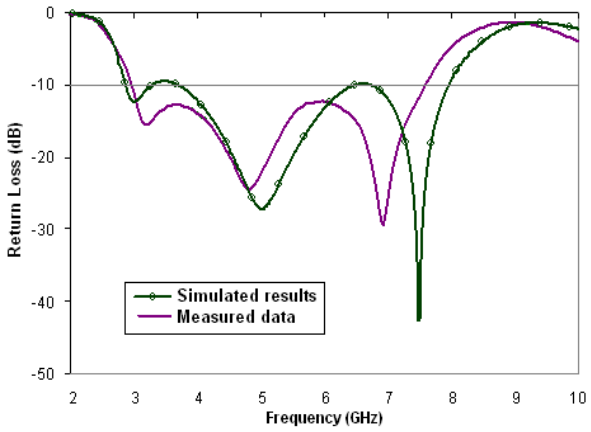

Figure 3: Simulated and measured return loss versus frequency of the proposed prototype UWB antenna.

3. RESULTS AND DISCUSSIONS

The proposed prototype antenna is simulated using IE3D software and also is fabricated using photolithographic technique as shown in Figure 2. The fabricated antenna was tested using vector network analyzer (HP8719) for the proposed UWB. Figure 3 illustrates the simulated results and measured data of the return loss as a function of frequencies. The simulation results show an impedance bandwidth from 2.85 GHz to 7.95 GHz whereas the measured data show a less bandwidth, in spite of the resemblance of the two curves. This minor discrepancy may be attributed to fabrication tolerance, and to the spatial closeness of the connector to the radiating slot and the patch.

Dimensions adjustment of the resonator slots can give the proposed antenna appropriate UWB performance and band notching suitable to avoid interference with the WLAN and HIBERLAN/2 services. Figure 4 and Figure 5 show the effect of a single split ring resonator placed on the antenna to control the band notching and bandwidth characteristics of the antenna. It is observed that, when the split ring external radius, r_{ext} decreases the center frequency of the band notch increases until it vanishes ($r_{ext} = 2.5\,\text{mm}$). On the other hand, the band notch location can be adjusted by tuning the split ring gap, g. For the split ring external radius $r_{ext} = 3.0\,\text{mm}$ and $g = 1.5\,\text{mm}$

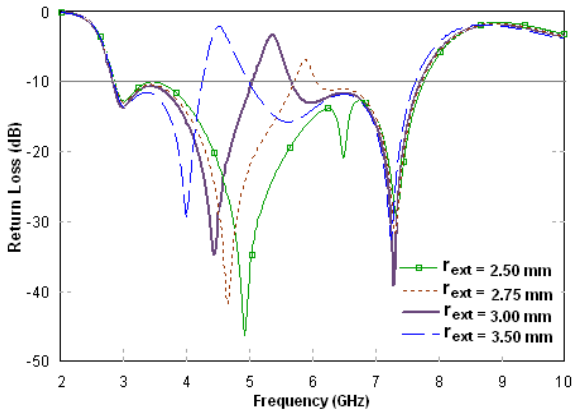

Figure 4: Simulated return loss versus frequency of the proposed antenna integrated with a single CSRR with $w = 0.5\,\text{mm}$, $g = 1.5\,\text{mm}$, $r = 6.0\,\text{mm}$, $R = 12.0\,\text{mm}$, $w_f = 3.0\,\text{mm}$, and $l_f = 11.5\,\text{mm}$, for different values of r_{ext}.

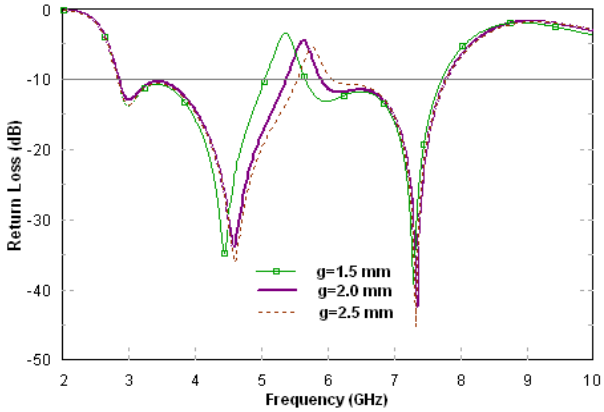

Figure 5: Simulated return loss versus frequency of the proposed antenna integrated with a single CSRR with $r_{ext} = 3.0\,\text{mm}$, $w = 0.5\,\text{mm}$, $r = 6.0\,\text{mm}$, $R = 12.0\,\text{mm}$, $w_f = 3.0\,\text{mm}$, and $l_f = 11.5\,\text{mm}$, for different values of g.

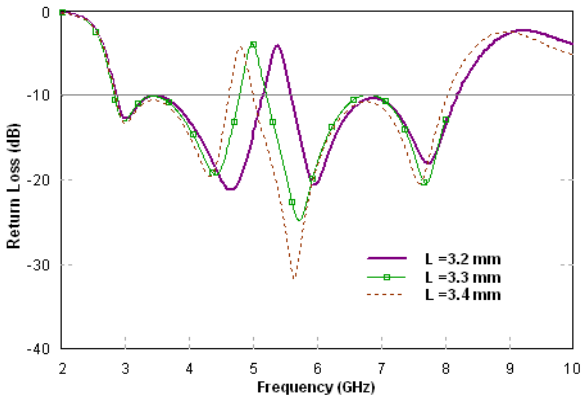

Figure 6: Simulated return loss versus frequency of the proposed antenna integrated with CSLR with $w = c = 0.4\,\text{mm}$, $d = 1.2\,\text{mm}$, $r = 6.0\,\text{mm}$, $R = 12.0\,\text{mm}$, $w_f = 3.0\,\text{mm}$, and $l_f = 11.5\,\text{mm}$, for different values of the spiral loop length L.

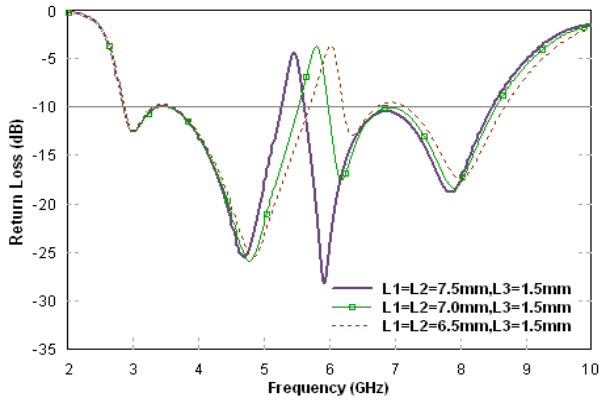

Figure 7: Simulated return loss versus frequency of the proposed antenna proximity-fed of a microstrip line integrated with a U-shaped slot with $w_f = 3.0\,\text{mm}$, $l_f = 11.5\,\text{mm}$, $r = 6.0\,\text{mm}$, and $R = 12.0\,\text{mm}$, for different values of the slot lengths L_1, L_2, L_3.

with keeping the other parameters unvaried, the antenna can cover the bandwidth from 2.83 GHz to 7.72 GHz with notched frequency band from 5.06 GHz to 5.65 GHz.

Etching a CSLR off the patch is the second proposed method to get a band-notch in the operated frequency band. The dimensions of the CSLR element are: $L = 3.2\,\text{mm}$, $w = 0.4\,\text{mm}$, $c = 0.4\,\text{mm}$, and $d = 1.2\,\text{mm}$. Figure 6 shows the effect of the variation of L on the return loss. The results show that as L decreases the center frequency of the band notch increases. By adjusting the dimensions to be $L = 3.2\,\text{mm}$, $w = 0.4\,\text{mm}$, $c = 0.4\,\text{mm}$, and $d = 1.2\,\text{mm}$ a bandwidth from 2.86 GHz to 8.19 GHz with band rejection from 5.16 GHz to 5.59 GHz is obtained.

To achieve a well defined band-notch a third alternative technique can be used in which a U-shaped slot is integrated on the microstrip feed-line as shown in Figure 1(e). The three lengths of the slot L_1, L_2, and L_3, are used to optimize the band-notch performance. Results of the simulated return loss of the proposed antenna using this technique are shown in Figure 7. The results illustrate that when the total length of the U-shaped slot decreases the central frequency of the band notch increases. The optimal dimensions of the U-shaped slot are $L_1 = L_2 = 7.5\,\text{mm}$ and $L_3 = 1.5\,\text{mm}$ with a uniform width 0.25 mm. This optimal design gives a bandwidth from 2.86 to 8.48 GHz with a sharp band rejection from 5.26 to 5.61 GHz. When the length of the U-shaped slot is a one third of the wavelength of the notch center frequency, a destructive interference occurs. This causes the antenna to be none-responsive at that frequency. Hence a narrow frequency band can be filtered out while maintaining good matching over the rest of the UWB frequency band.

The effect of the resonating slots on the return loss of the proposed antenna is investigated. Figure 8 shows the simulated return loss for the proposed UWB antenna as a function of frequency with and without the resonator slots. Each of the three techniques CSRR, CSLR, and U-shaped slots as illustrated earlier are used. It is noticed from the figure that a good impedance matching over the UWB can be achieved. For example the proposed antenna with a proximity-fed microstrip line integrated with U-shaped slot has a wider impedance bandwidth with a suitable band rejection of a central frequency at 5.5 GHz. The frequency response of the band-notched can be easily tuned by adjusting the dimensions of the slots.

The simulated peak gain versus frequency of the proposed antenna using each of the three techniques CSRR, CSLR, and U-shaped slots, is shown in Figure 9. The illustrated results reveal that the antenna gain varies from 3.05 dBi to 5.86 dBi over the operating frequency range within the UWB, almost the same as that of the prototype antenna. At the notched band, the antenna gain sharply reduced to about $-2.9\,\text{dBi}$. The maximum gain of the proposed antenna is 5.86 dBi at frequency 7.88 GHz. The radiation efficiency is almost 90% excluding the rejected band.

The radiation characteristics of the proposed antenna are also investigated. Figure 10 illustrates the simulated results of the far-field radiation patterns of E_θ and E_φ in the yz and xz planes at 6.0 GHz. The proposed antenna is characterized by omnidirectional patterns in the yz plane (E-plane), while it is a quasi-omnidirectional pattern in the xz plane (H-plane). Also the figure shows that the cross-polarized signal level is higher than the co-polarized signal level in some directions. It is obvious from the results that the radiation patterns are acceptable over the UWB bandwidth. Simulated results, not shown, showed that the radiation patterns of the proposed antenna with any

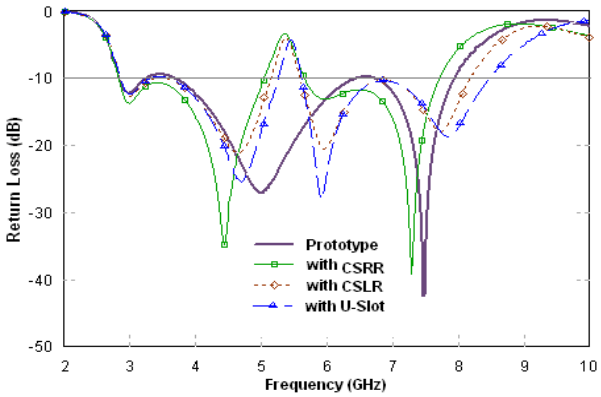

Figure 8: Simulated return loss versus frequency of the proposed prototype antenna with and without the resonating slots.

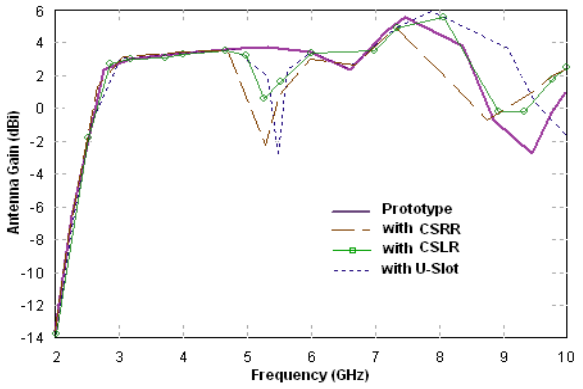

Figure 9: Simulated peak gain versus frequency of the proposed antenna with and without the resonating slots.

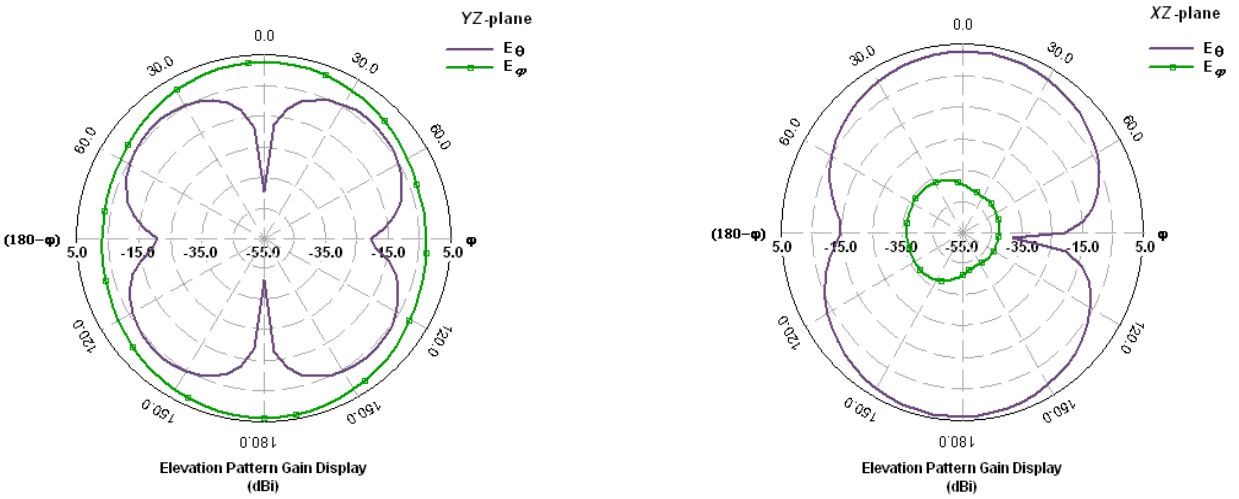

Figure 10: Simulated radiation patterns of E_θ and E_φ for the prototype antenna at 6.0 GHz. (a) yz plane, (b) xz plane.

of the three different resonating techniques are almost the same as those of the prototype antenna, whereas a little deviation was observed in the cross polarization in the xz-plane.

4. CONCLUSION

A novel ultra-wideband antenna with band-notch property was proposed. Matching between the circular radiator patch and the 50 ohm microstrip line is done through a proximity-feed technique. Three different techniques to introduce a band-notch were presented. The techniques are incorporating CSRR, CSLR and U-shaped slot in the design. The effect of adding these slots on the performance of the antenna is demonstrated. The designed antenna satisfies a 10 dB return loss requirement in the frequency band from 2.86 over to 8.48 GHz, with band-notch at 5.5 GHz frequency band. This band notch is corresponding to the WLAN and HIBERLAN/2 services. The prototype antenna is fabricated and the measured data of the return loss showed a good agreement with the simulated results. The proposed antenna featured suitable radiation patterns with good gain flatness over the UWB frequency band excluding the rejection band. Satisfactory antenna performance with a simple structure and small size makes the proposed proximity-feed antenna a good candidate for UWB applications.

REFERENCES

1. Schantz, H. G. and G. P. Wolenec, "Ultra-wideband antenna having frequency selectivity," U.S. Patent Publication No. 2003/0090436 A1, 2003.
2. Choi, W., K. Chung, J. Jung, and J. Choi, "Compact ultra-wideband printed antenna with band-rejection characteristic," *Electron. Lett.*, Vol. 41, No. 18, 990–991, Sep. 2005.
3. Chawanonphithak, K., C. Phongcharoenpanich, S. Kosulvit, and M. Krairiksh, "5.8 GHz notched UWB bidirectional elliptical ring antenna excited by circular monopole with curved slot," *Proc. Asia-Pacific Microwave Conf.*, 653–656, Dec. 2007.
4. Kim, Y. and D. H. Kim, "CPW-fed planar ultra wideband antennas having a frequency band notch function," *Electron. Lett.*, Vol. 40, No. 7, 403–405, Apr. 2004.
5. Ma, T. G. and S. J. Wu, "Ultrawideband band-notched folded strip monopole antenna," *IEEE Trans. Antennas Propag.*, Vol. 55, No. 9, 2473–2479, Sep. 2007.
6. Zhang, Y., W. Hong, C. Yu, Z.-Q. Kuai, Y.-D. Don, and J.-Y. Zhou, "Planar ultrawideband antennas with multiple notched bands based on etched slots on the patch and/or split ring resonators on the feed line," *IEEE Trans. Antennas Propag.*, Vol. 56, No. 9, 3063–3068, Sep. 2008.
7. Choi, J., S. Hong, and U. Kim, "The design of an UWB antenna with notch characteristic," *PIERS Online*, Vol. 3, No. 7, 987–990, 2007.
8. Kim, D.-O., N.-I. Jo, D.-M. Choi, and C.-Y. Kim, "Design of the novel band notched UWB antenna with the spiral loop resonators," *PIERS Online*, Vol. 6, No. 2, 173–176, 2010.

Optimization of Radiation Patterns of Array Antennas

V. Rajya Lakshmi[1] and G. S. N. Raju[2]

[1]Department of Electronics and Communication Engineering
Anil Neerukonda Institute of Technology and Sciences, Visakhapatnam, India
[2]Department of Electronics and Communications Engineering
AU College of Engineering (A), Andhra University, Visakhapatnam, India

Abstract— The array antennas exhibit flexibility in the design of radiation patterns. Conventionally, they are designed by controlling amplitude levels, phase levels space distribution of elements. In practice, for pre designed radiating elements in the array, one of the above parameters is considered for the design keeping the others fixed. However, in the present work the method of thinning is used to reduce side lobes without disturbing null to null beam width. When the elements of the array are uniformly excited, the first sidelobe level is found to be -13.5 dB. It is of interest here to reduce them considerably from the conventional level. The methodology involves the application of genetic algorithm to blind the required radiating elements in such a way the resultant pattern is optimized.

1. INTRODUCTION

Antenna array is formed by assembling of radiating elements in an electrical or geometrical configuration. Total field of the antenna array is found by vector addition of the fields radiated by each individual element [1]. In an array of identical elements, five controls that can be used to shape the overall pattern of the antenna are geometrical configuration of the overall array, relative displacement between elements, excitation amplitude of individual elements, excitation phase of individual elements, and relative pattern of the individual elements [2]. Thinning an array means turning off some elements in a uniformly spaced or periodic array to create a desired amplitude density across the aperture. Thinning an array to produce low sidelobes is much simpler than more general problem of non uniform spacing the elements [3]. Low sidelobe antenna arrays are becoming an increasingly important component of high performance electronic systems, particularly those operating in heavy clutter and jamming environments [4]. In the problem of large array thinning, the number of all possible combinations is large and it is 2^N where N is number of elements. Hence checking every possible combination to find the optimum one is nearly impossible. One needs a faster and more reliable method to find the optimum solution [5]. No deterministic method can be found for array thinning; instead there are probabilistic methods which focus on density of on elements in different parts of array and its effect on far field pattern. Also non gradient based optimization method, GA is referred to as one of the efficient methods which is capable of handling complex problems with many independent variables [6, 7].

The objective of this paper is to find a configuration for a thinned array which has a relative sidelobe level as low as possible and without enhancing the null to null beam width (NNBW) considerably.

2. GENETIC ALGORITHM

A Genetic algorithm offers an alternative to traditional search algorithms. It is a global optimization algorithm inspired by the well known biological processes of genetics and evolution. A combination of genetics and evolution is analogous to numerical optimization in that they both seek to find a good result within constraints on the variables. Input to an objective function is a chromosome. The output of the objective function is known as fitness. Each chromosome consists of genes or individual variables. A group of chromosomes is known as a population.

Genetic algorithms differ from most optimization methods, because it has the following characteristics [8].

1. It works with a coding of the parameters, not the parameters themselves.
2. It searches from many points instead of a single point.
3. It doesn't use derivatives.
4. It uses random transition rules, not deterministic rules.

GA (Genetic Algorithm) composed of three operators: Reproduction, Cross over and Mutation. Reproduction is the process in which the genetic information of an existing individual string is copied into the new population according to its fitness. After reproduction, the cross over operator creates two new individuals from two existing ones by genetic recombination. The mutation operator plays a key role in GAs, since it permits the creation of a new individual from an existing one by randomly one or more characters in a randomly chosen individual [9].

3. ARRAY THINNING AND GA

The radiating elements in the array of present interest are considered to be point sources spaced $d = \lambda/2$ apart. A symmetric linear array is shown in Fig. 2. Mathematically, the array factor of a $2N$ element array is given by [10].

$$E(\theta) = 2\sum_{n=1}^{N} A_n e^{j\varphi_n} \cos\left[k\left(n-0.5\right)d\left(\cos\theta - \cos\theta_0\right)\right] \tag{1}$$

Here,

k = wave number, $2\pi/\lambda$, λ = wave length.

θ = the angle measured from the axis of the array, θ_0 = steering angle.

(A_n, φ_n) = excitation of current for the nth element on either side of the array.

$A_n = 1$ or 0 for thinned arrays, $\varphi_n = 0$.

d = spacing between the elements of the array.

The fitness function associated with this array is the maximum SLL of its associated far field pattern to be minimized. The general form of the fitness function is given by

$$\text{Fitness} = \max\left(20\log_{10}\left(|E(\theta)|\right)/\left(\max|E(\theta_0)|\right)\right) \tag{2}$$

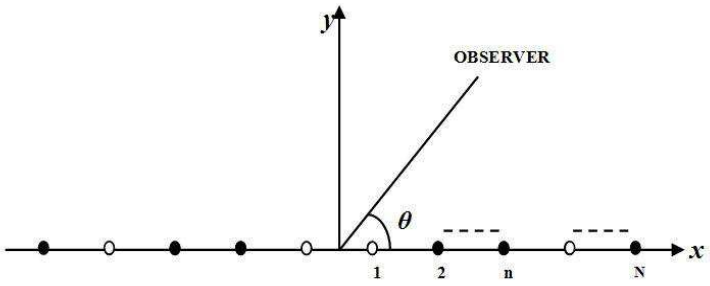

Figure 1: Geometry of $2N$ element symmetric linear array placed along the x-axis.

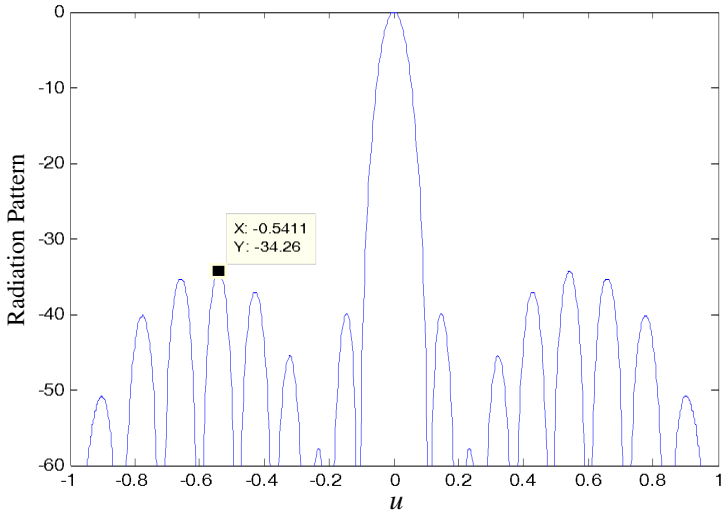

Figure 2: Radiation pattern of 20 elements linear array.

$$\max|E(\theta)| = |E(\theta_0)| \quad -\pi/2 \le \theta \le \pi/2,\ \theta \ne 0^\circ$$

4. RESULTS

Results for optimizing the relative sidelobe level of a linear array of 20, 50, 100 elements are presented below. Fig. 2 shows the radiation pattern of an array of 20 point sources after 50 iterations. The maximum relative sidelobe level is −34.26 dB. The thinned configuration of half of the array is shown in Fig. 3. Remaining array excitation levels are just mirror image of the right

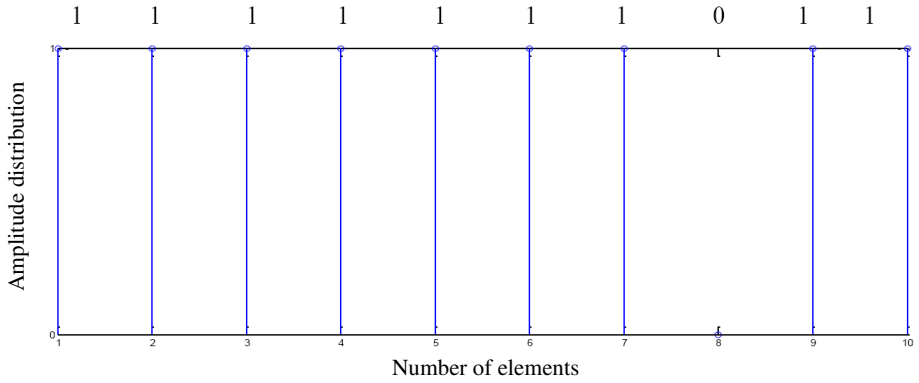

Figure 3: Thinned configuration of 20 elements linear array.

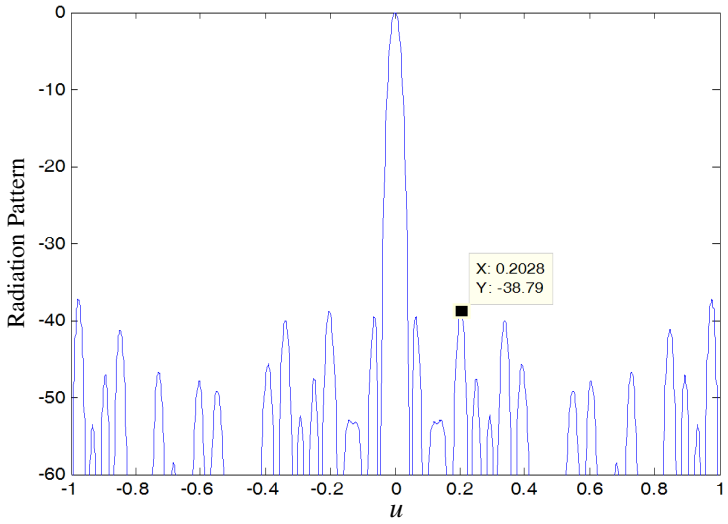

Figure 4: Radiation pattern of 50 elements linear array.

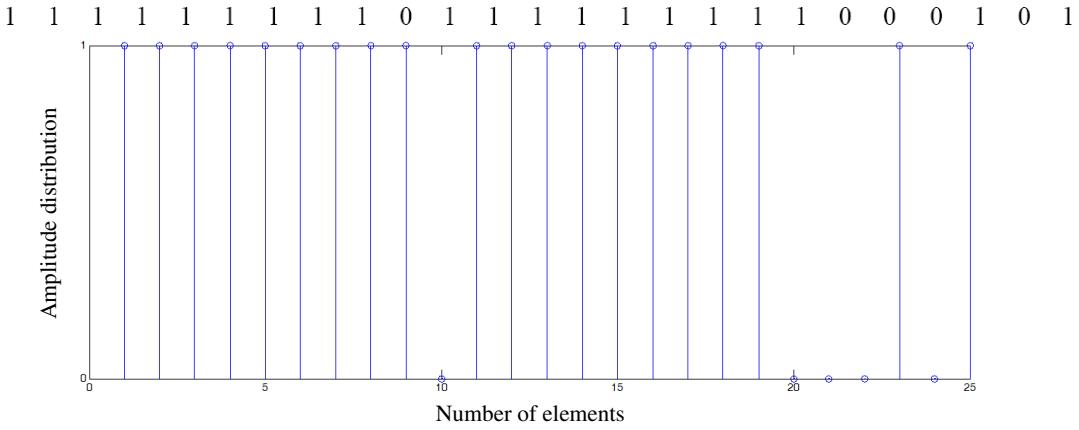

Figure 5: Thinned configration of the 50 element linear array.

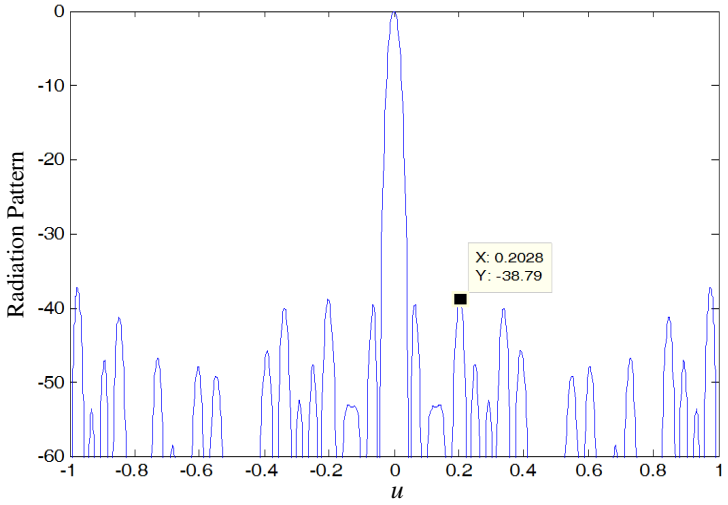

Figure 6: Radiation pattern of 100 element linear array.

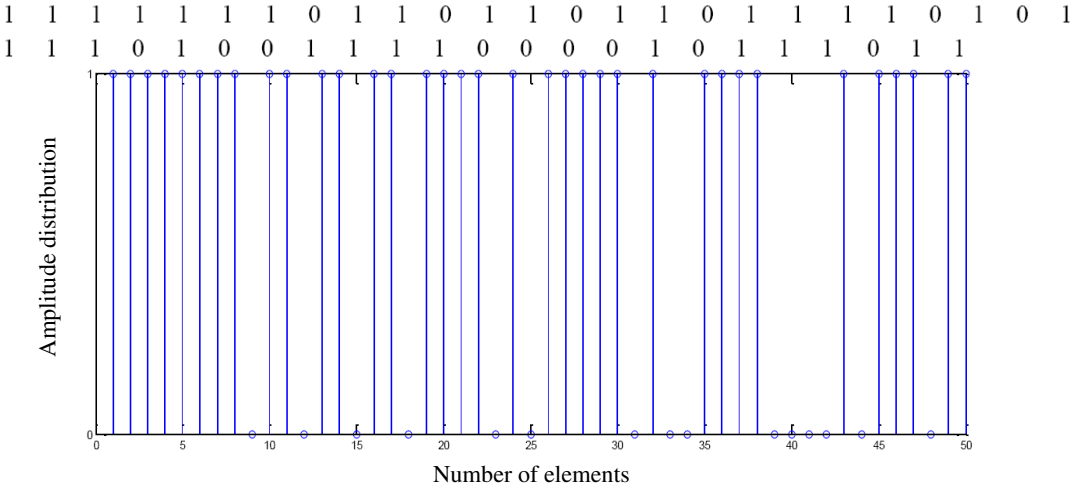

Figure 7: Thinned configuration of the 100 element linear array.

side because of the symmetry. Computations are carried out to obtain the patterns of the array when the elements of the array are 50. The corresponding Radiation pattern is shown in Fig. 4. The relative side lobe level observed is −38.79 dB. The excitation levels are plotted in Fig. 6. The procedure is repeated for 100 array elements. The obtained radiation pattern is shown in Fig. 7. The side lobe level is 37.24 dB. The excitation levels are plotted in Fig. 8. In all the cases, the beam width calculated is same as for a uniform array.

5. CONCLUSION

The thinned arrays provide cost effective solution compared to the uniform arrays. The application of genetic algorithm for optimization of radiation pattern characteristics of arrays is found to be very useful. The side lobe level is reduced from −13.5 dB to about −35 dB. The algorithm is found to be accurate and fast and the patterns are converged after 50 iterations. It is also evident from the results that the beam width of the main beam remains unaltered while reducing the first side lobe level. It is also possible to extend the algorithm to optimize the other parameters of the arrays.

REFERENCES

1. Raju, G. S. N., *Antennas and Propagation*, Pearson Education, 2005.
2. Balanis, C. A., *Antenna Theory Analysis and Design*, 2nd Edition, John Willy & Sons Inc., New York, 1997.
3. Haupt, R. L., "Thinned arrays using genetic algorithms," *IEEE Transactions on Antennas and Propagation*, Vol. 42, No. 7, Jul. 1994.

4. Haupt, R. L., "An introduction to genetic algorithm for electromagnetics," *IEEE Antennas and Propagation Magazine*, Vol. 37, No. 2, 7–15, Apr. 1995.
5. Ares-Pena, F. J., J. A. Rodriguez-Gonzalez, E. Villanueva-Lopez, and S. R. Rengarajan, "Genetic algorithms in the design and optimization of antenna array patterns," *IEEE Transactions on Antennas and Propagation*, Vol. 47, No. 3, 506–510, Mar. 1999.
6. Johnson, J. M. and Y. Rahmat-Samii, "Genetic algorithms in engineering electromagnetics," *IEEE Antennas and Propagation Magazine*, Vol. 39, No. 4, Apr. 1997.
7. Mahanti, G. K., A. Chakraborty, and S. Das, "Design of fully digital controlled reconfigurable array antennas with fixed dynamic range ratio," *Journal of Electromagnetic Waves and Applications*, Vol. 21, No. 1, 97–106, 2007.
8. Goldberg, D. E., *Genetic Algorithms*, Ch. 1–4, Addison-Wesley, New York, 1999.
9. Marcano, D., M. Jimenez, F. Duran, and O. Chang, "Synthesis of antenna arrays using genetic algorithms," *Proceedings of the IEEE International Caracas Conference on Devices, Circuits and Systems*, 328–332, 1995.
10. Soltankarimi, F., J. Nourinia, and C. Ghobadi, "Side lobe level optimization in phased array antennas using genetic algorithm," *ISSTA*, Sydney, Australia, Aug. 30–Sep. 2, 2004.

The Enhancement of the Light Scattering/Absorption from the Correlation Effect between Molecules

Wei-Xing Xu
NewTech Monitoring Inc., 1872 Birchview Dr, Oshawa, Ontario, L1K 3B9, Canada

Abstract— In this paper we first proposed the concepts of the correlated spectra/non-correlated spectra and discussed the correlation effect between molecules on the light scattering/absorption of the molecule. Furthermore, we also explored the potential application of this correlation effect in photo chemistry and related fields.

1. INTRODUCTION

In this paper, we will consider the situation where the light source and light scattering/absorption centre is correlated (Fig. 1) and study this correlation effect on the light scattering/absorption of molecule [1–8].

2. THEORY

2.1. Molecular Interaction System

In most cases, we have to consider the interaction among the molecules (Fig. 1). In this case, the wave function of molecule A becomes

$$\psi_A = \psi_A^{(0)} + \sum_{i \neq n} \frac{H_{in}^{'}}{E_n^0 - E_i^0} \psi_i^0 \tag{1}$$

$$E_n = E_n^0 + H_{nn}^{'} \tag{2}$$

In practice, we can set

$$H_{nn}^{'} \approx \overline{V_{ab}} \tag{3}$$

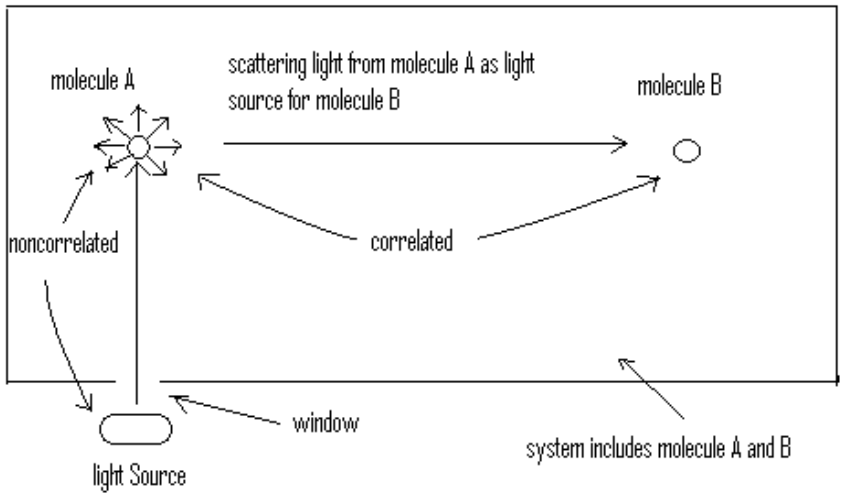

Figure 1: The illustration of the relations among the independent light source, correlated light source, molecule A and molecule B in the system.

where $\overline{V_{ab}} = \overline{V}_{ab}^{C,C} + \overline{V}_{ab}^{C,\mu} + \overline{V}_{ab}^{\mu,Q} + \overline{V}_{ab}^{\mu,\mu} + \overline{V}_{ab}^{\mu,Q} + \overline{V}_{ab}^{Q,Q}$, in which each term represented different molecular interactions [9–12].

$$\begin{aligned} C_k(t) &= \frac{H_{kl}^{"}}{i\hbar}\int_{-\infty}^{t} e^{i\omega_{kl}t'} f(t')dt' \\ &= \frac{1}{i\hbar}\left\langle \left(\psi_{Ak}^0 + \sum_{i\neq k}\frac{H_{ik}^{'}}{E_k^0 - E_i^0}\psi_i^0\right)\left|H^{"}(r)\right|\left(\psi_{Al}^0 + \sum_{i\neq l}\frac{H_{il}^0}{E_l^0 - E_i^0}\psi_i^0\right)\right\rangle \int_{-\infty}^{t} e^{i\omega_{kl}t'} f(t')dt' \\ &= \frac{1}{i\hbar}(H_1 + H_2 + H_3 + H_4) \end{aligned} \tag{4}$$

where

$$H_1 = \frac{1}{i\hbar}\left\langle \psi_{Ak}^0 \left|H^{"}(r)\right| \psi_{Al}^0\right\rangle \int_{-\infty}^{t} e^{i\omega_{kl}t'} f(t')dt \tag{5}$$

$$H_2 = \frac{1}{i\hbar}\left\langle \psi_{Ak}^0 \left|H^{"}(r)\right| \sum_{i\neq l}\frac{H_{il}^{'}}{E_l^0 - E_i^0}\psi_i^0\right\rangle \int_{-\infty}^{t} e^{i\omega_{kl}t'} f(t')dt \tag{6}$$

$$H_3 = \frac{1}{i\hbar}\left\langle \sum_{i\neq k}\frac{H_{ik}^0}{E_k^0 - E_i^0}\psi_i^0 \left|H^{"}(r)\right| \psi_{Al}^0\right\rangle \int_{-\infty}^{t} e^{i\omega_{kl}t'} f(t')dt \tag{7}$$

$$H_4 = \frac{1}{i\hbar}\left\langle \sum_{i\neq k}\frac{H_{ik}^0}{E_k^0 - E_i^0}\psi_i^0 \left|H^{"}(r)\right| \sum_{i\neq l}\frac{H_{il}^0}{E_l^0 - E_i^0}\psi_i^0\right\rangle \int_{-\infty}^{t} e^{i\omega_{kl}t'} f(t')dt \tag{8}$$

Comparing with the expressions of free molecule [8], the H_2, H_3 and H_4 come from contribution of the molecular interaction to the scattering/absorption probability of molecule A.

2.2. Correlated System

In this section, we would like to consider the system in which not only the molecular interaction was taken into account but also the correlation between the light source (molecule A, see Fig. 1) and scattering/absorption centre (molecule B, see Fig. 1) is included [13–19].

In this case,

$$\psi_{aa}^0 = \psi_A^0 + K\psi_B^0 \tag{9}$$

where $K = 2N\int \psi_A^0\psi_B^0 d\tau$, N is the number of molecules around the molecule A.

Considering the molecular interaction contribution,

$$\psi_{aa} = \psi_{aa}^0 + \sum_{i\neq n}\frac{H_{in}}{E_n^0 - E_i^0}\psi_i^0 = \psi_A^0 + K\psi_B^0 + \sum_{i\neq n}\frac{H_{in}}{E_n^0 - E_i^0}\psi_i^0 \tag{10}$$

Similarly, we can get

$$\begin{aligned} i\hbar\frac{dC_k}{dt} &= \lambda\sum_m \left(\left(\psi_{aak}^0 + \sum_{i\neq k}\frac{H_{ik}}{E_k^0 - E_i^0}\psi_{aai}^0\right)\left|H^{'}(r,t)\right|\left(\psi_{aal}^0 + \sum_{i\neq l}\frac{H_{il}}{E_l^0 - E_i^0}\psi_{aai}^0\right)\right) C_m \\ &= \lambda\sum_m \left(\psi_{Ak}^0 \left|H^{'}(r,t)\right| \psi_{Al}^0\right) C_m \\ &\quad +\lambda\sum_m \left(\psi_{Ak}^0 \left|H^{'}(r,t)\right| K\psi_{Bl}^0\right) C_m \\ &\quad +\lambda\sum_m \left(\psi_{Ak}^0 \left|H^{'}(r,t)\right| \sum_{i\neq l}\frac{H_{il}}{E_l^0 - E_i^0}\psi_i^0\right) C_m \end{aligned}$$

$$
\begin{aligned}
&+\lambda\sum_m\left(K\psi_{Bl}^0\left|H^{'}(r,t)\right|\psi_{Al}^0\right)C_m\\
&+\lambda\sum_m\left(K\psi_{Bk}^0\left|H^{'}(r,t)\right|K\psi_{Bl}^0\right)C_m\\
&+\lambda\sum_m\left(K\psi_{Bk}^0\left|H^{'}(r,t)\right|\sum_{i\neq l}\frac{H_{il}}{E_l^0-E_i^0}\psi_i^0\right)C_m\\
&+\lambda\sum_m\left(\sum_{i\neq k\frac{H_{ik}}{E_k^0-E_i^0}\psi_i^0}\left|H^{'}(r,t)\right|\psi_{Al}^0\right)C_m\\
&+\lambda\sum_m\left(\sum_{i\neq k\frac{H_{ik}}{E_k^0-E_i^0}}\psi_i^0\left|H^{'}(r,t)\right|K\psi_{Bl}^0\right)C_m\\
&+\lambda\sum_m\left(\sum_{i\neq k}\frac{H_{ik}}{E_k^0-E_i^0}\psi_i^0\left|H^{'}(r,t)\right|\sum_{i\neq l}\frac{H_{il}}{E_l^0-E_i^0}\psi_i^0\right)C_m
\end{aligned}
\tag{11}
$$

that is,

$$C_k=H_1+H_2+H_3+H_4+H_5+H_6+H_7+H_8+H_9 \tag{12}$$

where

$$H_1=\frac{1}{i\hbar}\left\langle\psi_{Ak}^0\left|H^{'}(r,t)\right|\psi_{Al}^0\right\rangle \tag{13}$$

$$H_2=\frac{1}{i\hbar}\left\langle\psi_{Ak}^0\left|H^{'}(r,t)\right|K\psi_{Bl}^0\right\rangle \tag{14}$$

$$H_3=\frac{1}{i\hbar}\left\langle\psi_{Ak}^0\left|H^{'}(r,t)\right|\sum_{i\neq l}\frac{H_{il}}{E_l^0-E_i^0}\psi_i^0\right\rangle \tag{15}$$

$$H_4=\frac{1}{i\hbar}\left\langle K\psi_{Bk}^0\left|H^{'}(r,t)\right|\psi_{Al}^0\right\rangle \tag{16}$$

$$H_5=\frac{1}{i\hbar}\left\langle K\psi_{Bk}^0\left|H^{'}(r,t)\right|K\psi_{Bl}^0\right\rangle \tag{17}$$

$$H_6=\frac{1}{i\hbar}\left\langle K\psi_{Bk}^0\left|H^{'}(r,t)\right|\sum_{i\neq l}\frac{H_{il}}{E_l^0-E_i^0}\psi_i^0\right\rangle \tag{18}$$

$$H_7=\frac{1}{i\hbar}\left\langle\sum_{i\neq k}\frac{H_{ik}}{E_k^0-E_i^0}\psi_i^0\left|H^{'}(r,t)\right|\psi_{Al}^0\right\rangle \tag{19}$$

$$H_8=\frac{1}{i\hbar}\left\langle\sum_{i\neq k}\frac{H_{ik}}{E_k^0-E_i^0}\psi_i^0\left|H^{'}(r,t)\right|K\psi_{Bl}^0\right\rangle \tag{20}$$

$$H_9=\frac{1}{i\hbar}\left\langle\sum_{i\neq k}\frac{H_{ik}}{E_k^0-E_i^0}\psi_i^0\left|H^{'}(r,t)\right|\sum_{i\neq l}\frac{H_{il}}{E_l^0-E_i^0}\psi_i^0\right\rangle \tag{21}$$

Comparing with the free molecule and the system in which only the molecular interaction was included, we know that the H_2, H_4, H_5, H_6 and H_8 can be taken as the contribution mainly from the correlation effect between the molecule as the light source and the molecule as the light scattering/absorption centre to the light scattering/absorption probability of molecule A, whereas the H_3, H_7 and H_9 are the contribution mainly from the molecular interaction to the light scattering/absorption of the molecule A. In the same way, we can get the expression of C_k for molecule B.

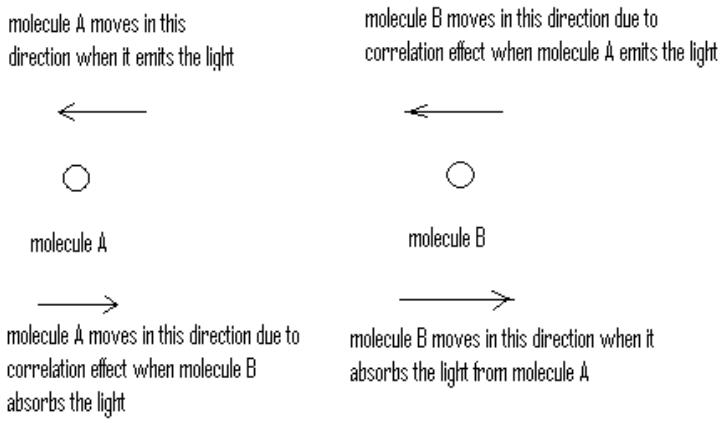

Figure 2: The illustration of the movement of molecule A and B in the processes of light emmission/absorption.

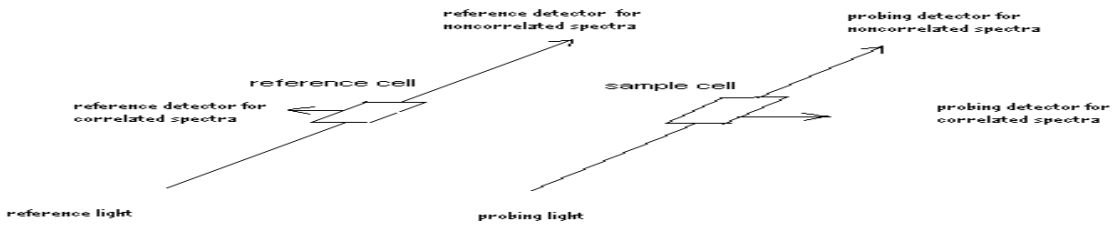

Figure 3: The illustration of the experimental scheme for the correlated and noncorrelated spectra.

For the correlated system, the scattering/absorption of molecule A gets the contribution from the molecule B by perturbation.

For the correlated spectra, the enhancement in absorption of molecule is easier to be observed than that in scattering of molecule, the reason is the scattering light is distributed in all directions, therefore, this distribution will reduce the intensity of the scattering light observed in the experiment.

3. FINAL REMARK

In this paper we discussed the correlation system and how the light scattering/absorption probability can be enhanced from the correlation effect. Even though we only include the first order correction based on the perturbation theory in our discussion, the researchers can include higher than first order correction following the same procedure. From the correlated spectra and noncorrelated spectra, we can get the detail information about the molecular structure and molecular interaction.

REFERENCES

1. Li, Y. Y., *Acta Physica Sinica*, Vol. 20, No. 2, 164, 1964.
2. Raman, C. V. and K. S. Krishnan, *Nature*, Vol. 122, 278, 1928.
3. Raman, C. V. and K. S. Krishnan, *Nature*, Vol. 122, 882, 1928.
4. Bloembergen, N., *Nonlinear Optics*, W. A. Benjamin, Inc., New York, 1965.
5. Born, M. and E. Wolf, *Principles of Optics*, Pergamon Press, London and New York, 1959.
6. Yariv, A. and J. P. Gordon, *Proc. IEE*, Vol. 51, 4, 1963.
7. Kundu, J., O. Neumann, et al., *J. Phys. Chem. C*, July 15, 2009, DOI:10.1021/jp903126f/.
8. Liboff, R. L., *Introductory Quantum Mechanics*, 4th Edition, Addison Wesley, 1301 Sansome St., San Francisco, CA94111, 2002.
9. Bird, R. B., J. O. Hirschfelder, and C. F. Curtiss, *Molecular Theory of Gases and Liquids*, John Wiley & Sons, Inc., New York, London, 1954.

10. Buckingham, A. D., P. W. Fowler, and J. M. Hutson, *Chem. Rev.*, Vol. 88, 963, 1988.
11. Chalasinski, G. and M. Gutowski, *Chem. Rev.*, Vol. 88, 943, 1988.
12. Buckingham, A. D., *Adv. Chem. Phys.*, Vol. 12, 107, 1967.
13. Glimsdal, E., P. Norman, and M. Lindgren, *J. Phys. Chem. B*, Sept. 28, 2009, DOI:10.1021/jp905437c/.
14. Revillod, G., N. Nishi, and T. Kakiuchi, *J. Phys. Chem. B*, Oct. 20, 2009, DOI:10.1021/jp907416m/.
15. Ishiyama, T. and A. Morita, *J. Phys. Chem. C*, Aug. 26, 2009, DOI:10.1021/jp9060957/.
16. Ishiyama, T. and A. Morita, *Chem. Phys. Lett.*, Vol. 431, 78, 2006.
17. Soos, M., M. Lattuada, and J. Sefcik, *J. Phys. Chem. B*, Oct. 21, 2009, DOI:10.1021/jp907284t/.
18. Hunt, K. L. C. and J. E. Bohr, *J. Chem. Phys.*, Vol. 84, No. 11, 6141, 1986.
19. Wang, C. H., *J. Chem. Phys.*, Vol. 98, No. 4, 3457, 1993.
20. http://www.rsc.org/membership/Networking/InterestGroups/MossbauerSpect/Intropart1.asp/.
21. Bloembergen, N., W. H. Lowdermilk, M. Matsuoka, and C. S. Wang, *Phys. Rev. A*, Vol. 3, No. 1, 404, 1971.
22. Herman, R. M. and M. A. Gray, *Phys. Rev. Lett.*, Vol. 19, No. 15, 825, 1967.
23. Cuevas, M. and R. A. Depine, *Phys. Rev. Lett.*, Aug. 28, 2009, DOI:10.1103/physRevLett.103.097401/.

Self-field Theory, General Relativity and Quantum Theory

A. H. J. Fleming
Biophotonics Research Institute, Melbourne, Australia

Abstract— There are theoretical similarities between general relativity (GR) and quantum field theory (QFT). Among the most fundamental are that both are based on 2nd order wave equations and their associated potential theories and gauge considerations. In comparison SFT is based on the 1st order Maxwellian with its field variables that have a much reduced emphasis on gauge. Both GR and QFT are based around single particle analyses rather than the mutual effects that couple particles together studied in SFT. Finally both GR and quantum theory employ a metric that in the view of SFT serves to accommodate the over constraint of the basic equations. In both cases this is linked to a theoretical requirement for a zero-mass photon. Thus both quantum theory and GR depend upon a zero mass photon and hence from the point of view of SFT both quantum theory and GR are theoretical approximations. For quantum theory zero mass springs from the earliest observations of beta decay and again when a negligible rest mass of the photon could hardly be compared with the seemingly endless radiation from within the nucleus of the bombs dropped on Hiroshima and Nagasaki in 1945. The cosmological principle that had its genesis in the Vatican's unscientific and dogmatic dealings with Galileo was a way to avoid having any universal centre of gravity thus making the same mistake again. Nevertheless it is only an approximation in the light of SFT where it is seen that non-homogeneity and anisotropy are both present in the gravitational structure itself where space is divided into different gravitational regions. This structure depends on the composite nature and non-zero mass of the photon. The space within the Universe cannot be thought of as the surface of an expanding balloon other than as a theoretical approximation that holds for GR. It is known that at smaller than cosmological domains the cosmological principle does not hold for instance for any possible surviving location of the Big Bang. We may think of a biological tissue such as liver where the dielectric constant is averaged over the microstructure such as biological cells. While such an approximation is useful for numerical estimation it cannot be assumed to hold in any fine detail across smaller domains; this holds for both a homogenous isotropic model of liver and of the Cosmos.

1. INTRODUCTION

Quantum field theory (QFT) derived around 1927 and general relativity (GR) around 1915 provided two different methods of applying relativity to physical problems. Dirac factorized the Klein-Gordon wave equation. In this form a particle of mass m has spin that is related to relativity.

$$\left[\nabla^2 + \frac{m^2c^2}{\hbar^2}\right]\psi(r) = 0 \tag{1a}$$

$$(\gamma_\mu \partial_\mu + im)\,(\gamma_\mu \partial_\mu - im)\,\psi = 0 \tag{1b}$$

On the other hand relativistic motion is introduced in special relativity (SR) and GR via a metric which applies to the whole space-time rather than any particular particle. For SR the metric is that of Minkowski space. In this particular form the space is a 'flat' metric. Moreover, the properties of space-time are invariant and thus the speed of light is considered constant throughout space-time. Of further note space-time is symmetric and bilinear.

$$-(e_0)^2 = (e_1)^2 = (e_2)^2 = (e_3)^2 = 1 \tag{2a}$$

$$\langle e_\mu, e_\mu \rangle = \eta_{\mu\nu} \tag{2b}$$

$$\eta = \begin{pmatrix} -1 & 0 & 0 & 0 \\ 0 & 1 & 0 & 0 \\ 0 & 0 & 1 & 0 \\ 0 & 0 & 0 & 1 \end{pmatrix}. \tag{2c}$$

General relativity applies a more general metric of curvilinear space-time to a wave equation containing second order derivatives amongst other terms called the Einstein field equations where R_{ab} is Ricci tensor, g_{ab} is the symmetric bilinear metric of space-time, and T_{ab} is the energy-momentum

Figure 1: Plot of the bispinorial motion of a particle, e.g., electron, in hydrogen atom.

tensor. The proportionality constant is given as $\kappa = 8\pi G/c^4$, with G the gravitational constant and c the speed of light.

$$R_{ab} - \frac{1}{2}Rg_{ab} = \kappa T_{ab} \tag{3a}$$

$$\langle g_\mu, g_\nu \rangle = g_{\mu\nu} \tag{3b}$$

As an example we take the special case applying to a spherically symmetric body such as a planet or a black hole, where the coordinates are (ct, r, θ, ϕ). The Schwarzschild metric can be written as

$$g_{ab} = \begin{pmatrix} \left(1 - \frac{2GM}{rc^2}\right) & 0 & 0 & 0 \\ 0 & -\left(1 - \frac{2GM}{rc^2}\right)^{-1} & 0 & 0 \\ 0 & 0 & -r^2 & 0 \\ 0 & 0 & 0 & -r^2 \sin^2\theta \end{pmatrix}. \tag{4}$$

In SFT each particle performs a bispinorial relativistic motion where in (5) each spinor refers to a centre of motion; an orbital centre of motion and a cyclotron motion both of which rotate. This gives a coupled spherical coordinate system (see Fig. 1). What must be realised is that at the atomic level the total separation is not a distance but two distances orthogonal to each other, a bilinear form similar to GR. Hence the assumption that these distances can be combined as Pythagorean distances is incorrect. They form an eigensolution to the problem for example the electron inside an atom. Moreover the space-time and speed of light can be inhomogeneous inside the one problem and solved, e.g., via finite differences

$$r\left(r_o, \omega_o, r_c, \omega_c\right) = r_o e^{j\omega_o t} + r_c e^{j\omega_c t} \tag{5}$$

There is an intimate relationship between Heisenberg's uncertainty principle and the equations of SFT which are not wave equations but the first order Maxwellian system comprising four Maxwell equations and the Lorentz equation. Instead of a single HUP inequality equation, there are two exact SFT equations. HUP is applied as commutation relationships in QFT. Moreover the Maxwellian is 1st order in comparison with the wave equations which are 2nd order. In terms of solution methods the 2nd order equations require integral equation methods whereas the 1st order Maxwellian requires differential methods; in fact there is an analytic solution to the Maxwellian greatly mitigating the computational work load compared with the integral equation methods associated with both GR and QFT.

2. CONSTRAINED EQUATIONS AND OVER-CONSTRAINED EQUATIONS

What is at issue from the point of view of SFT is an over-constrained model of the photon as a point source. This introduces uncertainty and the probabilistic nature of quantum theory. In addition the higher the order of the mathematics the more complex it becomes. This applies especially to differential forms of equations. So the question boils down to whether to use the EM wave equations or the first order ML equations as the basis of the mathematics. For instance many queries concern either gauge or symmetry. There is no such thing as a gauge theory in SFT because of the simplistic way gauge applies within SFT; further there are no vector and scalar potentials in SFT only the E- and H-fields. Again symmetry is achieved in a different way in SFT compared with QFT. Hence the issue of a non zero-mass photon is also answered in a mathematically different fashion to the symmetry-breaking presence of non zero mass fields within QFT. Finally relativity is inherent in the bispinorial form of mathematics and provides a novel way to incorporate relativity

within quantum theory. This also changes the way we view relativity to be physically palatable. Relativity's warping of space-time is intuitively digestible when it includes the hidden time and distance of internal photon motions.

Self-field theory provides a new way of viewing relativity. The internal and external motions of the photon help explain in a physically intuitive way how space is not actually warped but the vision our eyes see at relativistic speeds is warped. As Einstein knew, seeing is not always believing; straight lines could be curvilinear. In regards the general theory of relativity, Einstein's GR assumes a single form of gravitation acting across the entire Universe. To an approximation this is true but the actual situation is otherwise. SFT implies three main modifications to cosmological models based on GR as it currently stands: (1) Like CEM and its failure early in the 20th century to solve the atom, and quantum theory's lack of magnetic currents there is a lack of any stable solution due to the failure of models to examine mutual effects between masses. (2) The Universe contains more than one type of gravitation; a trispinorial form applies to galaxies, a 4-spinorial form may apply to super clusters, and maybe another form perhaps a 5-spinor applies to the Universe itself. The overall structure of the Universe is therefore not homogeneous or isotropic as assumed by GR. (3) Another important modification relates to the photon's non-zero mass and composite structure. If the Big Bang was hot enough there would have been an initial period where a sea of sub-photonic particles existed. This may be responsible for the inflationary period when the Universe expanded to near its present size at superluminal speeds. Sub-photonic particles of non-zero mass could travel at superluminal speeds and help solve the so-called horizon problem in a more intuitive way. Similarly the anisotropy observed within the Universe can be explained without recourse to quantum foam theories. These modifications all have implications for the various GR solutions obtained by Friedmann, Lemaître, De Sitter, Guth, and others including Einstein's own solution obtained in 1915. Instead of the similarity to fluid dynamics of current GR models a particle-field model can give another perspective on cosmological processes. Overall this suggests an early inflationary period that finished before an evolution towards the critical condition on density leading to a dynamic equilibrium within the Universe.

Both quantum theory and GR depend upon a zero mass photon and hence from the point of view of SFT both are theoretical approximations. For quantum theory zero mass springs from the earliest observations of beta decay and again when a negligible rest mass of the photon could hardly be compared with the seemingly endless radiation from within the nucleus of the bombs dropped on Hiroshima and Nagasaki in 1945. The cosmological principle that had its genesis in the Vatican's unscientific and dogmatic dealings with Galileo was a way to avoid having any universal centre of gravity thus making the same mistake again. Nevertheless it is only an approximation in the light of SFT where it is seen that non-homogeneity and anisotropy are both present in the gravitational structure itself where space is divided into different gravitational regions. This structure depends on the composite nature and non-zero mass of the photon. The space within the Universe cannot be thought of as the surface of an expanding balloon other than as a theoretical approximation that holds for GR. It is known that at smaller than cosmological domains the cosmological principle does not hold for instance for any possible surviving location of the Big Bang.

As an example of the way constrained and over constrained problems can be solved take a general linear system. $A_n^m \vec{x}_n = \vec{b}_n$

(a) where the system is square of order $m = 4$ and $n = 4$

$$\begin{bmatrix} a_{11} & a_{12} & a_{13} & a_{14} \\ a_{21} & a_{22} & a_{23} & a_{24} \\ a_{31} & a_{32} & a_{33} & a_{34} \\ a_{41} & a_{42} & a_{43} & a_{44} \end{bmatrix} \begin{bmatrix} x_1 \\ x_2 \\ x_3 \\ x_4 \end{bmatrix} = \begin{bmatrix} b_1 \\ b_2 \\ b_3 \\ b_4 \end{bmatrix}$$

The system has 4 real roots leading to physical solutions.

(b) where $m < n$, e.g., $m = 3$ and $n = 4$

$$\begin{bmatrix} a_{11} & a_{12} & a_{13} \\ a_{21} & a_{22} & a_{23} \\ a_{31} & a_{32} & a_{33} \end{bmatrix} \begin{bmatrix} x_1 \\ x_2 \\ x_3 \\ x_4 \end{bmatrix} = \begin{bmatrix} b_1 \\ b_2 \\ b_3 \end{bmatrix}$$

The system is under constrained and there is an infinite number of solutions.

(c) where $m > n$, e.g., $m = 4$ and $n = 3$

$$\begin{bmatrix} a_{11} & a_{12} & a_{13} & a_{14} \\ a_{21} & a_{22} & a_{23} & a_{24} \\ a_{31} & a_{32} & a_{33} & a_{34} \\ a_{41} & a_{42} & a_{43} & a_{44} \end{bmatrix} \begin{bmatrix} x_1 \\ x_2 \\ x_3 \end{bmatrix} = \begin{bmatrix} b_1 \\ b_2 \\ b_3 \\ b_4 \end{bmatrix}$$

The system is over constrained and there are no solutions. This over constrained case can be solved by choosing a metric, e.g., least squares, the Pythagorean distance, to minimize the error. This example is a direct analogue to the case of quantum theory where uncertainty is present and the photon is modeled without taking its internal structure into account. In case (a) exact solutions exist as in the case of SFT.

REFERENCES

1. Fleming, A. H. J., "Electromagnetic self-field theory and its application to the hydrogen atom," *Physics Essays*, Vol. 18, No. 3, 265-285, 2005
2. Fleming, A. H. J., "Self-field theory, analytic spectroscopy of the ordinary photon," *Proc. 2nd Electromagnetics Health and Environment Intl Conf.*, 18–23, Wroclaw, Poland, 2007
3. Fleming, A. H. J., "Analytic estimate for the mass of the photon," *PIERS Proceedings*, 1604–1607, Moscow, Russia, August 18–21, 2009.
4. Fleming, A. H. J., "Self-field theory — A possible gravitational structure for galaxies," *PIERS Proceedings*, 823–827, Cambridge, USA, July 5–8, 2010.
5. Fleming, A. H. J., *Self-field Theory — A New Mathematical Description of Physics*, Pan Stanford Publishing, 2011 (to be published).

Two-dimensional Tunable Plasma Photonic Crystal Filters

Limei Qi[1], **Fengqin Lu**[2], **and Liang Shang**[1]

[1]College of Physics and Engineering, Qufu Normal University
No. 57, West Jingxuan Road, Qufu 273165, China
[2]Group of Physics, Senior High School of Fengcheng, No. 1, Yingmou Road, Laiwu 271100, China

Abstract— Two types of two-dimensional plasma photonic crystal filters are studied in this paper, it is found that two-dimensional plasma photonic crystal consisting of plasma-filled dielectric rod structure can be used as filters in which the central frequency and bandwidth can be controlled by plasma frequency. When appropriate defect is introduced in it, a defect mode in the gap may appear, which can be adjusted by plasma density. These features of plasma-filled dielectric rod photonic crystal would have potential application in designing tunable photonic crystal filters.

1. INTRODUCTION

Since the pioneering work of Yablonovich [1] and John [2] in 1987, the past decades have witnessed an extended development in photonic crystal, also known as photonic band gap (PBG) materials. One of their important properties is to confine or to propagate electromagnetic waves within defects introduced in their structure, which opens many technical applications in photonic crystal filters, waveguides and cavities [3]. Early researches meanly focused on conventional photonic crystals consisting of dielectrics and metal metals materials. Since 2004, plasma photonic crystals (PPC) have been attracted much attention for its controllable PBG by plasma density [4]. One-dimensional (1D) PPC was usually composed of alternating thin plasma and dielectric material [5–12], for two-dimensional (2D) PPC, there are two types [13–16], the first type (type-1) is the periodic structure in which plasma rods are arranged in dielectric material, and the second type (type-2) is an antiparallel one consisting of dielectric rods in plasma. In this paper, 2D type-2 PPC is considered, it is found that this type structure with no defect can be used as tunable filters controlled by plasma frequency, and it would have narrow filter characteristics if appropriate defects are made in it.

2. THEORETICAL MODEL AND ANALYSIS

Figure 1(a) presents the type-2 PPC structure with Computer Simulation Technology (CST) model [17], the box is defined as plasma material with width $W = a$, length $L = 7a$ and height $H = 1.5a$, $a = 10\,\text{mm}$ is period length of the square lattice PPC, the circled rod is defined as dielectric with the relative dielectric constant $\varepsilon_a = 2.1$ and radius $r = 0.2a$. As for its boundary conditions [18], the xz and xy planes on each side of the box are assumed to be perfect magnetic condition (PMC) and perfect electric condition (PEC), respectively, and the yz planes are set as waveports, the excitation source is TM mode with electric field parallel to the rods. For plasma, the frequency-dependent dielectric function ε_b meets the Drude formula [4]:

$$\varepsilon_b(\omega) = 1 - \frac{\omega_p^2}{\omega^2}$$

where ω is the electromagnetic wave frequency, $\omega_p = (e^2 n_e/\varepsilon_0 m)^{1/2}$ is the electron plasma frequency with the electric density, electric quantity and electric quality are n_e, e and m respectively, ε_0 is the dielectric constant in vacuum.

Assumed $\omega_p a/2\pi c = 1$, transmission curve of the model is given in Fig. 1(b). The vertical axis denotes transmission magnitude varying from 0 to $-60\,\text{dB}$ and the horizontal axis means frequency varying from 0 to 45 GHz, it is seen that there are serials of pass and stop band regions. To demonstrate the transmission curve, dispersion curves calculated by modified plane wave method [15] are shown in Fig. 2. The left side shows dispersion curves in Γ-X direction which corresponds to the propagating direction of electromagnetic wave, the right side shows the transmission magnitude varying from 0 to $-30\,\text{dB}$. The transmission and dispersion curves have the same vertical axis, and the gray areas denote the band gaps, it is seen that band gaps in transmission curves are in agreement with those in dispersion curves.

If −30 dB is considered for Fig. 1(b), the transmission regions locate around 22 GHz ∼ 23 GHz, 32 ∼ 35 GHz, 37 ∼ 40 GHz and 41 ∼ 43 GHz, respectively. The first pass band is very narrow with the central frequency 22 GHz and width 1 GHz in the regions of 0 ∼ 32 GHz. To show how plasma frequency affects the pass band, transmission curves of different normalized plasma frequency $\omega_p a/2\pi c$ are given in Fig. 3, dot-dash, solid, and dash lines denote $\omega_p a/2\pi c = 0.8$, 1 and 1.2 respectively. It is seen the pass band shifts to the low frequency with central frequency 19.5 GHz and bandwidth 2.3 GHz for $\omega_p a/2\pi c = 0.8$, while the pass band shifts to the high frequency with central frequency 24.2 GHz and bandwidth 0.8 GHz for $\omega_p a/2\pi c = 1$. Therefore, with plasma frequency increasing, the first pass band shifts to high frequency with bandwidth decreasing, this type of 2D PPC can be used as tunable filters with the central frequency and bandwidth controlled by plasma frequency.

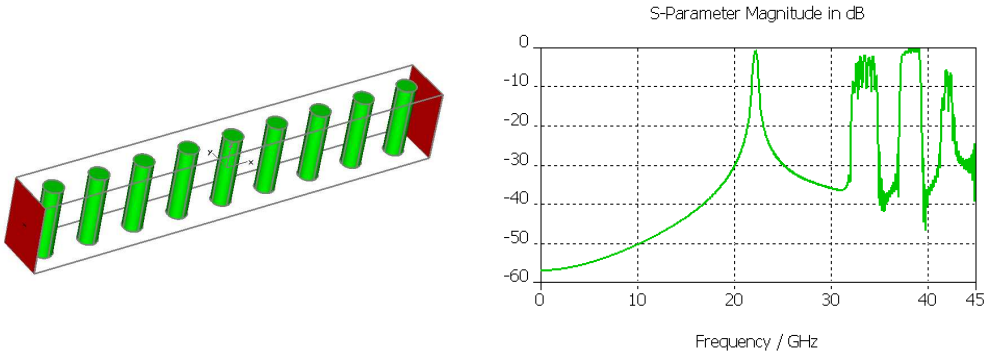

Figure 1: (a) CST model and (b) transmission curve for type-2 PPC with no defect.

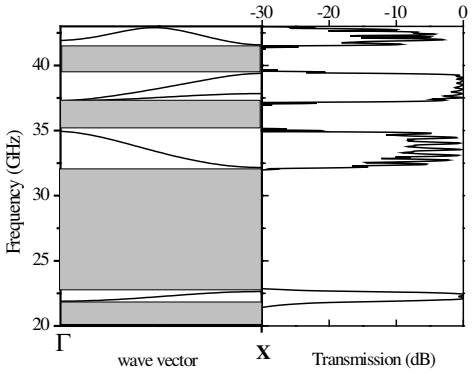

Figure 2: Transmission and dispersion curves.

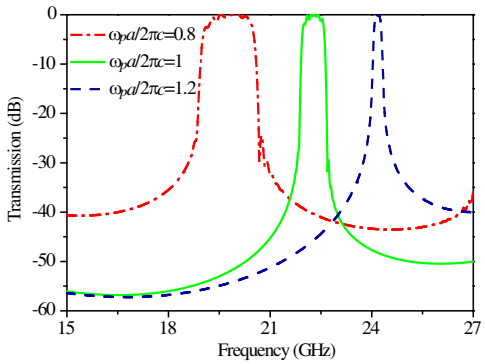

Figure 3: Transmission curves for different plasma frequency.

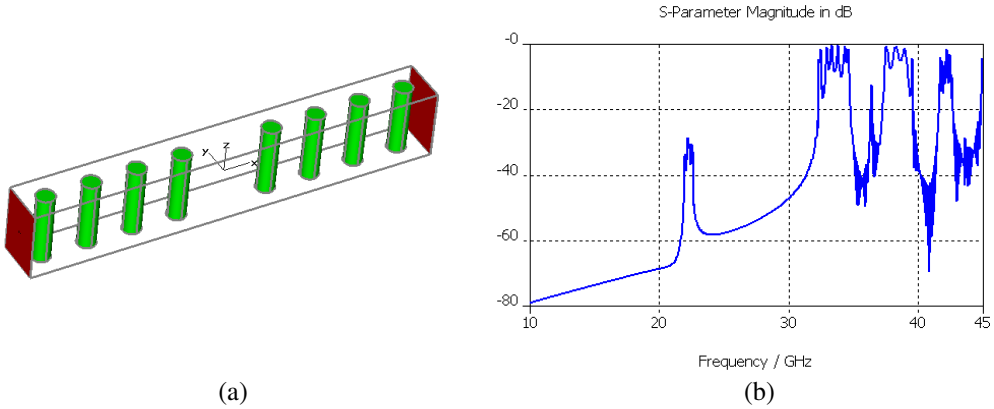

Figure 4: (a) CST model and (b) transmission curve for type-2 PPC with defect.

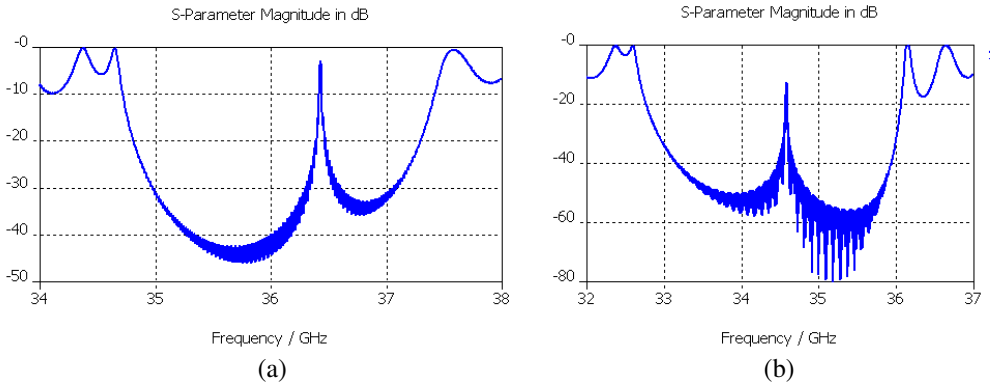

Figure 5: Transmission curve of type-2 PPC with defect for (a) $\omega_p a/2\pi c = 1$ and (b) $\omega_p a/2\pi c = 0.9$.

Figure 4(a) shows the type-2 PPC with the central rod removed, other parameters and boundary conditions are same with those in Fig. 1(a). Comparing with the transmission curve in Fig. 1(b), it is seen that the first pass band have a great attenuation smaller than −30 dB, but a very narrow pass band at 36.5 GHz appear in the gap between the second and third pass band. To see the narrow band clearly, Fig. 5(a) shows the transmission curve for $\omega_p a/2\pi c = 1$ with frequency varying from 34 GHz to 38 GHz, and Fig. 5(b) shows the transmission curve for normalized frequency $\omega_p a/2\pi c = 0.9$ with frequency varying from 32 GHz to 37 GHz, it is seen that the defect mode changes from 36.5 GHz to 34.5 GHz with plasma frequency decreasing. Therefore, a very narrow tunable PPC filters can be formed if central rod is missed for the type-2 PPC.

3. CONCLUSION

In summary, transmission characteristics of 2D type-2 PPC consisting of plasma-filled dielectric rod structure are studied, it is found that this structure can be used as tunable filters, and the desired central frequency and bandwidth can be obtained by changing plasma frequency. When the central rod is removed, a defect mode in certain gap would appear, and the defect mode would shift to low frequency with plasma frequency decreasing. These properties of 2D type-2 PPC would have potential application in tunable photonic crystal filters.

ACKNOWLEDGMENT

This work was supported by the National Natural Science Foundation of China (No. 11047193), and the Promotive Research Fund for Excellent Young and Middle-aged Scientists of Shandong Province (No. BS2010CL025).

REFERENCES

1. Yablonovitch, E., "Inhibited spontaneous emission in solid-state physics and electronics," *Phys. Rev. Lett.*, Vol. 58, 2059–2062, 1987.
2. John, S., "Strong localization of photons in certain disordered dielectric superlattices," *Phys. Rev. Lett.*, Vol. 58, 2486–2489, 1987.
3. Joannopoulos, J. D., S. G. Johnson, J. N.Winn, and R. D. Meade, *Photonic Crystals — Molding the Flow of Light*, Princeton University Press, Princeton, 2008.
4. Hojo, H. and A. Mase, "Dispersion relation of electromagnetic waves in one dimensional plasma photonic crystals," *J. Plasma Fusion Research*, Vol. 80, 89–90, 2004.
5. Laxmi, S. and M. Parmanand, "Photonic band gap effect in one-dimensional plasma dielectric photonic crystals," *Solid State Communications*, Vol. 138, 160–164, 2006.
6. Liu, S., W. Hong, and N. Yuan, "Finite-difference time-domain analysis of unmagnetized plasma photonic crystals," *International Journal of Infrared and Millimeter Waves*, Vol. 27, 403–422, 2006.
7. Liu, S., S. Zhong, and S. Liu, "Study of properties of the photonic band gap of unmagnetized plasma photonic crystal," *Plasma Science and Technology*, Vol. 11, 14–17, 2009.
8. Zhang, H., L. Ma, and S. Liu, "Study of periodic band gap structure of the magnetized plasma photonic crystals," *Optoelectronics Letters*, Vol. 5, 112–116, 2009.

9. Guo, B., "Photonic band gap structures of obliquely incident electromagnetic wave propagation in a one-dimension absorptive plasma photonic crystal," *Physics of Plasmas*, Vol. 16, 043508-1-6, 2009.
10. Hojo, H. and A. Mase, "Electromagnetic-Wave transmittance characteristics in one-dimensional plasma photonic crystals," *J. Plasma Fusion Res. Series*, Vol. 8, 477–479, 2009.
11. Qi, L., Z. Yang, F. Lan, X. Gao, and Z. Shi, "Properties of obliquely incident electromagnetic wave in 1D magnetized plasma photonic crystals," *Physics of Plasmas*, Vol. 17, 042501-1-8, 2010.
12. Qi, L. and X. Zhang, "Photonic band gaps of one-dimensional ternary plasma photonic crystals with periodic and periodic-varying structures," *Journal of Electromagnetic Waves and Applications*, Vol. 25, No. 4, 539–552, 2011.
13. Sakai. O., T. Sakaguchi, and K. Tachibana, "Verification of a plasma photonic crystal microplasmas," *Appl. Phys. Lett.*, Vol. 87, 241505-1-3, 2005.
14. Sakai, O., T. Sakaguchi, and K. Tachibana, "Photonic bands in two-dimensional microplasma arrays. I. Theoretical derivation of band structures of electromagnetic waves," *J. Appl. Phys.*, Vol. 101, 073304-1-9, 2007.
15. Qi, L. and Z. Yang, "Modified plane wave method analysis of dielectric plasma photonic crystal," *Progress In Electromagnetics Research*, Vol. 91, 319–332, 2009.
16. Qi, L., Z. Yang, L. Feng, X. Gao, and D. Li, "Dispersion characteristics of two-dimensional unmagnetized dielectric plasma photonic crystal," *Chinese Physics B*, Vol. 19, 034210-1-6, 2010.
17. CST Microwave Studio (Version 5.0), CST Computer Simulation Technology, 2006.
18. Shumpert, J. D., W. J. Chappell, and L. P. B. Katehi, "Parallel-plate mode reduction in conductor-backed slots using electromagnetic bandgap substrates," *IEEE Transactions on Microwave Theory Tech.*, Vol. 47, 2099–2104, 1999.

The Dependence of the Acoustomagnetoelectric Current on the Parameters of a Cylindrical Quantum Wire with an Infinite Potential in the Presence of an External Magnetic Field

N. Q. Bau[1], **N. V. Nhan**[2], **and N. V. Nghia**[3]

[1]Department of Physics, College of Natural Sciences, Hanoi National University, Hanoi, Vietnam
[2]Department of Physics, Academy of Defence Force, Air Force, Hanoi, Vietnam
[3]Department of Physics, Water Resources University, Hanoi, Vietnam

Abstract— The acoustomagnetoelectric effect in a cylindrical quantum wire with an infinite potential in the presence of an external magnetic field is investigated by using Boltzmann kinetic equation for an acoustic wave whose wavelength $\lambda = 2\pi/q$ is smaller than the mean free path l of the electrons and hypersound in the region $ql \gg 1$, (where q is the acoustic wave number). The analytic expression for the acoustomagnetoelectric current I^{ame} is calculated in the case: relaxation time of momentum τ is constant approximation and degenerates electrons gas. The nonlinear dependence of the expression for the acoustomagnetoelectric current I^{ame} on the acoustic wave numbers q and on the parameters of the cylindrical quantum wires is obtained. Numerical computations are performed for AlGaAs/GaAs cylindrical quantum wire with an infinite potential. The results are compared with the normal bulk semiconductors and the superlattices to show the values of the acoustomagnetoelectric current I^{ame} in the cylindrical quantum wire are different than they are in the normal bulk semiconductors and the superlattices.

1. INTRODUCTION

When an acoustic wave propagates through a conductor, it is accompanied by a transfer of energy and momentum to the conducting electrons. This gives rise to what is called the acoustoelectric effect [1–3]. Recently, [4–6] have investigated this effect in superlattices. However, in the presence of a magnetic field the acoustic wave is propagated in the conductor can produce another effect called the acoustomagnetoelectric (AME) effect. The AME effect is creating an AME current (if the sample is short circuited in the Hall direction), or an AME field (if the sample is open) when a sample placed in a magnetic field $\vec{H}$ carried an acoustic wave propagating in a direction perpendicular to the magnetic field $\vec{H}$. The AME effect was first foreseen by Grinberg and Kramer [7] for bipolar semiconductors and was observed experimentally in bismuth [8]. In past times, there are more and more interests in studying and discovering this effect in a bulk monopolar semiconductor [9], in a bulk semiconductor n-InSb [10]. In this specimen they observed that the AME effect occurs mainly because of the dependence of the electron relaxation time on the energy and when $\tau = constant$ the effect vanishes. Like the classical magnetic field, the effect also exists in the case of a quantized magnetic field, and the quantum acoustomagnetoelectric effects due to Rayleigh sound waves have investigated [11].

The AME effect problems in the bulk semiconductors [9, 10]; in superlattices [12] in the case non-degenerate electrons gas and in superlattices [13] in the case degenerate electrons gas have been investigated. However, the AME effect in the quantum wires has not been studied yet. Therefore, the purpose of this work is to examine this effect in the cylindrical quantum wire with an infinite potential for the case electron relaxation time which is not dependent on the energy and degenerate electron gas. Furthermore, we think the research of this effect may help us to understand the properties of quantum wire material. We have obtained the AME current I^{ame} in the cylindrical quantum wire with an infinite potential in the presence of an external magnetic field. The nonlinear dependence of the expression for the AME current I^{ame} on acoustic wave numbers q and on the parameters of cylindrical quantum wire with an infinite potential has been shown. Numerical calculations are carried out with a specific *AlGaAs/GaAs* quantum wire to clarify our results.

2. ANALYTIC EXPRESSION FOR THE ACOUSTOMAGNETOELECTRIC CURRENT

It is well known that, when the wavelength $\lambda = \pi/q$ of the acoustic wave will be considered shorter than the electron mean free path l (where $ql \gg 1$), the sound wave can be treated as a packet of coherent phonons (monochromatic phonon) having a function distribution $N(\vec{k}) =$

$(2\pi)^3 \phi\delta(\vec{k}-\vec{q})/\left(\hbar\omega_{\vec{q}}v_s\right)$. Where $h=1$, $\vec{k}$ is the current phonon wave vector, ϕ is the sound flux density, $\omega_{\vec{q}}$ and v_s are the frequency and the group velocity of sound wave with the wave vector $\vec{q}$, respectively. The problem will be solved in the quasi-classical case. The magnetic field will also be considered classically and weak thus limiting ourselves to the linear approximation of the magnetic field $\vec{H}$.

The density of the acoustoelectric current in the presence of magnetic field can be written in the form [12]

$$j^{AE} = \frac{2e}{(2\pi\hbar)^3}\int U^{AE}\psi_i d^3p \tag{1}$$

with

$$\begin{aligned} U^{AE} &= \frac{2\pi\phi}{\omega_{\vec{q}}v_s}\Big\{\left|G_{\vec{p}-\vec{q},\vec{p}}\right|^2\left[f(\varepsilon_{\vec{p}-\vec{q}})-f(\varepsilon_{\vec{p}})\right]\ \delta(\varepsilon_{\vec{p}-\vec{q}}-\varepsilon_{\vec{p}}+\hbar\omega_{\vec{q}}) \\ &\quad+\left|G_{\vec{p}+\vec{q},\vec{p}}\right|^2\left[f(\varepsilon_{\vec{p}+\vec{q}})-f(\varepsilon_{\vec{p}})\right]\ \delta(\varepsilon_{\vec{p}+\vec{q}}-\varepsilon_{\vec{p}}-\hbar\omega_{\vec{q}})\Big\} \end{aligned} \tag{2}$$

Here $f(\varepsilon_{\vec{p}})$ is the distribution function, $G_{\vec{p}\pm\vec{q},\vec{p}}$ is the matrix element of the electron-phonon interaction and ψ_i $(i=x,y,z)$ is the root of the kinetic equation given by [12]

$$\frac{e}{c}\left(\vec{V}\times\vec{H}\right)\frac{\partial\psi_i}{\partial p}+\hat{W}_{\vec{p}}\{\psi_i\} = \vec{V}_i. \tag{3}$$

Here $\vec{V}_i$ is the electron velocity and $\hat{W}_{\vec{p}}\{\ldots\} = (\partial f/\partial\varepsilon)^{-1}\hat{W}\{(\partial f/\partial\varepsilon)\ldots\}$. The operator $\hat{W}$ is assumed to be Hermitian [14]. In the case of the relaxation time of momentum τ is approximately constant, the collision operator has form $\hat{W}_{\vec{p}}=1/\tau$. Solving Eq. (3) by the method of iteration, we get for the zero and the first approximation with $\psi_i=\psi_i^{(0)}+\psi_i^{(1)}+\ldots$. Inserting into Eq. (1) and taking into account the fact that $\left|G_{\vec{p},\vec{p}'}\right|^2=\left|G_{\vec{p}',\vec{p}}\right|^2$, we obtain for the density of the acoustoelectric current the expression

$$\begin{aligned} j_i^{AE} &= -\frac{e\phi}{2\pi^2 v_s\omega_{\vec{q}}\hbar^3}\int\left|G_{\vec{p}+\vec{q},\vec{p}}\right|^2\left[f(\varepsilon_{\vec{p}+\vec{q}})-f(\varepsilon_{\vec{p}})\right]\left[V_i(\vec{p}+\vec{q})\tau-V_i(\vec{p})\tau\right]\delta(\varepsilon_{\vec{p}+\vec{q}}-\varepsilon_{\vec{p}}-\hbar\omega_{\vec{q}})d^3p \\ &\quad-\frac{e^2\phi\tau^2}{2\pi^2 mcv_s\omega_{\vec{q}}\hbar^3}\int\left|G_{\vec{p}+\vec{q},\vec{p}}\right|^2\left[f(\varepsilon_{\vec{p}+\vec{q}})-f(\varepsilon_{\vec{p}})\right] \\ &\quad\times\left[\left(\vec{V}(\vec{p}+\vec{q})\times\vec{H}\right)_i-\left(\vec{V}(\vec{p})\times\vec{H}\right)_i\right]\delta(\varepsilon_{\vec{p}+\vec{q}}-\varepsilon_{\vec{p}}-\hbar\omega_{\vec{q}})d^3p \end{aligned} \tag{4}$$

The matrix element of the electron-phonon interaction is given as $\left|G_{\vec{p},\vec{q}}\right|^2=|\Lambda|^2|\vec{q}|^2/2\rho\omega_{\vec{q}}$, where Λ is the deformation potential constant and ρ is the crystal density of the quantum wire.

In solving Eq. (4), we shall consider a situation whereby the sound is propagating along the quantum wire axis (Oz), the magnetic field $\vec{H}$ is parallel to the (Ox) axis and the AME current appears parallel to the (Oy) axis. Under such orientation the first term in Eq. (4) is responsible for the density of the acoustoelectric current and the solution is found in [2]. The second term in Eq. (4) is the density of the AME current and is expressed as

$$j_y^{\mathrm{AME}} = -\frac{e\phi\vec{q}^2\tau^2|\Lambda|^2\Omega}{4\pi v_s\omega_{\vec{q}}^2\rho\hbar^3}\int\left[f(\varepsilon_{\vec{p}+\vec{q}})-f(\varepsilon_{\vec{p}})\right]\left[V_z(\vec{p}+\vec{q})-V_z(\vec{p})\right]\delta(\varepsilon_{\vec{p}+\vec{q}}-\varepsilon_{\vec{p}}-\hbar\omega_{\vec{q}})d^3p\,. \tag{5}$$

where $\Omega=eH/mc$ is the cyclotron frequency and the Fermi-Dirac distribution function $f(\varepsilon_{\vec{p}})$ in the usual form is given by

$$f(\varepsilon_{\vec{p}}) = \left[\exp\left(\beta\left(\varepsilon_p-\mu\right)\right)+1\right]^{-1}, \tag{6}$$

where $\beta=1/kT$, k is the Boltzmann constant, T is the temperature of the cylindrical quantum wire, μ is the chemical potential. The energy $\varepsilon_{\vec{p}}$ of the cylindrical quantum wire with an infinite potential in the lowest miniband is given by [15]

$$\varepsilon_{\vec{p}} = \frac{\vec{p}_z^2}{2m}+\frac{\hbar^2A_{n,l}^2}{2mR^2}. \tag{7}$$

where $l = 1, 2, 3, \ldots$ is the radial quantum number, $n = 0, \pm 1, \pm 2, \ldots$ is the azimuth quantum number, m is the electron effective mass, R is the radius of the quantum wire, p_z is the longitudinal component of the quasi-momentum and $A_{n,l}$ is the l level root of Bessel function of the order n.

Substituting Eqs. (6) and (7) into Eq. (5) and taking into account the fact that $V_z(\vec{p}) = \partial\varepsilon(\vec{p})/\partial p$, we obtain for the AME current with the condition is satisfied then:

$$\varepsilon_F > \frac{\vec{p}_z^2}{2m} + \frac{\hbar^2}{2mR^2} A_{n,l}^2 + \hbar\omega_{\vec{q}} \tag{8}$$

where ε_F is the Fermi energy.

The inequalities in Eq. (8) are condition acoustic wave vector $\vec{q}$ to the AME effect exists. Therefore, we have obtained the expression the density of the AME current

$$j_y^{\mathrm{AME}} = \frac{e\phi\,|\Lambda|^2\, q^3\tau^2\Omega kT}{2\pi v_s \omega_{\vec{q}}^2 \rho\hbar^3} \exp\left(\beta\left(\mu - \frac{\hbar^2 A_{n,l}^2}{2mR^2}\right)\right)\left[1 - \exp\left(-\beta\hbar\,\omega_{\vec{q}}\right)\right]. \tag{9}$$

Thus,

$$I^{\mathrm{ame}} = \frac{e\phi\,|\Lambda|^2\, q^3\tau^2 R^2\Omega kT}{2 v_s \omega_{\vec{q}}^2 \rho\hbar^3} \exp\left(\beta\left(\mu - \frac{\hbar^2 A_{n,l}^2}{2mR^2}\right)\right)\left[1 - \exp\left(-\beta\hbar\,\omega_{\vec{q}}\right)\right]. \tag{10}$$

The Eq. (10) is the AME current in the cylindrical quantum wire with an infinite potential in the case degenerate electron gas, the expression only obtained if the condition in Eq. (8) is satisfied.

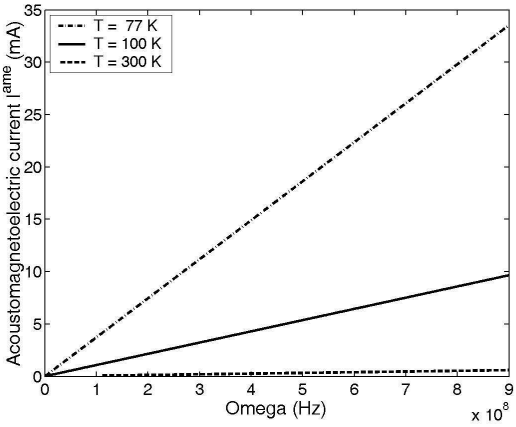

Figure 1: The dependence of the AME current I^{ame} on the cyclotron frequency Ω.

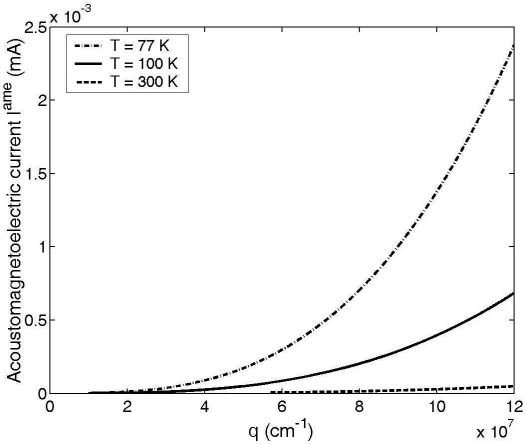

Figure 2: The dependence of the AME current I^{ame} on the acoustic wave number q.

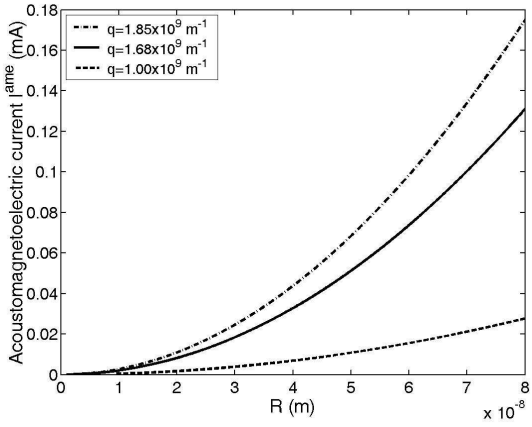

Figure 3: The dependence of the AME current I^{ame} on the radius of the cylindrical quantum wire.

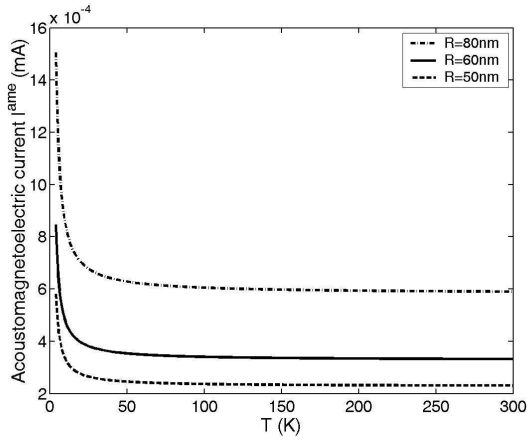

Figure 4: The dependence of the AME current I^{ame} on the temperature T.

3. NUMERICAL RESULTS

In the paper, we consider an *AlGaAs/GaAs* cylindrical quantum wire with an infinite potential. The parameters used in the calculations are as follows [11, 13]: $\tau = 10^{-12}\,\mathrm{s}$, $\phi = 10^{14}\,\mathrm{Wm}^{-2}$, $\Lambda = 8\,\mathrm{eV}$, $\omega_{\vec{q}} = 10^{10}\,\mathrm{s}^{-1}$, $\rho = 2 \times 10^{13}\,\mathrm{kgm}^{-3}$, $v_s = 5370\,\mathrm{ms}^{-1}$, $m = 0.067\,m_e$, m_e being the mass of free electron.

In the Figure 1, we show the dependence of the AME current on the cyclotron frequency Ω with the radius $R = 80\,\mathrm{\AA}$, the acoustic wave number $q = 1.68 \times 10^9\,\mathrm{m}^{-1}$ and the temperature $T = 77\,\mathrm{K}$, $T = 100\,\mathrm{K}$ and $T = 300\,\mathrm{K}$. When the intensity of the magnetic field rises up, the AME current I^{ame} increases linearly with the cyclotron frequency Ω. This value also decreases when the temperature T of the quantum wire increases.

In the Figure 2, we show the dependence of the AME current on the acoustic wave number q with the radius $R = 80\,\mathrm{\AA}$, the intensity of the magnetic field $H = 2\times10^3\,\mathrm{Am}^{-1}$ and the temperature $T = 77\,\mathrm{K}$, $T = 100\,\mathrm{K}$ and $T = 300\,\mathrm{K}$. The curve of the AME current I^{ame} strongly increases when the large value range of the acoustic wave number q and this value decreases when the temperature increases. Unlike the normal bulk semiconductors [9, 10], in the quantum wire the AME current is non-linear with the acoustic wave number q. These results are compared with those obtained in the superlattices [12, 13], the AME current have a non-linear with the acoustic wave number q. It is very different between the superlattices and the cylindrical quantum wire with an infinite potential.

In the Figure 3, we show the dependence of the AME current on the radius R of the cylindrical quantum wire with the temperature $T = 77\,\mathrm{K}$, the acoustic wave numbers $q = 1.00 \times 10^9\,\mathrm{m}^{-1}$, $q = 1.68\times10^9\,\mathrm{m}^{-1}$ and $q = 1.85\times10^9\,\mathrm{m}^{-1}$. The value of the AME current increases with the radius R of the cylindrical quantum wire when the radius R of the cylindrical quantum wire increases. This value increases when the acoustic wave number q rises up.

In the Figure 4, we show the dependence of the AME current on the temperature T of the cylindrical quantum wire with the acoustic wave number $q = 1.68 \times 10^9\,\mathrm{m}^{-1}$, the radius $R = 50\,\mathrm{nm}$, $R = 60\,\mathrm{nm}$ and $R = 80\,\mathrm{nm}$. The value of the AME current strongly decreases with the temperature when the temperature increases in the small value range the low temperature. This value is approximation constant in the temperature T interval from 30 K to 300 K.

4. CONCLUSION

In this paper, we have analytically investigated the possibility of the acoustomagnetoelectric (AME) effect in the cylindrical quantum wire with an infinite potential. We have obtained analytically expressions for the AME effect in the cylindrical quantum wire with an infinite potential for the case degenerate electron gas. The dependences of the expression for the AME current I^{ame} on the cyclotron frequency Ω, the frequency $\omega_{\vec{q}}$ of the acoustic wave, the temperature T and the radius R of the quantum wire are obtained. The result is different compared to those obtained in the normal bulk semiconductors [9, 10] and the superlattices [12, 13], according to [9] in the case $\tau = constant$ the effect only exists if the electron gas is non-degenerate, if the electron gas is degenerate, the effect is not appear, however, our result indicates that in the cylindrical quantum wire the AME effect exists both non-degenerate and degenerate electron gas when $\tau = constant$. Unlike the normal bulk semiconductors, in the quantum wire the AME current I^{ame} is nonlinear with the acoustic wave number q.

The numerical results have expressed the dependence of the AME current I^{ame} on the acoustic wave number q, the radius R and the temperature of the cylindrical quantum wire are performed for *AlGaAs/GaAs* cylindrical quantum wire with an infinite potential. The result shows that, the AME effect exists when the acoustic wave vector $\vec{q}$ complies with specific conditions in Eq. (8) which condition dependences on the frequency $\omega_{\vec{q}}$ of the acoustic wave, the mass of electrons, the temperature and the radius R of the quantum wire. The curve of the AME current I^{ame} strongly increases when the low temperature and the large value range of the acoustic wave number q. The value of the AME current I^{ame} is zero (the effect is not appear) when the small value range of the acoustic wave number q and the radius of the cylindrical quantum wire R. That is mean to have AME current I^{ame}, the acoustic phonons energy is high enough and satisfied in the some interval to impact much momentum to the conduction electrons.

ACKNOWLEDGMENT

This research is completed with financial support from the Program of Basic Research in Natural Science — Vietnam NAFOSTED.

REFERENCES

1. Parmenter, R. H. "The acousto-electric effect," *Phys. Rev.*, Vol. 89, 990–998, 1953.
2. Rotter, M., A. V. Kalameitsev, A. O. Grovorov, W. Ruile, and A. Wixforth, "Charge conveyance and nonlinear acoustoelectric phenomena for intense surface acoustic waves on a semiconductor quantum well," *Phys. Rev. Lett.*, Vol. 82, No. 10, 2171–2174, 1999.
3. Entin-Wohlman, O., Y. Levinson, and Y. M. Galperin, "Acoustoelectric effect in a finite-length ballistic quantum channel," *Phys. Rev. B*, Vol. 62, 7283–7288, 2000.
4. Mensah, S. Y., F. K. A. Allotey, and S. K. Adjepong, "Acoustoelectric effect in a semiconductor superlattice," *J. Phys.*, Vol. 6, No. 34, 6783–6787, 1994.
5. Mensah, S. Y., F. K. A. Allotey, and N. G. Mensah, "Nonlinear acoustoelectric effect in a semiconductor superlattice," *J. Phys.*, Vol. 12, No. 24, 5225–5232, 2000.
6. Mensah, S. Y., F. K. A. Allotey, N. G. Mensah, H. Akrobotu, and G. Nkrumah, "The influence of external electric field on acoustoelectric effect in a superlattice," *J. Phys.*, Vol. 37, No. 2, 87–97, 2005.
7. Grinberg, A. A. and N. I. Kramer, "Acoustomagnetic effect in piezoelectric semiconductors," *Sov. Phys. Dokl.*, Vol. 9, No. 7, 552, 1965.
8. Yamada, T. "Acoustomagnetoelectric effect in Bismuth," *J. Phys. Soc. Japan*, Vol. 20, 1424–1437, 1965.
9. Epshtein, E. M. and Y. V. Gulyaev, "Acoustomagnetoelectric effect in conductors with monopolar conductivity," *Fiz. Tverd. Tela.*, Vol. 9, No. 2, 376–381, 1967; *Sov. Phys. Solids State*, Vol. 9, No. 2, 288, 1967.
10. Kogami, M. and S. Tanaka, "Acoustomagnetoelectric and acoustoelectric effects in n-InSb at low temperatures," *J. Phys. Soc. Japan*, Vol. 30, 775–784, 1971.
11. Margulis, A. D. and V. I. A. Margulis, "The quantum acoustomagnetoelectric effect due to Rayleigh sound waves," *J. Phys.*, Vol. 6, No. 31, 6139–6150, 1994.
12. Mensah, S. Y., F. K. A. Allotey, and S. K. Adjepong, "Acoustomagnetoelectric effect in a superlattice," *J. Phys.*, Vol. 8, No. 9, 1235–1239, 1996.
13. Bau, N. Q. and N. V. Hieu, "Theory of the acoustomagnetoelectric effect in a superlattice," *PIERS Proceedings*, 342–346, Xi'an, China, Mar. 22–26, 2010.
14. Kaganov, M. I., S. T. Mevlyut, and I. M. Suslov, "The acoustoelectric current in a metal for an arbitrary conduction-electron dispersion law," *Sov. JETP*, Vol. 51, No. 1, 189–191, 1980.
15. Gold, A. and A. Ghazali, "Analytical results for semiconductor quantum-well wire: Plasmons, shallow impurity states, and mobility," *Phys. Rev. B*, Vol. 41, No. 11, 7626–7640, 1990.

The Parametric Resonance of Confined Acoustic Phonons and Confined Optical Phonons by an External Electromagnetic Wave in Cylindrical Quantum Wires with an Infinite Potential

N. Q. Bau[1], **L. T. Hung**[2], **and L. T. T. Phuong**[3]

[1]Department of Physics, Viet Nam National University Hanoi, 334 Nguyen Trai, Hanoi, Vietnam
[2]University of Education, Viet Nam National University Hanoi, 144 Xuan Thuy, Hanoi, Vietnam
[3]College of Education, Hue University, 34 Le Loi, Hue City, Vietnam

Abstract— The parametric resonance of confined acoustic phonons and confined optical phonons by an external electromagnetic wave in cylindrical quantum wires with an infinite potential is studied by using a set of quantum kinetic equations for confined phonons. The analytical expression of the threshold amplitude $E_{threshold}$ of the field in a cylindrical quantum wires with an infinite potential is obtained. The formula of $E_{threshold}$ contains two quantum numbers (m, k) characterizing confined phonons. The dependence of the threshold amplitude $E_{threshold}$ on the temperature T of the system, the wave vector $\vec{q}_z$, the frequency Ω of an external electromagnetic waves and the radius of the wires R is studied. Numerical computations and graphs are performed for GaAs-GaAsAl cylindrical quantum wires. The results are compared with the case of unconfined phonons.

1. INTRODUCTION

In quantum wires (QW), the motion of electrons and phonons is restricted in two dimensions, so that can flow freely in one dimension. The confinement of electrons in these systems has changed the electrons mobility remarkably. This has resulted in a number of new phenomena, which concern a reduction of sample dimensions. Many attempts have conducted dealing with these behaviors, for examples: the problems of the linear absorption coefficient in QW [1]; the nonlinear absorption in rectangular QW [2], in QW [3] have been studied. Electron interaction with confined acoustic phonons [4], the polar-optic phonons and high field electron transport [5] and self-consistent electronic structure [6] have also been researched in cylindrical quantum wires (CQW). And parametric interactions and transformations (PIT) are the interesting problems in CQW.

As we know that the electron gas becomes non-stationary in the presence of an external electromagnetic wave (EEW). When the conditions of the parametric resonance are satisfied, PIT of the same kinds of excitations, such as phonon-phonon and plasmon-plasmon excitations, or of different kinds of excitations, such as plasmon-phonon excitations, will arise, i.e., the energy exchange processes between these excitations will occur [7, 8]. For semiconductor nanostructures, there have been several works on the generation and amplification of acoustic phonons [9–11]. The PIT of acoustic and optical phonons have been considered in bulk semiconductors [12–14], in low dimensional semiconductors [15, 16] and CQW [17]. However, the parametric resonance of acoustic and optical phonons by an EEW in CQW with an infinite potential in the case of confined phonons have not studied yet. Therefore, in this paper, we continue to study the parametric resonance of confined acoustic and confined optical phonons in CQW with an infinite potential by an EEW. Numerical calculations are carried out with a specific GaAs/GaAsAl CQW. This result has been compared with the case of unconfined phonons [17], which shows clearly the effect of confined phonons as in [18, 19].

2. THE PARAMETRIC RESONANCE OF CONFINED ACOUSTIC PHONONS AND CONFINED OPTICAL PHONONS BY AN EXTERNAL ELECTROMAGNETIC WAVE IN CQW

We use a simple model for a CQW, in which a one-dimensional electron, phonon gas is confined by the infinity potential $V(x, y)$ along the x-y direction. So electrons and phonons are free only on the z plane. A laser field $\vec{E} = \vec{E}_o \sin(\Omega t)$ irradiates the sample in a direction, which is normal to the z plane, its polarization is along the (x, y) axis and its strength is expressed as a vector potential $\vec{A}(t) = c\vec{E}_o \cos(\Omega t)/\Omega$. If the confined electron-confined acoustic phonons and confined optical

phonons interaction potential is used, the Hamiltonian for the system of the confined electron and the confined acoustic and confined optical phonons is written as:

$$H = H_e + H_{aph} + H_{oph} + H_{e-aph} + H_{e-oph} \tag{1}$$

In order to establish a set of quantum kinetic equations for confined acoustic phonons and confined optical phonons, we use the general quantum distribution functions for the confined phonons [20] $\langle b_{m,k,\vec{q}_z}\rangle_t$ and $\langle c_{m,k,\vec{q}_z}\rangle_t$, where $\langle\psi\rangle_t$ denotes a statically, average at the moment $\langle\psi\rangle_t = Tr|\hat{W}\hat{\psi}\rangle$, ($\hat{W}$ is the density matrix operator); m, k are quantum number characterizing confined phonons. Using Hamiltonian in Equation (1) and realizing operator algebraic calculations, we obtain a set of coupled quantum transport equations.

Using Fourier transformation:

$$\left\langle \psi_{m,k,\vec{q}_z} \right\rangle_t = \frac{1}{2\pi}\int\limits_{-\infty}^{+\infty} \Psi_{m,k,\vec{q}_z}(\varpi)\, e^{-i\varpi t} d\varpi; \quad \Psi_{m,k,\vec{q}_z}(\varpi) = \int\limits_{-\infty}^{+\infty} \left\langle \psi_{m,k,\vec{q}_z} \right\rangle_t e^{i\varpi t} dt \tag{2}$$

to solve coupled quantum transport equations then we obtain the general dispersion equation for PIT of confined acoustic phonons and confined optical phonons in CQW:

$$\begin{aligned}
&\left(\varpi^2 - \varpi^2_{m,k,\vec{q}_z} - \frac{2}{\hbar}\sum_{\alpha,\alpha',m,k} \gamma^2 \left|I_{1D}(\vec{q}_z)\right|^2 \varpi_{m,k,\vec{q}_z} \Pi_0(\vec{q}_z,\varpi)\right) \\
&\left((\varpi - l\Omega)^2 - \nu^2_{m,k,\vec{q}_z} - \frac{2}{\hbar}\sum_{\alpha,\alpha',m,k} \beta^2 \left|I_{1D}(\vec{q}_z)\right|^2 \nu_{m,k,\vec{q}_z} \Pi_0(\vec{q}_z,\varpi - l\Omega)\right) \\
&= \frac{4}{\hbar^2}\sum_{\alpha,\alpha',m,k}\sum_{l=-\infty}^{+\infty} \left\{\gamma^2\beta^2 \left|I_{1D}(\vec{q}_z)\right|^4 \nu_{m,k,\vec{q}_z}\varpi_{m,k,\vec{q}_z} \Pi_l(\vec{q}_z,\varpi)\, \Pi_l(\vec{q}_z,\varpi - l\Omega)\right\}
\end{aligned} \tag{3}$$

where γ, β are the electron-phonon interaction constants; $|I_{1D}(\vec{q}_z)|$ is the electron form factor which can be written from [5, 21]; $\nu_{m,k,\vec{q}_z}$, $\varpi_{m,k,\vec{q}_z}$ are the frequency of confined phonons; α, α' characterizing the states of electron in the quantum wire before and after scattering with phonon.

Here:

$$\Pi_l(\vec{q}_z,\varpi) = \sum_{\nu=-\infty}^{\infty} J_\nu\left(\frac{\lambda}{\Omega}\right) J_{l+\nu}\left(\frac{\lambda}{\Omega}\right) \Gamma_{m,k,\vec{q}_z}(\varpi + \nu\Omega) \quad \text{with} \quad \lambda = \frac{e\vec{q}\vec{E}_o}{m^*\Omega^2} \tag{4}$$

$$\Gamma_{m,k,\vec{q}_z}(\varpi + l\Omega) = \sum_{\vec{k}_\perp} \frac{f_{\alpha'}\left(\vec{k}_z - \vec{q}_z\right) - f_\alpha\left(\vec{k}_z\right)}{\left[\varepsilon_\alpha\left(\vec{k}_z\right) - \varepsilon_{\alpha'}\left(\vec{k}_z - \vec{q}_z\right) - \hbar l\Omega - \hbar\varpi + i\hbar\delta\right]}, \tag{5}$$

If we write the dispersion relation of confined acoustic phonons and confined optical phonons:

$$\varpi_{m,k,\vec{q}_z} = \varpi_a + i\tau_a; \quad \nu_{m,k,\vec{q}_z} = \varpi_o + i\tau_o \tag{6}$$

$$\tau_a = -\frac{1}{\hbar}\sum_{\alpha,\alpha',m,k} \gamma^2 \left|I_{1D}(\vec{q}_z)\right|^2 \mathrm{Im}\Pi_0(\vec{q}_z,\varpi) \tag{7}$$

$$\tau_0 = -\frac{1}{\hbar}\sum_{\alpha,\alpha',m,k} \beta^2 \left|I_{ID}(\vec{q}_z)\right| \mathrm{Im}\Pi_0(\vec{q}_z,\varpi - l\Omega) \tag{8}$$

We obtain the resonance phonon mode:

$$\varpi_\pm^{(\pm)} = \varpi_a + \frac{1}{2}\left\{(v_a \pm v_o)\,\Delta(q) - i\,(\tau_a + \tau_o) \pm \sqrt{\left[(v_a \pm v_o)\,\Delta(q) - i\,(\tau_a - \tau_o)\right]^2 \pm \Lambda^2}\right\} \quad , \tag{9}$$

where $\Delta(q) = q - q_0$ being the wave number for which the resonance is satisfied, $v_a\,(v_0)$ is the group velocity of the acoustic (optical) phonon; ϖ_a is the renormalization (by the electron-phonon

interaction) frequency of the acoustic phonon and:

$$\Lambda = \frac{2}{\hbar} \sum_{\substack{\alpha,\alpha' \\ m,k}} \gamma\beta \left| I_{1D}(\vec{q}_z) \right|^2 \Pi_l(\vec{q}_z, \varpi_{m,k,\vec{q}_z}) \tag{10}$$

In Equation (10), the signs $(\pm)$ in the subscript of $\varpi_{\pm}^{(\pm)}$ correspond to the signs $(\pm)$ in the front of the root and the signs $(\pm)$ in subscript of $\varpi_{\pm}^{(\pm)}$ correspond to the other sign pairs. The signs depend on the resonant condition:

$$\lambda^2 > \frac{4\Omega^2 \mathrm{Im}\Gamma_{m,k,\vec{q}_z}\left(\varpi_{m,k,\vec{q}_z}\right) \mathrm{Im}\Gamma_{m,k,\vec{q}_z}\left(\nu_{m,k,\vec{q}_z}\right)}{\left[\mathrm{Re}\Gamma_{m,k,\vec{q}_z}\left(\varpi_{m,k,\vec{q}_z}\right)\right]^2}$$

For instance, the existence of a positive imaginary part of $\varpi_{\pm}^{(\pm)}$ implies a parametric amplication of the acoustic phonon. In such case that $\lambda \ll 1$, corresponding to the maximal resonance, we obtain:

$$F = \mathrm{Im}\omega_{+}^{-} = \mathrm{Im}\left\{\omega_a + \frac{1}{2}\left[-i\left(\tau_a + \tau_o\right) \pm \sqrt{\left(\tau_a + \tau_o\right)^2 + \Lambda^2}\right]\right\} \tag{11}$$

From Equation (11), the condition for the resonant acoustic phonon modes to have a positive imaginary part leads to $|\Lambda|^2 > 4\tau_a\tau_o$. Using this condition and Equations (1)–(11), we have found out the intensity of the threshold field $E_{threshold}$ for EEF:

$$E_{threshold} = \frac{2m^*\Omega}{e\sqrt{q_z^2 + q_{m,k}^2}} \times \frac{\sqrt{\xi\left(\varpi_{m,k,\vec{q}_z}\right) \cdot \xi\left(\nu_{m,k,\vec{q}_z}\right)}}{\sqrt{\left[\theta\left(\varpi_{m,k,q_z}\right) - \theta(\varpi_{m,k,\vec{q}_z} - \Omega)\right]^2 + \left[\xi\left(\varpi_{m,k,\vec{q}_z}\right) - \xi(\varpi_{m,k,\vec{q}_z} - \Omega)\right]^2}} \tag{12}$$

where:

$$\begin{aligned}
\xi(\varpi_{m,k,\vec{q}_z}) &= \frac{m^*}{2\hbar^2\sqrt{q_z^2 + q_{m,k}^2}} \exp\left(\frac{1}{k_BT}\left(\varepsilon_F - \frac{\hbar^2 B_\alpha^2}{2m^*R^2}\right)\right) \exp\left(-\frac{m^*\varepsilon_{\alpha\alpha'}^2\left(\nu_{m,k,\vec{q}_z} - \Omega\right)}{2k_BT\hbar^2\left(q_z^2 + q_{m,k}^2\right)}\right) \\
&\quad \left\{1 - \exp\left(\frac{\hbar\left(\varpi_{m,k,\vec{q}_z} - \Omega\right)}{k_BT}\right)\right\} \\
\theta(\varpi_{m,k,\vec{q}_z}) &= \frac{\sqrt{2m^*\pi k_BT}}{2\hbar\pi} \times \frac{1}{\varepsilon_{\alpha,\alpha'}\left(\varpi_{m,k,\vec{q}_z}\right)} \left[\exp\left(\frac{\varepsilon_F}{k_BT}\right)\left(\exp\left(-\frac{1}{k_BT}\left(\frac{\hbar^2 B_\alpha^2}{2m^*R^2}\right)\right)\right.\right. \\
&\quad \left.\left. - \exp\left(-\frac{1}{k_BT}\left(\frac{\hbar^2 B_{\alpha'}^2}{2m^*R^2}\right)\right)\right)\right] \\
\varepsilon_{\alpha\alpha'}(\varpi_{m,k,\vec{q}_z}) &= \frac{\hbar^2 B_\alpha^2}{2m^*R^2} - \frac{\hbar^2 B_{\alpha'}^2}{2m^*R^2} - \frac{\hbar^2\left(q_z^2 + q_{m,k}^2\right)}{2m^*} - \hbar\varpi_{m,k,\vec{q}_z}
\end{aligned}$$

Here k_B is Boltzmann constant, $q_{m,k}^2$ can be written from [21], B_α is corresponding to the equation $J_n(B_\alpha) = 0$, ε_F is the Fermi energy and R is the radius of the wires respectively.

In Equation (12), we can see the marked difference between the case of confined phonons and unconfined phonons, the formula of $E_{threshold}$ contains a quantum number (m, k) characterizing confined phonons.

3. NUMERICAL RESULTS AND DISCUSSIONS

In order to clarify the mechanism for parametric resonance of acoustic-optical phonons in case of the confined phonons, in this section, we consider a *GaAs/GaAsAl* CQW. The parametric used in the calculation are following [9, 18]: $m^* = 0.066m_o$, m_o being the mass of free electron; $\Omega = 8 \cdot 10^8\,\mathrm{Hz}$, $\hbar v_{\vec{q}_\perp}^m \approx \hbar v_0 = 36.25\,\mathrm{meV}$; $\omega_{\vec{q}_\perp}^m \approx v_a = 5370\,\mathrm{ms}^{-1}$, $k_B = 1.3807 \times 10^{-23}\,\mathrm{JK}^{-1}$; $e = 1.60219 \times 10^{-19}\,\mathrm{C}$; $\hbar = 1.05459 \times 10^{-34}\,\mathrm{Js}^{-1}$; $R = 5\,\mathrm{nm}$.

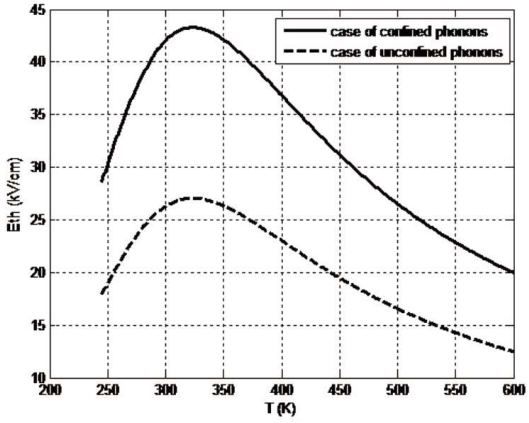

Figure 1: The dependence of $E_{threshold}$ on temperature T (K).

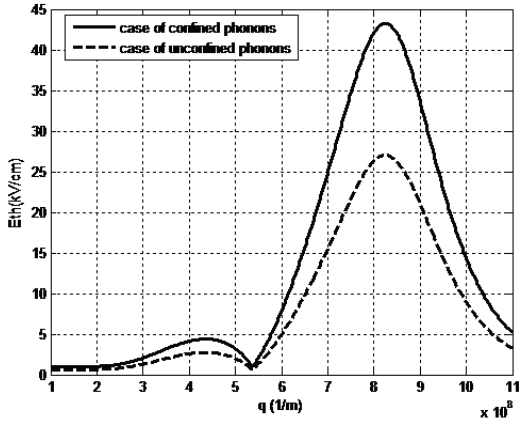

Figure 2: The dependence of $E_{threshold}$ on wave vector $\vec{q}_z$ (m^{-1}).

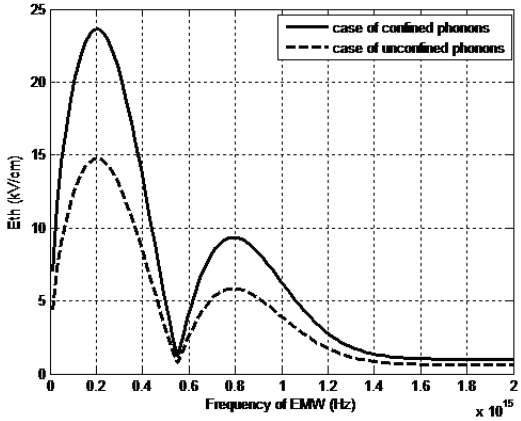

Figure 3: The dependence of $E_{threshold}$ on frequency Ω (Hz).

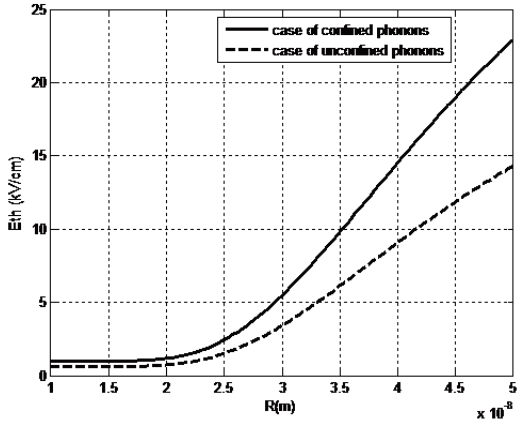

Figure 4: The dependence of $E_{threshold}$ on R (m).

In Fig. 1, It shows that $E_{threshold}$ as a function of temperature T in both cases of confined phonons and unconfined phonons. The graph shows that confined phonon increase the intensity of the threshold field $E_{threshold}$ in comparison with the case of unconfined phonons [17]. Namely, at the same temperature $T \sim 325\,\mathrm{K}$, $E_{threshold} \sim 43$ (kVcm^{-1}) in case of confined phonons, but $E_{threshold} \sim 22$ (kVcm^{-1}) in case of unconfined phonons.

In Fig. 2, present $E_{threshold}$ as a function of the wave vector at $T = 300\,\mathrm{K}$. The figure shows that the $E_{threshold}$ depends much strongly on wave vector that there are appearing two resonance peaks. Differing from the case of unconfined phonons [17], the curve has two lower resonance peaks. This is due to the fact that confined phonon has quantum wave number following the confined axis.

Figures 3 and 4 show that the strong dependences of $E_{threshold}$ on the frequency Ω and the radius of the wires are very clearly in case of confined phonons. There are two resonance peaks of $E_{threshold}$ at the difference values of frequency Ω in both cases of confined phonons and unconfined phonons. The $E_{threshold}$ increases fast following the radius of the wires and gets higher in case of confined phonons.

4. CONCLUSION

In this paper, we analytically investigated the possibility of parametric resonance of confined acoustic and confined optical phonons in CQW. We have obtained a set of quantum kinetic equations for transformation of phonons. However, the analytical solution applying to these equations can only be obtained with in some limitations. Using these limitations for simplicity we obtained the parametric resonant condition, the intensity of the threshold field $E_{threshold}$ for confined acoustic phonons and confined optical phonons in CQW. And we have also paid attention to $E_{threshold}$ in case of unconfined phonons to compare with the result above. We numerical calculated and graphed the intensity of the threshold field for $GaAs$/GaAs CQW. The results show that confined phonons cause some unusual effects. The threshold field $E_{threshold}$ depends strongly on the temperature T,

the wave vector $\vec{q}_z$, the frequency Ω and the radius of the wires. Confined phonons will increase the values of the threshold field $E_{threshold}$.

ACKNOWLEDGMENT

This work is completed with financial support from the Viet Nam NAFOSTED.

REFERENCES

1. Bau, N. Q., L. Dinh, and T. C. Phong, "Absorption coefficient of weak electromagnetic waves caused by confined electrons in quantum wires," *J. Korean. Phys. Soc.*, Vol. 51, 1325–1330, 2007.
2. Bau, N. Q. and H. D. Trien, "The nonlinear absorption of a strong electromagnetic wave by confined electrons in rectangular quantum wires," *PIERS Proceedings*, 336–341, Xi'an, China, Mar. 22–26, 2010.
3. Bau, N. Q. and H. D. Trien, "The nonlinear absorption coefficient of strong electromagnetic waves caused by electrons confined in quantum wires," *J. Korean. Phys. Soc.*, Vol. 56, No. 1, 120–127, 2010.
4. Yua, S. G., K. W. Kim, M. A. Stroscio, G. J. Iafrate, and A. Ballato, "Electron interaction with confined acoustic phonons in cylindrical quantum wires via deformation potential," *J. Appl. Phys.*, Vol. 80, No. 5, 2815–2822, 1996.
5. Wang, X. F. and X. L. Lei, "The polar-optic phonons and high field electron transport in cylindrical GaAs/AlAs quantum wires," *Phys. Rev. B*, Vol. 49, 4780–4789, 1994.
6. Proetto, C. R., "Self consistent electronic structure of cylindrical quantum wires," *Phys. Rev. B*, Vol. 45, No. 20, 1911–1917, 1995.
7. Phong, T. C., L. Dinh, N. Q. Bau, and D. Q. Vuong, "Rate of phonon excitation and conditions for phonon generation in rectangular quantum wires," *J. Kor. Phys. Soc.*, Vol. 49, 2367–2372, 2006.
8. Silin, V. P., "Parametric action of the high-power radiation on plasma," *National Press on Physics Theory Literature*, Moscow, 1973.
9. Komirenko, S. M., K. W. Kim, A. A. Dimidenko, V. A. Kochelap, and M. A. Stroscico, "Generation and amplification of sub-THz coherent acoustic phonons under the drift of two-dimensional electrons," *Phys. Rev. B*, Vol. 62, 7459, 2000.
10. Komirenko, S. M., K. W. Kim, A. A. Demidenko, V. A. Kochelap, and M. A. Stroscio, "Amplification of transverse acoustic phonons in quantum well heterostructures with piezoelectric interaction," *J. Appl. Phys.*, Vol. 90, 3934, 2001.
11. Shmelev, G. M. and N. Q. Bau, "The amplification of sound in semiconductors in the presence of two EMW," *Physics Effects in Semiconductors Kishinev*, 1981.
12. Epstein, E. M., "Parametric resonance of acoustic and optical phonons in semiconductors," *Sov. Phys. Semicond.*, Vol. 10, 1164, 1976.
13. Vyazovskii, M. V. and V. A. Yakovlev, "Parametric resonance of acoustic and optical phonons in impurity semiconductors in low temperature," *Sov. Phy. Semicond.*, Vol. 11, 809, 1977.
14. Shmelev, G. M., N. Q. Bau, and V. H. Anh, "Parametric transformations of plasmons and phonons in semiconductors (Firts part)," *Soviet Communication of JINR*, P-17-81-600, 1981.
15. Bau, N. Q. and T. C. Phong, "Parametric resonance of acoustic and optical phonons in a quantum well," *J. Kor. Phys. Soc*, Vol. 42, No. 5, 647–651, 2003.
16. Phong, T. C., L. V. Tung, and N. Q. Bau, "Parametric resonance of acoustic and optical phonons in a doped semiconductor superlattice," *J. Kor. Phys. Soc*, Vol. 53, 971–1975, 2008.
17. Thanh, L. D., D. Q. Vuong, N. V. Diep, and N. Q. Bau, "Parametric resonance of acoustic and optical phonons in cylindrical quantum wires," *Science (VNU)*, Vol. 20, No. 2, 33, 2004.
18. Bau, N. Q., D. M. Hung, and L. T. Hung, "The influences of confined phonons on the nonlinear absorption coefficient of a strong electromagnetic wave by confined electrons in doping superlattices," *Progress In Electromagnetics Research Letters*, Vol. 15, 175–185, 2010.
19. Bau, N. Q., L. T. Hung, and N. D. Nam, "The nonlinear absorption coefficient of a strong electromagnetic wave by confined electrons in quantum wells under the influences of confined phonons," *Journal of Electromagnetic Waves and Applications*, Vol. 24, No. 13, 1751–1761, 2010.
20. Anh, V. H., "A quantum approach to the parametric excitation problem in solids," Physic Report, Vol. 1, No. 64, 1–45, 1980.
21. Li, W. S. and S.-W. Gu, "Effects of the parabolic potential and confined phonons on the polaron in a quantum wire," *Phys. Rev. B*, Vol. 46, 4630–4637, 1992.

Advances in the Theory of A, B, C Numbers and Its Application to Waveguide Propagation

Mariana Nikolova Georgieva-Grosse[1] and Georgi Nikolov Georgiev[2]

[1]Consulting in Physics and Computer Sciences, Meterstrasse 4, D-70839 Gerlingen, Germany
[2]Faculty of Mathematics and Informatics
University of Veliko Tirnovo "St. St. Cyril and Methodius", BG-5000 Veliko Tirnovo, Bulgaria

Abstract— Harnessing a recently elaborated iterative technique, the dependence of the real positive numbers A_1, B_1, C_1, defined earlier by the positive purely imaginary zeros $\zeta_{k,n}^{(c)}$ in x ($n = 1, 2, 3, \ldots$) of the Kummer confluent hypergeometric function $\Phi(a, c; x)$, ($a = c/2 - jk$ — complex, $c = 3$, $x = jz$, k, z — real, $-\infty < k < +\infty$, $z > 0$), on the real positive parameters $|\alpha|$ and $\bar{r}_0$ ($0 < |\alpha| < 1$, $\bar{r}_0 > \zeta_{0,n}^{(c)}/2$), satisfying certain criterion, is analyzed numerically, stipulating that $n = 1$ and $\bar{r}_0 \geq 10$. The outcomes are pictured in a graphical form. A second limit of the domain of existence of A_1, B_1 and C_1 in the $|\alpha| - A_1$- and $\bar{r}_0 - A_1$-, $|\alpha| - B_1$- and $\bar{r}_0 - B_1$-, and $|\alpha| - C_1$- and $\bar{r}_0 - C_1$-planes, resp. is specified, linked with a representative of the $L_1(c, n)$ numbers, akin to the zeros $\zeta_{k,n}^{(c)}$ for $k \to -\infty$, in addition to the previously found first one, related to $\zeta_{0,n}^{(c)}/2$. It is established also that as for $\zeta_{0,n}^{(c)}/2 < \bar{r}_0 \leq 10$, so for $\bar{r}_0 \geq 10$, the impact of $|\alpha|$ on A_1, of $\bar{r}_0$ on B_1 and of both $|\alpha|$ and $\bar{r}_0$ on C_1, is slight. Interpreting physically $\bar{r}_0$, $|\alpha|$ and n in a suitable way, the employment of the quantities studied in the computation of the differential phase shift produced by the circular waveguide, wholly filled with ferrite of azimuthal magnetization and propagating normal TE_{0n} mode, is demonstrated. The investigation is a contribution to the theory of A, B, C numbers of which the A_1, B_1, C_1 ones constitute one of the two sub-classes, introduced by now.

1. INTRODUCTION

The object of the theory of A, B, C numbers are the definition, classification, modeling of the values, analysis of the properties and application of the quantities mentioned [1–5]. According to it the same are real and positive, and are advanced by the relations: $A = A_- - A_+$, $B = B_- - B_+$ and $C = C_- - C_+$ [2–5]. $A_\pm$, $B_\pm$ and $C_\pm$ are also real, positive ($A_- > A_+$, $B_- > B_+$ and $C_- > C_+$), and are determined with the help of the positive purely imaginary zeros of a complex Kummer confluent hypergeometric function [6] (of a complex function [2, 5], composed of Kummer and Tricomi ones [6]) of specially selected parameters [1–5]. Two kinds of numbers are considered, labeled by the subscript $1\pm$, resp. 1 ($2\pm$, resp. 2), if they conform to the first (second) case [5]. Their numerical equivalents are counted through iterative schemes [1–5]. These quantities are used to figure the differential phase shift, afforded by the azimuthally magnetized circular and coaxial ferrite waveguides for the normal TE_{0n} modes [1–5]. The field regarded is completely new and branched a short while back off the theory of geometries referred to [1–5].

In an extension to a previous study [3] here the effect of real, positive parameters $|\alpha|$ and $\bar{r}_0$ ($0 < |\alpha| < 1$, $\bar{r}_0 > \zeta_{0,n}^{(c)}/2$, $\zeta_{k,n}^{(c)}$ — nth positive purely imaginary zero in x of the Kummer function $\Phi(a, c; x)$ [6] with $a = c/2 - jk$ — complex, $c = 3$, $x = jz$, k, z — real, $k = 0$, $z > 0$, $n = 1, 2, 3, \ldots$ [3]), meeting the condition [3–5, 7]:

$$\zeta_{0,n}^{(c)}/2 < \bar{r}_0\sqrt{1 - \alpha^2} < L_1(c, n)/|\alpha|, \tag{1}$$

with $L_1(c, n)$ (written before also as $L(c, n)$) — certain positive real numbers [3, 4], on the quantities A_1, B_1, C_1 (A, B, C in the earlier notation [1, 3]) is examined, assuming $n = 1$ and $\bar{r}_0 \geq 10$. (Provided $c = 3$, $n = 1$, $\zeta_{0,n}^{(c)} = 7.66341\ 19404$ and $L_1(c, n) = 6.59365\ 41068$ [3].) An example of the putting into practice of numbers is given, as well.

2. NEW FEATURES OF THE A_1, B_1, C_1 NUMBERS

The solid lines in Figures 1–3 portray the change of the quantities A_1, B_1, C_1 with $|\alpha|$ and $\bar{r}_0$ on the understanding that $n = 1$ and $\bar{r}_0 \geq 10$. In Figures 1(a), (b), 2(a) and 3(a), (b) (Figures 1(c), (d), 2(b) and 3(c), (d)) $|\alpha|$ ($\bar{r}_0$) is regarded as a variable and $\bar{r}_0$ ($|\alpha|$) — as a parameter. The analysis

shows that for all $\zeta_{0,n}^{(c)}/2 < \bar{r}_0 < 2L_1(c,n)$ ($\bar{r}_0 \geq 2L_1(c,n)$) the functions $A_1 = A_1(|\alpha|)$, $B_1 = B_1(|\alpha|)$ and $C_1 = C_1(|\alpha|)$ are continuous with respect to $|\alpha|$, varying in the range(s) $0 < |\alpha| \leq |\alpha_{cr}|$, $|\alpha_{cr}| = \sqrt{1 - [\zeta_{0,n}^{(c)}/(2\bar{r}_0)]^2}$ ($0 < |\alpha| \leq |\alpha_2|$ and $|\alpha_1| \leq |\alpha| \leq |\alpha_{cr}|$, $\alpha_{1,2}^2 = 0.5[1 \pm \sqrt{1 - 4[L_1(c,n)/\bar{r}_0]^2}]$). This is visible from the first group of Figures. The formula for $|\alpha_{cr}|$ is obtained from the left-hand part of the inequality (1) with the sign "=" instead of "<" in it. The quantities $\alpha_{1,2}$ are roots of a biquadratic equation regarding $|\alpha|$, derived from the right-hand part of the same criterion, considered as an equality, ($|\alpha_1|$ corresponds to the sign "+" and $|\alpha_2|$ — to "−", ($|\alpha_2| < |\alpha_1|$)). In the limiting case $\bar{r}_0 = 2L_1(c,n)$, $|\alpha_1| \equiv |\alpha_2| = |\alpha_{\lim}| = 1/\sqrt{2}$. The points in Figures 1–3, depicted by squares, are graphical images of the A_1, B_1, C_1 numbers of such parameters. All $B_1(|\alpha|)$- ($C_1(|\alpha|)$-) characteristics possess a common beginning at $|\alpha| \to 0$, featured through a circle and designated by the symbol $\bar{r}_{0in} = 3.832$, omitted in Figure 3(b) to abstain from a too great ornateness. The ends of curves for all $\bar{r}_0$ (for $\bar{r}_0 > 2L_1(c,n)$) of abscissas equal to $|\alpha_{cr}|$ ($|\alpha_2|$ and $|\alpha_1|$), are denoted by circles (rhombs). (The squares mentioned replace two coinciding rhombs of the identical $|\alpha_2|$ and $|\alpha_1|$.) In each of the Figures the rhombs, situated to the left of the square answer to $|\alpha_2|$ and those to the right of it — to $|\alpha_1|$. In Figures 1(a), (b) and 3(a), (b), the parameter $\bar{r}_0$ relates to the entire line for $\bar{r}_0 < 2L_1(c,n)$ (to the two lines for $\bar{r}_0 \geq 2L_1(c,n)$). The values of $|\alpha_{cr}|$, $|\alpha_1|$, $|\alpha_2|$ and $|\alpha_{\lim}|$ are pertinent to the relevant points (circles, rhombs or square) only. The $|\alpha|$ — co-ordinates of the latter for specific $\bar{r}_0$ in the three cases are the same. To avoid overcrowding the numerical equivalents of all $|\alpha_2|$ and $|\alpha_1|$ and most of the ones of $|\alpha_{cr}|$ are written at the corresponding rhombs

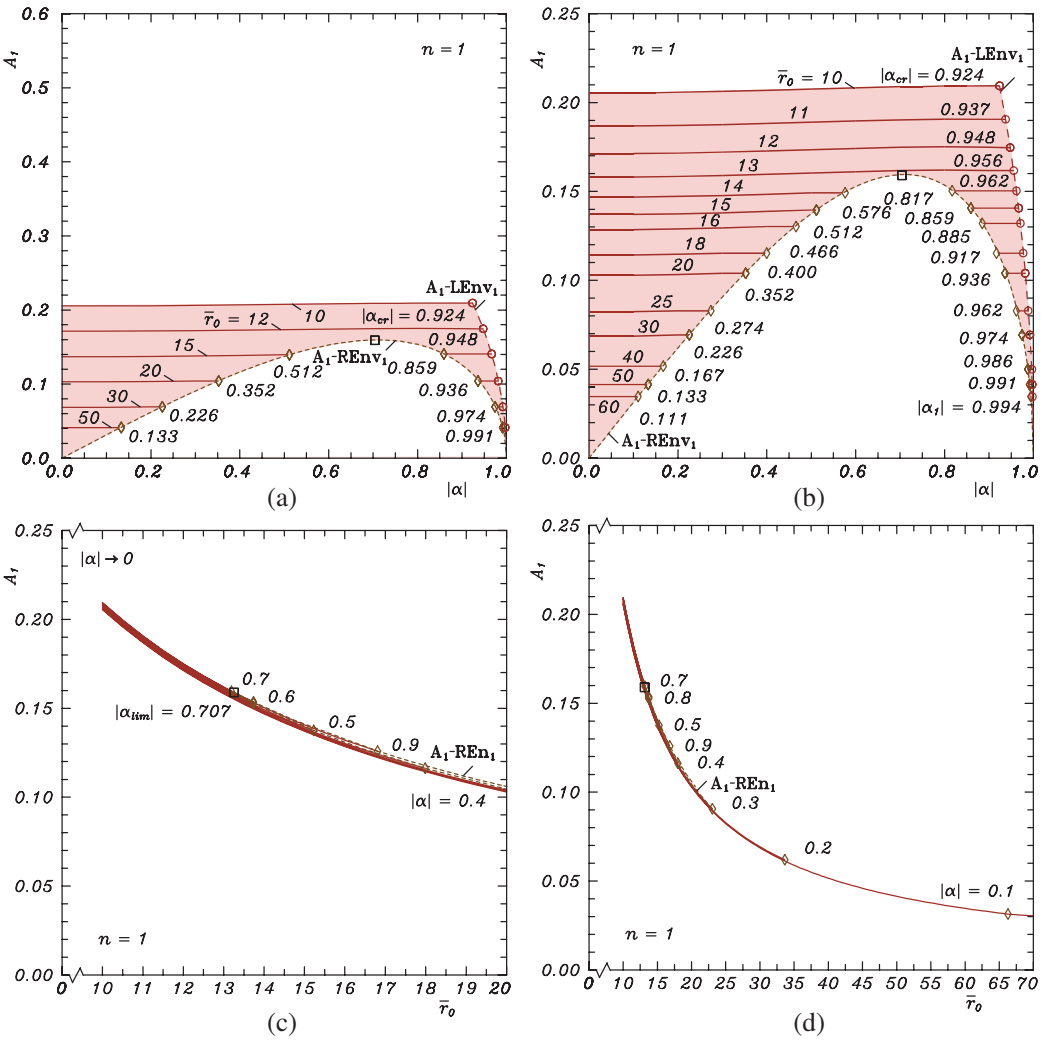

Figure 1: A_1 numbers for $n = 1$: (a) in the interval $\langle 0 \div 0.6 \rangle$ vs. $|\alpha|$ in the interval $\langle 0 \div 1.0 \rangle$ with $\bar{r}_0$ as parameter; (b) in the interval $\langle 0 \div 0.25 \rangle$ vs. $|\alpha|$ in the interval $\langle 0 \div 1.0 \rangle$ with $\bar{r}_0$ as parameter; (c) in the interval $\langle 0 \div 0.25 \rangle$ vs. $\bar{r}_0$ in the interval $\langle 10 \div 20 \rangle$ with $|\alpha|$ as parameter; (d) in the interval $\langle 0 \div 0.25 \rangle$ vs. $\bar{r}_0$ in the interval $\langle 10 \div 70 \rangle$ with $|\alpha|$ as parameter.

and circles, resp., in Figures 1(a), (b) solely. Further, the values of $|\alpha_2|$ and $|\alpha_1|$ for the even rhombs, counted from left and right, resp. to the middle, are given in Figure 3(a), and those of the odd ones — in Figure 3(b). The first (second) of these Figures contains also the numerical equivalents of the parameters mentioned, corresponding to the initial and the last rhombs (circles). To obviate flamboyance, the symbol $|\alpha_1|$ ($|\alpha_2|$), conforming to all $|\alpha|$ — co-ordinates of the A_1 and C_1 numbers, pictured by rhombs and located to the right (to the left) of the limiting squares in Figures 1(a), (b) and 3(a), (b), is presented in Figure 1 (b) (in Figure 3(b)) only. The left (right) rhombs of the pair in Figure 2(a), labeled by identical numbers indicate the end (the beginning) of the left (right) part of a $B_1|\alpha|$ — line for certain $\bar{r}_0 > 2L_1(c,n)$. The $A_1 - LEnv_1$- ($B_1 - LEnv_1$-, resp. $C_1 - LEnv_1$-) dashed envelope, connecting the circles, marks off the limit of the area of existence of numbers in the $|\alpha| - A_1$- ($|\alpha| - B_1$-, resp. $|\alpha| - C_1$-) plane from the side of larger values of $|\alpha|$. It is a continuation of the $A - LEnv_1$- ($B - LEnv_1$-, resp. $C - LEnv_1$-) line in Figures 1(a), 2(a) and 3(a), (b), drawn for $\zeta_{0,n}^{(c)}/2 \le \bar{r}_0 \le 10$ [3]. The $A_1 - REnv_1$- ($B_1 - REnv_1$-, resp. $C_1 - REnv_1$-) dotted curve, linking the rhombs, serves as a second boundary of the area mentioned. This is a new element in the Figures inspected. The square in Figures 1(a), (b) marks the maximum of the $A_1 - REnv_1$- envelope and in Figures 3(a), (b) — the minimum of the $C_1 - REnv_1$- one. The area in which A_1 (B_1, resp. C_1) are determined for $\bar{r}_0 \ge 10$ in the $|\alpha| - A_1$- ($|\alpha| - B_1$-, resp. $|\alpha| - C_1$-) plane is shown by pink in Figures 1(a), (b) (blue, resp. green in Figure 2(a), resp. Figures 3(a) and 3(b) for $10 \le \bar{r}_0 \le 20$).

For all $0 < |\alpha| < 1$ the functions $A_1 = A_1(\bar{r}_0)$, $B_1 = B_1(\bar{r}_0)$ and $C_1 = C_1(\bar{r}_0)$ are continuous with regard to $\bar{r}_0$, running through the interval $\bar{r}_{0cr} < \bar{r}_0 < \bar{r}_{0en-}$ where $\bar{r}_{0cr} = \zeta_{0,n}^{(c)}/[2(1-\alpha^2)^{1/2}]$ and $\bar{r}_{0en-} = L_1(c,n)/[|\alpha|(1-\alpha^2)^{1/2}]$. (The first (second) formula is deduced from the left- (right-) hand part of inequality (1), replacing the sign "<" by "=" in it.) This is illustrated in Figures 1(c), (d), 2(b) and 3(c), (d). The lines, depicting A_1 (B_1, resp. C_1) in the Figures considered originate in the $A_1 - LEn_1$- ($B_1 - LEn_1$-, resp. $C_1 - LEn_1$-) dashed envelope which forms the a first boundary of the area of existence of the numbers in the $\bar{r}_0 - A_1$- ($\bar{r}_0 - B_1$-, resp. $\bar{r}_0 - C_1$-) plane. It is computed from the expression for $\bar{r}_{0cr}$ and complements the $A - LEn_1$- ($B - LEn_1$-, resp. $C - LEn_1$-) curve in Figures 1(b)–(d), 2(b) and 3(c), (d) [3]. The set of Figures referred to contains the sources (pictured by circles) of the $A_1(\bar{r}_0)$- ($B_1(\bar{r}_0)$-, resp. $C_1(\bar{r}_0)$-) ($A(\bar{r}_0)$- ($B(\bar{r}_0)$-, resp. $C(\bar{r}_0)$-) curves for $|\alpha| = 0.1(0.1)0.9$, since the relevant values of $\bar{r}_{0cr}$ are less than 10. The $\bar{r}_0$- co-ordinates for chosen $|\alpha|$ of the ends of the same are computed from the formula for $\bar{r}_{0en-}$ and are pictured by rhombs. In Figures 1(c), (d) the parameters $|\alpha|$ of characteristics are written at their terminations. Those for $|\alpha| = 0.6$ and 0.8 coincide. In Figures 2(b) and 3(c), (d) the numerical equivalent of $|\alpha|$ ($\bar{r}_{0en-}$), corresponding to certain curve, is placed above it (at its end). Not to overburden the illustrative part of the paper, the denotation $\bar{r}_{0en-}$ itself is inserted in Figure 3(d) only. The $A_1 - REn_1$- ($B_1 - REn_1$-, resp. $C_1 - REn_1$-) dotted envelopes, linking the rhombs are new elements in the $\bar{r}_0 - A_1$- ($\bar{r}_0 - B_1$-, resp. $\bar{r}_0 - C_1$-) plane. For specific $\bar{r}_0 > 2L_1(c,n)$ they are double-valued.

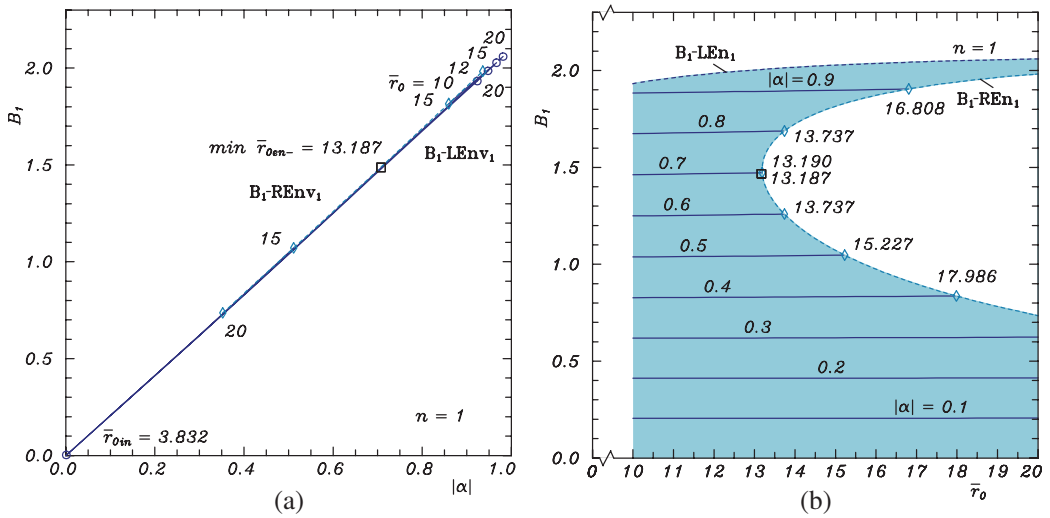

Figure 2: B_1 numbers for $n = 1$ vs.: (a) $|\alpha|$ in the interval $\langle 0 \div 1.0 \rangle$ with $\bar{r}_0$ as parameter; (b) $\bar{r}_0$ in the interval $\langle 10 \div 20 \rangle$ with $|\alpha|$ as parameter.

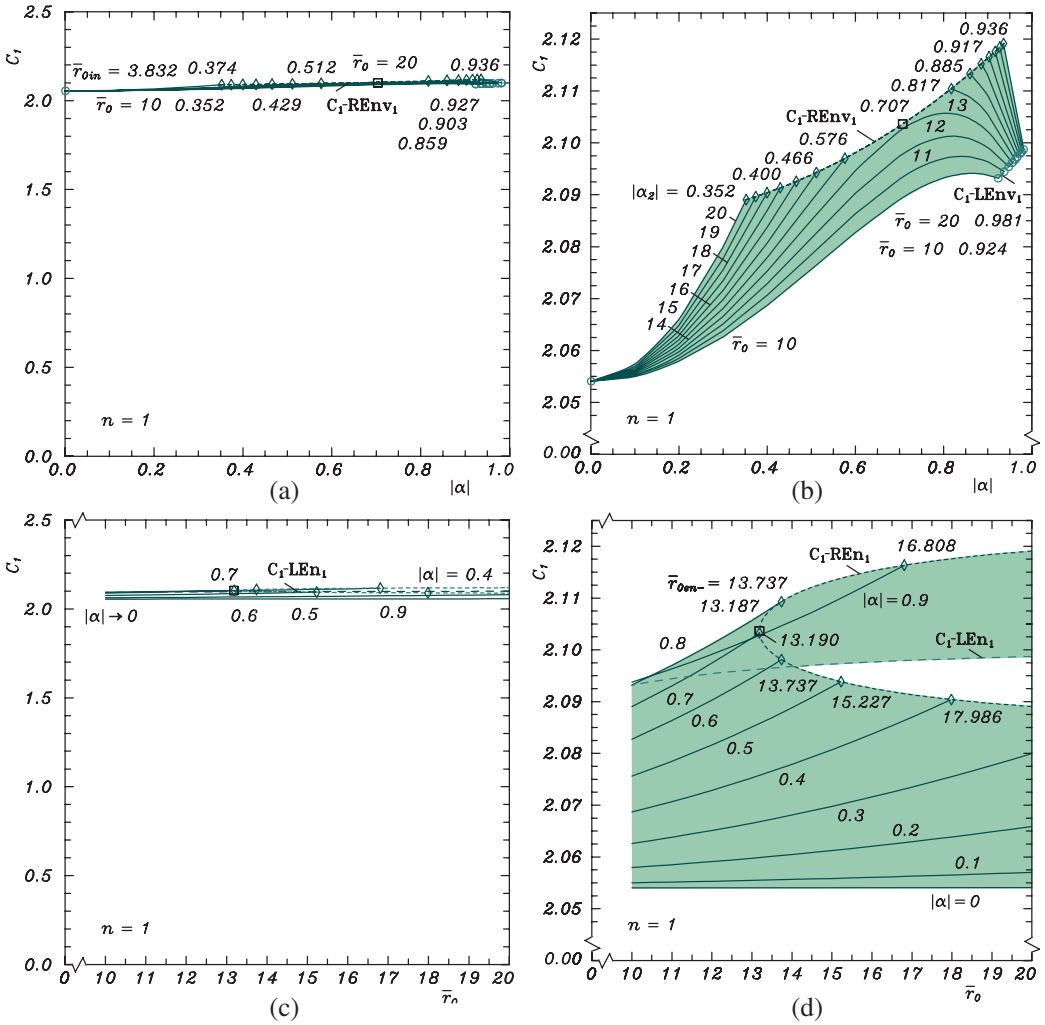

Figure 3: C_1 numbers for $n = 1$: (a) in the interval $\langle 0 \div 2.5\rangle$ vs. $|\alpha|$ in the interval $\langle 0 \div 1.0\rangle$ with $\bar{r}_0$ as parameter; (b) in the interval $\langle 2.05 \div 2.125\rangle$ vs. $|\alpha|$ in the interval $\langle 0 \div 1.0\rangle$ with $\bar{r}_0$ as parameter; (c) in the interval $\langle 0 \div 2.5\rangle$ vs. $\bar{r}_0$ in the interval $\langle 10 \div 20\rangle$ with $|\alpha|$ as parameter; (d) in the interval $\langle 2.05 \div 2.125\rangle$ vs. $\bar{r}_0$ in the interval $\langle 10 \div 20\rangle$ with $|\alpha|$ as parameter.

Their minimum is observed at $\min \bar{r}_{0en^-} = 2L_1(c, n)$, conforming to $|\alpha_{\lim}|$. For this reason it is designated by a square. The symbols $|\alpha_{\lim}| = 0.707$ and $\min \bar{r}_{0en^-} = 13.187$ may be regarded as designations of the parameters of all squares. Without risk of confusion in this form the first of them is presented in Figure 1(c) and the second one — in Figure 2(a). Their numerical values are given also in Figure 3(b) and Figures 2(a) and 3 (d), resp. If $\bar{r}_{0en^-}$ diminishes, e.g., from 20 to 13.187 ($|\alpha_2|$ grows from 0 and $|\alpha_1|$ lessens from 1 to 0.707), the two resulting rhombs tend to the square at which they overlap. The envelopes in question play the role of a second bound of the area of existence of numbers in the plane mentioned shown by pink in Figures 1(c), (d) (blue, resp. green in Figure 2(b), resp. Figures 3(c) and 3(d) for $10 \le \bar{r}_0 \le 20$). Note that the area of existence of C_1, (resp. its borders) is (are) more complicated, (cf. Figure 3(d)). The joint consideration of results presented here and in Refs. [1, 3, 4] shows that the influence of $|\alpha|$ on A_1, of $\bar{r}_0$ on B_1 and of both $|\alpha|$ and $\bar{r}_0$ on C_1, is slight.

3. APPLICATION

If $\bar{r}_0$ is the normalized in an appropriate way radius of a circular waveguide, $|\alpha|$ is the magnitude of the off-diagonal Polder permeability tensor element of the azimuthally magnetized ferrite, entirely filling it and n is the number of the propagating along it normal TE_{0n} mode, the sequence of inequalities (1) presents the condition for phase shifter operation of this structure, i.e., it yields the set of values of parameters $\{|\alpha|, \bar{r}_0\}$ for which it might provide differential phase shift $\Delta\bar{\beta} = \bar{\beta}_- - \bar{\beta}_+$ [1–5, 7]. Here $\bar{\beta}_-$ and $\bar{\beta}_+$ are the normalized phase constants of the wave for positive (clockwise) and negative (clockwise) magnetization of the anisotropic medium [1–5, 7]. Under these

assumptions the phase shift could be computed normalized form through the formula (written in the new notations for the numbers) [2, 3, 5]:

$$\Delta\bar{\beta} = A_1 B_1 / C_1. \tag{2}$$

Moreover, $\bar{r}_{0cr}$ ($|\alpha_{cr}|$) correspond to the cut-off state of configuration, $\bar{r}_{0in}$ stands for $\bar{r}_{0cr}$ in case of a dielectric load [3], $\bar{r}_{0en-}$ $|\alpha_1|$, $|\alpha_2|$ and $|\alpha_{\lim}|$ are connected with the envelope of phase curves, marking the end of propagation for negative magnetization from the side of higher frequencies [7]. Therefore, the dashed (dotted) envelopes in Figures 1–3 are connected with the first (second) limiting state of the configuration.

Numerical example: The case $\bar{r}_0 = 12$ and $|\alpha| = 0.1$ is regarded. Applying the iterative method from Refs. [3, 5] yields: $A_1 = 0.1712\ 7600$, $B_1 = 0.2055\ 3120$ and $C_1 = 2.0553\ 1204$. Hence, it is obtained $\Delta\bar{\beta} = 0.0171\ 2760$. Since finding the quantities A_1, B_1, C_1 for each set of parameters by the scheme mentioned is difficult, it is suggested to use for this purpose the above Figures. This allows to get $\Delta\bar{\beta}$ from Equation (2) for all $\bar{r}_0$ and $|\alpha|$ from the intervals $\langle 10 \div 20\rangle$ resp. $\langle 0 \div 1.0\rangle$ in which graphical results for all the numbers are available.

4. CONCLUSION

The introduced before by specific zeros of a definite complex Kummer function positive real numbers A_1, B_1, C_1 are studied numerically, depending on their parameters n — a positive integer and $|\alpha|$ and $\bar{r}_0$ — real positive quantities, subject to a certain criterion. The case $n = 1$, $0 < |\alpha| < 1$ and $\bar{r}_0 \geq 10$ is considered. The results are presented graphically. The most important conclusion of analysis is that the domain of existence of numbers is bilaterally restricted. An application of the outcomes in the theory of waveguides is manifested.

ACKNOWLEDGMENT

We express our gratitude to our mother Trifonka Romanova Popnikolova and to our late father Nikola Georgiev Popnikolov for their self-denial and for their tremendous efforts to support all our undertakings.

REFERENCES

1. Georgiev, G. N. and M. N. Georgieva-Grosse, "Formulae for differential phase shift computation in an azimuthally magnetized circular ferrite waveguide," *Proc. Millenn. Conf. Antennas Propagat. AP-2000*, 1002, in CDROM, Davos, Switzerland, August 9–14, 2000.
2. Georgieva-Grosse, M. N. and G. N. Georgiev, "The A, B, C numbers and their application in the theory of waveguides," *PIERS Proceedings*, 1043–1047, Moscow, Russia, August 18–21, 2009.
3. Georgieva-Grosse, M. N. and G. N. Georgiev, "On the A, B, C numbers and their application in the theory of circular waveguide with azimuthally magnetized ferrite," *PIERS Online*, Vol. 6, No. 4, 370–374, 2010.
4. Georgieva-Grosse, M. N. and G. N. Georgiev, "On the class of A_1 numbers: Definition, numerical modeling, domain of existence and application," *Proc. XXX URSI General Assembly*, in CDROM, Istanbul, Turkey, article ID BP1.47, 4 pages, August 13–20, 2011.
5. Georgieva-Grosse, M. N. and G. N. Georgiev, "Comparative study of the computational modeling and application of the classes of A, B, C numbers," *Proc. Thirteenth Int. Conf. Electromagn. Adv. Applicat. ICEAA'11*, 660–663, in CDROM, Turin, Italy, September 12–16, 2011, (Invited Paper in the Special Session "Future challenges in mathematical and computational electromagnetics and its applications," organized by G. N. Georgiev and M. N. Georgieva-Grosse).
6. Tricomi, F. G., *Funzioni Ipergeometriche Confluenti*, Edizioni Cremonese, Rome, Italy, 1954.
7. Georgiev, G. N. and M. N. Georgieva-Grosse, "A new property of the complex Kummer function and its application to waveguide propagation," *IEEE Antennas Wireless Propagat. Lett.*, Vol. 2, 306–309, December 2003.

An Extra Reduced Size Dual-mode Bandpass Filter for Wireless Communication Systems

Jawad K. Ali and Nasr N. Hussain
Department of Electrical and Electronic Engineering, University of Technology, Baghdad, Iraq

Abstract— A new miniaturized dual-mode microstrip bandpass filter is presented. The filter structure has been fractally generated based on the 4th iteration Minkowski-like pre-fractal geometry, using the conventional dual-mode square ring resonator as the initiator in the fractal generation process. It has been found that the presented filter possesses a size reduction of about 88% as compared with the dual-mode bandpass filter based on the conventional square ring resonator. In addition; simulation results show that the filter has acceptable return loss and transmission responses besides the miniaturized size gained.

1. INTRODUCTION

Dual-mode resonators have been characterized by many advantages such as small size, light weight, and low loss, making them widely used in realization of microwave filters for wireless communication systems, such as satellite and mobile communication systems. Each dual-mode resonator can be used as a doubly tuned resonant circuit, and therefore the number of resonators required for an N-order filter is reduced by half, resulting in a compact filter configuration. Microstrip dual-mode resonator filters have been first introduced in 1972 [1]. Since then, different configurations for the dual-mode resonators have been reported [2–9]. Numerous techniques have been proposed in order to reduce the size of the dual-mode resonator bandpass filters. These involve the use of meander resonators [2, 3], slotted patch [4, 5], stepped impedance resonators [6, 7], and many others [8, 9].

Fractal curves are characterized by a unique property that, after an infinite number of iterations, their length becomes infinite although the entire curve fits into the finite area. This space-filling property can be exploited for the miniaturization of microstrip resonators. Due to the technology limitations fractal curves are not physically realizable. Pre-fractals, fractal curves with finite order, are used instead [10]. Various fractal geometries have been applied to realize compact size bandpass filters [10–16]. Most of the published works concentrates on the application of different fractal geometries to construct single-mode resonator filters [10–15]. Furthermore, it has been reported that microstrip bandpass filters with fractal shaped dual-mode resonators can be realized [16]. Results show that these filters possess considerable size reductions as compared with the one based on the conventional dual-mode square ring resonator.

In this paper, a new dual-mode microstrip bandpass filter based on the 4th iteration Minkowski-like pre-fractal geometry has been presented. The filter is supposed to be suitable for microwave applications as a low cost mass-producible, high performance and compact component.

2. THE FILTER STRUCTURE

The dual-mode filter structure presented in this paper is composed of a single fractally generated microstrip dual-mode ring resonator. The resonator structure is the result of the 4th iteration Minkowski-like pre-fractal geometry. Details of the generation process have been outlined in Figure 1. As in the case of most of the deterministic pre-fractals, the resulting structures, corresponding to the different iteration levels are self-similar and are space-filling. These structures possess an additional property in each of the iteration levels; the symmetry of the whole structure about its diagonal. This property is of special importance in the design of dual-mode loop resonators [8].

The resulting pre-fractal structure has the characteristic that the perimeter increases to infinity while maintaining the volume occupied. This increase in length decreases the required volume occupied for the pre-fractal bandpass filter at resonance. It has been found that:

$$P_n = (1 + 2a_2)P_{n-1} \tag{1}$$

where P_n is the perimeter of the nth iteration pre-fractal and a_2 is equal to the ratio w_2/L_o. Theoretically as n goes to infinity the perimeter goes to infinity. The ability of the resulting structure to increase its perimeter, at all iterations, was found very triggering for examining its size reduction capability as a microstrip bandpass filter.

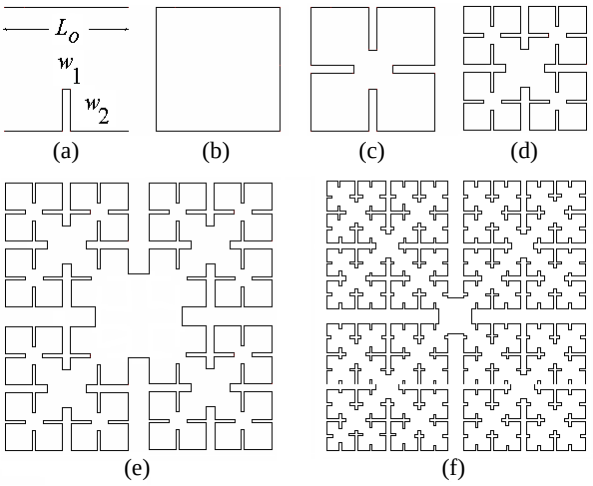

Figure 1: The generation process of the Minkowski-like pre-fractal structure. (a) the generator, (b) the square ring resonator, (c) the 1st iteration, (d) the 2nd iteration, (e) and (f) enlarged copies of the 3rd and 4th iterations.

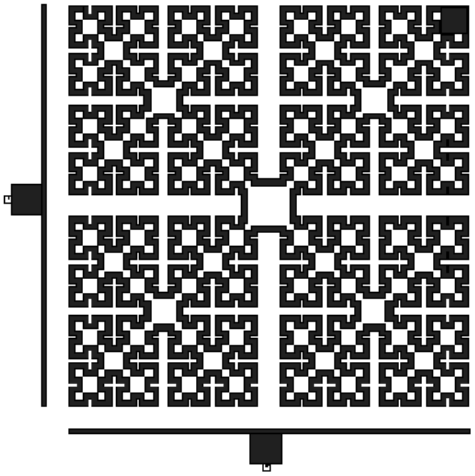

Figure 2: The layout of the modeled 4th iteration fractal-shaped resonator dual-mode microstrip bandpass filter.

The length, L_o of the conventional microstrip dual-mode square ring resonator has been determined using the classical design equations reported in the literature [8, 9], for a specified value of the operating frequency and given substrate properties. This length represents a slightly less than quarter the guided wavelength at its fundamental resonant frequency of the resonator.

As shown in Figure 1, applying geometric transformation of the generating structure (Figure 1(a)) on the square ring resonator (Figure 1(b)), results in the 1st iteration filter structure depicted in (Figure 1(c)). Similarly successive bandpass filter shapes, corresponding to the following iterations can be produced as successive transformations have been applied. Figure 1(f) shows an enlarged copy of the 4th iteration fractal structure, on which the proposed bandpass filter design is based. At the nth iteration, the corresponding filter side length, L_n has been found to be [16]

$$L_n = (0.6)^{n/2} L_0 \tag{2}$$

A large variety of prefractal structures can be produced corresponding to different values of a_1 and a_2. It is expected, then, that the resulting structures will resonate at different frequencies when L_o is maintained constant. In this paper, the values of a_1 and a_2 have been chosen to fit with the filter structures reported in [2, 16, 17]; making direct comparison of their performances with that of the presented filter easy.

3. FILTER DESIGN

A bandpass filter structure, based on dual-mode microstrip fractal-shaped resonator, has been designed for the ISM band applications at a design frequency of 2.4 GHz. At first, the side length of the square ring resonator L_o, that matches the passband frequency, has to be calculated. It has been found that this length is of about a quarter the guided wavelength. Then the side length, L_4, for the 4th iteration fractal-shaped resonator can be calculated based on the value of L_o, using (2). Then a small discontinuity (perturbation) is placed in the symmetry axis of the ring. Figure 2 shows the layout of the 4th iteration fractal-shaped dual-mode resonator with the perturbation applied at a location that is assumed at a 45° offset from its two orthogonal modes. The perturbation is in the form of a small patch added to the square ring, and the other subsequent iterations ring resonators. Low passband loss requires strong input/output coupling to the resonator. This is achieved by a narrow gap and a large coupling area that can be provided by the capacitive coupling. The spacing (gap) is very critical parameter: If it is too narrow, matching is insufficient, and fitting the poles to the desired stopband is not possible. On the other hand, if the gap is too wide, the two modes separate from each other so that the filter becomes broadband and the insertion loss in the passband increases dramatically.

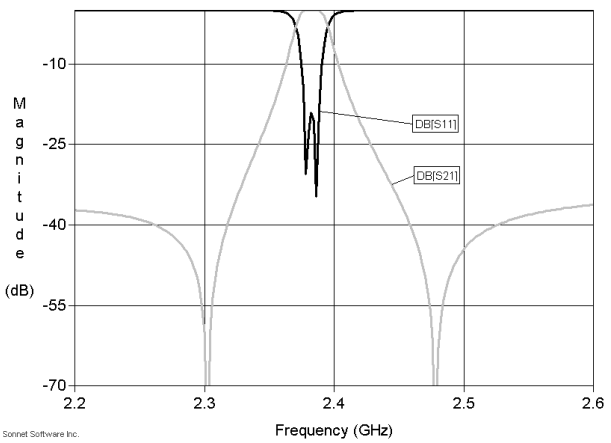

Figure 3: Performance responses of the dual-mode microstrip bandpass filter based on the 4th iteration.

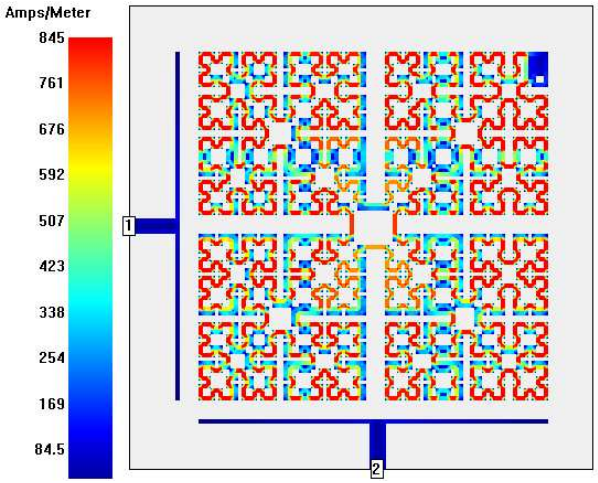

Figure 4: Simulated charge distribution for the 4th iteration dual-mode microstrip bandpass filter structure at the design frequency.

It is worth to mention that, the filter structures based on the 1st and 2nd iterations depicted in Figures 1(c) and 1(d), have similar structures with those reported in [2] and [17] respectively. The reported structures represent two separate attempts to produce compact size microstrip bandpass filters; each consists of a single design step and does not go on further. These filter structures have been found to possess size reductions of 40% and 64% respectively, as compared with the conventional dual-mode microstrip square ring resonator. In addition, dual-mode bandpass filter structure, based on a fractal-shaped resonator in the form depicted in Figure 1(e), offers a size reduction of about 79% as reported in [16]. Accordingly, the filter structure, based on the 4th iteration can be considered, up to the author's knowledge, a novel design. This filter offers further size reduction of about 88% as compared with the conventional dual-mode square ring resonator.

4. PERFORMANCE EVALUATION

A dual-mode microstrip bandpass filter, based on the fractal shape shown in Figure 1(f), has been modeled and analyzed at an operating frequency of 2.4 GHz using a full-wave electromagnetic EM simulator, from Sonnet Software Inc. [18], with a substrate having a thickness of 1.27 mm and a relative dielectric constant of 10.8. The resonator side length that matches the specified frequency has been found to be of about 4.55 mm with a trace width of 0.18 mm. For the present case, it has been found that the modeled filter performs well with a square perturbation patch having a length of about 0.33 mm. The input/output coupling structure is capacitive with an optimum gap of about 0.15 mm. Simulation results show that the resulting bandpass filter exhibits a quasi-elliptic response with two transmission zeros at finite frequencies near the passband as depicted in Figure 3. The filter shows a very good response with a return loss of about −10 dB and a fractional bandwidth of about 5% at a frequency of 2.38 GHz.

Figure 4 shows the current density pattern at the surface of the 4th iteration dual-mode microstrip bandpass filter at the design frequency. This figure implies that, at the design frequency the two degenerate modes are excited and coupled to each other leading to the required filter performance. The filter presented in this paper offers a size reduction of about 88% as compared with the conventional dual-mode microstrip square ring resonator, while those filters reported in [2, 16, 17, 19].

5. CONCLUSIONS

An extra reduced size microstrip bandpass filter structure has been presented in this paper, as a result of a new design technique for dual-mode microstrip bandpass filters. A dual-mode bandpass filter structure has been produced based on the 4th iteration Minkowski-like prefractal geometry, using the conventional dual-mode square ring resonator as an initiator. The proposed microstrip bandpass filter design has been modeled and analyzed using a full-wave EM simulator, at the ISM band. This dual-mode filter has been found to possess a size reduction which is better than that

reported in the literatures. It has been found that the presented filter design offers a size reduction of about 88% as compared with the conventional dual-mode microstrip square ring resonator under the same design specifications. The proposed filter can be generalized as a flexible design tool for compact microstrip bandpass filters for a wide variety of wireless communication systems.

REFERENCES

1. Wolff, I., "Microstrip bandpass filter using degenerate modes of a microstrip resonator," *Electron. Lett.*, Vol. 8, No. 12, 302–303, 1972.
2. Hong, J. S. and M. J. Lancaster, "Microstrip bandpass filter using degenerate modes of a novel meander loop resonator," *IEEE Microwave and Guided Wave Lett.*, Vol. 5, No. 11, 371–372, 1995.
3. Gorur, A. and C. Karpuz, "Miniature dual-mode microstrip filters," *IEEE Microwave and Wireless Comp. Lett.*, Vol. 17, No. 1, 37–39, 2007.
4. Tu, W. H. and K. Chang, "Miniaturized dual-mode bandpass filter with harmonic control," *IEEE Microwave and Wireless Comp. Lett.*, Vol. 15, No. 12, 838–840, 2005.
5. Zhu, L., P. M. Wecowski, and K. Wu, "New planar dual-mode filter using cross-slotted patch resonator for simultaneous size and loss reduction," *IEEE Trans. Microwave Theory Tech.*, Vol. 47, No. 5, 650–654, 1999.
6. Fok, S. W., P. Cheong, K. W. Tam, and R. P. Martins, "A novel microstrip square-loop dual-mode bandpass filter with simultaneous size reduction and spurious response suppression," *IEEE Trans. Microwave Theory Tech.*, Vol. 54, No. 5, 2033–2040, 2006.
7. Matsuo, M., H. Yabuki, and M. Makimoto, "Dual-mode stepped-impedance ring resonator for bandpass filter applications," *IEEE Trans. Microwave Theory Tech.*, Vol. 49, No. 7, 1235–1240, 2001.
8. Hong, J. S. and M. J. Lancaster, *Microstrip Filters for RF/Microwave Applications*, John Wiley and Sons Ltd., New York, 2001.
9. Chang, K. and L. Hsieh, *Microwave Ring Circuits and Related Structures*, John Wiley and Sons Ltd., New York, 2004.
10. Crnojevic-Bengin, V. and D. Budimir, "Novel compact resonators with multiple 2-d hilbert fractal curves," *Proceedings of the 35th European Microwave Conference, EuMA*, Paris, France, Oct. 2005.
11. Crnojevic-Bengin, V., V. Radonic, and B. Jokanovic, "Complementary split ring resonators using square sierpinski fractal curves," *Proceedings of the 36th European Microwave Conference, EuMA*, Manchester, UK, Sep. 2006.
12. Wu, G. L., W. Mu, X. W. Dai, and Y. C. Jiao, "Design of novel dual-band bandpass filter with microstrip meander-loop resonator and CSRR DGS," *Progress In Electromagnetics Research*, Vol. 78, 17–24, 2008.
13. Crnojevic-Bengin, V. and D. Budimir, "Novel microstrip resonators with embeded 3-D curves," *Proceedings of the 35th Asia-Pacific Microwave Conference, APMC*, New Delhi, India, Dec. 2004.
14. Yousefzadeh, N., C. Ghobadi, and M. Kamyab, "Consideration of mutual coupling in a microstrip patch array using fractal elements," *Progress In Electromagnetics Research*, Vol. 66, 41–46, 2006.
15. Barra, M., C. Collado, J. Mateu, and J. M. O'Callaghan, "Miniaturization of superconducting filter using hilbert fractal curves," *IEEE Trans. Appl. Supercon.*, Vol. 15, No. 3, 3841–3846, 2005.
16. Ali, J. K., "A new miniaturized fractal bandpass filter based on dual-mode square ring resonator," *Proceedings of the 5th Inter. Multi-Conference on Systems, Signals and Devices, SSD'08*, Amman, Jordan, Jun. 2008.
17. Hong, J. S. and M. J. Lancaster, "Recent advances in microstrip filters for communications and other applications," *Proceedings of the IEE Colloquium on Advances in Passive Microwave Components*, London, UK, May 1997.
18. *EM User's Manual*, Version 11.0, Sonnet Software, Inc., Mar. 2007.
19. Hettstedt, F., T. Lehmann, and R. Knoechel, "Novel dual-mode microstrip bandpass filter," *IEEE Microwave Mag.*, Vol. 10, No. 1, 155–157, 2009.

New Defected Microstrip Structure Bandstop Filter

J.-K. Xiao[1] and W.-J. Zhu[2]

[1]School of Electronical & Mechanical Engineering, Xidian University, Xi'an 710071, China
[2]School of Computer and Information, Hohai University, Changzhou 213022, China

Abstract— Defected microstrip structure (DMS) has similar properties with defected ground structure (DGS) but without any leakage through the ground plane. In this report, the stop-band performance of DMS is studied, and new single band, dual-band and tri-band bandstop filters with DMS are proposed. The dual-band and tri-band bandstop filters are fabricated, and the measured results are similar to the simulation. The new DMS bandstop filters have advantages of good frequency selectivity, low loss and simple circuit topology, and simultaneously, has a miniature circuit size of no more than 30 mm × 1.2 mm.

1. INTRODUCTION

Currently, the defected ground structure (DGS) [1–3] has been widely employed to improve filter performance and reduce filter size. DGS is proved efficiency for harmonic suppression and has stop-band performance in microwave circuits design, and especially the periodical DGSs, which extend the stopband greatly. DGS increases the effective capacitance and inductance of microstrip line, and the performances of filters or other microwave components are effectively improved. However, DGS introduces wave leakage through the ground plane.

Compared with DGS circuit, the traditional defected microstrip structure (DMS) [4–6] unit is made by etching two vertical narrow slots in the microstrip line. DMS is more easily integrated with other microwave circuits, and has an effectively reduced circuit size compared with DGS, and simultaneously, DMS exhibits the properties of slow-wave, rejecting microwaves in certain frequencies and has an increasing electric length of certain circuits which are similar to the well known DGS but without any manipulation of the ground plane.

In the present report, new defected microstrip structure is studied, and new bandstop filters with single band, dual-band and tri-band are designed. Dual-band and tri-band bandstop filters are fabricated and measured, and the experiment demonstrates the new design.

2. DEFECTED MICROSTRIP STRUCTURE

Defected microstrip structure (DMS) consists of a horizontal slot and a vertical slot in the middle of conductor line, as Figure 1 shows. Similar to the defected ground structure (DGS), DMS increases the electric length of microstrip line, and disturbs its current distribution, and the effective capacitance and inductance of a mirostrip line increase. Accordingly, the DMS has stopband and slow-wave characteristics [1], as is shown in Figure 2, and new microwave components especially bandstop filters and low pass filters can be designed by using these characteristics. In order to show the difference and do a comparison, the simulated results are got by using a 50-ohm microstrip line with a substrate relative permittivity of 2.2 and 10.2, and a thickness of 0.8 mm and 1.27 mm,

Table 1: Stop band characteristics of DMS using 50 Ω microstrip line ($\varepsilon_r = 2.2$, $H = 0.8$ mm).

DMS Dimensions (mm)	$a = 0.2$, $c = 0.8$, $d = 1.0$		
	$b = 5.9$	$b = 9.2$	$b = 13.9$
f_0 (GHz)	10.58	8.92	6.49
f_c (GHz)	6.01	4.73	3.01

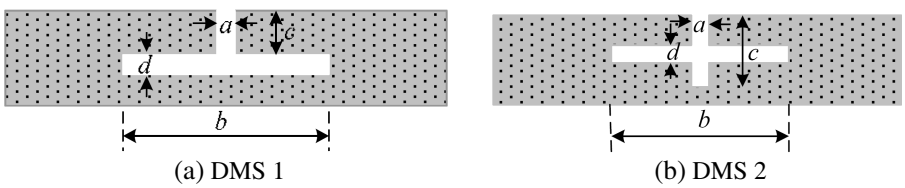

(a) DMS 1 (b) DMS 2

Figure 1: Defected microstrip structures (DMS).

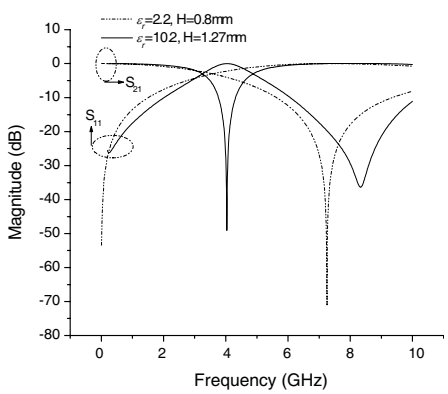

Figure 2: Simulated S-parameters of 50-ohm Microstrip line with DMS unit 1, for $\varepsilon_r = 2.2$, $a = 0.2\,\text{mm}$, $b = 13\,\text{mm}$, $c = 0.8\,\text{mm}$, $d = 1\,\text{mm}$, for $\varepsilon_r = 10.2$, $a = 0.2\,\text{mm}$, $b = 14\,\text{mm}$, $c = 0.3\,\text{mm}$, $d = 0.3\,\text{mm}$

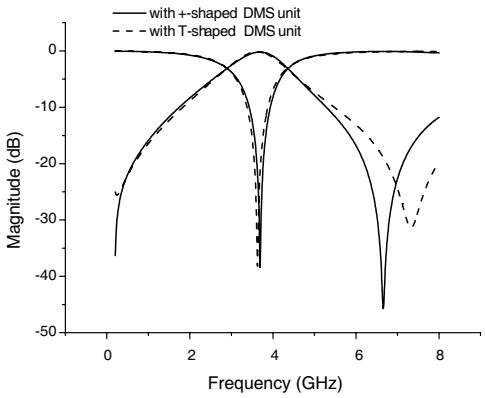

Figure 3: Simulated S-parameters comparison of DMS 1 and DMS 2, $\varepsilon_r = 10.2$, $a = 0.4\,\text{mm}$, $b = 16\,\text{mm}$, $c = 1.1\,\text{mm}$, $d = 0.3\,\text{mm}$.

respectively. It can be seen from Figure 2 that DMS has obvious stop band performance, and a bandstop filter can be easily obtained using high permittivity substrate. It can be seen from Figure 3 that the proposed DMS 2 has better stopband performance. In the research, we observed that DMS can be described by horizontal slot length b and vertical slot width a, and it shows the horizontal slot length affects the effective inductance, and which increases with b increasing, and introduces a lower stop band. While, the vertical slot width affects the effective capacitance, and which decreases with a increasing, and lower capacitance induces to a higher resonant frequency f_0. Stopband characteristics of DMS using $50\,\Omega$ microstrip line are shown in Table 1.

The electrical performance of stop band for DGS is performed as a parallel LC resonant circuit [2, 5], because the stop band performance of new DMS is similar to that of the DGS unit, so the equivalent circuit model of DGS [2] can be used to extract the equivalent circuit parameters of DMS, and inductance L and capacitance C can be expressed as

$$C = \frac{\omega_c}{Z_0 g_1} \cdot \frac{1}{\omega_0^2 - \omega_c^2}, \quad L = \frac{1}{4\pi^2 f_0^2 C} \tag{1}$$

The equivalent circuit parameters of the DMS shown in Figure 1 can be calculated from expression (1).

3. DMS BANDSTOP FILTERS

In order to demonstrate the stopband validity of DMS, bandstop filters with a single band, dual-band and tri-band are designed with dielectric relative permittivity of 10.2 and thickness of 1.27 mm, as shown in Figure 4 and Figure 6, respectively. Simulated frequency responses comparison with b of the single band bandstop filter are shown in Figure 5, and it shows operation frequency increases with parameter b decreasing, and for $b = 15\,\text{mm}$, the filter has a relative bandwidth of 5.68% and low loss of no more than 0.8 dB at center frequency 5.66 GHz, and a pair of transmission zeros with attenuation of no less than 36 dB.

For dual-band and tri-band bandstop filter implementation, a pair of vertical slot is introduced, and the horizontal slot affects the effective inductance, while, the vertical slot affects the effective capacitance. Simulated frequency responses of the dual-band bandstop filter are shown in Figure 7, and relationships of operation frequency with parameter b are shown in Figure 8. It can be seen the operation frequency of the dual-stopband decrease with horizontal slot length b increasing, and for $b = 15.8\,\text{mm}$, the dual-band operate at 1.89 GHz and 5.69 GHz, respectively, and has low loss. In order to verify the design, the dual-band bandstop filter is fabricated and measured, as Figure 9 shows, and the measurement is got by Agilent E5071C vector network analyzer, and it can be seen the measurement is similar to the simulation.

When b increases to more than 18 mm, a tri-band bandstop filter is introduced for the effective inductance increases. Figure 10 shows the simulated frequency responses of the tri-band bandstop filter, and Figure 11 shows the relationships of operation frequency and parameter b. It can be

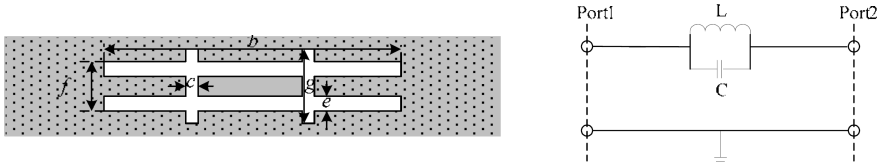

(a) Filter topology (b) Sketch equivalent circuit

Figure 4: Single band bandstop filter with DMS.

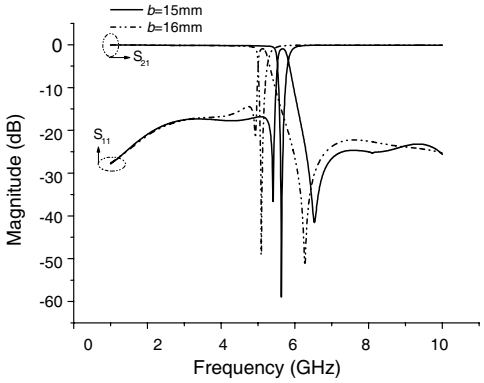

Figure 5: Frequency responses comparison of the bandstop filter with b, $c = 0.3\,\text{mm}$, $e = 0.2\,\text{mm}$, $f = 0.6\,\text{mm}$, $g = 1\,\text{mm}$.

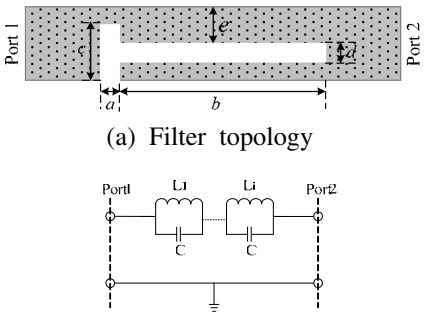

(a) Filter topology

(b) Equivalent circuit

Figure 6: Topology and equivalent circuit of the dual or tri-band bandstop filter with DMS when b is different, where, $i = 2$ or 3.

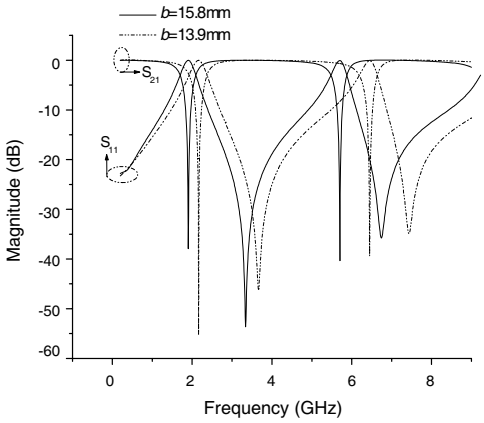

Figure 7: Simulated frequency responses of the dual-band bandstop filter, $a = 0.4\,\text{mm}$, $c = 1\,\text{mm}$, $d = 0.3\,\text{mm}$, $e = 0.6\,\text{mm}$.

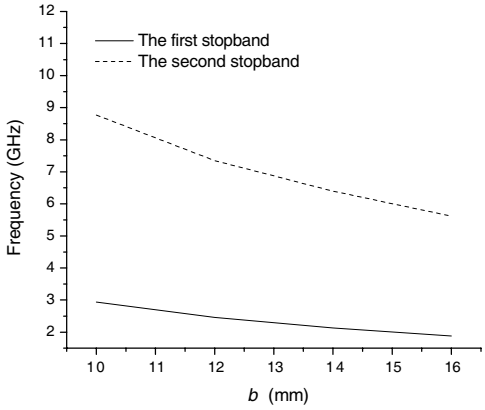

Figure 8: Relationships of operation frequency and parameter b, $a = 0.4\,\text{mm}$, $c = 1\,\text{mm}$, $d = 0.3\,\text{mm}$, $e = 0.6\,\text{mm}$.

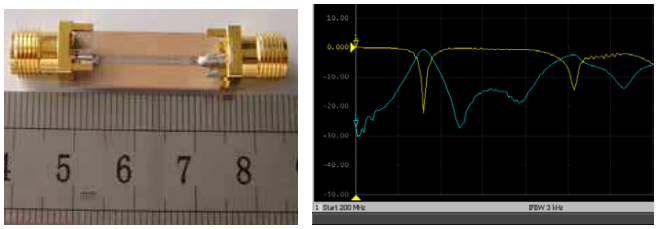

(a) Photograph of the hardware (b) Measured results

Figure 9: Fabrication and measurement of the dual-band bandstop filter.

seen when $b = 20\,\text{mm}$, the tri-band bandstop filter operates at 1.55 GHz, 4.59 GHz, and 7.59 GHz, respectively, and its operation frequency has similar variation trend with that of the dual-band one, and the operation frequency variation of the third band is more obvious than the other operation bands. It also shows the filter has wide passband between each operation stopband which is more

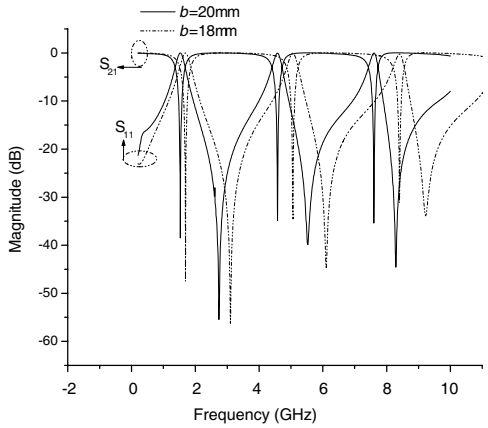

Figure 10: Simulated frequency responses of the tri-band bandstop filter, $a = 0.4\,\text{mm}$, $c = 1\,\text{mm}$, $d = 0.3\,\text{mm}$, $e = 0.6\,\text{mm}$.

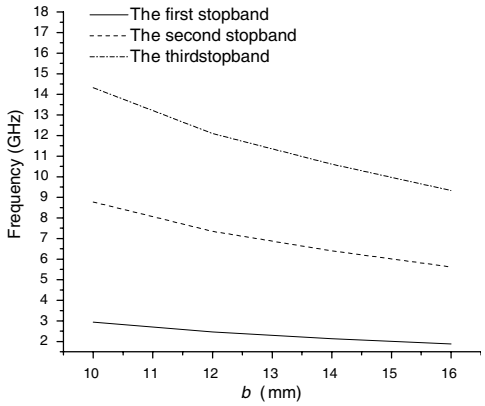

Figure 11: Relationships of operation frequency and parameter b, $a = 0.4\,\text{mm}$, $c = 1\,\text{mm}$, $d = 0.3\,\text{mm}$, $e = 0.6\,\text{mm}$.

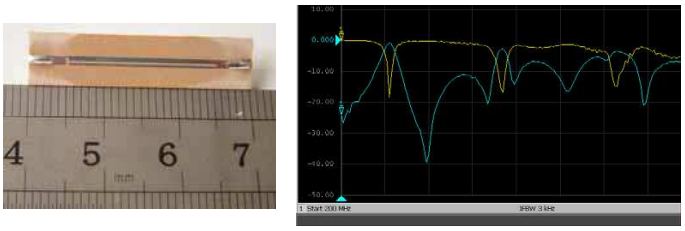

(a) Photograph of the hardware (b) Measured results

Figure 12: Fabrication and measurement of the tri-band bandstop filter.

than two times the filter's first operation frequency, and the excellent band-gap performance of DMS is demonstrated. Fabrication and measurement of the tri-band bandstop filter are shown in Figure 12, and the measured results are similar to the simulation.

4. CONCLUSION

In this report, defected microstrip structure (DMS) which has no enclosure problem is studied, and new bandstop filters with a single band, dual-band and tri-band are proposed. The measurement demonstrates the design. The new DMS bandstop filters have advantages of simple topology, miniature size and good performances of transmission zeros and low loss.

REFERENCES

1. Kim, C.-S., J.-S. Park, D. Ahn, and J.-B. Lim, "A novel 1D periodic defected ground structure for planar circuits," *IEEE Microwave Guided Wave Letters*, Vol. 10, No. 4, 131–133, 2000.
2. Ahn, D., J. S. Park, C. S. Kim, Y. Qian, and T. Itoh, "A design of the low-pass filter using the novel microstrip defected ground structure," *IEEE Trans. on MTT*, Vol. 49, No. 1, 86–93, 2001.
3. Lim, J. S., C. H. Kim, D. Ahn, Y. C. Jeong, and S. Nam, "Design of low-pass filters using defected grounded structure," *IEEE Trans. on MTT*, Vol. 53, No. 8, 2539–2554, 2005.
4. Zhang, S., J. K. Xiao, Z. H. Wang, and Y. Li, "Novel low-pass filters using defected microstrip structure," *Microwave Journal*, Vol. 49, No. 9, 118–128, 2006.
5. Tirado-Mendez, J. A. and H. Jardon-Aguilar, "Comparison of defected ground structure (DGS) and defected microstrip structure (DMS) behavior at high frequencies," *1st International Conference on Electrical and Electronics Engineering (ICEEE)*, 7–10, 2004.
6. Tirado-Mendez, J. A., H. Jardon-Aguilar, F. Iturbide-Sanchez, et al., "A proposed defected microstrip structure (DMS) behavior for reducing rectangular patch antenna size," *Microwave and Optical Technology Letters*, Vol. 43, No. 6, 481–484, 2004.

Dual-band Bandpass Filter Using SIR Structure

J.-K. Xiao[1] and W.-J. Zhu[2]

[1]School of Electronical & Mechanical Engineering, Xidian University, Xi'an 710071, China
[2]School of Computer and Information, Hohai University, Changzhou 213022, China

Abstract— Compact dual-band bandpass filters are proposed by using new S-shaped stepped-impedance resonators with dual and tri-section, and the designed dual-band bandpass filters are demonstrated by measurement. The proposed filters have advantages of simple and compact structures, low passband insertion losses, and dual-band operation, all these have prospect to apply in wireless communication systems.

1. INTRODUCTION

Currently, with the rapid development of modern wireless communications, bandpass filters with dual-band [1–3] operation become important in communication systems and have been paid much attention for the requirement of portable equipment, and users can access more services with a single handset. The traditional microstrip parallel-coupled half-wavelength resonator bandpass filters have narrow stopband between the fundamental response and the first spurious response, so the stepped-impedance resonator (SIR) [4–6] was presented in the past years to not only restrain the spurious responses, but also shorten the resonator size. SIR also can be used to design tri-band even multi-band filters for tuning the higher order resonant modes conveniently. However, the deficiency of this kind of resonator is its resonant frequencies are dependent, and transmission zeros are difficult to implement. Literature [7] proposed a miniaturized hairpin SIR with inner coupling, and a network model of this resonator is researched. Commonly, there are three methods for dual-band filter design, one is using cascade bandpass and bandstop filter, the second is using stepped impedance resonator, and the third is using two sets of different resonators or introducing two paths coupling.

This report presents new S-shaped dual and tri-section SIR bandpass filters with dual-band operation, and compared with dual-band filters with two sets of different resonators or two paths coupling, the filter sizes of the new design are greatly reduced.

2. DUAL-BAND BANDPASS FILTER USING DUAL-SECTION SIR

A fundamental microstrip stepped-impedance resonator unit is formed by joining together two microstrip transmission lines with different characteristic impedance Z_1 and Z_2 (the corresponding characteristic admittances are Y_1 and Y_2), and the corresponding electric lengths are θ_1 and θ_2, respectively. l_1 and l_2 are physical lengths corresponding to electric length θ_1 and θ_2, respectively. Z_i is input impedance, and Y_i is input admittance. Fig. 1(a) shows the half-wavelength SIR, and Fig. 1(b) shows the S-shaped two-section SIR. For the S-shaped SIR, the impedance ratio can be defined as $k = Z_2/Z_1$, and the input admittance can be written as

$$Y_i = jY_2 \cdot \frac{2(k\tan\theta_1 + \tan\theta_2)\cdot(k - \tan\theta_1\tan\theta_2)}{k(1-\tan^2\theta_1)\cdot(1-\tan^2\theta_2) - 2(1+k^2)\cdot\tan\theta_1\tan\theta_2} \tag{1}$$

Parallel resonant condition can be obtained on the base of $Y_i = 0$, and it can be expressed as

$$k = \tan\theta_1 \cdot \tan\theta_2 \tag{2}$$

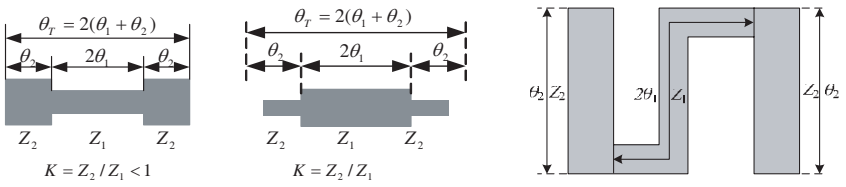

(a) Half-wavelength SIR (b) S-shaped SIR

Figure 1: Fundamental SIR structures and the new SIR.

where, $\theta_1 \approx \theta_2 = \theta$, and expression (1) can be rewritten as

$$Y_i = jY_2 \frac{2(1+k)\cdot(k-\tan^2\theta)\cdot\tan\theta}{k-2(1+k+k^2)\cdot\tan^2\theta+k\tan^4\theta} \tag{3}$$

The resonant condition on this case can be obtained as

$$\theta = \theta_0 = \arctan(\sqrt{k}) \tag{4}$$

The first three resonant frequencies of the S-shaped SIR are expressed as f_{S1}, f_{S2} and f_{S3}, and the corresponding electric length are θ_{S1}, θ_{S2} and θ_{S3}, respectively. From expression (3) when $Y_i = 0$, the following expressions can be obtained

$$\tan\theta_{S1} = \infty, \quad \tan^2\theta_{S2} - k = 0, \quad \tan\theta_{S3} = 0 \tag{5}$$

And the corresponding electric length can be obtained as

$$\theta_{S1} = \frac{\pi}{2}, \quad \theta_{S2} = \arctan(-\sqrt{k}) = \pi - \theta_0, \quad \theta_{S3} = \pi \tag{6}$$

From expressions (4) and (6), the ratio of spurious frequency versus the fundamental frequency can be got as

$$\frac{f_{S1}}{f_0} = \frac{\theta_{S1}}{\theta_0} = \frac{\pi}{2\arctan\sqrt{k}}, \quad \frac{f_{S2}}{f_0} = \frac{\theta_{S2}}{\theta_0} = \frac{\pi-\theta_0}{\theta_0} = 2\left(\frac{f_{S1}}{f_0}\right)-1, \quad \frac{f_{S3}}{f_0} = \frac{\theta_{S3}}{\theta_0} = \frac{\pi}{\theta_0} = 2\left(\frac{f_{S1}}{f_0}\right) \tag{7}$$

For the S-shaped SIR as shown in Fig. 1(b), we know that $k < 1$, and the calculated relationships of f_s/f_0 and k are shown in Fig. 2. All of the filters in this report are designed on ceramic substrates with dielectric constant of 10.2 and thickness of 1.27 mm, and all I/O feed lines are microstrip lines with characteristic impedance of 50 Ω. Here, simple and compact S-shaped SIR bandpass filter with dual-band operation is proposed, as Fig. 3 shows, where, $a = 5.4$ mm, $b = c = d = 1$ mm, $e = 1.5$ mm, $f = 6$ mm and $g = 4.4$ mm. Simulated filter frequency responses comparison with parameters e and a are shown in Fig. 4(a) and Fig. 4(b), respectively, and it shows the center frequency distance between the dual-passband increases with parameter e increasing, while, operation frequencies of the dual-passabnd decrease with parameter a increasing. For $a = 5.4$ mm, the dual-band bandpass filter operates at 2.5 GHz and 5.25 GHz, respectively, which has a passband insertion loss of no more than 0.9 dB. In order to verify the design, the S-shaped SIR dual-band bandpass filter is fabricated and tested, as Fig. 5 shows, and the measurement is got by Agilent E5071C vector network analyzer, and it shows the measurement is similar to the simulation.

3. DUAL-BAND BANDPASS FILTER USING TRI-SECTION SIR

Tri-section SIR can get better harmonics suppression, as shown in Fig. 6(a), where, characteristic impedance of a tri-section SIR are Z_1, Z_2 and Z_3, respectively, and the corresponding electric length

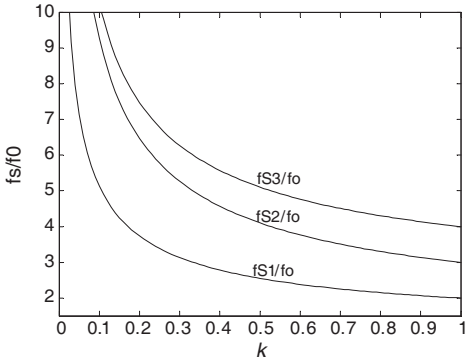

Figure 2: Relationship curves of f_s/f_0 versus k.

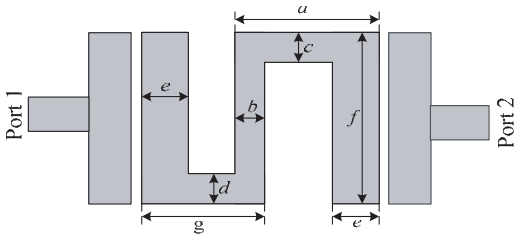

Figure 3: S-shaped SIR dual-band bandpass filter.

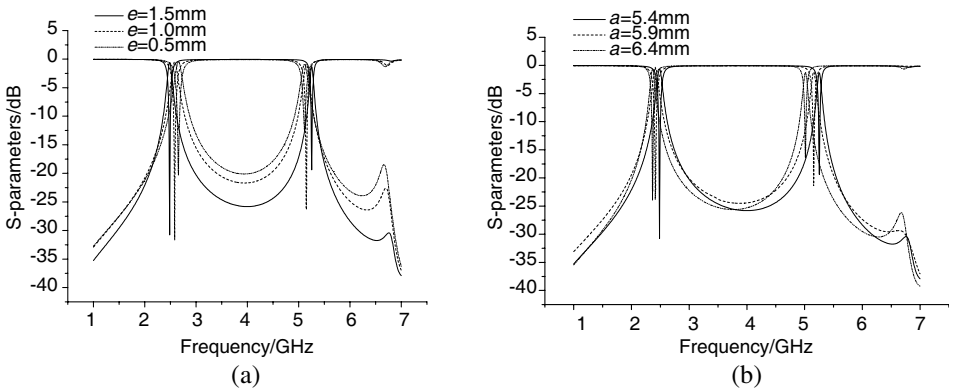

Figure 4: Simulated frequency responses.

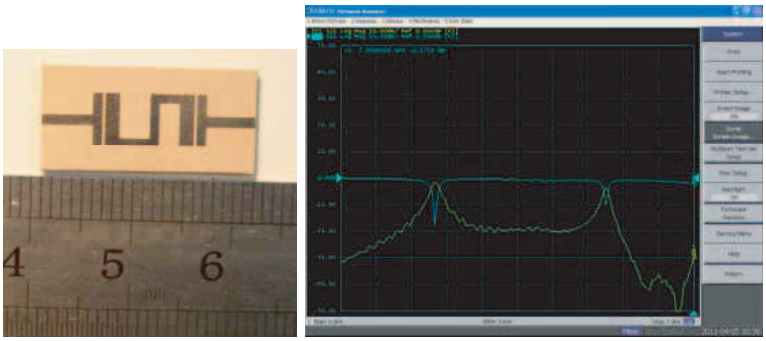

(a) Fabricated hardware (b) Measured results

Figure 5: Fabrication and measurement.

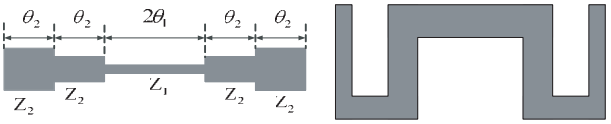

(a) Traditional tri-section SIR (b) S-shaped tri-section SIR

Figure 6: Tri-section SIR.

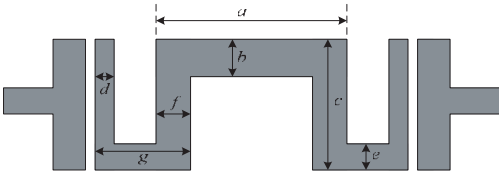

Figure 7: S-shaped Tri-section SIR bandpass filter.

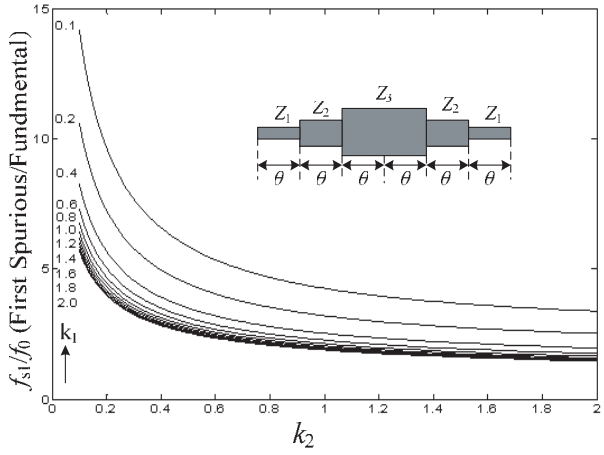

Figure 8: Relationship curves of f_{s1}/f_0 versus k_2 for the tri-section SIR.

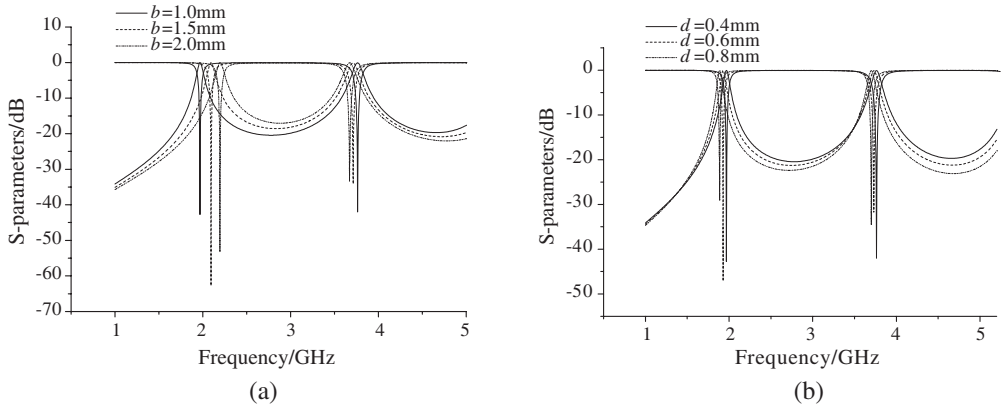

Figure 9: Simulated frequency responses of the dual-band bandpass filter with tri-section SIR.

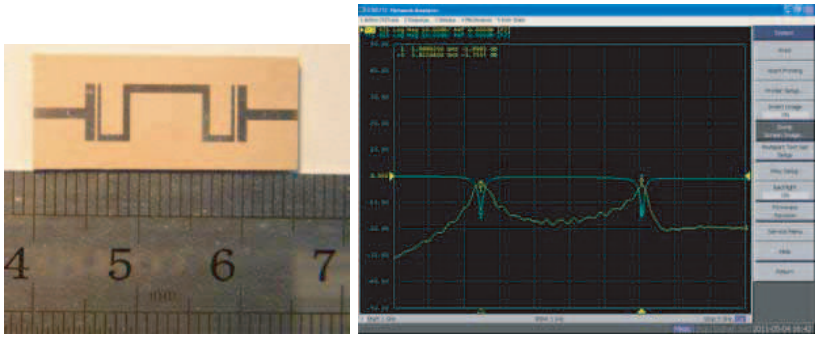

(a) Fabricated hardware (b) Measured results

Figure 10: Fabrication and measurement.

are θ_1, θ_2 and θ_3, respectively. If $k_1 = Z_3/Z_2$, $k_2 = Z_2/Z_1$, and $\theta_1 = \theta_2 = \theta_3 = \theta$, and θ can be written as $\theta = \tan^{-1}(\sqrt{\frac{k_1 k_2}{k_1+k_2+1}})$, and the total electric length can be got as [8]

$$\theta_T = 6\tan^{-1}\left(\sqrt{\frac{k_1 k_2}{k_1 + k_2 + 1}}\right). \tag{8}$$

Figure 6(b) shows the symmetrical S-shaped tri-section SIR, and the designed dual-band bandpass filter using that kind of resonator is shown in Fig. 7, where, $a = 8.4\,\text{mm}$, $b = 1\,\text{mm}$, $c = 6\,\text{mm}$, $d = 0.4\,\text{mm}$, $e = f = 0.8\,\text{mm}$. The calculated relationships of f_{s1}/f_0 versus k_2 for the tri-section SIR are shown in Fig. 8. Simulated frequency responses of the proposed filter are shown in Fig. 9, and it can be seen from Fig. 9(a) that for the first band, filter operation frequency increases with parameter b increasing, while, Fig. 9(b) shows that the variation of parameter d has slight influence on filter center frequencies. It shows when $b = 1.0\,\text{mm}$, the filter operates at 1.97 GHz and 3.76 GHz, respectively, and the filter passband insertion loss is no more than 0.3 dB. Fig. 10 shows the fabricated hardware and measured results, and the measurement agrees with the simulation.

4. CONCLUSION

S-shaped resonator bandpass filters with dual-band, low passband insertion losses by using dual and tri-section SIR are designed. The proposed filters are fabricated and tested, and the designs are demonstrated by measurement. The proposed models have simple and compact structures without the coupling of different resonators, and can be applied in wireless communication systems.

REFERENCES

1. Kuo, J. T. and H. Lin, "Dual-band bandpass filter with improved performance in extended upper rejection band," *IEEE Trans. on Microwave Theory and Techniques*, Vol. 57, No. 4, 824–829, 2009.

2. Liu, H. W., Y. F. Lv, and W. Zheng, "Compact dual-band bandpass filter using trisection hairpin resonator for GPS and WLAN applications," *Electronics Letters*, Vol. 45, No. 7, 360–361, 2009.
3. Zhang, X. Y., J. X. Chen, J. Shi, et al., "High-selectivity dual-band bandpass filter using asymmetric stepped-impedance resonators," *Electronics Letters*, Vol. 45, No. 1, 63–64, 2009.
4. Sagawa, M., M. Makimoto, and S. Yamashita, "Geometrical structures and fundamental characteristics of microstrip stepped-impedance resonators," *IEEE Trans. Microwave Theory and Techniques*, Vol. 45, 1078–1085, 1997.
5. Kuo, J. T. and E. Shih, "Microstrip stepped impedance resonator bandpass filter with an extended optimal rejection bandwidth," *IEEE Trans. Microwave Theory and Techniques*, Vol. 5, No. 1, 1554–1559, 2003.
6. Choil, W.-W., K.-W. Tam, and R. P. Martins, "A novel microstrip transversal bandpass filter with simultaneous size reduction and spurious responses suppression," *2005 Asia-Pacific Microwave Conference Proceedings*, Vol. 1, 508–511, 2005.
7. Lee, S.-Y. and C.-M. Tsai, "New cross-coupled filter design using improved hairpin resonators," *IEEE Trans. Microwave Theory and Techniques*, Vol. 48, No. 12, 2482–2490, 2000.
8. Chu, Q. X. and X. M. Lin, "Advanced triple-band bandpass filter using tri-section SIR," *Electronics Letters*, Vol. 44, No. 4, 295–296, 2008.

An Investigation of Unloaded Quality Factor of $\lambda/2$ and $\lambda/4$ Resonators

Somboon Theerawisitpong[1], **Toshitatsu Suzuki**[2], **and Yozo Utsumi**[2]

[1]Department of Technical Education, Faculty of Technical Education
Rajamangala University of Technology Thanyaburi
39 Moo 1, Rangsit-Nakorn Nayok Road, Klong Hok, Thanyaburi, Pathumtani 12110, Thailand
[2]Department of Electrical and Electronic Engineering, Nippon Institute of Technology
4-1 Gakuendai, Miyashiro-machi, Minami Saitama-gun, Saitama-ken 345-8501, Japan

Abstract— This paper proposes an investigation of Q_0 of $\lambda/2$ and $\lambda/4$ resonators with respect to electric current density flowed on resonator. The assumption of decreased Q_0 of $\lambda/4$ resonator has been proved at this time. In our study, it is found that Q_0 of $\lambda/4$ resonator (120) is decreased, due to a loss of electric current density occurred through a short circuit of via-holes made at the end, which is lower than that of $\lambda/2$ resonator (150).

1. INTRODUCTION

It is well known that microstrip filters can be designed based either half-wavelength ($\lambda/2$) or quarter-wavelength ($\lambda/4$) resonators [1–5]. Most of conventional filters are designed based $\lambda/2$ resonator while some miniaturized filters are designed based $\lambda/4$ resonator. The length of $\lambda/4$ resonator is shorter than that of $\lambda/2$ resonator by two times but unloaded quality factor (Q_0) of $\lambda/4$ resonator may be lower than that of $\lambda/2$ resonator [6]. However, this assumption of decreased Q_0 is not yet proved and revealed in any reports.

In our study, single $\lambda/2$ and $\lambda/4$ resonators are realized on a NPC-F260A having dielectric constant (ε_r) = 2.6, substrate thickness (h) = 1.2 mm, tangential loss factor ($\tan\delta$) = 0.0015, and copper thickness (t) = 9 µm. Q_0 of those resonators is determined to confirm the decreased of Q_0 of $\lambda/4$ resonator and circumstance of electric current density (J) flowed on those resonators is also demonstrated using IE3D software. The result shows that Q_0 of $\lambda/4$ resonator is decreased, due to a loss of electric current density through a via-hole.

2. RESONATOR AND UNLOADED QUALITY FACTOR (Q_0)

In our study, $\lambda/2$ and $\lambda/4$ resonators are a uniform line having a 50-Ω impedance and are corresponding to the same fundamental resonant frequency of 2 GHz. Schematics of those resonators are shown in Figure 1. In this figure, the total length (L_T) of $\lambda/2$ and $\lambda/4$ resonators is approximately 50 mm, and 25 mm while strip-width (W) is 3.32 mm. And three small via-holes having a diameter of 0.4 mm are made at the end of $\lambda/4$ resonator in order to realize a short circuit.

In our investigation, Q_0 can be determined by Equation (1) where C_n is maximally filter coefficient, Q_L is loaded quality factor, and L_0 is attenuation at fundamental resonant frequency [7].

$$Q_0 = 8.686 \times C_n \times \frac{Q_L}{L_0} \tag{1}$$

In the above equation, Q_L can be calculated by fundamental resonant frequency (f_0) and 3-dB bandwidth (Δf) as follow: $Q_L = f_0/\Delta f$. By the way, f_0 and Δf can be determined using IE3D software.

3. INVESTIGATION OF Q_0

At first, frequency response of $\lambda/2$ and $\lambda/4$ resonators are simulated using IE3D software. The simulated result of frequency response of these resonators is shown in Figure 2. The fundamental resonant frequency, bandwidth, and attenuation of these resonators are as follows: $f_{0,\lambda/2} = 1.989$ GHz, $f_{0,\lambda/4} = 1.997$ GHz, $\Delta f_{\lambda/2} = 10$ MHz, $\Delta f_{\lambda/4} = 18$ MHz, $L_{0,\lambda/2} = 11.51$ dB, and $L_{0,\lambda/4} = 8.167$ dB. Thus, Q_0 of those resonators can be calculated using Equation (1) as follows: $Q_{0,\lambda/2} = 150$ and $Q_{0,\lambda/4} = 120$ where $C_n = 1$. This result shows that Q_0 of $\lambda/4$ resonator is lower than that of $\lambda/2$ resonator.

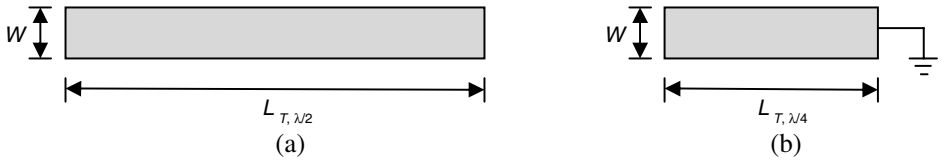

Figure 1: Schematic of (a) a $\lambda/2$ resonator, and (b) a $\lambda/4$ resonator. The total length of $\lambda/2$ and $\lambda/4$ resonators is respectively 50 mm, and 25 mm while strip-width is same at 3.32 mm. A short circuit at the end of $\lambda/4$ resonator are made by three small via-holes having a 0.4 mm-dia.

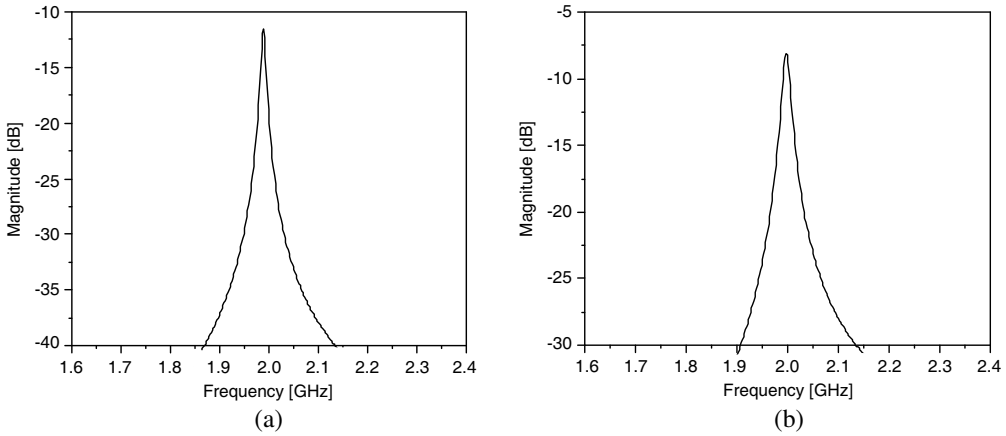

Figure 2: Simulated result of fundamental resonant frequency of (a) $\lambda/2$, and (b) $\lambda/4$ resonators where $f_{0,\lambda/2} = 1.989\,\text{GHz}$, $f_{0,\lambda/4} = 1.997\,\text{GHz}$, $\Delta f\lambda/2 = 10\,\text{MHz}$, $\Delta f\lambda/4 = 18\,\text{MHz}$, $L_{0,\lambda/2} = 11.51\,\text{dB}$, and $L_{0,\lambda/4} = 8.167\,\text{dB}$.

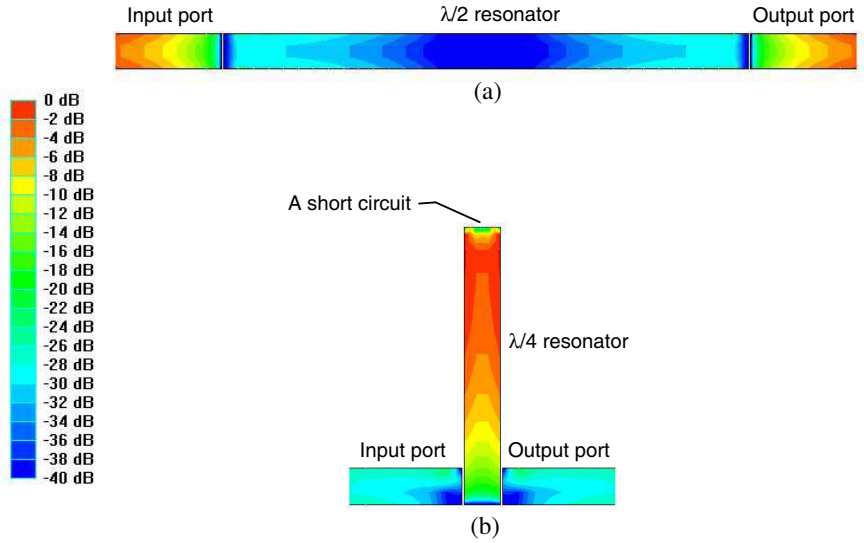

Figure 3: Electric current density flowed on strip-width of $\lambda/2$ and $\lambda/4$ resonators. Red shows maximum electric current density and blue shows minimum electric current density.

In this paper, we propose investigation Q_0 of $\lambda/2$ and $\lambda/4$ resonators with respect to electric current density. The result of this investigation is shown in Figure 3. In this figure, red shows maximum electric current density and blue shows minimum electric current density.

The result in Figure 3 shows that attenuation of electric current density on $\lambda/2$ resonator is very low which means electric current density can flow well on this resonator while attenuation of electric current density on $\lambda/4$ resonator is very high indicated by red which means electric current

density may be lost through a short circuit of via-holes. In addition, investigation of Q_0 of $\lambda/2$ and $\lambda/4$ SIRs is also re-examined in both simulation and experiment, which is avoided to apply $\lambda/4$ resonator in our previous work [6]. Consequently, we can summarize that decreased Q_0 of $\lambda/4$ resonator is due to a loss of electric current density through a short circuit made by via-holes.

4. CONCLUSIONS

An investigation of Q_0 of $\lambda/2$ and $\lambda/4$ resonators has been reported in this paper. It is confirmed that decreased Q_0 of $\lambda/4$ resonators is due to a loss of electric current density through a short circuit made of via-holes at the end. Therefore, $\lambda/4$ resonator should be avoided for developing of high-Q_0 filters.

REFERENCES

1. Jayatilaka, H. C., D. M. Klymyshyn, M. Börner, and J. Mohr, "Compact thick metal diplexer with multi-coupled folded half wavelength resonators," *Progress In Electromagnetics Research C*, Vol. 18, 1–8, 2011.
2. Deng, P.-H. and P.-T. Chiu, "New bandpass filters using half-wavelength and branch-line resonators," *Progress In Electromagnetics Research C*, Vol. 16, 241–249, 2010.
3. Chen, Y.-W., Y.-J. Liu, and M.-H. Ho, "The quasi-elliptic bandpass filter using quarter-wavelength stepped impedance resonators," *PIERS Online*, Vol. 2, No. 6, 605–608, 2006.
4. Wu, H.-W., Y.-K. Su, M.-H. Weng, and R.-Y. Yang, "Design of dual-band bandpass filter using diverse quarter-wavelength resonators for GPS/WLAN applications," *Microw. Opt. Tech. Lett.*, Vol. 50, No. 10, 2694–2696, 2008.
5. Theerawisitpong, S., T. Suzuki, N. Morita, and Y. Utsumi, "Microstrip BPF using SIRs with wide and deep harmonics suppression band," *Proc. of ISAP-2009*, 899–920, Bangkok, Thailand, October 2009.
6. Theerawisitpong, S., T. Suzuki, N. Morita, and Y. Utsumi, "Design of microstrip bandpass filters using SIRs with even-mode harmonics suppression for cellular systems," *IEICE Trans. Electron.*, Vol. 93, No. 6, 867–876, 2010.
7. Matthaei, G. L., L. Young, and E. M. T. Jones, *Microwave Filters, Impedance Matching Networks and Coupling Structure*, McGraw-Hill, New York, 1964.

Design of an Extra-low-loss Broadband Y-branch Waveguide Splitter Based on a Tapered MMI Structure

Pengfei Wang[1, 2], **Gilberto Brambilla**[1], **Yuliya Semenova**[2], **Qiang Wu**[2], **and Gerald Farrell**[2]

[1]Optoelectronics Research Centre, University of Southampton, Southampton, SO17 1BJ, UK
[2]Photonics Research Center, School of Electronic and Communications Engineering
Dublin Institute of Technology, Kevin Street, Dublin 8, Ireland

Abstract— An optimal design for an extra-low loss buried waveguide Y-branch splitter is presented over a broadband wavelength range from 1500 ∼ 1600 nm. A tapered multimode waveguide section, earlier used to reduce the excess loss, is optimized when the light distribution at the end of the multimode waveguide section is matched to the profile of the symmetric supermode for the structure of the two branching waveguides. An optimization that combines genetic algorithm and a gradient-based search method are used to obtain the optimal geometrical parameters for the multimode waveguide section as well as the widths for the input and branching waveguides. An excess loss of 0.015 dB@1550 nm was obtained after the proposed optimization. For these optimized parameters, even when packaging induces a typical offset between input standard singlemode fibre and waveguide, the wavelength dependence of the output ratio between the two branches is small (less than 0.03 dB).

1. INTRODUCTION

A Y-branch structure fabricated by planar technology is a fundamental element in constructing photonic integrated circuits such as power splitters, Mach–Zehnder interferometers, and hybrid-integrated optical transceivers. Previously, the conventional Y-branch was found to suffer severe radiation loss when the branching angle is larger than 2° [1]. To reduce the loss, the branching angle must be small and the length of splitter device must be extended. To date, several efforts have been made to overcome the loss problem, especially when the branching angle is large [2, 3]. Adding a microprism at the junction is one of the possible approaches. The function of the microprism is to compensate the phase mismatch caused by branching to reduce the radiation loss. However, the fabrication process is quite complex and suffers from misalignment of the microprisms at the junction. Low loss bending has been also achieved by utilizing coherently coupled bends [4]. Q. Wang [5] has presented a low loss Y-branch waveguide splitter utilising a multimode interference (MMI) waveguide section as a transition region with appropriate widths for the input and the branching waveguides. The designed Y branch has an excellent performance in a very wide wavelength range, which means the Y-branch waveguide splitter can be further integrated into a ratiometric wavelength measurement system [6]. In this paper, an extra-low-loss buried waveguide Y-branch splitter based on a tapered MMI structure is proposed and presented operating over a broadband wavelength range from 1500 ∼ 1600 nm. With optimized parameters, the wavelength dependence of the output ratio between the two branches (∼ 0.03 dB over ∼ 100 nm) is negligible even with a mismatching offset between the input standard singlemode fibre and a waveguide introduced during packaging.

2. BACKGROUND OF DESIGN

A conventional Y-branch structure consists of an input waveguide and two branching waveguides, as shown in Fig. 1. The two branching waveguides can either have the shape of a cosine arc or they can be straight waveguides with a certain branching angle. However, a Y-branch with cosine-arc branching waveguides has a more compact size as compared with the one with straight branching waveguides.

Silica-on-silicon waveguides have a number of advantages, such as low propagation loss and high fibre matching efficiency. Therefore the silica-on-silicon buried waveguide is considered in this paper. Conventionally there is a gap between the two branching waveguides for convenience of fabrication. The gap between the buried branching waveguides fabricated by plasma enhanced chemical vapor deposition technology should not be less than 2 µm, to avoid air voids at the tip of the branch after the cladding layer is deposited. The excess loss is an important characteristic of the Y-branch structure. Many methods for minimizing the excess loss have been recently proposed [7].

However, the existence of the gap degrades greatly the actual performance of the device, further induces the insertion loss and the non-uniformity of a splitter consisting of cascaded Y branches.

The MMI waveguide has many advantages and can be used to construct planar lightwave circuits for different purposes such as splitting, combining, and routing [8–11]. The self-image theory is usually used to determine the geometrical parameters of the MMI section and the positions of the input and output waveguides. Power splitters based on a multimode waveguide section between the input and output waveguides have been proposed and fabricated earlier [9, 10]. In this paper a tapered MMI waveguide section is adopted: such a tapered MMI waveguide has a narrow width and therefore can support only two or three eigenmodes between the input and the branching waveguides. The excess loss of the device is then reduced by optimizing the geometrical parameters of the tapered multimode waveguide section, the end width of the tapered waveguide, the width of the branching gap, and the width of the branching waveguides. This paper presents an optimal design for a low-loss Y-branch structure with a tapered multimode waveguide section and the branching gap mentioned above.

3. OPTIMAL DESIGN OF THE GEOMETRICAL PARAMETERS

The buried waveguide cross section is shown in Fig. 2(a); the core and cladding refractive indices and the waveguide width and height were assumed to be: $n_{core} = 1.4553$; $n_{clad} = 1.4444$, $W_0 = 5.5\,\mu\text{m}$ and $H_0 = 5.5\,\mu\text{m}$, respectively. In order to obtain a splitter with a low excess loss, several parameters such as the widths W_2 of the tapered waveguide section, W_1 of the tapered input waveguides, the gap s between the branching waveguides and the width W_3 of the branching waveguides need to be optimized.

A genetic algorithm and a gradient-based search method are chosen as the optimization method. In the optimization process, the length of the multimode waveguide section is chosen on the basis of the principle of operation of MMI couplers, such as 1000 μm. However, the other four geometrical parameters W_1, W_2, W_3, and s have large variation ranges and therefore large search ranges in the genetic algorithm, thus good initial values (which are close enough to the global maximum) are difficult to find for these parameters. It is well known that a gradient search method can be easily trapped by a local maximum in such a case. Therefore, in the present paper, we first use the genetic algorithm for the design. After a number of iterations, when the convergence of the genetic algorithm slows down, we use a gradient search method to speed up the convergence by using the parameters obtained from the genetic algorithm as good initial values for the gradient search method.

Figure 3 shows the optical intensity field distribution of the proposed Y-branch splitter calculated

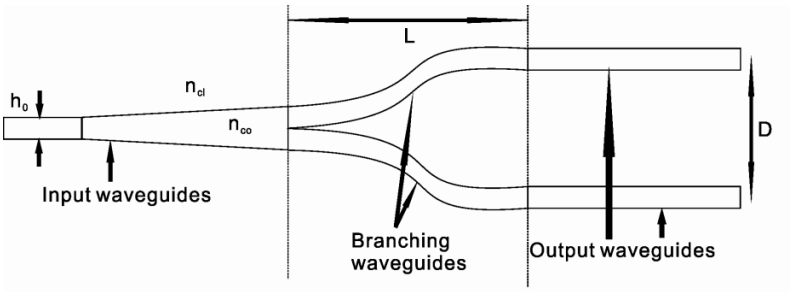

Figure 1: Schematic of conventional Y-branch waveguide splitter.

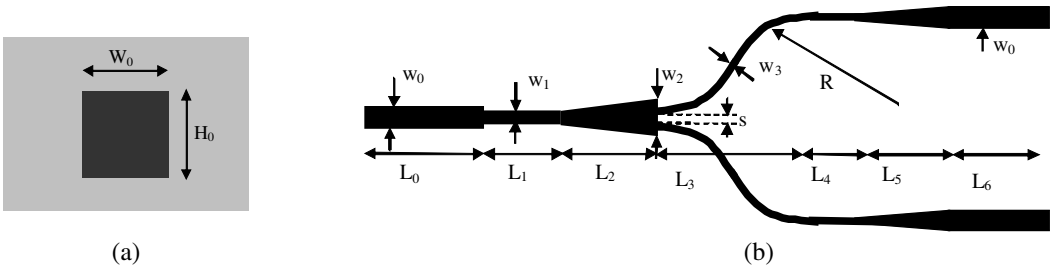

Figure 2: (a) Cross section of input waveguide. (b) Schematic of the proposed Y-branch waveguide splitter.

using the Beam Propagation (BPM) method. In this simulation, $L_1 = 1500\,\mu m$, $w_1 = 4\,\mu m$; $W_0 = 5.5\,\mu m$; $W_2 = 14\,\mu m$, $s = 2\,\mu m$, $W_3 = 4\,\mu m$; $L_0 = 1000\,\mu m$; $L_2 = 1000\,\mu m$; $L_3 = 1529.6\,\mu m$; $R = 30000\,\mu m$; $L_4 = 1000\,\mu m$; $L_5 = 1000\,\mu m$. The excess loss versus wavelength is shown in Fig. 4 which illustrates the excess loss between the sum of two output ports and input port of the integrated device. The excess loss of the proposed Y-branch splitter is only 0.015 dB at a wavelength of 1550 nm, which is much lower than the calculated results presented in Ref. [5].

A major challenge in the use of silica on silicon buried waveguides for photonic lightwave circuit technology is the efficient coupling of light to/from an optical singlemode fibre because of the large mode mismatch between the input optical fibre and the silica buried waveguide. The alignment precision of the optical fibre to a buried waveguide may be limited in practice by the device packaging technique used. To help minimize manufacturing costs therefore it is important to estimate the tolerance of the splitter performance to a typical alignment errors induced by the limitations of the packaging technique. Therefore an estimate of the effect of a typical offset between the input standard singlemode fibre and the packaged waveguide needs to be considered and calculated.

With the developed optimization method, the corresponding light propagation in the case of fibre position shift by $\pm 0.4\,\mu m$ from the centre is presented in Fig. 5, when $L_1 = 3000\,\mu m$ and $w_1 = 3.5\,\mu m$. From the input port of the integrated device, L_0, illustrated in Fig. 2(b), one can see that the optical mode field propagating with in the waveguide of L_0 section, is disturbed by the mismatching significantly, compare with the optical mode pattern of L_0 shown in Fig. 3. It was found that the wavelength dependence of the imbalance is still small (see Fig. 6 the fibre shift is assumed to be $\pm 0.4\,\mu m$), even when there is a typical mismatching offset of $\pm 0.4\,\mu m$ between the input fibre and input port of integrated splitter device.

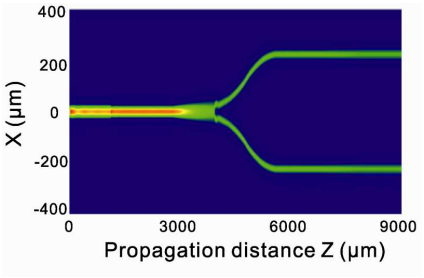

Figure 3: Optical intensity field distribution of the proposed Y-branch waveguide splitter when $L_1 = 1500\,\mu m$ and $w_1 = 4\,\mu m$.

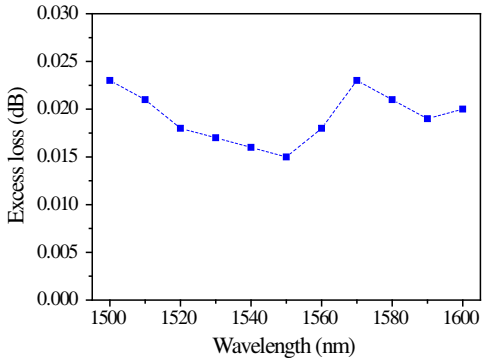

Figure 4: Calculated excess loss as a function of wavelength.

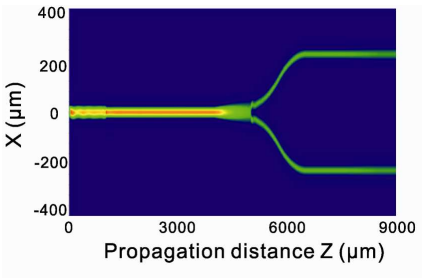

Figure 5: Optical intensity field distribution of the proposed Y-branch splitter, when $L_1 = 3000\,\mu m$ and $w_1 = 3.5\,\mu m$; a typical offset of $\pm 0.4\,\mu m$ between the input singlemode fibre and the input port of the splitter is assumed.

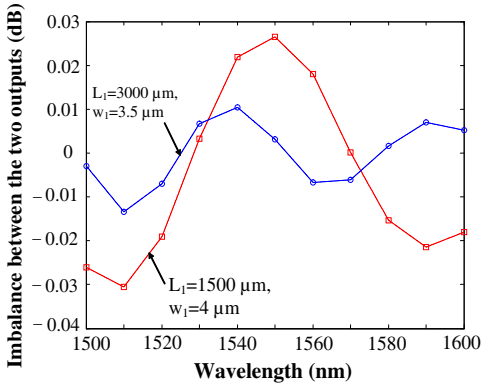

Figure 6: Imbalance between the splitter output ports after the optimization for the two cases of: $L_1 = 3000\,\mu m$ and $w_1 = 3.5\,\mu m$ (blue line); and $L_1 = 1500\,\mu m$ and $w_1 = 4\,\mu m$ (red line).

4. CONCLUSION

An optimal design for an extra-low-loss buried Y-branch splitter based on a tapered multimode waveguide has been presented over a wide wavelength range (1500 $\sim$ 1600 nm). An optimization method that combines a genetic algorithm and a gradient-based search method have been used to obtain the optimal geometrical parameters for the multimode waveguide section as well as the widths for the input and branching waveguides. An extra-low excess loss of 0.015 dB at a wavelength of 1550 nm has been obtained after the optimization. An offset between the input standard singlemode fibre and waveguide in packaging has been considered and the result shows that there is very small wavelength dependence ($\sim$ 0.03 dB) of the output ratio between the two branches. There is significant potential for the useful application of the proposed Y-branch structure in integrated optical devices, such as $1 \times N$ power splitters and switches, in the future.

ACKNOWLEDGMENT

P. Wang is funded by the Irish Research Council for Science, Engineering and Technology, co-funded by the Marie-Curie Actions under FP7. Q. Wu gratefully acknowledges the support of Science Foundation Ireland under grant No. 07/SK/I1200.

REFERENCES

1. Sasaki, H. and N. Mikoshiba, "Normalized power transmission in single mode optical branching waveguide," *Electron. Lett.*, Vol. 17, 136–138, Feb. 1981.
2. Ni, T. D., D. Sturzebecher, M. Cummings, and B. Perlman, "Design, fabrication, and test of wide-angle low-loss Y-junction hybrid polymer couplers," *Appl. Phys. Lett.*, Vol. 67, No. 12, 1651–1652, Sep. 1995.
3. Lin, H. B., R. S. Cheng, and W. S. Wang, "Wide-angle low-loss single mode symmetric Y-junction," *IEEE Photon. Technol. Lett.*, Vol. 6, 825–827, Jul. 1994.
4. Taylor, H. F., "Power loss at directional change in dielectricwaveguides," *Appl. Opt.*, Vol. 13, 642–647, Mar. 1974.
5. Wang, Q., J. Lu, and S. He, "Optimal design method of a low-loss broadband Y branch with a multimode waveguide section," *Appl. Opt.*, Vol. 41, No. 36, 7644–7649, 2002.
6. Wang, Q., G. Farrell, T. Freir, G. Rajan, and P. Wang, "Low-cost wavelength measurement based on a macrobending singlemode fiber," *Optics Letters*, Vol. 31, No. 12, 1785–1787, 2006.
7. Gamet, J. and G. Pandraud, "Field matching Y-branch for low loss power splitter," *Optics Communications*, Vol. 248, 423–429, 2005.
8. Soldano, L. B. and E. C. M. Pennings, "Optical multi-mode interference devices based on self-imaging: principles and applications," *J. Lightwave Technol.*, Vol. 13, 615–627, 1995.
9. Chung, Y., R. Spickermann, D. B. Young, and N. Dagli, "A low-loss beam splitter with an optimized waveguide structure," *IEEE Photon. Technol. Lett.*, Vol. 4, 1009–1011, 1992.
10. Fardad, M. A. and M. Fallahi, "Sol-gel multimode interference power splitters," *IEEE Photon. Technol. Lett.*, Vol. 11, 697–699, 1999.
11. Besse, P. A., M. Bachhamn, H. Melchior, L. B. Soldano, and M. K. Smit, "Optical bandwidth and fabrication tolerances of multimode interference couplers," *J. Lightwave Technol.*, Vol. 12, 1004–1009, 1994.

Scanning Near-field Millimeter Wave Microscope Combining Dielectric Tapered Probes and Metal Tips

B. Zhu[1], **S. Vanloocke**[2], **V. Matvejev**[1], **J. Stiens**[1], **D. De Zutter**[2], **and R. Vounckx**[1]

[1]Laboratory for Micro-and Photon Electronics, Department of Electronics and Informatics
Vrije Universiteit Brussel, Pleinlaan 2, 1050 Elsene, Brussels, Belgium
[2]Department of Information Technology (INTEC), UGent, Sint-Pietersnieuwstraat 41, Gent 9000, Belgium

Abstract— In this paper, we built a free-space scattering-type scanning near-field millimeter wave microscope using two tapered dielectric probes facing each other and a sample in between based on MVNA. Nylon, Teflon and PVC dielectric tapered probes are compared in this system. We adopted a PVC probe and a Teflon probe as incident and receiving probes. The resolution is frequency dependent. In order to increase the resolution and contrast, we additionally positioned a metal probe tip between the dielectric tapered probe and the object under test. First experiment results on this signal improvement concept will be reported for a 2 µm tungsten probe, yielding an increased field enhancement and leading to the contrast improvement.

1. INTRODUCTION

The microwave regime in the frequency spectrum has been extensively utilized for communication, imaging, nondestructive testing, and security purposes. Millimeter- (30–300 GHz) and Terahertz- (300–3000 GHz) waves provide unique opportunities for the development of novel applications in the active near-field imaging and spectroscopy of microscopic objects. Conventional optical imaging systems in the mm- and THz range ($0.1 < \lambda < 10$ mm) cannot resolve microscopic details as the resolution in the far field is limited by the wavelength (Rayleigh criterion). The amplitude and phase of the near field (evanescent wave) contain high resolution spatial information which is highly dependent on the local structure. Hence, recently, near field microscopes with higher resolution have been frequently reported [1, 2]. Scattering type scanning near-field microscopy imaging is a powerful technique to obtain sub-wavelength resolution images of a sample. The method is based on measuring the scattered near-field very close to a sample or converting the near-field evanescent wave to propagating wave and detected in far field. However, extracting this information from the scattered fields requires near-field probes capable of coupling to the local field at a tiny point. The higher the resolution, the more sophisticated and expensive the probes are [3, 4].

For imaging, object investigation and nondestructive testing using millimeter and THz technologies, electromagnetic beams are required to be collimated and focused to attain higher resolution. Typically, illuminating sources in imaging systems use biconvex lenses, parabolic mirrors, incorporate meta materials and a variety of lenses [5]. Recently, many groups have demonstrated different imaging probe techniques, such as aperture probes and apertureless probes, particularly, a circular aperture, a modulated scatter probe, a coaxial cable, an open waveguide, a small loop, and a micro-strip resonator, a narrow resonant slit, a metal micro-slit probe, a thin-slit aperture in a convex and plate of a rectangular wave guide, resonant waveguide probe and so on [2]. Although many probes are mentioned above, the highest resolution probes are various sharp metallic tips and dielectric waveguides with sub-wavelength aperture sizes and were placed within 0.5 mm of the sample surface. Conical Teflon probes in [3] get 0.2 to 0.5 mm resolution at 260 GHz and 0.5 mm resolution at 150 GHz in [4].

In this research, we built a free-space scattering-type scanning near-field millimeter wave microscope using two tapered dielectric probes and a sample in between based on an MVNA (Millimeter Wave Vector Network Analyzer) from AB millimeter as shown in Fig. 1, the operated frequency is in the W-band ($70 \sim 110$ GHz). Teflon probes and 3D printed ABS probes were compared in previous works [6, 7] and we can distinguish at least 256 µm metal strips on a PCB at 100 GHz. We found that the 3D printed ABS probe had higher resolution in Amplitude image because of the sharper end of the probe. The noise in the ABS phase image is much bigger than in Teflon probes phase images due to its non-homogenous inner structure. Nylon, Teflon and PVC tapered probes are compared in this paper; the transmission and reflection properties are analyzed and the factors that affect the image resolution are illustrated in part 2. In order to improve the contrast and resolution of the near-field images, we additionally positioned a metal probe tip between the dielectric taper and the object under test, the results are illustrated in part 3. At last, we draw the conclusions.

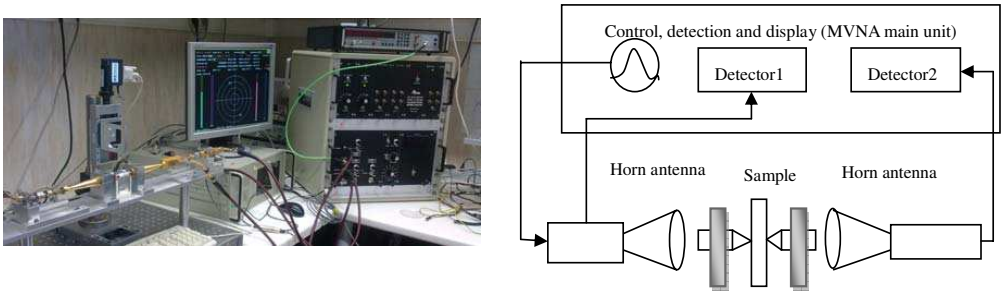

Figure 1: Experiment setup of near-field scanning imaging system in millimetre and Terahertz wave.

Table 1: Real and imaginary part of dielectric permittivity for Teflon, Nylon and PVC at 100 GHz [8].

Specimen	ε'	ε''	Loss tangent
Teflon	2.0303	0.0004	1.97e-5
Nylon	1.4405	0.0285	0.0198
PVC	2.88	0.032	0.0111

Table 2: Amplitude of S_{11} and S_{21} for different materials as illuminating and receiving probes.

Illuminating-receiving	Teflon-Teflon$'$	Teflon-Teflon$''$	Teflon-PVC	Teflon-Nylon	Nylon-Teflon	PVC-Teflon	Nylon-Nylon	PVC-PVC
S_{21} (dB)	−7.82	−3.18	−8.1	−8.99	−5.56	−3.99	−15.81	−12.91
S_{11} (dB)	−4.61	−5.4	−4.59	−4.55	−4.43	−6.16	−4.78	−5.72

2. COMPARISON OF DIFFERENT PROBES

Teflon is widely used because of its nearly transparent properties in the millimeter wave spectrum, but it is hard to mill or cut sub-millimeter dimensions on a lathe due to its softness and even more that it is easy to be rubbed to destroy the probe when it is in contact with the scanning sample. Nylon and PVC probes can be very sharp because of the hardness. Teflon, Nylon and PVC probes are compared using the near-field scanning imaging system as shown in Fig. 1. The real permittivity ε' and the imaginary permittivity ε'' are shown in Table 1 for these three materials in W-band (70–110 GHz).

Before the reflection (S_{11}) and transmission (S_{21}) coefficients are measured, the system is calibrated using the baseline calibration method without any probes to remove the effects of mismatches. The transmission is calibrated using an open or empty sample holder fixture while the reflection is calibrated using a metal mirror plate placed at the sample plane. The illumination frequency is locked at 100 GHz, all measurement are performed at room temperature. After calibration, we fixed our probes as an illuminating probe and a receiving probe. Nylon-Teflon means that the illuminating probe is Nylon and the receiving probe is Teflon. In the previous simulation work [7], we reported that the side leakage is determined by the real part of the permittivity and when the permittivity is bigger, the side leakage is less. The loss tangent only impact the intensity. We use tapered probes with a 45° opening angle, 9 mm radius and length of 9.75 mm in the following experiments.

The amplitude results of S_{11} and S_{21} for different probes are descripted in Table 2. Teflon$''$ is much sharper than Teflon$'$ and Teflon is a sharp probe like Teflon$''$ in the table. It is reasonable that when the probe is sharper, the transmission decay is less. Although the loss tangent of Nylon and PVC is much higher than that of Teflon, the transmission decay is not proportional to the loss tangent because of the tapered shape. In order to get higher resolution, we choose a PVC tapered probe as the incident waveguide and Teflon tapered probe as the receiving waveguide to do the experiments for the rest part of this paper. Since PVC probes are much harder and sharper than Teflon probes, they are better to focus the incident beam and Teflon probes can decrease the transmission decay acting as a receiving probe.

We found that the resolution not only depends on the sharpness of the probe but also on the distance of tip-sample because of the illuminating source beam size. When the beam size is smaller,

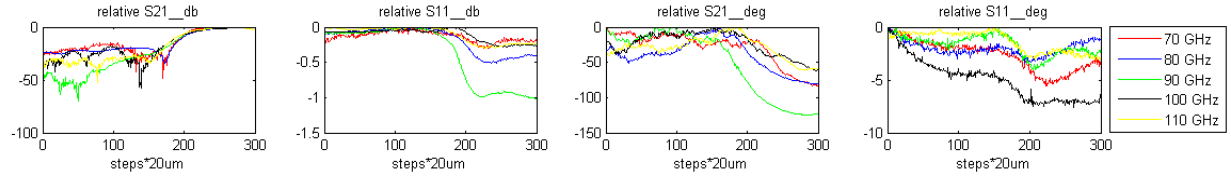

Figure 2: 6 mm metal edge linear scanning graphs at different frequencies (tip-sample distance is 0.5 mm).

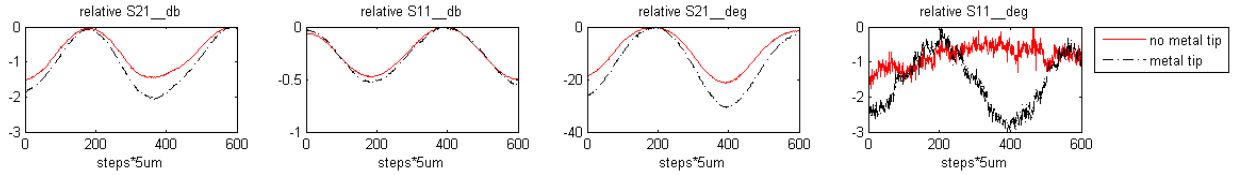

Figure 3: Linear scanning of 1 mm metal strips on a PCB with and without the metal tip.

the resolution is higher. The results of experiments agree with the simulation work in [7]. We used a sharper probe and kept the probe very close to the sample. We used a tip-sample distance of 0.5 mm in this work. We found that the frequency also affects the resolution and contrast; we did a linear scan (6 mm range with 20 µm per step) of the metal plate edge at 70, 80, 90, 100 and 110 GHz. As can be seen from Fig. 2, the resolution (according to 10% to 90% criterion) and the contrast are frequency dependent using a PVC probe (incident probe) and a Teflon Probe (receiving probe). The reflection phase information is noisy. In order to increase the resolution and contrast, we use a metal tip to create the enhancement of the near-field.

3. ENHANCEMENT OF THE METAL NEEDLE IN THE NEAR-FIELD SETUP

In the classic scattering scanning near-field optic microscopes (s-SNOM), a metal tip, usually tungsten, locally perturbs the electromagnetic field surrounding the specimen. According to the field enhancement by the static metal tip, an apertureless THz near-field microscope, which allows for spatial resolutions as small as 150 nm with keeping the metal tip the constant distance to the surface of the sample at 2 THz was reported in [9, 10]. We additionally positioned a metal probe tip between the dielectric taper and the object under test. This metal probe acts as an antenna to generate a locally concentrated near field usable for scanning microscopy [11, 12]. We notice that the reflection phase is not good in Fig. 3, we couldn't see any information about the sample from the reflection phase. When we add a 2 µm tungsten tip, we found out that the reflection phase graph improved a lot. From transmission information of Fig. 3, we can see there is a little contrast improvement (1.81 times).

4. CONCLUSION

We built a near-field imaging system based on MVNA and experiments reveal that the image resolution depends on many factors such as the distance of the tip and the sample, the material of the tip, and the sharpness of the probe, and the source frequency. The results of experiments agree with the previous simulations in [7]. In order to improve the contrast and resolution of the near-field images, we additionally positioned a 2 µm tungsten probe between the dielectric taper and the sample. We found out that the reflection phase improves a lot and transmission contrast has a little bit improvement, but it is not enough. This setup has more reflection interference, we have to perfect it and higher resolution is expected by using a dithering system and lock-in amplifier in the near future.

ACKNOWLEDGMENT

This work is funded by the FWO-Vlaanderen project "FWOAL465- Scattering type near-field mm wave microscopy" of the Flemish region in Belgium and is also executed in the framework of NEWFOCUS ESF Research Networking Program (RNP).

REFERENCES

1. Shiku, H., J. R. Krogmeier, and R. C. Dunn, "Noncontact near-field scanning optical microscopy imaging using an interferometric optical feedback mechanism," *Langmuir*, Vol. 15,

No. 6, 2162–2168, 1999.
2. Park, W., J. Kim, and K. Lee, "Millimeter-wave scanning near-field microscope using a resonant waveguide probe," *Applied Physics Letters*, Vol. 79, No. 16, 2642–2644, 2001.
3. Weiss, M. D., B. Zadler, S. Schafer, et al., "Near field millimeter wave microscopy with conical Teflon probes," *Journal of Applied Physics*, Vol. 106, No. 4, 2009.
4. Greeney, N. S. and J. A. Scales, "Dielectric microscopy with submillimeter resolution," *Applied Physics Letters*, Vol. 91, No. 22, 2007.
5. Banik, B. K., J. Vukusic, H. Merkel, et al., "A novel catadioptric dielectric lens for microwave and terahertz applications," *Microwave and Optical Technology Letters*, Vol. 50, No. 2, 416–419, 2008.
6. Zhu, B., J. Stiens, G. Poesen, et al., "Dielectric analysis of 3D printed materials for focusing elements operating in mm & THz wave frequency bands," *Proceedings of Symposium IEEE/LEOS Benelux Chapter*, 13–16, 2010.
7. Zhu, B., S. Vanloocke, J. Stiens, et al., "A novel 3D printed focusing probe in scattering-type scanning near-field millimeter & Terahertz wave microscope," *EuCAP2011*, 775–778, Rome, Italy, 2011.
8. Elhawil, A., L. Zhang, J. Stiens, et al., "A quasi-optical free-space method for dielectric constant characterization of polymer materials in mm-wave band," *Proceedings of Symposium IEEE/LEOS Benelux Chapter*, 187–190, 2007.
9. Kersting, R., F. F. Buersgens, G. Acuna, et al., "Terahertz near-field microscopy," *Advances in Solid State Physics, Advances in Solid State Physics*, R. Haug, Ed., 203–222, Springer-Verlag, Berlin, 2008.
10. Cho, G. C., H.-T. Chen, K. Simon, et al., "Apertureless terahertz near-field microscopy," *Semiconductor Science and Technology*, Vol. 20, No. 7, S286, 2005.
11. Knoll, B., F. Keilmann, A. Kramer, et al., "Contrast of microwave near-field microscopy," *Applied Physics Letters*, Vol. 70, No. 20, 2667–2669, 1997.
12. Knoll, B. and F. Keilmann, "Enhanced dielectric contrast in scattering-type scanning near-field optical microscopy," *Optics Communications*, Vol. 182, No. 4–6, 321–328, 2000.

New Method to Calculate the Low Frequency Noise Hooge Parameter: Applications to SiGe HFET

Luis Manuel Rodríguez, Mauro A. Enciso-Aguilar, and Martha C. Galaz Larios
Escuela Superior de Ingeniería Mecánica y Eléctrica, Instituto Politécnico Nacional, México D. F.

Abstract— A new extraction method for the Hooge parameter based on high frequency and low frequency measurements is presented for the first time. We emphasis on the role played by the resistive and electrostatic parasitics on the accuracy of the Hooge parameter. We illustrate this new approach by calculating the Hooge parameter for a $Si/Si_{0.6}Ge_{0.4}$ n-HFET and we compare these values with those calculated by classical method.

1. INTRODUCTION

The Hooge parameter (α_H) is frequently calculated for low frequency (LF) noise characterization of the field effect transistor when the nature of the LF noise is supposed to be due to mobility fluctuation. This factor is supposed to be independent of bias, frequency, size of devices and it is a very useful figure of merit to compare the $1/f$ noise behaviour. We present in this letter a new method to evaluate the α_H parameter based on a small signal equivalent extracted from HF measurement. First we review the classical methods used to evaluate the α_H parameter, then we give details of the new method developped for SiGe HFET and to conclude, we provide some results obtained in the SiGe Heterojunction Field Effect Transistor (HFET). All data presented here are related to measurements and treatment made on Si/SiGe n-HFET with $0.1 \times 100\,\mu m^2$ gate area. The description of the structure can be found in [1]. These HFET exhibit excellent performance in HF domain such as maximum oscillation frequency $f_{\max}$ of 188 GHz and minimum noise figure $NF_{\min}$ of 0.3 dB at 2.5 GHz with associated gain G_{ass} of 19 dB [2].

2. REVIEW OF CLASSICAL MEASUREMENT METHODS

In Hooge's theory [3], the $1/f$ noise is related to mobility fluctuations in crystal lattice. The LF noise shows a $1/f^{\gamma}$ frequency dependence, where the parameter γ is usually between 0.9 and 1.1. Regardless of the origin of the $1/f$ noise one can consider α_H parameter as a comparison tool of experimental results coming from several types of devices or materials. With unit γ, α_H parameter is defined as follows

$$\alpha_H = fN\frac{S_{Id}}{I_{DS}^2} \tag{1}$$

where N is the total number of free charge carriers controlled by the gate in the channel of the FET, S_{Id} is the current noise power spectral density and I_{DS} is the drain current. According to measurement setup, S_{Id} can be deduced from the input noise voltage spectral density S_{Vg} with $S_{Id} = S_{Vg} \times g_m^2$, where g_m is the extrinsic transconductance which can be directly measured.

The main effort in α_H determination is evaluating correctly N. In linear regime, N can be expressed as follows [4].

$$N = \frac{I_{DS}\,L_G}{q\,\mu(E_X)\,E_X} \tag{2}$$

where $\mu(E_x)$ is the field-dependent carrier mobility, E_x is the electrical field along the source-drain axis and L_G is the channel length. Drain bias should be very low to assume that all the carriers in the channel are in mobility regime and to expect quasi constant electric field along the source-drain axis. At low drain voltage, the drain current is also low and the effective electric field beneath the gate can be estimated using the following expression: $E_X = [V_{DS} - (R_S + R_D)I_{DS}]/L_{eff}$ where R_S and R_D are the source and drain resistance, I_{DS} the drain current and L_{eff} the effective gate length. Once the lateral electric field is known, one has to choose an accurate model for the mobility. Many models exist. One can consider the field-dependent mobility [5]: $\mu(E_X) = \mu_0/[1 + (\frac{E_X}{E_S})^{\gamma}]^{\frac{1}{\gamma}}$ where μ_0 is the low field mobility, E_S and γ are fitting parameters. These approach have been used by [6].

On the other hand, even in linear regime, channel doping profile and gate dielectric control all together the HFET mobility and current drive in a very complex manner. It seems to be better to quantify directly the carrier mobility by measurements mainly in short channel devices. But

a direct extraction of the mobility is difficult because the extracted mobility value is sensitive to the definition and values of the effective channel length L_{eff}, extrinsic source resistance (R_S) and drain resistance (R_D). Some authors [7, 8] have computed the effective mobility, μ_{eff}, by the ratio of extrinsic drain conductance g_D and of the gate oxide capacitance C_{OX} in MOSFETs

$$\mu_{eff} = L_{eff}^2 \frac{\partial I_{DS}/\partial V_{DS}}{C_{OX} V_G} = L_{eff}^2 \frac{g_D}{C_{OX} V_G} \tag{3}$$

where V_G is the effective gate voltage, g_D and C_{OX} are obtained from I-V and C-V measurements performed on the same device. Disagreements in α_H commonly appear since L_{eff} and series resistance R_S and R_D are not taken into account. A better extraction of the mobility can however be done, if a careful estimations of R_S and R_D contribution on the output conductance g_D is made. If one notes, g_{mint} and g_{Dint} are the intrinsic transconductance and output conductance of the transistor. These parameters can be extracted using the followings relations

$$g_{m\text{int}} = \frac{g'_m}{1 - (R_S + R_D) g_D (1 + R_S g'_m)} \tag{4}$$

$$g_{Dint} = \frac{g'_D}{1 - R_S g_m (1 - (R_S + R_D) g'_D)} \tag{5}$$

where $g'_m = \frac{g_m}{1 - g_m R_S}$ and $g'_D = \frac{g_D}{1 - g_D (R_S + R_D)}$.

3. NEW METHOD

First, the limitations of classical methods used to extract the α_H parameter are due, in a large extend, to the increasing role of parasitics in ultra short gate length devices, leading to a misestimation of effective mobility, or effective number of free carriers N controlled by the gate. Both resistive and electrostatic parasitics should be taken into account for accurate extraction of α_H. Second, if classical methods are well suited for MOSFET, they are not directly applicable for buried channel HFET with significant 2D effects. Therefore we have developed a new approach which can be used for any kind of FET. This method exploits HF measurements and is well suited for small gate length III-V or silicon based HFET. Let's explain this method: Starting with (1), and in the case of MOSFET, we could first obtain N directly through the gate capacitance C_T (C_G or C_{OX})

$$N = C_T V_G / q \tag{6}$$

Substituting Eqs. (6) to (1) then becomes

$$\alpha_H = \frac{S_{Id} C_T V_G f}{q I_{DS}^2} \tag{7}$$

The crucial parameter of (6) is C_T. It is better to measure this capacitance than to calculate it (permittivity/thickness), since not necessarily the effective channel length and the oxide thickness are accurately known. Moreover, the C_{OX} may include the incidence of the polysilicon depletion layer for MOS.

We turn now to the extraction of the effective capacitance C_T: The capacitance measurements contain parasites. Some of these parasitic contributions should not be considered for the calculation of N. We explain below, how the capacitances are extracted and thus, we use the following expression to determine N in the HFET

$$N = \frac{(C_{GS} + C_{GD} - C_{elec}) \times V_G}{q} \tag{8}$$

where C_{GS}, C_{GD} and C_{elec} are the total gate-source, total gate-drain and the electrostatic capacitances respectively, determined with HF measurements. S-parameter measurements and small signal circuit modelling are used to extract capacitances and resistances. The determination of intrinsic parameters of the equivalent circuit is carried out using transformation of S-parameters into Z and Y-parameters at each bias point [9]. The whole capacitances represent not only intrinsic capacitances but also extrinsic electrostatic parasitics.

The whole parasitic capacitance is extracted thanks to measurement and extraction of C_{GS} and C_{GD} performed on several gate length and gate width devices. Devices with several gate lengths and several gate widths have been measured at several drain and gate biases. The parasitic capacitance values are extracted from the intercept with zero gate length and zero gate width of the $C_{GS}+C_{GD}$ versus gate length and gate width respectively as illustrated in Fig. 1. This value doesn't depend on bias condition.

The whole parasitic capacitance is due to three contributions: 1/electrostatic coupling between the two metallization finger gate and the taper terminating the center strip of the coplanar waveguide which is mainly observable with the gate width dependence, 2/an electrostatic capacitance between shape of the mushroom gate metallization and the 2-DEG in the channel below the access zone and with the surface states in the cap layer, and 3/a fringe contribution arising from the depletion zone within the semiconductor. Contributions 2/ and 3/ can be observed on the gate length dependence of the whole capacitances. It should be mentioned that surface states may play also a significant role in the value of fringe capacitances. Electrostatic and fringe capacitances reduce HF performances by screening the strain enhanced transport properties of the SiGe HFETs.

Electrical modelling on several gate length and gate width devices shows that these electrostatic parameters vary from 70 to 150 fF/mm. For a typical device the sum of the total gate-source and gate-drain capacitance ($C_{GS}+C_{GD}$) is 125 fF/mm and the sum of resistances (R_S+R_D) is 3.3 Ω·mm. One must underline that only electrostatic contributions and the fringe effect associated to the poor aspect ratio in buried channel HFET have to be taken into account and have been removed.

The current noise spectral density for the SiGe n-HFET measured exhibits $1/f$ and generation-recombination noise. All traces are at same E_X conditions. The constant E_X was obtained biasing: $E_X = \frac{V_{DS}-I_{DS}(R_S+R_D)}{L_{eff}}$.

Figure 2 compares α_H parameter versus V_G, α_H is calculated using the expression (1) and (2) using L_G directly. α_H is also calculated using the expression (7) and (8) with and without taking into account C_{elec}. We can note around 33% underestimation for α_H value using C_T instead of C_{OX} without taking into account C_{elec} contribution and taking into account g_{Dint} and L_{eff}. A higher underestimated α_H value was founded considering L_G and extrinsic drain conductance g_D.

Table 1 depicts the estimated α_H parameter for several FET technologies. As the α_H parameter can be used to evaluate the crystalline quality of the transistor, the best quality has been observed for conventional Si p-MOSFET and the worst crystalline quality has been observed in SiGe p-FETs fabricated on sapphire, it is known that Silicon has à 10% lattice mismatch with sapphire. The α_H parameter calculated in the SiGe n-HFET of this work, is comparable with the parameters observed in Si n-MOSFET and InGaAs PHEMT transistors.

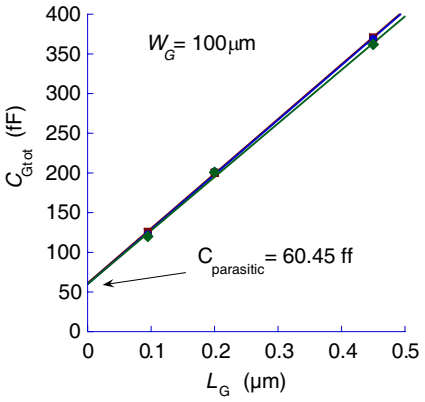

Figure 1: Parasitic capacitance obtained from the $C_{Gtot} = C_{GS} + C_{GD}$ versus gate length.

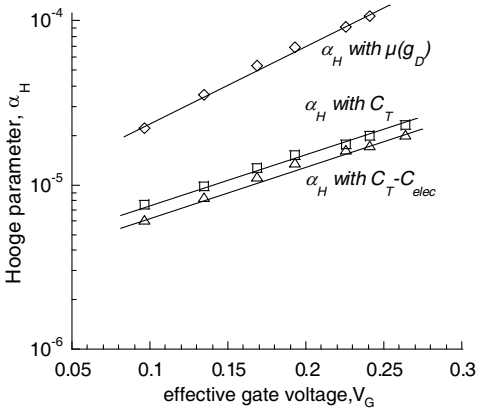

Figure 2: α_H parameter versus V_G, (△) α_H value calculated with our proposed method (using Eq. (7)), (□) α_H value calculated without taking into account C_{elec} (using Eqs. (7) and (8)), (♢) α_H value calculated without taking into account L_{eff} (using Eqs. (1) and (2)).

Table 1: Hooge parameter for several microwave FETs on GaAs, InGaAs, Si and SiGe. Except in [12] results are calculated in linear region at $V_{DS} \ll V_G$.

Transistor	$\mathbf{W \times L}$ ($\mu\mathbf{m}^2$)	$\boldsymbol{\alpha}_H$
SiGe n-HFET *this work*	100×0.1	$\mathbf{6.1\ 10^{-6}}$
Si n-MOSFET [10]	10×0.2	$7.0\ 10^{-6}$
Si p-MOSFET [11]	20×3	$4.0\ 10^{-7}$
GaAs MESFET [12]	280×0.5	$5.7\ 10^{-4}$
InGaAs PHEMT	200×0.35	$9.0\ 10^{-6}$
GaAlAs HEMT	200×0.5	$1.3\ 10^{-5}$
SiGe p-MOSFET [7]	54×1	$2.5\ 10^{-5}$
SiGe p-FET on SOS [8]	20×1.3	$9.4\ 10^{-5}$
SiGe p-FET on SOS	20×1.25	$8.1\ 10^{-5}$
Si p-FET on SOS	20×1.04	$2.9\ 10^{-4}$

4. CONCLUSION

We have presented a new method to calculate α_H parameter well suited for buried channel HFET. The Hooge parameter evaluation based on capacitance calculation leads to an overestimation of α_H values, by misestimating the effective gate length and because of the influence of electrostatic capacitance. The new method presented in this article considers these problems in short gate length devices and then the α_H parameter becomes correctly proportional to the mobility and the total number of free charge carriers controlled by the gate as theoretically assumed.

ACKNOWLEDGMENT

The financial support of SIP-IPN, COFAA-IPN and CONACyT 106698 project.

REFERENCES

1. Kummer, M., C. Rosenblad, A. Dommann, T. Hackbarth, G. Höck, M. Zeuner, E. Müller, and H. Von Känel, "Low energy plasma enhanced chemical vapour deposition," *Materials Sci. Eng. B*, Vol. 89, 288–295, 2002.
2. Enciso, M., F. Aniel, P. Crozat, R. Adde, M. Zeuner, T. Fox, and T. Hackbarth, "0.3 dB minimum noise figure of 0.13 µm gate-length strained $Ge/Si_{0.58}Ge_{0.42}$ n-MODFETs," *Electron. Lett.*, Vol. 37, 1089–1090, 2001.
3. Hooge, F. N., "$1/f$ noise is no surface effect," *Phys. Lett. A*, Vol. 29, 139, 1969.
4. Van der Ziel, A., "Unified presentation of $1/f$ noise in electronic devices: Fundamental $1/f$ noise sources," *Proceedings of the IEEE*, Vol. 76, 233–258, 1988.
5. Jacobini, C., C. Canali, G. Ottaviani, and A. Quaranta, "A review of some transport properties of silicon," *Solid-State Electronics*, Vol. 20, 77–89, 1977.
6. Li, P. W. and W. M. Liao, "Low-frequency noise analysis of Si/SiGe channel pMOSFETs," *Solid-State Electronics*, Vol. 46, 2281–2285, 2002.
7. Lukyanchikova, N. B., M. V. Petrichuk, N. P. Garbar, L. S. Riley, and S. Hall, "Noise in p-channel SiGe and si MOSFETs with gate oxide grown by low temperature plasma anodisation," *Proc. EDMO*, 181–186, 2001.
8. Mathew, S. J., G. Niu, et al., "Hole confinement and low-frequency noise in SiGe pFET's on silicon-on-sapphire," *IEEE Electron. Device Lett.*, Vol. 20, 173–175, 1999.
9. Dambrine, G., A. Cappy, F. Heliodore, and E. Playez, "A new method for determining the FET small-signal equivalent circuit," *IEEE Trans. Microwave Theory Tech.*, Vol. 36, 1151–1159, 1988.
10. Akue Allogo, Y., M. Murcia, J. C. Vildeuil, M. Valenza, P. Llinares, and D. Cottin, "$1/f$ noise measurements in n-channel MOSFETs processed in 0.25 µm technology," *Solid-State Electronics*, Vol. 46, 361–366, 2002.
11. Chang, J., A. A. Abidi, and C. R. Viswanathan, "Flicker Noise in CMOS transistors from Sub-threshold to strong inversion at various temperatures," *IEEE Trans. Electron Device*, Vol. 41, 1965–1971, 1994.
12. Plana, R., L. Escotte, et al., "Noise in AlGaAs/InGaAs/GaAs pseudomorphic HEMT's from 10 Hz to 18 GHz," *IEEE Trans. Elec. Dev.*, Vol. 41, 90–101, 1993.

Small Antenna Chamber Design and Measurement

Guan-Yu Chen[1], **Kuo-Liang Wu**[1], **Y. D. Chen**[2], **and Jwo-Shiun Sun**[1]

[1]Department of Electronic Engineering, National Taipei University of Technology, Taiwan
[2]Antenna and EMC Laboratory, HTC Corporation, Taiwan

Abstract— The mobile phone under test of far-field range testing has been the plan at the Cellular Telecommunications & Internet Association (CTIA) certification program test requirements for performing radiated power and receiver performance measurement. It is a 3D system for measuring low gain antennas and is well matched for PDA Phone or wireless antenna testing.

1. 3D ANTENNA MEASUREMENT

In the US, the Certification Program of the CTIA-The Wireless Association was the first organization to publish a test plan for Over-The-Air (OTA) testing of mobile terminals. During the last few years there has been significant progress towards developing standardized testing methods for wireless devices. A key element in such testing is the accurate evaluation of radiated performance while operating in the respective communications. Such testing is commonly referred to as testing and is becoming a mandatory part of the product certification required by most network operators. In those papers [1–4], facilities of mobile phone measurement have recently commissioned a spherical far-field measurement system (Figure 1 and Figure 2). In this paper describes a spherical antenna measurement system that addresses the challenges in testing antennas for wireless communications. It is a 3D system for measuring low gain antennas and is well matched for PDA Phone or wireless antenna testing. It has effectively demonstrated testing and characterization of far-field performance, CTIA Over-The-Air (OTA) performance data, radiated power (EIRP), and sensitivity (EIS). In passive mode measurements of antennas are performed by a vector network analyzer. It provides radiation pattern data in any polarization, as well as antenna efficiency. In system mode measurements, commonly referred to as OTA Performance Testing, of mobile phones and other cellular terminals can be performed. It is connected to a radio communications tester (Agilent 8960). The communications tester sets up a phone call through the 3D polarization scanning, enabling measurements of radiated transmitter power (EIRP) and receiver sensitivity (EIS) over the entire spherical measurement surface surrounding the mobile phone.

2. 3D FAR-FIELD ANTENNA MEASUREMENT SYSTEM AND EXPERIMENTS

In this study, the author has established a 3D far-field antenna measurement system [5–8]. Based on this 3D spherical far-field measurement system, the low-profile mobile antennas measurements and mobile phone for wireless network are applied. The 3D antenna measurement system and study can be applied to wireless OTA measurement.

3. 3D ANTENNA MEASUREMENT PRINCIPLE

3D antenna system [9–11] is a measurement of the RF device's transmitter performance. This measurement procedure records 3D antenna pattern every 15 and 30 degrees for the total of 528

Figure 1: The 3D small OTA chamber design.

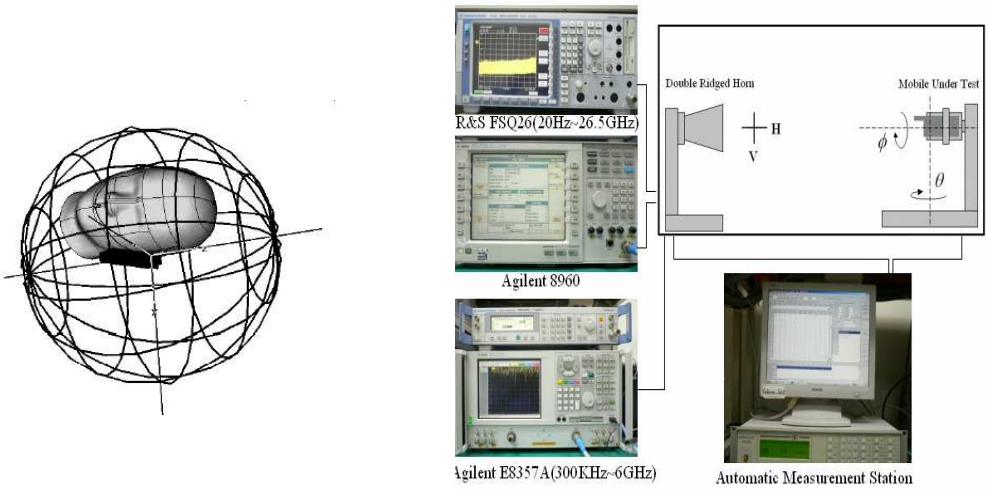

Figure 2: The 3D measurement system and wireless system networking.

and 120 points (2 orthogonal linear polarizations × 12 theta's data × 24 phi's data and 2 orthogonal linear polarizations × 5 theta's data × 12 phi's data). As a result, a 3D pattern is obtained showing maximum and minimum points of transmitter performance. This section discusses the methodology of 3D polarization measurement and environment. Directivity (D), equation is defined as the ratio of the wave radiation intensity in certain direction to the average radiation intensity, and show the spherical coordinates used for measurement.

4. MEAN EFFECTIVE GAIN

Based on measurement method [12, 13] is described for analying the mean effective gain (MEG) of antenna in 3D far field chamber environment. The MEG of an antenna in a certain environment can be computed based on the 3D gain pattern of the mobile antenna and the average angular distribution of incident power in the environment. By using Equations (1) and (2) the expression for the MEG can be calculate. And the mean incident power ratio P_V/P_H represents the cross polarization power ratio (XPR), by using Equation (3). In this paper, we present experimental results of the XPR rate at the mobile antenna in a simple dipole antenna environment at center frequency. Based on response of mobile antenna, the 3D measured results of MEG and XPR are measured.

$$G_e = \frac{P_{rec}}{P_V + P_H} \tag{1}$$

$$\begin{aligned} P_{rec} &= \int_0^{2\pi}\int_0^{\pi} \{P_1 G_\theta(\theta,\phi)P_\theta(\theta,\phi) + P_2 G_\theta(\theta,\phi)P_\theta(\theta,\phi)\}\sin\theta d\theta d\phi \\ G_e &= \int_0^{2\pi}\int_0^{\pi} \left\{\frac{XPR}{1+XPR}G_\theta(\theta,\phi)P_\theta(\theta,\phi) + \frac{1}{1+XPR}G_\phi(\theta,\phi)P_\phi(\theta,\phi)\right\}\sin\theta d\theta d\phi \end{aligned} \tag{2}$$

$$XPR = \frac{P_V}{P_H} \tag{3}$$

5. SMALL 3D ANTENNA CHAMBER

The mobile phone under test of far-field range testing has been the plan at the Cellular Telecommunications & Internet Association (CTIA) certification program test requirements for performing radiated power and receiver performance measurement. In this paper, facilities of antenna pattern measurement have recently commissioned a spherical far-field measurement system. The low profile far-field spherical scan system provides significant advantages over the older far-field testing including elimination of problem of simple theta (θ) and phi (ϕ) rotary axis with indoor far-field range testing, complete measurement characterization of the antenna, and improved accuracy. This paper

will discuss the antenna and wireless system integration tested, spherical antenna measurement for far-field system, and the results being achieved.

6. CONCLUSIONS

The low profile far-field spherical scan system provides significant advantages over the older far-field testing including elimination of problem of simple theta and phi rotary axis with indoor far-field range testing, complete measurement characterization of the antenna, and improved accuracy. This paper will discuss the antenna and wireless system integration tested with the TRP/TIS and spherical antenna measurement for far-field system, and the results being achieved.

ACKNOWLEDGMENT

The authors acknowledge the Antenna and EMC Department of HTC, Taiwan for sport the wireless technique and measurement environment.

REFERENCES

1. Chen, G. Y., S. Y. Huang, W. F. Yen, J. S. Sun, Y. D. Chen, C. H. Lin, J. Y. Yang, and C. Y. Lin, "The spherical antenna measurement and spherical absorption rate (SAR) for near field radiation evaluation," *2005 Asia Pacific Symposium on EMC (2005 APEMC)*, 128–135, Taipei, Taiwan, Dec. 2005.
2. Chen, G. Y., J. S. Sun, C. J. Huang, S. Y. Huang, Y. T. Chung, K. L. Wu, Y. D. Chen, C. H. Lin, and J. Y. Yang, "The 3D far-field antenna system for total radiation efficiency, mean effective gain and multi-input multi-output measurement operation," *2006 National Symposium on Telecommunications (2006 NST)*, 143, Kaohsiung, Taiwan, Dec. 2006.
3. Chen, G. Y., J. S. Sun, and Y. D. Chen, "The 3D far-field antenna measurement technology for radiation efficiency, mean effective gain and diversity antenna operation," *2006 The 7th International Symposium on Antennas, Propagation, and EM Theory (2006 ISAPE)*, 42–45, Guilin, China, Oct. 2006.
4. Chen, G. Y., J. S. Sun, S. Y. Huang, Y. D. Chen, C. H. Lin, and J. Y. Yang, "Flexible monopole antenna for mobile phone co-design and 3D far-field antenna scanning technique apply to total radiation efficiency and mean effective gain measurement," *2006 China-Japan Joint Microwave Conference (2006 CJMW)*, 89–92, Chengdu, China, Aug. 2006.
5. Chen, G. Y., J. S. Sun, S. Y. Huang, Y. D. Chen, C. H. Lin, and J. Y. Yang, "Manufacture, design, measurement and FPC antennas integration for PDA phone," *2006 China-Japan Joint Microwave Conference (2006 CJMW)*, 416–419, Chengdu, China, Aug. 2006.
6. Chen, G. Y., J. S. Sun, S. Y. Huang, Y. D. Chen, C. H. Lin, and J. Y. Yang, "Mobile handset measurement for wireless system networking," *2006 China-Japan Joint Microwave Conference (2006 CJMW)*, 698–701, Chengdu, China, Aug. 2006.
7. Chen, G. Y., C. H. Lin, J. S. Sun, K. K. Tiong, and Y. D. Chen, "3D far-field antenna scanning technique apply to radiation efficiency and mean effective gain measurement," *IEEE TENCON 2007*, Taipei, Taiwan, Oct. 2007.
8. Chen, G. Y., C. H. Lin, J. S. Sun, K. K. Tiong, and Y. D. Chen, "Mobile handset and radiation power absorption measurement," *IEEE TENCON 2007*, Taipei, Taiwan, Oct. 2007.
9. Wu, K.-L., G.-Y. Chen, J.-S. Sun, C.-H. Lin, K.-K. Tiong, and Y. D. Chen, "The GPS antenna design and measurement," *PIERS Proceedings*, 162–164, Hangzhou, China, Mar. 24–28, 2008.
10. Wu, K.-L., G.-Y. Chen, J.-S. Sun, C.-H. Lin, K.-K. Tiong, and Y. D. Chen, "The helical antenna for handset design and phantom effect," *PIERS Proceedings*, 221–222, Hangzhou, China, Mar. 24–28, 2008.
11. Chen, G.-Y., J.-S. Sun, C.-H. Lin, K.-K. Tiong, and Y. D. Chen, "Small antenna measurement facilities," *PIERS Proceedings*, 157–158, Hangzhou, China, Mar. 24–28, 2008.
12. Chen, G.-Y., J.-S. Sun, K. Chang, and Y. D. Chen, "Antenna pattern measurement," *PIERS Proceedings*, 331–333, Beijing, China, Mar. 23–27, 2009.
13. Chen, G.-Y., K.-L. Wu, J.-S. Sun, and Y. D. Chen, "Antenna measurement system for CTIA OTA operation," *PIERS Proceedings*, 1823–1825, Xi'an, China, Mar. 22–26, 2010.

Calculation and Analysis of the Coupling Effects of High Voltage Transmission Lines in Joint-use Corridors Shared by Multi-systems

Jun Zhu, **Xiaobin Cao**, **Zihui Zhao**, **Li Chen**, **and Guangning Wu**
School of Electrical Engineering, Southwest Jiaotong University, China

Abstract— Electromagnetic coupling effects among transmission lines threaten the stability and reliability of each system, which the corridor is shared by. This paper investigates the effects of various parameters on the electromagnetic interference among transmission lines in detail. The influencing factors include erection parameters, soil parameters and operation parameters of power system. A multi-conductor transmission line model is established to calculate the coupling effects of transmission lines with EMTP. The model consists of 500 kV double-circuit AC transmission lines and 1000 kV one-circuit AC transmission lines. And then, the effects of various parameters on the generated interferences are analyzed, when 1000 kV AC transmission lines are de-energized. The general rules of induction components among transmission lines changing with different parameters are obtained. This paper provides an insight on how to make the safe distance of transmission lines in the corridors.

1. INTRODUCTION

With the rapid development of economy and society, joint-use corridors shared by multi-system have the characteristic of saving land, which is occupied by power, communication, transportation and energy transport systems. Meanwhile, in order to meet energy demand, UHV transmission lines are gradually put into use. This leads to the load current and fault current of transmission lines increased significantly, and exacerbates the electromagnetic coupling effects among transmission lines in joint-use corridors. So the electromagnetic interference threatens the stability and reliability of each system in the corridors.

In order to ensure each system operating safely in the corridors, many countries have started research and have developed regulations and standards [1, 2]. Researchers mainly study on the coupling effects among parallel transmission lines. The generation mechanism of electromagnetic induction components between two parallel conductors was analyzed in [3] and [4]. These papers described a method of calculating the transverse voltage caused by electric field induction based on charge equivalent method. The electromagnetic interference among parallel transmission lines was analyzed in [5] and [6]. These papers pointed out that the induced longitudinal EMF increases with the parallel length in approximate direct proportion. But, all the research above is not concerning the electromagnetic interference among multi-circuit lines.

Transmission lines in the corridor are close to each other, so the electromagnetic interference level is more serious. This threatens reliable operation of each system and the safety of line maintenance. It is necessary to study on the electromagnetic induction among lines in the corridors, and analyze the general rules of induction components changing with different parameters.

2. SYSTEM SITUATION AND SIMULATION MODEL

This paper mainly studies on the general rules of induction components among lines changing with different parameters, so there is no need to correspond with the actual lines. Typical erection situation and line parameters are confirmed from relevant articles. Then, a parallel transmission lines system has been set up, as shown in Fig. 1(a). The total length of transmission lines in parallel is l (km), and the separation distance between 500 kV and 1000 kV ac transmission lines is d (m).

A cross section of the joint-use corridor is shown in Fig. 1(b), and various parameters of transmission lines in the common corridor were given by [6] and [7] in detail. This paper adopts nine-phase line to simulate 500 kV double-circuit ac transmission lines on the same tower in parallel with 1000 kV one-circuit ac transmission lines with EMTP.

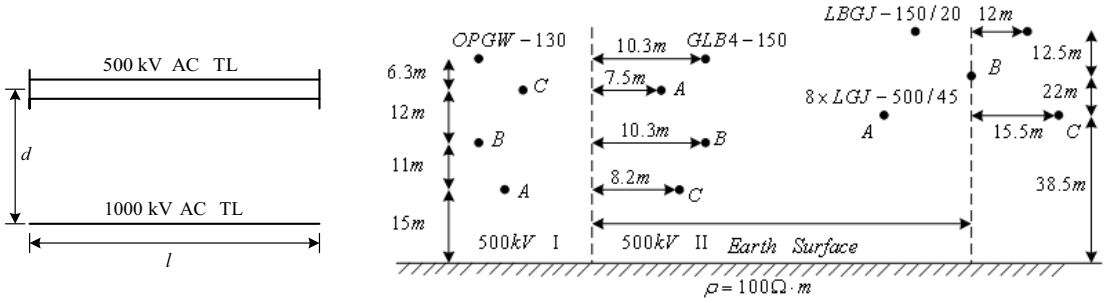

Figure 1: 500 kV double-circuit ac TL on the same tower in parallel with 1000 kV one-circuit ac TL. (a) Parallel transmission lines system. (b) Cross section of parallel transmission lines system.

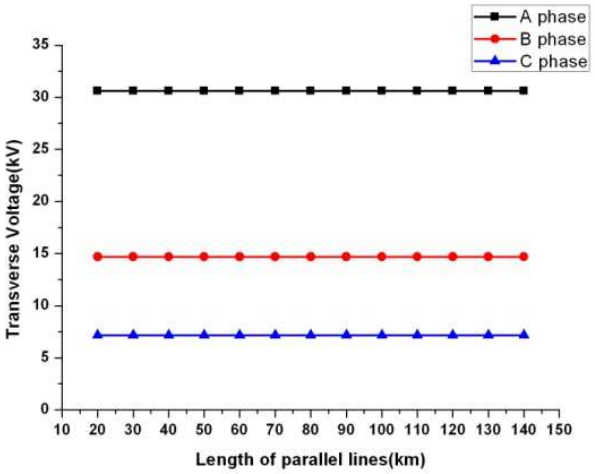

Figure 2: Relation between transverse voltage and length of parallel lines ($d = 40\,\text{m}$, $h = 38.5\,\text{m}$, $\rho = 100\,\Omega\cdot\text{m}$).

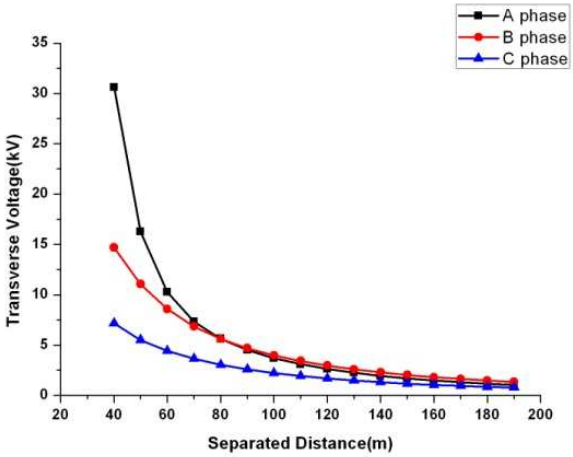

Figure 3: Relation between transverse voltage and separation distance ($l = 60\,\text{km}$, $h = 38.5\,\text{m}$, $\rho = 100\,\Omega\cdot\text{m}$).

3. ELECTROMAGNETIC INDUCTION COMPONENT ON 1000 KV DE-ENERGIZED LINES

3.1. Transverse Voltage Due to Electric-field Induction

When 1000 kV ac transmission lines are de-energized and insulated against ground, the transverse voltage is generated in every phase of UHV transmission lines due to electric-field induction. The rules of transverse voltage changing with length of parallel lines and separate distance are respectively shown in Figs. 2 and 3. The length of parallel lines is varying from 20 m to 140 m, and separeted distance from 40 m to 190 m.

3.2. Longitudinal EMF and Induced Current Due to Magnetic-field Induction

When 1000 kV ac transmission lines are de-energized and grounded at a single terminal or at two terminals, the longitudinal EMF and induced current are generated in every phase of UHV transmission lines due to magnetic-field induction. The rules of longitudinal EMF and induced current changing with parallel length, separation distance, soil resistivity and current in energized lines are respectively shown in Figs. 4, 5, 6, and 7. Parallel length is varying from 20 m to 140 m, separeted distance from 40 m to 190 m, soil resistivity from $10\,\Omega\cdot\text{m}$ to $10^5\,\Omega\cdot\text{m}$, and current from 400 A to 3000 A in every phase.

4. DISCUSSION

The effects of various parameters on the generated electromagnetic interference are discussed in this section. The parallel transmission line system described in Section 2 is taken as an example to analyze. All the calculation results are the induced interferences on the A phase conductor of 1000 kV lines with neighboring 500 kV ac lines in the steady state.

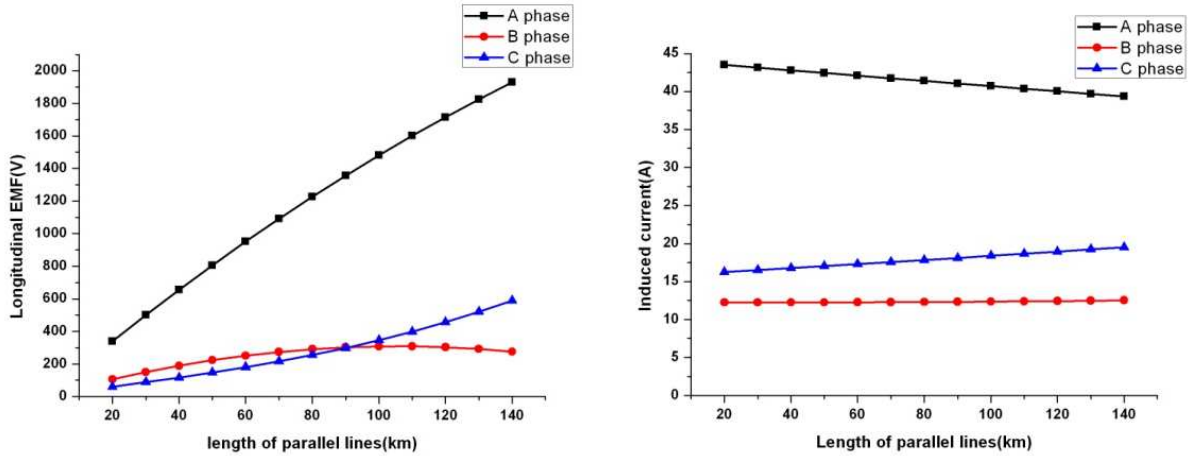

Figure 4: Relation between longitudinal EMF/induced current and length of parallel lines. ($d = 40\,\mathrm{m}$, $h = 38.5\,\mathrm{m}$, $\rho = 100\,\Omega\cdot\mathrm{m}$, $I = 1000\,\mathrm{A}$).

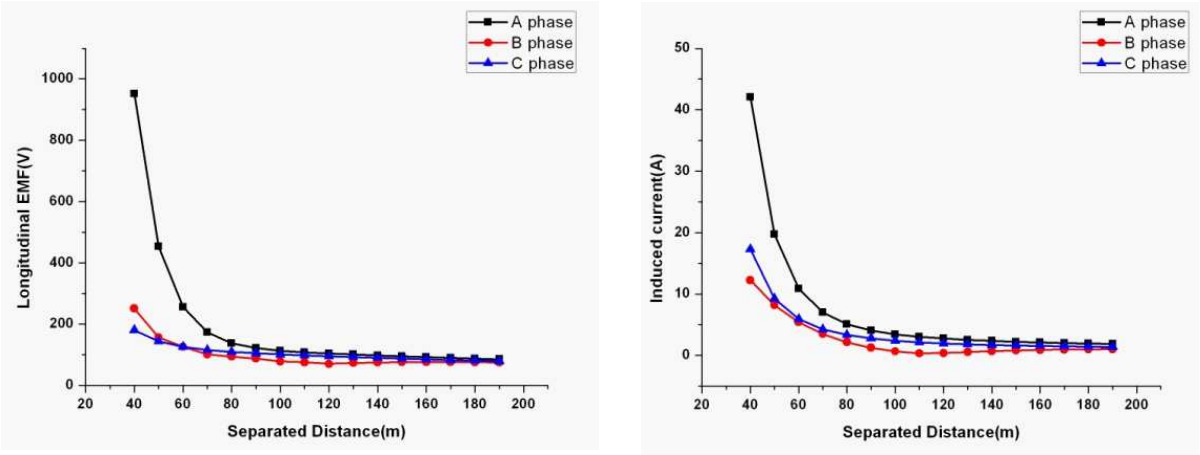

Figure 5: Relation between Longitudinal EMF/induced current and separation distance. ($l = 60\,\mathrm{km}$, $h = 38.5\,\mathrm{m}$, $\rho = 100\,\Omega\cdot\mathrm{m}$, $I = 1000\,\mathrm{A}$).

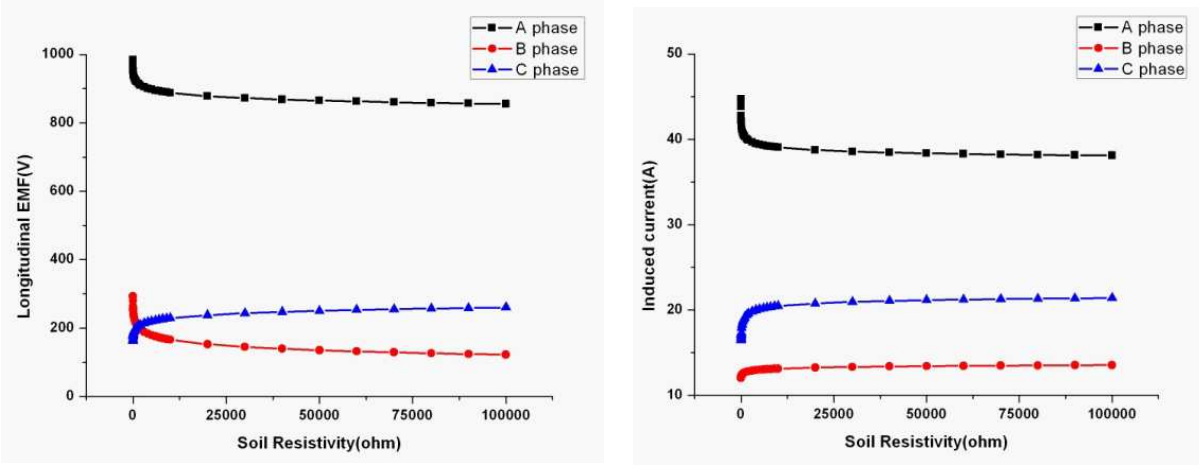

Figure 6: Relation between longitudinal EMF/induced current and soil resistivity. ($l = 60\,\mathrm{km}$, $d = 40\,\mathrm{m}$, $h = 38.5\,\mathrm{m}$, $I = 1000\,\mathrm{A}$).

4.1. Length of Parallel Lines

Relation between electromagnetic induction components and length of parallel lines is shown in Figs. 2 and 4. The transverse voltage does not vary with the parallel length markedly, while the longitudinal EMF increases with the parallel length and do not present direct proportion. When the de-energized lines are grounded at two terminals, the current amplitude is very large. So, when the de-energized lines are maintained, it is important to take measures to reduce the current amplitude in the grounding loop.

4.2. Separation Distance

Relation between the electromagnetic induction components and separation distance is shown in Figs. 3 and 5. With the increase of separation distance, all the components above decrease and do not present direct proportion. The effects of separation distance upon the electromagnetic induction components on the A phase conductor are shown in Tab. 1. When the distance is smaller than 80 m, all components are very large and decrease rapidly with the increase of separation distance. When the distance is larger than 80 m, all components are small and decrease slowly with the increase of separation distance. So transmission lines in the corridors should keep a certain distance. In this paper, the separation distance is suggested to be larger than 80 m in the parallel transmission line system.

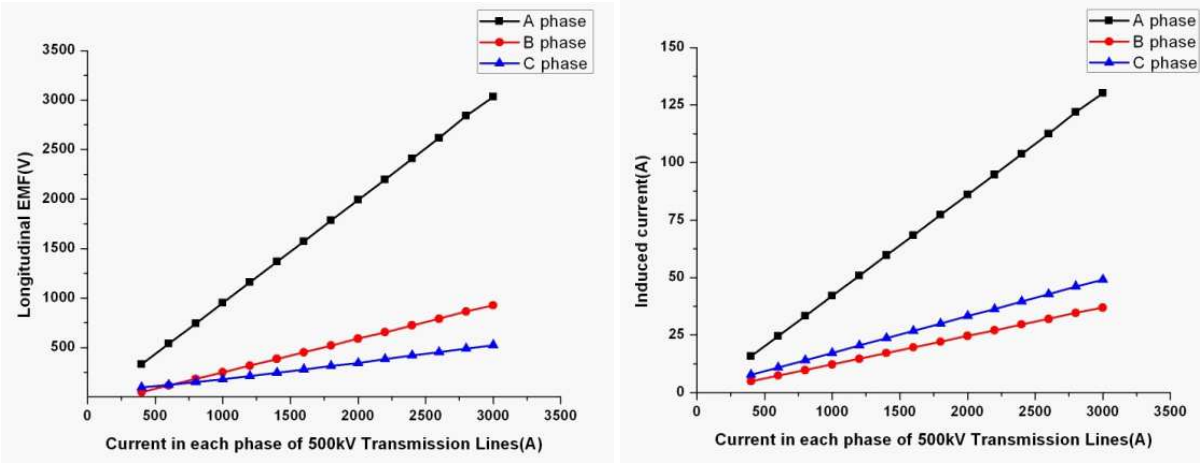

Figure 7: Relation between longitudinal EMF/induced current and current in 500 kV TL. (l = 60 km, d = 40 m, h = 38.5 m, ρ = 100 Ω·m).

Table 1: Effects of separation distance upon the electromagnetic induction components on A phase conductor.

Separation Distance (m)	40	60	80	100	120	140	160	180
Transverse Voltage (kV)	30.6	10.3	5.63	3.71	2.63	1.94	1.49	1.17
Longitudinal EMF (kV)	0.95	0.26	0.14	0.11	0.1	0.098	0.093	0.088
Induced Current (A)	42.1	10.9	5.11	3.46	2.76	2.38	2.12	1.94

Table 2: Effects of soil resistivity upon the electromagnetic induction components on the A phase conductor.

Soil Resistivity (Ω·m)	10	20	50	80	10^2	2×10^2	5×10^2	8×10^2
Longitudinal EMF (V)	983.9	973.7	961.1	954.7	951.6	942.1	929.5	923.0
Induced Current (A)	44.7	43.8	42.8	42.3	42.1	41.5	40.8	40.4
Soil Resistivity (Ω·m)	10^3	2×10^3	5×10^3	8×10^3	10^4	2×10^4	5×10^4	8×10^4
Longitudinal EMF (V)	919.9	910.2	897.4	890.8	887.7	877.9	865.1	858.5
Induced Current (A)	40.3	39.9	39.4	39.1	39.0	38.7	38.4	38.2

4.3. Soil Resistivity

Relation between the induced longitudinal EMF/current and soil resistivity is shown in Fig. 6. With the increase of soil resistivity, the longitudinal EMFs and induced currents in each phase of 1000 kV ac transmission lines present different trends, and are slightly affected by it. The effects of soil resistivity upon the electromagnetic induction components on the A phase conductor are shown in Tab. 2. While the variation range of soil resistivity is in the same order of magnitude, the induction components change slightly. While the variation range exceeds one order of magnitude, the induction components are changed obviously. It is because that the mutual impedances between transmission lines change with soil resistivity. The formulas of the mutual impedance and the complex depth are shown in [5]. It is obviously obtained that the complex depth of earth return current circuit is very large in power frequency. While the variation range of soil resistivity is in the same order of magnitude, the complex depth changes slightly. Therefore, the mutual impedance is essentially constant, leading to the induction components changing slightly. While the variation range of soil resistivity exceeds one order of magnitude, even reaching several orders of magnitude, the complex depth changes in several orders of magnitude. Thus, the mutual impedance changes greatly, leading to the induction components changing obviously.

4.4. Current in Energized Lines

Relation between the induced longitudinal EMF/current and current in energized lines is shown in Fig. 7. The induced longitudinal EMF and induced current increased with current of 500kV lines in approximate direct proportion.

5. CONCLUSION

In this paper, the electromagnetic coupling effects of HV transmission lines in the corridors have been studies with a computing model established in EMTP. From the calculation results, the following conclusions can be drawn.

1. The transverse voltage does not vary with the parallel length markedly, while the longitudinal EMF increases with the parallel length and do not present direct proportion.
2. The induced current is very large and essentially constant with parallel length. It is important to take measures to reduce the current amplitude in the grounding loop when de-energized lines are maintained.
3. All the induction components decrease and do not present direct proportion with separation distance increased. When the distance is larger than 80 m, all components are small and decrease slowly with the increase of separation distance. Thus, the separation distance is suggested to larger than 80 m in the parallel transmission line system of this paper.
4. With the increase of soil resistivity, the longitudinal EMFs and induced currents in each phase of 1000 kV ac transmission lines present different trends, and are slightly affected by it. While the variation range of soil resistivity is in the same order of magnitude, the induction components change slightly. While the variation range exceeds one order of magnitude, the induction components are changed obviously.
5. The induced longitudinal EMF and induced current increased with current of energized lines in approximate direct proportion.

ACKNOWLEDGMENT

The authors would like to thank Professor Guangning Wu in Southwest Jiaotong University for kindly comments and suggestions. This research was supported by the International Cooperation Ministry of Science and Technology PRC (Grant No. 2009DFA72230).

REFERENCES

1. Southey, R. D., F. P. Dawalibi, and W. Vukonich, "Recent advances in the mitigation of ac voltages occurring in pipelines located close to electric transmission lines," *IEEE Trans. on Power Delivery*, Vol. 9, No. 2, 1090–1097, 1994.
2. CIGRE, "Guide on the influence of high voltage AC power systems on metallic pipelines," 1995.
3. Horton, R., M. Halpin, and K. Wallace, "Induced voltage in parallel transmission lines caused by electric field induction," *IEEE 11th International Conference on Transmission & Distribution Construction, Operation and Live-Line Maintenance*, Oct. 15–19, 2006.

4. Horton, R. and K. Wallace, "Induced voltage and current in parallel transmission lines: Causes and concerns," *IEEE Trans. on Power Delivery*, Vol. 23, No. 4, 2339–2346, 2008.
5. Tang, J., R. Zeng, H. Ma, et al., "Analysis of electromagnetic interference on dc line from parallel AC line in close proximity," *IEEE Trans. on Power Delivery*, Vol. 22, No. 4, 2401–2408, 2007.
6. Ban, L., X. Wang, H. Bai, et al., "Simulative analysis of induced voltages and currents among multi circuit 220 kV and 500 kV transmission lines on same tower," *Power System Technology*, Vol. 33, No. 6, 45–49, 2009.
7. Li, X., W. Jiang, T. Li, et al., "Influence of AC transmission lines on parallelly erected UHVDC transmission lines and suppression measures," *Power System Technology*, Vol. 32, No. 11, 1–6, 2008.